Imperial College London

Anti-Oxidised Low-Density Lipoprotein Antibodies and Antibody Fragment Targeted Nanoparticles for the Translational Study of Atherosclerosis

A thesis submitted to Imperial College London
for the degree of Doctor of Philosophy

January 2024

Dr Adam Douglas Hartley

Supervised by
Dr Ramzi Y Khamis
Prof Dorian O Haskard
Prof Justin C Mason

Imperial College London
National Heart and Lung Institute

STATEMENT OF ORIGINALITY

I, Adam Hartley, confirm that the work presented in this thesis is my own. Where figures or data have been reproduced from the work of others, the source is clearly stated and referenced. The vast majority of this work has been carried out at in the Vascular Sciences Section of the National Heart and Lung Institute, Faculty of Medicine, Imperial College London, London, UK, whilst some has been performed at Queens University, Belfast, UK and Bristol University, Bristol, UK. Much of the work contained here has been presented at seminars, conferences and published in peer-reviewed journals.

COPYRIGHT DECLARATION

The copyright of this thesis rests with the author. Unless otherwise indicated, its contents are licensed under a Creative Commons Attribution-Non-Commercial 4.0 International Licence (CC BY-NC). Under this licence, you may copy and redistribute the material in any medium or format. You may also create and distribute modified versions of the work. This is on the condition that: you credit the author and do not use it, or any derivative works, for a commercial purpose.

When reusing or sharing this work, ensure you make the licence terms clear to others by naming the licence and linking to the licence text. Where a work has been adapted, you should indicate that the work has been changed and describe those changes. Please seek permission from the copyright holder for uses of this work that are not included in this licence or permitted under UK Copyright Law.

ACKNOWLEDGEMENTS

Supervisors

First and foremost, I would like to express my sincere gratitude to my supervisors, Dr Ramzi Khamis, Prof Dorian Haskard and Prof Justin Mason, for their expert supervision, guidance and support throughout this PhD.

In particular, I will be forever indebted to Dr Khamis for his direction, mentorship, support and leadership in both the science laboratory and cardiac catheter laboratory, teaching me how to become an academic scholar, interventional cardiologist and a better person. He has shown me how to balance these roles, whilst also ensuring I understand the importance of strong family values and providing an often required wider-field perspective when problems arise and new strategies are required.

Prof Mason very sadly and unexpectedly passed away during my research time, and his wise words, direction and advice have, and will continue to be, greatly missed.

Financial support

The work contained within this thesis would have not been possible without the generous funding provided by the Wellcome Trust, who awarded me a Clinical Research Fellowship (220572/Z/20/Z) as part of the Wellcome 4i Clinical PhD Programme. In addition, earlier career support from the National Institute for Health Research who provided funding for my Academic Clinical Fellowship, permitted time and resources to develop the ideas and pilot data which culminated in the work in this thesis. Laboratory funding from the British Heart Foundation and the National Institute for Health Research Imperial Biomedical Research Centre also substantially supported this work.

Contribution from collaborators

Assistance for the statistical analyses conducted in Chapter 3 was provided by Dr Matthew Shun-Shin (ORBITA substudy) and Dr Amit Kaura (SCOT-HEART substudy), both Imperial College London. Collaborators, Prof Christopher Scott and Dr Michelle Greene, both Queen's University Belfast, Northern Ireland, UK, assisted with nanoparticle design and initial *in vitro*

testing, as outlined in Chapter 4. Additional characterisation of LO1Fab carried out in Chapter 4 was performed with the support of Prof Jason Johnson (Bristol University, UK) – immunohistochemistry on human atherosclerotic sections and Dr Sean Devenish (Fluidic Analytics, Cambridge, UK) – microfluidic antibody affinity profiling.

Contribution from members from the Vascular Sciences Section, National Heart and Lung Institute

I would like to thank the entire Vascular Sciences Section for their help throughout the duration of my PhD. I would especially like to acknowledge members of the Khamis group, namely Mikhail Caga-Anan, Samuel Owen, Nasser Al-Shahrani, Yasmin Morris, Dr Samata Pandey and Dr Cinzia Marceddu for all of their support. Without their friendship, hard work, and expertise this PhD would have been a much harder undertaking. Other members of the Vascular Sciences Section who have gone above and beyond in their support of my laboratory work include Dr Charis Pericleous and Dr Ali Ashek, to whom I am very grateful.

Other support

Most importantly, I am eternally grateful for the support and understanding of my wife, Lochani, without whom, this PhD would not have been possible. Lochani has been a pillar of strength, looking after our wonderful son, Maximilian, throughout the long days, nights and weekends either spent on-call, performing research or writing this thesis. Finally, I would like to thank my parents, who provided the platform for me to be where I am today. My father sadly passed away during my time spent undertaking this PhD. I know that he was immensely proud of all that I had achieved, both academically and clinically, and I will miss his love and support forever.

PRIZES AWARDED IN RELATION TO THIS THESIS

British Atherosclerosis Society/ British Society for Cardiovascular Research Rapid Fire Oral Abstract Prize Finalist at the British Cardiovascular Society Annual Meeting, 2021

European Society of Cardiology Basic Science Registration Grant, 2022

Royal Society of Medicine John Glyn Trainee Prize Event Finalist, 2022

Royal Society of Medicine Cardiology President's Prize Finalist, 2023

British Cardiovascular Intervention Society Young Investigator Award Finalist, 2023

ABSTRACT

There is an unmet need in prevention of cardiovascular disease, through predicting and preventing future index events; as well as a requirement for better prevention of recurrent events. This project focuses on these two needs, through development of antibodies against malondialdehyde-modified low-density lipoprotein (MDA-LDL) as biomarkers of atherosclerosis and antibody-conjugated nanoparticles for molecular targeting of atherosclerosis. One further objective is to develop a novel translational model, aiming to reduce reliance on animals in preclinical atherosclerosis research.

Firstly, I explored the relationship between IgG/ IgM antibodies against MDA-LDL with atherosclerosis and exercise. Serum was utilised from patients with chest pain undergoing computerised tomography coronary angiography in the SCOT-HEART trial and patients with coronary artery disease in the ORBITA trial. The SCOT-HEART study reports that both anti-MDA-LDL antibodies protectively related to atherosclerotic plaque characteristics. The ORBITA study demonstrates that exercise results in reduced anti-MDA-LDL antibody levels, which was unaffected by percutaneous coronary intervention.

Secondly, I harnessed LO1Fab as a targeting ligand for fluorescent nanoparticles, aiming to localise to MDA-LDL-rich atherosclerotic plaques. LO1Fab is a humanised fragment of LO1, which is a monoclonal murine antibody that recognises MDA-LDL. The final optimised nanoparticle construct underwent vigorous *in vitro* testing prior to *in vivo* evaluation, where nanoparticles localised to atherosclerotic regions *in vivo*, confirmed on *ex vivo* analysis.

Lastly, I developed an amputated human limb model of atherosclerosis, consisting of perfusing a limb with oxygenated blood via a pulsatile pump under physiological conditions. The model has been successfully performed, with X-ray angiography, intravascular ultrasound and optical coherence tomography. In a proof-of-concept study, circulated indocyanine green localised to atherosclerotic regions on fluorescence reflectance imaging.

In summary, this thesis demonstrates the utility of antibodies against MDA-LDL as serological and molecular targeting agents of atherosclerosis *in vivo*, whilst also developing a novel experimental model of atherosclerosis.

TABLE OF CONTENTS

CHAPTER 1 – BACKGROUND 27

1.1 Cardiovascular disease 27
1.1.1 Epidemiology 27
1.1.2 Atherosclerotic cardiovascular disease 28
1.1.3 Sequelae of atherosclerotic cardiovascular disease 29

1.2 Atherosclerosis 30
1.2.1 Atherosclerosis pathobiology 30
1.2.1.1 On the macroscopic level 30
1.2.1.2 On the microscopic level 31
1.2.2 Low-density lipoprotein in atherosclerosis 34
1.2.2.1 Structure and function of low-density lipoprotein 34
1.2.2.2 Oxidised low-density lipoprotein 36
1.2.2.3 Malondialdehyde-modified low-density lipoprotein 36
1.2.2.4 Measuring circulating oxidised low-density lipoprotein 37
1.2.3 Vulnerable atherosclerotic plaque 39
1.2.4 Inflammation in atherosclerosis 42
1.2.5 Gaps in atherosclerosis research 46

1.3 The role of antibodies in atherosclerosis 49
1.3.1 Antibody biology 49
1.3.2 Natural antibodies 51
1.3.3 Anti-oxidised low-density lipoprotein antibodies 51

1.4 Currently available diagnostic techniques and treatments of atherosclerotic cardiovascular disease 53
1.4.1 Diagnosis of atherosclerotic cardiovascular disease 53
1.4.1.1 Non-invasive techniques for the detection of atherosclerosis 54
1.4.1.2 Invasive techniques for the detection of atherosclerosis 56
1.4.1.2.1 Intravascular ultrasound 56
1.4.1.2.2 Optical coherence tomography 57
1.4.1.2.3 Near-infrared spectroscopy 57
1.4.1.2.4 Near-infrared fluoroscopy 57
1.4.1.2.5 Hybrid imaging techniques 58
1.4.2 Currently available therapies for the treatment of atherosclerotic cardiovascular disease 59
1.4.2.1 Lifestyle modification 59
1.4.2.2 Pharmacological therapy 60
1.4.2.3 Myocardial revascularisation 60

1.5 The unmet clinical diagnostic and therapeutic needs in atherosclerotic cardiovascular disease 61

1.6 Experimental modelling of atherosclerosis 63
1.6.1 Small animal models 64
1.6.1.1 Mouse models of experimental atherosclerosis 64
1.6.1.2 Rabbit models of experimental atherosclerosis 65
1.6.2 Large animal models 66
1.6.2.1 Pig models of experimental atherosclerosis 66
1.6.2.2 Non-human primate models of experimental atherosclerosis 67
1.6.3 Issues with currently available preclinical models 67
1.6.4 The need for replacement, reduction and refinement in animal research 69

1.7 From stable atherosclerotic plaque to vulnerable atherosclerotic plaque 70
1.7.1 Imaging vulnerable atherosclerotic plaques 70
1.7.2 Treating vulnerable atherosclerotic plaques 77

1.8 Molecular imaging of atherosclerotic plaque 83
1.8.1 Requirements for successful molecular imaging of atherosclerosis 84
1.8.2 Radionuclear-based molecular imaging 84
1.8.3 Magnetic resonance-based molecular imaging 86
1.8.4 Optical imaging-based molecular imaging 87

1.9 Targeted antibodies in atherosclerosis 89
1.9.1 Rationale for antibody-based oxidised LDL targeted constructs in atherosclerosis 89
1.9.2 Targeted antibodies against oxidised LDL in atherosclerosis 90
1.9.3 Engineered antibody fragments 93
1.9.4 Whole antibody versus antibody fragment-based targeting of atherosclerosis 96

1.10 Nanoparticle-based imaging and therapeutics in atherosclerosis 97
1.10.1 Nanoparticle background 97
1.10.2 Targeted nanoparticles in atherosclerosis 100
1.10.3 PLGA nanoparticles in atherosclerosis 102

1.11 Work leading up to this project 109
1.11.1 The relationship between anti-MDA-LDL antibodies, atherosclerotic plaque and cardiovascular events 110
1.11.2 LO1 development 111
1.11.3 Preclinical modelling of atherosclerosis 113

1.12 Aims and hypotheses of this PhD 113

CHAPTER 2 – MATERIALS AND METHODS 115

2.1 Antibodies used during this thesis 115

2.2 Oxidised LDL and anti-oxidised LDL antibodies as biomarkers of atherosclerosis 116
2.2.1 Scottish COmputed Tomography of the HEART (SCOT-HEART) substudy 116
2.2.1.1 Study background 116
2.2.1.2 Study protocol 118
2.2.1.2.1 Inclusion criteria 118
2.2.1.2.2 Exclusion criteria 119
2.2.1.2.3 Randomisation 119
2.2.1.2.4 CT scanning 119
2.2.1.3 Quantitative plaque analysis 120
2.2.1.4 Blood sampling 120
2.2.1.5 Ethical approvals 121
2.2.1.6 Statistical analysis 122
2.2.2 Objective Randomised Blinded Investigation with optimal medical Therapy of Angioplasty in stable angina (ORBITA) substudy 123
2.2.2.1 Study background 123
2.2.2.2 Study protocol 125
2.2.2.2.1 Inclusion criteria 125
2.2.2.2.2 Exclusion criteria 125
2.2.2.2.3 Randomisation and masking 126
2.2.2.3 Exercise protocol and blood sampling 126
2.2.2.4 Dobutamine stress echocardiography protocol 127
2.2.2.5 Ethical approvals 128
2.2.2.6 Statistical analysis 128
2.2.3 Blood samples 129
2.2.4 Enzyme-linked immunosorbent assays 129
2.2.4.1 Enzyme-linked immunosorbent assay for MDA-LDL 129
2.2.4.2 Enzyme-linked immunosorbent assay for Apolipoprotein B-100 131
2.2.4.3 Enzyme-linked immunosorbent assay for IgG/ IgM anti-MDA-LDL 132
2.2.5 Generation of MDA-LDL 132

2.3 Antibody and antibody fragment targeted nanoparticles for delivery to atherosclerosis 133

2.3.1 Generation of LO1/ LO1Fab 133
2.3.1.1 LO1 133
2.3.1.2 LO1Fab 133
2.3.2 LO1/ LO1Fab binding kinetics 133
2.3.3 Generation of control Fab fragments 134
2.3.4 Fluorescent labelling of antibody fragments for in vivo studies 135
2.3.5 Nanoparticle design and formulation 136
2.3.5.1 Nanoparticle design 136
2.3.5.2 Nanoparticle generation 137
2.3.5.3 Antibody conjugation 140
2.3.5.3.1 Antibody fragment reduction 140
2.3.5.3.2 Nanoparticle-antibody conjugation 140
2.3.5.3 Nanoparticle biophysiochemical properties 141
2.3.5.3.1 Dynamic light scattering 141
2.3.5.3.2 Nanoparticle tracking analysis 141
2.3.5.4 Micro-bicinchoninic protein assay 142
2.3.6 In vitro characterisation 142
2.3.6.1 Generation of MDA-LDL 142
2.3.6.2 Enzyme-linked immunosorbent assays 142
2.3.6.2.1 Modified fluorescence enzyme-linked immunosorbent assay 143
2.3.6.2.2 Anti-PEG enzyme-linked immunosorbent assay 143
2.3.6.2.3 Anti-CH1 enzyme-linked immunosorbent assay 144
2.3.6.2.4 Anti-ApoB enzyme-linked immunosorbent assay 144
2.3.6.2.5 Competitive enzyme-linked immunosorbent assay 144
2.3.6.3 Gel electrophoresis 145
2.3.6.3.1 Sodium dodecyl sulphate–polyacrylamide gel electrophoresis (SDS-PAGE) 145
2.3.6.3.2 Native–polyacrylamide gel electrophoresis (native-PAGE) 145
2.3.6.3.3 Nanoparticle reduction 146
2.3.6.4 Immunohistochemistry 147
2.3.6.4.1 LO1 and LO1Fab immunohistochemistry in human atherosclerosis 147
2.3.6.4.2 LO1 and LO1Fab immunohistochemistry in murine atherosclerosis 148
2.3.6.4.3 Nanoparticle staining in murine atherosclerosis 148
2.3.6.4.4 Oil Red O staining 149
2.3.6.4.5 Fluorescence microscopy 149
2.3.7 Foam cell assay 149
2.3.7.1 Isolation of monocytes and macrophage differentiation 149
2.3.7.2 Quantitative real-time polymerase chain reaction 150
2.3.7.2.1 Cell lysis 150
2.3.7.2.2 RNA extraction 151
2.3.7.2.3 Reverse transcription 151
2.3.7.2.4 Quantitative real-time polymerase chain reaction 152
2.3.7.3 Fluorescent labelling of native and MDA-modified LDL 153
2.3.7.4 Foam cell generation and quantification 153
2.3.7.5 Macrophage treatment with nanoparticle constructs 154
2.3.7.6 Fluorescence microscopy 154
2.3.7.7 Statistical analysis 155
2.3.8 In vivo characterisation 155
2.3.8.1 Ethical approvals 155
2.3.8.2 Murine model of atherosclerosis 155
2.3.8.3 Construct half-life determination 156
2.3.8.4 Fluorescence molecular tomography - computerised tomography 156
2.3.8.5 Mouse whole-body perfusion and aortic root sectioning 158
2.3.8.6 Ex vivo tissue fluorescence imaging 159
2.3.8.7 Ex vivo aortae Oil Red O staining 159
2.3.8.8 Statistical analysis 159

CHAPTER 3 – RELATIONSHIPS BETWEEN OXIDISED LDL AND ANTIBODIES TO OXIDISED LDL WITH ATHEROSCLEROTIC PLAQUE CHARACTERISTICS AND EXERCISE 162

3.1 Chapter summary 162

3.2 Introduction 164

3.3 Assay optimisation and variability 168

3.4 The relationship between oxidised LDL and antibodies to oxidised LDL with atherosclerotic plaque characteristics – a substudy of the SCOT-HEART trial 169

3.4.1 Patient population 169
3.4.1.1 Representativeness of study population to overall SCOT-HEART population 171
3.4.2 Study CTCA and antibody data summary 174
3.4.3 Relationship between MDA-LDL and anti-MDA-LDL antibody levels and clinical characteristics 175
3.4.3.1 MDA-LDL 175
3.4.3.2 IgG anti-MDA-LDL 177
3.4.3.3 IgM anti-MDA-LDL 178
3.4.4 Relationship between anti-MDA-LDL antibody levels and coronary, aortic, aortic valve and mitral valve calcification 180
3.4.5 Relationship between anti-MDA-LDL antibody levels and plaque subtype burden 187
3.4.5.1 IgG anti-MDA-LDL 189
3.4.5.2 IgM anti-MDA-LDL 191
3.4.6 Relationship between anti-MDA-LDL antibody levels and obstructive coronary disease 192
3.4.7 Relationship between anti-MDA-LDL antibody levels and clinical events 194
3.4.8 Conclusions 195

3.5 The relationship between oxidised LDL and antibodies to oxidised LDL with exercise in coronary artery disease – a substudy of the ORBITA trial 198

3.5.1 Patient population 198
3.5.2 Effect of exercise on MDA-LDL and anti-MDA-LDL antibodies 200
3.5.3 Effect of PCI versus placebo on pre-exercise and post-exercise MDA-LDL and anti-MDA-LDL antibody levels 203
3.5.4 Relationship between MDA-LDL and anti-MDA-LDL antibody levels and baseline dobutamine stress echocardiography 204
3.5.5 Conclusions 205

3.6 Discussion 206

3.6.1 SCOT-HEART study summary 206
3.6.1.1 IgG anti-MDA-LDL 206
3.6.1.2 IgM anti-MDA-LDL 207
3.6.2 Potential mechanistic roles of IgM anti-MDA-LDL antibodies in atherogenesis 208
3.6.3 Relationship of IgG anti-MDA-LDL antibodies with atherosclerosis 210
3.6.4 Importance of the SCOT-HEART study findings 212
3.6.5 SCOT-HEART study limitations 212
3.6.6 ORBITA study summary 213
3.6.7 Pathophysiological basis for oxidation biomarker changes with exercise 214
3.6.8 Lack of PCI effect on biomarker levels 215
3.6.9 ORBITA study limitations 216
3.6.10 Importance of the ORBITA study findings 216

3.7 Conclusions 216

3.8 Related presentations and publications 217

3.8.1 Presentations 217
3.8.2 Publications 218

CHAPTER 4 – TARGETED NANOPARTICLE CONSTRUCTS FOR THE MOLECULAR TARGETING OF VULNERABLE ATHEROSCLEROTIC PLAQUE 221

4.1 Chapter summary 221

4.2 Introduction 222

4.3 Nanoparticle design 224
4.3.1 Targeting antibody fragment 224
4.3.2 Nanoparticle platform 226
4.3.3 Nanoparticle cargo 227

4.4 First iteration nanoparticle construct 228
4.4.1 First iteration nanoparticle composition 228
4.4.2 First iteration nanoparticle characterisation 229
4.4.2.1 Nanoparticle size and polydispersity index 230
4.4.2.2 Modified nanoparticle fluorescence-linked immunosorbent assay 231
4.4.2.3 Nanoparticle function is dependent on TCEP reduction and the maleimide reaction 232
4.4.2.4 Development of the anti-PEG ELISA 234
4.4.2.5 Initial nanoparticle stability 236
4.4.2.5.1 Nanoparticle centrifugation and filtration 238

4.5 Nanoparticle optimisation 241
4.5.1 Further nanoparticle optimisation 242
4.5.1.1 Nanoparticle function on fluorescence ELISA is independent of the fluorophore 243
4.5.2 Antibody fragment conjugation efficiency 245
4.5.3 Final nanoparticle physical properties 253
4.5.4 Final nanoparticle composition 254

4.6 Control Fab production 254
4.6.1 $F(ab')_2$ reduction with 2-MEA 255
4.6.2 Ultracentrifugation of reduced $F(ab')_2$ fragments 258
4.6.3 Quantification of free sulfhydryl groups on reduced $F(ab')_2$ fragments 261
4.6.4 Fluorescent labelling of the control Fab fragment 263

4.7 Effect of Fab fragment reduction for nanoparticle conjugation 264
4.7.1 Fab fragment reduction 264
4.7.2 Reduced Fab fragment nanoparticle conjugation 272

4.8 LO1 and LO1Fab binding properties 279
4.8.1 Microfluidic antibody affinity profiling 280
4.8.2 Immunohistochemistry 282

4.9 Nanoparticle in vitro characterisation 285
4.9.1 Physical nanoparticle properties 285
4.9.1.1 ELISA 286
4.9.1.2 Dynamic Light Scattering analysis 287
4.9.1.3 Nanoparticle tracking analysis 288
4.9.1.4 Antibody conjugation estimations 289
4.9.2 Nanoparticle MDA-LDL recognition on ELISA 291
4.9.2.1 Indirect ELISAs 291
4.9.2.2 Competitive ELISAs 293
4.9.2.2.1 Versus LO1 293
4.9.2.2.2 Versus LO1Fab 295
4.9.3 Varying antigenic loads 296
4.9.3.1 Binding to MDA-LDL rather than native LDL 296
4.9.3.2 Binding to differentially modified MDA-LDL 297
4.9.4 Nanoparticle stability 299
4.9.5 Fluorescence Microscopy 300
4.9.5.1 LO1Fab 301
4.9.5.2 LO1Fab-nanoparticle 303

4.10 Foam cell assay 305
4.10.1 Isolation of monocytes and macrophage differentiation 306

4.10.2 Defining the macrophage population 306
4.10.3 Foam cell formation 308
4.10.3.1 Fluorescent labelling of MDA-LDL 308
4.10.3.2 Foam cell formation 311
4.10.4 Macrophage uptake of nanoparticles 314
4.11 LO1Fab-750 in vivo characterisation in murine atherosclerosis 315
4.11.1 The LDL-receptor deficient mouse model 316
4.11.2 Whole body FMT 318
4.11.3 Confocal microscopy of in vivo injected mice 321
4.12 Nanoparticle in vivo characterisation in murine atherosclerosis 324
4.12.1 Blood clearance of constructs 325
4.12.2 In vivo imaging at 24-hours 328
4.12.3 Construct organ distribution at 24-hours 330
4.12.4 In vivo imaging at 4-hours 331
4.12.5 Ex vivo imaging at 4-hours 333
4.12.6 Construct organ distribution at 4-hours 335
4.12.7 In vivo imaging co-localised with a commercial plaque-targeted NIRF agent 337
4.12.8 Ex vivo imaging co-localised with a commercial plaque-targeted NIRF agent 343
4.12.9 Fluorescence microscopy of in vivo injected mice 345
4.13 Discussion 350
4.14 Conclusions 356
4.15 Related presentations and publications 357
4.15.1 Presentations 357
CHAPTER 5 – A NOVEL EXPERIMENTAL MODEL OF ATHEROSCLEROSIS, THE EX VIVO PUMP-PERFUSED AMPUTATED HUMAN LIMB MODEL 360
5.1 Chapter summary 360
5.2 Introduction 361
5.2.1 Background 361
5.2.2 Concept of the ex vivo pump-perfused amputated human limb model 362
5.2.3 Aims of the ex vivo pump-perfused amputated human limb model 364
5.3 Ethical permission 365
5.4 The ex vivo pump-perfused amputated human limb model 366
5.4.1 Ex situ perfusion system 366
5.4.2 Limb procurement 368
5.4.3 Limb perfusion 369
5.4.4 Imaging 370
5.5 Experimental progress 371
5.6 Maintenance within physiological parameters 374
5.7 Angiography 377
5.8 Intravascular imaging 380
5.9 Proof-of-principle atherosclerotic fluorescence molecular imaging 383
5.10 Discussion 386
5.11 Conclusions 390
5.12 Related presentations and publications 391
5.12.1 Presentations 391
CHAPTER 6 – CONCLUDING REMARKS AND FUTURE WORK 393

6.1 Concluding remarks **393**
6.2 Suggestions for future work **396**
CHAPTER 7 – REFERENCES ***401***
APPENDIX ***423***
Appendix 1 – Related publications **423**
Appendix 2 – Related presentations **425**

LIST OF ABBREVIATIONS

ACS	Acute coronary syndrome
ANOVA	Analysis of variance
Apo(a)	Apolipoprotein (a)
ApoB	Apolipoprotein B
ApoE	Apolipoprotein E
ASCOT	Anglo-Scandinavian Cardiac Outcomes Trial
ASCVD	Atherosclerotic cardiovascular disease
AU	Absorbance units
BCA	Bicinchoninic acid
B_{max}	Maximum specific binding
BSA	Bovine serum albumin
CABG	Coronary artery bypass grafting
CACS	Coronary artery calcification score
CAD	Coronary artery disease
CANTOS	Canakinumab ANti-Inflammatory Thrombosis Outcomes Study
CCS	Chronic coronary syndrome
CD	Cluster of differentiation
cDNA	Complementary deoxyribonucleic acid
CH	Constant heavy
CI	Confidence interval
CIRT	Cardiovascular Inflammation Reduction Trial
CL	Constant light
COLCOT	COLchicine Cardiovascular Outcomes Trial
COURAGE	Clinical Outcomes Utilizing Revascularization and Aggressive Drug Evaluation
CPET	Cardiopulmonary exercise testing
CRP	C-reactive protein
CT	Computerised tomography
CTCA	Computerised tomography coronary angiography
CVD	Cardiovascular disease
CXCR4	C-X-C motif chemokine receptor-4
DAPI	4′,6-diamidino-2-phenylindole
DES	Drug-eluting stent
dH_2O	Distilled H_2O
DLS	Dynamic light scattering
DMEM	Dulbecco's Modified Eagle Medium
DMSO	Dimethyl sulfoxide
DSE	Dobutamine stress echocardiography
DTT	Dithiothreitol

EDTA	Ethylenediaminetetraacetic acid
ELISA	Enzyme-linked immunosorbent assay
Fab	Fragment antigen binding
Fc	Fragment crystallisable
FDG	Fluorodeoxyglucose
FFR	Fractional flow reserve
FMT	Fluorescence molecular tomography
FRI	Fluorescence reflectance imaging
GAPDH	Glyceraldehyde 3-phosphate dehydrogenase
GLACIER	Goal of Oxidized LDL and Activated Macrophage Inhibition by Exposure to a Recombinant Antibody
HDL	High-density lipoprotein
HR	Hazard ratio
HRP	Horseradish peroxidase
hsCRP	high sensitivity C-reactive protein
IDL	Intermediate-density lipoprotein
Ig	Immunoglobulins
IHD	Ischaemic heart disease
IL	Interleukin
ISCHEMIA	International Study of Comparative Health Effectiveness With Medical and Invasive Approaches
IQR	Interquartile range
IVUS	Intravascular ultrasound
K_d	Dissociation constant
LCBI	Lipid core burden index
LDL	Low-density lipoprotein
LDL-R	Low-density lipoprotein receptor
LoDoCo2	Low-Dose Colchicine-2
Lp(a)	Lipoprotein (a)
LRP	Lipid Rich Plaque study
MAAP	Microfluidic antibody affinity profiling
MACE	Major adverse cardiovascular events
MCP-1	Monocyte chemo-attractant protein-1
M-CSF	Macrophage colony-stimulating factor
MDA	Malondialdehyde
MDA-LDL	Malondialdehyde-modified low-density lipoprotein
MEA	Mercaptoethylamine
MES	2-(N-Morpholino)ethanesulfonic acid
MeSH	Medical Subject Headings
MI	Myocardial infarction
MLA	Minimal lumen area
MMP	Matrix metalloproteinase

MRI	Magnetic resonance imaging
mRNA	Messenger ribonucleic acid
NC3Rs	National Centre for the Replacement Reduction & Refinement of Animals in Research
NIR	Near-infrared
NIRAF	Near-infrared autofluorescence
NIRF	Near-infrared fluoroscopy
NIRS	Near-infrared spectroscopy
nLDL	Native low-density lipoprotein
NLRP3	NLR-family pyrin domain-containing protein 3
NP	Nanoparticle
NP-Ab	Nanoparticle-antibody complex
NSTE-ACS	Non-ST-segment elevation acute coronary syndrome
OCT	Optical coherence tomography
OD	Optical density
OR	Odds ratio
ORBITA	Objective Randomised Blinded Investigation with optimal medical Therapy of Angioplasty in stable angina
OMT	Optimal medical therapy
OSE	Oxidation-specific epitopes
oxLDL	Oxidised low-density lipoprotein
PAGE	Polyacrylamide gel electrophoresis
PBMC	Peripheral blood mononuclear cell
PBS	Phosphate-buffered saline
PCI	Percutaneous coronary intervention
PCR	Polymerase chain reaction
PCSK9	Proprotein convertase subtilisin/kexin type 9
PDI	Polydispersity index
PEG	Polyethylene glycol
PET	Positron emission tomography
PLGA	Poly(lactic-co-glycolic acid)
PREVENT	Preventive Coronary Intervention on Stenosis With Functionally Insignificant Vulnerable Plaque
RR	Relative risk
RF-IVUS	Radiofrequency intravascular ultrasound
R_h	Hydrodynamic radius
ROI	Region of interest
RNA	Ribonucleic acid
RPMI	Roswell Park Memorial Institute
RT	Room temperature
scFv	single-chain variable fragments
SCOT-HEART	Scottish COmputed Tomography of the HEART

SD	Standard deviation
SDS	Sodium dodecyl sulphate
SEM	Standard error of the mean
SNR	Signal: noise ratio
SPECT	Single-photon emission computed tomography
STEMI	ST-segment elevation myocardial infarction
TBR	Target: background ratio
TCEP	Tris(2-carboxyethyl)phosphine
TCFA	Thin-capped fibroatheroma
TNFα	Tumour necrosis factor-α
TMB	3,3′,5,5′-Tetramethylbenzidine
VCAM-1	Vascular cell adhesion molecule-1
VSMC	Vascular smooth muscle cell
VH	Variable heavy
VH-IVUS	Virtual histology intravascular ultrasound
VL	Variable light
VLDL	Very-low-density lipoprotein
ZEUS	Zlitivekimab Cardiovascular Outcomes Study

LIST OF FIGURES

Figure 1-1. Atherosclerosis pathogenesis. 31
Figure 1-2. Low-density lipoprotein structure. 35
Figure 1-3. The central role of oxidised low-density lipoprotein in atherosclerotic plaque pathobiology. 38
Figure 1-4. The vulnerable atherosclerotic plaque. 40
Figure 1-5. IgG and antibody fragment structure. 94
Figure 1-6. Major organic and non-organic nanoparticle classes. 98
Figure 2-1. Consort diagram for SCOT-HEART substudy. 121
Figure 2-2. Blood sampling timepoints in the ORBITA Study. 127
Figure 2-3. ELISA formats. 130
Figure 2-4. Degree of labelling calculations. 136
Figure 2-5. Sonication of organic and aqueous phases with Rhodamine 6G whilst stirring on ice. 139
Figure 3-1. Malondialdehyde modification of LDL. 169
Figure 3-2. Adjusted association between antibody level and presence of calcification in the coronary arteries, aorta, aortic valve and mitral valve using restricted cubic splines. 184
Figure 3-3. Unadjusted and adjusted association between antibodies and log-transformed coronary artery calcium score using restricted cubic splines. 186
Figure 3-4. Adjusted association between antibodies and coronary atherosclerotic plaque subtypes using restricted cubic splines. 188
Figure 3-5. Schematic illustration of the potential mechanistic roles of IgG and IgM anti-MDA-LDL antibodies with important CTCA features of coronary atherosclerosis. 198
Figure 3-6. Dynamic change in biomarkers between P1 (baseline pre-randomisation assessment, pre-exercise) and P2 (baseline pre-randomisation assessment, post-exercise). 202
Figure 4-1. Schematic representation of the initial nanoparticle design. 229
Figure 4-2. Size and dispersity of the first iteration of Rhodamine 6G nanoparticle constructs. 230
Figure 4-3. MDA-LDL recognition by the first iteration of Rhodamine 6G nanoparticle constructs. 232

Figure 4-4. Nanoparticle function is dependent on both the maleimide reaction and antibody fragment TCEP reduction. 233
Figure 4-5. Checkerboard titration ELISA for the novel anti-PEG ELISA. 235
Figure 4-6. Nanoparticle function on ELISA is similar when detected via fluorescence or polyethylene glycol binding. 236
Figure 4-7. Aggregation of nanoparticles when left prior to use. 238
Figure 4-8. Nanoparticles are in suspension. 240
Figure 4-9. Schematic representation of the final nanoparticle design. 242
Figure 4-10. Nanoparticle function is independent of the conjugated fluorophore. 244
Figure 4-11. LO1Fab conjugation to Cy5 nanoparticles. 246
Figure 4-12. Optimisation of maleimide percentage and antibody fragment conjugation in nanoparticle formulation. 247
Figure 4-13. Evaluation of varying nanoparticle compositions. 249
Figure 4-14. Optimisation of LO1Fab conjugation efficiency to Cy5 nanoparticles. 252
Figure 4-15. F(ab')2 reduction with 2-MEA. 256
Figure 4-16. Optimisation of F(ab')2 reduction with 2-MEA. 258
Figure 4-17. Ultracentrifugation of the reduced F(ab')2 fragments. 260
Figure 4-18. Quantification of free sulfhydryl groups on reduced F(ab')2 fragments. 262
Figure 4-19. Fluorescent labelling of Fab constructs. 263
Figure 4-20. Fab fragment reduction using TCEP. 266
Figure 4-21. Gel electrophoresis of reduced LO1 Fab fragments. 268
Figure 4-22. 10M TCEP-reduced Fab fragment recognition of MDA-LDL on ELISA. 269
Figure 4-23. The reactivity of differentially reduced LO1Fab on ELISA. 270
Figure 4-24. Effect of minimally reduced LO1Fab on MDA-LDL recognition in ELISA format. 272
Figure 4-25. The effect of LO1Fab TCEP reduction prior to nanoparticle conjugation on ELISA. 273
Figure 4-26. Gel electrophoresis of nanoparticle constructs. 275
Figure 4-27. Gel electrophoresis with fluorescent imaging of nanoparticle constructs. 276
Figure 4-28. Gel electrophoresis of reduced nanoparticle constructs. 278
Figure 4-29. Binding curves for the interaction of MDA-LDL with LO1 and LO1Fab using microfluidic antibody affinity profiling. 281

Figure 4-30. Immunohistochemistry with LO1 and LO1Fab on stable human coronary artery atherosclerotic plaques. 284
Figure 4-31. Confirmation of Fab presence on both LO1Fab and control Fab conjugated nanoparticles. 286
Figure 4-32. Nanoparticle construct size assessed by nanoparticle tracking analysis. 288
Figure 4-33. Example calculations for the estimation of amount of Fab per each nanoparticle in the LO1Fab-nanoparticle construct. 291
Figure 4-34. Nanoparticle function on ELISA. 292
Figure 4-35. LO1Fab-NP competes with LO1 for MDA-LDL binding. 294
Figure 4-36. LO1Fab-NP competes with LO1Fab for MDA-LDL binding. 295
Figure 4-37. Nanoparticle binding to MDA-modified LDL but not native LDL on ELISA. ... 297
Figure 4-38. Preservation of nanoparticle binding to MDA-modified epitopes on MDA-LDL. 298
Figure 4-39. LO1Fab but not pre-conjugated LO1Fab-NP is resistant to freeze-thaw cycles. 299
Figure 4-40. Immunohistochemistry with LO1Fab and control Fab in murine aortic root atherosclerosis (20x magnification). 302
Figure 4-41. Fluorescence confocal microscopy with nanoparticle constructs in murine aortic root atherosclerosis (20x magnification). 304
Figure 4-42. PCR of targeted macrophage genes. 307
Figure 4-43. Fluorescent labelling of MDA-LDL. 310
Figure 4-44. Equivalent fluorescent labelling of native and MDA-modified LDL. 311
Figure 4-45. Increased macrophage uptake MDA-modified LDL versus native LDL. 312
Figure 4-46. Macrophage MDA-LDL uptake is concentration dependent. 313
Figure 4-47. Confocal microscopy of macrophages treated with MDA-LDL and nanoparticle constructs. 314
Figure 4-48. The atherosclerotic mouse model used for molecular imaging in this chapter. 317
Figure 4-49. FMT quantitative imaging of LO1Fab-750 versus control Fab-750. 320
Figure 4-50. Fluorescent confocal microscopy of an aortic root section from a mouse injected in vivo with LO1Fab-750. 322

Figure 4-51. Fluorescent confocal microscopy of an aortic root section from a mouse injected in vivo with control Fab-750. 323
Figure 4-52. Nanoparticle construct in vivo half-lives. 326
Figure 4-53. FMT imaging of LO1Fab targeted nanoparticles at 24-hours post-injection. 329
Figure 4-54. Organ distribution of nanoparticle constructs at 24-hours post-injection. 330
Figure 4-55. In vivo FMT imaging of LO1Fab targeted versus untargeted nanoparticles at 4-hours post-injection. 332
Figure 4-56. Ex vivo fluorescence analysis of aortae from mice injected with LO1Fab-targeted or untargeted nanoparticles. 334
Figure 4-57. Organ distribution of nanoparticle constructs at 4-hours post-injection. 336
Figure 4-58. In vivo FMT imaging of LO1Fab-conjugated versus control Fab-conjugated nanoparticles, co-injected with MMPSense-750FAST at 4-hours post-injection. 339
Figure 4-59. In vivo FMT-CT imaging of LO1Fab-conjugated versus control Fab-conjugated nanoparticles, co-injected with MMPSense-750FAST at 4-hours post-injection. 342
Figure 4-60. FRI and FMT of ex vivo aortae from mice injected with LO1Fab or control Fab conjugated nanoparticles and MMPSense-750FAST. 344
Figure 4-61. Fluorescent confocal microscopy of an aortic root section from a mouse injected in vivo with LO1Fab-targeted nanoparticles. 347
Figure 4-62. Fluorescent confocal microscopy of an aortic root section from a mouse injected in vivo with control Fab-targeted nanoparticles. 349
Figure 5-1. Schematic representation of the ex vivo pump-perfused amputated human limb model. 367
Figure 5-2. Annotated photograph of the ex vivo pump-perfused amputated human limb model. 367
Figure 5-3. The amputated human limb model. 373
Figure 5-4. Physiological parameters measured during one limb perfusion experiment. .. 376
Figure 5-5. Angiography of the amputated human limb model. 378
Figure 5-6. Intravascular imaging of the amputated human limb model using intravascular ultrasound. 381
Figure 5-7. Intravascular imaging of the amputated human limb model using optical coherence tomography. 382

Figure 5-8. Targeting atherosclerosis near-infrared fluorescence imaging of atherosclerosis using the ex vivo pump-perfused amputated human limb model. 385

LIST OF TABLES

Table 1-1. Non-invasive imaging modalities in clinical use to assess coronary artery disease and vulnerable atherosclerotic plaque. 71
Table 1-2. Invasive imaging modalities in clinical use to assess coronary artery disease and vulnerable atherosclerotic plaque. 73
Table 1-3. Vulnerable plaque prospective natural history studies. 77
Table 1-4. Completed prospective randomised controlled trials of local interventions for vulnerable plaques. 79
Table 1-5. Ongoing prospective randomised controlled trials of local interventions for vulnerable plaques. 81
Table 1-6. Randomised clinical trials of medical therapy for stabilisation of vulnerable plaques. 82
Table 1-7. Antibody fragment properties. 97
Table 1-8. Systematic review summary table of research studies exploring PLGA-based nanoparticles in atherosclerosis. 107
Table 2-1. Primary antibodies used during this thesis. 115
Table 2-2. Secondary antibodies used during this thesis. 116
Table 2-3. Polymers used for nanoparticle generation. 137
Table 2-4. Gene expression probes used in this thesis for quantitative real-time polymerase chain reaction. 153
Table 3-1. Patient characteristics for included participants in the SCOT-HEART substudy. 171
Table 3-2. Patient characteristics of the total SCOT-HEART population and the substudy population. 173
Table 3-3. Patient characteristics of participants who underwent coronary CT angiography in the SCOT-HEART population and the substudy population. 174
Table 3-4. Patient characteristics per tertile of MDA-LDL. 176
Table 3-5. Patient characteristics per tertile of IgG anti-MDA-LDL. 178
Table 3-6. Patient characteristics per tertile of IgM anti-MDA-LDL. 179
Table 3-7. Adjusted odds ratio for the presence of coronary/ aortic/ aortic valve/ mitral valve calcification per tertile of IgG/ IgM anti-MDA-LDL antibodies. 182

Table 3-8. Coronary calcification per tertile of IgG and IgM anti-MDA-LDL antibodies. 185
Table 3-9. Coronary plaque subtypes per tertile of IgG anti-MDA-LDL antibodies. 190
Table 3-10. Adjusted odds ratio for high risk of fatal or non-fatal myocardial infarction based on 4% low-attenuation plaque burden cut-off per tertile of IgG anti-MDA-LDL antibodies. 191
Table 3-11. Coronary plaque subtypes per tertile of IgM anti-MDA-LDL antibodies. 192
Table 3-12. Results of multinomial logistic regression of antibodies on the probability of severity of coronary disease. 193
Table 3-13. Results of multinomial logistic regression of antibodies on the probability of 1-, 2- or 3-vessel disease in patients with obstructive disease. 194
Table 3-14. Relationship between fatal or non-fatal myocardial infarction and antibody levels. 195
Table 3-15. Patient characteristics of participants included in the ORBITA substudy. 200
Table 3-16. Average biomarker values at each study timepoint. 200
Table 4-1. Fluorescently labelled LO1 and LO1Fab bind MDA-LDL using microfluidic diffusional sizing technology. 280
Table 4-2. Summary of microfluidic antibody affinity profiling assay results for LO1 and LO1Fab. 282
Table 4-3. Average size and polydispersity index of nanoparticle constructs by Dynamic Light Scattering analysis. 287
Table 4-4. Average size and concentration of nanoparticle constructs by nanoparticle tracking analysis. 289
Table 4-5. Antibody fragment conjugation and conjugation efficiency of nanoparticle constructs 290

Chapter 1

Background

CHAPTER 1 – BACKGROUND

1.1 Cardiovascular disease

1.1.1 Epidemiology

Cardiovascular disease (CVD) is the leading cause of mortality worldwide, accounting for 17.9 million or 32% of all deaths globally (1). With novel cutting-edge therapies and greater emphasis on CVD prevention, mortality rates in developed countries are beginning to plateau, generating a mortality gap with many developing countries where rates are continuing to rise (2). Accordingly, worldwide >75% of all deaths from CVD occur in under-developed or developing countries (1), making the ongoing prevention and treatment of CVD a global public health priority. Better treatments for communicable diseases allow survival to later life in developing countries, permitting the development of CVD, and coupled with aging populations across the globe, ensures that the burden of CVD will remain large. In addition, from a public health perspective, whilst mortality from CVD is clearly hugely prominent, premature mortality (often defined as <70 years old), as well as incidence and prevalence of CVD, with the associated morbidity, quality of life impairment and burden on healthcare systems, are also significant. These epidemiological parameters are also generally seen to be plateauing and even decreasing across Europe over the last 50 years, however, are continuing to rise globally (3, 4).

CVD is often considered to be more prevalent in males than females, and indeed age-specific rates are higher in males, however actual lifetime risk is similar between the sexes. These sex differences are primarily considered to be due to an overall greater preponderance of traditional cardiovascular risk factors in males, including higher rates of smoking, diabetes,

hypertension and hypercholesterolaemia. In addition, a protective effect of sex steroid hormones (mainly oestrogens) is thought to be important, rendering less CVD in younger females, which then wanes following the menopause. For example, premenopausal females generally have more favourable cholesterol profiles than males, but lipid levels then increase following the menopause to levels higher than their male counterparts (5).

CVD comprises a heterogenous group of cardiovascular conditions, with coronary heart disease, cerebrovascular disease and peripheral arterial disease forming major components, linked by atherosclerosis as a unifying pathology. Indeed, myocardial infarction (MI) and strokes accounted for 85% of CVD mortality in 2019 (1). Other aspects of CVD with less relevant relations to atherosclerosis include rheumatic, valvular and congenital heart disease, as well as venous thromboembolic disease.

1.1.2 Atherosclerotic cardiovascular disease

Atherosclerosis is the key aetiology of the vast majority of CVD (atherosclerotic CVD, [ASCVD]), and results in the formation of fibrous/ fatty/ calcific plaques within the arterial subendothelial space. As these lesions expand in size, related to various systemic, inflammatory or mechano-anatomical features, they may cause significant luminal narrowing with a degree of blood flow restriction (6). The clinical manifestations of this depend on the affected vascular bed and degree of dynamic blood flow requirement (such as high cardiac output states during exercise or systemic infection): for example, significant stenoses in the coronary circulation may lead to ischaemic chest pain (angina pectoris), whilst in the peripheral circulation may result in intermittent limb claudication. However, atherosclerotic coronary luminal narrowing per se represents a relatively safe phenotype, demonstrated by

recent randomised clinical trials of percutaneous coronary intervention ([PCI], the catheter-based implantation of intra-coronary arterial stents) to relieve significant stenoses, in patients with flow-limiting stable ischaemic heart disease. Indeed, an invasive strategy with PCI made no significant difference to MI or CVD death rates versus medical therapy, over three-year follow up (7). The clinical manifestations of coronary artery disease (CAD) (coronary arterial atherosclerotic plaque) are divided into unstable presentations – acute coronary syndromes (ACS) or MI, where there is evidence of acute myocardial ischaemia due to coronary thrombosis often accompanied by electrocardiographic changes and serum cardiac troponin elevation; and stable presentations – termed chronic coronary syndromes (CCS), with symptomatic/ asymptomatic CAD in the absence of acute coronary thrombosis.

1.1.3 Sequelae of atherosclerotic cardiovascular disease

Atherosclerotic plaques may remain stable, or can rupture, related to a constellation of phenomena, regarded classically as Virchow's triad – 1, endothelial injury; 2, local flow disturbances including blood stasis; and 3, systemic hypercoagulability (8). This rupture event exposes the highly thrombogenic lipid and tissue factor-rich plaque core to the bloodstream, and in the presence of other members of Virchow's triad, massive thrombosis may occur, resulting in acute vessel occlusion. MI ensues if this takes place within the coronary vascular bed, thrombotic stroke in the cerebral vasculature, or acute limb ischaemia in the peripheral arterial circulation. The formed blood clot may also embolise distally, as is more commonly seen in peripheral and cerebral vascular diseases. The symptomatic sequelae of these major vessel occlusive events again relate to the affected vascular bed, but typically result in acute-onset cardiac chest pain/ loss of neurological function/ limb pain in the coronary/ cerebral/ peripheral vasculature respectively. However, clinically silent

atherosclerotic plaque rupture and vessel occlusion can occur, often in the presence of advanced diabetes mellitus with resultant microvascular disease and impaired nociception. There is also evidence that atherosclerotic plaques may rupture or erode at other times, perhaps when components of Virchow's triad are not present, and accordingly can heal without triggering massive thrombosis and vessel occlusion (9).

1.2 Atherosclerosis

As described above, the clinical consequences of atherosclerosis have an overwhelming global public health burden. Atherosclerosis is a chronic inflammatory process of which the hallmark is retention of fatty lipids and cholesterol beneath vascular endothelium, leading to plaque development.

1.2.1 Atherosclerosis pathobiology

1.2.1.1 On the macroscopic level

The origins of atherosclerotic plaques are first detectable as fatty streaks from adolescence, although this can appear much earlier in the presence of various conditions, for example Familial Hypercholesterolaemia. With time, plaques develop, usually at predilection sites where there is turbulent disturbed blood flow, altered local haemodynamic forces and low wall shear stress, such as at branching points or outer walls of bifurcation sites (10). In a proatherogenic milieu of uncontrolled modifiable and unmodifiable cardiovascular risk factors and chronic inflammation, these plaques continue to grow in size and complexity. Often the vessel will positively remodel to accommodate the evolving plaque and prevent encroachment into the lumen; however, this adaptability will be exceeded with continued plaque development. Plaques will often remain clinically silent, until there is sufficient blood

flow limitation to cause ischaemia in tissue supplied distal to the stenotic lesion, or there is plaque rupture leading to thrombus formation and vessel occlusion. Figure 1-1 below displays the macroscopic development of an atherosclerotic plaque.

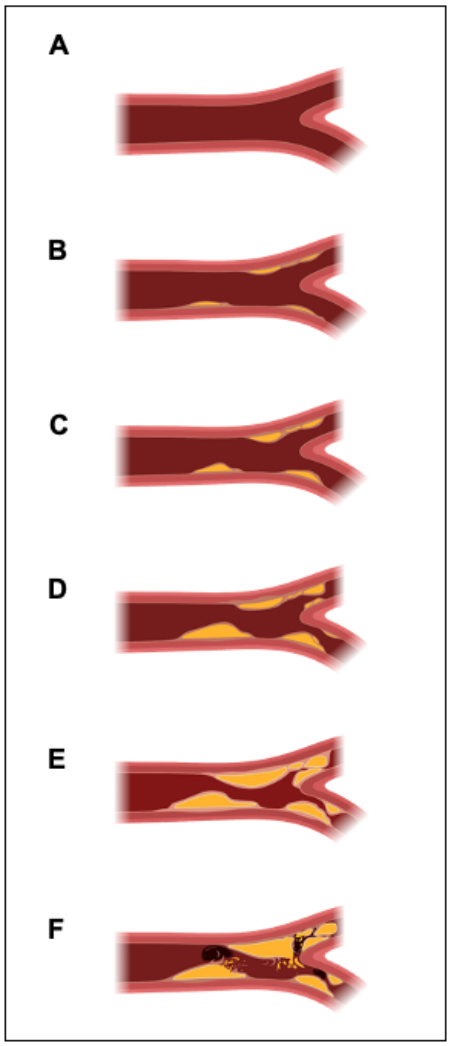

Figure 1-1. Atherosclerosis pathogenesis.

Atherosclerotic plaque developing at an arterial bifurcation site. Normal coronary artery (A) develops fatty streaks (B), to more advanced plaques (C,D), prior to severe flow-limiting disease (E), when the patient may experience symptoms (for example angina pectoris in the coronary vascular bed). Alternatively, the plaque may rupture (F), leading to thrombosis and arterial occlusion, resulting in myocardial infarction, ischaemic stroke or acute limb ischaemia depending on the affected vascular bed. Made using Biorender.

1.2.1.2 On the microscopic level

On a cellular level, injury to vascular endothelium lining large and medium-sized arteries by local flow disturbances leads to the overexpression of adhesion molecules, such as vascular

cell adhesion molecule-1 (VCAM-1), on endothelial surfaces. This in turn leads to increased recruitment of T-cells and monocytes to sites of endothelial injury, with release of pro-inflammatory chemokines, such as monocyte chemo-attractant protein-1 (MCP-1), establishing the inflammatory cascade. Adhered activated monocytes then migrate through the endothelium into the sub-intimal space, differentiate into macrophages and further drive the translocation of additional inflammatory cells down a chemokine gradient.

Vascular endothelial cells themselves also become activated in this process, changing to an atheroprone phenotype, with impaired nitric oxide bioavailability, promotion of further leucocyte adhesion and migration as well as promotion of vascular smooth muscle cell (VSMC) proliferation. The now dysfunctional endothelial barrier becomes more porous, permitting the passage of particles <70nm in diameter such as Apolipoprotein B (ApoB)-100 containing lipoproteins, including low-density lipoprotein (LDL), passively endocytosed down a concentration gradient, as well as being actively transcytosed by caveolae, activin-like kinase 1 or scavenger receptor B1 (11). LDL is retained here in the sub-intimal space due to the interaction between positively charged lysine and arginine residues on ApoB-100 and negatively charged groups within proteoglycans in the endothelial cell basement membrane (12). Activated VSMCs migrate to form the fibrous cap overlying the lesion, protecting the thrombogenic plaque contents from the bloodstream.

LDL within the evolving plaque microenvironment is vulnerable to various modifications including peroxidation, glycation or self-assembly, rendering itself pro-inflammatory and capable of immune recognition (6). Peroxidation of LDL generates oxidised LDL (oxLDL), a heterogenous group of various post-translational oxidative modifications to various aspects

of the LDL particle, which possess diverse oxidation-specific epitopes (OSEs). These are capable of being recognised by various immune cells of both the innate and adaptive immune systems, as well as complement system proteins. Complement and antibodies can be protective, although in this scenario, can drive further endothelial damage and pro-inflammatory leucocyte recruitment. What is more, oxLDL and other oxidised phospholipids get engulfed by resident macrophages or VSMCs via scavenger receptors, such as lectin-like oxLDL receptor-1, leading to the formation of foam cells as lipid accumulates, due to unchecked lipid uptake and impaired lipid efflux. These dysfunctional foam cells with ineffective efferocytosis become hubs for further cytokine-mediated pro-inflammatory cell recruitment, matrix metalloproteinase (MMP), myeloperoxidase and interferon-γ release, generation of neutrophil extracellular traps and programmed cell death. MMP activity leads to collagen degradation and thinning of the protective fibrous cap. As foam cells get degraded, dysregulated cell death occurs, including cellular processes such as apoptosis, autophagy and pyroptosis, releasing cellular debris within the plaque extracellular space, termed the atherosclerotic necrotic core. Cholesterol crystals are also formed in this process, which are pro-inflammatory and can further promote tumour necrosis factor-α (TNFα) and NLR-family pyrin domain-containing protein 3 (NLRP3) inflammasome activation (12-14).

As described above, the plaque can continue to expand with a stable phenotype, or can develop more vulnerable features, predisposing the plaque to rupture. Rupture events tend to occur where the fibrous cap is thinnest and with the greatest necrotic core burden, often in the cap shoulder region (8).

1.2.2 Low-density lipoprotein in atherosclerosis

Retention of LDL in the arterial subendothelial space is a key initiating event in atherogenesis. LDL can traverse through the damaged intimal endothelial layer from the bloodstream, particularly in the context of hyperlipidaemia (15), where it may undergo oxidative modification to oxLDL (as detailed above) and becomes trapped.

1.2.2.1 Structure and function of low-density lipoprotein

Lipoproteins transport cholesterol and triglycerides around the body via the blood. There are five lipoprotein classes: LDL, high-density lipoprotein (HDL), very low-density lipoprotein (VLDL), intermediate density lipoprotein (IDL) and chylomicrons. In simple terms: LDL transports lipids to peripheral tissues, HDL performs the reverse action, VLDL carries triglycerides and cholesteryl esters to peripheral tissues and breaks down to IDL, IDL carries mainly cholesteryl esters to peripheral tissues and is converted to LDL, and chylomicrons are triglyceride-rich and carry dietary triglycerides from the intestine to peripheral tissues. Thus, LDL is the main carrier responsible for taking lipids to peripheral tissues. It is also the most exposed particle to external influences that can alter its molecular structure and render it pathogenic (16).

LDL comprises three elements: 1) a lipid core of cholesteryl esters, triglycerides and unesterified cholesterol, 2) ApoB (~520kDa), the principal protein and 3) an exterior phospholipid monolayer. LDL is very heterogenous and varies considerably in size (18-25nm) (~3,000kDa) and density, with smaller, denser LDL molecules being more vulnerable to modification with increased atherogenicity (16). LDL is formed when triglycerides are removed from VLDL/ IDL via hydrolysis by lipoprotein lipase in tissues, becoming smaller and

denser. LDL particles are removed from the circulation in normal lipid homeostasis upon binding to the LDL-Receptor (LDL-R), a cell surface glycoprotein receptor present on hepatic and peripheral tissues, which recognises the ApoB-100 protein and leads to endocytosis of the entire particle, prior to lysosomal degradation (17). As such, conditions that lead to ineffective LDL transport to tissues, for example reduced/ defective LDL-R genes in Familial Hypercholesterolaemia, will result in significantly elevated LDL plasma levels. Additionally, transgenic mice that either lack the gene encoding LDL-R, or have it disrupted in a homozygous fashion, demonstrate significantly accelerated atherosclerosis, especially when coupled with a high-fat diet (18). As such, the LDL-$R^{-/-}$ mouse model is a valuable research tool and is the animal model used in thesis. Figure 1-2 below displays the basic structure of LDL.

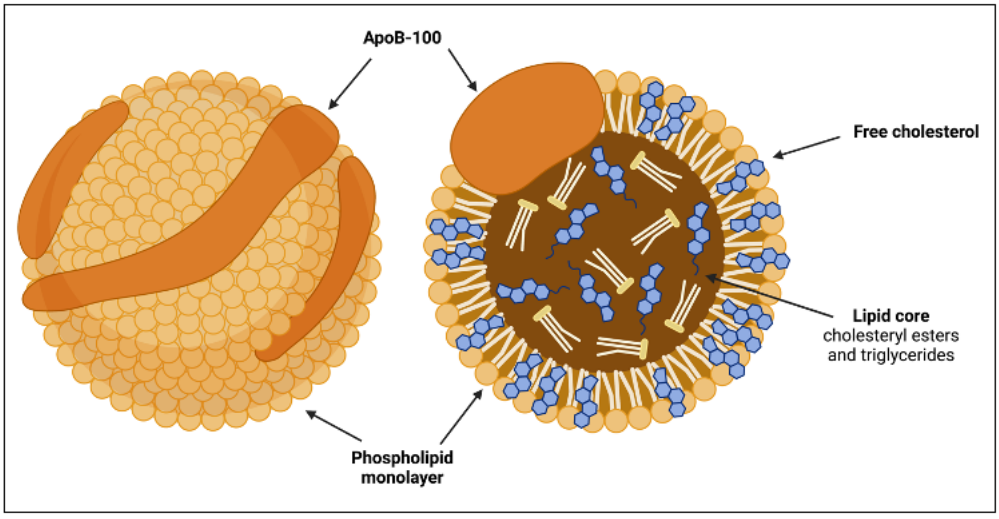

Figure 1-2. Low-density lipoprotein structure.

The structure of an LDL particle, demonstrating the outer shell on the left, and inner structure on the right. Key components are highlighted. Made using Biorender.

Lipoprotein(a) (Lp[a]) is an important variant of LDL that contains both Apolipoprotein (a) (Apo[a]) and ApoB, and thus as well as being proatherogenic, can also compete with

plasminogen for its binding site (due to structural homology between Apo(a) and plasminogen/ tissue plasminogen activator), rendering it prothrombotic (19). Lp(a) is also an important circulating lipoprotein carrier of oxidised phospholipid, via binding to the Apo(a) moiety (20).

1.2.2.2 Oxidised low-density lipoprotein

Modification of LDL can occur through various post-translational changes, including enzymatic digestion, for example with myeloperoxidase, lipoxygenase and peroxidases, as well as oxidation and lipolysis. These modifications range from minimal modification, to more wholescale adaptation of the lipid or ApoB components, to such an extent that it is no longer recognisable by the LDL-R (21). Once retained in the vascular subendothelial space by binding to proteoglycans or other matrix components, especially under hyperlipidaemic conditions, these oxidative changes predominate, forming oxLDL.

These modifications render oxLDL antigenic through various OSEs that are capable of recognition via innate immune system components. More specifically, pattern recognition receptors on macrophages, circulating pentraxins (e.g. C-reactive protein, [CRP]), natural immunoglobulins, complement proteins and toll-like receptors may recognise any of the variety of danger associated molecular patterns on oxLDL, that may perform similar roles to bacterial pathogen-associated molecular patterns via molecular mimicry (22).

1.2.2.3 Malondialdehyde-modified low-density lipoprotein

Lipid peroxidation generates very reactive aldehyde products, such as malondialdehyde (MDA). Adduction of this reactive electrophilic aldehyde group to LDL via interaction with

nucleophilic groups generates MDA-LDL (23). This is but one of the many possible oxidative modifications on LDL; however, it does comprise a significant component of the group of lipid peroxidation-specific epitopes on oxLDL that can undergo recognition by the innate immune system (24). Other well characterised particles in the oxLDL spectrum include oxidised phosphatidylcholine, enzymatically modified LDL, electronegative LDL and minimally modified LDL.

To further emphasise the pathological importance of MDA-LDL, it is abundant in atherosclerotic plaque (25), is endocytosed by macrophages via scavenger receptors (21), whilst anti-MDA-LDL antibodies prevent scavenger-mediated oxLDL macrophage uptake (26), foam cell formation and atherogenesis (27). Immunohistochemical analysis of human atherosclerotic plaques has shown that MDA-LDL accumulates within macrophage-rich areas and the lipidic necrotic core, and specifically relates to unstable and ruptured plaques (28). Additionally, plasma levels of MDA-LDL have been found to correlate to severity of coronary atherosclerosis (29). As will be discussed later, targeting oxLDL via antibodies directed against MDA-LDL is central to this thesis.

1.2.2.4 Measuring circulating oxidised low-density lipoprotein

Detection of oxLDL in plasma is possible via various enzyme-linked immunosorbent assay (ELISA)-based techniques. The origin for circulating oxLDL is uncertain, but is likely the result of *in situ* oxidative modification in plasma, rather than release from atherosclerotic plaques. This of course has implications for the specificity of oxLDL as a biomarker of atherosclerosis. Although there is significant heterogeneity in results obtained from different assays used to assess plasma levels of oxLDL, owing in part to the plethora of possible investigable OSEs,

higher circulating titres of oxLDL have widely been found to associate with various disease states (30). Pertinently, a meta-analysis of observational studies revealed an association between elevated plasma oxLDL and ASCVD (effect size 1.79 [confidence interval (CI) 1.56-2.05]) (31). Moreover, higher levels of oxidised phospholipids on ApoB (oxLDL) have been found to independently predict 15-year cardiovascular events (a composite of ischaemic stroke, MI, new-onset unstable angina, acute coronary interventions, and vascular death) in apparently healthy individuals (32). Although a causal relationship between measured oxLDL and cardiovascular events has not been demonstrated, long-term elevated LDL cholesterol levels is causally linked with incident ischaemic heart disease (IHD), shown through mendelian randomisation analysis of nine polymorphisms on six different genes (33). Figure 1-3 below outlines the central role of oxLDL in the pathobiology of atherosclerosis.

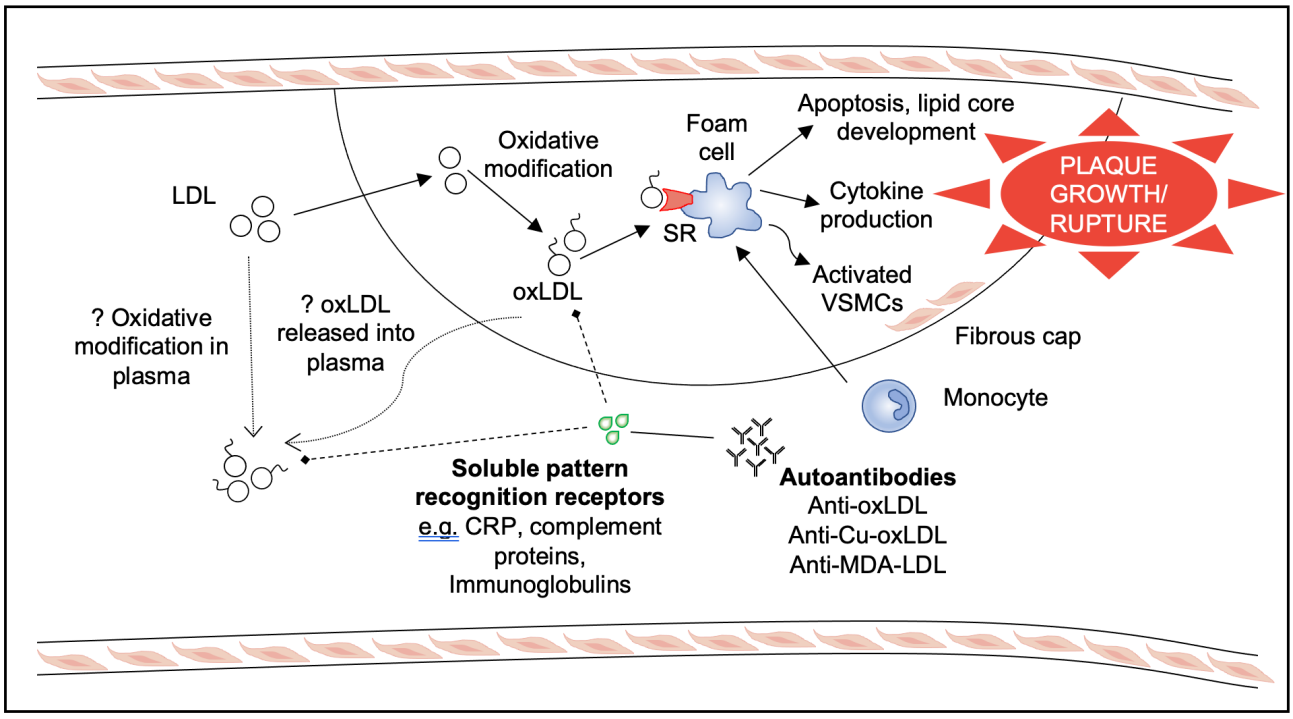

Figure 1-3. The central role of oxidised low-density lipoprotein in atherosclerotic plaque pathobiology.

Modified from Hartley A, Haskard D, Khamis R. Oxidized LDL and anti-oxidized LDL antibodies in atherosclerosis–Novel insights and future directions in diagnosis and therapy. Trends in Cardiovascular Medicine. 2019 Jan 1;29(1):22-6. CRP, C-reactive protein; LDL; low-density lipoprotein; MDA-LDL;

malondialdehyde-modified LDL; oxLDL, oxidised LDL; SR, scavenger receptor; VSMCs, vascular smooth muscle cells.

1.2.3 Vulnerable atherosclerotic plaque

The pathobiology of atherogenesis rests on retention of LDL within the subintimal space, leading to a cascade of inflammatory steps centred around foam cell generation. Post-mortem studies, and later clinical natural history studies, have provided features of atherosclerotic plaques that relate to rupture and subsequent MI (34, 35). Plaques possessing combinations of these rupture-prone characteristics have subsequently been termed the 'vulnerable atherosclerotic plaque' (35). These features are highlighted in Figure 1-4 below. Detection of these vulnerable plaques in the clinical setting, prior to their rupture and onset of adverse sequalae, remains an important avenue of research interest.

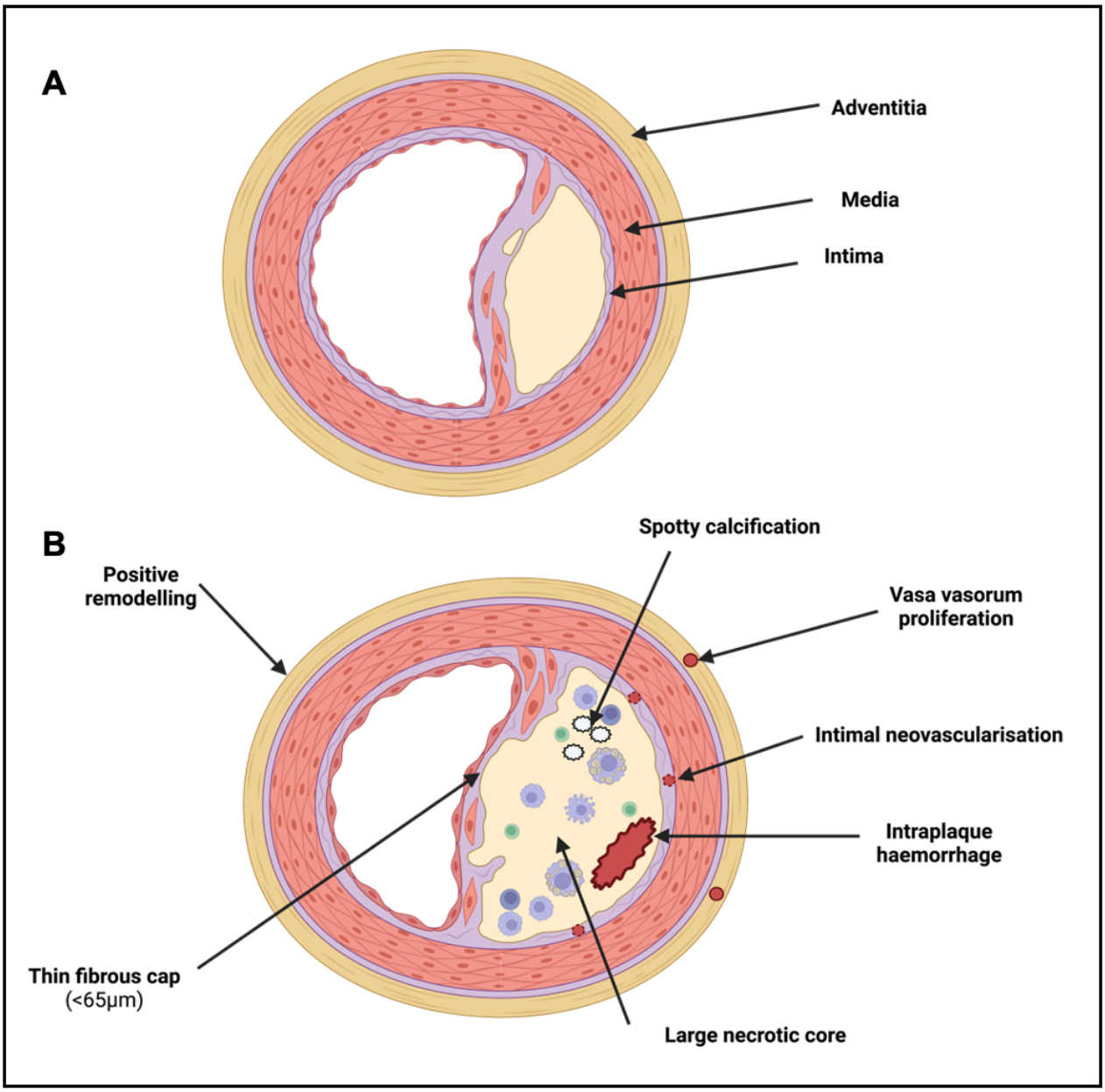

Figure 1-4. The vulnerable atherosclerotic plaque.

Cross-sections through a developing atherosclerotic plaque are shown in (A) and (B).
(A) shows a less advanced and stable plaque, with a thick fibrous cap and absence of plaque vulnerability factors. Arterial wall layers are demonstrated.
(B) conversely, shows a vulnerable plaque that is more predisposed to rupture. Key vulnerability factors are highlighted.
Made using Biorender.

The hallmark and most important vulnerable plaque feature is a thin fibrous cap overlying a lipidic necrotic core, termed a thin-capped fibroatheroma (TCFA). Based on a seminal sudden

cardiac death autopsy study by Virmani and colleagues, the average ruptured cap thickness was 23μm, whilst 95% were <65μm (36), and thus this threshold has been used to define a TCFA (8). After the presence of a TCFA, larger necrotic core (for example >3.5mm^2) and evidence of macrophage infiltration are major plaque vulnerability factors (37). Accordingly, TCFA accompanied by a large necrotic core with associated inflammation (evidenced by monocyte/ macrophage/ T cell infiltration) is thought to underpin 60-70% of all plaque rupture events associated with major acute coronary thromboses (34, 38).

There is evidence that subclinical plaque rupture events occur with subsequent plaque healing and growth, but without acute vessel occlusion (39). It is likely that plaque ruptures occur, without occlusive thrombus formation, and therefore are devoid of major clinical sequelae. Moreover, whilst coronary arterial plaque rupture events are considered to be the key aetiology of MI (~60%), plaque erosions (~30-35%) and eruption of calcific nodules (~5%) can also precipitate acute vessel thrombosis (35, 40, 41). The mechanisms behind plaque erosion and nodular calcification are less clearly understood; but erosion is more common in younger patients and coronary spasm may be implicated in the pathogenesis, whilst they more often present with incomplete vessel occlusion as non-ST-segment ACS (NSTE-ACS) (8).

Crucially, vulnerable plaques are often non-stenotic and not flow-limiting, which typically would mean a less advanced plaque without a thick calcified fibrous cap, and therefore may not be appreciated with standard clinical techniques and would not be considered for PCI by conventional approaches. However, ruptured plaques do tend to carry significant plaque

burden, with only 10% of TCFA being associated with <50% area stenosis on post-mortem analysis (37).

Other vulnerable plaque features include positive or expansive remodelling (as the vessel wall expands outwards to accommodate the evolving plaque), larger plaque sizes but with limited lumen encroachment (greater plaque burden), and the presence of superficial or spotty calcification (42). As plaques enlarge, they undergo angiogenesis, via proliferation of the vasa vasorum and intimal neovascularisation. These blood vessels permit the passage of immune cells directly to the plaque. However, these new blood vessels are leaky and fragile, and thus more predisposed to rupture, leading to intraplaque haemorrhage, which further promotes necrotic core growth and plaque inflammation (43). Lastly, greater plaque metabolic or inflammatory activity with accompanying perivascular inflammation has been linked with increased plaque vulnerability to rupture (8).

1.2.4 Inflammation in atherosclerosis

As can be appreciated above, inflammation and the immune system play prominent roles in atherogenesis. Vascular inflammation is considered to be both a triggering and exacerbating factor for the development of atherosclerosis. The consequences of pro-inflammatory cytokines, such as TNFα, can be directly appreciated, for example in the upregulation of LDL trans-endothelial transport. More indirectly, immune cells perform a plethora of proatherogenic actions, including antigen presentation, such as that performed by B cells and dendritic cells. Cluster of differentiation (CD)8^+T cells are involved with regulation of macrophage activity; B cells are implicated in LDL oxidation, promotion of T Helper 1 cells (which are involved in cytokine-driven inflammatory cell recruitment) as well as regulation of

$CD4^+$T cells or regulatory T cells (44). The interleukin (IL)1β–IL6– CRP axis, moving down the inflammatory cascade, has been heavily implicated in atherosclerosis, particularly its important role in the NLRP3 inflammasome (45). Indeed, linking inflammation and cholesterol in atherogenesis, CRP-induced NLRP3 inflammasome activation has been shown to augment LDL transcytosis across endothelial cells (46).

Evidence for the importance of inflammation in clinical ASCVD has come somewhat indirectly, with important randomised clinical trials demonstrating efficacy of anti-inflammatory therapies in reducing the occurrence of cardiovascular events. For example, the Canakinumab ANti-Inflammatory Thrombosis Outcomes Study (CANTOS) (47), Low-Dose Colchicine-2 (LoDoCo2) (48) and COLchicine Cardiovascular Outcomes Trial (COLCOT) (49) studies have demonstrated reduced major adverse cardiovascular events (MACE) using canakinumab, a fully human IgG monoclonal antibody targeting IL-1β (CANTOS), or colchicine, an anti-microtubule broad spectrum anti-inflammatory agent (LoDoCo2/ COLCOT). These agents, whilst acting on the IL1β–IL6–CRP axis, are also thought to interfere with NLRP3 inflammasome activation.

In CANTOS, 10,061 patients with previous MI and high sensitivity C-reactive protein (hsCRP) ≥2mg/L were randomised to canakinumab with optimised medical therapy (OMT) versus OMT alone. Those randomised to the intervention arm had a significant 15% reduction (hazard ratio [HR] 0.85; 95% CI 0.74 to 0.98; p=0.021) in CVD events over median 3.7 years of follow up, co-existent with reduced hsCRP levels and independent of lipid-lowering (47). A recent meta-analysis of randomised trials using colchicine for coronary disease reported a 22% reduction in MI, 46% reduction in stroke and 23% reduction in coronary

revascularisation. There was also an 18% reduction in cardiovascular death; however, there was an increase in non-cardiovascular death, resulting in the absence of a net effect on all-cause mortality (50).

The anti-inflammatory effect of HDL is well established and may underlie some of the cardioprotective benefit of higher circulating HDL levels (51). Indeed a recent study found an inverse association of HDL anti-inflammatory capacity (measured *in vitro* by the ability to suppress TNFα–induced VCAM-1 messenger ribonucleic acid [RNA; mRNA] expression in endothelial cells) with incident cardiovascular events. Indeed, adding this anti-inflammatory parameter further refined cardiovascular risk prediction provided by the Framingham Risk Score, independent of hsCRP (52). To further strengthen the role of inflammation and the vulnerable plaque, a prediction tool for atherosclerotic lesion progression and rupture based on intravascular ultrasound (IVUS) and virtual histology data has identified that an inflammatory plaque microenvironment (monocytes and macrophages) strongly correlates with necrotic core expansion in unstable plaques (53).

Inhibition of IL-6, downstream of IL-1β, with ziltivekimab, a human monoclonal antibody directed against the IL-6 ligand, has been shown to safely and effectively reduce hsCRP levels, along with other biomarkers of inflammation and thrombosis, in patients at high atherosclerotic risk with chronic renal disease and elevated hsCRP (≥ 2mg/L) (54). Whether this translates into reduced cardiovascular events is being investigated in the currently recruiting multi-centre placebo controlled Zlitivekimab Cardiovascular Outcomes Study (ZEUS) (55). It is important to note that methotrexate, an anti-folate immunosuppressant, has been unsuccessfully trialled to treat ASCVD in the Cardiovascular Inflammation Reduction

Trial (CIRT), a well-powered study for clinical cardiovascular endpoints (56). Indeed, the trial was stopped early due to inefficacy. However, alongside the absence of a reduction in MACE, no effect on key inflammatory biomarkers was observed, including but not limited to, CRP, IL-1β or IL-6. Moreover, CIRT did not use an elevated hsCRP level cut-off as a prerequisite in the inclusion criteria for recruitment, as was present in CANTOS. The ongoing ZEUS trial has used the same cut-off for inclusion. In addition, patients enrolled in the intervention arm of CANTOS that did not see an on-treatment reduction in hsCRP gained no MACE reduction (57). Finally, in a recent collaborative analysis of patients enrolled in clinical trials with contemporary statin therapy (n=31,245), inflammation assessed by hsCRP was found to be a stronger predictor of future MACE than cholesterol assessed by LDL (58). Thus, taking the evidence together, there is mounting support for the importance of inflammation, and treating inflammation, in ASCVD.

Identifying relationships between various serological inflammatory biomarkers and ASCVD have also added weight to the inflammatory hypothesis in atherosclerosis. As mentioned above, CRP, a hepatically-produced acute phase reactant, has been examined closely in this regard, owing to its relatively short circulating half-life and routine use in clinical practice. Early studies identified that higher CRP levels predicted worse cardiovascular outcomes in both stable and unstable populations (59-61), and incorporation of CRP levels into basic cardiovascular risk models provides additional risk prediction (62). More recently, we have demonstrated that even very small hsCRP elevations provide additional prognostic data beyond troponin levels in patients presenting with suspected ACS (63). However, these studies all suffer from the understanding that CRP is an indiscriminative blood biomarker, and thus the source for the inflammation could be atherosclerotic plaques/ vascular

endothelium; but could also arise from some other source. Additionally, CRP per se is not mechanistically associated with coronary heart disease, unlike the upstream IL-6 receptor, as studied in mendelian randomisation analyses (64, 65). Conversely, a pilot study of CRP apheresis in patients following admission with an ACS found that CRP levels related to infarct size and left ventricular dysfunction, with a larger study ongoing (66).

In an attempt to localise the source of inflammation to atherosclerotic plaques and link this with recurrent cardiovascular events, a recent multi-centre prospective cohort study examined coronary atherosclerotic plaque activity using ^{18}F-sodium fluoride positron emission tomography (PET) in patients with a recent MI and multivessel CAD and followed them up for a median of four years. Although plaque activity did not relate to the composite primary endpoint (which included unplanned coronary revascularisation), it did relate to the important hypothesis generating secondary endpoints of cardiac death or non-fatal MI (high plaque activity [11.2%] versus low plaque activity [6.7%]; HR 1.82; 95% CI [1.07-3.10]; p=0.03) (67).

1.2.5 Gaps in atherosclerosis research

Given the far-reaching impact of ASCVD, much research effort has been invested, with resultant novel diagnostic tests and therapeutic agents. However, there needs to be greater understanding of pathophysiological drivers of atherosclerosis-mediated CVD. As above, the clinical focus before or after a cardiovascular event is in optimising risk profiles based on conventional risk factors (such as diabetes mellitus, hypertension or hypercholesterolaemia). This is clearly an imperfect approach given the ongoing extensive epidemiological impact discussed above.

Nonetheless, aggressively optimised risk factor-based management undeniably has the potential to substantially reduce cardiovascular events. To this end, what constitutes OMT is constantly evolving as new therapeutic avenues emerge. For example, lipid modification techniques have progressed from cholesterol biosynthesis inhibition (statins), to gut cholesterol absorption inhibition (ezetimibe), to low-density lipoprotein receptor degradation inhibition (Proprotein convertase subtilisin/kexin type 9 [PCSK9] inhibitors) and most recently acetyl coenzyme A generation inhibition, a precursor of cholesterol biosynthesis (bempedoic acid). These most recent drug classes have only emerged as viable clinical therapies in recent years. Yet, there is hope of further novel options, such as small interfering RNAs to Lp(a), which is an important carrier of oxidised phospholipid in the circulation and a genetically-determined risk factor for ASCVD (68). Moreover, a very recent gene editing therapy to permanently deactivate PCSK9, via a single dose of VERVE-101 to change a single base (adenine to guanine) in the PCSK9 gene sequence, has reported very promising phase I trial results, with phase II trials expected over the coming years (69). This approach has demonstrated a substantial reduction in circulating LDL levels, which therefore would leave less LDL susceptible to oxidation and atherogenesis. As can be readily appreciated, as clinical approaches for lipid management become more diverse (and expensive), what comprises optimal management will need clarification, where the most effective agents, both therapeutically and economically, are prioritised.

Moving away from the isolated cholesterol hypothesis of atherogenesis, which has been the central tenet of preventative cardiology for many years, there may be additional atherosclerotic triggers that are treatable. The role of the inflammatory hypothesis of

atherogenesis is very interesting in this regard, and may help to provide a missing link between atherosclerosis, plaque rupture and cardiovascular events. Moreover, with the rise of anti-inflammatory agents to treat ASCVD, such as colchicine (48, 49) and canakinumab (47), a greater understanding of the mechanism of action of these agents directly on atherosclerotic plaques is required. We also need to appreciate which patients will benefit most from these treatments. Additionally, whether hsCRP is the best biomarker for patient selection, and the associated cut-off levels, demands further study. Finally, the prospect of immune-based therapies or indeed a 'vaccine' for atherosclerosis is an alluring one, that has not seen clinical translation, with work ongoing (70).

The interplay of less traditional cardiovascular risk factors with more established conditions, such as sleep, environmental pollution and psychosocial stress, also demands greater research attention (71). Moreover, the role of sex as a biological variable needs much greater consideration, particularly with the burden of data suggesting different clinical CVD presentations and manifestations between the sexes (72). The role of diet in ASCVD development may also prove to be important, with an increasing appreciation of dietary modifications affecting intestinal microbiota as possible therapeutic targets (73). With the rise of genomic testing and the establishment of genetic risk markers, the prospect of multigene risk assessment, combined with clinical assessment, producing a patient-centred approach to risk stratification, is possible (71). The promise of combining data provided by less traditional and established cardiovascular risk factors with inflammatory and genetic signatures of risk may not only provide a precision approach to risk assessment, but also permit a tailored approach to allow focusing of molecular targeted therapeutic interventions. This could be viewed as the future of cutting-edge ASCVD management.

1.3 The role of antibodies in atherosclerosis

Inflammation and both the adaptive and innate immune systems closely interplay in atherosclerosis. Antibodies are key mediators principally of the adaptive immune system, released by B cell lymphocytes in response to antigen presentation; however low affinity "natural" antibodies are part of the innate immune system. Natural antibodies are largely protective and are considered to play an important role in atherogenesis.

1.3.1 Antibody biology

In human biology, there are five classes of antibodies, or immunoglobulins (Ig), grouped according to their heavy chain types. These are: α (IgA), γ (IgG), δ (IgD), ε (IgE) and μ (IgM). Each isotype has a different structure and performs distinctive physiological functions. All antibodies are formed of four polypeptides, comprising two heavy and two light chains. Antibodies are further divided into constant (Fragment crystallisable [Fc]) regions and fragment antigen binding (Fab) regions. The Fab region performs antigen binding, whilst the Fc region carries out antibody effector functions. Immunoglobulin class switching is a mechanism whereby a B cell's immunoglobulin production is converted from one isoform to another, via changing the Fc portion, keeping the variable region unchanged and maintaining antigen specificity. Typically, class switch recombination changes IgM to IgG/ IgA/ IgE, enabling different effector binding and signalling.

The IgG isotype (150kDa) represents ~75% of the human serological and extracellular fluid antibody population, and indeed 10-20% of all plasma proteins. IgG is formed of two identical 50kDa heavy chains and two identical 25kDa light chains, joined together by disulphide bonds

at the hinge region. Each heavy chain comprises an N-terminal variable domain (variable heavy [VH]) and three constant domains (constant heavy [CH]; CH1, CH2, CH3) (74). Each light chain is comprised of a constant light (CL) and variable light (VL) domains. The VH and VL chains each provide three of the hypervariable loops which form the antigen binding sites. There are four further IgG subclasses – IgG1-4, which vary according to their antigen binding, ability to bind to C1q and activate the complement system as well as their Fc or constant region receptors. IgG1 (~60%) and IgG2 (~32%) are the most abundant. IgG1 is primarily responsible for antibody responses to soluble and membrane protein antigens, whilst IgG2 are secreted in response to bacterial capsular polysaccharide antigens (74). IgG4 is most clinically relevant for its role in IgG4-related disease, a chronic inflammatory vasculitis with multi-organ involvement (75).

IgA (160kDa) is the second most abundant (~15%) immunoglobulin isoform in the blood, however it is the predominant class in mucosal secretions in regions lined by mucosal membranes, such as the intestinal and respiratory tracts. There are two subclasses (IgA1 and IgA2) and exists as both a monomer and dimer. Its main function is to protect mucosal surfaces by binding and neutralising bacterial toxins, preventing epithelial cell adhesion (76).

IgM (180kDa) is the third most abundant (~10%) immunoglobulin isoform and the first antibody secreted by plasma cells in response to a foreign antigen. It is usually secreted as a pentamer (~900kDa) linked via disulphide bonds, with very high avidity owing to the presence of ten antigen binding sites. This compensates for its low antigen affinity, given its early secretion prior to B cell somatic hypermutation. It is mainly present intravascularly, rather than tissues, owing to its large size (76).

IgD (185kDa) and IgE (190kDa) are much less abundant in blood. IgD is present on B-cell membranes, serving as an antigen receptor, but has an undefined role after secretion. IgE binds to mast cells causing degranulation and is involved with immune defence against parasites and hypersensitivity reactions (76).

1.3.2 Natural antibodies

Natural antibodies are germline-encoded immunoglobulins that are thought to exist prior to exogenous antigenic exposure as part of the innate immune system. They provide an immediate first line of defence via broad and unrefined (low affinity but polyreactive) immune responses to infection, whilst the adaptive immune system response develops sensitively and antigen-specifically. Natural antibodies are synthesised predominantly by B1 cells and marginal zone B cells, and although the IgM isotype is the most widely recognised in humans, IgA and IgG natural antibodies have also been found (77). Aside from direct antimicrobial properties, natural antibodies also regulate B cell responses, selection and development, as well as perform roles in clearance of apoptotic debris and suppression of self-immune responses (78). It is hypothesised that natural antibodies are evolutionarily conserved owing to their important immunoregulatory, homeostatic and housekeeping properties (79). To this end, natural antibodies against oxLDL, such as MDA-LDL, have been identified and relate to atherosclerosis, forming a significant component of the entire natural antibody reservoir (80).

1.3.3 Anti-oxidised low-density lipoprotein antibodies

One overarching hypothesis linking natural antibodies with atherosclerosis is that an initial juvenile oxLDL insult results in an innate immune response, stimulating the production of anti-

oxLDL antibodies by B1 cells. Indeed, circulating IgG antibodies against modified LDL (including MDA-LDL) have been found to be much higher in healthy normocholesterolaemic children than a comparable adult cohort, perhaps suggesting protective benefits (81). An inverse relationship between plasma oxLDL and IgG anti-oxLDL antibodies has also been demonstrated in healthy adults (82). These antibodies are thought to complex with, neutralise and traffic, oxLDL to the reticuloendothelial system, in concert with the complement system (79). *In vivo* studies have shown that immunisation of atherosclerosis-prone LDL-R deficient mice with MDA-LDL results in reduced atherogenesis (83), whilst B lymphocyte deficiency was proatherogenic in a similar transgenic model (84). There is also mechanistic evidence from preclinical studies that anti-oxLDL antibodies can block uptake of oxLDL by macrophage scavenger receptors, inhibit phagocytosis of apoptotic cells, reduce foam cell formation and atherosclerotic lesion development (26, 27, 85, 86).

The production of atheroprotective IgM from the bone marrow of Apolipoprotein E $(ApoE)^{-/-}$ mice has been found to be inhibited by B-cell-specific knockout of the chemokine receptor C-X-C motif chemokine receptor-4 (CXCR4), which regulates cell trafficking. Adding clinical significance, CXCR4 expression on human B1 cells positively correlated with circulating IgM anti-MDA-LDL and inversely related to coronary atherosclerosis on IVUS (87). Furthermore, levels of free and microvesicle (extracellular vesicles with important roles in thrombosis) - bound IgM have been shown to vary inversely with measured plasma coagulation levels. The same study also demonstrated that IgM anti-MDA-LDL antibodies inhibit microvesicle-dependent coagulation and thrombosis, and mechanistically, competed for the binding of coagulation factor X/Xa to circulating microvesicles (88).

As circulating levels of oxLDL have been measured in various disease groups, antibody titres against oxLDL have been assessed, with the limitations of different assayed antibodies against diverse OSEs. Overall, IgM anti-oxLDL antibodies are considered to provide atheroprotection, whilst the balance with IgG anti-oxLDL antibodies is more controversial, and studies have reported both positive and negative associations with CVD (89, 90). One example is the Bruneck cohort study, where IgM anti-MDA-LDL related to less CVD, and IgG anti-MDA-LDL associated with a greater risk of developing CVD over 15-years of follow-up (32). Conversely, the Haskard-Khamis laboratory has reported a protective association of both IgG and IgM anti-MDA-LDL in the Anglo-Scandinavian Cardiac Outcomes Trial (ASCOT) (91). We have published a systematic review that highlighted the protective association of higher IgM anti-oxLDL antibody levels with CAD and cardiovascular events (90). A recent study has emphasised the beneficial relationship of IgM against methylglyoxal-modified ApoB (a reactive aldehyde encompassed by oxLDL), with higher titres conferring less severe coronary stenoses (92).

1.4 Currently available diagnostic techniques and treatments of atherosclerotic cardiovascular disease

1.4.1 Diagnosis of atherosclerotic cardiovascular disease

The clinical diagnosis of ASCVD can either be made based on imaging evidence of atherosclerosis in coronary/ cerebral/ peripheral arterial beds, prior to the onset of an index cardiovascular event, or following an event. However, whether demonstration of atherosclerosis without an accompanying appropriate clinical syndrome dictates primary or secondary preventative therapy is debated.

1.4.1.1 Non-invasive techniques for the detection of atherosclerosis

Cardiovascular imaging modalities for CAD are broadly grouped into 'functional' or 'anatomical' tests. Functional tests include modalities that assess the effects of regional blood flow limitation on myocardium, such as regional wall motion abnormalities (stress echocardiography or stress cardiac magnetic resonance imaging [MRI]), and perfusion defects (positron nuclear techniques including PET or single-photon emission computed tomography [SPECT], or perfusion MRI). Anatomical tests use contrast either injected intravenously and imaged with x-rays (non-invasive computed tomography [CT] coronary angiography [CTCA]) or selectively into coronary arteries with fluoroscopy (invasive coronary angiography). However, although CTCA or coronary angiography primarily provide data on blood flow and luminal narrowing, developments including invasive pressure/ flow assessments during coronary angiography and CT-based fractional flow reserve (FFR) add functional ischaemia information (93). Moreover, the quality of anatomical data obtained from coronary angiography is substantially improving, with more widespread use of invasive imaging modalities, such as IVUS and optical coherence tomography (OCT), providing detailed atherosclerotic plaque characterisation. Another, although not yet widely clinically utilised, invasive tool is near-infrared (NIR) spectroscopy (NIRS), which provides complementary data on atherosclerotic plaque lipid burden, which is not as well appreciated by other invasive modalities. In addition, quantitative analysis of CTCA-derived atherosclerotic plaque characterisation has entered the clinical arena and correlates with clinical outcomes (94, 95). CTCA can be used to better diagnose the likely cause of chest pain (96) and more accurately identify patients that will derive greater benefit from invasive coronary angiography (97). Moreover, demonstration of atherosclerosis by CTCA in patients with stable chest pain has been shown to provide prognostic benefit versus functional testing

(98). MRI-based coronary angiography is an exciting emerging modality that could provide both functional and anatomical CAD assessment, free from radiation and nephrotoxic contrast agents, although there is a risk of nephrogenic systemic fibrosis with gadolinium-based contrast agents (99).

Thus, there are now a wide variety of imaging modalities that are clinically available for the detection of ASCVD or its consequences, each with their own diagnostic niche for cardiovascular risk assessment and guiding coronary revascularisation. However, the vast majority of these relate to CCS, and have limited utility in ACS; although the obvious exception is coronary angiography, which is a cornerstone of ACS management (100). The reason that there are so many options for cardiovascular assessment relates both to the widespread burden of CVD, and the imperfect nature of available tests. All modalities have drawbacks which limit their use, including the lack optimal sensitivity/ specificity, use of ionising radiation, cost, or risk of complications. Whilst coronary angiography combined with pressure wire studies and invasive imaging provides the most detailed coronary assessment, it carries a 1/1000 risk of serious complications for angiography-only, with higher rates for more interventional techniques. This risk, combined with radiation and cost implications, makes coronary angiography unsuitable for screening of at-risk populations, or even as a first-line investigation in patients presenting with stable chest pain, unless the pre-test probability is very high. As such, invasive coronary angiography is reserved for those with the highest risk clinical features or after having undergone suggestive non-invasive testing in stable IHD, or those presenting with MI, where risks and costs are outweighed by potential benefits (101).

1.4.1.2 Invasive techniques for the detection of atherosclerosis

Invasive coronary angiography, as outlined above, involves the passage of a catheter from a peripheral artery retrogradely to the ascending aorta, permitting the intubation of the left main stem and right coronary ostia. Iodinated contrast is then injected via the catheter and angiography performed. However, this essentially only provides imaging of the vessel lumen, without data on atherosclerotic plaque features, that is derivable from CTCA for example. Thus, for example, non-obstructive atheroma and vulnerable plaque characteristics will not be appreciated, which has the potential to change clinical management and outcomes. Coronary angiography can be supplemented with the passage of various intravascular imaging catheters over a coronary guidewire to improve its sensitivity for atherosclerosis detection and plaque morphology visualisation.

1.4.1.2.1 Intravascular ultrasound

The most commonly used intravascular imaging technique is IVUS, for both the identification of severe stenoses for PCI, as well as the guidance and optimisation of PCI when it is performed as well as the assessment of procedural complications. Piezoelectric transducers in the catheter tip produce and detect reflected ultrasound waves (10-60MHz), generating a three-dimensional image. It has reasonable spatial resolution (100-200μm), which is improved at higher frequencies with a trade-off of reduced depth penetration. Virtual histology (VH-IVUS) or radiofrequency IVUS (RF-IVUS) is a more advanced imaging technique to examine plaque composition, whereby spectral analysis of ultrasound backscatter is performed, with different plaque components exhibiting identifiable spectral characteristics (102), although the reliability of this technique to detect necrotic core and TCFA has been questioned using validation histology (103).

1.4.1.2.2 Optical coherence tomography

OCT is a NIR light-based intravascular modality that permits very high spatial resolution (10-20μm) imaging of atherosclerotic plaques. However, this is accompanied by reduced depth penetration and the need for a blood-free field for imaging (given blood-induced scatter attenuating the OCT signal), which may be overcome using image augmentation methods. As such, OCT is most frequently performed with iodinated contrast media, which itself carries nephrotoxicity considerations, although imaging with saline is feasible.

1.4.1.2.3 Near-infrared spectroscopy

NIRS is an invasive imaging technique that relies on the reflection of near-infrared light of fatty plaques across the optical spectrum, producing a 'chemogram' of lipid content (104). NIRS analysis generates a lipid core burden index (LCBI) based on the amount of lipid in the artery, and the 4 mm segment with highest LCBI is known as the $MaxLCBI_{4mm}$. $MaxLCBI_{4mm}$ values ≥400 are related to segments that are culprit plaques for ST-segment elevation MI (STEMI) (105). However, NIRS must be combined with other imaging modalities to provide anatomical atherosclerotic plaque data. NIRS is available clinically but has yet to enter widespread practice.

1.4.1.2.4 Near-infrared fluoroscopy

NIR fluoroscopy (NIRF) is an emerging molecular intravascular imaging modality that has not yet been translated clinically, owing in large part to a lack of suitable well-validated molecular probes. Alongside anatomical data provided by IVUS and OCT, plaque pathobiological activity can be analysed via NIRF, using fluorophore-conjugated agents that can target

plaque-related molecular processes. As with NIRS, combination of NIRF with either IVUS or OCT is required for co-registration of signal to atherosclerotic plaques or anatomical landmarks. Following injection of a fluorophore-tagged molecular probe, light in the near-infrared spectrum (650–900 nm) is directed at the arterial wall and stimulates fluorophores to an excited state (fluorescence excitation) with emission of photon energy (fluorescence emission), which is detectable by an appropriate high sensitivity charge-coupled camera and emission filter. NIRF imaging has the potential to be highly sensitive, owing to reduced tissue or red cell autofluorescence in the NIR spectrum, minimising background signal and increasing penetration depth, thus maximising the signal: noise ratio (SNR) (106).

This exciting technique has the potential to revolutionise our clinical assessment of atherosclerotic plaques, through evaluation of plaque biology (for example plaque inflammatory or macrophage activity), but as stated above, is currently limited by suitable probe development, as well as signal blood penetrance and the required duration of image acquisition.

1.4.1.2.5 Hybrid imaging techniques

Hybrid techniques have the potential to combine the advantages of different imaging modalities into a single catheter, if the necessary engineering challenges can be overcome. As stated above, this is essential for co-registration with NIRS/ NIRF, which provide no anatomical information. For example, NIRS-IVUS and OCT-NIRS catheters have been developed, which simultaneously combine the lipid pool detection of NIRS with detailed plaque morphological information provided by IVUS/ OCT, resulting in improved vulnerable plaque detection over the modalities separately (107-109).

Similarly, NIRF-IVUS (110) and NIRF-OCT (111) hybrid catheters have been developed for molecular-structural plaque colocalisation, and are still in clinical translation. NIRF-OCT has relative advantages over NIRF-IVUS, given its improved spatial resolution and being a completely optical fibre-based modality, makes engineering more straightforward. However, the requirement for blood pool clearance and low depth of penetration remain (106). OCT has also been combined with NIR autofluorescence (NIRAF) in a dual-modality hybrid catheter (112). Endogenous NIRAF signal is thought to correlate with intraplaque haemorrhage, as well as insoluble oxidised lipid and ceroid (113), all features of vulnerable plaque, thereby adding another tool to the vulnerable plaque imaging armamentarium. Finally, tri-modality NIRF-OCT-IVUS is under development for a more complete morphological and molecular coronary assessment (114).

1.4.2 Currently available therapies for the treatment of atherosclerotic cardiovascular disease

The management of ASCVD can be broadly grouped into lifestyle modification, pharmacological therapy and myocardial revascularisation.

1.4.2.1 Lifestyle modification

Lifestyle management focuses on cardiovascular risk factor control, and includes smoking cessation, healthy diet, physical activity and maintaining a healthy weight. Cardiac rehabilitation consisting of structured exercise sessions with nurses, dieticians, physiotherapists and psychologists has been shown to significantly reduce cardiovascular mortality (115).

1.4.2.2 Pharmacological therapy

Pharmacological therapy consists of strategies to prevent symptoms with anti-ischaemic drugs (such as beta-adrenoceptor antagonists, calcium channel antagonists, long-acting nitrates or ranolazine), as well as therapies that focus on event prevention. These include anti-thrombotic therapies with aspirin, platelet $P2Y_{12}$ adenosine diphosphate chemoreceptor inhibitors (such as clopidogrel, prasugrel or ticagrelor) as well as low-dose anticoagulant therapy (rivaroxaban). Furthermore, renin-angiotensin-aldosterone antagonism and beta-adrenoceptor antagonism have roles to play in cardiac remodelling and improved prognosis following an acute MI (101). More recently, colchicine has been added to the secondary preventative medication arsenal, in patients at high risk of further cardiovascular events despite being on OMT (116). Of course, optimised pharmacological therapy for ASCVD will include medications to improve cardiovascular risk factor control, such as hypertension, diabetes and hypercholesterolaemia. Lipid lowering drugs, including statins as a mainstay, with the addition of other agents such as ezetimibe, PCSK9 inhibitors, icosapent ethyl or bempedoic acid as appropriate, comprise an evolving aspect of preventative cardiology. Interestingly, aside from their lipid lowering effect, statins have been demonstrated to have pleiotropic effects, including atherosclerotic plaque stabilisation and anti-inflammatory properties (117).

1.4.2.3 Myocardial revascularisation

Myocardial revascularisation consists of either relieving severe or haemodynamically significant coronary stenoses with PCI (with balloon angioplasty or drug-eluting stents [DES]), or surgically re-routing blood distal to these lesions via coronary artery bypass grafting

(CABG), following coronary angiography. Both of these techniques carry substantial major complication rates (at least 1/100 for PCI and greater for CABG) and therefore should only be performed where the expected benefits outweigh the risks. The prognostic benefit of myocardial revascularisation in the setting of CCS has been questioned recently (7, 118), and as such should be viewed as an adjunct to OMT in symptom-refractory patients in the vast majority of cases. However, revascularisation remains a cornerstone of ACS management, with a clear mortality benefit (119).

These evidence-based therapies discussed above are on the whole, only accessible as secondary prevention, once a patient has declared themselves as having ASCVD, usually after having an ACS or undergoing revascularisation for a CCS.

1.5 The unmet clinical diagnostic and therapeutic needs in atherosclerotic cardiovascular disease

Despite improving mortality and morbidity rates, CVD remains the leading cause of death in both developed and developing countries. Thus, there is a clear mandate for better prevention and treatment options in developed countries, and enhanced provision of existing management strategies in developing countries. Population screening programmes aligned with primary care initiated cardiovascular risk modification can go some way to treat CVD before it develops (primary prevention). However, there is variable uptake and engagement with advised lifestyle changes or treatments to manage these risk factors, particularly in asymptomatic individuals. Nonetheless, patients can also have very high-risk cardiovascular profiles, but never go on to develop symptomatic CVD, or have very low-risk profiles and have an MI at a young age. Thus, our understanding of the disease processes involved, and

entirely risk factor-based management, is imperfect. Better screening tests that may be able detect those at the greatest risk, incorporated into risk prediction algorithms with the inclusion of traditional cardiovascular risk factors would have a clear benefit. A screening test for high-risk CVD would ideally be inexpensive, highly sensitive for future cardiovascular events with reasonable specificity, and be acceptable to both patients and physicians – as such, a blood biomarker would be ideal. However, at present there are no blood biomarkers in routine clinical use that are able to assist in the accurate prediction of future CVD (120), aside from the identification of cardiovascular risk factors.

There are however a wide variety of imaging modalities that are clinically available for the detection of ASCVD or its consequences, each with their own diagnostic niche for cardiovascular risk assessment and guiding coronary revascularisation, as well as drawbacks. Unfortunately, none are suitable for cardiovascular population screening. A singular imaging modality, or indeed a simultaneous hybrid approach, if non-invasive and cost efficient, would have the potential to bridge this gap.

Despite modern therapeutic options, recurrent cardiovascular events in those undergoing coronary interventions for MI is as high as 20% at three years (121). Therefore, a further unmet clinical need is the prevention of recurrent cardiovascular events following an index insult. The index event permits the initiation of a plethora of potent cardiovascular risk-modifying therapies, yet recurrent events remain common. Indeed, the strongest predictor of a cardiovascular event is a prior event, associated with approximately a risk doubling (122). Better means of calculating which of these high-risk individuals will go on to have a further cardiovascular event is necessary, where more invasive, and expensive therapies may be

justified. It is in this patient group where invasive hybrid imaging with NIRF co-registered with IVUS or OCT, using a suitable molecular targeted probe or multiplexed probe panel, to provide atherosclerotic plaque morphological and functional data may present the most nuanced picture of future cardiovascular risk. Potentially, secondary preventative medications could then be tailored in an individualised manner, permitting a precision medicine approach to ASCVD. Moreover, with growing clinical evidence for vulnerable plaque characteristics portending a significantly increased risk of plaque rupture and cardiovascular events, as will be discussed later, there is a real need to identify vulnerable plaques, with imaging techniques or otherwise, prior to their rupture or erosion. If these plaques could be identified prior to causing an event, perhaps via molecular targeted imaging, it is plausible that the same targeting ligand could be harnessed to deliver appropriate therapies directly to vulnerable atherosclerotic plaques, potentially modifying plaque morphology or biology in a beneficial manner.

1.6 Experimental modelling of atherosclerosis

Preclinical studies investigating the pathobiology and pharmacology of ASCVD have followed traditional research frameworks, moving from identification of a target of interest, to analysing its relevance in *in vitro* studies, followed by, if successful, advancing to *in vivo* studies prior to further clinical translation. Given the clinical importance of CVD, there are a plethora of *in vivo* models of atherosclerosis, yet none are perfectly representative of the human disease state, and each has their advantages and drawbacks.

1.6.1 Small animal models

Small animal models of experimental atherosclerosis consist predominantly of the mouse and rabbit, and of these, the mouse is the most frequently used of all animal species.

1.6.1.1 Mouse models of experimental atherosclerosis

Mouse models of atherosclerosis are transgenic, most commonly with genetic ablation of either ApoE or the LDL-R. Non-genetically manipulated mice are relatively resistant to atherogenesis, owing to relatively atheroprotective lipid profiles, with very low VLDL and LDL levels (123). Absence of ApoE, a glycoprotein that binds and removes plasma chylomicrons and VLDL remnants from the circulation, results in hypercholesterolaemia, particularly of the chylomicron and VLDL fractions. Absence of the LDL-R results in failure of LDL removal from the circulation, resulting in hypercholesterolaemia, predominantly LDL. Whilst ApoE deficiency in humans is rare, underlying Familial Dysbetalipoproteinemia, LDL-R deficiency is more common, causing Familial Hypercholesterolaemia, as mentioned above. Both strains, accompanied by a high-fat diet, develop an atherosclerotic phenotype in a reasonably short timeframe, making them favourable for preclinical study. However, $ApoE^{-/-}$ models exhibit very rapid atherogenesis, often without the need for a high-fat diet. This is likely due to the anti-inflammatory properties of ApoE (inhibition of platelet aggregation, lipoprotein oxidation and VSMC proliferation) as well as playing an important role in efferocytosis and apoptotic cell remnant accumulation (18). Thus, $LDL\text{-}R^{-/-}$ models are more suited to study inflammatory atherosclerotic processes, and, coupled with their inherent more human-like lipid profiles (124), make $LDL\text{-}R^{-/-}$ mice an ideal experimental model for this thesis.

Other advantages of mice for the study of atherosclerosis include that they are easy to breed, have a relatively low maintenance cost, and owing to their small size, lesser amounts of research probes are required for experimentation. However, atherosclerotic lesions are often less complex with these models, partly owing to their rapid development, and there is little spontaneous plaque rupture or other atherothrombotic complications, making these experimental models of atherogenesis rather than plaque instability per se. The sites of atherogenesis are also different from humans, developing lesions most commonly in the aortic root, lesser curvature of the aortic arch and major aortic arch vessels, versus coronary, carotid, and peripheral vessels in humans (124). Newer LDL-R and ApoE deficient models have more recently been developed to gain leptin-deficiency, to develop more accurate models of metabolic syndrome (18). In addition, more advanced transgenic mouse models that exhibit complex plaque phenotypes and spontaneous plaque rupture have been developed by cross-breeding $ApoE^{-/-}$ mice with mice containing a heterozygous mutation in the fibrillin-1 gene, the gene responsible for elastic fibre fragmentation in Marfan's syndrome (125).

1.6.1.2 Rabbit models of experimental atherosclerosis

Rabbit models of experimental atherosclerosis are also common, owing to their relatively inexpensive maintenance and easy handling. Experimental use is declining however, likely related to the ready commercial availability of cheaper and more acceptable transgenic mouse models. Rabbit models include Watanabe heritable hyperlipidaemic rabbits, which develop significant hypercholesterolaemia and hypertriglyceridaemia accompanied by widespread atherosclerotic lesions with a normal diet (126). Other approaches include New Zealand White rabbits fed a high-fat diet and more recently, ApoE-deficient rabbits have been

generated using genome editing (127). Rabbit models develop largely foam cell atherosclerotic lesions, rather than the fibrous lesions in mice and more complex mixed lesions in humans. Rabbits are obviously larger in size than mice, and therefore iliac vessel cannulation is possible, permitting catheter-based intravascular imaging of the aorta, but not the coronary arteries. This has been harnessed to generate a novel model of atherosclerosis, whereby catheter-directed balloon injury is performed to disrupt the endothelium of the iliac vessels, resulting in rapid neointimal thickening, lipid accumulation, smooth muscle cell infiltration and foam cell generation. This creates atherosclerotic lesions in an accelerated fashion (within two-weeks), much faster than the four to eight months that would be required otherwise (128). Rabbit lipoprotein metabolism is closer to human than mouse lipoprotein metabolism, however there are important differences. For example, rabbits lack Apolipoprotein A-II (an important component of HDL in humans) and have low levels of hepatic lipase (129). Again, different to humans, rabbits develop significant atherosclerotic lesions in the aortic arch and descending thoracic aorta (123).

1.6.2 Large animal models

Larger animal models of experimental atherosclerosis are principally pigs and non-human primates. The advantages of using these larger species are that more complex intravascular catheter-based techniques can be employed, owing to their increased size and more human-like cardiovascular anatomy.

1.6.2.1 Pig models of experimental atherosclerosis

Pigs are the most used larger species for experimental atherosclerosis modelling, owing to their human-like anatomy, closer genetic resemblance to humans and similar atherosclerosis

predilection sites, in the coronary, abdominal aorta and iliofemoral arteries. However, atherosclerotic plaques in porcine models often do not advance to become more complex lesions, at least in a reasonable experimental timescale. Furthermore, spontaneous plaque rupture and thrombosis is rare. Pig models consist of lines with natural mutations in the ApoB and LDL-R genes, diabetic hypercholesterolaemic pigs, as well as genetically engineered strains, for example, LDL-R knock-out or PCSK9 transgenic pigs (130). In contrast to mice and rabbits, pigs are more expensive to maintain and more difficult to handle (123). Porcine models however have been successfully utilised to study atherosclerotic plaque development in response to disturbed coronary flow using clinical calibre *in vivo* intravascular imaging (131), model ischaemia-reperfusion injury and restenosis following angioplasty, as well as being used in stent development (132).

1.6.2.2 Non-human primate models of experimental atherosclerosis

Non-human primates, for example, cynomolgous and rhesus monkeys, develop atherosclerosis on high-fat diets, and can be useful experimental models for human atherosclerosis. However, they are used very infrequently, owing to the necessary level of regulation, expense, ethical considerations, as well as high level of specialised training required. Nonetheless, non-human primate studies have been utilised to study psychosocial and behavioural aspects of atherosclerosis (132).

1.6.3 Issues with currently available preclinical models

A key issue relating to preclinical atherosclerosis research is the lack of successful translation that has been seen from vast experimental research efforts to the clinical arena. There are a plethora of examples of novel therapeutic agents or targeting probes within the field of

ASCVD that show fantastic preclinical efficacy, yet do not translate into clinical practice, for inefficacy, toxicity or other concerns. It is imperative that this is addressed to better focus and streamline research efforts going forwards.

In preclinical animal research, a greater awareness and understanding of more complex, but perhaps less advanced, disease states will be necessary to model the human clinical situation more accurately. At present, most animal models focus on one pro-atherosclerotic phenotype, such as hypercholesterolaemia, and do not appreciate the plethora of dysmetabolic conditions present in patients. This oversimplification, coupled with the lack of appreciation of sex-specific models (133) amongst other characteristics that lead to lack of representativeness of animal models to human disease states (particularly with rodent models), may explain the failure of many promising therapeutic agents to bridge the gap from preclinical research to clinical practice. As mentioned above, newer more sophisticated mouse models of metabolic syndrome and plaque rupture are being developed which may help in this regard.

Much greater importance also needs to be placed in both preclinical and clinical research in primary prevention strategies prior to clinical disease onset, particularly with the soon to be overwhelming burden of aging and sedentary lifestyles giving rise a pandemic of dysmetabolic conditions. Prevention will be much more efficacious than cure, and thus should be prioritised. How these are modelled in preclinical research will require some consideration, where more advanced disease states are often modelled to render larger treatment effects.

Moreover, models with more human-like physiology and size encounter more ethical and financial issues. In addition, long and expensive translational pipelines from bench to the clinic are often prohibitive, leading to loss of potential candidate agents. Taking these points together, it is clear that more representative preclinical modelling of atherosclerosis is required.

1.6.4 The need for replacement, reduction and refinement in animal research

Aside from the necessity to fine-tune animal experimental atherosclerosis research to be more useful and representative of human disease, there is an ethical requirement to optimise how animals are utilised in research. The 3Rs: Replacement, Reduction and Refinement, principles created by Russell and Burch in 1959 (134) outline a widely accepted ethical framework to maintain animal welfare during experimentation. In the UK, there is the 'National Centre for the Replacement Reduction & Refinement of Animals in Research' (NC3Rs), a national organisation which aims to advance and instil the 3Rs in research practices. Replacement aims to strive for experimental designs that answer study questions without the requirement for animals. The principle of reduction prioritises appropriately powered experimental designs where the minimum number of animals are required, yet producing results that are robust and reproducible. Refinement aims to minimise pain, suffering and distress experienced by the animals during experimentation, by advancing understanding and implementation of best animal welfare practices (135).

These ethical principles govern animal studies globally and must always be considered at all stages of research design and execution. Thus, in preclinical atherosclerosis research there

is a requirement to not only optimise animal welfare and power experiments appropriately, but to replace animals with other methods or experimental designs where possible.

1.7 From stable atherosclerotic plaque to vulnerable atherosclerotic plaque

As outlined above, rupture of an atherosclerotic plaque is central to the pathogenesis of ASCVD, and there are various structural lesion features that predispose these plaques to rupture, termed vulnerable plaques. However, evidence suggests that plaque rupture events occur frequently, without precipitating acute vessel occlusion, followed by plaque healing and often lesion expansion (39). Thus, it remains a priority to understand and predict which of these plaques will eventually precipitate a MI, with the aim of potentially preventing this occurring. Key plaque vulnerability morphological factors include a TCFA overlying a large necrotic core accompanied by inflammatory infiltrates, amongst other features (136). Importantly for this thesis, greater lipidic necrotic core size has been found to relate to plaque rupture in post-mortem studies of patients experiencing sudden cardiac death (34).

1.7.1 Imaging vulnerable atherosclerotic plaques

The ability to recognise plaque vulnerability factors using clinically available techniques is essential, for both cardiovascular risk prediction and potential risk mitigation. This was once the reserve of invasive imaging modalities; however, there is an expanding role for non-invasive techniques. Tables 1-1 and 1-2 below provide an outline of the available modalities for the imaging of CAD and plaque vulnerability features, reviewing their advantages and disadvantages, for non-invasive and invasive techniques, respectively.

	CTCA	MRI	PET
Source of image	X-ray	Magnetic	Nuclear
Key clinical indications	• Visualise coronary anatomy • Assessment of need for invasive coronary angiography ± PCI • Cardiovascular risk stratification	• Assessment of myocardial function and viability • Myocardial tissue characterisation • Stress imaging in CCS	• Assessment of myocardial function and viability • Stress imaging in CCS
Spatial resolution	0.4mm	1mm	5mm
Radiation burden	+	-	++
Contrast agent/ tracers	Iodinated contrast	Gadolinium-based	Radioisotope-based, e.g., ^{18}FDG-PET, ^{18}F-NaF, ^{68}Ga-DOTATATE
Sensitivity for contrast agent detection	Millimolar	Micromolar	Nanomolar - Picomolar
Plaque vulnerability features: • ***Positive remodelling*** • ***Lipid core*** • ***Plaque rupture*** • ***TCFA*** • ***Inflammation*** • ***Neovascularisation*** • ***Intraplaque haemorrhage*** • ***Spotty/ micro-calcification***	(Depending on radiotracer) ++ + - - - - - ++	(Depending on radiotracer) - + - - + - + -	(Depending on radiotracer) - - - - + - - ++
Key advantages	• Widely available • Cost-efficient • Provides cardiovascular risk stratification • Novel emerging techniques, e.g., CT-based physiology and virtual histology • Novel photon counting CT has the potential to permit higher resolution imaging with radiation dose reduction • Potential for molecular targeting with iodinated probes	• No radiation • Excellent tissue characterisation • Novel emerging techniques – e.g., sequences to enable coronary artery assessment • Potential for molecular targeting with metallic-based probes	• Main strength lies in its ability to gain functional data, dependent on the radiotracer and molecular probe used
Key disadvantages	• Radiation (albeit relatively low dose), restricting serial scanning	• Coronary artery visualisation is currently limited • Not widely available • Expensive	• Radiation dose, restricting serial scanning • Poor spatial resolution • Need for hybrid CT imaging for colocalisation • Not widely available • Expensive • Infrastructure required for probe manufacture

Table 1-1. Non-invasive imaging modalities in clinical use to assess coronary artery disease and vulnerable atherosclerotic plaque.

Modified from Bom MJ, Van Der Heijden DJ, Kedhi E, Van Der Heyden J, Meuwissen M, Knaapen P, Timmer SA, Van Royen N. Early detection and treatment of the vulnerable coronary plaque: can we prevent acute coronary syndromes?. Circulation: cardiovascular imaging. 2017 May;10(5)

	Angiography	**OCT**	**IVUS**	**NIRS**
Source of image	X-ray	Near-infrared light	Ultrasound (10-60MHz)	Near-infrared light
Key clinical indications	• Assessment of coronary artery anatomy • Facilitation of other imaging/ physiology techniques and PCI	• PCI guidance • Assessment of PCI failure and complications	• PCI guidance • Assessment of PCI failure and complications	• Assessment of plaque lipid component
Spatial resolution	0.16mm	10-20µm	100-200µm	N/A
Depth of penetration	N/A	2-3mm	7-10mm	1-2mm
Pullback speed	N/A	10-40mm/s (although 100mm/s is possible)	0.5mm/s	0.5mm/s
Plaque vulnerability features: • ***Positive remodelling*** • ***Lipid core*** • ***Plaque rupture*** • ***TCFA*** • ***Macrophage infiltration*** • ***Neovascularisation*** • ***Intraplaque haemorrhage*** • ***Spotty calcification***	 ++ - +/- - - - - -	 - + ++ ++ ++ + - +	 ++ + + - - - - ++	 - +++ - - - - - -
Key advantages	• Facilitate other invasive imaging/ physiology techniques • Facilitates PCI • Excellent spatial and temporal resolution vs non-invasive techniques • Widely available • Cheaper than other techniques	• Excellent spatial resolution permitting detailed plaque characterisation • Can identify plaque features associated with vulnerability • PCI guidance • Novel emerging techniques, e.g. OCT-derived coronary physiology	• Can identify plaque features associated with vulnerability (especially VH-IVUS) • Good visualisation of deep plaque components • PCI guidance • Novel emerging techniques, e.g. IVUS-derived coronary physiology	• Can identify plaque features associated with vulnerability
Key disadvantages	• Imaging of vessel lumen only • Need for iodinated contrast	• Blood clearance required • Limited tissue penetration • Cost	• Limited spatial resolution, especially at lower frequencies • Cost	• Need for hybrid imaging with other intravascular imaging modalities for colocalisation • Limited tissue penetration • Cost

Table 1-2. Invasive imaging modalities in clinical use to assess coronary artery disease and vulnerable atherosclerotic plaque.

Modified from Bom MJ, Van Der Heijden DJ, Kedhi E, Van Der Heyden J, Meuwissen M, Knaapen P, Timmer SA, Van Royen N. Early detection and treatment of the vulnerable coronary plaque: can we prevent acute coronary syndromes?. Circulation: cardiovascular imaging. 2017 May;10(5)

The ability to recognise the clinical correlates of the histopathological plaque vulnerability factors has been comprehensively investigated in prospective natural history studies using intravascular coronary imaging.

In the seminal PROSPECT study, Stone and colleagues followed up 697 patients who were admitted to hospital following an ACS and underwent three-vessel angiography and IVUS. When patients subsequently had a recurrent MACE (20.4%) over median 3.4 years of follow up, the event was attributed to either the original culprit or non-culprit lesion. Approximately half of recurrent events related to prior non-culprit lesions with mild angiographic stenoses (mean [± standard deviation (SD)] diameter stenosis, 32.3±20.6%). On multivariate analysis, factors related to future rupture were: 1) a plaque burden (plaque and media cross-sectional area divided by external elastic membrane cross-sectional area) ≥70%; 2) minimal lumen area (MLA) ≤4.0mm^2 and 3) TCFA. Plaques comprising all three of these criteria accounted for 18.2% (HR 11.05 [95% CI 4.39–27.82]) of all recurrent events (121).

Further studies have identified other clinically identifiable vulnerability factors. The Lipid Rich Plaque study (LRP) established the LCBI as an invasive imaging biomarker of plaque vulnerability, using NIRS-IVUS of non-flow limiting segments on coronary angiography. The LCBI reflects the histopathologic necrotic lipid-rich core of atherosclerotic plaques. This study demonstrated that lesions with the max$LCBI_{4mm}$ >400 strongly related to MACE, with adjusted

HR 3.39 (95% CI 1.85–6.20; p<0.0001) (137). PROSPECT II (138), a second large natural history study, used NIRS-IVUS and assessed cardiovascular outcomes over a median of 3.7 years, and reported a MACE rate of 13.2% (95% CI 11.0-15.6). The majority of these events were related to non-culprit plaques (8.0% vs 4.2%, non-culprit versus prior culprit plaques). Furthermore, when lesions had maxLCBI$_{4mm}$ ≥325 (upper quartile) and plaque burden ≥70%, non-culprit major adverse events occurred in 7.0% of patients but only 0.2% of patients without either of these high-risk features. Patients who had one or more lesions with maxLCBI$_{4mm}$ ≥325 in combination with plaque burden ≥70% had a 4-year non-culprit lesion-related MACE rate of 13.2% (95% CI 9.4-17.6) (139). COMBINE OCT-FFR followed diabetic patients with intermediate obstructive coronary lesions that were assessed for physiology and imaging with FFR and OCT. The excellent spatial resolution of OCT permits the identification of TCFA (<65μm), that is not as readily appreciated with the other invasive imaging modalities. In this study, lesion-related major events were 13.3% versus 3.1% (HR 4.7; 95% CI 2.0-10.9) in patients with TCFA and without TCFA respectively. Pertinently, there was no difference in outcomes with flow-limiting and non-flow limiting disease based on FFR (140). Furthermore, in the PECTUS-obs study, patients with bystander FFR-negative coronary disease following an ACS had OCT performed and were followed up for 2-years. The presence of a high-risk plaque (defined as at least two of: lipid arc ≥90°, TCFA and plaque rupture/ thrombus) predicted future MACE (15.4% versus 8.3% without a high-risk plaque; HR 1.93 [95% CI, 1.08-3.47]; p=0.02) (141). These recent studies add further support to the significance of lesion morphology, rather than blood flow limitation, in the vulnerable plaque hypothesis.

A recent retrospective analysis of 3-vessel OCT data from patients undergoing coronary angiography for ACS supported these findings, with TCFA (adjusted HR 8.15; 95% CI 3.67-18.07) and MLA ≤3.5mm^2 (adjusted HR 4.33; 95% CI 1.81-10.38) strongly predicting the combined outcome of cardiac death, non-culprit lesion-related non-fatal MI and unplanned coronary revascularisation over median 3.3 years of follow-up (142).

Table 1-3 below provides an overview of all the prospective natural history studies, highlighting the plaque features that were found to predict the primary study endpoints. As can be appreciated, both OCT and NIRS-IVUS have been demonstrated to identify vulnerable plaques that predict clinical events. Together, the key identified intravascular imaging vulnerability components from the studies included: the presence of TCFA, higher maxLCBI, greater plaque burden, smaller lumen areas, and larger arcs of lipid. These draw direct parallels with pathological vulnerable plaque features described earlier. A recent meta-analysis of both invasive and non-invasive atherosclerotic plaque imaging studies has confirmed these findings, and has identified low MLA (HR [95% CI]) (HR 2.26 [1.18, 4.34]), TCFA (HR 3.19 [1.25, 8.11]) and large LCBI (2.00 [1.43, 2.80]) as the most important invasively-detected plaque vulnerability factors for MACE at the patient level, whilst low-attenuation plaque (2.58 [1.82, 3.67]) was the most important individual non-invasively detected factor for MACE at the patient level. All features were more strongly related to events at the lesional level (143).

Study	Size	Population	Follow up	Imaging	Primary endpoint	Vulnerable plaque features
Uchida et al. (1995) (144)	157	Patients with stable angina and "regular" plaques on angioscopy	1 year	Angioscopy	ACS	**"Yellow" plaques** vs white plaques 11/39 vs 4/118; p=0.00021

						<u>"Glistening yellow" plaques</u> vs non-glistening yellow plaques 9/13 vs 2/26; p=0.00026
VIVA (2011) (145)	170	Patients undergoing coronary angiography ± PCI	625 days	VH-IVUS	Death, MI or unplanned revascularisation)	**<u>TCFA</u>** HR 8.16 (1.78–37.32; p=0.007) **<u>Plaque burden ≥70%</u>** HR 7.48 (2.50–22.31; p<0.001) **<u>MLA ≤ 4 mm^2</u>** HR 2.91 (1.07–7.91; p=0.036)
PROSPECT (2011) (121)	697	Patients with ACS undergoing PCI	3.4 years	RF-IVUS	Cardiac death, cardiac arrest, MI, or rehospitalization due to unstable or progressive angina	**<u>Plaque burden ≥70%</u>** HR 5.03 (2.51–10.11; p<0.001) **<u>MLA ≤4 mm^2</u>** HR 3.21 (1.61–6.42; p=0.001) **<u>TCFA</u>** HR 3.35 (1.77–6.36; p<0.001)
ATHEROREMO-NIRS (2014) (146)	203	Patients undergoing coronary angiography ± PCI with NIRS of a non-culprit artery	1 year	NIRS	Death, ACS, stroke, unplanned revascularisation	**<u>maxLCBI$_{4mm}$ ≥median</u>** HR 4.04 (1.33–12.29; p=0.01)
ATHEROREMO-IVUS (2018) (147)	581	Patients undergoing coronary angiography ± PCI with RF-IVUS in 1 non-stenotic segment of a non-culprit artery	4.7 years	RF-IVUS	Death, MI or unplanned revascularisation	**<u>MLA ≤4 mm^2</u>** HR 1.49 (1.07–2.08; p=0.02) ***(Not TCFA or plaque burden)***
CLIMA (2019) (148)	1003	Patients undergoing coronary angiography ± PCI with OCT of untreated proximal LAD	1 year	OCT	Cardiac death + target segment MI	**<u>MLA <3.5 mm^2</u>** HR 2.1 (1.1–4.0; p=0.032) **<u>Fibrous cap thickness <75 μm</u>** HR 4.7 (2.4–9.0; p<0.001) **<u>Lipid arc >180°</u>** HR 2.4 (1.2–4.8; p=0.013) **<u>OCT-defined macrophages</u>** HR 2.7 (1.2–6.1; p=0.021)
LRP (2019) (137)	1,271	Patients undergoing coronary angiography ± PCI with analysable maxLCBI$_{4mm}$ segments	692 days	NIRS-IVUS	Non-culprit MACE (cardiac death, cardiac arrest, ACS, CABG, PCI, hospital admission with angina with >20% diameter stenosis progression)	**<u>maxLCBI$_{4mm}$ >400</u>** **Patient level** HR 1.89 (1.26–2.83; p=0.0021) **Plaque level** HR 3.39 (1.85–6.20; p<0.0001)
Kubo et al. (2021) (149)	1,378	Patients undergoing coronary angiography ± PCI with OCT	6 years	OCT	ACS attributed to a non-culprit coronary plaque that was imaged by OCT at baseline	**<u>Lipid arc >180°</u>** HR 12.67 (6.82–23.57; p<0.001) **<u>Fibrous cap thickness <65 μm</u>** HR 10.41 (6.48–16.73; p<0.001)
COMBINE OCT-FFR (2021) (150)	390	Patients with diabetes undergoing coronary angiography ± PCI and ≥1 FFR-negative lesions and valid OCT	18 months	OCT	Cardiac death, target vessel MI, target lesion revascularization, unstable angina requiring hospitalization	**<u>Predominantly lipid-rich plaque with fibrous cap thickness ≤65 μm and lipid arc >90°</u>** HR 4.65 (1.99–10.89; p<0.001)

PROSPECT II (2021) (138)	898	Patients undergoing coronary angiography ± PCI with recent (<4 weeks) MI with 3 vessel NIRS-IVUS	3.7 years	NIRS-IVUS	Non-culprit MACE (cardiac death, MI, unstable angina, progressive angina)	**Plaque burden ≥70%** **Patient level** OR 3.49 (1.83–6.63; p=0.0001) **Plaque level** OR 12.94 (6.36–26.32; p<0.0001) **MLA ≤4 mm^2** **Patient level** OR 6.00 (2.12–17.00; p=0.0007) **Plaque level** OR 4.97 (2.59–9.53; p<0.0001) **maxLCBI$_{4mm}$ ≥324.7** **Patient level** OR 2.27 (1.25–4.13; p=0.0071) **Plaque level** OR 7.83, 4.12–14.89; p<0.0001)
PECTUS-obs (2023) (141)	438	Patients with ACS undergoing PCI with at least 1 non-culprit lesion that was FFR-negative. High-risk plaque defined as at least 2 of: 1) lipid arc ≥90° 2) fibrous cap thickness less than 65µm 3) either plaque rupture or thrombus presence	2 years	OCT	MACE (all-cause mortality, non-fatal MI or unplanned revascularisation)	**High-risk plaque** HR 1.93, 1.08–3.47; p=0.02

Table 1-3. Vulnerable plaque prospective natural history studies.

Studies performed to follow-up invasively identified vulnerable plaques, with composite clinical outcomes. Key plaque vulnerability factors identified in each study that related to the composite primary endpoint (at the plaque/ patient level or both) are highlighted, with odds ratios (OR) or hazard ratios (HR) for the primary composite endpoint and 95% confidence intervals.
IVUS, intravascular ultrasound; MACE, major adverse cardiovascular events; maxLCBI$_{4mm}$, maximum 4mm lipid core burden index; MLA, minimal lumen area; NIRS, near-infrared spectroscopy; OCT, optical coherence tomography; RF-IVUS, radiofrequency IVUS; TCFA, thin-capped fibroatheroma; VH-IVUS, virtual histology IVUS

1.7.2 Treating vulnerable atherosclerotic plaques

Following the successful identification of plaques prone to precipitating an ACS prior to their rupture, it then becomes important to establish if any interventions may be performed to ameliorate or indeed negate this risk. Exclusion of the highest risk plaques from the coronary vascular bed is an attractive means of doing this, and has been explored in the PROSPECT ABSORB substudy of the PROSPECT II study (139). 182 patients with angiographically mild

(median stenosis 41.6%) vulnerable plaques (based on plaque burden ≥65%) were randomised to OMT ± PCI using a fully bioresorbable scaffold. These scaffolds are appealing for use in the prophylactic stenting of high-risk non-obstructive plaques given the expected neointimal hyperplasia, thickening the fibrous cap and thus rendering the plaque more stable, with complete resorption of the structure over time and avoiding long term adverse sequelae. However, subsequent to study enrolment, these stent designs had poor long term clinical results, owing to concern over increased device thrombosis and target lesion revascularisation, resulting in withdrawal from the market (151). Nonetheless, in PROSPECT ABSORB angiographic follow-up was completed at 25 months in 91.8% of patients, with a median clinical follow-up of 4.1 years. Lesions treated by bioresorbable scaffolds had significantly greater MLA, but similar lesion-related cardiovascular events and target lesion failure. However, this pilot study was not powered to explore clinical endpoints but does suggest safety of a primary invasive approach for treating vulnerable plaques. PREVENT (The Preventive Coronary Intervention on Stenosis With Functionally Insignificant Vulnerable Plaque) is another randomised controlled trial examining bioresorbable scaffolds or DES in addition to OMT versus OMT alone in patients with vulnerable plaque, that is ongoing and is powered for clinical events (NCT02316886). PECTUS (OCT-guided angioplasty of vulnerable plaques) was also due to investigate bioresorbable scaffolds in vulnerable plaque, but terminated early in 2017, after recruiting only 34 of the 500 planned patients, following withdrawal of the bioresorbable scaffold from the market (152). Table 1-4 below summarises the completed trials of local interventions to vulnerable atherosclerotic plaques. In addition, the randomised FAVOR V AMI trial plans to investigate the benefit of PCI for lesions with impaired coronary flow and increased radial wall strain (but without vulnerable plaque

imaging criteria), evaluating clinical outcomes up to five-years (ClinicalTrials.gov identifier: NCT05669222).

Study	Size	Design	Population	Therapy	Follow up	Primary endpoint	Outcome
PROSPECT ABSORB (2020) (139)	182	1:1 RCT of OMT alone vs BVS + OMT for an angiographically non-obstructive stenosis not intended for PCI, but with plaque burden ≥65%	Patients undergoing coronary angiography ± PCI with recent (<4 weeks) MI with 3 vessel NIRS-IVUS	PCI with bioresorbable scaffold	25 months	MLA at randomized non-culprit lesion site	3.0±1.0 mm^2 vs 6.9±2.6 mm^2 (least square means difference 3.9 mm^2 (3.3–4.5; p<0.0001)
PECTUS (2020) (152)	34 (500 planned)	1:1 RCT of OMT alone vs bioresorbable scaffold + OMT for 30-90% stenotic lesions with FFR≥0.80 and 2 of OCT plaque vulnerability features	Patients undergoing coronary angiography ± PCI for ACS	PCI with bioresorbable scaffold if 2 of 3 vulnerable plaque features: • lipid arc >90° • fibrous cap thickness <65 µm • plaque rupture/ thrombus formation	1 year	All-cause mortality, non-fatal MI, unplanned revascularisation	Halted early due to retraction from the market of bioresorbable scaffolds

Table 1-4. Completed prospective randomised controlled trials of local interventions for vulnerable plaques.

Prospective trials randomising patients with vulnerable plaques to local therapy with percutaneous coronary intervention (bioresorbable scaffolds or conventional drug eluting stents).
FFR, fractional flow reserve; MLA, minimal lumen area; OMT, optimal medical therapy; RCT, randomised controlled trial.

Aside from the aforementioned PREVENT trial that is due to report in 2024, there are multiple ongoing randomised studies exploring the utility of PCI to treat non-flowing limiting coronary stenoses with vulnerable plaque features. Table 1-5 below provides an overview of these ongoing trials. These studies will add needed clarity to any potential role of mechanical intervention to non-obstructive vulnerable lesions. However, it is obvious from Table 1-5 that each trial has its own individual definition of what constitutes a vulnerable plaque, which will require uniformity going forwards. In addition, the initial follow-up durations may be too short

in order to observe if there is a true difference between the arms, considering prophylactic therapy is being delivered, and longer follow-up may be required. Aside from conventional PCI with DES or bioresorbable scaffolds, no other clinical studies have explored the potential of other local plaque-directed therapies.

Study	Size	Design	Population	Therapy	Follow up	Primary endpoint
PREVENT (NCT02316886) (ongoing – results expected in 2024)	1,608	1:1 RCT of OMT alone vs PCI + OMT for >50% stenotic lesions with FFR>0.80	Patients undergoing coronary angiography ± PCI (symptomatic or asymptomatic)	**PCI with bioresorbable scaffold or DES, if 2 of 4 vulnerable plaque features:** • MLA <4 mm^2 • plaque burden >70% • max$LCBI_{4mm}$>315 • TCFA – OCT (fibrous cap thickness <65 μm and lipid arc>90°)/ VH-IVUS (≥10% confluent necrotic core with>30° abutting to the lumen in 3 consecutive slices)	2 years	Cardiac death, target vessel related MI, ischaemia-driven target vessel revascularisation, unplanned hospitalisation for angina.
INTERCLIMA (NCT05027984) (ongoing – first results expected in 2023 and to complete in 2025)	1,420	1:1 RCT of OCT vs physiology guided treatment of intermediate (40-70% stenosis) non-culprit lesions	Patients undergoing coronary angiography ± PCI for ACS	**OCT or FFR-guided PCI with DES, if:** **OCT arm** Fibrous cap thickness <75 μm plus ≥2 of 3 other OCT criteria: • MLA <3.5 mm^2 • lipid arc >180° • OCT defined macrophages **Physiology arm** iFR/ RFR ≤0.89 or FFR ≤0.80	2 and 5 years	Cardiac death and target vessel MI
COMBINE INTERVENE (NCT05333068) (ongoing – results expected 2026)	1,222	1:1 RCT of a PCI revascularisation strategy based FFR (with sham OCT) vs combined FFR and OCT assessment	Patients undergoing PCI with ≥2 target lesions (MI culprit lesion or >50% lesion where FFR will be performed) in different native vessels suitable for PCI	**PCI** **FFR arm** All lesions with FFR ≤0.80 **FFR + OCT arm** All lesions with FFR ≤ 0.75 + 1 of: • fibrous cap thickness ≤ 75 μm • ruptured plaque • plaque erosion with > 70% plaque burden or MLA <2.5 mm^2	2 years	Cardiac death, MI, clinically driven revascularisation
VULNERABLE (NCT05599061) (ongoing – results expected 2028)	600	1:1 RCT of PCI revascularisation strategy for intermediate lesions (40-69% stenosis) with FFR > 0.80+ OCT with findings indicative of	Patients with STEMI undergoing successful revascularisation and multivessel disease	OMT ± PCI	4 years	Target vessel failure (composite of: cardiovascular death, target-vessel related MI, target vessel revascularisation)

		vulnerable plaque				

Table 1-5. Ongoing prospective randomised controlled trials of local interventions for vulnerable plaques.

Prospective trials randomising patients with vulnerable plaques to local therapy with percutaneous coronary intervention (bioresorbable vascular scaffolds or conventional drug eluting stents).
FFR, fractional flow reserve; iFR, instantaneous wave free ratio; maxLCBI$_{4mm}$, maximum 4mm lipid core burden index; MLA, minimal lumen area; OCT, optical coherence tomography; OMT, optimal medical therapy; RCT, randomised controlled trial, RFR; resting full cycle ratio; STEMI, ST-segment elevation myocardial infarction; TCFA, thin-capped fibroatheroma; VH-IVUS, virtual histology IVUS

Coronary angiography with intravascular imaging followed by PCI is an expensive and relatively high-risk undertaking, especially when there is no strong evidence base for intervention to non-obstructive lesions at least at the present time. On the other hand, medical therapy may be a relatively better option to treat vulnerable plaques, although again, conclusive evidence or widespread adoption are lacking. Potential agents include lipid lowering agents as well as anti-inflammatory agents, such as colchicine or the anti-IL1β monoclonal antibody canakinumab (47). However, these anti-inflammatory agents have shown promise in treating ASCVD, rather than vulnerable atherosclerotic plaques per se. Moreover, whilst colchicine is now an emerging clinical treatment of ASCVD, canakinumab did not receive regulatory or guideline approval, related to a perceived lack of supportive data and cost effectiveness (153). LDL-lowering drugs including statins, ezetimibe and PCSK9 inhibitors have also been proposed to affect vulnerable plaque through reduced plaque burden and increased fibrous cap thickness, although the clinical efficacy of these therapies is likely mediated by LDL reduction rather than direct plaque effects (136). Indeed, statin therapy has been demonstrated to slow progression of coronary atherosclerosis, but with increased coronary artery calcification on CT, perhaps representing a more stable plaque

phenotype (154). Moreover, PCSK9 inhibition with evolocumab in the GLAGOV trial was the first study to demonstrate coronary plaque regression on IVUS, albeit with a relatively small effect size of -1.0% atheroma volume (95% CI, -1.8% to -0.64%; p<0.001), after 78-weeks of treatment (155).

Table 1-6 below summarises the prospective randomised controlled trials that have explored the effect of medical therapies (all of which are lipid-lowering agents) on plaque vulnerability factors, using NIRS-IVUS, OCT, or both, at baseline and at follow-up.

Study	Size	Population	Therapy	Follow up	Change in fibrous cap thickness (μm)	Change in maxLCBI$_{4mm}$
YELLOW (2013) (156)	87	Patients with multivessel CAD undergoing PCI + ≥ 1 non-target lesion	Standard of care vs Rosuvastatin 40mg OD	7 weeks	-	2.4 (–36.1 to 44.7) vs –149.1 (–210.9 to –42.9); p<0.01 (median, 95% CI)
EASY-FIT (2014) (157)	60	Patients with untreated dyslipidaemia, unstable angina and an untreated, non-culprit lesion identified by OCT	Atorvastatin 5mg OD vs Atorvastatin 20mg OD	1 year	19 (–1 to 48) vs 73 (28 to 113); p<0.001 (median, IQR)	-
HUYGENS (2022) (158)	161	Patients with NSTE-ACS and an untreated, non-culprit vulnerable plaque identified by OCT	Placebo + statin vs Evolocumab + statin	1 year	21.5 (10.9–32.1) vs 42.7 (32.4–53.1); p=0.02 (median, IQR)	-
PACMAN-AMI (2022) (159)	300	Patients undergoing PCI for acute MI and untreated, non-culprit lesions identified by NIRS–IVUS and OCT	Placebo + statin vs Alirocumab + statin	1 year	62.4 (46.2–78.5) vs 91.0 (73.0–108.9); p=0.01 (mean, 95% CI)	–37.6 (–57.4 to –17.8) vs –79.4 (–100.4 to –58.5); p=0.006 (mean, 95% CI)

Table 1-6. Randomised clinical trials of medical therapy for stabilisation of vulnerable plaques.

Adapted from Gaba P, Gersh BJ, Muller J, Narula J, Stone GW. Evolving concepts of the vulnerable atherosclerotic plaque and the vulnerable patient: implications for patient care and future research. Nature Reviews Cardiology. 2022 Sep 23:1-6.

maxLCBI$_{4mm}$, maximum 4 mm lipid core burden index; IVUS, intravascular ultrasound; NIRS, near-infrared spectroscopy; NSTE-ACS, non-ST-segment elevation acute coronary syndrome; OCT, optical coherence tomography.

Overall, these trials demonstrate increased fibrous cap thickness, accompanied by reduced lipid core maxLCBI$_{4mm}$ signal, with more intensive lipid-lowering therapies, representing more favourable, less vulnerable, plaque characteristics. Whether these changes at the plaque level will translate to a clinically meaningful reduction in cardiovascular events is not certain however, and will be hard to discern from the clear systemic benefits of the therapies at the patient level.

1.8 Molecular imaging of atherosclerotic plaque

Molecular imaging of various facets of atherosclerotic plaques, using targeted probes that localise to lesions and can be detected by imaging systems, has the potential to move beyond anatomical morphological plaque assessment and provide an understanding of plaque biological activity. Evaluating plaque biological activity becomes increasingly important when, for example, we consider that more inflammatory plaques are thought to harbour a more unstable phenotype, and thus could select patients for more intensive preventative therapies (67). Any of the previously discussed pathways that lead to plaque rupture or erosion could be targeted for molecular imaging agent development, such as MMP/ cathepsin activity, reactive oxygen species/ oxidised lipids, inflammatory cascades, neovascularisation, as well as apoptotic/ necrotic cellular processes (160).

Moreover, anatomic imaging, with intravascular NIRS-IVUS or OCT, or non-invasive modalities as discussed above, provide imaging correlates of some vulnerable plaque

features, yet many of the histopathologically recognised elements remain undetectable. This may be overcome using carefully selected and developed molecular probes. Of course, if suitable molecular targeting agents are developed, these can be further harnessed for other theranostic (a combination of therapeutic and diagnostic) purposes, such as potentially being a direct therapeutic agent themselves, or utilised as a targeting ligand for delivery of other therapeutic agents. Unfortunately, no molecular imaging platform for atherosclerosis has been successfully translated to routine clinical practice yet.

1.8.1 Requirements for successful molecular imaging of atherosclerosis

Probes for molecular imaging of atherosclerosis are dependent on three components: a targeting ligand; a signal generating moiety or other means of permitting detection; and finally, a suitable imaging system to detect the signal generating moiety. An ideal molecular imaging probe for clinical atherosclerosis will have the following attributes. Firstly, the targeting ligand must have biological and pathological relevance to plaque formation or vulnerability, but without biological activity itself. Secondly, a high SNR must be generated upon probe ligation, ideally with signal amplification (for example by chemical activation) with favourable pharmacokinetics (smaller internalisable molecules or peptides are often preferable). Thirdly, the ligand and imaging moiety can be readily synthesised without the requirement for complicated chemistry. Lastly, the agent is readily translatable, with scalability, biocompatibility and is free from toxicity (160).

1.8.2 Radionuclear-based molecular imaging

Radionuclear-based techniques using PET and SPECT are well suited to molecular imaging. PET in particular is an attractive modality, where it already performs an important role in

clinical oncological practice, owing to its high sensitivity to tracers, permitting detection in the picomolar range, as well as its deep tissue penetration, meaning that non-invasive imaging is readily feasible (see Table 1-1) (161). PET however is limited by its inherent poor spatial resolution, but hybrid imaging with high resolution CTCA permits PET signal co-localisation to coronary arterial beds, allowing the simultaneous generation of anatomical and functional plaque data. These nuclear techniques are also quantitative modalities, which is particularly useful in tracking disease processes over time.

A major drawback of PET imaging (particularly if combined with CT scanning), is the incurred radiation dose, which can be >10mSv (by comparison an invasive coronary angiogram typically conveys 2-6mSv) (162). However, radiation doses are expected to significantly reduce with ongoing technical improvements (161). The short isotope radiotracer half-life also often necessitates an onsite cyclotron for isotope generation, which poses logistical issues.

As with all modalities used for molecular imaging, the strength of the imaging technique is reliant on the quality of the molecular targeting agent. Examples of preclinical nuclear probes that have been developed for atherosclerosis imaging include ^{11}C-acetate, binding to fatty acid synthetase; [^{11}C]-(R)-PK11195, binding to macrophages via a translocator protein, and ^{99m}Tc-NC100692, targeting αvβ3 integrin that is important in angiogenesis and vascular inflammation (163).

Unlike other imaging modalities, molecular imaging of atherosclerosis with PET has been translated to humans, and has been performed in clinical studies, often harnessing probes that were initially developed for oncological purposes. Examples of these include ^{68}Ga-

DOTATATE (based on binding to the somatostatin receptor, that was initially developed for neuroendocrine tumours, however these receptors are also upregulated on the surface of activated macrophages) (164), as well as the more widely used ^{18}F-fluorodeoxyglucose (FDG) (based on vascular inflammation and metabolic activity, binding to glucose transporter-1) and ^{18}F-sodium fluoride (NaF) (based on vascular micro-calcification, binding to hydroxyapatite) tracers (165). Most recently, molecular imaging using ^{18}F-GP1 (a glycoprotein IIb/IIIa receptor antagonist) PET has been trialled in patients following an ACS, and was able to detect coronary thrombosis and identify culprit lesions (166).

1.8.3 Magnetic resonance-based molecular imaging

MRI-based techniques offer an ideal opportunity for the imaging atherosclerotic plaques, owing to its high contrast sensitivity, good spatial and temporal resolution and excellent tissue characterisation, coupled with iodine and ionizing radiation-free imaging. Sensitivity is lower, whilst resolution is far superior to nuclear techniques. There has been a rapidly emerging presence of cardiac MRI in clinical practice over recent years, yet there are significant hurdles that need to be overcome to permit satisfactory imaging of coronary arteries. These include cardiac and respiratory motion, prolonged scanning times as well the lack of sub-millimetre spatial resolution, which is required for coronary imaging. However, novel methods that permit coronary magnetic resonance angiography vessel wall imaging are currently in clinical translation (167).

Molecular magnetic resonance probes are broadly grouped into T1-shortening paramagnetic gadolinium-based agents and T2-shortening superparamagnetic iron-oxide-based agents. A plethora of plaque features have been targeted with MRI probes, including, but not limited to:

inflammation, the necrotic core, extra-cellular matrix and plaque rupture/ thrombosis (168). Examples of preclinical MRI molecular atherosclerosis agents are superparamagnetic iron oxides and ultrasmall superparamagnetic iron oxides, which are nanoparticles of iron oxide crystals coated in biocompatible dextran, that localise to macrophages, and Gd_4-TESMA, which binds to tropoelastin, a marker of impaired plaque elastogenesis (169). Briley-Saebo and colleagues developed their antibody fragments that target OSEs on LDL or oxidised phospholipids (discussed in the next section) as MRI molecular agents by incorporating them into gadolinium-containing micelles and evaluated *in vivo* localisation to atherosclerotic plaques using MRI in $ApoE^{-/-}$ mice. All targeted constructs accumulated within plaques, which was confirmed to be in the vicinity of lipid and macrophages on *ex vivo* confocal microscopy (170). In further translational steps, gadolinium micelles were exchanged to manganese micelles (171) and lipid-coated ultra-small superparamagnetic iron particles (172).

However, a major drawback of molecular imaging with MRI is the high dose of molecular probe required, owing to its poorer sensitivity than other techniques. As such, hybrid imaging with PET-MRI has been developed, to harness the advantages of each imaging modality, whilst avoiding the additional nephrotoxic contrast, ionizing radiation and potential for misalignment artefact with PET-CT (168).

1.8.4 Optical imaging-based molecular imaging

Optical imaging-based molecular imaging is an exciting and evolving field. Fluorescence imaging is very much in its clinical infancy, with no probe, or indeed method of detection, having been successfully translated to the clinical arena, except for in the ophthalmic assessment of retinochoroidal diseases. Optical molecular imaging relies on the detection of

a molecular targeting agent which has been conjugated with a NIR-emitting fluorophore. This is a promising technique, at least for preclinical research purposes, as whole-body fluorescence detection can be performed, for example with fluorescence molecular tomography (FMT), that permits the simultaneous detection of different molecular probes, which have been labelled with NIRF agents that excite/ emit in different aspects of the NIR spectrum. Thus, multiplexing different targeting agents is possible, providing a more comprehensive and tailored analysis of plaque biological activity, depending on the molecular probes chosen.

For clinical translation, it is much more likely that intravascular, rather than whole-body, imaging will be performed, with much greater sensitivity and spatial resolution. Anatomical co-registration of fluorescence is required in order to localise signal to structures, and hybrid NIRF-IVUS (110) and NIRF-OCT (111) catheters have been developed for this purpose, as discussed earlier. NIRF imaging, compared to visible light fluorescence imaging, has significant advantages, including reduced background signal owing to less light absorption by neighbouring structures (for example, haemoglobin), resulting in increased tissue penetration and improved sensitivity with a high target: background ratio (TBR) (106). As mentioned above, NIRAF imaging has been investigated in humans, where plaque autofluorescence (at 633nm) co-localised with OCT, related to fibroatheroma and plaque rupture (112).

There are multiple preclinical NIRF molecular agents that have successfully identified different facets of atherosclerotic plaques. Examples include commercially available probes, such as MMPSense (a caged probe that activates in the presence of MMP 2, 3, 7, 9, 12, and

13; pro-inflammatory endopeptidases implicated in atherogenesis) and Prosense (an activatable probe that is optically silent until cleavage by cathepsins, located within macrophage lysosomes) (both PerkinElmer, Massachusetts, USA). These are available with different conjugated fluorophores. Indocyanine green is a near-infrared agent (excitation 780/ emission 830nm), which, although it does not target a specific molecular pathway, localises to lipid and macrophages in areas of increased endothelial permeability (for example, atherosclerotic plaques). It has already been used experimentally by Verjans and colleagues to image carotid atherosclerosis in humans, via intravenous injection prior to carotid endarterectomy, with indocyanine green accumulating in all specimens versus saline control *ex vivo*. On histological analysis, increased signal related to areas with significant burden of macrophages, lipid and intraplaque haemorrhage (173). Indocyanine green has already been approved by the US Food and Drug Administration for ophthalmological NIRF applications. As will be discussed later, the Haskard-Khamis laboratory has developed LO1, a monoclonal murine IgG antibody that recognises MDA-LDL, and later the LO1 humanised Fab fragment, for NIRF imaging of atherosclerosis via labelling with VivoTag-S-750 (PerkinElmer, Massachusetts, USA), a NIR-emitting fluorophore (174). Other preclinical NIRF molecular targets in atherosclerosis include fibrin deposition, microcalcification and impaired endothelial permeability (106).

1.9 Targeted antibodies in atherosclerosis

1.9.1 Rationale for antibody-based oxidised LDL targeted constructs in atherosclerosis

Targeting atherosclerotic lesions with ligands that may be directly atheroprotective, or carry tagged imaging reporters or therapeutic cargo, is a very attractive means of imaging and

treating ASCVD. Monoclonal antibodies or antibody fragments are ideal for this purpose, given their relatively small size and high antigen specificity. Unlike monoclonal antibodies that recognise a single epitope, polyclonal antibodies are derived by different B cell lineages and bind to different epitopes on a single antigen. As a result, they have high binding affinity and multiple different immunoglobulins can recognise a single antigen. This can potentially result in signal amplification, which is ideal for molecular targeting. However, the lack of specificity can result in cross-reactivity. Moreover, the lack of structural homogeneity can be problematic for use as a clinical imaging or therapeutic agent, where construct specificity, characterisation, integrity and reproducibility is paramount (175). Recombinant monoclonal antibodies, although expensive to manufacture, do not suffer from clonal drift or gene deletion that can affect hybridoma produced monoclonal antibody function.

Therefore, using recombinant monoclonal antibodies/ antibody fragments that bind oxLDL is an ideal means of targeting at-risk atherosclerotic lesions, given the central role of oxLDL and necrotic core development in plaque vulnerability to rupture. The probe may localise to plaques via the leaky endothelial intimal layer or via the vaso vasorum, where it will either remain extracellular, or it may get actively endocytosed (with oxLDL) by resident macrophages, with subsequent progression to foam cells and eventually the necrotic core. Thus, the construct may preferentially target atherosclerotic lesions with greater macrophage burden and larger necrotic cores – a key feature of vulnerable plaques.

1.9.2 Targeted antibodies against oxidised LDL in atherosclerosis

Monoclonal antibodies that target various OSEs on oxLDL have been developed as both assays quantifying circulating levels as a plasma biomarker of oxLDL burden, and for

targeted molecular *in vitro*/ *in vivo* imaging. The murine monoclonal antibody 4E6 was the first to be developed by Holvoet and colleagues, recognising a conformational epitope on ApoB-100, resulting from the substitution of lysine residues to aldehydes (176, 177). Circulating levels measured by ELISA were found to be associated with Lp(a), a major carrier of oxLDL in plasma, as well as a range of CVD and cardiovascular risk factors, including acute and stable CAD (176), metabolic syndrome (177) and obesity (178, 179). Mercodia (Uppsala, Sweden) subsequently developed a commercial ELISA based on 4E6 for the quantification of plasma oxLDL. Further antibody development has centred on oxidative modifications on LDL, rather than the ApoB protein fragment. These include FOH1a/DLH3, a murine monoclonal antibody directed against oxidised phosphatidylcholine (180); EO6, a murine monoclonal antibody against phosphorylcholine, the hydrophilic moiety of phospatidylcholine, as well as MDA2, a murine monoclonal antibody to MDA-lysine residues (179, 181, 182). However, given the heterogenous nature of different potential oxidative modifications on oxLDL and disparate assay development, assays are not easily comparable and utilise different units of measurement (15,17).

Furthermore, in a translational step, IK17 was discovered, a human monoclonal Fab against MDA-LDL that was isolated from a phage display antibody library from a patient with high anti-MDA-LDL antibody levels. Human antibodies should be superior to murine alternatives for clinical purposes, with less immune system induction and an absence of human anti-murine antibody production. IK17 was found to bind to oxLDL but not native LDL, inhibit phagocytosis of oxLDL by macrophages, and localise to atherosclerotic plaques when injected intravenously in LDL-$R^{-/-}$ mice (26). Moreover, IK17 was found to reduce foam cell formation and atherosclerotic lesion formation when injected intraperitoneally in LDL-$R^{-/-}$ mice

lacking the ability to make anti-human antibodies (27). Following on from these *in vitro* mechanistic studies, IK17 fragments were used to target both lipid-coated ultra-small superparamagnetic iron particles and manganese micelles for the *in vivo* MRI detection of atherosclerotic lesions in ApoE$^{-/-}$ and LDL-R$^{-/-}$ mice, respectively (171, 172).

The most potentially promising translational move came with the testing of MLDL1278A, a monoclonal recombinant IgG1 anti-MDA-LDL antibody in the Goal of Oxidized LDL and Activated Macrophage Inhibition by Exposure to a Recombinant Antibody (GLACIER) multicentre randomised double-blind placebo-controlled clinical trial (183). 147 patients with stable atherosclerosis and evidence of plaque inflammation on FDG-PET/CT were randomised to MLDL1278A (administered by single or multiple infusions) or placebo along with continued OMT and followed up at 12 weeks with FDG-PET/CT to assess the effect on arterial FDG uptake, as well as inflammatory plasma biomarkers. However, there was no effect on imaging or blood biomarker endpoints (including CRP). Potential explanations for this negative result include an unfavourable patient population, with relatively low background inflammatory activity (recruited patients had stable atherosclerosis), the effectiveness of the standard of care medical therapy (which included statins), the relatively short follow up period, as well as perhaps suboptimal endpoint selection (183). Further clinical research with this humanised monoclonal antibody, now called Orticumab, is ongoing.

More recently, the protective autoantibody A12 (against autoantigen ALDH4A1) has been identified as novel targeted antibody in atherosclerosis, using proteomic analysis of the antibody repertoire of high-fat fed LDL-R$^{-/-}$ mice that showed plaque reactivity. ALDH4A1 is a mitochondrial matrix dehydrogenase that regulates the degradation of essential amino acid

proline, which is involved in the regulation of vascular homeostasis. Circulating levels of ALDH4A1 were found to be elevated in both mice and humans with atherosclerosis, and infusion of A12 attenuated murine atherosclerotic lesion formation (184).

As has been mentioned above and will be discussed in greater depth later in this chapter, the Haskard-Khamis group has developed murine IgG LO1 and humanised LO1Fab which recognise MDA-LDL, as oxLDL-directed molecular targeting agents (174). This prior work forms the foundation for the nanoparticle studies in this thesis.

1.9.3 Engineered antibody fragments

Antibodies possess a modular structure, meaning that different components or domains can be altered, with the creation of customised immunoglobulins, without necessarily affecting overall antibody antigen recognition. Antibody structure can be adapted to modify a plethora of antibody physiochemical characteristics, for example, half-life and distribution, as well as affinity, avidity, valency, and tissue penetration. One of the most common antibody engineering steps is fragmentation, resulting in smaller antibody fragments.

Figure 1-5 provides an overview of IgG structure and different related engineered antibody fragments. Fab fragments are the most common engineered fragment, formed of one arm of the ‘Y’-shaped IgG structure, thus retaining the antigen binding domain, but without the Fc fragment. Fab fragments were first created via antibody cleavage using papain, digesting the hinge peptide bond, creating two Fab fragments (2× 50kDa) and one Fc fragment (50kDa). However, Fab' (55kDa) with a free sulfhydryl group, is often more desirable for further conjugation and modification. These fragments are created by digestion of a full IgG by

pepsin, to form a $F(ab')_2$ (110kDa) fragment, which comprises two antigen-binding regions joined at the hinge region. Reduction of this hinge region results in two Fab' fragments. However, both Fab and Fab' suffer from reduced affinity versus full IgG antibodies, given their monovalency (185).

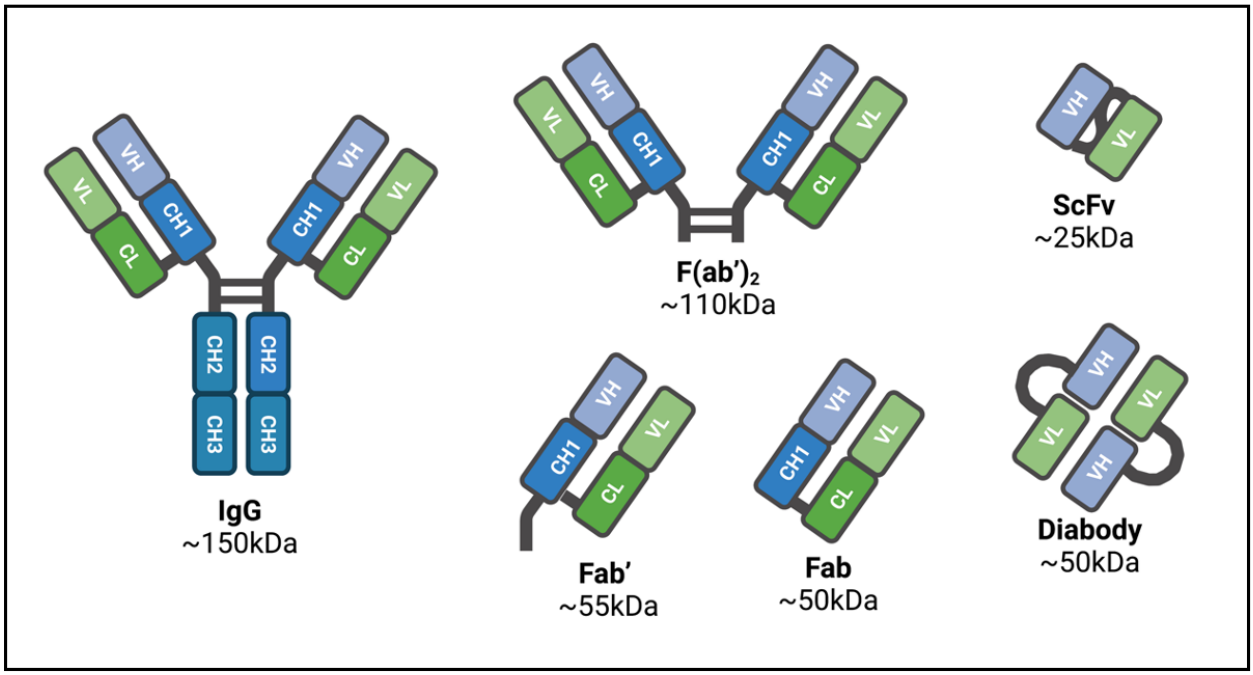

Figure 1-5. IgG and antibody fragment structure.

Key antibody fragments that are discussed in this thesis. Blue and green subunits represent heavy and light chains respectively. Made using Biorender.

Nonetheless, the production of Fab fragments has key advantages, including and most importantly, greater tissue penetrance owing to their small size, as well as often easier manufacture, given the lack of glycosylation and small size versus a full IgG, enabling expression to be performed in prokaryotic rather than mammalian expression systems. Moreover, the lack of an Fc region results in loss of antibody effector function, as well as anti-

Fc mediated antibody detection, which is desirable for their use as solely molecular targeting agents. However, the absence of the Fc fragment can result in reduced fragment thermostability and Fc receptor-mediated recycling, resulting in much shorter *in vivo* half-lives, as well as increased aggregation during manufacture processes (185).

Additional antibody fragments include single-chain variable fragments (scFv)s (25kDa) and diabodies (50kDa), each of which may have certain benefits for molecular targeting. Both structures are inherently less stable than their Fab counterparts, owing to the loss of stabilisation between the VH/VL and CH1/CL interfaces (186). ScFvs are recombinant fusion structures, formed from the variable regions of the light and heavy chains joined by a flexible linker, resulting in just the antigen-binding domains in a single polypeptide, without any constant regions. The small size of these structures can result in even greater tissue penetrance and very short half-lives, which may be optimal to ensure a high TBR for molecular imaging. Further antibody engineering can render diabodies, which are paired scFv fragments, with the variable light chains non-covalently bound to each other through complementary regions via a pentameric glycine-rich linker to form dimerised bivalent molecules (2× VH and VL chains). This results in two opposite antigen binding sites, serving to increase binding avidity. Moreover, scFvs with different specificities may be combined, producing bivalent bispecific structures with two different antigen binding sites, which may have additional benefits for detection of two simultaneous antigens. Even more sophisticated antibody engineering can render tri- and tetra-valent immunoglobulin fragments, as well as more stable molecules with a central disulphide bridge. As with Fabs, very short *in vivo* half-lives can be expected, given their small size and lack of Fc receptor-mediated recycling. If

necessary, various elements can be conjugated to their structure, such as polyethylene glycol (PEG), or fused to an albumin binding protein, in an attempt to adapt these properties (186).

1.9.4 Whole antibody versus antibody fragment-based targeting of atherosclerosis

As can be readily appreciated above, antibody structure can be modulated to affect a vast array of properties, not least through engineering into antibody fragments. These fragments may carry certain advantages over whole antibodies for molecular targeting applications; however, fragmentation does not come without its drawbacks. The principal benefit in molecular targeting is reduced molecular size and weight, resulting in greater tissue penetrance and accessibility to cryptic epitopes, which is obviously of utmost importance. Other benefits include a reduced potential for immunogenicity and, particularly for imaging applications, shorter half-lives, whereby background signal is reduced (owing to clearance from the circulation), and more expedient imaging is permitted. However, these advantages are caveated by more difficult development, the potential loss of beneficial antibody-mediated responses as well as reduced antigen avidity.

Table 1-7 below provides an overview of the basic antibody fragment *in vivo* characteristics when used as targeting agents in humans. Smaller constructs clearly have reduced blood half-lives and are removed from the circulation via renal rather than hepatic clearance (187).

Antibody fragment	Composition	Molecular weight (kDa)	Valency	Blood $t_{1/2}$	Blood clearance
IgG	$(VH + CH1\text{-}3 + VL + CL)_2$	~150	Bivalent	1-3 weeks	Hepatic
F(ab')$_2$	$(VH + CH1 + VL + CL)_2$	~110	Bivalent	8-10 hours	Hepatic

Fab'	VH + CH1 + VL + CL	~55	Monovalent	12-20 hours	Renal
Fab	VH + CH1 + VL + CL	~50	Monovalent	12-20 hours	Renal
scFv	VH + VL	~28	Monovalent	2-4 hours	Renal
Diabody	$(scFv)_2$	~50	Bivalent	3-5 hours	Renal

Table 1-7. Antibody fragment properties.

Different engineered antibody fragments and their typical properties in humans. Table adapted from Freise AC, Wu AM. In vivo imaging with antibodies and engineered fragments. Molecular immunology. 2015 Oct 1;67(2):142-52.

Additionally, antibody fragments, as compared to whole monoclonal antibodies, may permit the binding of a greater amount of antibody for a fixed amount of antigen, owing to their smaller size, as well as the opportunity for greater antigen accessibility with less steric hinderance imposed by an already bound antibody. As such, when considering targeting agents for nanoparticles as will be developed in this thesis, it would be expected that Fab fragments would offer significant advantages over complete monoclonal antibodies.

1.10 Nanoparticle-based targeting for imaging and therapeutics in atherosclerosis

1.10.1 Nanoparticle background

Nanoparticles are structures of 10-100nm (in at least one dimension, although sometimes extending to 500nm by some definitions) in size with evolving use in contemporary medical practice. Current clinical uses include imaging contrast agents (188) and drug or gene delivery, particularly in the field of oncology (189). Of note, lipid nanoparticle approaches have been used to develop two successful COVID-19 vaccines (190). Nanoparticles have three key shared features that govern their physical properties: 1) high mobility in free state;

2) extremely large surface areas; 3) exhibition of quantum behaviours. Significant advantages of nanoparticles over other techniques for targeted delivery are their customisability with a wide spectrum of possible manipulations, with various effects on their biochemical or physical properties. Such modifications can be utilised to optimise controlled drug carriage and release as well as site-specific targeting (191). Additional advantages of nanoparticle-mediate drug delivery include encapsulation to avoid off-target effects and controlled drug release kinetics.

Various organic or inorganic nanoparticle structures have been designed, as outlined in Figure 1-6 below.

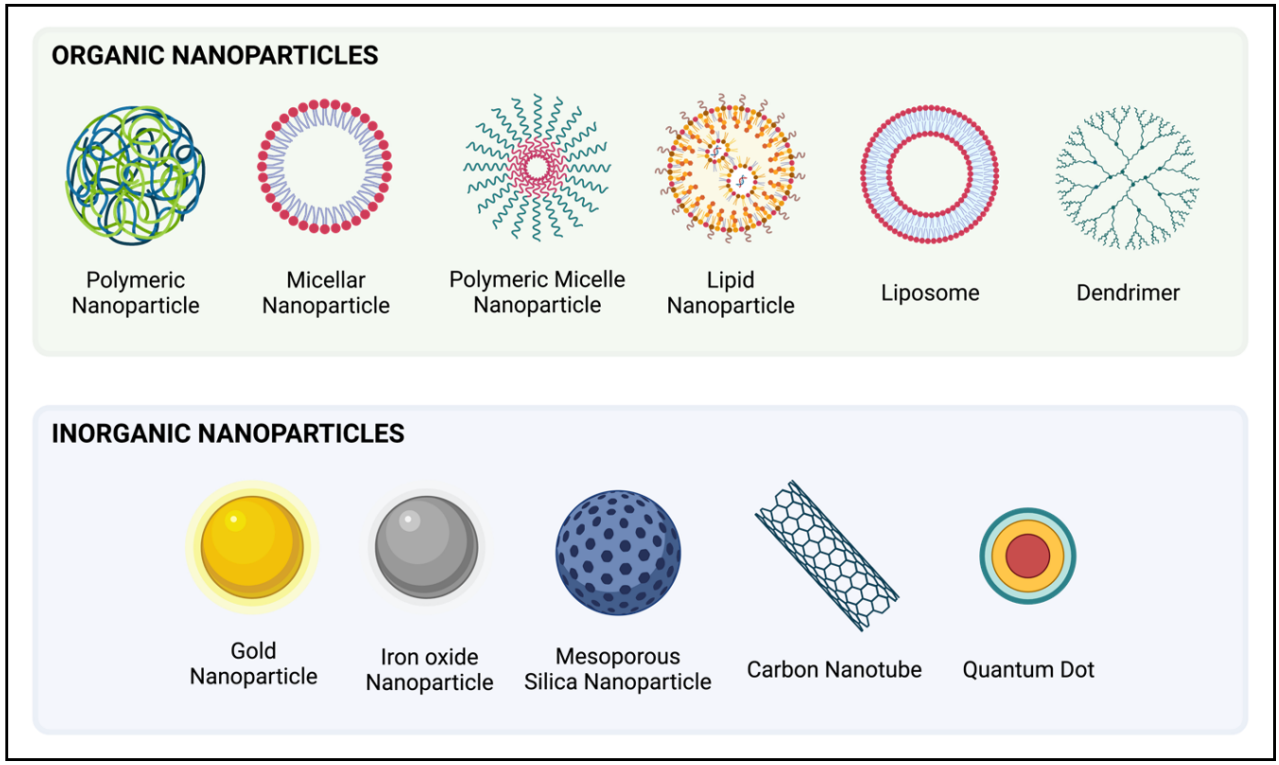

Figure 1-6. Major organic and non-organic nanoparticle classes.

Made using Biorender.

Nanoparticle *in vivo* properties are essentially governed by their composition, surface properties, flexibility, as well as size and shape (192). Each nanoparticle design has its individual advantages and drawbacks, including production costs, degree of required engineering as well as ease of modification for site-specific targeting or payload delivery. Inorganic nanomaterials generally have greater construct stability than carbon-containing organic nanomaterials and are usually hydrophilic and possess good biocompatibility. Conversely, organic nanomaterials are often biodegradable and non-toxic, meaning that they function very well as nanocapsules (carrying a cargo within their central cavity) releasing their payload in living systems upon construct break down, making them ideal agents for molecular targeting applications (193).

Organic nanoparticles may be synthesised from a variety of materials, however lipids and synthetic polymers predominate, with polymeric micellar nanoparticle formulations of polylactic-co-glycolic acid (PLGA) and PEG among the most widely used (192). PLGA, formed by copolymerisation of two cyclic dimers of glycolic and lactic acid via ester bonds, is an ideal basis for nanoparticle development, given its biocompatibility, complete biodegradability, and that it can self-assemble into micelles. However, the use of PLGA nanoparticles is limited by their relatively large diameter (150-200nm), very poor water solubility and rapid uptake by the liver and spleen *in vivo*. To counter these drawbacks, PLGA may be combined with PEG. PEG is hydrophilic, and therefore forms an outer shell with the hydrophobic PLGA in the core, increasing particle stability. Moreover, PEGylation renders the structure undetectable by the immune system, increasing circulating blood half-life and

permitting on-target binding (194). In addition, PLGA-PEG nanoparticles can be readily functionalised by the addition of reactive groups on the outer PEG chains.

1.10.2 Targeted nanoparticles in atherosclerosis

Particular advantages of applications of nanomedicines in atherosclerosis will include targeted therapy to the disease site (i.e., the plaque, perhaps with precision tailored therapeutic agents), increased efficacy of the therapeutic agent with fewer off-target effects and adverse events, as well as the ability to combine diagnosis and therapy. However, despite the above advantages, no nanoparticle-based approaches have made the transition from bench to bedside in the field of CVD. Examples of trialled constructs include organic nanoparticles designed for the delivery of various statin formulations to sites of interest, with resultant reductions in atherosclerotic lesion size, intimal macrophages, MMP activity and disrupted fibrous caps (195, 196). Other nanoparticle constructs include ultra-small superparamagnetic iron oxide-based nanoparticles, liposomes, or lipid-based nanoparticles. Various payloads have also been tested, including imaging contrast agents, drugs, stem cells or gene therapies (197).

One of the most successful nanoparticle-based approaches for CVD that has been tested clinically were liposomal nanoparticles encapsulating prednisolone. In a randomised placebo-controlled trial, infusion of the nanoparticle encapsulated prednisolone led to improved prednisolone pharmacokinetics and successful delivery to their target, as shown by *ex vivo* analysis of macrophages isolated from iliofemoral plaques of patients undergoing vascular surgery; however, prednisolone did not reduce plaque inflammation or permeability (198). This study suggests promise in an untargeted nanoparticle approach, where perhaps another

therapeutic cargo may be able to demonstrate therapeutic efficacy, whilst potential adverse off-target effects need to be considered.

Different nanoparticle targeting ligands have also been explored. These include targeting inflamed endothelial cells via adhesion molecules (such as anti-VCAM-1 or anti-platelet endothelial cell adhesion molecule antibodies) or macrophages via scavenger receptors (such as anti-lectin-like oxidised receptor-1 and anti-CD36 antibodies). Other approaches include targeting activated platelets with glycoprotein IIb/IIIa receptor ligands; MMPs or cathepsins via hydroxamic acid-based agents; or stabilin-2, a transmembrane protein expressed in endothelial cells and macrophages that is upregulated in atherosclerotic plaques, via targeting peptides (197). Passive nanoparticle targeting is also possible, relying on increased vascular permeability at sites of inflammation, however this will likely result in greater off-target effects.

The nanoparticle drug delivery system is likely to be of most importance with gene-based agents and drugs with severe systemic side effects, particularly in ASCVD, where there is a potential very broad, otherwise well, patient population that could benefit. For example, in CANTOS, the randomised-controlled trial of canakinumab in ASCVD, 25.4% of all excluded patients (1,873 out of 7,377 patients) were excluded owing to active tuberculosis or risk factors for tuberculosis reactivation. These patients accounted for 10.7% of all those screened for trial inclusion (47). Thus, if canakinumab could be administered without the risk of systemic immune modulation, there is a large target population who may benefit. Conversely, potential limitations to the widespread use of nanotherapies for atherosclerosis

include the cost of largescale production, currently unestablished clinical safety and long-term stability (199).

1.10.3 PLGA nanoparticles in atherosclerosis

As touched on above, PLGA-based nanoparticles have been assessed preclinically to image or treat atherosclerosis, with and without targeting and cargo, predominantly in murine models. I conducted a systematic review to gain a full appreciation of the breadth of the literature regarding PLGA nanoparticles in atherosclerosis, using the following Medical Subject Headings (MeSH) search terms:

- (("polylactic acid polyglycolic acid copolymer" **OR** ["polylactic" ***AND*** "acid polyglycolic" ***AND*** "acid" ***AND*** "copolymer"]) **OR** "polylactic acid polyglycolic acid copolymer" **OR** "plga")

  AND

- ("nanoparticle ***OR*** "nanoparticles")

  AND

- ("atherosclerosis" ***OR*** "atherosclerоses")

I initially performed the search on 22/10/22 without language or date restrictions and carried out an update on 24/10/2023. The final search yielded 59 results, of which 52 were included in the final analysis. Seven studies were excluded (five were reviews, two were not directly related to atherosclerosis). Table 1-8 below provides a summary of the results.

No.	Study	Nanoparticle	Size	Target	Cargo	Model	Effect
1	**Di Mascolo et al. (2013)** (200)	PLGA-PVA	~200 nm	Untargeted (endothelial cells)	Rosiglitazone (peroxisome proliferator-activated receptor-γ agonist)	LDL-R$^{-/-}$ mice with 12-week high fat diet	↓ proinflammatory gene expression (IL1β, MCP-1)
2	**Zhang et al. (2015)** (201)	PLGA-PEG	156.6 ± 10.3 nm	Untargeted (endothelial cells)	GW3965 (liver X receptor agonist)	LDL-R$^{-/-}$ mice with 16-week high fat diet	↓ plaque macrophage content ↓ MCP-1 expression ↓ TNF-α ↑ ABCA1 gene induction
3	**Sanchez-Gaytan et al. (2015)** (202)	PLGA-HDL mimetic	88 to 156 nm	Untargeted (HDL mimetic)	N/A – NP delivery only	ApoE$^{-/-}$ mice with 15-week high fat diet	N/A – NP delivery demonstrated
4	**Nakashiro et al. (2016)** (203)	PLGA	NR	Untargeted (endothelial cells)	Pioglitazone (peroxisome proliferator-activated receptor-γ agonist)	ApoE$^{-/-}$ mice with 8-week high fat diet	↓ macrophages ↓ disrupted/ buried fibrous caps ↓ MMP/ cathepsin activity ↓ inflammatory cytokine expression
5	**Koga et al. (2016)** (196)	PLGA	200 nm	Untargeted (endothelial cells)	Pitavastatin	ApoE$^{-/-}$ mice with 8-week high fat diet	↓ macrophages ↓ disrupted/ buried fibrous caps Therapeutic arteriogenesis
6	**Zhao et al. (2017)** (204)	PLGA-dextran sulphate reconstituted HDL	156.5 ± 0.5 nm	Scavenger Receptor A1	Atorvastatin	*In vitro* only	↓ IL-6, TNF-α ↑ IL10
7	**Zhang et al. (2017)** (195)	Hyaluronan-reconstituted HDL-PLGA	138.2±2.3 nm	Endothelial cells with ↑ permeability (HDL mimetic), overexpressing CD44 receptors in plaques	Simvastatin	Atherosclerotic rabbits with 8-week high fat diet	↓ lesion size ↓ intimal macrophages ↓ MMP activity
8 9	**Imanparast et al. (2016)** (205) **Imanparast et al. (2017)** (206)	PLGA- mZD7349 peptide (VCAM-1 ligand)	233±18 nm	VCAM-1	Simvastatin	*In vitro* only	↑ phosphorylated endothelial nitric oxide synthetase
10	**Koenig et al. (2017)** (207)	PLGA-film on layered stents	N/A	Layered on stent	siRNA against ICAM-1	*In vitro* only	↓ ICAM-1

11	**Li et al. (2017)** (208)	PEG-PLGA-RGD (ligand to integrin αvβ3 receptor) USS-stimulated cargo release	221.6 ± 0.9 nm	Integrin αvβ3 receptor	dexamethasone acetate	*In vitro* only	↑ cell viability with oxLDL-induced cell oxidative injury
12	**Dou et al. (2017)** (209)	PLGA with β-cyclodextrin	204 nm	Untargeted	Rapamycin	ApoE$^{-/-}$ mice with 12-week high fat diet	N/A (proof of concept)
13	**Le et al. (2017) [Peripheral Arterial Disease]** (210)	PLGA	90-150 nm	Untargeted (endothelial cells)	Antioxidant and nitric oxide donor	In vitro only	↑ endothelial cell viability ↑ angiogenesis
14	**Ameruoso et al. (2017) [Alzheimer's Disease]** (211)	PEG-PLGA	184.19 ± 15.06 nm	Macrophages in the presence of amyloid-β fibrils	Curcumin (anti-inflammatory)	In vitro only	↓ IL-1β, IL-6, TNF-α via amyloid-β fibres
15	**Ochin et al. (2018)** (212)	PEG-PLGA-PVA surfactant	42-63 nm	Untargeted (endothelial cells)	Berberine Chloride (anti-PCSK9)	In vitro only	↓ PCSK-9 mRNA ↑ intracellular LDL-r mRNA
16	**Zhang et al. (2018)** (213)	Tocopheryl-PEG-liposome-PLGA	99 nm	Untargeted (Endothelial cells - lipophilic)	Simvastatin	Atherosclerotic rabbits with 8-week high fat diet	↓ intima-media thickness ↓ oxidative stress level (dihydroethidium fluorescence)
17	**Ye et al. (2019)** (214)	Perfluorohexane with dextran sulfate - PLGA	258.60−374.63 nm	Scavenger Receptor-A	N/A – Imaging (USS, MRI)	ApoE$^{-/-}$ mice with 8-12-week high fat diet	N/A (imaging)
18 **19** **20**	**Chen et al. (2013)** (215) **Wu et al. (2019)** (216) **Wu et al. (2020)** (217)	EGFP-EGF1-PLGA	106.08 ± 1.33 nm	Vascular smooth muscle cells (via tissue factor)	silencing chemokine (C-C motif) receptor 2	In vitro only	silenced target gene in the atherosclerotic macrophages
21	**Wang et al. (2019)** (218)	PLGA-superparamagnetic nano-silica ➔ ↑ bioavailability	100-200 nm	Untargeted (endothelial cells)	Quercetin (flavonoid)	In vitro only	N/A (proof of concept)

22	**Wang et al. (2019)** (219)	PLGA cloaked with erythrocyte vesicles ➔ biomimetic nanocomplexes (reduce nonspecific clearance)	97.4 ± 2.4 nm	Untargeted (endothelial cells)	Rapamycin	ApoE$^{-/-}$ mice with 10-week high fat diet	↓ lesion size ↓ necrotic core size ↓ macrophage/ smooth muscle cell ↓ MMP-9
23	**Esfandyari-Manesh et al. (2020)** (220)	PLGA-Maleimide-PEG	183 nm	Stabilin 2 (glycoprotein in endothelial cells in atherosclerotic plaques)	Imatinib	In vitro only	N/A (proof of concept)
24	**Om et al. (2020)** (221)	PLGA (↑ bioavailabilty)	120-220nm	Untargeted (endothelial cells)	Diosmin (from citrus fruit, flavonoid with anti-inflammatory effect, low water solubility)	Diabetic rat model	↑ anti-inflammatory effect (↓ angiotensin II, PAI-1, TGF-β, NFκB)
25	**Yang et al. (2020) [Aortic stenosis]** (222)	PLGA-PEG NPs coated with platelet membrane glycoproteins	144.3 ± 6.2 nm	Aortic valve	N/A – NP delivery only	ApoE$^{-/-}$ mice with 36-week high fat diet	N/A – NP delivery demonstrated
26	**Chen et al. (2020)** (223)	PLGA-PEG decorated with carbohydrate-based targeting moieties e.g. mannose, galactose	136 ± 10.9 nm	Macrophages	Enhanced green fluorescent protein mRNA	In vitro only	↑ mRNA transfection with coated NPs
27	**Wang et al. (2020)** (224)	PLGA NPs embedded within the shells of the magnetic NP coated microbubbles	267.5 ± 35.6 nm	Stented coronary arterial segments	Paclitaxel	Ex vivo only	N/A – NP delivery demonstrated
28	**Chen et al. (2020)** (225)	PLGA NPs loaded with a a β-galactosidase-activatable nanoprobe	153.2 ± 6.5 nm	Senescent cells and vasculature	N/A	ApoE$^{-/-}$ mice with 8-week high fat diet	N/A – NP delivery demonstrated
29	**Yi et al. (2020)** (226)	PLGA NPs with adsorbed ApoB derived P210 peptides on surface	Not reported	Vaccine based delivery	Retinoic acid (as immune enhancer)	ApoE$^{-/-}$ mice	↑ P210 specific IgM/ ↑ P210 specific IgG autoantibodies ↓ IFNɣ
30	**Khang et al. (2020)** (227)	Tetrazine-labelled glycoprotein 1b α conjugated PLGA NPs	173 ± 64 nm	Injured endothelium	Pretargeting with tetrazine-labelled NPs, followed by transcyclo-octene labelled HUVECs	In vitro and ex vivo only	Successful delivery of HUVECs at sites of arterial injury
31	**Wang et al. (2021)** (228)	Macrophage membrane coated PLGA NPs	95.69 nm	Activated endothelial cells	Rapamycin (mTORi)	ApoE$^{-/-}$ mice with 10-week high fat diet	↓ atherosclerosis progression
32	**Yin et al. (2021)** (229)	PLGA	92.69 ± 3.1 nm	Vascular endothelial cells	N/A	ApoE$^{-/-}$ mice with 12-week high fat diet	↑ TNFα ↑ IL6 ↑ macrophage → foam cell

33	**Gao et al. (2021)** (230)	PLGA NPs containing contrast Fe3O4 and perfluoropentane and coated with specific plaque-targeted peptides	289.54 ± 1.69 nm	Scavenger Receptor A	N/A	$ApoE^{-/-}$ mice with 16-week high fat diet	↑ macrophage apoptosis Disaggregation of activated platelets on atherosclerotic plaques
34	**Pillai et al. (2021)** (231)	PLGA	140–450 nm	Untargeted	Curcumin and Bioperine PLGA	In vitro only	↑ macrophage → foam cell ↑ inflammatory cell mediators
35	**Katsuki et al. (2022) [Abdominal aortic aneurysm]** (232)	PLGA	159 nm	Monocytes/ macrophages	Pitavastatin	$ApoE^{-/-}$ mice with 8-week high fat diet	↓ aneurysm formation ↓ MCP-1 ↓ macrophage accumulation
36	**Li et al. (2022)** (233)	PLGA NPs coated with CD47 and Integrin α4/β1 modified macrophage membranes	Not reported	Endothelial cells	Colchicine	$ApoE^{-/-}$ mice with 6-week high fat diet and left carotid surgical constriction	↓ plaque lipid size ↑ plaque stability
37	**Shen et al. (2022)** (234)	PLGA NPs coated with U937 (human monocytes) cell membranes	112.7 ± 0.4 nm	Vascular endothelial cells	ginsenoside and catalase	$ApoE^{-/-}$ mice with 8-week high fat diet	↓ ICAM-1, TNF-α and IL-1β ↓ plaque size
38	**Leal et al. (2022)** (235)	PLGA functionalised with an antibody to VCAM-1	196 ± 14 nm	Activated vascular endothelial cells	miRNA-124a and atorvastatin	In vitro only	↓ IL-6, TNF-α, ROS ↓ macrophage LDL accumulation
39	**Chen et al. (2022)** (236)	H_2O_2 responsive PLGA-PEG NPs	205.2 ± 1.9	Untargeted	VEGF and nerve growth factor	Mouse ischaemic hindlimb model	↓ collagen deposition ↓ muscle injury
40	**Zhou et al. (2022)** (237)	Platelet biomimetic PLGA NPs with USS-targeted microbubble destruction	287nm	Atherosclerotic plaques through platelet plaque adhesion	Rapamycin	$ApoE^{-/-}$ mice with 12-week high fat diet	NP delivery demonstrated
41	**Li et al. (2022)** (238)	PLGA NPs	152.4 ± 0.4 nm	αvβ3 receptor with low pH sensitivity	Rapamycin	$ApoE^{-/-}$ mice with 12-week high fat diet	↓ atherosclerosis progression
42	**Fang et al. (2022)** (239)	PLGA-PEG NPs	274.9 nm	integrin αvβ3 targeted and cathepsin k responsive	Rapamycin	$ApoE^{-/-}$ mice with 12-week high fat diet	↓ atherosclerosis progression ↓ local and systemic inflammation
43	**De Negri Atanasio et al. (2022)** (240)	PLGA NPs functionalised with immunouteroglobin-1 -PEG	217-265 nm	Fibronectin	Bevacizumab (mAb against VEGF)	In vitro only	N/A

44	**Craciun et al. (2022)** (241)	PLGA NPs coated on angioplasty balloon	161.9 ± 26.6 nm	Diseased peripheral arterial segments	Quercetin	In vitro only	Successful NP and drug delivery
45	**Zhang et al. (2023)** (242)	PLGA/PLA NPs	~60-150 nm	Untargeted (macrophage lysosomes)	N/A	ApoE$^{-/-}$ mice with 8-week high fat diet	↓ plaque apoptosis, necrotic core formation, and cytotoxic protein aggregates ↑ fibrous cap formation
46	**Liu et al. (2023)** (243)	PLGA/PVA NPs	116.4 nm	Untargeted – aimed for increased Atorvastatin oral bioavailability	Atorvastatin	Wistar rats with 1-month high-fat diet	↑ Atorvastatin absorption and ↓ lipid levels
47	**Zhu et al. (2023)** (244)	PLGA-PEG NPs	144.0 ± 0.212 nm	scavenger receptors A-I targeting peptide	ABCA1 upregulator	ApoE$^{-/-}$ mice with 8-week high fat diet	↓ foam cell formation ↓ cholesterol foam cell deposition ↓ atherosclerosis
48	**Dash et al. (2023)** (245)	PLGA NPs	197.7 nm	Untargeted	Atorvastatin-Curcumin with chitosan as a drug release modifier	Swiss Albino mice fed a high-fat diet for 12-weeks	↓ oxidative stress ↓ foam cell formation ↓ atherosclerosis
49	**Groner et al. (2023)** (246)	PLGA-PEG NPs	85 nm	Untargeted	Pioglitazone	In vitro only	↑ drug effect
50	**Huang et al. (2023)** (247)	PLGA NPs	220 nm	M2 macrophage membrane coating	TRIM24, an E3 ubiquitin ligase of a Trim family protein	ApoE$^{-/-}$ mice with 8-week high fat diet	Polarization of M2 macrophages ↓ atherosclerosis
51	**Karami et al. (2023)** (248)	PLGA NPs	292 nm	Monocyte membrane coating	Gliclazide	New Zealand white rabbits with 8-week high-fat diet	↓ inflammation ↓ atherosclerosis ↑ M2/M1 macrophage polarization
52	**Li et al. (2023)** (249)	PLGA NPs coated onto a stent	99.83 ± 19.76 nm	Platelet membrane coating	Rapamycin	Sprague-Dawley rats	↓ smooth muscle cell proliferation ↑ endothelial healing after stent implantation

Table 1-8. Systematic review summary table of research studies exploring PLGA-based nanoparticles in atherosclerosis.

In total 52 studies are included in the final synthesis (seven studies were excluded – five were reviews whilst two did not relate directly to atherosclerosis). Where studies are incremental to previous studies already included in the systematic review, the studies feature within the same row.
ABCA1, ATP binding cassette subfamily A member 1; ApoE, apolipoprotein E; CD, cluster of differentiation; HDL, high-density lipoprotein; ICAM-1, Intercellular Adhesion Molecule 1; IL, interleukin; IFN, interferon; LDL-R, low-density lipoprotein receptor; NF-κB, Nuclear factor kappa-light-chain-enhancer of activated B cells; NP, nanoparticle; MCP, monocyte chemoattractant protein; MMP; matrix metalloproteinase; oxLDL, oxidised low-density lipoprotein; PAI-1, plasminogen activator inhibitor-1; PCSK9, Proprotein convertase subtilisin/kexin type 9; PEG, polyethylene glycol; PLA, polylactic acid; PLGA, poly(lactic-co-glycolic acid); PVA, Polyvinyl alcohol;

TNF, tumour necrosis factor; ROS, reactive oxygen species; TGF-β, transforming growth factor-β; VCAM, vascular cell adhesion molecule; VEGF, vascular endothelial growth factor

As can be appreciated in Table 1-8, there was an initial relatively slow publication rate, with 21 of the studies published 2013-2019; however, this then has accelerated, and 31 studies were subsequently published in the following three years to 2023. A significant proportion of the studies did not utilise a targeting ligand for nanoparticle delivery, but often aimed for delivery to endothelial cells or macrophages. Nanoparticle dimensions ranged widely, spanning 50-400nm, however most frequently ranged between 100-200nm.

Whilst some studies used *in vitro* models of nanoparticle delivery alone, the majority utilised murine models of atherosclerosis, predominantly with the ApoE$^{-/-}$ mouse model. Common therapeutics for nanoparticle-mediated delivery were statins, anti-diabetic agents, anti-proliferative as well as anti-inflammatory agents. Frequent *in vivo* study endpoints were a reduction in atherogenesis and plaque development, as well as a more favourable inflammatory cytokine profile.

One early successful study by Mulder and colleagues developed hybrid HDL-PLGA nanoparticles, relying on the intrinsic natural targeting of HDL to atherosclerotic plaque macrophages. Utilisation of a PLGA core led to controlled drug release properties and permitted cargo versatility (202). Earlier work in the group had previously demonstrated that statin-loaded HDL mimetic nanoparticles inhibited atherosclerotic plaque inflammation in ApoE$^{-/-}$ mice (250). Another innovative approach that has been explored in some studies is coating angioplasty balloons or stents with PLGA-based nanoparticles comprising a cargo of

anti-inflammatory or anti-proliferative agents, in an attempt to reduce in-stent restenosis (207, 241, 249).

Recently, Yi and colleagues developed a nanoparticle-based vaccine for atherosclerosis, using PLGA nanoparticles with ApoB derived peptide 210 (as an autoantigen to activate an antigen-specific atheroprotective immune response, based on earlier work in the Nilsson laboratory (251)) adsorbed on the surface as a targeting ligand, with encapsulated retinoic acid as an immune enhancer, to increase the efficacy of the P210 vaccine. Accordingly, in ApoE$^{-/-}$ mice, the authors demonstrated a reduction in atherosclerotic lesion size accompanied by increased specific P210 IgM, versus mice immunised with the non-nanoparticle based P210 vaccine (226). However, to date, the delivery of an imaging or therapeutic agent via PLGA-based nanoparticles with a specific targeting ligand against oxLDL has not been explored.

1.11 Work leading up to this project

The foundation for this PhD project has been many years in the making. Research in the Haskard laboratory exploring the role of IgG autoantibodies against oxLDL, using hybridomas from the spleen of an unimmunised elderly high fat-fed LDL-R$^{-/-}$ mouse, led to the discovery of LO1 in 2012. This monoclonal IgG3κ antibody selectively reacted with copper-oxLDL, and even more strongly with MDA-LDL, but not native unmodified LDL, on ELISA. Binding was found to be time and concentration-dependent and unaffected by LDL trypsinisation. Moreover, LO1 could bind to its antigen in tissue, and bound oxLDL deposits using immunocytochemistry of murine and human atherosclerotic lesions (252). Earlier work in the Haskard laboratory had also identified the importance of IgM in atherogenesis, where high

fat-fed mice that were deficient in both serum IgM and the LDL-R developed significantly larger and more complex atherosclerotic plaques with greater cholesterol crystal formation than mice only deficient in LDL-R. Interestingly, levels of IgG antibodies against oxLDL decreased in the double knock-out model, suggesting homeostatic compensatory utilisation and consumption of IgG in the absence of IgM (86).

Much subsequent work in the Khamis-Haskard laboratory has centred around two key research interests. The first explores the relationships between circulating oxLDL, as well as IgG and IgM anti-oxLDL antibodies, with ASCVD, investigating their potential utility as clinically meaningful biomarkers. The second explores the development of LO1 as a tool for the translational study of atherosclerosis, harnessing LO1 for molecular targeting of atherosclerosis.

1.11.1 The relationship between anti-MDA-LDL antibodies, atherosclerotic plaque and cardiovascular events

To explore this research aim further, a sandwich ELISA was developed to detect MDA-LDL in serum using LO1 (253). Alongside the LO1 sandwich ELISA, indirect ELISAs were designed to detect circulating IgG and IgM antibodies to MDA-LDL. Subsequently, these assays have been performed using blood from various human populations, both free-from and with, CVD at baseline. These assays have been shown to be sufficiently sensitive to detect dynamic changes in blood levels in response to oxidative stress, for example with major vascular or CABG surgery (253, 254). Both of these studies demonstrate homeostatic consumption of anti-MDA-LDL antibodies with these systemic stressors, likely via binding to their abundant antigen in the bloodstream, forming complexes, and being cleared from the

circulation by the reticuloendothelial system. However, the impact of exercise, as a cellular stressor, on anti-MDA-LDL antibody levels in patients with significant CAD, before and after PCI, has not been well studied.

In the population studies, both IgG and IgM anti-MDA-LDL antibodies have been shown to reflect protection from incident CVD on long term follow-up (91, 255). The protective associations between CVD and IgM anti-oxLDL antibodies has been demonstrated in multiple studies by other groups, whilst the relationship with IgG is less distinct and still requires further clarification (90). Moreover, in a potentially mechanistic step, we have shown that serum IgM anti-MDA-LDL antibodies relate inversely to atherosclerotic necrotic core size in humans as assessed using NIRS-IVUS (255). Thus, we have provided a potential link whereby having a larger circulating reservoir of IgM anti-MDA-LDL antibodies relates to smaller necrotic cores in atherosclerotic plaques at the lesional level, and to less CVD at the patient level. However, to date, this relationship at the plaque level has only been demonstrated with one invasive imaging modality, in a relatively small study, where a further large corroborative study, ideally with a non-invasive modality, would be ideal.

1.11.2 LO1 development

There have been significant developments in this research aim, focusing on the molecular targeting of oxLDL. Firstly, a NIRF derivative of LO1 was developed via conjugation of a NIR-emitting reporter (termed LO1-750), via maleimide chemistry. After demonstration of retention of LO1 binding to its antigen in the vicinity of macrophages on immunohistochemical analysis of human, mouse and rabbit atherosclerotic plaques, binding was confirmed with staining of *ex vivo* murine atherosclerotic aortic tissue. LO1-750 proceeded to *in vivo* study,

which demonstrated selective uptake in the aortic arch and major branches of high fat-fed LDL-R$^{-/-}$ mice versus control IgG and wild type mice, using quantitative FMT co-localised with micro-CT. Extensive *ex vivo* validation confirmed binding to atherosclerotic lesions in the vascular sub-endothelial space. Further experiments identified that *in vivo* injected LO1-750 could discern more advanced from less advanced atherosclerotic lesions, and also led to the development of LO1-750 for *in vivo* intravascular catheter-based rabbit atherosclerosis studies (174).

Since then, further research in the Khamis laboratory has seen the development of humanised fragments of LO1 (Fab and scFv). Humanisation aims to prevent the development of human anti-mouse antibodies which may prevent repeat administration with clinical translation. Fragmentation, as discussed above, aims to create smaller constructs that retain antigen affinity, to improve lesion penetration and reduce the TBR for *in vivo* imaging studies. These fragments, particularly given their smaller size, can then be harnessed as targeting ligands for other vehicles, such as nanoparticles. To date, humanised LO1Fab has shown impressive retention of function *in vitro* versus LO1 and has been successfully developed for *in vivo* fluorescence study via conjugation of a NIRF reporter, termed LO1Fab-750 (S Pandey's thesis), and thus will play a key role in the nanoparticle development in this thesis. Using these antibody fragments as targeting ligands for nanoparticle-mediated *in vivo* delivery will further broaden their possible theranostic implications, with greater imaging payload delivery, as well as therapeutic agent delivery, a possibility.

1.11.3 Preclinical modelling of atherosclerosis

As can be seen above, much work in the Haskard-Khamis laboratory has utilised *in vivo* animal studies to demonstrate successful probe localisation to atherosclerotic plaques, following *in vitro* studies and with comprehensive *ex vivo* validation. However, as reviewed above in *Section 1.6*, experimental modelling of atherosclerosis provides an imperfect representation of the complex human disease process, with each animal model having various advantages and drawbacks. Alongside the significant ethical considerations and involved costs, we as a research community should be seeking alternatives to animal models wherever possible, as we strive to replace, reduce and refine our experimental animal practices (135).

1.12 Aims and hypotheses of this PhD

My aims were to test the hypotheses that is possible to:

- identify relationships between oxLDL and antibodies to oxLDL with non-invasively assessed atherosclerotic plaque characteristics, as well as the assess the dynamic relationship between antibodies and exercise in coronary artery disease.

- target oxLDL-rich atherosclerotic plaque with antibody-based constructs that facilitate lesion identification and future delivery of local therapies.

- develop a pump-perfused amputated human limb model that can be utilised as a novel experimental model for molecular targeting in atherosclerosis.

Chapter 2

Materials and Methods

CHAPTER 2 – MATERIALS AND METHODS

2.1 Antibodies used during this thesis

Primary antibody specificity	Company (ID)	Host species	Species reactivity	Mono-/ polyclonal	Dilution	Conjugate	Application in thesis
ApoB	Abcam (ab20898)	Goat	Human	Poly	1:2000	Biotin	ELISA
ApoB	Abcam (ab7616)	Goat	Human	Poly	1:2000	-	ELISA
IgM	SouthernBiotech (9022-08)	Mouse	Human	Mono	1:2000	Biotin	ELISA
IgG	SouthernBiotech (9042-01)	Mouse	Human	Mono	1:2000	-	ELISA
IgG-CH1	Thermo Fisher Scientific (11496548)	-	Human	Mono	1:100 (IHC) 1:1000 (ELISA)	Biotin	IHC, ELISA
PEG	Abcam (190652)	Rabbit	-	Mono	1:500	-	ELISA

Table 2-1. Primary antibodies used during this thesis.

ELISA, enzyme-linked immunosorbent assay; IHC, immunohistochemistry.

Secondary antibody specificity	Company (ID)	Host species	Species reactivity	Mono-/ polyclonal	Dilution	Conjugate	Application in thesis
Ig	Dako (P0161)	Rabbit	Mouse	Poly	1:2000	Horseradish peroxidase	ELISA
Ig	Abcam (ab205718)	Goat	Rabbit	Poly	1:1000	Horseradish peroxidase	ELISA
Ig	Thermo Fisher Scientific	Goat	Mouse	Poly	1:400	Biotin	IHC

Table 2-2. Secondary antibodies used during this thesis.

ELISA, enzyme-linked immunosorbent assay; IHC, immunohistochemistry.

2.2 Oxidised LDL and anti-oxidised LDL antibodies as biomarkers of atherosclerosis

My involvement in this study was to be design the study, plan, and perform the ELISAs and carry out initial statistical analysis. Some of the ELISAs were carried out with research technician support under my supervision. Final and detailed statistical analysis was provided through collaboration with Dr Amit Kaura (SCOT-HEART substudy) and Dr Matthew Shun-Shin (ORBITA substudy), both Imperial College London, UK.

2.2.1 Scottish COmputed Tomography of the HEART (SCOT-HEART) substudy

2.2.1.1 Study background

The Scottish COmputed Tomography of the HEART (SCOT-HEART) study was a multicentre open-label prospective randomised controlled trial that assessed the role of CTCA in patients with chest pain (ClinicalTrials.gov identifier: NCT01149590) (96). Patients were recruited

from rapid access chest pain clinics across Scotland and randomised 1:1 to standard care ± CTCA. The primary study outcome was the proportion of patients diagnosed with angina secondary to CAD at 6-week follow-up. Long-term health outcomes were also collected from the Information and Statistics Division of the National Health Service Scotland, with case review of health records as appropriate.

The rationale behind the study was to evaluate the effect of CTCA on the management and outcomes of patients referred to outpatient cardiology services with chest pain that was suspected to be due to CAD. This study is of particular importance given the increasing and evolving role that CTCA has in the diagnosis of CAD, particularly in the UK, where the National Institute for Health and Care Excellence guidance now recommends CTCA as a first-line investigation for patients presenting with suspected stable angina (256). Subsequently, in part related to the impressive outcomes of the SCOT-HEART trial detailed below, CTCA has seen an expanding role within best practice guidelines, where CTCA is the only non-invasive imaging modality with a Class 1A recommendation within the American College of Cardiology/ American Heart Association joint committee guidelines for diagnosis of chest pain (257).

The primary study findings have been published, reporting an increased certainty of chest pain diagnosis due to CAD (relative risk [RR] 1.79, 95% CI 1.62–1.96; p<0.0001) with CTCA. There was also a trend for a lower frequency of angina diagnosis (RR 0.93, CI 0.85–1.02; p=0.1289) and lower fatal or non-fatal MI rate at a median 1.7 (range 0.1–4.1) years of follow-up (26 versus 42, HR 0.62, 95% CI 0.38–1.01; p=0.0527) (96). The long-term outcomes have subsequently been reported – at a median 4.8 (range 3–7) years: 48 (2.3%) versus 81 (3.9%)

patients had experienced a fatal or non-fatal MI in the CTCA and standard care arms respectively (HR 0.59, 95% CI 0.41–0.84; p=0.004). Concomitantly, there were more prescriptions for anti-anginal and cardiovascular preventative therapies, but no significant increase in coronary angiography or revascularisation (258).

In a post hoc study, semi-automated quantitative plaque-level analysis was performed, differentiating atherosclerotic lesions into calcified, non-calcified and low-attenuation plaque with corresponding plaque volumes. Burden of low-attenuation plaque was found to be the strongest predictor of fatal or non-fatal MI, withstanding correction for clinical cardiovascular risk score, coronary artery calcification score (CACS) or coronary artery stenosis. A 4% low-attenuation plaque burden threshold for fatal or non-fatal MI was identified following receiver operator characteristic analysis, with a HR of 4.65 (95% CI 2.06–10.5; p<0.001) (95).

2.2.1.2 Study protocol

A total of 4,146 patients were recruited to the SCOT-HEART trial, with 2,073 randomised into each trial arm. Participants were recruited from specialist cardiology chest pain clinics and underwent standard of care investigations as per local clinical protocols, including stress electrocardiography, stress imaging and invasive coronary angiography and were randomised to standard of care ± CTCA.

2.2.1.2.1 Inclusion criteria

Patients aged 18–75 years old and referred by a primary care physician to a cardiology chest pain clinic with stable suspected angina.

2.2.1.2.2 Exclusion criteria

Exclusion criteria were inability to undergo CT scanning, renal failure, allergy to iodinated contrast media, known pregnancy, ACS within the preceding three months or an inability to give informed consent.

2.2.1.2.3 Randomisation

Randomisation was performed 1:1 each trial arm with minimisation to ensure balance for all major cardiovascular risk factors.

2.2.1.2.4 CT scanning

Participants underwent both non-contrast CT and contrast enhanced CTCA. Tube voltage, current and contrast volume were adjusted based on body mass index.

CTCA images were assessed by at least two trained observers with excellent intra- and inter-observer agreement, as reported previously (259). CACS was assessed on non-contrast CT using the well-validated Agatston scoring method (260). Degree of coronary stenosis was visually assessed and reported as either normal (unobstructed), non-obstructive (<70% in major epicardial segments or <50% in left main stem) or obstructive (≥70% or ≥50% in the left main stem). The number of coronary arteries with obstructive disease was also assessed (1, 2 or 3-vessel disease).

Clinical cardiovascular risk assessment was provided by the ASSIGN (Assessing cardiovascular risk using SIGN guidelines) score. This cardiovascular risk score identifies people who are likely to develop CVD over the following 10 years, including risk from social

deprivation. Importantly, it has been calibrated to the Scottish population and is superior to the Framingham risk score at cardiovascular risk discrimination in Scotland (261, 262).

2.2.1.3 Quantitative plaque analysis

Semi-automatic quantitative evaluation of atherosclerotic plaques was performed by a trained assessor (Autoplaque, Version 2.5, Cedars-Sinai Medical Center) (95). Excellent interobserver variability has also been previously demonstrated using this technique (263). Briefly, quantitative analysis was performed for patients with CACS >0 or with ≥1 segment of obstructive or non-obstructive disease. Vessel wall, lumen and plaque constituents were automatically identified, as was narrowest area stenosis in the region, with manual adjustment as required. Plaque volumes were measured for calcified plaque, non-calcified plaque, low-attenuation plaque (attenuation of <30 Hounsfield Units (94)) and total plaque. Percentage plaque burden for each plaque subtype was then computed by dividing the relevant plaque volume by vessel volume of the region assessed.

2.2.1.4 Blood sampling

Blood specimens were obtained at the time of CTCA scanning in one centre (Edinburgh Imaging Facility). In total, 830 patients had available blood samples for analysis, who therefore comprised the study population for this project, as demonstrated in the consort diagram, Figure 2-1, below.

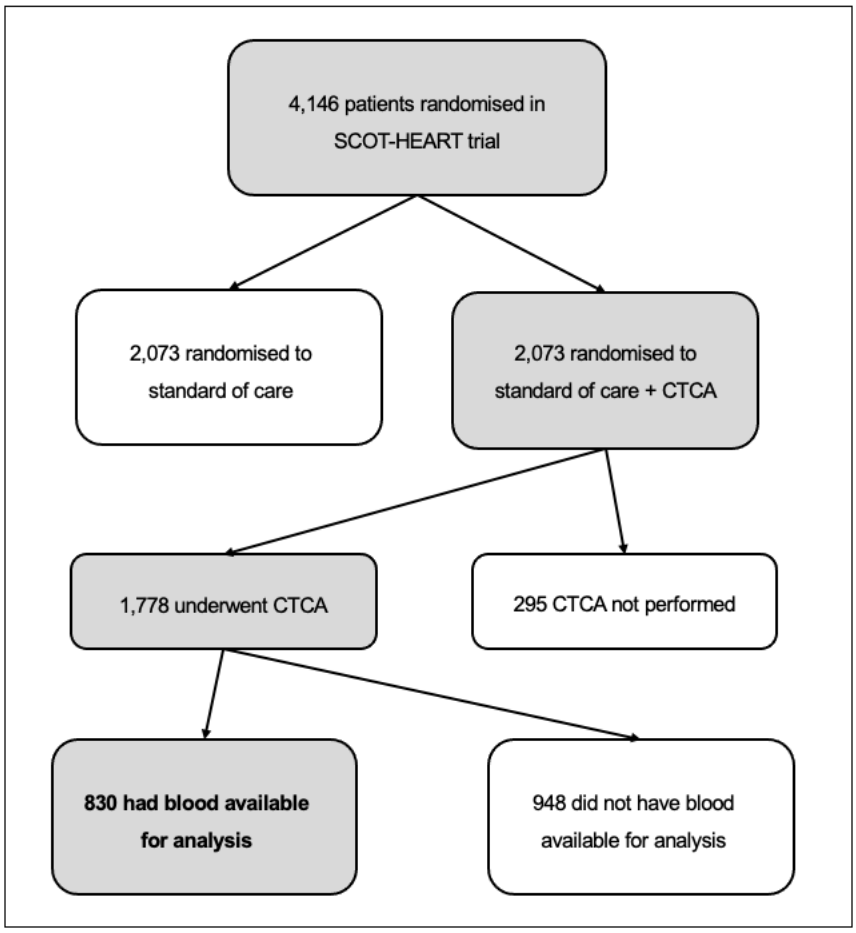

Figure 2-1. Consort diagram for SCOT-HEART substudy.

CTCA, Computerised tomography coronary angiography.

2.2.1.5 Ethical approvals

The original SCOT-HEART study protocol conformed to the Declaration of Helsinki and was approved by the local ethics committee. All participants provided and written informed consent.

2.2.1.6 Statistical analysis

Continuous variables were presented as mean ± standard deviation (SD) or median with interquartile range (IQR), depending on skew of the data. Categorical variables were presented as numbers with percentages.

Values obtained from ELISA analyses (protocols described on page 129) were blank subtracted (sample optical density [OD] minus the mean OD of the plate-specific blank wells that included all reagents except samples). All measurements were performed in duplicate. Concentrations of MDA-LDL and ApoB were derived by interpolation from log transformation of OD values onto a sigmoidal, four-parametric logistic curve using GraphPad Prism 8 (La Jolla, California, USA). Raw blank-subtracted OD values were used for anti-MDA-LDL antibodies.

Statistical analysis comparing antibody concentrations with clinical or CT characteristics was performed using R version 4.0.3 (R Foundation for Statistical Computing, Vienna, Austria). Measured biomarkers were divided into tertiles with the lowest tertile used as reference, as performed previously (255). Log transformation of CACS was performed for analysis given its skewed distribution (264). A multinomial logistic regression model was used to evaluate the relationship between antibody levels and different outcomes, adjusted for ASSIGN cardiovascular risk score. Separate odds ratios (OR) and 95% CI were calculated for the non-obstructive disease and obstructive disease groups, comparing each with the reference group of no disease. In patients with obstructive disease, ORs were also calculated for the 2-vessel disease and 3-vessel disease groups, comparing each with the reference group, 1-

vessel disease. The ORs were adjusted for the ASSIGN cardiovascular risk score, which was modelled using a restricted cubic spline with four knots.

Plaque subtype burdens across antibody tertiles were assessed in an unadjusted linear regression model (Trend model 1) and an adjusted model with the inclusion of the ASSIGN cardiovascular risk score (Trend model 2). The analysis was replicated for low-attenuation plaque with a predefined cut-off of 4% (95). Adjusted restricted cubic splines with four knots were also used to display these associations with antibody concentrations on a continuous scale. Splines were used in the regression model as the assumption of linearity between antibody concentration and plaque subtype burden was not satisfied. Splines transform the explanatory variable (antibody level) by splitting the range of values in intervals and fitting a separate curve in each interval. The spline is defined so that the overall resulting curve is smooth and continuous. The points that delimit the intervals are called knots. Preliminary investigation suggested that four knots should be used to model antibody levels in the restricted cubic spline analyses. A statistically significant difference was defined as a two-sided p value <0.05.

2.2.2 Objective Randomised Blinded Investigation with optimal medical Therapy of Angioplasty in stable angina (ORBITA) substudy

2.2.2.1 Study background

PCI, as outlined in Chapter 1 (page 60), in the stable (non-ACS) setting, is principally performed for angina relief. Largescale multicentre randomised controlled trials have been conducted in attempt to discover a potential prognostic effect of elective PCI on future MI or

mortality. Most notably, these are the Clinical Outcomes Utilizing Revascularization and Aggressive Drug Evaluation (COURAGE) (265) and International Study of Comparative Health Effectiveness With Medical and Invasive Approaches (ISCHEMIA) (7) trials, both of which randomised patients with stable CAD and angina/ inducible ischaemia to OMT ± revascularisation. However, despite 15 year-follow up of the COURAGE trial (266) and objective evidence of moderate/ severe ischaemia coupled with contemporary PCI/ CABG practice in the ISCHEMIA trial, there was no evidence of any prognostic benefit with revascularisation in either study. Previous meta-analysis of trial data had confirmed these findings (267); however, a more recent meta-analysis of 25 trials and 19,806 patients has suggested a degree of reduction in cardiac mortality with PCI (RR 0.79, 95% CI 0.67–0.93; $p<0.01$), with differences to earlier studies attributed to longer follow-up duration (118).

Nonetheless, current consensus and clinical practice is that PCI for stable CAD is performed to improve symptoms, and as such establishing if there is any true symptomatic benefit of PCI should therefore be paramount. To this end, and given that all previous trials of angina improvement with PCI were unblinded, as well as that the amelioration of chest pain is a subjective endpoint with the potential for a significant placebo effect, the Objective Randomised Blinded Investigation with optimal medical Therapy of Angioplasty in stable angina (ORBITA) trial (ClinicalTrials.gov identifier: NCT02062593) was designed and conducted (268). Accordingly, the ORBITA study randomised patients with severe single vessel CAD to PCI or placebo procedure and was powered for the primary endpoint of improvement in exercise time.

2.2.2.2 Study protocol

A total of 200 patients were randomised in the ORBITA trial (105 assigned to PCI, 95 to placebo procedure). Patients were approached and recruited following diagnostic coronary angiography. Following enrolment, patients entered a 6-week medical optimisation phase, where anti-anginal medical therapy was introduced and doses optimised. Patients then underwent baseline pre-randomisation assessment, which included quality of life questionnaires, cardiopulmonary exercise testing (CPET) and dobutamine stress echocardiography (DSE). The blinded procedure then took place, followed 6-weeks later by a follow-up assessment (like the pre-randomisation assessment), followed thereafter by unblinding. Dual antiplatelet therapy was maintained for both groups until unblinding at the end of the trial (where upon it was ceased for the placebo procedure group).

2.2.2.2.1 Inclusion criteria

Eligible patients were aged 18–85 years old with angina (or equivalent symptoms) and at least one angiographically significant lesion (≥70%) in a single vessel that was suitable for PCI.

2.2.2.2.2 Exclusion criteria

Exclusion criteria were significant coronary stenosis (≥50%) in a non-target vessel, left main stem disease, chronic total coronary occlusions, presentation with ACS, previous CABG surgery, contraindications to DES, severe valvular disease/ left ventricular systolic impairment, moderate-severe pulmonary hypertension, life expectancy less than 2 years and inability to give informed consent.

2.2.2.2.3 Randomisation and masking

During the ORBITA trial, on the day of the blinded procedure, patients underwent invasive physiological assessment (which was blinded to the operator), and then were sedated with auditory isolation and randomised 1:1 to each trial arm without stratification or blocking. In those allocated to the revascularisation arm, PCI was performed, aiming for complete revascularisation, followed by a final invasive physiological assessment. In those allocated to the placebo arm, patients remained sedated for at least 15-minutes prior to catheter withdrawal.

2.2.2.3 Exercise protocol and blood sampling

Blood samples were obtained on the day of pre-randomisation assessment, prior to exercise (timepoint P1) and 3-hours after exercise (timepoint P2). At post-randomisation assessment (6-weeks following the PCI or placebo procedure) further blood tests were obtained: before (timepoint P3) and 3-hours after (timepoint P4) exercise (see Figure 2-2 below). Exercise consisted of a CPET, performed with the QUARK CPET breath-by-breath metabolic measurement system (COSMED, Rome, Italy) during both pre- and post-randomisation assessments. Blinded physiologists and physicians performed all exercise tests. The test was stopped due to the development of limiting symptoms (angina, shortness of breath or fatigue), heart rhythm abnormalities, significant blood pressure changes or marked ST-segment deviation (≥0.20 mV associated with typical angina or in the first stage of exercise).

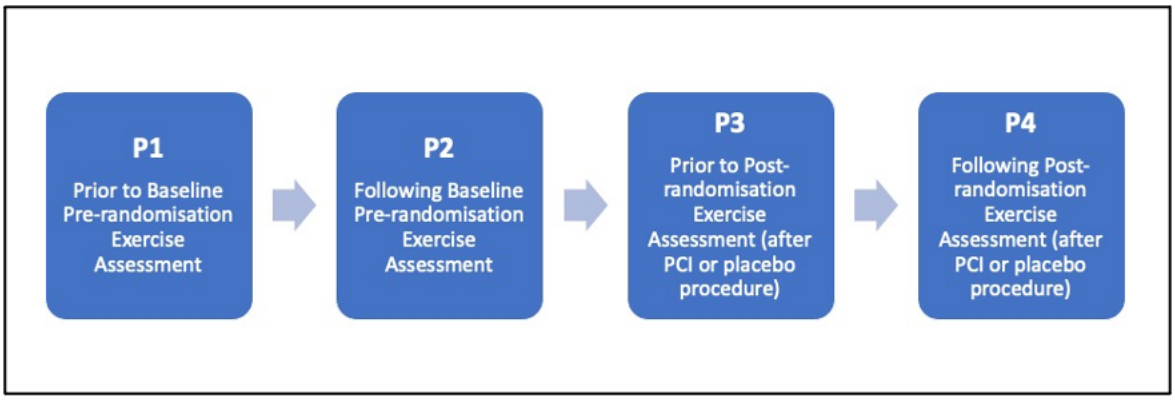

Figure 2-2. Blood sampling timepoints in the ORBITA Study.

Modified from Hartley A, Shun-Shin M, Caga-Anan M, Rajkumar C, Nowbar AN, Foley M, Francis DP, Haskard DO, Khamis RY, Al-Lamee RK. The Placebo-Controlled Effect of Percutaneous Coronary Intervention on Exercise Induced Changes in Anti-Malondialdehyde-LDL Antibody Levels in Stable Coronary Artery Disease: A Substudy of the ORBITA Trial. Frontiers in Cardiovascular Medicine. 2021:1330.
PCI, percutaneous coronary intervention.

2.2.2.4 Dobutamine stress echocardiography protocol

Blinded physicians and sonographers performed all scans during the ORBITA trial. Patients omitted β-blockers for at least 24-hours prior to the DSE. Sulphur hexafluoride microbubble preparation (SonoVue, Bracco Imaging SpA) was used to optimise endocardial border definition. After acquisition of resting images to exclude significant valvular disease, intravenous dobutamine was infused initially at 10µg/kg/min followed by increasing doses of 20µg/kg/min, 30µg/kg/min, up to a maximum of 40µg/kg/min in 3-minute stages. Intravenous atropine was administered in 300µg boluses up to a maximum of 1,200µg for patients not achieving 85% of the predicted maximal heart rate. DSE reporting was performed by cardiologists blinded to treatment allocation and pre/ post-randomisation phase (269).

Peak dobutamine-induced wall motion was graded according to the score: normal=0, hypokinetic=1, akinetic=2, dyskinetic=3, or aneurysmal=4, per segment in the standard left

ventricular 17-segment model. The segment scores were totalled for each scan. Each scan was reported on 2 occasions, independently, in a blinded fashion by 6 imaging cardiologists, and the average between all reports was calculated (269).

2.2.2.5 Ethical approvals

The main ORBITA study was approved by the London Central Research Ethics Committee (reference 13/LO/1340) and conformed to the principles outlined in the Declaration of Helsinki. Written informed consent was obtained from all participants following diagnostic coronary angiography and prior to trial enrolment.

2.2.2.6 Statistical analysis

Statistical analysis was performed using R 4.0.3 (R Foundation for Statistical Computing, Vienna, Austria) using the modelling package “rms” (270, 271). Change in biomarkers with exercise from timepoint P1 to P2, and P3 to P4 were assessed using paired student's t-test. All other analyses were performed using ordinary least squares regression modelling. The effect of PCI versus placebo on the pre-exercise (P3) biomarkers was assessed by including the treatment arm, and the P1 time point in the regression model. The effect of PCI on the post-exercise biomarker was assessed by including treatment arm and P1, P2, and P3 in the regression model. The effect of DSE score on the pre-randomisation post-exercise (P2) biomarker was assessed by including the P1 timepoint, and the stress echo score with a restricted cubic spline with 3 knots. The effect of DSE score on the placebo-controlled impact of PCI on the post-exercise (P4) biomarker levels was also assessed using regression modelling, including the treatment arm, timepoints (P1, P2, P3) as well as pre-randomisation DSE score and their interaction.

2.2.3 Blood samples

Blood plasma samples were collected and stored at -80°C, prior to thawing to room temperature before use for both SCOT-HEART and ORBITA studies.

2.2.4 Enzyme-linked immunosorbent assays

ELISA protocols have already been developed and optimised for IgG and IgM anti-MDA-LDL, MDA-LDL and ApoB-100 through prior work in the Khamis laboratory (91, 253). Tables 2-1 and 2-2 detail all primary and secondary antibodies used for these.

2.2.4.1 Enzyme-linked immunosorbent assay for MDA-LDL

The ELISA for MDA-LDL is performed in the sandwich format (see Figure 2-3 below), immobilising the full LO1 antibody to capture MDA-LDL in plasma, followed by a biotinylated anti-ApoB secondary antibody. The ELISA in sandwich format permits high specificity and sensitivity, with two antibodies required to bind the antigen (MDA-LDL). For this ELISA, and all ELISAs performed in this thesis, Nunc Maxisorb™ 96-well plates (44-2404-21 – Thermo Fisher Scientific, Massachusetts, USA) were used. Plates were coated overnight with LO1 (100µL of 10µg/mL) at 4ºC, diluted in phosphate-buffered saline (PBS) (Dulbecco's PBS; Thermo Fisher Scientific, Massachusetts, USA). Values for MDA-LDL were divided by those obtained for ApoB (see below) on a per sample basis. This adjustment for the protein element of the MDA-LDL particle permits analysis of the oxidatively modified LDL component, as performed previously (254, 272).

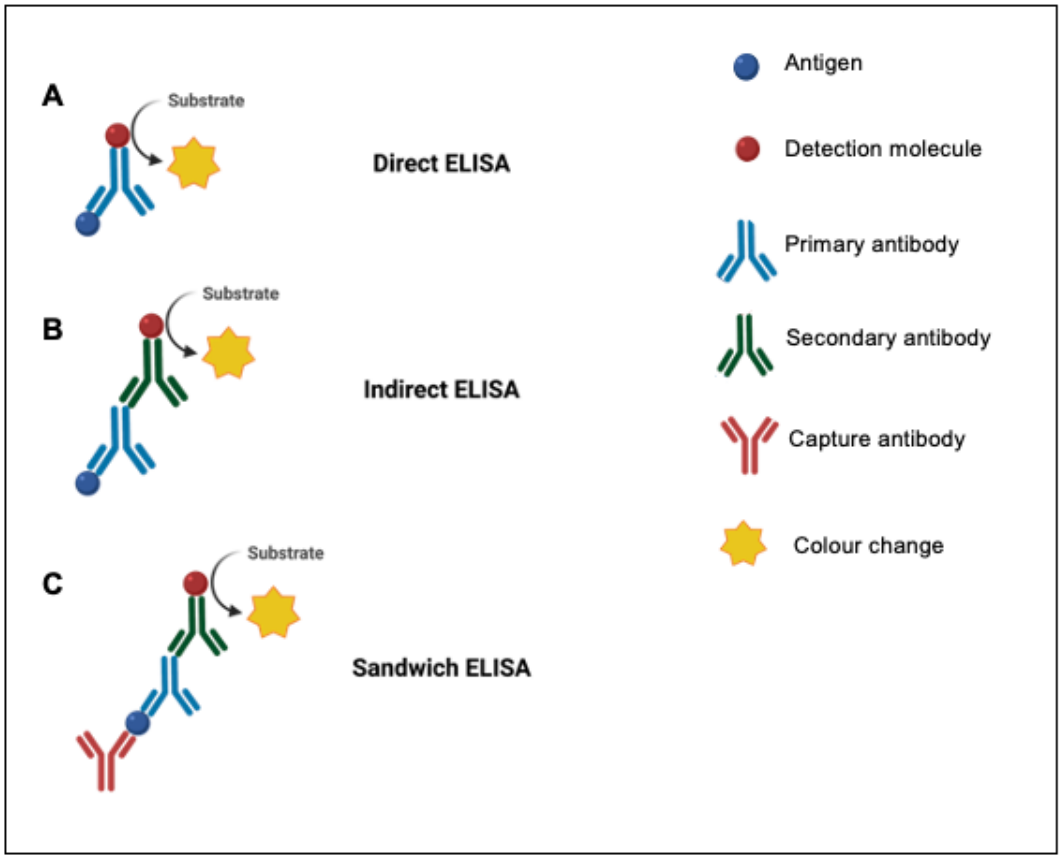

Figure 2-3. ELISA formats.

A) – Direct ELISA. The immobilised antigen is detected by a specific antibody that is directly conjugated to a detection molecule, such as horseradish peroxidase. Addition of a substrate, such as TMB (3,3′,5,5′-tetramethylbenzidine), results in a colour change which is detectable with a plate reader.
B) – Indirect ELISA. This uses a two-step process for detection. The immobilised antigen is detected by a primary antibody, that is then itself detected by a labelled secondary antibody against the host species of the primary antibody. As before, addition of a substrate results in a colour change.
C – Sandwich ELISA. This uses a three-step process for detection. The capture antibody is coated on the surface of the well, which binds to added antigen, prior to primary and secondary antibody binding as in B).
Made using Biorender.
ELISA, Enzyme-linked immunosorbent assay.

The next day, the plates were washed ×3 with 300µL PBS-Tween-20 (0.05% Tween-20 in PBS; Sigma-Aldrich, UK) to remove non-adherent material, followed by blocking of non-specific binding with 300µL 3% bovine serum albumin (BSA) (3% in PBS, 22µm sterile-filtered; A9418 – Sigma-Aldrich, UK) for 1-hour at room temperature (RT). Following this, the wells were washed ×3 with PBS-Tween-20 (for this and all subsequent steps), prior to the

addition of 100µL patient plasma samples for 1-hour at 1:40 dilution at RT. This dilution step, and all subsequent dilutions in the ELISA, were performed in assay buffer (0.5% BSA, 0.05% Tween-20 in PBS). Next, after washing, 100µL biotinylated polyclonal anti-ApoB antibody (Abcam, Cambridge, UK) at 1:2000 dilution was added and incubated for 1-hour at RT. For signal generation, 100µL horseradish peroxidase (HRP)-conjugated streptavidin (DY998 – R&D Systems, MN, USA, 1:200) for 20-minutes, followed by 100µL 3,3′,5,5′-tetramethylbenzidine (TMB; T0440 – Merck, Darmstadt, Germany), were used. The reaction was stopped with 100µL 0.5M H_2SO_4. Plates were read at an OD of 450nm using a Synergy HT microplate reader (Beckman-Coulter, California, USA) for this and all biomarker ELISAs.

Values were corrected to the averages of blank wells that were run on every plate and received all reagents except for the test reagents. All measurements were carried out in the minimum of duplicates.

2.2.4.2 Enzyme-linked immunosorbent assay for Apolipoprotein B-100

The ELISA for ApoB is also measured in sandwich format (see Figure 2-3 above), with polyclonal anti-ApoB (ab7616 – Abcam, Cambridge, UK) at 1:2000 dilution added on solid phase overnight at 4ºC, diluted in PBS. After blocking with 300µL 3% BSA, 100µL of blood samples were added at 1:320 dilution in assay buffer, followed by 100µL biotinylated anti-ApoB antibody (ab20898 – Abcam, Cambridge, UK) at 1:2000 dilution in assay buffer. Signal generation was with 100µL HRP-conjugated streptavidin at 1:200 dilution in assay buffer for 20-minutes, followed by 100µL TMB. The reaction was stopped with 100µL 0.5M H_2SO_4. Plates were read at an OD 450nm using a Synergy HT microplate reader as above.

2.2.4.3 Enzyme-linked immunosorbent assay for IgG/ IgM anti-MDA-LDL

These ELISAs are performed in indirect ELISA format (see Figure 2-3 above). Plates were coated with 100µL of 10µg/mL MDA-LDL overnight at 4ºC, diluted in PBS. After blocking with 300µL 3% BSA, 100µL of plasma samples were added (1:80 dilution for IgG and 1:120 dilution for IgM, both in assay buffer). Mouse anti-human IgG (9042-01 – Southern Biotech, Alabama, USA, 1:2000) or biotinylated mouse anti-human IgM (9022-08 – Southern Biotech, Alabama, USA, 1:2000) were used for primary detection. HRP-conjugated polyclonal rabbit anti-mouse antibody (P0161 – Dako, Cambridge, UK, 1:2000 for 1-hour) and streptavidin-HRP (1:200 for 20-minutes) for IgG and IgM respectively were utilised for secondary detection. Signal generation and readouts were performed as above.

2.2.5 Generation of MDA-LDL

MDA-LDL is produced through the adduction of MDA to native LDL (nLDL), as performed previously (273). 1,1,3,3-tetramethoxypropane (malondialdehyde bis[dimethyl acetal]) (Sigma-Aldrich, UK) underwent acid hydrolysis through incubation with 4M HCl for 10 minutes at RT. The pH was then adjusted to 7.4 using 1.5M NaOH to create 0.5M MDA, which is then incubated with human LDL (437644 – Merck, Darmstadt, Germany) at 37°C for 3 hours, at a ratio of 100µL of 0.5MDA to 1mg of LDL. This forms MDA-LDL, which is then buffer exchanged into PBS using 7kDa molecular weight cut-off Zeba™ Spin Desalting columns (89889 – Thermo Fisher Scientific, Massachusetts, USA). 0.01% ethylenediaminetetraacetic acid (EDTA; 324503 – Merck, Darmstadt, Germany) was added to prevent further oxidation. Protein concentration was then measured using the Pierce™ bicinchoninic acid (BCA) protein assay kit (23225 – Thermo Fisher Scientific, Massachusetts, USA), as per the manufacturer's instructions.

2.3 Antibody and antibody fragment targeted nanoparticles for delivery to atherosclerosis

2.3.1 Generation of LO1/ LO1Fab

LO1 and LO1Fab are both manufactured externally following the identification, development, and optimisation of production techniques that have previously taken place in the Haskard-Khamis laboratory.

2.3.1.1 LO1

LO1 was isolated from frozen hybdridoma cell supernatants by affinity chromatography on protein G sepharose as previously described (252). Non-specific murine IgG3κ was used as an isotype control (Merck, Darmstadt, Germany). Details for these processes can be found in Khamis et al (174).

2.3.1.2 LO1Fab

LO1Fab was produced in HEK293/6E cells using pcDNA 3.1 as a vector, prior to Capto L purification and size exclusion chromatography. Details for these processes can be found in S Pandey's PhD thesis.

2.3.2 LO1/ LO1Fab binding kinetics

The binding kinetics of LO1 and LO1Fab with MDA-LDL can be assessed indirectly through saturation ELISA binding experiments, or more directly and precisely using surface plasmon resonance. Unfortunately, the antigen (MDA-LDL) is very large and has a degree of

heterogeneity that makes surface plasmon resonance unreliable and inaccurate in prior experience of the Khamis laboratory. Therefore, we sought other experimental techniques to establish the strength of binding relationships. In collaboration with 'Fluidic Analytics' (Cambridge, UK), microfluidic diffusional sizing of the two antibody constructs was performed, using the 'Fluidity One-M' device (274). This novel technique involves the passage of fluorescently labelled antibodies with their antigen through microfluidic channels, and sorts the particles by size (hydrodynamic radius) as they flow across the diffusion chamber. Smaller particles will diffuse rapidly, whereas larger species diffuse more slowly and travel less far across the diffusion chamber. As the antibodies bind to their epitope, there is a resultant change in size of the particles (change in hydrodynamic radius), which is detected as a change in diffusion speed and distance.

2.3.3 Generation of control Fab fragments

To serve as a negative control for both LO1Fab itself and LO1Fab-conjugated nanoparticles, a human control Fab' was produced. The free cysteine group on the Fab' is important to permit maleimide-based fluorophore labelling for *in vivo* studies and for conjugation to nanoparticles. Unfortunately, I could not identify any commercially available human Fab' fragments, and as such produced them from human IgG $F(ab')_2$ fragments (009000006 – Jackson ImmunoResearch, Philadelphia, USA). Selective cleavage of the two disulphide bonds of the hinge region produces two Fab' fragments, as performed previously (275).

Firstly, $F(ab')_2$ fragments were buffer exchanged into reaction buffer (100mM sodium phosphate, 150mM NaCl and 10mM EDTA in PBS, pH 7.2). Separately, 50nM 2-mercaptoethylamine•HCl (2-MEA; 20408 – Thermo Fisher Scientific, Massachusetts, USA)

was made up in reaction buffer as above. 2-MEA was then added to the $F(ab')_2$ fragments to give a final concentration of 4mM 2-MEA. The mixture was then incubated at 37ºC for 1-2-hours. 2-MEA reduction conditions were optimised, as detailed in *Section 4.6 Control Fab production.* Following incubation, the mixture was cooled to RT and Fab' separated from 2-MEA via ultracentrifugation with an Amicon 50kDa molecular weight cut-off filter (UFC5050 – Merck, Darmstadt, Germany). The retentate was then resolubilised with reaction buffer to prevent further reduction, in order to preserve Fab' free thiol groups, and was buffer exchanged into PBS prior to use.

The persistence of free sulfhydryl groups on the Fab' fragments for maleimide chemistry was assessed using an Ellman's assay (5,5-dithio-bis-[2-nitrobenzoic acid]; 22582 – Thermo Fisher Scientific, Massachusetts, USA) according to the manufacturer's instructions. This colorimetric assay is based upon the reaction between Ellman's Reagent and thiol groups, with cysteine hydrochloride monohydrate forming the reference standard.

2.3.4 Fluorescent labelling of antibody fragments for in vivo studies

For the assessment of LO1Fab versus control Fab *in vivo* with FMT, the antibody fragments require conjugation with a NIR fluorophore. This was performed as carried out previously for LO1Fab, using maleimide chemistry with VivoTag-S-750-MAL (NEV11223 – PerkinElmer, Massachusetts, USA) (S Pandey's thesis). A 10mM stock of VivoTag-S-750 MAL was prepared in dimethyl sulfoxide (DMSO; D8418 – Sigma-Aldrich, Missouri, USA) and added to Fab fragments, resulting in a molar ratio of protein: dye of 20:1. The mixture was light-protected and rotated for 2-hours at RT. Zeba™ Spin Desalting columns were then used to buffer exchange into PBS, prior to assessing the maximum absorbance at 280nm and 750nm

using a NanoDrop 2000 spectrophotometer (Thermo Fisher Scientific, Massachusetts, USA). The degree of labelling of dye: protein, which enables correction of *in vivo* quantified fluorescence signal to protein, was determined using the calculations shown in Figure 2-4 below.

$$Degree\ of\ labelling = \frac{[Dye]}{[Protein]}$$

$$[Protein] = \frac{A_{280} - (A_{750} \times correction\ factor)}{\epsilon Protein}$$

$$[Dye] = \frac{A_{750}}{\epsilon Dye}$$

Figure 2-4. Degree of labelling calculations.

0.05 is the correction factor for the absorbance of VivoTag-S-750-MAL at 280nm (equal to 5.0% of its absorbance at 750nm). $\epsilon Protein$ and ϵDye are molar extinction coefficients for the protein and dye, respectively. $\epsilon Protein$ is 203,000 $M^{-1}cm^{-1}$ and ϵDye is 240,000 $M^{-1}cm^{-1}$.

2.3.5 Nanoparticle design and formulation

2.3.5.1 Nanoparticle design

Polymers were chosen for nanoparticle formation based upon composition and presence of functional groups, as well as molecular weight. Polymer molecular weight can be evaluated by gel permeation chromatography and assessed according to their number average molecular weight (M_n) or their weight average molecular weight (M_w). M_n is purely based on the statistical average molecular weight of all polymer chains in the sample; whilst M_w considers the relative molecular weight of each chain in the sample (thus larger polymer

chains contribute more to the overall M_w). Table 2-3 below displays the molecular weights of the polymers used in this study.

Polymer	Manufacturer, catalogue number	Number average molecular weight (M_n)	Weight average molecular weight (M_w)
PLGA	Sigma-Aldrich (St. Louis, USA) Resomer 502 H 719897	Not provided by manufacturer	7-17,000 Da
PLGA-PEG-MAL	PolySciTech (Lafayette, USA) AI020	8,491 Da	23,875 Da
PLGA-Cy5	PolySciTech (Lafayette, USA) AV034	46,640 Da	60,485 Da
PLGA-IRdye 800CW	PolySciTech (Lafayette, USA) AV043	10,040 Da	11,445 Da

Table 2-3. Polymers used for nanoparticle generation.

PLGA, poly(lactic-co-glycolic acid); PEG, poly(ethylene glycol); MAL, maleimide; Cy5, cyanine 5 – a near-infrared fluorescent dye (excitation 649nm/ emission 666nm); IRdye 800CW, an indocyanine-type near-infrared fluorophore (excitation 775nm/ emission 792nm).

2.3.5.2 Nanoparticle generation

The nanoparticles produced in this thesis were made in collaboration with Prof Christopher Scott at Queen's University Belfast, Northern Ireland, UK. Following initial nanoparticle

development at Queen's University Belfast, optimisation and further nanoparticle testing was performed at Imperial College London.

Nanoparticles were generated using the single emulsion-solvent evaporation technique as described previously (276). This consists of adding a polymer dissolved in an organic solvent to an aqueous phase (either oil to water or water to oil) to generate emulsion droplets. Surfactants such as the water-soluble poly(vinyl alcohol) can be used to prevent coalescence and encourage the formation of nanoparticle droplets.

Nanoparticles were made in batches of 20mg, using different compositions of the polymers outlined in the table above, with or without the addition of 100μL of 2mg/mL Rhodamine 6G in dichloromethane (R4127 – Sigma-Aldrich, St. Louis, USA) for fluorescent detection in some *in vitro* assays (excitation 525nm/ emission 548nm).

The polymer (20mg) was dissolved in 1mL dichloromethane to form the organic phase of the reaction. The aqueous phase was formed by adding 7mL of 2.5% poly(vinyl alcohol) (363170 – Sigma-Aldrich, St. Louis, USA) in 50mM 2-(N-Morpholino)ethanesulfonic acid (MES) hydrate buffer (M8250 – Sigma-Aldrich, St. Louis, USA), adjusted to pH 5. Using a 1mL syringe with 25G needle, the organic phase was added dropwise to the aqueous phase whilst stirring at 600rpm on ice (Jeio Tech multi-channel stirrer MS-53M; Daejeon, South Korea), to form droplets. The liquid was then sonicated (FB120 Sonic Dismembrator; Fisher Scientific, Massachusetts, USA) for 54 seconds (pulse duration of 3 seconds with 2 second pause between pulses and a pulse amplitude of 50%) whilst stirring continuously at 600rpm on ice (see Figure 2-5 below). This decreases droplet size and promotes emulsion formation. The

liquid was then left stirring overnight, protected from light at 600rpm, uncovered, to allow the dichloromethane to evaporate and precipitate the polymers as nanoparticles.

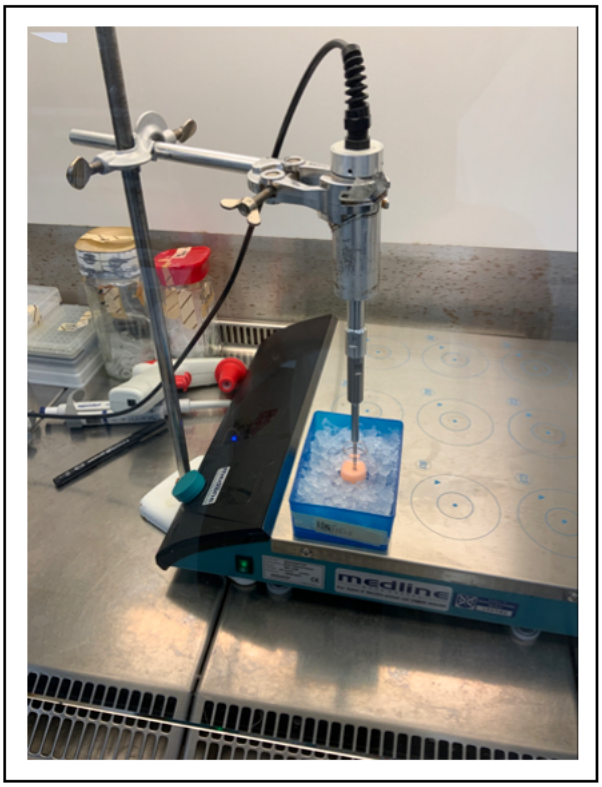

Figure 2-5. Sonication of organic and aqueous phases with Rhodamine 6G whilst stirring on ice.

The following day, the suspension was aliquoted into 1.5mL Eppendorf microtubes (800μL per tube) and centrifuged at 20,000g for 20-minutes at 4°C to wash the nanoparticles. The supernatant was then discarded, and 1mL PBS added to the pellet. Following nanoparticle rehydration for 30-minutes at 4°C, the nanoparticles were sonicated again with pulse duration of 1 second at 1 second intervals and an amplitude of 35%, until the nanoparticle pellet was completely resuspended. The process was then repeated, with centrifugation (20,000g for 20-minutes at 4°C), removal of the supernatant, pellet rehydration with 1mL PBS for 30-

minutes at 4°C and finally sonication (1 second pulse duration at 1 second intervals with 35% amplitude); leaving a final nanoparticle concentration of 2mg/mL. If the nanoparticles were not for immediate antibody conjugation, they were centrifuged again (20,000g for 20-minutes at 4°C) and the pellet stored at -20°C until use.

2.3.5.3 Antibody conjugation

2.3.5.3.1 Antibody fragment reduction

Prior to nanoparticle mixing, antibody fragments were optimised for conjugation with maleimide chemistry, via partial reduction using tris(2-carboxyethyl)phosphine (TCEP) hydrochloride (51805-45-9; Fluorochem, Derbyshire, UK). TCEP is a stable, irreversible, powerful reducing agent that selectively cleaves disulphide bonds, via oxidation of the phosphine group and release of the thiol group. This process therefore increases the availability of free thiol groups for cysteine labelling with maleimide chemistry. Moreover, and dissimilar to other reducing agents such as β-mercaptoethanol, TCEP does not readily react with maleimide groups and thus does not need to be removed prior to the maleimide reaction, making it an ideal reducing agent for nanoparticle conjugation in this study (277).

Therefore, as a preparatory step in targeted nanoparticle generation, antibody fragments were incubated with TCEP for 1-hour at RT, generally at 10M excess, based on prior testing and experience in the Scott laboratory.

2.3.5.3.2 Nanoparticle-antibody conjugation

Nanoparticle pellets were defrosted and rehydrated with 1mL PBS at 4°C, prior to sonication (pulses of 1 second with 1 second pause, at 35% amplitude on the FB120 Sonic

Dismembrator (Queen's University Belfast) or <5 microns on the Soniprep 150 (MSE, Nuaillé, France) (Imperial College London).

Empirically, based on previous experience in the Scott laboratory, antibody/ antibody fragments were added to nanoparticles in a 25μg:1mg ratio. Following TCEP reduction, the antibody/ fragments were incubated with the resuspended nanoparticles overnight at 4°C on a rotator. The next day, the nanoparticles were centrifuged at 12,000g for 20-minutes at 4°C and the supernatant was discarded, to remove unbound antibody. The nanoparticles were then rehydrated with 1mL PBS for 30-minutes at 4°C, prior to sonication (pulses of 1 second with 1 second pause at 20% amplitude on the FB120 Sonic Dismembrator (Queen's University Belfast) or 2-4 microns on the Soniprep 150 (Imperial College London). This process was then repeated with centrifugation, rehydration (with desired volume of solvent, usually 0.5mL PBS to give a nanoparticle concentration of 1mg/mL) and resuspension of the pellet, in a further effort to wash the antibody-bound nanoparticles.

2.3.5.3 Nanoparticle biophysiochemical properties

2.3.5.3.1 Dynamic light scattering

Dynamic Light scattering (DLS) was performed using the NanoBrook Omni (Brookhaven Instruments, New York, USA) using 100μg/mL nanoparticles.

2.3.5.3.2 Nanoparticle tracking analysis

Nanoparticle tracking analysis was performed as an alternative method of assessing nanoparticle size, as well as generating a particle count per unit volume (rather than a weight

of nanoparticles per unit volume). This was performed using 10µg/mL nanoparticles on the Nanosight NS300 (Malvern Panalytical, Malvern, UK).

2.3.5.4 Micro-bicinchoninic protein assay

The Micro-BCA protein assay (23235 – Thermo Fisher Scientific, Massachusetts, USA) was carried out to quantify the mass of antibody fragments conjugated to nanoparticles. This was performed according to the manufacturer's instructions, except for the reference protein standard, which was made through spiking known amounts of Fab in 2-fold dilution series into untargeted nanoparticles. As the micro-BCA assay provides a colorimetric readout, this new reference standard corrects for the colour of the nude nanoparticles. This technique cannot therefore be used with fluorescent nanoparticles. Fab conjugation efficiency was calculated as ([amount of Fab on nanoparticles/ amount of Fab added to initial conjugation reaction] × 100).

2.3.6 In vitro characterisation

2.3.6.1 Generation of MDA-LDL

All the proposed targeted antibody-nanoparticle constructs react with MDA-LDL, produced as described above on page 132.

2.3.6.2 Enzyme-linked immunosorbent assays

Following nanoparticle conjugation, ELISAs were performed to establish conservation of MDA-LDL binding. There are four key ELISA designs that are used to assess nanoparticle function in this thesis, as outlined below.

2.3.6.2.1 Modified fluorescence enzyme-linked immunosorbent assay

This modified indirect ELISA relies on the fluorescence of bound nanoparticles as its readout. 100µL of 10µg/mL MDA-LDL was added on solid phase overnight at 4ºC, diluted in PBS. The next morning, the wells were blocked with 300µL 3% BSA for 1-hour, followed by 100µL nanoparticle constructs for 2-hours at RT. In general, wells were washed with 3× 300µL PBS-Tween-20 between all ELISA steps. However, at this stage in this ELISA design, wells were washed ×9, to remove as much unbound nanoparticle as possible. The attached nanoparticles were then dissolved in a 1:1 volume ratio of acetonitrile: DMSO (50µL per well) and fluorescence measured at the appropriate wavelength depending on the conjugated fluorophore, using either a Synergy HT plate reader (Biotek, Santa Clara, USA); an Odyssey CLx Imaging System (LI-COR, Nebraska, USA) or a CLARIOstar Plus (BMG Labtech, Aylesbury, UK).

2.3.6.2.2 Anti-PEG enzyme-linked immunosorbent assay

To provide an alternative means of comparing nanoparticles conjugated with different targeting agents (that can also be non-fluorescent), I designed and developed a novel ELISA with detection based upon the presence of PEG in the nanoparticle outer shell. Following testing and optimisation of different primary and secondary antibody pairs (as detailed later in *4.4.2.4 Development of the anti-PEG ELISA*), the following protocol was devised.

Wells were coated overnight with 100µL 10µg/mL MDA-LDL, then, following blocking with 300µL 3% BSA, were exposed to the nanoparticle constructs for 1-hour (100µL). Next, a rabbit anti-PEG antibody (Ab190652 – Abcam, Cambridge, UK) (1/500, 100µL) was added, prior to a goat anti-rabbit IgG-HRP (Ab205718 – Abcam, Cambridge, UK) (1/500, 100µL) for

secondary detection, for 1-hour each. 100μL TMB was then added for signal generation, with 100μL 0.5M H_2SO_4 used to terminate the reaction.

2.3.6.2.3 Anti-CH1 enzyme-linked immunosorbent assay

This ELISA designs permits nanoparticle recognition via the conjugated antibody fragments. Wells were coated with MDA-LDL, followed by blocking non-specific binding and nanoparticle constructs, as above. Detection was performed using a biotinylated anti-IgG-CH1 antibody (11496548 – Thermo Fisher Scientific, Massachusetts, USA) for 1-hour at 1:1000 dilution, prior to Streptavidin-HRP for 20-minutes at 1:200 dilution. TMB and 0.5M H_2SO_4 were used for signal generation/ termination.

2.3.6.2.4 Anti-ApoB enzyme-linked immunosorbent assay

This sandwich ELISA relies on detection via the bound ApoB particle, with nanoparticles/ antibody fragments immobilised on solid phase. The ELISA design is as per *2.2.4.2 Enzyme-linked immunosorbent assay for Apolipoprotein B-100*.

2.3.6.2.5 Competitive enzyme-linked immunosorbent assay

Various competitive ELISAs were performed in this thesis to assess the ability of LO1/ LO1Fab to compete with targeted nanoparticles for MDA-LDL binding. One key design involved coating wells overnight with MDA-LDL (5μg/mL) prior to blocking with 2% BSA and then the addition of LO1Fab in two-fold dilution series for 1-hour. Following this, LO1Fab-conjugated nanoparticles were added at a fixed concentration for 1 further hour. Nanoparticle binding was then evaluated using the anti-PEG ELISA detailed above.

2.3.6.3 Gel electrophoresis

2.3.6.3.1 Sodium dodecyl sulphate–polyacrylamide gel electrophoresis (SDS-PAGE)

NuPAGE Novex 4-12% Bis-Tris mini protein gels (NP0322PK2 – Thermo Fisher Scientific, Massachusetts, USA) were loaded with a total protein mass of 5-10μg or 1mg nanoparticle constructs with 5μL 4× NuPAGE lithium dodecyl sulphate sample buffer (NP0008 – Thermo Fisher Scientific, Massachusetts, USA) and run using NuPAGE MES Running Buffer (NP0002 – Thermo Fisher Scientific, Massachusetts, USA) for ~1-hour at 200V in an XCell SureLock™ Mini-Cell (EI0001 – Thermo Fisher Scientific, Massachusetts, USA). The standard protein ladder used was SeeBlue Plus2 Protein Standard (LC5925 – Thermo Fisher Scientific, Massachusetts, USA). For fluorescent imaging, the gels were run with Chameleon Duo pre-stained protein standard (92860000 – Li-Cor Biosciences, Nebraska, USA).

SDS-PAGE gels were then washed with distilled H_2O ×3 on a shaker, prior to Coomassie staining with SimplyBlue™ SafeStain (LC6060 – Thermo Fisher Scientific, Massachusetts, USA) for 1-hour. Following de-staining in distilled H_2O overnight, the gels were imaged on the Gel Doc-It Imaging System (UVP, Jena, Germany). Alternatively, for fluorescence imaging, the gels were imaged on the Odyssey CLx (Li-Cor Biosciences, Nebraska, USA) at 700 and 800nm.

2.3.6.3.2 Native–polyacrylamide gel electrophoresis (native-PAGE)

Samples were prepared using 2.5μL NativePAGE™ Sample Buffer (4×) (BN2003) and 0.25-1μL NativePAGE™ 5% G-250 sample additive (BN2004), loading a total protein mass of 5-10μg or 1mg nanoparticle constructs on NativePAGE™ 4-16%, Bis-Tris, 1.0mm mini protein gels (BN1002BOX). Anode buffer was prepared by mixing 50mL NativePAGE™ Running

Buffer (20×) (BN2007) with 950mL deionized water. Dark blue cathode buffer was prepared from 10mL NativePAGE™ Running Buffer (20×) and 10mL NativePAGE™ Cathode Additive (20×) (BN2007) in 180mL deionized water. The ladder used was NativeMark™ unstained protein standard (LC0725) (all reagents Thermo Fisher Scientific, Massachusetts, USA).

The gels were run for 105-120 minutes in an XCell SureLock™ Mini-Cell. Gels were then Coomassie stained. The gels were placed in 100 mL 'Fix' solution (40% methanol, 10% acetic acid) and then microwaved on high power (950–1100 watts) for 45-seconds. Following this, the gels were shaken for 15-minutes at RT. The 'Fix' solution was then decanted and 100mL 'De-stain' solution (8% acetic acid) added, prior to microwaving on high power (950–1100 watts) for 45-seconds. The gels were then left to further de-stain to reduce background signal on an orbital shaker overnight. The gels were imaged on the Gel DOC-It Imaging System (Bioimaging Systems, California, USA) the following day.

2.3.6.3.3 Nanoparticle reduction

Nanoparticles were boiled and reduced to fragment the constructs into their constituent components, prior to gel electrophoresis. Following conjugation and centrifugation-resuspension cycles, 4mg nanoparticles were finally resuspended in 95μL (4×) Laemmli sample buffer (1610747 – Bio-Rad, California, USA) and 5μL 2-mercaptoethanol (1610710 – Bio-Rad, California, USA). They were then heated to 95ºC for 10-minutes (PTC-200 Peltier Thermal Cycler, MJ Research, Florida, USA).

2.3.6.4 Immunohistochemistry

2.3.6.4.1 LO1 and LO1Fab immunohistochemistry in human atherosclerosis

Immunohistochemistry for LO1 and LO1Fab on human coronary stable atherosclerotic plaques was performed in collaboration with Prof Jason Johnson, Bristol University, using slides from the Bristol Coronary Artery BioBank (National Research Ethics Service approval [08/H0107/48]).

Slides were dewaxed in 3 changes of Clearene solvent, followed by rehydration with 3 changes of graduated industrial methylated spirit (100%, 90% and 70%) and then rinsing in tap water, followed by distilled H_2O (dH_2O). The slides were then microwaved on full power for 6-minutes with 10mM citrate buffer at pH 6.0. After topping up with dH_2O and heating again for 6-minutes on full power, the slides were rinsed in dH_2O, sections were circled with a hydrophobic pen and covered with Bloxall (SP-6000-100 – Vector Laboratories, California, USA), to inhibit endogenous peroxidase activity. Following rinsing ×3 in PBS, blocking was applied with 100μL horse serum at RT for 30-minutes. After tapping off excess liquid, 100μL primary antibody (LO1 or LO1Fab) (1:50) was pipetted onto the sections and incubated overnight in a humidity chamber at 4ºC. The next morning, following washing in PBS, 100μL secondary antibody was incubated for 1-hour at RT (1:400 biotinylated polyclonal goat anti-mouse antibody [31800 – Thermo Fisher Scientific, Massachusetts, USA] for LO1; 1:100 anti-IgG-CH1 for LO1Fab). Next, 100μL 1:100 Dylight™ 488 streptavidin (SA-5488-1 – Vector Laboratories, California, USA) was incubated for 1-hour at RT. Slides were then mounted with VECTASHIELD, a 4′,6-diamidino-2-phenylindole (DAPI)-stained mountant (H-1200-10 – Vector Laboratories, California, USA), for 10-minutes at RT. Adjacent slides had already

been stained with mouse anti-human CD68 (M0814 – Dako, Cambridge, UK) at 0.3μg/mL in prior work in the Johnson Laboratory.

2.3.6.4.2 LO1 and LO1Fab immunohistochemistry in murine atherosclerosis

Frozen aortic root atherosclerotic slides were obtained from LDL-$R^{-/-}$ mice fed a high-fat diet for 30-weeks, as outlined in *Section 2.3.8.5 Mouse whole-body perfusion and aortic root* sectioning below.

Slides were dipped in dH_2O prior to 100% isopropanol for 1-hour and then, after dipping in dH_2O and airdrying, boundary lines were drawn with a hydrophobic pen. Slides were blocked with 2% BSA at 4°C for 1-hour, followed by the Avidin/ Biotin Blocking Kit (SP-2001 – Vector Laboratories, California, USA) (15-minutes per solution in a humidified chamber). The primary antibodies (LO1Fab 20μg/mL in 0.5% BSA; control Fab 20μg/mL in 0.5% BSA) were then incubated overnight in a humidity chamber at 4ºC. The next morning, following dip/ wash/ dip in PBS (as with all subsequent steps), the secondary antibodies were incubated for 1-hour at RT (1:100 anti-IgG-CH1 for both LO1Fab and control Fab). Next, 1:500 Streptavidin-AlexaFluor-647 (S21374 – Thermo Fisher Scientific, Massachusetts, USA) was incubated for 1-hour at RT. Slides were then mounted with a nuclear-stained mountant (Fluoromount-G mounting medium with DAPI; 00-4959-52 – Thermo Fisher Scientific, Massachusetts, USA) and glass cover slip for 10-minutes at RT, as above.

2.3.6.4.3 Nanoparticle staining in murine atherosclerosis

Slides were dipped in dH_2O prior to 100% isopropanol for 1-hour, followed by dipping in dH_2O and airdrying. Boundary lines were drawn with a hydrophobic pen. Slides were then blocked

with 5% BSA at 4°C overnight in a humidified chamber. After dip/ wash/ dip in PBS (as with all subsequent steps), the sections were incubated with an Avidin/ Biotin Blocking Kit as above. Next, the nanoparticle constructs were added (1mg/mL in 1% BSA) for 2-hours at RT, prior to mounting with a nuclear-stained mountant and glass cover slip as above.

2.3.6.4.4 Oil Red O staining

Slides were stained with Oil Red O to identify lipid deposits and counter-stained using haematoxylin, as per the manufacturer's instructions (ab150678 – Abcam, Cambridge, UK).

2.3.6.4.5 Fluorescence microscopy

Fluorescence imaging at Bristol University was performed using the Olympus phase contrast and darkfield BX41 microscope. Fluorescence imaging at Imperial College London was performed in the Facility for Imaging by Light Microscopy. Widefield and colour microscopy was performed using the Zeiss Axio Observer inverted microscope. Confocal microscopy was performed using the Leica Stellaris 8 microscope.

2.3.7 Foam cell assay

2.3.7.1 Isolation of monocytes and macrophage differentiation

Whole blood was collected from healthy donors in 9mL sodium heparin and 5mL serum Vacutainer tubes (BD, New Jersey, USA). Autologous serum was prepared by centrifugation at 2,000g for 15-minutes, which was then mixed with PBS to form 2% serum. Blood from the sodium heparin tubes was mixed 1:1 with 2% serum in PBS. Sepmate™ peripheral blood mononuclear cell (PBMC) isolation tubes (STEMCELL Technologies, Vancouver, Canada) were prepared using 15mL Ficoll-Paque Plus (GE17-1440-02 – Merck, Darmstadt, Germany)

followed by 35mL of blood/ 2% autologous serum. Density gradient centrifugation was performed at 1200g for 10-minutes with maximum acceleration and brake, prior to being transferred to a fresh 50mL Falcon tube, and topped up to 50mL with 2% autologous serum. This was then centrifuged at 350g with maximum acceleration and brake. The supernatant was then aspirated, and pellet resuspended in 5mL 2% serum. Centrifugation at 350g for 10-minutes with resuspension 5mL 2% serum was repeated two further times. Cells were then counted manually with a haemocytometer (Hausser Scientific, Pennsylvania, USA) and diluted accordingly with Dulbecco's Modified Eagle Medium (DMEM; 10313021 – Thermo Fisher Scientific, Massachusetts, USA)/ 10% autologous serum and plated at 1×10^6 cells per well on a specialised 96-well imaging plate (black μ-plate, 89626 – Ibidi, Wisonsin, USA) for 1-hour. Cell adherence was confirmed under light microscopy (Olympus CKX53 inverted cell culture microscope), prior to washing with warmed DMEM. Cells were then incubated for 7-days at 37°C with Roswell Park Memorial Institute 1640 medium (RPMI; 31870025 – Thermo Fisher Scientific, Massachusetts, USA), containing: 300mg/mL L-glutamine (25030081 – Thermo Fisher Scientific, Massachusetts, USA), 10% autologous serum, 1% penicillin-streptomycin (15070063 – Thermo Fisher Scientific, Massachusetts, USA) and 20ng/mL macrophage colony-stimulating factor (M-CSF; 300-25 – Peprotech, London, UK), to encourage macrophage differentiation. Culture media was changed every 2-3 days.

2.3.7.2 Quantitative real-time polymerase chain reaction

2.3.7.2.1 Cell lysis

Macrophages were plated in a 6-well plate (140674 – Thermo Fisher Scientific, Massachusetts, USA). RLT buffer (RNeasy Mini Kit, 74104 – Qiagen, Hilden, Germany) was made with β-mercaptoethanol (10μL/mL). Cells were washed 2-3 times with ice-cold PBS

prior to adding 350µL RLT buffer per well. The cells were then scraped, and lysates harvested.

2.3.7.2.2 RNA extraction

RNA extraction was performed using the RNeasy Mini Kit and RNase-free DNase (79254 – Qiagen, Hilden, Germany). Sufficient DNase was made by combining 10µL DNase with 70µL RDD buffer per sample. Next, 350µL of 70% ethanol (in 350µL RLT buffer) was added to the samples and mixed by pipetting, and transferred into RNeasy columns prior to centrifugation at 12,000g for 30-seconds at RT. Flow through was discarded, prior to adding 700µL RW1 buffer, and further centrifugation at 12,000g for 30-seconds at RT. Flow through was then discarded again. 80µL DNase was then added and incubated for 15 minutes at RT. 350µL RW1 buffer was then added and centrifuged at the same settings, with removal of flow through. Next, 700µL RPE buffer was added and centrifuged at 14,000g for 30 seconds at RT with disposal of flow through. This step was repeated with 350µL RPE buffer, with centrifugation for 2-minutes. Without buffer addition, the columns were spun again at 17,000g for 1-minute at RT and transferred to 1.5mL collection tubes. Finally, 30µL of RNase free water (129112 – Qiagen, Hilden, Germany) was added to the centre of the column and allowed to stand for 30-seconds. This was then spun at 12,000g for 1-minute. The eluted 30µL H_2O was re-added to the centre of the column and re-spun at 12,000g for 1-minute. RNA was then stored at -80°C until use.

2.3.7.2.3 Reverse transcription

The RNA concentration was quantified using the NanoDrop 2000 spectrophotometer using a 1.5µL sample. From this concentration, the volume required for 1µg of RNA was calculated.

This was made up to 16µL with RNAase free water. 4µL qSCRIPT cDNA Supermix (733-1177 – VWR, Pennsylvania, USA) was added to the 16µL RNA sample plus RNase-free H_2O. Following centrifugation (at 10,000g for 30-seconds), the tubes were added to the Veriti 96-well thermal cycler (Applied Biosystems, Thermo Fisher Scientific, Massachusetts, USA) and reverse transcription performed for 40-minutes (5-minutes at 25°C, followed by 30-minutes at 42°C and 5-minutes at 85°C) to generate complementary deoxyribonucleic acid (cDNA), which was stored at -20°C until use.

2.3.7.2.4 Quantitative real-time polymerase chain reaction

qPCR Master Mix (4444557 – Thermo Fisher Scientific, Massachusetts, USA) was prepared on ice. 4.5µL cDNA (corresponding to 10ng) and 5.5µL mastermix (comprising 5µL qPCR Master Mix and 0.5µL Taqman gene expression probe) (10µL final volume) were added per well to a 364-well plate (4309849 – Applied Biosystems, Thermo Fisher Scientific, Massachusetts, USA). The gene expression probes used are detailed in Table 2-4 below.

Gene	Probe
Hs02786624_g1	GAPDH (glyceraldehyde-3-phosphate dehydrogenase)
Hs04192464_mH	HLA-DRB1
Hs00219575_m1	HLA-DRA
Hs00167304_m1	CD11b (Integrin αM)
Hs00169122_g1	CD14
Hs04334165_m1	CD16 (FcγRIIIb)
Hs04189704_m1	CD45 (Protein tyrosine phosphatase receptor type C)
Hs02836816_g1	CD68
Hs00911250_m1	CD115 (Colony stimulating factor 1 receptor)

Table 2-4. Gene expression probes used in this thesis for quantitative real-time polymerase chain reaction.

Probes used for quantitative real-time polymerase chain reaction to confirm macrophage lineage. All Taqman probes, Thermo Fisher Scientific (Massachusetts, USA).
CD, cluster of differentiation; FcγR, Fragment crystallisable gamma receptor; GAPDH, glyceraldehyde-3-phosphate dehydrogenase; HLA, human leucocyte antigen.

The plate was then sealed and centrifuged at 1,000g for 2-minutes and polymerase chain reaction (PCR) performed on QuantStudio 6 Flex Real-time PCR system (Thermo Fisher Scientific, Massachusetts, USA). The PCR protocol included a denaturation step of 95°C for 2-minutes with 40 cycles of amplification at 95°C for 15-seconds and 60°C for 1-minute. Target gene expression was normalised to glyceraldehyde 3-phosphate dehydrogenase (GAPDH) gene expression and fold change was calculated.

2.3.7.3 Fluorescent labelling of native and MDA-modified LDL

Native or MDA-modified LDL were labelled with DiI (D282 – Thermo Fisher Scientific, Massachusetts, USA), a lipophilic carbocyanine fluorescent dye, by incubation with 10μL DiI per 1mL LDL for 24-hours at RT. The resultant DiI-nLDL or DiI-MDA-LDL complexes were then eluted through a 7kDa molecular weight cut-off Zeba™ Spin Desalting column to remove unbound dye. Equivalent DiI labelling and retention of DiI-MDA-LDL recognition by both LO1 and LO1Fab was confirmed on ELISA prior to cell treatment.

2.3.7.4 Foam cell generation and quantification

On Day 6 of PBMC culture, media was changed and 10μg/mL DiI-nLDL/ DiI-MDA-LDL added to wells. Cells were then incubated at 37°C for a further 24-hours. At this point, the plate was washed with PBS (300μL/well) followed by the addition of phenol red-free media (100μL/well)

(21063029 – Thermo Fisher Scientific, Massachusetts, USA). DiI fluorescence intensity (excitation 532nm/ emission 574nm) was then evaluated on the CLARIOstar Plus fluorescence plate reader.

2.3.7.5 Macrophage treatment with nanoparticle constructs

Constructs (250μg/mL) were incubated with DiI-MDA-LDL (10μg/mL) for 1-hour rotating at RT, prior to incubation with cells ($1x10^6$ per well) on Day 6 for 24-hours at 37°C. Plates were analysed for fluorescence intensity at the DAPI, DiI and Cy5 channels using the CLARIOstar Plus fluorescence plate reader, prior to fluorescence microscopy as below.

2.3.7.6 Fluorescence microscopy

Following analysis for fluorescence intensity, wells were washed with PBS (300μL/well) and 10μg/mL DAPI nuclear stain (D1306 – Thermo Fisher Scientific, Massachusetts, USA) (100μL/well) incubated for 10-minutes at 37°C. After another PBS wash (300μL/well), 4% formaldehyde (100μL/well) was incubated for 10-minutes to fix the cells, protected from light at RT. Next, formaldehyde was aspirated and plate washed with PBS again (300μL/well), prior to finally adding 100μL PBS. Plates were then stored, light-protected, at 2-8°C prior to microscopy.

All fluorescent microscopy images for analysis were obtained with identical microscope settings. Plates were imaged using widefield fluorescent microscopy (Zeiss Axio Observer inverted microscope) at the DAPI channel, as well as confocal microscopy (Leica Stellaris 8 microscope) at DAPI, DiI and Cy5 channels, as appropriate.

2.3.7.7 Statistical analysis

Cell counting was performed on 10x magnification widefield microscopy whole-well images at the DAPI channel, using Image J software (278), as described previously (279). Threshold pixel intensity was set between 50-255 units and particles analysed between 20-1200 pixels in size. These counts were used to standardise fluorescence intensity per 1,000 cells in each well. Data analysis was performed using GraphPad Prism 9 (La Jolla, California, USA) and are presented as mean ± SEM. One-way analysis of variance (ANOVA) was used to assess statistical significance between treatment groups, which was defined as a two-tailed p value <0.05.

2.3.8 In vivo characterisation

2.3.8.1 Ethical approvals

All animal experimental protocols undertaken at Imperial College London were ethically approved by the Central Biomedical Services and were carried out under the authority of UK Home Office licenses (Project Licenses 708969 and 8942649).

2.3.8.2 Murine model of atherosclerosis

Mice homozygous for $Ldlr^{tm1Her}$ (B6.129S7-Ldlrtm1Her/J) were purchased and bred (002207 – Jackson Laboratories, Maine, USA). This genetic knock-out model encodes a truncated non-functional LDL-R protein without a membrane spanning segment, such that it cannot bind LDL. As a result, the mice develop a serum cholesterol of 200-400 mg/dL (normal range 80-100 mg/dL) on a regular chow diet, or >2,000 mg/dL when fed an atherogenic diet (280). Mice were housed in a controlled environment under pathogen-free conditions in the Central Biomedical Services, Imperial College London. Female mice from 10-weeks of age until

experimental age were switched from a chow diet to a high-fat Western diet, formulated with 15% cocoa butter, 1% corn oil, 0.25% cholesterol and 40.5% sucrose (TD 190191 – Envigo, Indiana, USA). Female LDL-$R^{-/-}$ mice were used due to their propensity to develop larger plaques than their male counterparts (133).

2.3.8.3 Construct half-life determination

LDL-$R^{-/-}$ mice fed a high-fat diet for 35-40 weeks were injected intravenously via a tail vein with 2mg nanoparticle constructs or 50μg Fab fragments (doses scaled to a 25g mouse, and based on prior experience in the Khamis/ Scott laboratories). Venesection was performed from the opposite tail vein 15 minutes post-injection, and then at hourly intervals thereafter till 6 hours, and then again and 24- and 48-hours. On each occasion 20μL blood was drawn and immediately mixed 1:1 with 1000units/mL heparin and added to separate wells in triplicate on a black ELISA plate with clear-bottom wells (165305 – Thermo Fisher Scientific, Massachusetts, USA). Immediately following each tail bleed, fluorescence was quantified on the Odyssey CLx Imaging System at 700/ 800nm.

2.3.8.4 Fluorescence molecular tomography - computerised tomography

Nanoparticle constructs (2mg) or NIR fluorophore-conjugated Fab fragments (50μg) were injected intravenously in high-fat fed LDL-$R^{-/-}$ mice, with doses scaled to a 25g mouse. At approximately 2 half-lives following injection (4-hours) the mice were imaged using FMT (FMT 4000 – PerkinElmer, Massachusetts, USA) ± micro-CT (Siemens Inveon, Munich, Germany). In some experiments, the commercially available atherosclerotic plaque reporter MMPSense-750 FAST (PerkinElmer, Massachusetts, USA) was also co-injected alongside

nanoparticle constructs. All *in vivo* imaging was performed in the Biological Imaging Centre, Imperial College London.

Prior to imaging, mice were placed under general anaesthesia via isoflurane inhalation (in 100% oxygen: flow rate 1.5-3L/minute). Fur was then removed via a combination of shaving and depilatory creams, to reduce autofluorescence. Mice were then carefully transferred to the imaging cassette and imaged with FMT using appropriate laser channels (680nm for nanoparticles; 750nm for Fab fragments conjugated with Vivotag-S-750 or MMPSense-750 FAST). Fluorescence reflectance imaging (FRI) was performed prior to FMT for all scans. Transillumination settings were maintained at 'very high sensitivity' for all imaged constructs. Similarly, pixel density was set to 'fine' (2mm) for all scans. Following FMT scanning, some mice underwent micro-CT using the same imaging cassette and continued general anaesthesia. CT acquisition used 80kV voltage and 500μA current. CT projections were reconstructed using the Feldkamp algorithm and Shepp Logan filter with no down sampling. CT scanning was performed with the assistance of Dr Ali Ashek, Imperial College London. Colocalisation of CT and FMT scans was performed via fiducial markers on the imaging cassette using 'Imalytics Preclinical' image analysis software (Gremse-IT GmbH, Aachen, Germany).

Fluorescence imaging was reconstructed using TrueQuant 3.0 (PerkinElmer, Massachusetts, USA). Quantification of fluorescent signal is possible with FMT, owing to construct-specific calibration that is performed prior to imaging. Prior to injection, nanoparticles were analysed on the NanoDrop 2000 spectrophotometer to obtain 280nm and 680nm values (280nm and 750nm for labelled Fab fragments) to enable FMT calibration of fluorescence signal. Separate

calibration runs were performed for each batch of nanoparticles, to reduce the possibility of batch-to-batch variation affecting imaging data. Using TrueQuant 3.0 software, 3-dimensional regions of interest (ROI) were drawn that included the heart and aortic arch vessels, which was standardised across all datasets. Thresholding to background signal was performed for each scan individually in a blinded fashion. 2 separate areas of low signal were identified from the whole-body scan (usually in the abdomen, in regions away from primary metabolic organs) and fluorescence intensity averaged. This averaged value was then used to correct the ROI value for that scan.

2.3.8.5 Mouse whole-body perfusion and aortic root sectioning

For whole-body perfusion, mice were sacrificed via CO_2 inhalation. Following death, a sternotomy was performed, and anterior rib cage removed. The right atrium was incised for outflow and a 30G cannula inserted into the left ventricle for inflow. The mouse was then infused with 20mL PBS over 10-minutes using a 10mL syringe, followed by 20mL 2% formalin-saline at 37°C for a further 10-minutes. The heart, comprising the aortic root was then harvested, and left rotating in optimal cutting temperature embedding medium (KMA-0100-00A – CellPath, Powys, UK) overnight at 4°C. The next day, the heart was transected across the apex and mounted using fresh optimal cutting temperature embedding medium in a mould (58950 – Epredia, Portsmouth, UK) and covered with a cork disc. This was then placed into isopentane on dry ice to freeze the tissue, prior to storage at -80°C.

Cryosections were made from cardiac tissue, transecting the aortic root on short axis using a microtome cryostat (OTF5000 – Bright, Cambridge, UK). Once at the desired level on light microscopy, consecutive 5μm sections were made, mounting on Superfrost™Plus adhesion

microscope slides (J1800AMNZ – Epredia, Portsmouth, UK) and left to airdry for at least 2-hours, prior to storage at -80°C.

2.3.8.6 Ex vivo tissue fluorescence imaging

Following sacrifice, organs were harvested and washed in PBS prior to undergoing FMT (at appropriate wavelengths) using an opaque tissue block inside the imaging cassette, as above. Identical lengths of aorta, from the extra-cardiac ascending aorta to the iliac bifurcation were dissected and opened en face via a longitudinal incision, with the lumen surface facing upwards. Liver, kidneys and spleen were imaged with 'medium' (3mm) pixel density, whilst the heart and aortae were imaged with 'fine' pixel density. All organs were kept protected from light until imaging. Again, FRI was carried out prior to FMT. Standardised ROIs were used to quantify fluorescent signal on TrueQuant 3.0 software.

2.3.8.7 Ex vivo aortae Oil Red O staining

Following fluorescence imaging, aortae were stained with Oil Red O to identify lipid deposits. Firstly, the tissue was fixed in 4% formaldehyde for 30-minutes on a microscope slide, followed by washing in 100% propylene glycol for 5-minutes. Next, the tissue was submerged in Oil Red O solution for 1-hour, prior to washing in 85% isopropyl alcohol for 5-minutes. Finally, the aortae were rinsed with tap water and then PBS. The aortae were then imaged and photographed using a Leica S9D light microscope.

2.3.8.8 Statistical analysis

For construct half-life analysis, fluorescent measurements were blank subtracted from blood without any fluorescent probe delivered and analysed on GraphPad Prism 9 (La Jolla,

California, USA) using non-linear least squares regression to generate construct half-lives. For *in vivo* quantitative imaging studies, background-subtracted fluorescence intensity within identical ROIs were compared between groups. For *ex vivo* quantitative imaging studies, identical ROIs were compared between groups. These analyses were performed using an unpaired t-test with Welch's correction if normally distributed or Mann Whitney U test If not normally distributed. Statistical significance was achieved with a two-tailed p value <0.05.

Chapter 3

Relationships between oxidised LDL and antibodies to oxidised LDL with atherosclerotic plaque characteristics and exercise

CHAPTER 3 – RELATIONSHIPS BETWEEN OXIDISED LDL AND ANTIBODIES TO OXIDISED LDL WITH ATHEROSCLEROTIC PLAQUE CHARACTERISTICS AND EXERCISE

3.1 Chapter summary

This thesis chapter outlines two serological studies exploring the relationship between circulating antibodies to MDA-LDL with atherosclerotic plaque characteristics and exercise. ELISAs that have been previously developed and optimised in the Haskard-Khamis laboratory were utilised to establish biomarker levels in both studies.

The first study evaluates MDA-LDL and IgG/ IgM anti-MDA-LDL antibodies in blood from patients who underwent CTCA scanning as part of the SCOT-HEART trial. In total, 830 samples were available, with a high prevalence of cardiovascular risk factors and substantial coronary atherosclerosis (27% had evidence of obstructive disease). Relationships between the antibodies and different CTCA-imaged atherosclerotic characteristics are evaluated, investigating the hypothesis that both anti-MDA-LDL antibodies will protectively associate with atherosclerosis. Blank-subtracted and corrected values obtained from ELISA analyses were compared to clinical or CT characteristics in tertiles, with the lowest tertile as reference. A multinomial logistic regression model was used to evaluate the relationship between antibody levels and different outcomes, adjusted for a clinical cardiovascular risk score.

Levels of both IgG and IgM anti-MDA-LDL antibodies were found to inversely relate to different facets of atherosclerosis that are detectable on CTCA, including overall markers of

disease burden and valve calcification as well as more specific plaque characteristics. The most important finding was that IgG anti-MDA-LDL levels specify to less low-attenuation non-calcified plaque, the plaque necrotic core as detected on CTCA. What is more, this relationship remained using a 4% low-attenuation plaque burden threshold, which strongly relates to future MI, independent of coronary luminal obstruction, CACS, or traditional cardiovascular risk factors. The importance of the study findings lies in the potential to add further refinement to existing cardiovascular risk prediction algorithms, without the need to undertake expensive non-invasive imaging involving the use of ionizing radiation, or indeed invasive assessments, incorporating both radiation and increased clinical risk.

The second study evaluates dynamic changes in MDA-LDL and IgG/ IgM anti-MDA-LDL antibodies in blood from participants with severe flow-limiting single vessel CAD in the ORBITA trial. Blood was available at four timepoints – on the day of pre-randomisation assessment, prior to exercise (timepoint P1); 3-hours after exercise (timepoint P2); at post-randomisation assessment (6-weeks following the PCI or placebo procedure), before (timepoint P3); and 3-hours after (timepoint P4) exercise. Performing the ELISAs as above on these blood samples permitted assessment of the temporal variations in biomarkers, pre- and post-exercise, before and after PCI or placebo procedure. The study set out to investigate the hypothesis that there is an acute depletion of anti-MDA-LDL antibodies with vigorous exercise in patients with significant CAD, through homeostatic consumption, which may be ameliorated by coronary intervention.

Levels of both IgG and IgM anti-MDA-LDL antibodies did decrease with exercise (P1-P2 and P3-P4). No change in circulating MDA-LDL was observed with exercise. However, PCI did

not influence the antibody levels compared to placebo procedure, at baseline or with exercise. Additionally, neither antibody related to baseline ischaemia on DSE nor exercise duration or intensity. The significance of the results of this study is in demonstrating a potential function of anti-MDA-LDL antibodies in providing an immunological response to vigorous exercise, as seen previously with other substantial cellular stressors (for instance, major vascular surgery). Coupled with the atheroprotective associations demonstrated in the SCOT-HEART study, there are growing signals of a mechanistic role of anti-MDA-LDL antibodies in atherosclerosis.

3.2 Introduction

Risk stratification for the future onset of cardiovascular disease, particularly in healthy patients prior to a first cardiovascular event (primary prevention), has been the focus of enormous research interest. Risk stratification in current mainstream clinical practice is undertaken using event prediction algorithms, based primarily on the presence of traditional cardiovascular risk factors (281). However, there is increasing interest in in the incorporation of more novel risk factors into these algorithms, such as markers of social deprivation or autoimmune inflammatory diseases, with improved specificity and sensitivity for future cardiovascular events (282). Nonetheless, current risk prediction models are imperfect, and can often result in the over-treatment of those with minimal risk, or under-treatment of those at greatest risk. Diverse biological characteristics have been investigated as potential biomarkers for integration and optimisation of these risk matrices, with varying success. Indeed, we have investigated the utility of a highly-sensitive immunoassay for CRP to help predict future MACE in patients presenting to hospital with suspected MI (63); but clinical use has not been adopted.

As outlined above, vulnerable coronary atherosclerotic plaques are considered to be the causative lesions in precipitating MI, in combination with other features of Virchow's triad, with plaque rupture leading to thrombus formation and acute vessel occlusion. Post-mortem studies in patients following sudden cardiac death have identified plaque rupture to be common in lesions with, amongst other characteristics, large lipid necrotic cores and TCFAs (34). The ability to detect the presence of these vulnerable plaques prior to an MI, and incorporate them as risk modifiers into the clinical risk algorithms above, potentially accompanied by plaque and patient modulating therapies, would be of great clinical utility.

Natural antibodies, particularly of the IgM subclass, against MDA-adducted LDL, a post-translational oxidative modification to the LDL particle which renders it antigenic, have been found to relate to freedom from cardiovascular events in large population-based studies (90). In a unifying study, we have previously demonstrated that IgM anti-MDA-LDL levels protectively and independently relate to both cardiovascular events and $maxLCBI_{4mm}$ on NIRS-IVUS, which itself has been found to relate to future MACE (137). However, further confirmatory validation with anti-MDA-LDL antibodies in different patient populations is required before adoption into the clinical domain, particularly with an alternative imaging modality. Accordingly, CTCA imaging, coupled with new plaque analysis software, such as 'Autoplaque', can permit the quantitative plaque burden evaluation of different subtypes of atherosclerotic plaques, including low-attenuation plaque, the CT correlate of the lipidic necrotic core (283).

In the first half of this chapter, the relationship between anti-MDA-LDL antibodies with CTCA-derived atherosclerotic plaque subtypes will be explored, using sera from patients enrolled in the SCOT-HEART trial, in collaboration with the principal investigator, Prof David Newby (University of Edinburgh, UK). Briefly, as outlined above, the SCOT-HEART trial was a large multicentre open-label prospective randomised controlled trial that assessed the role of CTCA in patients with chest pain. Patients were recruited from outpatient clinics and randomised to standard care ± CTCA. 'Autoplaque' analysis has already been performed on all CT scans performed in the trial, making it an ideal population for this study (95). ELISAs that have been previously developed and optimised in the Haskard-Khamis laboratory are performed on these samples, assaying for IgG/ IgM anti-MDA-LDL antibodies, as well as MDA-LDL and ApoB. Relationships between the antibodies and different CTCA-imaged atherosclerotic characteristics will be evaluated, investigating the hypothesis that anti-MDA-LDL antibodies relate to various atherosclerotic characteristics, particularly low-attenuation plaque, in a protective fashion.

If robust consistent relationships between different phenotypes of atherosclerotic plaque and anti-MDA-LDL antibodies exist, independent of cardiovascular risk factors, then this adds significant supporting evidence for the incorporation of these assays into clinical risk matrices. Importantly, this data could be derived from a simple blood test, without the need for an invasive procedure or non-invasive scan, nephrotoxic contrast or ionizing radiation; in a cost-effective fashion.

In the second half of this chapter, the dynamics of MDA-LDL, ApoB and anti-MDA-LDL antibodies are evaluated in relation to strenuous exercise, in patients with severe flow-limiting

CAD. We have previously demonstrated that anti-MDA-LDL antibodies decrease perioperatively following major vascular surgery (254) and major cardiac surgery (253). This is theorised to be a potentially homeostatic consumptive phenomenon, whereby the antibodies bind to the pathogenic MDA-LDL that is produced in the presence of the significant cellular stressors, forming complexes that are then removed from circulation by the reticuloendothelial system. Robust exercise in patients with pre-existing single-vessel CAD may be expected to act as a similar significant physiological stressor. However, more excitingly, the interplay of exercise with coronary revascularisation via PCI for the only flow-limiting stenosis, thus relieving all expected substrate for ischaemia on exercise, will be evaluated in this chapter. This study was made possible through analysis of blood samples from participants undergoing randomisation to PCI or placebo procedure in the ORBITA trial (268), through collaboration with the principal investigator, Dr Rasha Al-Lamee (Imperial College London, UK).

Briefly, the ORBITA trial was the first blinded placebo-controlled trial for PCI in stable angina. 200 patients were enrolled following coronary angiography, which had to demonstrate at least one angiographically significant lesion (≥70%) in a single vessel that was suitable for PCI. Following this, patients underwent a 6-week anti-anginal optimisation phase, prior to baseline CPET, DSE and the blinded procedure (PCI or placebo). In those undergoing PCI, complete revascularisation was aimed for, with post-PCI physiology performed. Six weeks later, repeat CPET and DSE were performed in the follow-up assessment. Blood samples are available before and after the pre- and post-randomisation exercise assessments. The hypothesis being explored in this substudy of the ORBITA trial is that anti-MDA-LDL antibodies will

decrease from baseline levels following strenuous exercise; however, this acute reduction will be abrogated through relieving coronary ischaemia with PCI.

As mentioned above, both studies were only possible through collaboration with the trial investigators. In addition, Dr Amit Kaura and Dr Matthew Shun-Shin (both Imperial College London, UK) assisted with the statistical analyses for the SCOT-HEART and ORBITA sub-studies respectively.

3.3 Assay optimisation and variability

The ELISAs used in this chapter have been validated extensively previously in prior work in the Haskard-Khamis laboratory. The ELISAs for IgG and IgM anti-MDA-LDL utilise MDA-LDL on solid phase. A single batch of generated MDA-LDL was used for each study to optimise inter-plate variability, with EDTA added to limit further oxidation after the 3-hour MDA incubation.

Figure 3-1 below details the results of a BCA assay and functional ELISA of a batch of generated MDA-LDL. Given the very large and heterogenous lipoprotein structure of MDA-LDL, concentration must be determined via the protein component (ApoB), using a BCA assay. The ability of LO1 to detect MDA-LDL versus native unmodified LDL is then tested on ELISA, to confirm satisfactory LDL modification.

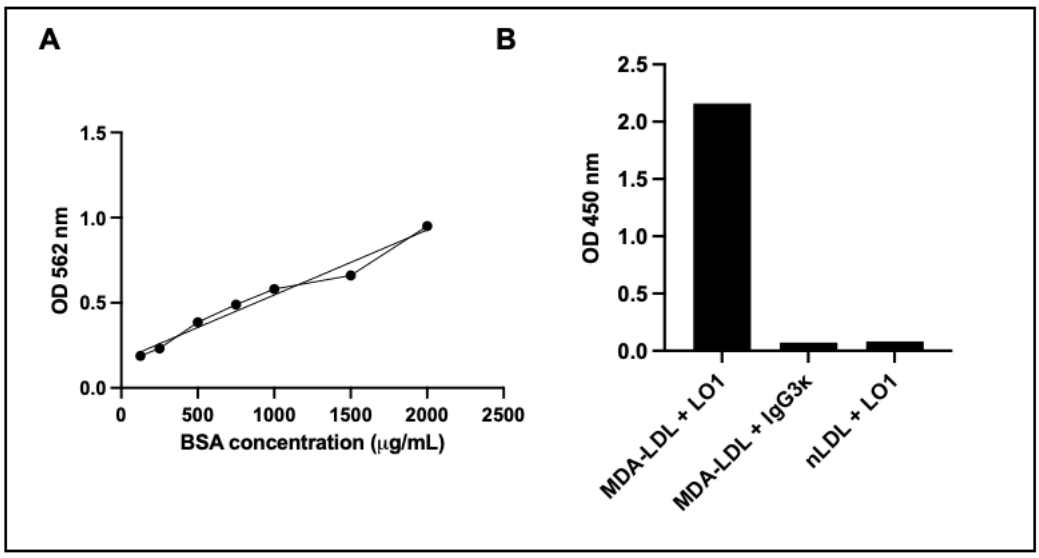

Figure 3-1. Malondialdehyde modification of LDL.

A) – displays the BSA standard curve that was used to interpolate the unknown MDA-LDL concentration using non-linear least squares regression (R^2 = 0.970). Of note, the concentration of the protein component (ApoB) of the modified LDL structure is quantified. Performed in duplicate. Error bars represent SEM.
B) – displays the results of an ELISA with MDA-LDL or native LDL on solid phase, with either LO1 or control IgG3κ as the primary antibodies. There is greater signal with LO1 than control antibody for MDA-LDL or for LO1 with native LDL, thus demonstrating effective modification of LDL to MDA-LDL.

All ELISAs were performed by researchers blinded to treatment allocation/ patient characteristics. Intra-plate and inter-plate coefficients of variance were <5% and <15% respectively.

3.4 The relationship between oxidised LDL and antibodies to oxidised LDL with atherosclerotic plaque characteristics – a substudy of the SCOT-HEART trial

3.4.1 Patient population

This substudy of the SCOT-HEART trial included all patients from the CT arm with blood available for analysis (see Figure 2-1). In total, the trial recruited 4,146 patients, of which, 2,073 were randomised to the standard of care + CTCA arm. Of these, 1,778 participants

finally underwent CTCA scanning, and of these, 830 had blood available for analysis. These patients all underwent CTCA scanning at a single site (Edinburgh Clinical Research Imaging Centre, Edinburgh, Scotland). Table 3-1 below details the patient characteristics of the substudy population.

	All participants
Number	830
Male, n (%)	438 (53)
Age, years (mean ± SD)	57.6 ± 9.8
Body mass index, kg/m^2 (mean ± SD)	29.6 ± 5.6
Atrial fibrillation, n (%)	16 (1.9)
Previous coronary heart disease, n (%)	67 (8.1)
Previous cerebrovascular disease, n (%)	40 (4.8)
Previous peripheral vascular disease, n (%)	15 (1.8)
Smoking habit, n (%)	
Current smoker	165 (20)
Ex-smoker	291 (35)
Non-smoker	374 (45)
Hypertension, n (%)	297 (36)
Diabetes Mellitus, n (%)	96 (12)
Family history of coronary heart disease, n (%)	341 (42)
Chest pain diagnosis, n (%)	

Atypical angina	207 (25)
Non-anginal	283 (34)
Typical angina	340 (41)
ASSIGN cardiovascular risk score (mean ± SD)	18.2 ± 11.4

Table 3-1. Patient characteristics for included participants in the SCOT-HEART substudy.

The 830 patients were 53% male with an average age of 57.6 (SD 9.8) years. There was a high prevalence of cardiovascular risk factors, with 55% current or ex-smokers, 36% hypertension, 12% diabetes mellitus and 8% previous coronary heart disease. The most common chest pain diagnosis was typical angina (41%), graded according to the National Institute for Health and Care Excellence definition (256). The average ASSIGN score was 18.2 (SD 11.4), with scores ≥ 20 representing a high likelihood of developing future CVD over the following 10-years (261).

3.4.1.1 Representativeness of study population to overall SCOT-HEART population

Given that this is a substudy in a proportion (n=830) of the larger SCOT-HEART population (n=4,146), we first compared the study population to the overall population, to confirm representativeness (Table 3-2 below). There were few major differences, with similar ages and cardiovascular risk profiles. The substudy population was slightly less male (53% versus 56%, p=0.035) and had a greater incidence of prior cerebrovascular disease (5% versus 3%, p=0.012). There was more typical angina in the substudy population also (41% versus 35%). However, there were no substantial clinically important differences between the populations.

	Overall (n=4146)	**Not included** (n=3316)	**Study Population** (n=830)	**P value**
Male, n (%)	2325 (56)	1887 (57)	438 (53)	0.035
Age, years (mean ± SD)	57 ±10)	57 ± 10	58 ± 10	0.055
Body mass index, kg/m2 (mean ± SD)	30 ± 6	30 ± 6	30 ± 6	0.400
Atrial fibrillation, n (%)	85 (2)	69 (2)	16 (2)	0.888
Previous coronary heart disease, n (%)	401 (10)	334 (10)	67 (8)	0.093
Previous cerebrovascular disease, n (%)	139 (3)	99 (3)	40 (5)	0.012
Previous peripheral vascular disease, n (%)	53 (1)	38 (1)	15 (2)	0.187
Smoking habit, n (%)				0.130
Current smoker	855 (21)	690 (21)	165 (20)	
Ex-smoker	1330 (32)	1039 (31)	291 (35)	
Non-smoker	1954 (47)	1580 (48)	374 (45)	
Hypertension, n (%)	1395 (34)	1098 (33)	297 (36)	0.166
Diabetes Mellitus, n (%)	444 (11)	348 (10)	96 (12)	0.406
Family history of coronary heart disease, n (%)	1716 (42)	1375 (42)	341 (42)	0.935
Chest pain diagnosis, n (%)				<0.001
Atypical angina	988 (24)	781 (24)	207 (25)	
Non-anginal	1692 (41)	1409 (43)	283 (34)	
Typical angina	1462 (35)	1122 (34)	340 (41)	

ASSIGN cardiovascular risk score (median [IQR])	15 [9, 22]	14 [9, 22]	16 [10, 24]	0.002

Table 3-2. Patient characteristics of the total SCOT-HEART population and the substudy population.

Next, we examined for any differences between those who underwent CTCA scanning (n=1,769) with blood available for analysis (n=830), versus those without available blood samples (n=948) (Table 3-3 below). Again, there were few major differences between the groups, with similar ages and prevalence of cardiovascular risk factors. Sex, 53% male versus 56% male (p=0.005), and previous coronary heart disease, 8% versus 10% (p=0.011), varied between the substudy and overall CTCA populations, respectively. As above, there were more frequently typical angina diagnoses in the substudy population (41% versus 37%). However, there were no substantial differences between the cohorts which would be expected to affect the validity of our analyses.

	Overall (n=1778)	**Not included** (n=948)	**Study Population** (n=830)	**P value**
Male, n (%)	997 (56)	559 (60)	438 (53)	0.005
Age, years (mean ± SD)	58 ± 9	58 ± 9	58 ± 10	0.902
Body mass index, kg/m2 (mean ± SD)	30 ± 6	30 ± 5	30 ± 6	0.936
Atrial fibrillation, n (%)	34 (2)	18 (2)	16 (2)	1.000
Previous coronary heart disease, n (%)	178 (10)	111 (12)	67 (8)	0.011
Previous cerebrovascular disease, n (%)	79 (4)	39 (4)	40 (5)	0.562

Previous peripheral vascular disease, n (%)	31 (2)	16 (2)	15 (2)	1.000
Smoking habit, n (%)				0.093
Current smoker	330 (19)	165 (18)	165 (20)	
Ex-smoker	593 (34)	302 (32)	291 (35)	
Non-smoker	845 (48)	471 (50)	374 (45)	
Hypertension, n (%)	608 (35)	311 (34)	297 (36)	0.281
Diabetes Mellitus, n (%)	196 (11)	100 (11)	96 (12)	0.591
Family history of coronary heart disease, n (%)	765 (44)	424 (45)	341 (42)	0.130
Chest pain diagnosis, n (%)				0.001
Atypical angina	432 (24)	225 (24)	207 (25)	
Non-anginal	683 (39)	400 (43)	283 (34)	
Typical angina	654 (37)	314 (33)	340 (41)	
ASSIGN cardiovascular risk score (median [IQR])	16 [10, 23]	16 [10, 22]	16 [10, 24]	0.635

Table 3-3. Patient characteristics of participants who underwent coronary CT angiography in the SCOT-HEART population and the substudy population.

3.4.2 Study CTCA and antibody data summary

Unsurprisingly, given the high preponderance of cardiovascular risk factors in the substudy population, as well as that they had possible symptomatic CAD, a sizeable proportion of participants had evidence of coronary atherosclerosis on CTCA. There was non-obstructive coronary artery disease present in 41% and obstructive disease in 27%. Of those with obstructive CAD (n=221), 117 patients had one-vessel obstructive disease, 77 had two-

vessel obstructive disease and 27 patients had three-vessel obstructive disease. The median CACS was 30 (IQR, 0-251) Agatston units. The median total plaque burden was 39.8 (0-48.7)%, non-calcified plaque burden was 36.5 (0-45.3)%, calcified plaque burden was 0.6 (0-2.9)% and low-attenuation plaque burden was 4.5 (0-6.9)%.

Median IgG anti-MDA-LDL was 0.932 (0.702-1.234) AU whilst IgM anti-MDA-LDL was 1.614 (1.147-2.211) absorbance units (AU).

3.4.3 Relationship between MDA-LDL and anti-MDA-LDL antibody levels and clinical characteristics

For the initial analysis, measured biomarker levels were divided into tertiles and any relationships with the clinical parameters outlined in the tables above were evaluated.

3.4.3.1 MDA-LDL

MDA-LDL was adjusted to ApoB, as described above, and was evaluated in tertiles versus clinical parameters (Table 3-4 below). MDA-LDL related to age, with higher levels in older participants (56.2 [SD 9.6] versus 58.8 [SD 10.3] years from the lowest to highest tertile, p=0.005). A positive relationship between increasing age and oxLDL levels has been identified previously, and is consistent with the concept of increasing oxidative stress and free radical generation (284, 285). Levels also related to smoking habit ($p<0.001$) and there was a trend for higher levels with a greater prevalence of diabetes mellitus (p=0.057). The association between MDA-LDL and these cardiovascular risk factors is not surprising, given that baseline circulating oxLDL has been demonstrated to be a predictor of future MI (286).

	Lowest	Middle	Highest	P value
Male, n (%)	152 (55)	148 (54)	138 (50)	0.463
Age, years (mean ± SD)	56.2 ± 9.6	57.9 ± 9.5	58.8 ± 10.3	0.005
Body mass index, kg/m2 (mean ± SD)	30 ± 5.6	29.3 ± 5.4	29.5 ± 5.9	0.296
Atrial fibrillation, n (%)	5 (1.8)	5 (1.8)	6 (2.2)	0.939
Previous coronary heart disease, n (%)	15 (5.4)	23 (8.3)	29 (11)	0.09
Previous cerebrovascular disease, n (%)	9 (3.3)	12 (4.4)	19 (6.9)	0.129
Previous peripheral vascular disease, n (%)	3 (1.1)	5 (1.8)	7 (2.5)	0.449
Smoking habit, n (%)				<0.001
Current smoker	69 (25)	58 (21)	38 (14)	
Ex-smoker	73 (26)	110 (40)	108 (39)	
Non-smoker	135 (49)	108 (39)	131 (47)	
Hypertension, n (%)	91 (33)	111 (40)	95 (35)	0.183
Diabetes Mellitus, n (%)	23 (8.3)	32 (12)	41 (15)	0.057
Family history of coronary heart disease, n (%)	114 (42)	119 (44)	108 (40)	0.633
Chest pain diagnosis, n (%)				0.091
Atypical angina	79 (29)	62 (23)	66 (24)	
Non-anginal	94 (34)	106 (38)	83 (30)	
Typical angina	104 (38)	108 (39)	128 (46)	
ASSIGN cardiovascular risk score (mean ± SD)	18.8 ± 11.5	18.5 ± 11.5	17.2 ± 11.2	0.247

Table 3-4. Patient characteristics per tertile of MDA-LDL.

MDA-LDL levels were calculated as MDA-LDL: ApoB ratio.

3.4.3.2 IgG anti-MDA-LDL

IgG anti-MDA-LDL was evaluated in tertiles versus clinical parameters (Table 3-5 below). There were no statistically significant relationships evident.

	Lowest	Middle	Highest	P value
Male, n (%)	145 (52)	152 (55)	1141 (51)	0.608
Age, years (mean ± SD)	57.2 ± 10	57.2 ± 9.6	58.4 ± 9.9	0.240
Body mass index, kg/m2 (mean ± SD)	29.3 ± 5.7	29.5 ± 5.7	29.9 ± 5.5	0.425
Atrial fibrillation, n (%)	5 (1.8)	7 (2.5)	4 (1.4)	0.636
Previous coronary heart disease, n (%)	26 (9.4)	20 (7.2)	21 (7.6)	0.610
Previous cerebrovascular disease, n (%)	9 (3.3)	16 (5.8)	15 (5.5)	0.315
Previous peripheral vascular disease, n (%)	4 (1.4)	8 (2.9)	3 (1.1)	0.240
Smoking habit, n (%)				0.201
Current smoker	54 (20)	59 (21)	52 (19)	
Ex-smoker	86 (31)	94 (34)	111 (40)	
Non-smoker	137 (50)	123 (45)	114 (41)	
Hypertension, n (%)	103 (38)	93 (34)	101 (37)	0.649
Diabetes Mellitus, n (%)	36 (13)	35 (13)	25 (9)	0.267
Family history of coronary heart disease, n (%)	112 (41)	108 (40)	121 (44)	0.555
Chest pain diagnosis, n (%)				0.510
Atypical angina	74 (27)	65 (24)	68 (25)	

Non-anginal	92 (33)	104 (38)	87 (31)	
Typical angina	111 (40)	107 (39)	122 (44)	
ASSIGN cardiovascular risk score (mean ± SD)	17.4 ± 10.5	18.6 ± 12.2	18.5 ± 11.5	0.378

Table 3-5. Patient characteristics per tertile of IgG anti-MDA-LDL.

3.4.3.3 IgM anti-MDA-LDL

IgM anti-MDA-LDL was evaluated in tertiles versus clinical parameters (Table 3-6 below). IgM anti-MDA-LDL antibodies were significantly associated with a range of clinical parameters. Across tertiles from low-to-high there were significant inverse relationships with male sex (62.1% vs 42.2%, p<0.001), cerebrovascular disease (7.2% vs 2.5%, p=0.036), hypertension (41.9% vs 27.7%, p=0.001), diabetes mellitus (15.5% vs 7.9%, p=0.02) and ASSIGN cardiovascular risk score (19.8±11.9 vs 17.5±11.0, p=0.011). These results are in accordance with the pre-existing literature. Females are known to have a greater reservoir of IgM anti-MDA-LDL antibodies (287). In addition, IgM anti-MDA-LDL antibodies have been shown to be highest in paediatric populations (81), and to decline with increasing age (287). Moreover, levels have been previously shown to be lower in diabetic, obese and hypertensive patients (288, 289). The inverse relationships with age, male sex, as well as other cardiovascular risk factors (all as identified here) have been postulated to provide evidence of a protective mechanism, or at least a protective association, between IgM anti-MDA-LDL antibodies, atherogenesis and CVD (89).

	Lowest	**Middle**	**Highest**	**P value**

Male, n (%)	172 (62)	149 (54)	117 (42)	<0.001
Age, years (mean ± SD)	58.6 ± 9.5	56.9 ±10.2	57.4 ± 9.7	0.112
Body mass index, kg/m2 (mean ± SD)	29.4 ± 5.1	29.6 ± 6.0	29.8 ± 5.7	0.727
Atrial fibrillation, n (%)	6 (2.2)	7 (2.5)	3 (1.1)	0.434
Previous coronary heart disease, n (%)	25 (9.0)	24 (8.7)	18 (6.5)	0.494
Previous cerebrovascular disease, n (%)	20 (7.2)	13 (4.8)	7 (2.5)	0.036
Previous peripheral vascular disease, n (%)	4 (1.4)	7 (2.5)	4 (1.4)	0.536
Smoking habit, n (%)				0.054
Current smoker	41 (15)	60 (22)	64 (23)	
Ex-smoker	96 (35)	93 (34)	102 (37)	
Non-smoker	140 (51)	123 (45)	111 (40)	
Hypertension, n (%)	116 (42)	105 (39)	76 (28)	0.001
Diabetes Mellitus, n (%)	43 (16)	31 (11)	22 (8)	0.02
Family history of coronary heart disease, n (%)	115 (42)	105 (39)	121 (44)	0.374
Chest pain diagnosis, n (%)				0.07
Atypical angina	66 (24)	72 (26)	69 (25)	
Non-anginal	79 (29)	102 (37)	102 (37)	
Typical angina	132 (48)	102 (37)	106 (39)	
ASSIGN cardiovascular risk score (mean ± SD)	19.8 ± 11.9	17.2 ± 11.2	17.5 ± 11	0.011

Table 3-6. Patient characteristics per tertile of IgM anti-MDA-LDL.

3.4.4 Relationship between anti-MDA-LDL antibody levels and coronary, aortic, aortic valve and mitral valve calcification

Relationships between serum anti-MDA-LDL antibody levels and CT-derived coronary calcification, using the Agatston score, have been identified previously, with IgG showing very weak positive correlation and IgM inverse correlation (287). Coronary artery calcification itself has gained an important clinical role in cardiovascular risk stratification, over and above conventional cardiovascular risk factor-based algorithms (290). As such, I explored relationships between IgG/ IgM anti-MDA-LDL antibodies and coronary artery calcification, as well as other CT-derived areas of calcification, including aortic, aortic valve and mitral valve calcification. Aside from hopefully demonstrating associations between blood and other imaging biomarkers of atherosclerosis, left-sided heart valve calcification is garnering increasing clinical interest through catheter-based structural heart valve interventions. For example, degree of aortic valve calcification relates to aortic stenosis severity and is helpful in predicting long term implanted device outcomes and post-procedural complications (291). Moreover, a previously unidentified heavily calcified “porcelain” aorta at the time of open-heart CABG or aortic valve surgery can lead to a significantly more complex operation or indeed procedure termination (292). Therefore, the identification of these important CT-derived imaging features with a simple blood test would have clinical relevance.

Table 3-7 below provides the associations between tertiles of IgG/ IgM anti-MDA-LDL antibodies and the presence or absence of regions of calcification identified on CTCA. These were assessed using a logistic regression model with adjustment for the ASSIGN cardiovascular risk score, which itself was modelled using a restricted cubic spline with four knots. Using the lowest tertile as reference, the OR of presence of calcification was evaluated

between the middle and highest tertiles. There were no relationships between IgG and any calcification, except for an inverse association with the presence of mitral valve calcification with OR 0.36 (95% CI, 0.10-0.99, p=0.05); however, the trend across tertiles was not statistically significant (p=0.25). For IgM, there was a robust inverse relationship with mitral valve calcification, with the middle tertile (OR 0.35 [95% CI 0.11-0.92], p=0.05), and more so the highest tertile (OR 0.26 [95% CI 0.07-0.72], p=0.02), being protective, with a significant p value for trend (p=0.05). The highest IgM tertile also inversely related to aortic valve calcification with OR 0.59 (95% CI 0.36-0.96, p=0.04), however the trend across tertiles was not significant (p=0.07). There were no relationships with the presence of coronary or aortic vessel calcification.

		Coronary calcification		**Aortic calcification**		**Aortic valve calcification**		**Mitral valve calcification**	
	Tertile	OR (95% CI)	P val	OR (95% CI)	P val	OR (95% CI)	P val	OR (95% CI)	P val
IgG anti-MDA-LDL (AU)	Lowest	1.00 (Ref)		1.00 (Ref)		1.00 (Ref)		1.00 (Ref)	
	Middle	0.93 (0.62 –1.40)	0.71	0.85 (0.52 –1.38)	0.51	0.91 (0.55 –1.49)	0.70	0.61 (0.23 –1.53)	0.30
	Highest	0.93 (0.62 –1.41)	0.75	1.13 (0.71 –1.81)	0.60	0.99 (0.61 –1.62)	0.98	0.36 (0.10 –0.99)	**0.05**

Trend			0.38		0.50		0.46	0.25
	Lowest	1.00 (Ref)		1.00 (Ref)		1.00 (Ref)		1.00 (Ref)	
IgM anti-MDA-LDL (AU)	Middle	0.90 (0.60 –1.37)	0.63	1.15 (0.72 –1.84)	0.55	0.78 (0.48 – 1.26)	0.32	0.35 (0.11 –0.92)	**0.05**
	Highest	0.71 (0.47 –1.07)	0.10	0.93 (0.57 –1.49)	0.75	0.59 (0.36 –0.96)	**0.04**	0.26 (0.07 –0.72)	**0.02**
Trend			0.22		0.92		0.07		**0.05**

Table 3-7. Adjusted odds ratio for the presence of coronary/ aortic/ aortic valve/ mitral valve calcification per tertile of IgG/ IgM anti-MDA-LDL antibodies.

P values based on a logistic regression model across the three tertiles of the antibodies with adjustment for cardiovascular risk score. Cardiovascular risk score was modelled using a restricted cubic spline with four knots.

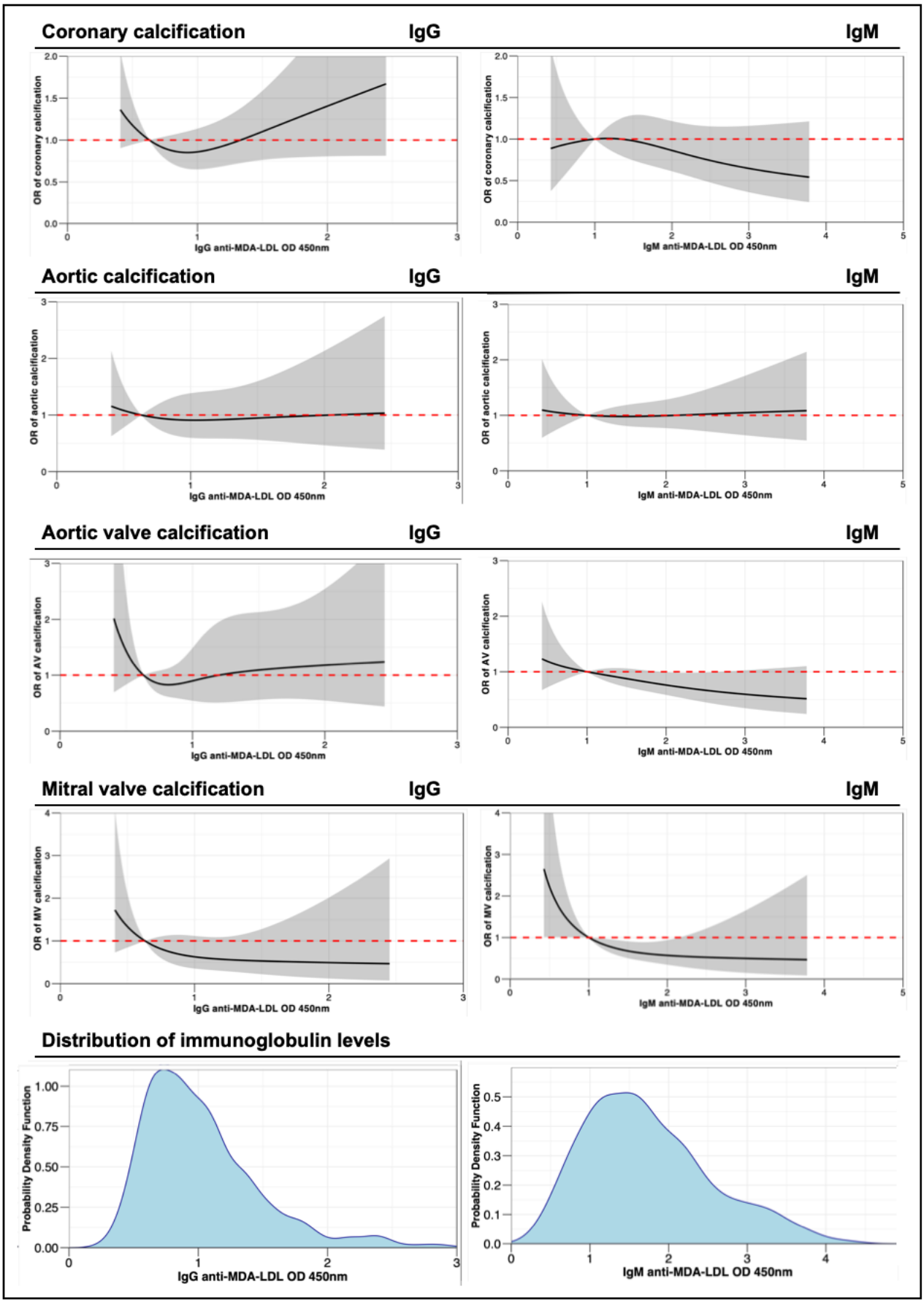
Coronary calcification
IgG
IgM
OR of coronary calcification
IgG anti-MDA-LDL OD 450nm
IgM anti-MDA-LDL OD 450nm
Aortic calcification
IgG
IgM
OR of aortic calcification
IgG anti-MDA-LDL OD 450nm
IgM anti-MDA-LDL OD 450nm
Aortic valve calcification
IgG
IgM
OR of AV calcification
IgG anti-MDA-LDL OD 450nm
IgM anti-MDA-LDL OD 450nm
Mitral valve calcification
IgG
IgM
OR of MV calcification
IgG anti-MDA-LDL OD 450nm
IgM anti-MDA-LDL OD 450nm
Distribution of immunoglobulin levels
Probability Density Function
IgG anti-MDA-LDL OD 450nm
Probability Density Function
IgM anti-MDA-LDL OD 450nm

Figure 3-2. Adjusted association between antibody level and presence of calcification in the coronary arteries, aorta, aortic valve and mitral valve using restricted cubic splines.

Splines were used in the model as the assumption of linearity between antibody concentration and plaque subtype burden was not satisfied. Splines were adjusted for cardiovascular risk score. Preliminary investigation suggested that three knots (intervals) should be used to fit the spline curve. The shaded area around the spline curve represents the 95% confidence interval. The probability density distribution is displayed to describe the distribution of measurements of antibody levels to model antibody concentrations in the restricted cubic spline analyses. AV, aortic valve; MV, mitral valve; OD, optical density; OR, odds ratio.

Next, the antibody-calcification relationships were evaluated graphically using restricted cubic splines with three knots and adjustment for the ASSIGN cardiovascular score, to visually assess the direction of any potential associations, displayed in Figure 3-2 above. Although not apparent in Table 3.7, divergent associations between the antibodies and coronary calcification are clear, albeit with wide confidence intervals, with IgG appearing to positively relate to the presence of calcification whilst IgM relates negatively. There is no ostensible relationship between either antibody with aortic calcification. However, there is a suggestion that IgM protectively relates to aortic valve calcification, as highlighted in Table 3-7. The protective relationships between both antibodies and mitral valve calcification are visible. A positive skew of both antibodies across the study population is also evident.

The relationships between the antibodies and quantitatively assessed coronary artery calcification using the Agatston score were subsequently evaluated, in an unadjusted model (Trend model 1) and with adjustment for the ASSIGN cardiovascular risk score (Trend model 2). This analysis is shown in Table 3-8, and visually in Figure 3-3, below. Log transformation of the Agatston score was performed, as is commonly conducted owing to its non-normal and positively skewed distribution (264).

		Coronary artery calcification score (log transformed) Median (IQR)
IgG anti-MDA-LDL (AU)	Lowest	5.00 (0 – 7.86)
	Middle	5.13 (0 – 7.85)
	Highest	4.75 (0 – 8.14)
Trend model 1		0.38
Trend model 2		0.57
IgM anti-MDA-LDL (AU)	Lowest	5.67 (0 – 8.31)
	Middle	4.95 (0 – 7.63)
	Highest	4.00 (0 – 7.80)
Trend model 1		**0.014**
Trend model 2		0.11

Table 3-8. Coronary calcification per tertile of IgG and IgM anti-MDA-LDL antibodies.

P values based on a linear trend test across the three tertiles of the antibodies in a linear regression model. Model 1: unadjusted; Model 2: adjustment for cardiovascular risk score. Cardiovascular risk score was modelled using a restricted cubic spline with four knots. The coronary calcification score was log2 transformed in the linear regression model.

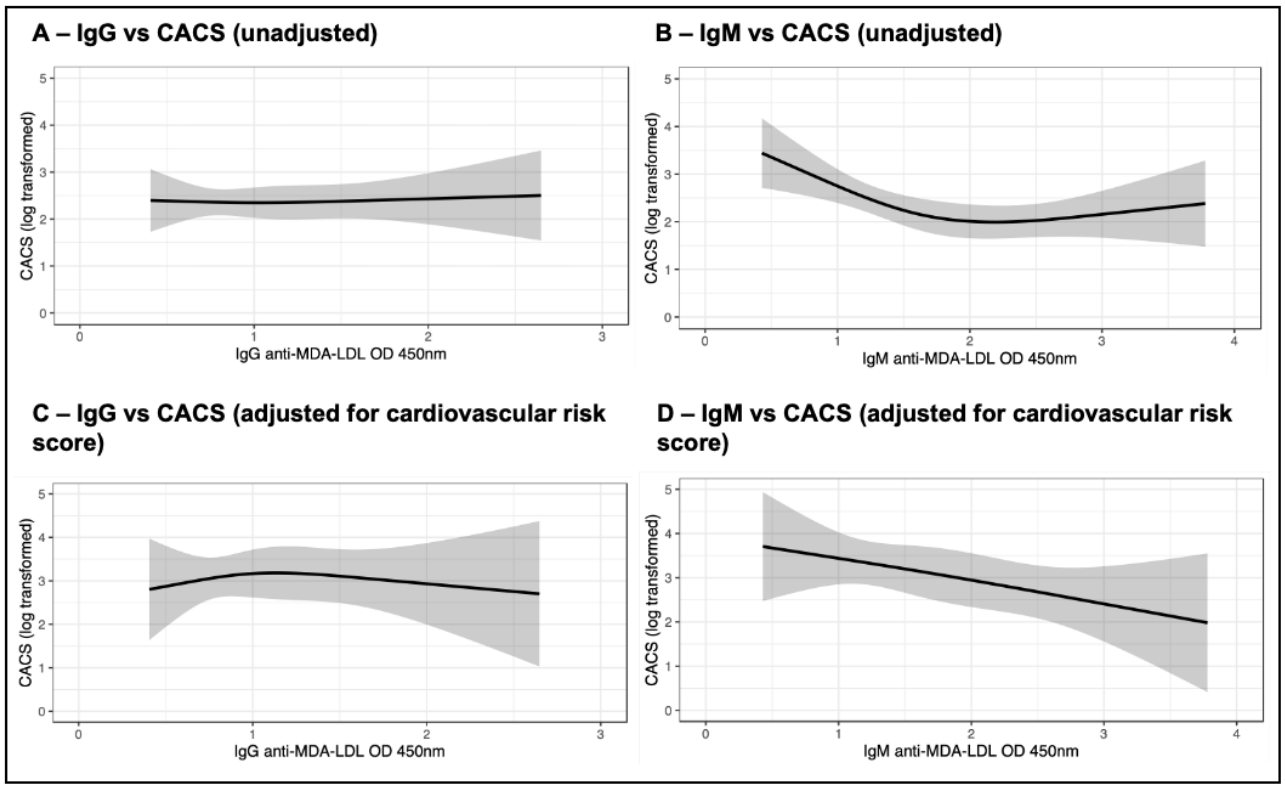

Figure 3-3. Unadjusted and adjusted association between antibodies and log-transformed coronary artery calcium score using restricted cubic splines.

Splines were used in the model as the assumption of linearity between antibody concentration and coronary artery calcification score was not satisfied. Splines were either unadjusted or adjusted for cardiovascular risk score. Preliminary investigation suggested that three knots (intervals) should be used to fit the spline curve. The shaded area around the spline curve represents the 95% confidence interval. CACS, coronary artery calcification score.

There was no association with IgG and log-transformed quantitatively assessed coronary calcification. However, an inverse relationship was identified with IgM, as had been suggested in the qualitative analysis above. In the unadjusted analysis this is a statistically significant relationship (p=0.014), which attenuates in Trend model 2 (p=0.11). Interestingly, in Figure 3-3, there is a more obvious linear negative relationship with IgM in the adjusted model, yet with wider confidence intervals, which explains the loss of statistical significance in Table 3-8.

3.4.5 Relationship between anti-MDA-LDL antibody levels and plaque subtype burden

Next, I investigated relationships between the antibodies and quantitatively assessed atherosclerotic plaque burdens. As detailed in *Section 2.2.1.3 Quantitative plaque analysis*, plaque volumes were measured for calcified, non-calcified, low-attenuation and total plaque. Percentage plaque burden for each plaque subtype was then computed by dividing the relevant plaque volume by the vessel volume of the region assessed. Antibodies in tertiles were then compared to each percentage plaque burden in a linear regression model without adjustment (Trend model 1), with additional adjustment for age (Trend model 2), additional adjustment for sex (Trend model 3), additional adjustment for each conventional cardiovascular risk factor (Trend model 4), and finally the ASSIGN cardiovascular risk score (Trend model 5). Figure 3-4 below presents the relationship between antibodies and plaque subtype graphically, adjusted for the ASSIGN cardiovascular risk score, using restricted cubic splines with four knots, as performed above.

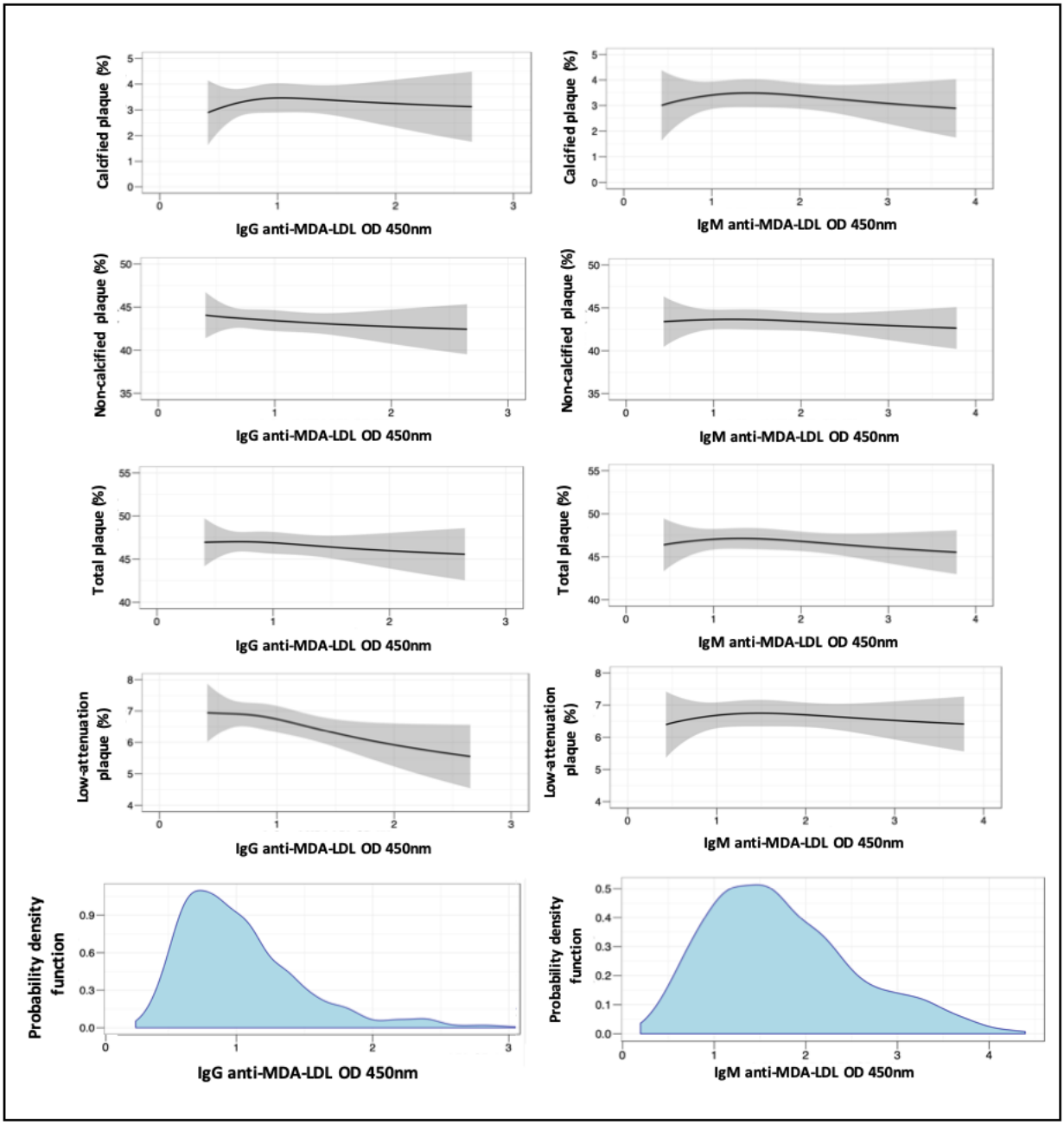

Figure 3-4. Adjusted association between antibodies and coronary atherosclerotic plaque subtypes using restricted cubic splines.

Splines were used in the regression model as the assumption of linearity between antibody concentration and plaque subtype burden was not satisfied. Splines were adjusted for cardiovascular risk score. Preliminary investigation suggested that four knots (intervals) should be used to fit the spline curve. The shaded area around the spline curve represents the 95% confidence interval. The probability density distribution is displayed to describe the distribution of measurements of antibody levels to model antibody concentrations in the restricted cubic spline analyses. OD, optical density.

3.4.5.1 IgG anti-MDA-LDL

Table 3-9 below presents the relationships between IgG anti-MDA-LDL in tertiles and plaque subtypes. Although the highest tertile of IgG anti-MDA-LDL had a numerically lower total plaque burden, there was no significant relationship (unadjusted, p=0.39; adjusted for cardiovascular risk score, p=0.64). The highest tertile of IgG anti-MDA-LDL also tended to have lower burdens of all plaque subtypes (calcified, non-calcified and low-attenuation plaque), although the most marked associations were seen with low-attenuation plaque (unadjusted, p=0.021; adjusted for cardiovascular risk score, p=0.031). This relationship withstood individual correction for all available lipid parameters (total cholesterol, HDL and non-HDL cholesterol), as well as other components of the cardiovascular risk score. This inverse relationship with low-attenuation plaque is readily appreciable in Figure 3-4 above.

		Total plaque	**Calcified plaque**	**Non-calcified plaque**	**Low-attenuation plaque**
	Tertile	Median (IQR)	Median (IQR)	Median (IQR)	Median (IQR)
IgG anti-MDA-LDL (AU)	Lowest	46.6 (39.6 – 52.7)	2.3 (0.6 – 4.7)	42.6 (37.2 – 48.6)	6.4 (4.7 – 8.6)
	Middle	47.1 (40.0 – 52.1)	1.9 (0.6 – 4.5)	43.0 (37.2 – 48.5)	6.2 (4.6 – 8.3)
	Highest	44.4 (38.1 – 53.1)	1.8 (0.5 – 4.6)	40.7 (34.8 – 47.7)	5.8 (4.2 – 7.5)
P value for trend					
Model 1: Unadjusted		0.39	0.66	0.27	**0.021**
Model 2: (Model 1 + age)		0.43	0.99	0.41	**0.029**
Model 3: (Model 2 + sex)		0.60	0.78	0.50	**0.030**

Model 4: (Model 3				
+ Total cholesterol)	0.58	0.22	0.54	**0.038**
+ HDL cholesterol)	0.64	0.70	0.52	**0.025**
+ Non-HDL cholesterol)	0.54	0.93	0.50	**0.034**
+ Family history of IHD)	0.73	0.88	0.68	**0.046**
+ Cigarette smoking)	0.85	0.85	0.78	**0.028**
+ Diabetes)	0.58	0.62	0.43	**0.030**
+ Systolic blood pressure)	0.57	0.74	0.46	**0.030**
Model 5: ASSIGN Risk score	0.64	0.80	0.55	**0.031**

Table 3-9. Coronary plaque subtypes per tertile of IgG anti-MDA-LDL antibodies.

P values based on a linear trend test across the three tertiles of the antibodies in a linear regression model. Model 1: unadjusted; Model 2: Model 1 + age; Model 3: Model 2 + sex; Model 4: Model 3 + cardiovascular risk factors; Model 5: ASSIGN cardiovascular risk score. Continuous variables were modelled using restricted cubic splines.

Given the relationship between IgG anti-MDA-LDL and low-attenuation plaque, the analysis was then repeated with a pre-defined low-attenuation plaque threshold of 4% (Table 3-10 below). This 4% low-attenuation plaque burden cut-off was chosen *a priori*, as it has been shown to strongly relate to future MI, independent of traditional clinical risk factors and the extent of obstructive coronary artery disease (95). Accordingly, the highest tertile of IgG anti-MDA-LDL was associated with the lowest burden of low-attenuation plaque, which remained after adjustment for the cardiovascular risk score (OR 0.58 [95% CI 0.34-0.96], p=0.037, p=0.027 for trend).

	Low-attenuation plaque >4%	
	OR (95% CI)	P value

IgG anti-MDA-LDL OD 450nm (AU)	Lowest	1.00 (Ref)	
	Middle	0.93 (0.53 – 1.63)	0.80
	Highest	0.58 (0.34 – 0.96)	**0.037**
Trend			**0.027**

Table 3-10. Adjusted odds ratio for high risk of fatal or non-fatal myocardial infarction based on 4% low-attenuation plaque burden cut-off per tertile of IgG anti-MDA-LDL antibodies.

P values based on a logistic regression model across the three tertiles of the antibodies with adjustment for cardiovascular risk score. Cardiovascular risk score was modelled using a restricted cubic spline with four knots.

3.4.5.2 IgM anti-MDA-LDL

Table 3-11 below presents the relationships between IgM anti-MDA-LDL in tertiles and plaque subtypes. There were no relationships with total plaque burden (unadjusted, p=0.64; adjusted for cardiovascular risk score, p=0.88), with or without adjustment, or with any plaque subtype. These findings are supported by Figure 3-4 above.

	Tertile	**Total plaque** Median (IQR)	**Calcified plaque** Median (IQR)	**Non-calcified plaque** Median (IQR)	**Low-attenuation plaque** Median (IQR)
IgM anti-MDA-LDL (AU)	Lowest	45.4 (39.7 – 52.1)	2.1 (0.6 – 4.7)	42.1 (37.2 – 47.7)	6.0 (4.3 – 8.3)
	Middle	46.6 (39.4 – 53.1)	1.9 (0.5 – 4.4)	42.6 (36.2 – 48.7)	6.4 (4.6 – 8.5)
	Highest	46.6 (39.8 – 52.0)	2.0 (0.5 – 4.7)	43.0 (35.6 – 48.8)	6.0 (4.5 – 7.5)
P value for trend					
Model 1: Unadjusted		0.64	0.73	0.76	0.99

Model 2: (Model 1 + age)	0.59	0.70	0.70	0.96
Model 3: (Model 2 + sex)	0.82	0.69	1.00	1.00
Model 4: (Model 3				
+ Total cholesterol)	0.80	0.43	0.93	0.90
+ HDL cholesterol)	0.29	0.65	0.93	0.94
+ Non-HDL cholesterol)	0.77	0.60	0.96	0.95
+ Family history of IHD)	0.68	0.80	0.75	0.90
+ Cigarette smoking)	0.61	0.75	0.70	0.99
+ Diabetes)	0.85	0.45	0.89	0.99
+ Systolic blood pressure)	0.89	0.69	0.97	0.99
Model 5: ASSIGN Risk score	0.88	0.72	1.00	0.98

Table 3-11. Coronary plaque subtypes per tertile of IgM anti-MDA-LDL antibodies.

P values based on a linear trend test across the three tertiles of the antibodies in a linear regression model. Model 1: unadjusted; Model 2: Model 1 + age; Model 3: Model 2 + sex; Model 4: Model 3 + cardiovascular risk factors; Model 5: ASSIGN cardiovascular risk score. Continuous variables were modelled using restricted cubic splines.

3.4.6 Relationship between anti-MDA-LDL antibody levels and obstructive coronary disease

	No disease (n=272)		**Non-obstructive disease** (n=337)		**Obstructive disease** (n=221)	
	OR (95% CI)	P value	OR (95% CI)	P value	OR (95% CI)	P value
IgG anti-MDA-LDL (AU)	Reference	-	0.96 (0.63–1.46)	0.86	1.05 (0.65–1.69)	0.84

IgM anti-MDA-LDL (AU)	Reference	-	0.74 (0.51–1.07)	0.11	0.63 (0.42–0.95)	**0.028**

Table 3-12. Results of multinomial logistic regression of antibodies on the probability of severity of coronary disease.

P values based on a multinomial regression model, with the reference group being no disease (A). Adjusted for cardiovascular risk score, which was modelled using a restricted cubic spline with four knots.

There was a trend for IgM anti-MDA-LDL antibodies conferring protection from non-obstructive coronary disease versus no coronary disease (OR 0.74 [95% CI 0.51-1.07], p=0.11), but was only significantly associated with obstructive disease (OR 0.63 [95% CI 0.42-0.95], p=0.028). There were no significant relationships found between IgG anti-MDA-LDL and obstructive or non-obstructive coronary disease (Table 3-12).

Conversely, although there was a suggestion of both antibodies being inversely related to the number of obstructed coronary arteries, only IgG anti-MDA-LDL reached statistical significance, and strongly indicated protection (OR for 3-vessel disease versus 1-vessel disease 0.20 [95% CI 0.07-0.62], p=0.0048), (Table 3-13 below).

	1-vessel disease (n=117)		**2-vessel disease** (n=77)		**3-vessel disease** (n=27)	
	OR (95% CI)	P value	OR (95% CI)	P value	OR (95% CI)	P value
IgG anti-MDA-LDL (AU)	Reference	-	0.60 (0.30–1.20)	0.15	0.20 (0.07–0.62)	**0.0048**

IgM anti-MDA-LDL (AU)	Reference	-	0.62 (0.35–1.10)	0.10	0.68 (0.31–1.51)	0.35

Table 3-13. Results of multinomial logistic regression of antibodies on the probability of 1-, 2- or 3-vessel disease in patients with obstructive disease.

P values based on a multinomial regression model, with the reference group being 1-vessel disease. Adjusted for cardiovascular risk score, which was modelled using a restricted cubic spline with four knots.

3.4.7 Relationship between anti-MDA-LDL antibody levels and clinical events

I have now demonstrated a protective relationship between both IgG and IgM anti-MDA-LDL antibodies with atherosclerotic features known to relate to hard cardiovascular endpoints, including coronary calcification (293), aortic valve calcification (294), mitral valve calcification (295) and low-attenuation atherosclerotic plaque (95). However, valve calcification is associated with concomitant coronary atherosclerosis, and the relationship between valve calcification per se with cardiovascular events may not be independent of coronary artery disease (296). Nonetheless, in an exploratory analysis, we evaluated the association between the antibodies and incident MI, until the end of SCOT-HEART trial follow-up (median 4.8 years). Table 3-14 below displays the results of this analysis, with no relationship evident, in tertiles or continuously. However, this is not surprising, given the very low clinical event rate, with only 19 fatal or non-fatal MIs recorded in the 830 participants over the follow-up period. This low event rate may be due to the optimised preventative medical therapy that had been instituted during the SCOT-HEART trial, particularly in those who underwent CT scanning. This is thought to explain the protective effect on future MI seen in those undergoing CTCA in the trial (258). Of course, all 830 patients included in the present analysis are from the CT arm of the original trial.

		No. of events	Fatal or non-fatal Myocardial Infarction	
			OR (95% CI)	P value
IgG anti-MDA-LDL (AU)	Lowest	7	1.00 (Ref)	
	Middle	8	1.18 (0.42 – 3.44)	0.75
	Highest	4	0.56 (0.15 – 1.90)	0.37
	Continuous	19	0.69 (0.22 – 2.03)	0.51
IgM anti-MDA-LDL (AU)	Lowest	5	1.00 (Ref)	
	Middle	9	2.03 (0.69 – 6.71)	0.21
	Highest	5	1.04 (0.29 – 3.81)	0.95
	Continuous	19	1.33 (0.54 – 0.92)	0.49

Table 3-14. Relationship between fatal or non-fatal myocardial infarction and antibody levels.

P values based on a logistic regression model across the three tertiles of the antibodies with adjustment for cardiovascular risk score. Cardiovascular risk score was modelled using a restricted cubic spline with four knots.

3.4.8 Conclusions

In summary, this substudy of the SCOT-HEART trial including all patients from the CT arm with blood available for analysis (n=830) has investigated relationships between both IgG and IgM anti-MDA-LDL antibodies and cardiovascular atherosclerosis. Most importantly, we demonstrate for the first time a protective relationship between antibodies against MDA-LDL and low-attenuation non-calcified atherosclerotic plaque on CTCA, which is known to relate to risk of future MI. This study also suggests that MDA-LDL antibodies are associated with less coronary atherosclerotic plaque, a more favourable plaque phenotype and lower valve calcification. Figure 3-5 below highlights these findings, along with the potential mechanistic roles of IgG and IgM anti-MDA-LDL antibodies in atherogenesis. No relationship with clinically

driven events could be demonstrated; however, this particular analysis is limited by the low frequency of MI in the study population.

IgM anti-MDA-LDL
↓ CACS
IgG anti-MDA-LDL
↓ low-attenuation plaque
Calcification
Necrotic core
Transcytosis across endothelium
LDL
Oxidative modification
MDA-LDL
? Released into plasma
? Oxidative modification in plasma
MDA-LDL
Taken up by foam cells
Complexes with IgG and IgM anti-MDA-LDL antibodies
Homeostatic clearance via the liver and spleen
IgM anti-MDA-LDL
↓ obstructive coronary disease
IgG anti-MDA-LDL
↓ number of obstructed vessels

Figure 3-5. Schematic illustration of the potential mechanistic roles of IgG and IgM anti-MDA-LDL antibodies with important CTCA features of coronary atherosclerosis.

On the left, there is a CTCA image of an atherosclerotic plaque in the left anterior descending artery that has been reconstructed to demonstrate atherosclerotic plaque characteristics. Blue corresponds to vessel lumen; yellow is calcified plaque; red is non-calcified plaque and orange represents low-attenuation plaque.
On the right, there is an illustration of a representative atherosclerotic plaque, highlighting the potential roles of IgG and IgM anti-MDA-LDL antibodies in plaque biology as well as the key findings of this study.
This diagram demonstrates how circulating low-density lipoprotein crosses leaky vascular endothelium to the sub-endothelial space, where it becomes oxidatively modified to oxidized LDL, of which malondialdehyde adduction to form MDA-LDL is one prevalent modification. Subsequently, macrophages uptake MDA-LDL via scavenger receptors and form foam cells, which are key in the evolving atherosclerotic plaque. Ensuing cell death and apoptosis results in increased necrotic core formation, which is crucial to plaque vulnerability, and is detected on CTCA as low-attenuation plaque. MDA-LDL may transcytose back across the leaky vascular endothelium into the vessel lumen, or become oxidised in plasma to form MDA-LDL, where it is detectable in blood. Here IgG and IgM anti-MDA-LDL antibodies from the circulating antibody reservoir can detect and bind MDA-LDL, forming immune complexes, which are then removed from the circulation via the reticuloendothelial system in a homeostatic phenomenon.
In this study, higher levels of IgG anti-MDA-LDL associated with less low-attenuation plaque and fewer number of vessels with obstructive disease; whilst higher IgM anti-MDA-LDL levels related to lower CACS and less obstructive coronary disease.
CACS, coronary artery calcium score; LDL, low-density lipoprotein; MDA-LDL, malondialdehyde-modified LDL.

3.5 The relationship between oxidised LDL and antibodies to oxidised LDL with exercise in coronary artery disease – a substudy of the ORBITA trial

3.5.1 Patient population

In total, 200 patients were randomised in the ORBITA trial, between January 6th 2014 and August 11th 2017. Of these 200, 196 had blood samples available for analysis (PCI, n=102; Placebo, n=94). Table 3-14 below displays the patient and lesion characteristics. The mean ages of the PCI and placebo arm were similar at 66.0 (SD 9.50) and 66.2 (SD 8.45) respectively. Again, sex was similar with 70% and 76% male per group. There was a high and similar preponderance of cardiovascular risk factors between the two arms, with each having ~70% hypertension, ~70% hypercholesterolaemia, ~5% previous MI, ~20% diabetes mellitus and ~15% current smokers. Left ventricular systolic function was good in approximately 90% and moderately impaired in 3%. Severe left ventricular systolic dysfunction was an exclusion criterion for recruitment. In terms of location of the severe

coronary artery lesion, ~68% were in the left anterior descending artery, ~10% in the left circumflex and ~15% in the right coronary artery, with no substantial differences between the two arms. At pre-randomisation assessment there was a very high prescription of preventative medications, with 98% taking aspirin and 95% taking a statin. For anti-anginal medication at baseline, 78% were taking β-blockers whilst 91% were taking calcium channel blockers. The median number of anti-anginal medications was three prior to randomisation.

	PCI (n=102)	**Placebo (n=94)**	**All patients (n=196)**
Age (years, SD)	66.0 (9.50)	66.2 (8.45)	66.1 (8.99)
Male (%)	71 (70%)	71 (76%)	142 (72%)
Hypertension (%)	70 (69%)	65 (69%)	135 (69%)
Hypercholesterolaemia (%)	79 (77%)	62 (66%)	141 (72%)
Previous myocardial infarction (%)	5 (5%)	7 (7%)	12 (6%)
Previous PCI (%)	9 (9%)	15 (16%)	24 (12%)
Diabetes Mellitus (%)	15 (15%)	21 (22%)	36 (18%)
Current smoker (%)	10 (10%)	15 (16%)	25 (13%)
Angina duration (months, SD)	9.7 (15.9)	8.4 (7.6)	9.1 (12.6)
Left ventricular systolic function			
- Normal (%)	96 (94%)	84 (89%)	180 (92%)
- Mildly impaired (%)	3 (3%)	7 (7%)	10 (5%)
- Moderately impaired (%)	3 (3%)	3 (3%)	6 (3%)
Significant coronary stenosis			
- LAD (%)	69 (68%)	65 (69%)	134 (68%)

- D1 (%)	2 (2%)	2 (2%)	4 (2%)
- Intermediate (%)	1 (1%)	2 (2%)	3 (2%)
- LCx (%)	9 (9%)	10 (11%)	19 (10%)
- OM1 (%)	4 (4%)	0 (0%)	4 (2%)
- RCA (%)	17 (17%)	15 (16%)	32 (16%)

Table 3-15. Patient characteristics of participants included in the ORBITA substudy.

PCI, percutaneous coronary intervention; LAD, left anterior descending; D1, 1st diagonal; LCx, circumflex; OM1, 1st obtuse marginal; RCA, right coronary artery.

3.5.2 Effect of exercise on MDA-LDL and anti-MDA-LDL antibodies

	P1 (n=188)	**P2** (n=186)	**P3** (n=186)	**P4** (n=183)
MDA-LDL (as ratio to ApoB)	0.155 (0.085)	0.154 (0.083)	0.158 (0.116)	0.160 (0.123)
IgG anti-MDA-LDL (AU)	0.454 (0.214)	0.432 (0.198)	0.473 (0.223)	0.467 (0.216)
IgM anti-MDA-LDL (AU)	0.773 (0.457)	0.759 (0.460)	0.832 (0.517)	0.808 (0.492)

Table 3-16. Average biomarker values at each study timepoint.

Blood samples were obtained on the day of pre-randomisation assessment, prior to exercise (timepoint P1) and three hours after exercise (timepoint P2). At post-randomisation assessment (six weeks following the PCI or placebo procedure) further blood tests were obtained: before (timepoint P3) and three hours after (timepoint P4) exercise. Values are mean (standard deviation). MDA-LDL is expressed as a ratio of MDA-LDL to Apolipoprotein B; anti-MDA-LDL antibodies are expressed as optical density values at 450nm in Absorbance Units.

Table 3-16 above displays the average biomarker values at each study timepoint P1-P4. Blood sampling for P1 occurred on the day of pre-randomisation assessment prior to exercise, whilst P2 was three-hours following exercise. P3 and P4 occurred before and after exercise at the post-randomisation assessment. Adjusted MDA-LDL levels did not change significantly across the timepoints. However, both IgG and IgM anti-MDA-LDL antibodies decreased following exercise at the pre-randomisation assessment (0.454 AU to 0.432 AU

and 0.773 AU to 0.759 AU respectively). A similar reduction was observed following exercise at the post-randomisation assessment (0.473 AU to 0.467 AU and 0.832 AU to 0.808 AU respectively).

Figure 3-6 below displays the temporal changes between P1 and P2 graphically, with a one-sample t-test used to assess statistical difference in biomarker values before and after exercise. There was no significant change in adjusted MDA-LDL levels with exercise (-0.001 AU, 95% CI -0.004 to 0.001; p=0.287). As above, a significant decrease in the levels of both antibodies was observed. IgG ant-MDA-LDL reduced by 0.022 AU (95% CI -0.029 to -0.014; p<0.0001) whilst IgM ant-MDA-LDL decreased by 0.016 AU (95% CI -0.024 to -0.008; p=0.0002).

These findings establish a reduction in both IgG and IgM anti-MDA-LDL with exercise. This could represent a beneficial homeostatic phenomenon, with antibody consumption via binding to circulating oxLDL, that has been generated by exercise. Once bound, the antibodies complex with their antigen, and are trafficked to the reticuloendothelial system for excretion. It is possible that the timing of blood sampling has resulted in a lack of appreciation of dynamic changes in MDA-LDL.

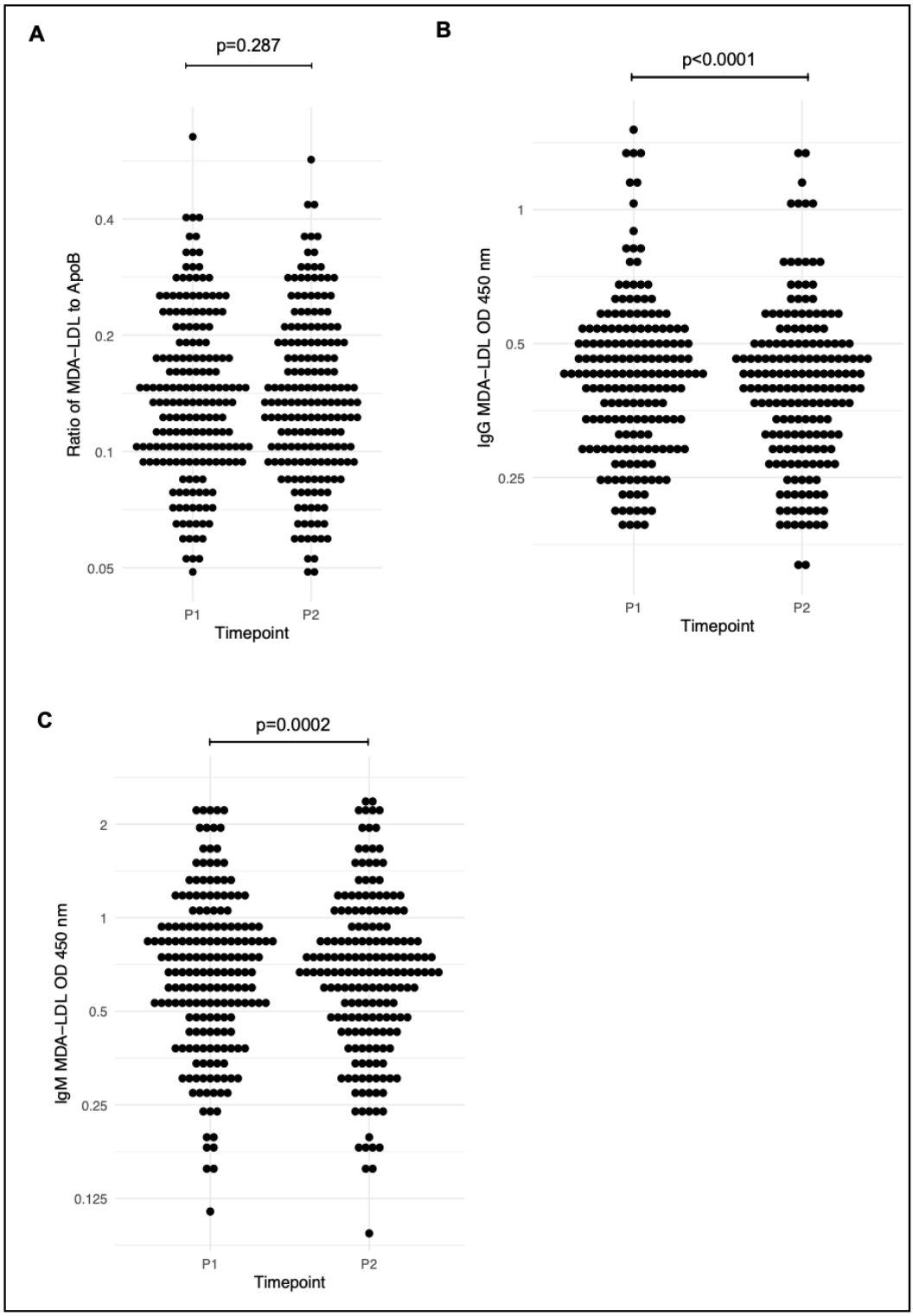

Figure 3-6. Dynamic change in biomarkers between P1 (baseline pre-randomisation assessment, pre-exercise) and P2 (baseline pre-randomisation assessment, post-exercise).

A) – Adjusted MDA-LDL
B) – IgG anti-MDA-LDL
C) – IgM anti-MDA-LDL
One sample t-test used to assess statistical significance.

Next, any associations between biomarker levels and exercise intensity were assessed (P2 controlling for P1), to evaluate whether more strenuous exercise induced more free radical generation, therefore resulting in a greater anti-MDA-LDL antibody level reduction required for complexing and clearance. However, there were no relationships between exercise duration and adjusted MDA-LDL, IgG or IgM anti-MDA-LDL (p=0.0355, p=0.386 and p=0.657, respectively). Equally, there were no observable associations with exercise intensity assessed via maximum oxygen consumption ($VO2_{max}$) (p=0.121, p=0.701 and p=0.07, respectively). However, the relationship with IgM anti-MDA-LDL was trending and close to statistical significance. It is possible however that perhaps the highly optimised anti-ischaemic therapy in the patients enrolled in the ORBITA trial abolished any association between anti-MDA-LDL antibodies and exercise intensity.

3.5.3 Effect of PCI versus placebo on pre-exercise and post-exercise MDA-LDL and anti-MDA-LDL antibody levels

After ascertaining that robust exercise induced a reduction in both IgG and IgM anti-MDA-LDL antibodies, potentially in a homeostatic response to the exercise-induced oxidative stress in patients with significant myocardial ischaemia, I next wanted to evaluate whether rendering these patients relatively non-ischaemic through PCI could ameliorate the immune response. Firstly, any effect of PCI on resting, pre-exercise, biomarkers were assessed. This was achieved by comparing values at baseline pre-exercise (P1) with those at post-randomisation pre-exercise (P3). Accordingly, there were no significant differences in pre-exercise values between the PCI and placebo arms (MDA-LDL [p=0.102], IgG anti-MDA-LDL [p=0.444], IgM anti-MDA-LDL [p=0.909]), when analysing P3 levels controlled for P1 levels.

Next, the placebo-controlled effect of PCI was evaluated on exercise-induced biomarker changes, via analysing P4 values and adjusting for P1-3. Comparably, treating the obstructive CAD with PCI, and therefore resolving the ischaemic substrate, did not alter the post-exercise biomarker levels (MDA-LDL [p=0.605], IgG anti-MDA-LDL [p=0.725], IgM anti-MDA-LDL [p=0.171]). Of note, the exercise-induced reductions in both antibodies remained between P3 and P4, similar to P1 and P2, across the whole study population. IgG anti-MDA-LDL decreased 0.006 AU (95% CI -0.013 to -0.0004, p=0.036), whilst IgM anti-MDA-LDL decreased 0.015 AU (95% CI -0.024 to -0.006, p=0.002). As before, there was no significant change in MDA-LDL levels (0.0007 AU, 95% CI -0.003 to 0.004; p=0.707). As discussed above, perhaps the baseline anti-anginal therapy reduced the ischaemic burden with exercise, and therefore nullified any potential effect of PCI in this population. This is relevant, as PCI for stable CAD is now generally only clinically indicated in patients with ongoing symptoms despite optimised anti-anginal therapy. Thus, the optimised anti-anginal medical therapy may prevent symptoms, as well as significant oxLDL generation, with exercise. This also may help to explain a lack of beneficial prognostic effect of PCI in the context of optimised medical therapy (7).

3.5.4 Relationship between MDA-LDL and anti-MDA-LDL antibody levels and baseline dobutamine stress echocardiography

Of the patients included in the study, 180 had DSE performed at baseline, as outlined in *Section 2.2.2.4 Dobutamine stress echocardiography protocol*. The presence of a relationship between MDA-LDL or related antibody levels and ischaemia on DSE was evaluated, at baseline pre-randomisation and at the post-randomisation assessment. It could

be hypothesised that more ischaemic myocardium at baseline may relate to lower anti-MDA-LDL antibody concentrations following exercise, with greater antibody consumption in response to the increased ischaemic burden. This follows the earlier findings that exercise across all participants resulted in consumption/ loss of these antibodies. However, the pre-randomisation stress echo score did not affect any of the post-exercise biomarker levels (MDA-LDL [p=0.349], IgG anti-MDA-LDL [p=0.852], IgM anti-MDA-LDL [p=0.255]) (P2 adjusting for P1). Likewise, the pre-randomisation stress echo score did not impact the placebo-controlled effect of PCI on post-exercise levels (P4) of any biomarkers (MDA-LDL [p=0.484], IgG anti-MDA-LDL [p=0.750], IgM anti-MDA-LDL [p=0.759]). Thus, even in patients with greater ischaemic myocardium at baseline who have subsequently been revascularised, removing the ischaemic substrate with PCI induced no effect on the exercise-induced biomarker change. As above, the interplay of optimised anti-anginal therapy at baseline (in both arms) needs to be considered and may be effectively masking any biomarker changes.

3.5.5 Conclusions

Using the unique opportunity afforded by the availability of blood samples collected from patients with CAD enrolled in the ORBITA trial (n=196), we assessed for any changes in MDA-LDL or related antibodies with exercise, and whether this could be influenced by PCI. Accordingly, this study demonstrated that exercise resulted in an acute reduction in both IgG and IgM MDA-LDL antibodies, with no change in adjusted MDA-LDL levels. The magnitude of this change was not related to exercise duration or intensity, or indeed degree of baseline ischaemia on stress echocardiography. Moreover, relieving the flow-limiting stenosis with PCI

did not significantly affect the change in IgG/ IgM anti-MDA-LDL antibody levels with exercise, or their baseline levels prior to exercise.

These findings determine an acute reduction in anti-MDA-LDL antibodies occurs with exercise, possibly via an induction of clearance of generated oxLDL via the innate immune system. This is of course observational with an undefined mechanism and the significance remains to be determined. However, this effect was not significantly modulated by PCI. The role of the aggressively optimised medical therapy during the 6-week medical optimisation phase pre-randomisation needs to be considered, and may mask any biomarker changes.

3.6 Discussion

This chapter has explored the relationships between MDA-LDL and related anti-MDA-LDL antibodies with CTCA-detected atherosclerosis; as well as exercise and ischaemia in the presence of severe coronary atherosclerosis, modulated by coronary intervention with PCI.

3.6.1 SCOT-HEART study summary

I report that both IgG and IgM anti-MDA-LDL antibodies relate to atherosclerosis in a protective fashion in the SCOT-HEART substudy.

3.6.1.1 IgG anti-MDA-LDL

IgG anti-MDA-LDL related to less necrotic core burden (low-attenuation plaque on CTCA), independent of standard lipid measures (including total cholesterol, HDL and non-HDL cholesterol) and traditional cardiovascular risk factors. The importance of this lies in the fact that low-attenuation plaque corresponds to the necrotic atherosclerotic core, which has been

identified on invasive clinical studies to confer an increased risk of future cardiovascular events (137, 138). We also demonstrate that higher IgG anti-MDA-LDL antibodies predict a lower incidence of a low-attenuation plaque 4% threshold, which is strongly related to future MI, independent of standard clinical risk factors and the extent of obstructive coronary artery disease (95). IgG anti-MDA-LDL also related to the number of coronary arteries with obstructive disease and a trend was present with mitral valve calcification.

3.6.1.2 IgM anti-MDA-LDL

IgM anti-MDA-LDL antibody levels on the other hand, inversely related to multiple cardiovascular risk factors and obstructive coronary disease, with a trend for number of coronary arteries with obstructive disease as well as CACS, whilst levels were also associated with both aortic and mitral valve calcification. Unfortunately, no direct link could be drawn to clinically driven endpoints in this study, which is likely due to the low event rate, even with 5-year in-trial follow-up. However, these associations have been evaluated previously by our group in a large systematic review and protective relationships between IgM antibodies against various epitopes on oxLDL have been demonstrated in various clinical studies, although the relationship with IgG is more difficult to elucidate (90). Similar findings have very recently been reported in a large case-control study of the Pakistan Risk of Myocardial Infarction Study, where IgM anti-MDA-LDL levels were measured within 24-hours of a first MI in 4559 patients, and compared to 4617 age and sex-matched controls. Males, smokers and individuals with hypertension and diabetes had lower antibody levels ($p<0.001$), as we report in the present study. Compared to the lowest quintile, the highest quintiles of IgM MDA-LDL had a significant reduction in MI, with an OR of 0.67 (95% CI, 0.58-0.77). Most interestingly, IgM antibodies against other OSEs were similarly protective from future MI,

suggesting a class effect of natural IgM targeted against oxidative epitopes. Indeed, when the IgM OSE levels were added to traditional cardiovascular risk factors in this study, there was an impressive net reclassification index of 15.5% (95% CI 11.4 to 19.6) for future MI (297).

Altogether, taking the current SCOT-HEART substudy findings and the existing literature into account, there is a mounting evidence base to strongly suggest that having a greater reservoir of IgM anti-oxLDL antibodies relates to less atherosclerosis and atherosclerosis-driven cardiovascular events. Our study is in keeping with previous studies that have demonstrated an inverse correlation between IgM anti-MDA-LDL antibodies and obstructive angiographically-imaged CAD (298) as well as CT-derived CACS (287). Pertinently, IgM anti-MDA-LDL antibodies are lower in males than females, lower in various diseases that predispose to manifest cardiovascular disease, and decrease with increasing age, all suggesting an important relationship with atherosclerosis (287).

3.6.2 Potential mechanistic roles of IgM anti-MDA-LDL antibodies in atherogenesis

We have previously shown that IgM anti-MDA-LDL antibodies are associated with a lower burden of lipid-rich plaque on invasive assessment using NIRS-IVUS in the IBIS-3 study, which is known to relate to increased plaque rupture and subsequent vessel thrombosis (255). What is not known however, is whether this relationship is purely an epiphenomenal association, the effect of some other interaction without any mechanistic role or causation itself, or indeed whether increasing this pool of IgM antibodies is advantageous.

To this end, subcutaneous immunisation of LDL-R$^{-/-}$ mice with MDA-LDL has been recently shown to reduce aortic atherosclerotic plaque size, accompanied by substantial increases in serum memory B cells, plasma cells and specific IgG and IgM anti-MDA-LDL antibodies. Furthermore, these effects were abolished (with accelerated atherosclerosis) in mice lacking germinal centre-derived plasma cells, supporting the crucial role of the adaptive immune system in this response (299). This concept is being used for the development of therapeutic antibody treatments for passive immunisation in atherosclerosis (183). Accordingly, a future planned avenue of research in the Khamis laboratory is to explore the potential atheroprotective effect of passive immunisation of LO1 or LO1Fab in the LDL-R$^{-/-}$ mouse model of atherosclerosis.

Again, demonstrating a potential mechanistic link between IgM anti-oxLDL antibodies and atherosclerosis, the source for IgM antibodies targeting OSEs has been very recently identified to be circulating human CD24 marginal zone B cells. Anti-CD24 treatment led to reduced marginal zone B cells and accordingly protection from vascular inflammation in atherosclerotic mice; whilst the presence of these marginal zone B cells producing IgM anti-OSE antibodies was found to inversely relate to severity of CAD in humans (300).

Horkko and colleagues have explored the cellular effects of EO6, a natural murine IgM antibody that binds to the phosphatidylcholine headgroup of oxidised phospholipids. Following binding, EO6 inhibits macrophage oxLDL uptake and minimises resultant oxidised phospholipid induced inflammation (301). As discussed above, the same group also identified a human monoclonal IgG Fab, IK17, in a phage display antibody library from a patient with high plasma anti–MDA-LDL titres. IK17 selectively bound to MDA-modified LDL, stained

human and rabbit atherosclerotic necrotic cores on immunohistochemistry and localised to atherosclerotic plaque in mouse *in vivo* experiments. Similar to EO6, IK17 prevented macrophage mediated uptake of oxLDL (26). Immunohistochemical staining of coronary artery sections from sudden death victims has revealed abundant IK17 epitopes in macrophage-rich areas and the plaque necrotic core, with more specific staining in unstable and ruptured plaques than other oxidised phospholipid or macrophage markers (28). In a separate study, intraperitoneal infusion of IK17 to high fat-fed LDL-$R^{-/-}$ mice three times per week for 14 weeks resulted in reduced foam cell formation and attenuated *in vivo* atherogenesis (27). In a further example of the mechanistic role of anti-MDA-LDL antibodies, transgenic mice on the LDL-$R^{-/-}$ background were developed that expressed an scFv of EO6. EO6 scFv was secreted by the liver and macrophages and inhibited *in vivo* oxLDL macrophage uptake, with less atherogenesis, aortic valve calcification, systemic inflammation and even prolonged life (302). Thus, these studies provide plausible mechanistic evidence for atheroprotective effects of IgM anti-oxLDL antibodies.

3.6.3 Relationship of IgG anti-MDA-LDL antibodies with atherosclerosis

Conversely, the relationship of IgG anti-MDA-LDL antibodies with atherosclerotic cardiovascular disease requires further clarification. In earlier work in the Haskard-Khamis laboratory, IgG anti-MDA-LDL antibodies were shown to relate to freedom from clinical cardiovascular events in an analysis of the ASCOT trial (91), however, in some studies IgG anti-oxLDL antibodies have even been found to relate to worse cardiovascular outcomes (89).

Importantly, as described above, in a prior study in our group, IgM anti-MDA-LDL antibody levels related to smaller necrotic core sizes on invasive assessment using NIRS-IVUS (whilst IgG did not) (255). In the present study, IgG anti-MDA-LDL antibody levels related to smaller necrotic core sizes on non-invasive assessment using CTCA (whilst IgM did not). It is conceivable that IgM anti-MDA-LDL antibody levels are reflective of more advanced atherosclerosis, as evidenced by the multiple relationships found in this study with both coronary and valve calcification as well as cardiovascular risk factors. However, the link between advanced atherosclerosis and clinical events is not straightforward, with more advanced, obstructive calcific atherosclerotic plaques appearing to possess a more stable phenotype. Indeed, plaque rupture events more often occur at areas possessing plaque vulnerability factors (as covered in the first chapter), often with mild-moderate luminal stenosis (121). What is more likely however, is that both IgG and IgM antibodies against oxLDL are working in concert. It has been demonstrated previously in animal models that depleting IgM antibodies results in the recruitment of IgG antibodies to achieve homeostasis (86). The homeostatic protective mechanism of IgM, as well as IgG, is likely to involve antigenic clearance via the reticuloendothelial system and complement pathways (88). The pathophysiological role of different anti-oxLDL IgG subclasses (which vary across species) may well be important in deciphering any relationships with atherosclerotic disease, and considering the subclasses as a single entity may be an over-simplification. Another potential confounding element is the patient population, and therefore inflammatory/ immune milieu from which the blood samples were obtained. For example, blood was collected from patients in the IBIS-3 study prior to coronary angiography in patients presenting with stable CAD as well as ACS, whilst in SCOT-HEART blood was drawn at the time of CT scanning in patients with suspected stable CAD. It is also possible therefore that the patients in IBIS-3 had more

advanced or unstable atherosclerosis, as they were either presenting acutely or had already been referred for an invasive assessment of CAD, whilst the patients in SCOT-HEART had been referred to CTCA as their first diagnostic CAD assessment following an initial clinic visit.

3.6.4 Importance of the SCOT-HEART study findings

The value of the SCOT-HEART study results is in confirming, for the first time, a protective role of anti-oxLDL antibodies in predicting atherosclerotic plaque characteristics with a non-invasive imaging modality. The dual relationship of both IgG and IgM anti-MDA-LDL antibody levels to protective phenotypes of atherosclerosis could present a valuable tool in screening patients for cardiovascular risk. This could mean that patients at previously unappreciated greater risk are appropriately targeted with more aggressive preventative medical therapy, which gains mounting relevance as we enter the era of expensive injectable and gene-based therapeutics for cardiovascular risk mitigation. Future work will need to confirm these findings in other CTCA-based imaging cohorts, before potentially integrating these assays in more established coronary risk scoring algorithms. The latter will require validation in large patient cohorts in the hope of eventually rolling out their clinical use.

3.6.5 SCOT-HEART study limitations

The main limitations from this substudy of SCOT-HEART lie in that we have assessed serological biomarkers in relation to coronary atherosclerosis, but of course circulating biomarkers likely reflect whole-body atherosclerotic burden, and there is a need to assess associations with other vascular beds. However, there is an increasing awareness that overall plaque burden is predictive of an adverse coronary prognosis, on both a lesional and patient level, rather than stenosis severity (7, 137, 138). Therefore, measures of overall coronary

artery disease burden and plaque volumes take on increasing significance, especially for the prediction of future MI (138). This may relate to the findings here, where both IgG and IgM are acting in concert, demonstrating a correlation where both reflect reduced atherosclerotic burden, but also a reduced presence of high-risk features on CT. Clearly extrapolating mechanistic pathways from this correlative investigation is beyond the scope of this work. However, the implication of a protective antibody reservoir being present in some patients, conferring a reduced global pathological picture of atherogenesis, is an interesting concept worthy of further exploration.

Our study population size is modest, and the clinical event rate is low, even at 5-year follow-up. Lastly, similar to most prior studies assessing antibody levels to oxLDL, only one OSE is assessed, with the possibility of other significant oxidative modifications. However, anti-MDA-LDL antibodies do comprise a significant component of the natural antibody reservoir against oxLDL (80). Furthermore, MDA-LDL is a pathologically important epitope, is abundant in atherosclerotic plaque and the focus of therapeutic studies (183, 303).

3.6.6 ORBITA study summary

In the ORBITA study we report that high intensity exercise resulted in significant circulating oxidative biomarker changes in patients with severe CAD on optimised anti-anginal medical therapy, with both IgG and IgM anti-MDA-LDL antibodies significantly decreasing following exercise. Revascularisation of the isolated flow-limiting epicardial coronary stenosis with DES did not affect the antibodies at baseline prior to exercise, or their exercise-induced change.

3.6.7 Pathophysiological basis for oxidation biomarker changes with exercise

The vigorous exercise performed in the ORBITA study protocol (until limiting symptoms, heart rhythm/ blood pressure abnormalities or significant electrocardiographic changes) likely generates robust cellular oxidative stress, free radical production and oxidised (MDA-) LDL formation in plasma. Next, circulating anti-MDA-LDL antibodies bind to their antigen, forming complexes and clearing them from the blood via the reticuloendothelial system in a homeostatic phenomenon. We have previously demonstrated similar dynamic biomarker changes in response to major vascular surgery (254) and CABG (253). Interestingly in the vascular surgery study, larger reductions in IgG anti-MDA-LDL antibody levels from pre-operative baseline, suggesting greater peri-operative consumption and clearance, related to more peri-operative MACE (254).

However, in this ORBITA study we do not report any change in MDA-LDL with exercise. This could be due to sample timing, taking place three-hours after exercise, with rapid immune homeostatic clearance already having occurred. Conversely, an increase in oxLDL levels with exercise has previously been reported in diseased populations, including those with hypertension and hypercholesterolaemia (304), heart failure (305), diabetes mellitus (306) and older age (307). Interestingly, exercise training of older individuals has been shown to reduce exercise induced oxidative LDL modification (308); whilst cardiac rehabilitation in those with CVD reduces baseline serum oxLDL levels (309). Moreover, a greater increase in oxLDL levels with exercise has been shown to relate to worse cardiovascular prognosis (305). Aside from blood sample timing, another plausible explanation for the lack of observed oxLDL increase in this study is that the optimised medical therapy that the patients in this trial received prior to randomisation rendered them relatively non-ischaemic on exercise.

Accordingly, one study has previously demonstrated no increase in oxLDL levels with high intensity exercise in healthy athletically trained individuals (310).

Moving one step further, the interaction of exercise with atherogenesis is interesting. As discussed above, regular exercise and cardiovascular fitness can reduce baseline oxLDL levels. However, there is emerging evidence that very high levels of physical activity, for example that undertaken by endurance athletes, may actually promote atherosclerotic cardiovascular disease (311). This is supported by the Master@Heart prospective observational cohort study (312), assessing the impact of long-term endurance sport participation in addition to a healthy lifestyle and low cardiovascular risk profile. Compared to healthy non-athletes, lifelong and late-onset endurance athletes had evidence of greater coronary atherosclerosis on CTCA, including non-calcific plaque in proximal arteries. The reasons for this apparent exercise-atherosclerosis paradox are unclear, but perhaps immune response to regular high intensity exercise plays a role.

3.6.8 Lack of PCI effect on biomarker levels

In this study PCI did not modulate either baseline biomarker values, or their exercise-induced changes, which remained in both treatment arms following intervention. However, in prior studies, PCI has been shown to induce acute plasma increases in oxLDL (313), likely attributed to either direct mechanical release or disruption from instrumented atherosclerotic plaque or increased plasma generation. This can generate immune induction, with raised IgG and IgM anti-oxLDL antibodies present six months following the PCI procedure (314, 315). Equally, it could be considered that PCI, by relieving the coronary stenosis, would reduce any ischaemic substrate and therefore the stimulus for immune induction. However, there were

no demonstrable relationships between antibody levels and baseline ischaemia on stress echocardiography or duration/ intensity of exercise in this study, suggesting that this may not be the case. Other factors to consider include the timing of blood sampling, with blood drawn at 6-weeks following the PCI procedure where any acute biomarker changes pre-exercise may be missed, as well as the interaction of highly optimised anti-anginal therapy.

3.6.9 ORBITA study limitations

The key limitation of the ORBITA study rests in the fixed timing of blood samples for analysis. The availability of samples immediately following exercise, as well as the PCI/ placebo procedure, would help interpret the immune response to the various stimuli, as would having more frequent samples to help delineate peak and trough plasma levels. As with the SCOT-HEART study, another drawback of this study is that MDA modification is only one of a range of possible oxidative modifications on LDL.

3.6.10 Importance of the ORBITA study findings

On a more mechanistic basis than the SCOT-HEART study, the ORBITA study provides a potential role of anti-MDA-LDL antibodies in providing an immunological response to vigorous exercise in patients with CAD, potentially via complexing to the excess generated MDA-LDL, with consumption in a homeostatic phenomenon.

3.7 Conclusions

This chapter has investigated the relationships of MDA-LDL and anti-MDA-LDL with coronary atherosclerosis, in a stable setting of patients being investigated for possible chest pain of

cardiac origin in the SCOT-HEART trial, and in a more dynamic setting pre- and post-exercise, before and after PCI in patients with single vessel CAD.

Anti-MDA-LDL antibody levels have been shown to inversely relate to cardiovascular risk factors, measures of atheroma burden as well as aortic valve and mitral valve calcification, all of which are known to carry an adverse prognosis. The most significant finding of the SCOT-HEART study, however, was the protective association with CTCA-derived atherosclerotic necrotic core, which is the strongest independent predictor of future MI. Both IgG and IgM anti-MDA-LDL antibody levels decreased following robust exercise in the ORBITA study, possibly due to consumption, which was unaffected by PCI.

Combining the results of the observational SCOT-HEART and ORBITA studies, together with the existing literature, there is growing body of evidence to suggest that anti-MDA-LDL antibodies relate to atherogenesis. The exciting progression of these studies, moving on from cardiovascular risk stratification, will be establishing whether increasing the circulating reservoir of anti-MDA-LDL antibodies, by passive immunisation or some other means, is effective in limiting atherosclerosis development in clinical trials, using serial non-invasive CTCA imaging. The panacea will be demonstrating efficacy in preventing atherosclerotic CVD in patients at high cardiovascular risk, on top of modern fully optimised preventative medical therapy, in large event-driven placebo-controlled randomised clinical trials.

3.8 Related presentations and publications

3.8.1 Presentations

The work contained within this chapter has been presented at the following meetings:

Anti-MDA-LDL antibody levels indicate protection from coronary CT-derived valve calcification in the SCOT-HEART Trial. ***European Society of Cardiology, Amsterdam, Netherlands, 2023*** (moderated poster presentation)

Antibodies against oxidised low-density lipoprotein and valve calcification in the SCOT-HEART trial. **British Society of Cardiovascular Research/ British Atherosclerosis Society/ British Cardiovascular Society, 2023** (poster presentation)

IgG and IgM anti-oxidized low-density lipoprotein antibodies predict protective atherosclerotic characteristics on cardiac CT: a substudy of the Scottish COmputed Tomography of the HEART (SCOT-HEART) trial. **British Society of Cardiovascular Research/ British Atherosclerosis Society/ British Cardiovascular Society, 2021** (oral presentation)

The Interaction of Exercise and Percutaneous Coronary Intervention with Oxidized LDL and Anti-oxidized LDL Antibodies: A Secondary Analysis of the ORBITA Study. ***European Atherosclerosis Society, 2020*** (poster presentation)

3.8.2 Publications

The work contained within this chapter has been published as original research in the following journal articles:

Hartley A., Williams MC., Kaura A., Caga-Anan M., Dey D., Dweck MR., Haskard DO., Newby DE., Khamis RY. Anti-malondialdehyde low-density lipoprotein antibody levels predict low-attenuation plaque in the SCOT-HEART trial. **Journal of American College of Cardiology: Cardiovascular Imaging**, 2023; DOI: 10.1016/j.jcmg.2023.07.006. PMID: 37656117.

Hartley A., Shun-Shin M., Caga-Anan M., Rajkumar C., Nowbar AN., Foley M., Francis DP., Haskard DO., Khamis RY., Al-Lamee RK. The Placebo-Controlled Effect of Percutaneous Coronary Intervention on Exercise Induced Changes in Anti-Malondialdehyde-LDL Antibody Levels in Stable Coronary Artery Disease: A Substudy of the ORBITA Trial. **Frontiers in Cardiovascular Medicine**, 2021; DOI: 10.3389/fcvm.2021.757030. PMID: 34708098.

Chapter 4

Targeted nanoparticle constructs for the molecular targeting of vulnerable atherosclerotic plaque

CHAPTER 4 – TARGETED NANOPARTICLE CONSTRUCTS FOR THE MOLECULAR TARGETING OF VULNERABLE ATHEROSCLEROTIC PLAQUE

4.1 Chapter summary

This chapter describes the design, development, and preclinical testing of nanoparticles that utilise molecular targeting to deliver an imaging payload to vulnerable, oxidised lipid-rich, atherosclerotic plaque. The final nanoparticle structure consists of three key components: the nanoparticle platform itself, a cargo, and a targeting antibody fragment.

For this study, organic polymeric nanoparticles were utilised, as they are relatively inexpensive, have a simple design, have reasonably straightforward production and are readily modifiable. The final formulation included PLGA, PLGA-PEG-MAL (maleimide) and PLGA conjugated to the cargo. The payloads used for this study were NIR-emitting fluorophores, with Cy5 used in the final design. Cy5, with excitation and emission ranges 610nm/ 675nm, is readily detectable *in vivo* and avoids much of the blood generated autofluorescence which is a greater issue at lower wavelengths. After testing whole antibody and antibody fragment-based constructs, humanised LO1Fab demonstrated superior nanoparticle biophysical characteristics and function, and thus was chosen as the molecular targeting agent.

The final nanoparticle construct then underwent vigorous *in vitro* testing, with assessment on ELISA with detection via all three nanoparticle components to demonstrate binding to MDA-

LDL, gel electrophoresis to ensure nanoparticle integrity, and immunohistochemistry in both murine and human atherosclerosis to show MDA-LDL binding was preserved in tissue. The ability of the nanoparticle to localise to MDA-LDL within foam cells was also assessed using cell culture techniques. Following successful *in vitro* testing, the most promising nanoparticle formulation was then taken to the *in vivo* phase. After half-life calculation and pilot study, nanoparticles were injected in age and sex-matched LDL-$R^{-/-}$ mice fed a high-fat diet for 40-weeks, and underwent FMT, demonstrating increased signal in the ROI, versus the untargeted and control Fab-targeted constructs. Localisation to lipidic deposits was confirmed *ex vivo* using FRI of the extracted aortae and fluorescent confocal microscopy of cryosectioned aortic root tissue. Finally, atherosclerotic mice were co-injected with MMPSense, a commercially available NIRF atherosclerotic plaque reporter, alongside the nanoparticle constructs, and underwent FMT co-localised with micro-CT, which confirmed *in vivo* uptake localised to the aortic root, ascending aorta and aortic arch vessels.

The result of the work in this chapter is a polymeric nanoparticle with an imaging payload that can molecularly target oxLDL within atherosclerotic plaque *in vivo*. The next phase of this study will involve demonstrating targeting efficacy in other animal models, namely rabbit models of atherosclerosis, for which experimental plans and ethical permissions are already in place. In addition, changing the nanoparticle cargo from an imaging to a drug payload, potentially with therapeutic potential, is an important and logical next step.

4.2 Introduction

The concept of the vulnerable plaque, an atherosclerotic plaque that is prone to rupture and thus precipitate an acute vascular occlusive event, is a growing and increasingly supported

paradigm (316). After establishing the pathological features defining plaque vulnerability (8), and with clinical intravascular imaging identified correlates being recognised (316), there is a growing clinical interest in these high risk lesions. However, the current clinical methods of visualising these lesions are not optimal – non-invasive CTCA lacks spatial resolution and cannot provide detailed in-depth plaque morphology, necessitating both ionizing radiation and iodinated nephrotoxic contrast; whilst intravascular imaging has much greater spatial and temporal resolution, but is inherently invasive, with a risk of serious complications coupled with the radiation and contrast concerns. Moreover, once these vulnerable plaques are identified, it is not known how best to address and mitigate the increased risk that these lesions pose. Separate to this, is the inflammatory hypothesis of atherosclerosis, with emerging data suggesting 'hot' inflammatory metabolically active plaques are more likely to progress, develop a vulnerable phenotype and rupture, leading to a major cardiovascular event (67), is also garnering increasing support. In parallel, anti-inflammatory therapies have been successfully trialled to treat clinical atherosclerosis, for example the anti-IL1β monoclonal antibody canakinumab (47) or colchicine (48, 49), and are gaining traction in clinical guidelines (116). However, these anti-inflammatory agents often have unwanted adverse off-target effects, which can be severe, especially in the case of monoclonal therapies.

Thus, there are clear unmet clinical needs – 1) the ability to sensitively detect vulnerable atherosclerotic plaques, ideally with a non-invasive approach, and 2) the ability to modify either plaque metabolic activity or structure in such a way that it is rendered less vulnerable to rupture. A molecular targeted nanoparticle-based approach with an imaging or therapeutic payload is one strategy that may satisfy both of these unmet needs.

In this chapter, the design and *in vitro* testing of novel NIRF nanoparticle constructs are detailed, prior to proof of principle studies, demonstrating successful molecular targeting *in vivo* with atherosclerotic mice, utilising highly sensitive FMT with anatomical co-localisation provided by micro-CT, with extensive *ex vivo* validation.

Nanoparticle design and initial *in vitro* testing was performed with the help of Prof Christopher Scott and Dr Michelle Greene (Queen's University Belfast). Additional characterisation of LO1Fab was performed with the help of Prof Jason Johnson (Bristol University – immunohistochemistry on human atherosclerotic sections) and Dr Sean Devenish (Fluidic Analytics – microfluidic antibody affinity profiling).

4.3 Nanoparticle design

For this study, nanoparticle design was performed in collaboration with Prof Christopher Scott, Queen's University Belfast. Nanoparticle synthetic chemistry and initial testing was performed in collaboration with Dr Michelle Greene at Queen's University Belfast. Subsequent nanoparticle optimisation and all further *in vitro*/ *in vivo*/ *ex vivo* studies were performed by me, with research technician support for a minority of experiments.

4.3.1 Targeting antibody fragment

The key novel component of the nanoparticle used in this thesis is the targeting antibody fragment, based upon prior work in the Haskard-Khamis laboratories. This stemmed from the development of the murine monoclonal IgG3κ antibody that reacted with MDA-LDL, termed LO1 (252). Subsequent to this, LO1 was developed for *in vivo* molecular targeting via the

conjugation of a NIR-emitting fluorophore for optical imaging, which successfully localised to plaques in both atherosclerotic mice and rabbits (174). Next, the full antibody was developed into a humanised Fab fragment (termed LO1Fab) via complementarity determining region grafting onto a human framework scaffold (S Pandey's thesis). Again, LO1Fab was conjugated with a NIR-emitting fluorophore, as above, and successfully demonstrated atherosclerotic lesion targeting *in vivo*. Importantly, both LO1 and LO1Fab have an engineered free unpaired end C-terminal cysteine residue for utilisation in maleimide reaction chemistry. Maleimide reaction chemistry is a form of click reaction with the production of a thioether bond between a thiol group (present on cysteine residues) and a maleimide group. This bond is rapidly formed and relatively stable at neutral pH (317). In both LO1 and LO1Fab, the free cysteine residue is away from the antigen binding site, and thus any conjugated binding partner should not interfere with the tertiary structure of the fragment or impact antibody function. Furthermore, cysteine residues are not particularly abundant in proteins (compared to lysine residues for example), and any naturally occurring cysteine residues within the antibody structure will have formed disulphide bridges, preventing binding at these sites (317). Maleimide reaction chemistry was successfully utilised for NIRF probe conjugation with LO1 and LO1Fab, and can also be harnessed for other binding partners, such as nanoparticle components with available maleimide groups.

Both LO1 and LO1Fab were chosen for initial nanoparticle development, with the expectation that LO1Fab would be more favourable, given its lower molecular weight, which is likely to enhance antibody-nanoparticle conjugation and thus degree of labelling, as well as potentially producing smaller sized nanoparticles, with greater lesion penetration and less steric hinderance accordingly.

4.3.2 Nanoparticle platform

As discussed earlier, there are a wide variety of potential nanoparticle platforms, which are broadly grouped by their composition into organic- and inorganic-based nanomaterials. Organic-based nanoparticles may be favoured for their enhanced biocompatibility, biodegradability, and non-toxic nature. However, as compared to inorganic-based nanomaterials, they often have lower stability and cargo entrapment can be more challenging (318). Polymeric nanoparticles are a subset of organic-based synthetic nanomaterials, formed of biocompatible polymers, typically PLGA, polyglycolic acid and polylactic acid. PLGA has intermediate properties of polyglycolic acid and polylactic acid, with average density, flexibility, and degradation. The main strength of polymeric nanoparticles is their significant customisability, through changing their formulation. For example, by changing block co-polymer lengths, alterations in size, shape, charge, cargo encapsulation and flexibility may be affected (192). However, PLGA often suffers from short blood circulation times due to immune clearance by resident splenic and hepatic macrophages, which is not ideal for theranostic applications. As such, PLGA is often combined with 'stealth' polymers, such as PEG, to reduce immune clearance and prolong circulating times. Moreover, PEG is a hydrophilic polymer, and thus forms a coating over the hydrophobic PLGA core, forming a micellar structure, potentially facilitating the incorporation of a (ideally hydrophobic) cargo. As a result, PEGylation has been shown to prevent immune opsonisation, aggregation, and phagocytosis (319).

To effectively target atherosclerotic plaques with a therapeutic agent, the key nanoparticle design requirements are likely to be small size (ideally <200nm diameter) and a long-

circulation time (half-life 2-24 hours) to optimise plaque penetration and accumulation. For imaging applications a shorter half-life, enhancing TBR is likely to be more favourable.

Thus, a nanoparticle formulation based on PLGA-PEG co-polymers was chosen, with the incorporation of PLGA-PEG-MAL polymers, to permit antibody conjugation on the outer shell, via maleimide reaction chemistry.

4.3.3 Nanoparticle cargo

The selection of nanoparticle cargo must include various considerations: 1) what is ideal to deliver to atherosclerotic plaques clinically; 2) the added benefit of nanoparticle local delivery over systemic delivery (especially if a pharmacological agent is used); 3) what is practically possible to either load directly or encapsulate into the nanoparticle core; and 4) how to demonstrate effective payload delivery. However, targeted drug delivery relies on successful binding of the nanoparticle to its molecular target at the site of action (the atherosclerotic necrotic core in the case of LO1Fab-targeted nanoparticles). Hence, the most important test of nanoparticle function will be to demonstrate successful MDA-LDL binding. Firstly, this can be assessed on various *in vitro* assays, including ELISA-based experimental designs and in tissue with immunohistochemistry, prior to testing the ability of the nanoparticle to access atherosclerotic plaques *in vivo*. Therefore, to enable detection of nanoparticle molecular targeting for all of these studies, a NIR-emitting fluorophore was chosen as the principal nanoparticle payload, with detection using fluorescence-based experimental endpoints.

Ideally, the chosen NIR-emitting fluorophore would have a sufficiently long wavelength, into the NIR spectrum (>~600nm), to reduce scatter and autofluorescence produced by oxy- and

deoxyhaemoglobin, and thus improve the SNR with *in vivo* fluorescence imaging (320). In addition, using a fluorophore that is commercially pre-conjugated to a polymer should improve nanoparticle *in vivo* stability. This is especially true if this polymer is hydrophobic, and thus the fluorophore will be safely enclosed within the core of the micellar PLGA-PEG structure.

Accordingly, Cy5 (excitation 651nm/ emission 670nm) was chosen, with a commercially available PLGA-Cy5 polymer (AV034 – PolySciTech, Lafayette, USA). However, for ease of initial *in vitro* characterisation, Rhodamine 6G (excitation 525nm/ emission 548nm) was added to the nanoparticle composition during production, rather than PLGA-Cy5, given its shorter excitation and emission wavelengths which are more readily detectable on various laboratory fluorescence plate readers.

4.4 First iteration nanoparticle construct

4.4.1 First iteration nanoparticle composition

The nanoparticle construct was designed in collaboration with Prof Christopher Scott's laboratory (Belfast, UK). The first design was composed of 5mg PLGA-PEG-MAL and 15mg PLGA, to make a 20mg batch of nanoparticles, with 100μL 2mg/mL Rhodamine 6G entrapped during production. Overnight incubation of 50μg antibody constructs per mg of nanoparticles was chosen as the initial conjugation ratio, based on prior experience in the Scott laboratory. Antibody constructs were reduced with a 10x molar excess of TCEP for 1-hour prior to nanoparticle conjugation, with the aim of reducing any disulphide bonds that may have formed between exposed cysteine residues on Fab fragments/ IgG molecules in solution. This will aim to break any antibody dimers into their constituent parts and facilitate

maleimide reaction chemistry between the cysteine residues and the nanoparticle maleimide groups. Figure 4-1 below illustrates the first iteration nanoparticle design.

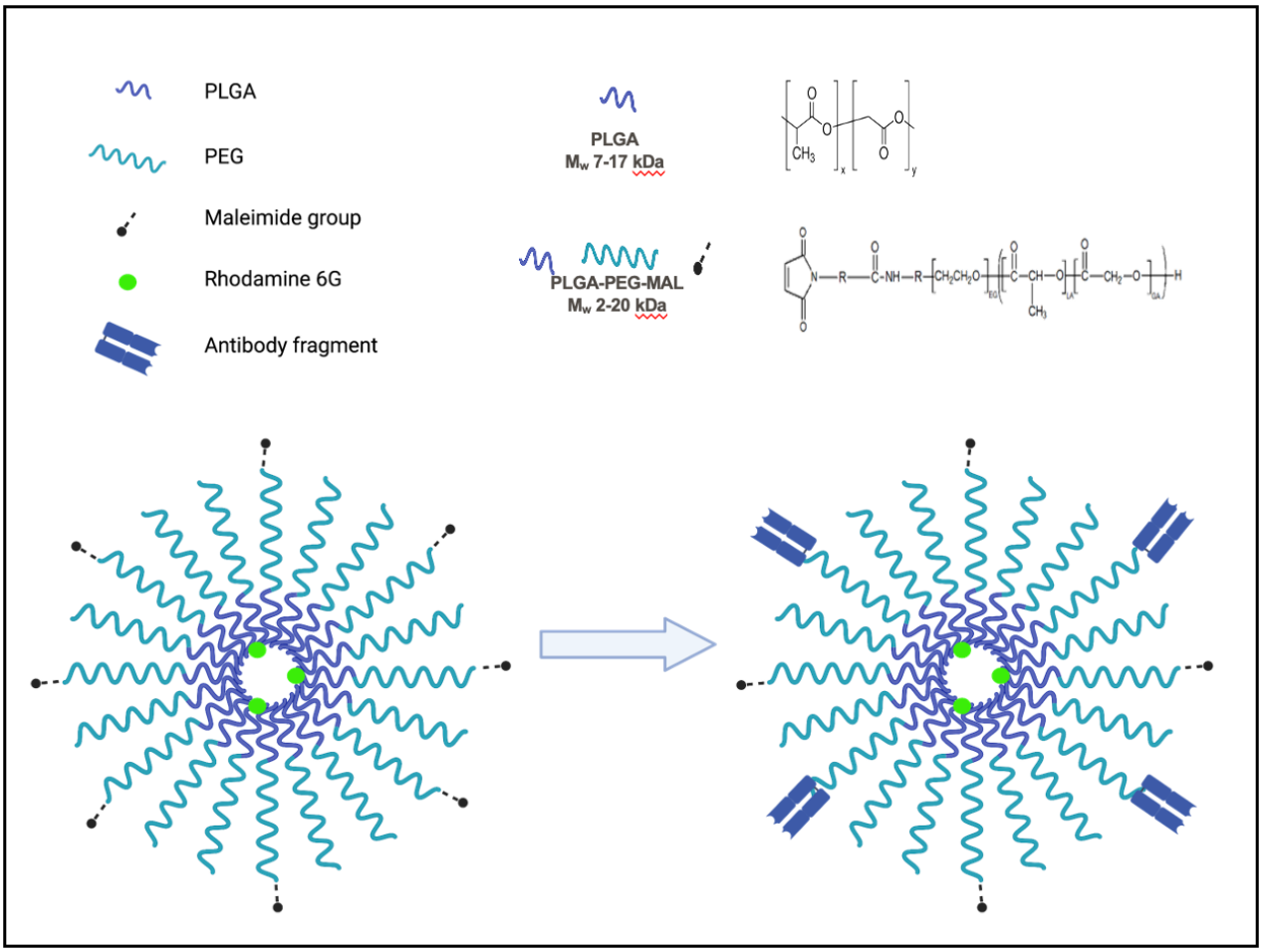

Figure 4-1. Schematic representation of the initial nanoparticle design.

The initial iteration of the polymeric fluorescent nanoparticles is shown, formed of PLGA and PLGA-PEG-MAL, with Rhodamine 6G entrapped within the core. The unconjugated nanoparticles are then rotated overnight at 4°C with Fab fragments or IgG molecules to allow the maleimide reaction to take place. Made using Biorender.

4.4.2 First iteration nanoparticle characterisation

After production, the nanoparticle constructs were initially characterised for size and degree of uniformity, followed by assessing the ability to bind to MDA-LDL in ELISA format.

4.4.2.1 Nanoparticle size and polydispersity index

Nanoparticle size and uniformity were assessed using DLS. Ideal parameters include size <200nm, with smaller particles being more desirable, given their increased ability to cross leaky endothelial barriers to access atherosclerotic plaques; whilst a low degree of nanoparticle dispersity (polydispersity index [PDI] <0.2) is desirable, to ensure that a uniform batch of nanoparticles is manufactured, and a more robust and standardised effect produced. Figure 4-2 displays the size and PDI of the first iteration of nanoparticles, with the following constructs: untargeted NP (control nanoparticle with no conjugated antibody), LO1-NP (full murine LO1 IgG conjugated) and LO1Fab-NP (humanised LO1Fab conjugated).

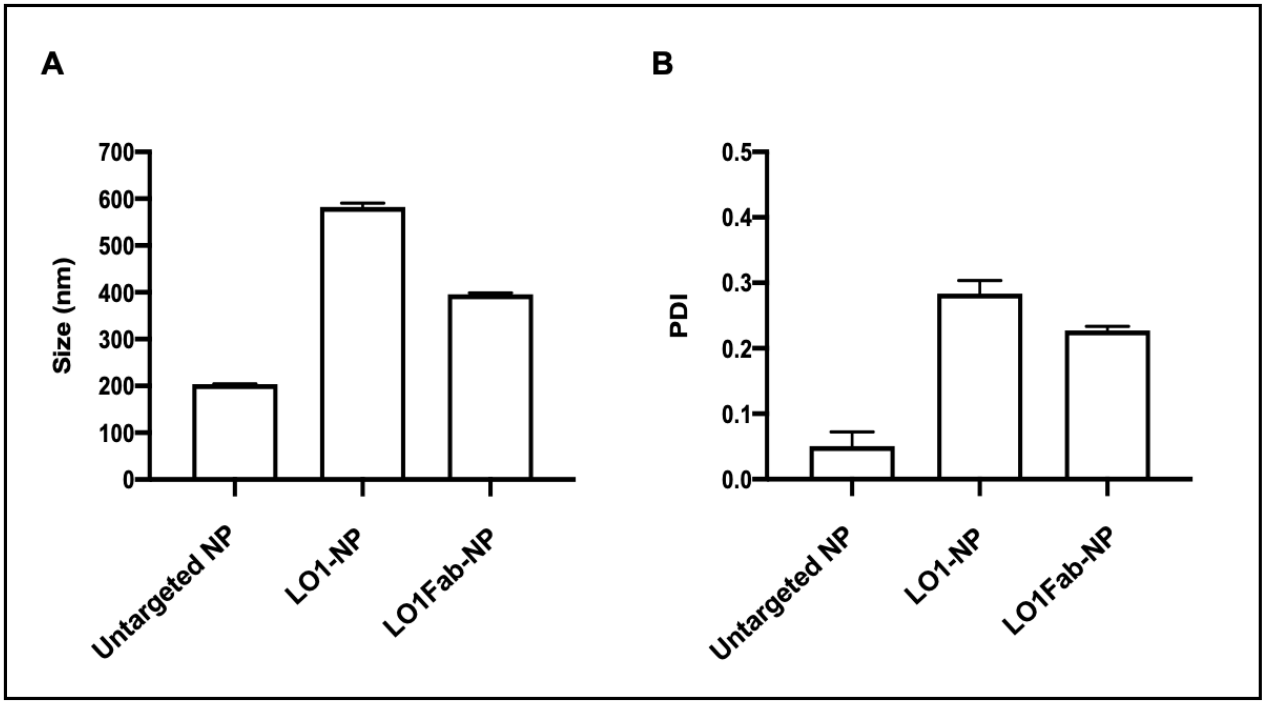

Figure 4-2. Size and dispersity of the first iteration of Rhodamine 6G nanoparticle constructs.

(A) – Displays the average size of untargeted, LO1 and LO1Fab conjugated nanoparticle constructs.
(B) – Displays the average polydispersity index of nanoparticle constructs.
Assessed using Dynamic light scattering. Performed in triplicate. Error bars represent SEM.

There is a large increase in construct size following antibody conjugation (from ~200nm to ~550nm for LO1 and ~390nm for LO1Fab), suggesting successful antibody conjugation has taken place, albeit beyond the desirable size range. This increase in particle size could be due nanoparticle aggregation, or indeed be the direct effect of antibody binding. PDI however was more acceptable, with ~0.28 for LO1-NP and ~0.22 for LO1Fab-NP (from ~0.05 with the untargeted-NP), suggesting that there is no significant nanoparticle clumping. Based on this initial characterisation, the nanoparticles were assessed for MDA-LDL binding.

4.4.2.2 Modified nanoparticle fluorescence-linked immunosorbent assay

A modified fluorescence ELISA was used to assess nanoparticle antigen recognition, whereby MDA-LDL (or PBS acting as a control for non-specific binding) was added on solid phase overnight, prior to blocking and the addition of nanoparticle constructs for 2-hours. The plates were then thoroughly washed to remove unbound constructs, prior to nanoparticle dissolution and the assessment of Rhodamine 6G fluorescence on a plate reader. Figure 4-3 below demonstrates a concentration-dependent increase in fluorescent signal (nanoparticle binding) with both LO1 ($p=0.0086$) and LO1Fab ($p=0.0478$) conjugated nanoparticles. Additionally, there is increased binding of the LO1Fab-nanoparticle versus LO1-nanoparticle ($p=0.0046$ at 250μg/mL and $p=0.009$ at 500μg/mL). However, more non-specific binding is evident with LO1Fab than with the LO1-nanoparticle.

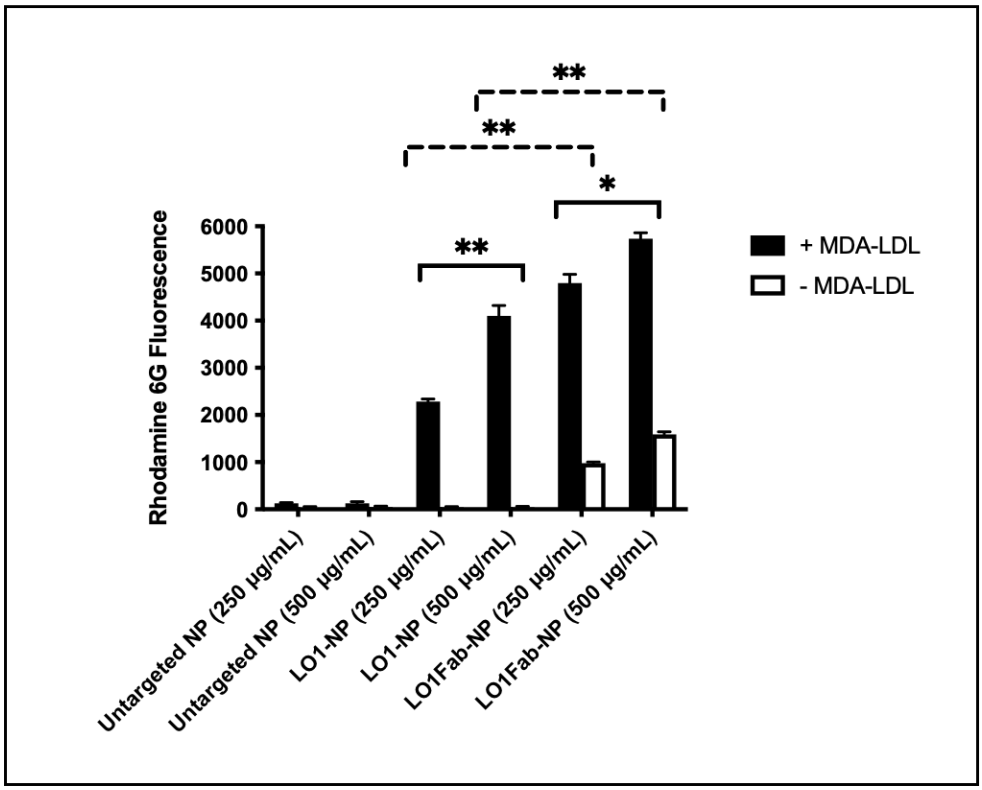

Figure 4-3. MDA-LDL recognition by the first iteration of Rhodamine 6G nanoparticle constructs.

*This fluorescence ELISA is designed with MDA-LDL (+ MDA-LDL, 10µg/mL) or PBS (negative control, - MDA-LDL) on solid phase and detection via Rhodamine 6G fluorescence. There is a concentration-dependent increase in binding with both LO1 (**p=0.0086) and LO1Fab (*p=0.0478) conjugated nanoparticles (solid brackets), with no binding of the untargeted construct. Additionally, there is increased binding of the LO1Fab-NP versus LO1-NP at both concentrations (**p=0.0046 at 250µg/mL and **p=0.009 at 500µg/mL) (dashed brackets). There is more non-specific binding of LO1Fab-NP than LO1-NP however. Unpaired t-test used to assess significance. Performed in triplicate. Error bars represent SEM.*

4.4.2.3 Nanoparticle function is dependent on TCEP reduction and the maleimide reaction

To confirm that MDA-LDL binding was due to Fab function, rather than non-specific binding, nanoparticles were formulated using the same quantity of PLGA-PEG-NHS (amide) polymer, rather than PLGA-PEG-MAL, and were conjugated with and without prior reduction with TCEP. These constructs were then evaluated using fluorescence ELISA.

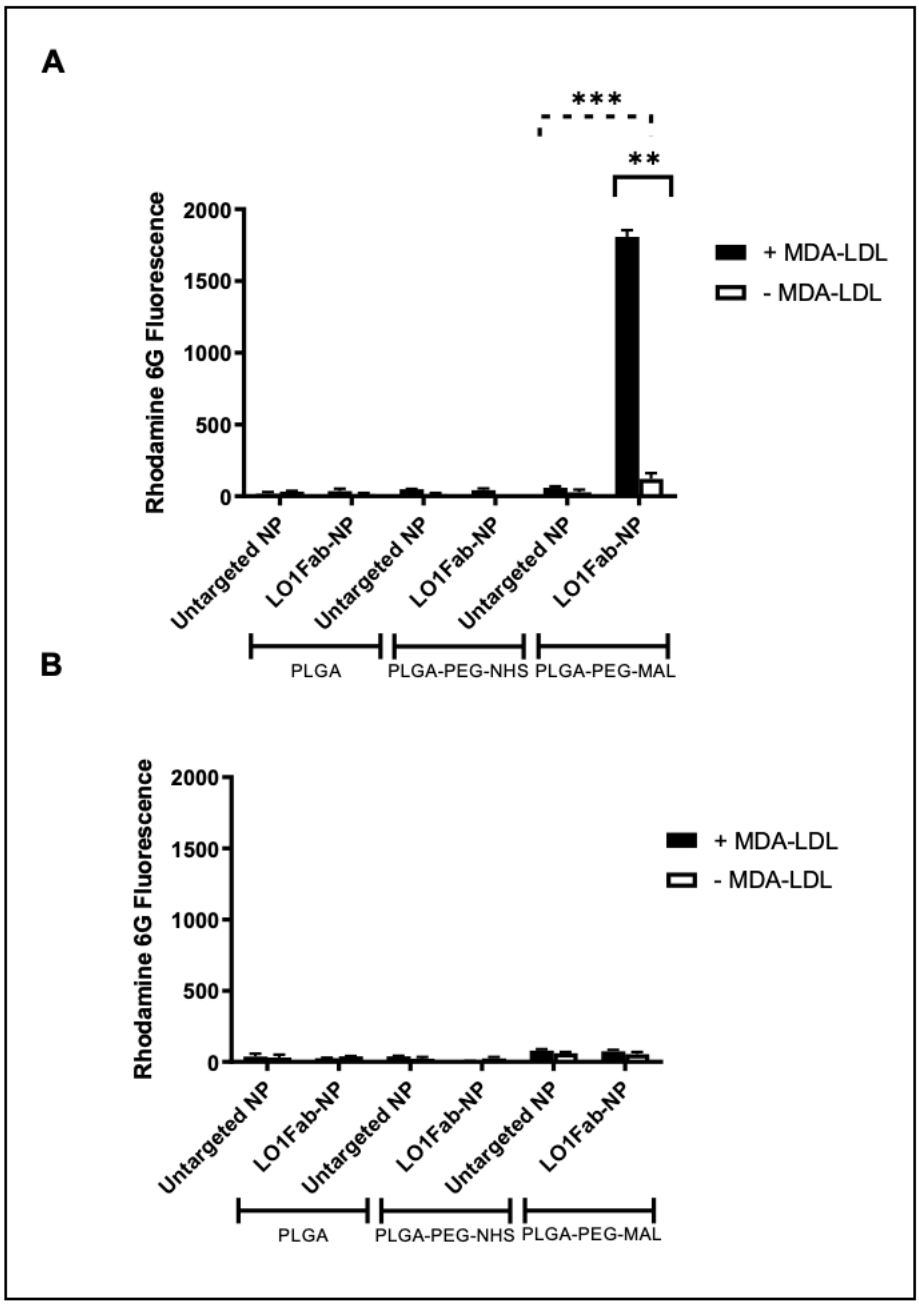

Figure 4-4. Nanoparticle function is dependent on both the maleimide reaction and antibody fragment TCEP reduction.

*This figure displays with MDA-LDL (10μg/mL) or PBS on solid phase with detection via Rhodamine 6G fluorescence, with (A) and without (B) Fab TCEP reduction prior to nanoparticle conjugation. In both A and B nanoparticles are formulated with PLGA only, PLGA-PEG-NHS or PLGA-PEG-MAL. These fluorescence ELISAs demonstrate that when there is no LO1Fab reduction prior to nanoparticle conjugation (A) there is no function on fluorescence ELISA. Moreover, MDA-LDL binding on fluorescence ELISA is only present when the PLGA-PEG-MAL polymer is included in the nanoparticle formulation (**p=0.0027 versus PBS-coated wells, solid bracket; ***p=0.0009 versus untargeted nanoparticle, dashed bracket). Unpaired t-test used to assess significance. Performed in triplicate. Error bars represent SEM.*

Figure 4-4 above demonstrates complete abolishment of binding with nanoparticles formulated without maleimide groups and when the LO1Fab was not reduced prior to conjugation. There was robust binding to MDA-LDL with TCEP-reduced LO1Fab-conjugated PLGA-PEG-MAL nanoparticles (p=0.0027 versus PBS-coated wells) and when compared to untargeted PLGA-PEG-MAL nanoparticles (p=0.0009).

4.4.2.4 Development of the anti-PEG ELISA

I next set out to find an alternative method of further quantifying nanoparticle binding to MDA-LDL on ELISA, in addition to fluorescence, to enable comparison of constructs with differing fluorophores. As such, I developed a new experimental design based on detection via the PEG in the outer nanoparticle corona, which should be accessible for antibody binding and thus ELISA detection. After reviewing commercially available antibodies, I settled upon a rabbit anti-PEG primary antibody, with a goat anti-rabbit secondary antibody conjugated with HRP. The first anti-PEG antibody (PA5-32247 – Thermo Fisher Scientific, Massachusetts, USA) trialled was not successful in ELISA format, generating significant background signal, likely due to the interaction of the anti-PEG antibody with the Tween-20 in the wash and assay buffers. As such a monoclonal anti-PEG antibody was tested (190652 – Abcam, Cambridge, UK) with little Tween-20 reactivity. Figure 4-5 displays the successful checkerboard titration ELISA produced by coating varying concentrations of this monoclonal rabbit anti-PEG antibody overnight, followed by blocking with 3% BSA, and then detection with polyclonal goat anti-rabbit-HRP for 1-hour. TMB was added for signal generation, prior to 0.5M H_2SO_4 after 2-minutes.

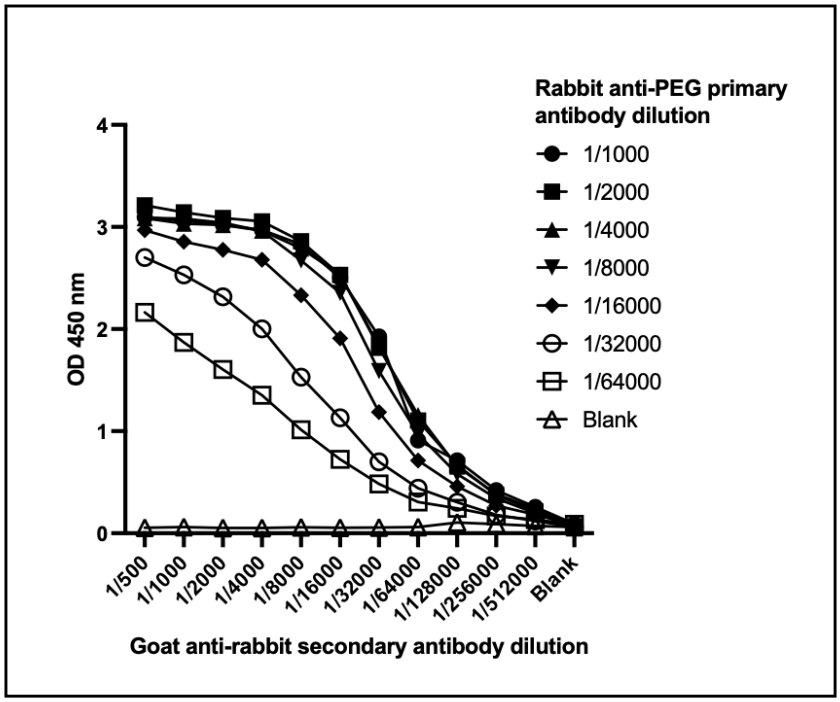

Figure 4-5. Checkerboard titration ELISA for the novel anti-PEG ELISA.

This ELISA was performed with varying dilutions of rabbit anti-PEG antibody coated overnight, prior to blocking with 3% BSA and detection via varying concentrations of goat anti-rabbit-HRP for 1-hour, prior to TMB for 2-minutes. Performed without replicates.

Figure 4-5 demonstrates good recognition by the secondary antibody for the primary antibody and permitted the selection of appropriate antibody concentrations for ELISA development. Accordingly, the nanoparticle constructs were then tested in an indirect ELISA format, coating with MDA-LDL, with both primary and secondary antibodies at 1/500 concentration. Figure 4-6 below shows two similar ELISAs, with a fluorescence ELISA in A and an anti-PEG ELISA in B, comparing the three initial nanoparticle constructs. Similar binding patterns are observed between the two assays, with LO1Fab-NP demonstrating greater signal than LO1-NP, with little (or no) signal above background with the untargeted constructs. These results also confirm the initial nanoparticle fluorescence ELISA performed in *Section 4.4.2.2*.

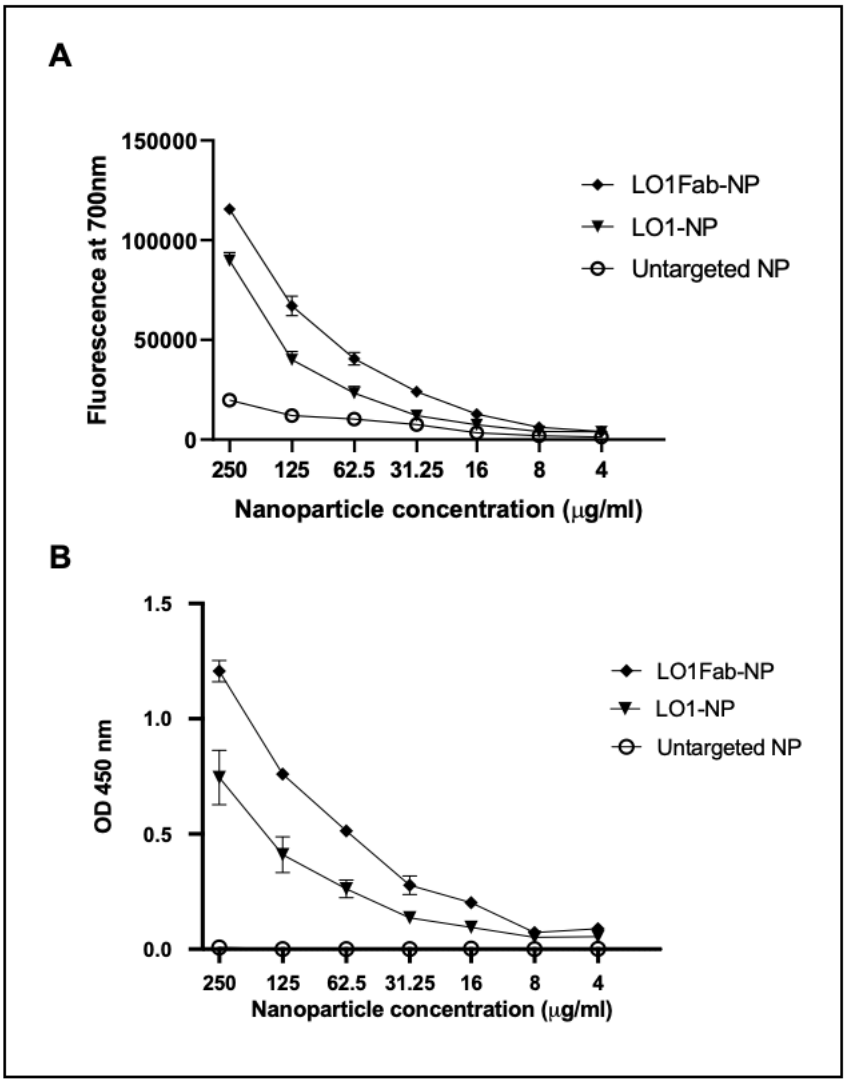

Figure 4-6. Nanoparticle function on ELISA is similar when detected via fluorescence or polyethylene glycol binding.

MDA-LDL (10μg/mL) was coated overnight, prior to blocking with 3% BSA and then Cy5 nanoparticles were added in dilution series. Whether detection is via fluorescence at 700nm using the Odyssey CLx Imaging System (A), or rabbit anti-PEG followed by goat anti-rabbit-HRP antibodies (B), there are similar binding patterns, with LO1Fab-NP providing a stronger signal than LO1-NP, with little untargeted nanoparticle signal. Performed in duplicate. Error bars represent SEM.

4.4.2.5 Initial nanoparticle stability

I then wanted to assess the stability and batch variability of the nanoparticle constructs after they have been conjugated with the targeting antibody. From prior work in the Scott

Laboratory, the unconjugated dehydrated nanoparticle pellets are known to be stable at -20°C for prolonged periods (~months), however post-rehydration and conjugation, this is much more variable. As a first step, I compared older (1-month) and more recently conjugated constructs (1-week) in dilution series, by imaging on a fluorescent scanner (Odyssey CLx Imaging System), displayed in Figure 4-7 below.

It is evident that the fluorescence does dilute out for the fresher constructs, as would be expected. On pipetting the older constructs however, an obvious pellet had formed, and thus only the supernatant was used for imaging. It is clear that the pellet must have contained the majority of the nanoparticle constructs, with very little fluorescence still appreciable. Another interesting observation was that the fresher antibody-conjugated nanoparticles had aggregated. No such clumping was seen with the untargeted nanoparticle, suggesting that the aggregation was, at least in part, due to antibody presence.

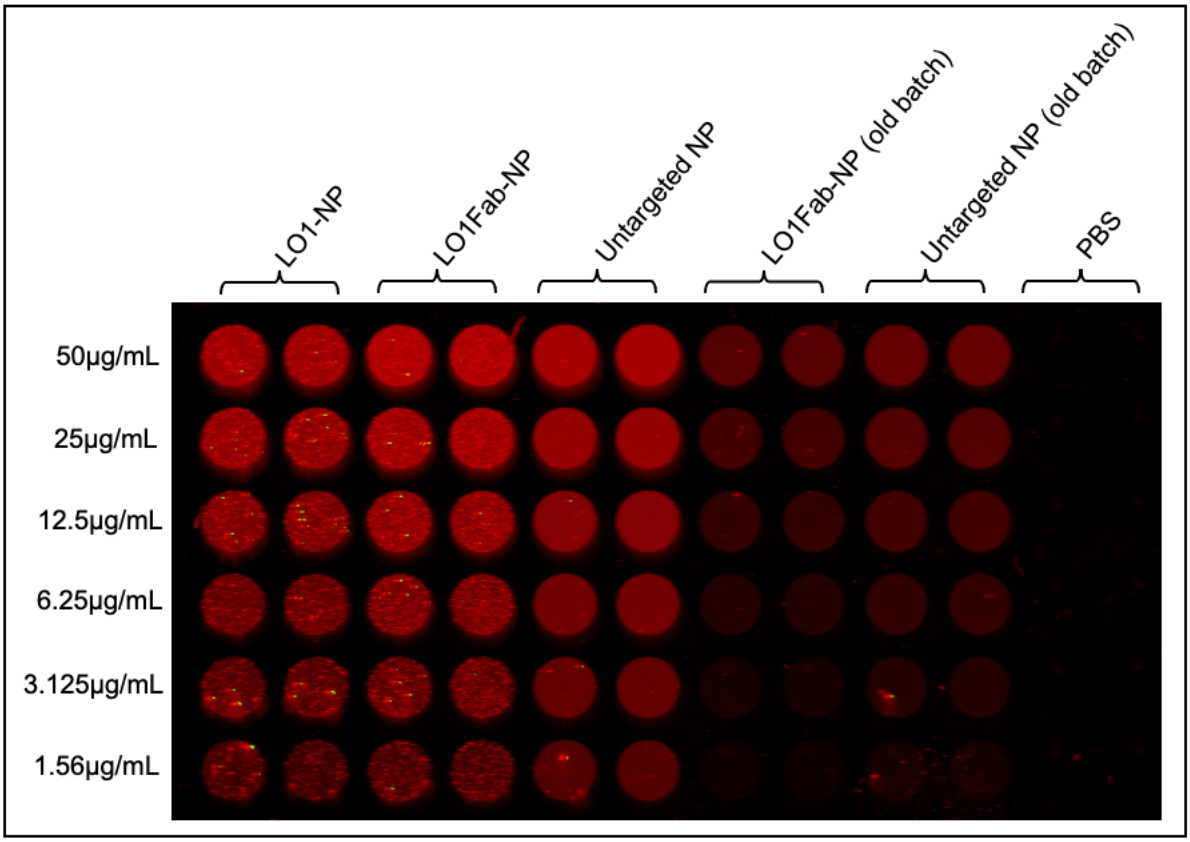

Figure 4-7. Aggregation of nanoparticles when left prior to use.

Following antibody-nanoparticle conjugation, nanoparticles were left at 4°C for 1-week (first 3 conditions) and compared to nanoparticles that had been kept for 1-month (next 2 conditions) and PBS. The constructs were added in dilution series to an ELISA plate and then imaged at 700nm using the Odyssey CLx Imaging System. There is clear aggregation of the antibody-conjugated nanoparticles in the more freshly conjugated conditions. However, in the nanoparticles that had been conjugated 1-month earlier, there is much less aggregation, but also substantially less fluorescence, likely due to pelleting of the previously suspended nanoparticles.

4.4.2.5.1 Nanoparticle centrifugation and filtration

In an attempt to render these nanoparticles still viable for further study, especially for *in vivo* applications where aggregation would pose significant issues (for example, vascular occlusion with the clumped nanoparticles), I trialled centrifugation and filtration of the constructs that had been conjugated 1-week previously. Centrifugation was performed at 5000 rpm for 30-seconds and then 6000 rpm for an additional 30-seconds, prior to harvesting the supernatant. Filtration was carried out in a sterile manner using a Minisart syringe filter

with pore size of 22μm (Sartorius, Goettingen, Germany). Figure 4-8 displays a comparison of the filtered/ centrifuged LO1Fab-NP and untargeted NP, imaged at 700nm in A, and nanoparticle function on ELISA in B. Both techniques resulted in loss or breakdown of antibody-nanoparticle structure, with substantially reduced fluorescence as well as MDA-LDL binding.

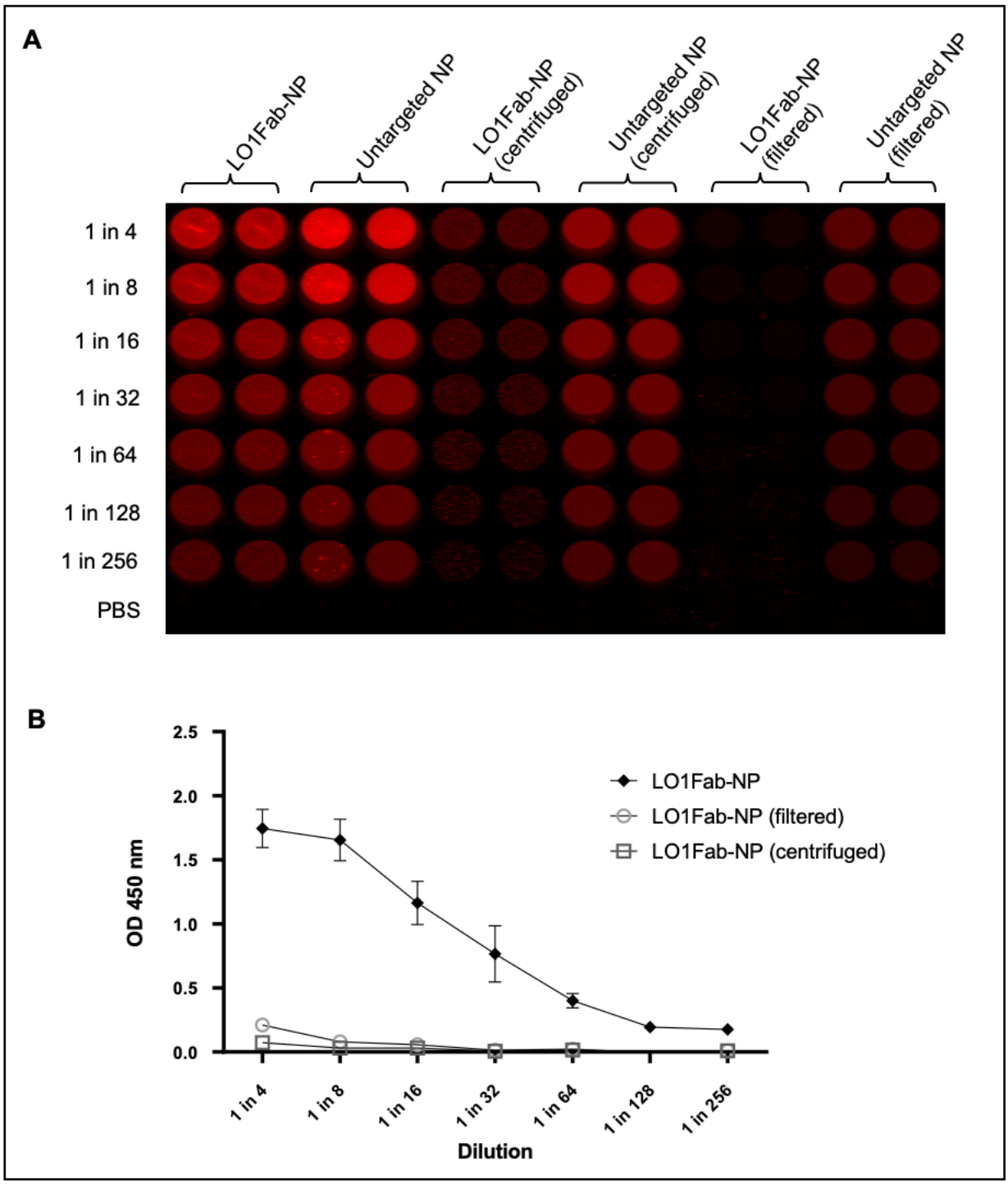

Figure 4-8. Nanoparticles are in suspension.

Following antibody conjugation, LO1Fab or untargeted nanoparticles were left at 4°C for 1-week (A – first 2 conditions), and were then either centrifuged (5,000rpm for 30-seconds followed by 6,000rpm for 30-seconds) and supernatant collected (A – third and fourth conditions), or filtered with a 22µm filter (A – last 2 conditions). The nanoparticles were added in dilution series to an ELISA plate and imaged at 700nm on the Odyssey CLx Imaging System (A), or tested on the anti-PEG ELISA versus MDA-LDL (10µg/mL) on solid phase (B). With both centrifugation and filtration there is significant loss of fluorescence (especially for antibody-conjugated nanoparticles, and more so with filtration). This loss of fluorescence is mirrored in the functional ELISA. (B) is performed in duplicate. Error bars represent SEM.

From these experiments it was clear that the nanoparticles are in suspension, with the pellet containing all nanoparticle constructs which were left prior to centrifugation, or were filtered out with filtration, rather than in solution. As such, I moved to only using freshly rehydrated and conjugated nanoparticles (especially for the planned *in vivo* studies) and re-sonicated the nanoparticles prior to all experiments.

4.5 Nanoparticle optimisation

The first nanoparticle design was a success, with antibody-nanoparticle conjugation and good function on ELISA, with detection via fluorescence and PEG presence, albeit with too large construct diameter and the need for fresh manufacture. The LO1Fab-nanoparticle appeared to be the more promising construct, with greater signal on both ELISA-based assays and smaller size. However, Rhodamine 6G was used as the imaging cargo, with poor fluorescence characteristics for *in vivo* imaging. Thus, further nanoparticle constructs were designed and tested, focusing on LO1Fab as the targeting antibody fragment and including Cy5, aiming to generate smaller constructs that retain function.

The important design considerations to reduce construct diameter were to decrease the percentage of PLGA-PEG-MAL polymer in the formulation, and to reduce the amount of LO1 or LO1Fab added to the nanoparticle conjugation reactions (from 50 to 25µg). This served to reduce the nanoparticle maleimide groups available for antibody fragment conjugation, as well as reducing the amount of antibody available for conjugation. This should render smaller constructs with less antibody fragment per particle, hopefully without significant loss of nanoparticle function.

4.5.1 Further nanoparticle optimisation

After rounds of development and optimisation, the final nanoparticle design was comprised of PLGA-PEG-MAL, PLGA-Cy5 and PLGA, conjugated to LO1Fab, displayed in Figure 4-9 below. I initially used 10mg PLGA-Cy5 in place of 10mg of PLGA; resulting in 5mg PLGA-PEG-MAL, 10mg PLGA-cyanine 5 and 5mg PLGA being used to make a 20mg batch of nanoparticles.

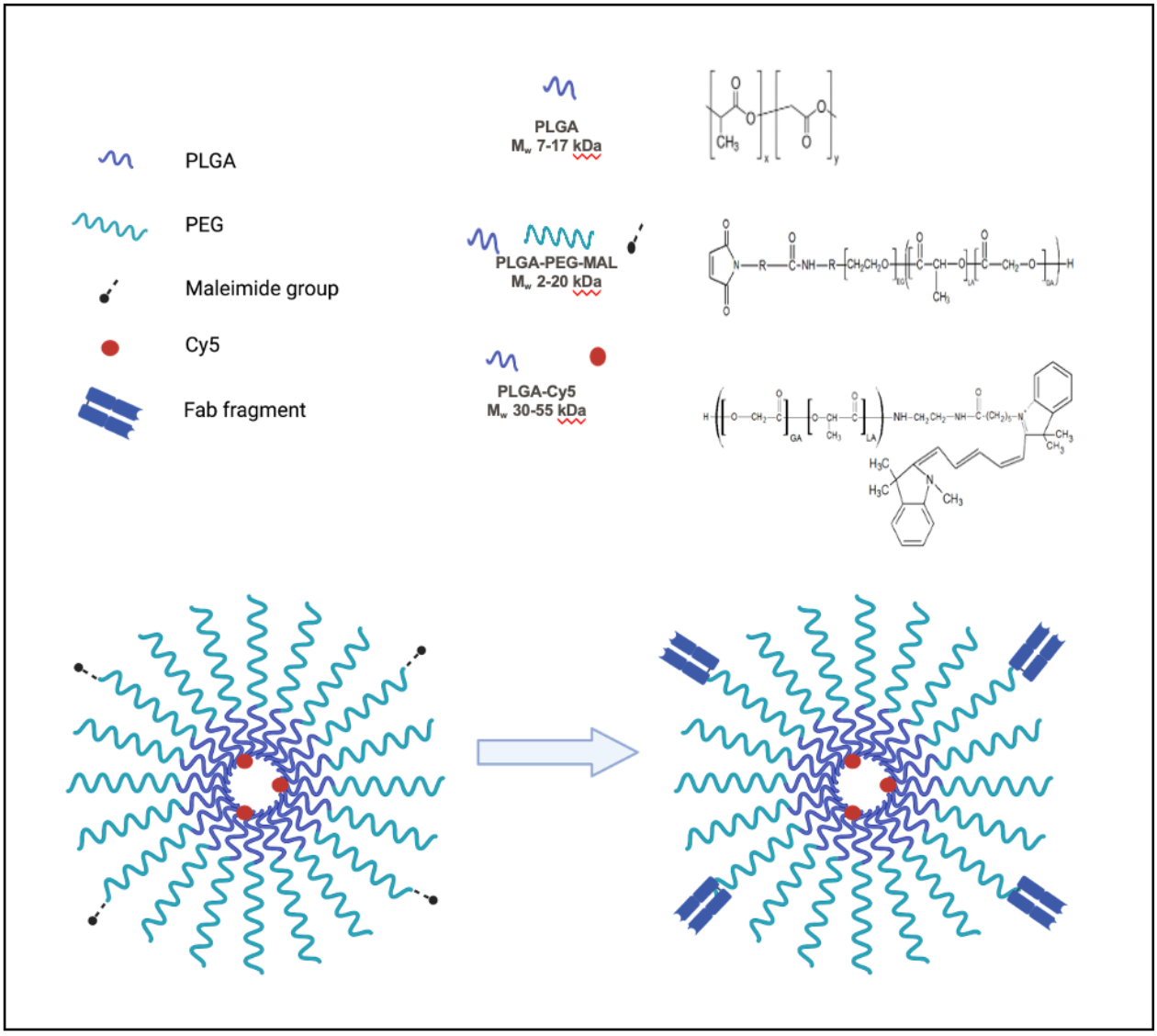

Figure 4-9. Schematic representation of the final nanoparticle design.

The final iteration of the polymeric fluorescent nanoparticles is shown, formed with a core of PLGA and PLGA-Cy5, with PLGA-PEG-MAL providing the outer shell. The unconjugated nanoparticles are then rotated overnight at 4°C with Fab fragments to allow the maleimide reaction to take place. Made using Biorender.

4.5.1.1 Nanoparticle function on fluorescence ELISA is independent of the fluorophore

I set out first to demonstrate function of the revised nanoparticle design, with incorporation of PLGA-Cy5. Initially, I wanted to show that switching fluorophores did not affect binding, assessed on fluorescence ELISA. Figure 4-10 shows the results of the fluorescence ELISAs, using the initial nanoparticle construct with Rhodamine 6G (A) versus Cy5 nanoparticles (B), each functionalised with both LO1 or LO1Fab, with and without TCEP reduction prior to conjugation.

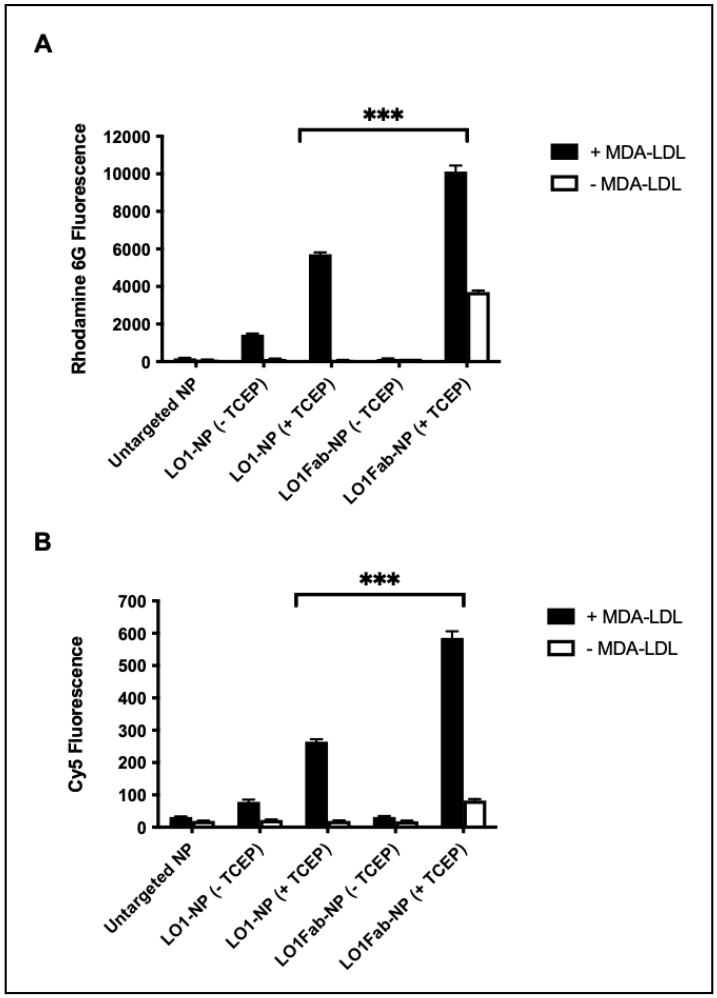

Figure 4-10. Nanoparticle function is independent of the conjugated fluorophore.

*This figure displays fluorescence ELISAs that were performed with MDA-LDL (10µg/mL) or PBS on solid phase, with detection using fluorescence read-outs at the appropriate wavelengths of the conjugated fluorophores. This demonstrates that whether the nanoparticles were formulated with Rhodamine 6G (A) or Cy5 (B), similar MDA-LDL binding on fluorescence ELISA is observed for all constructs. For both formulations, LO1Fab-NP provides more robust binding than LO1-NP (A – ***p=0.0002; B – ***p=0.0001). There is much greater binding with antibody TCEP reduction prior to nanoparticle conjugation for both targeted constructs and for both fluorescent formulations. Unpaired t-test used to assess significance. Performed in triplicate. Error bars represent SEM.*

There are several interesting patterns to note. Firstly, the overall binding patterns are similar between A and B, suggesting similar function, regardless of the fluorophore. Secondly, there is little background binding signal with both constructs, shown in the wells coated with PBS. Thirdly, TCEP conjugation generates much greater binding for both LO1 and LO1Fab-

conjugated nanoparticles, and there is significantly more signal with LO1Fab rather than LO1 conjugation ($p<0.001$ for both Rhodamine 6G and Cy5 nanoparticles).

4.5.2 Antibody fragment conjugation efficiency

Given the much stronger binding of LO1Fab over LO1 conjugated nanoparticles on all analyses, the smaller construct size in initial experiments, as well as the theoretical binding advantages of smaller targeting fragments, LO1Fab constructs were taken forwards in all further studies. Thus, it next became important to optimise the amount of Fab added to the conjugation process, in order to optimise nanoparticle function and conjugation efficiency.

During the nanoparticle optimisation process the amount of antibody construct added to the overnight conjugation step per 1mg of nanoparticle construct was decreased from 50 to 25µg, aiming to reduce construct size. However, this may potentially still be too much, with the coexistent reduction of PLGA-PEG-MAL percentage, and also may be suboptimal, with a reduction in nanoparticle targeted binding capacity. Therefore, I conjugated nanoparticles with 25 or 50µg TCEP-reduced LO1Fab and assessed *in vitro* function. I carried out the indirect ELISA with detection using the anti-PEG primary antibody; fluorescence ELISA using Cy5 fluorescence; and finally, an indirect ELISA with detection with anti-IgG-CH1, all shown in Figure 4-11 below. In this way, nanoparticle presence has been evaluated by all of its constituent components (PEG on the outer nanoparticle corona, Cy5 fluorescence in the nanoparticle core and conjugated Fab fragments on the outer surface).

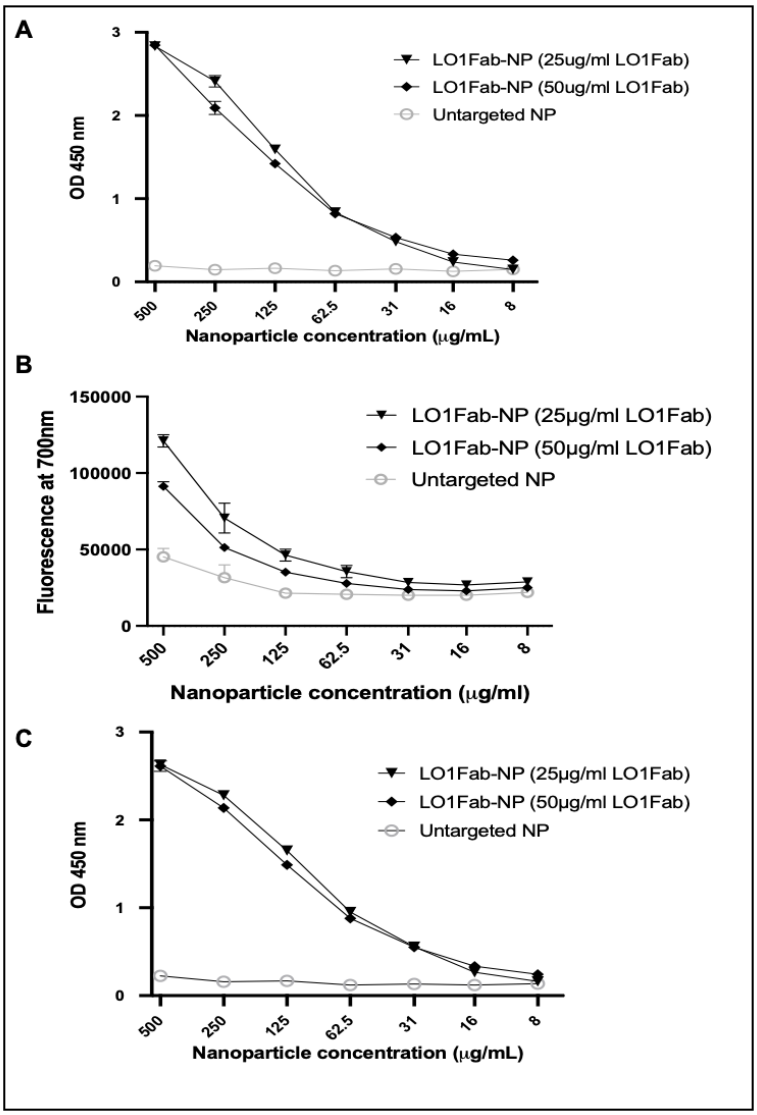

Figure 4-11. LO1Fab conjugation to Cy5 nanoparticles.

Cy5 nanoparticles were conjugated with either 25 or 50μg/mL LO1Fab, and then tested for MDA-LDL recognition with 3 different ELISA designs. MDA-LDL (10μg/mL) was coated overnight, followed by blocking with 3% BSA and nanoparticles in dilution series. Detection was with anti-PEG (A), Cy5 fluorescence (B) and anti-IgG-CH1 (C). There was no additional benefit of an increased quantity of Fab fragment in the conjugation reaction, as evident in all 3 ELISAs. All performed in duplicate. Error bars represent SEM.

Similar binding patterns are observed across all three ELISA designs, with little additional benefit of the higher Fab concentration. There will therefore be a reduced conjugation efficiency, assuming no additional Fab is able to bind to the nanoparticle surface, as would be suggested by the similar ELISA curves. This could be explained by either, 1) all the

maleimide groups being saturated by Fab at the lower Fab concentration, or 2) by steric hinderance from the already bound Fab fragments preventing additional Fab binding.

I next sought to assess whether I could further reduce the amount of Fab added to nanoparticle conjugation to reduce wastage, whilst still maintaining function, and varying the maleimide percentage at the same time, again to see if antibody fragment conjugation efficiency could be optimised.

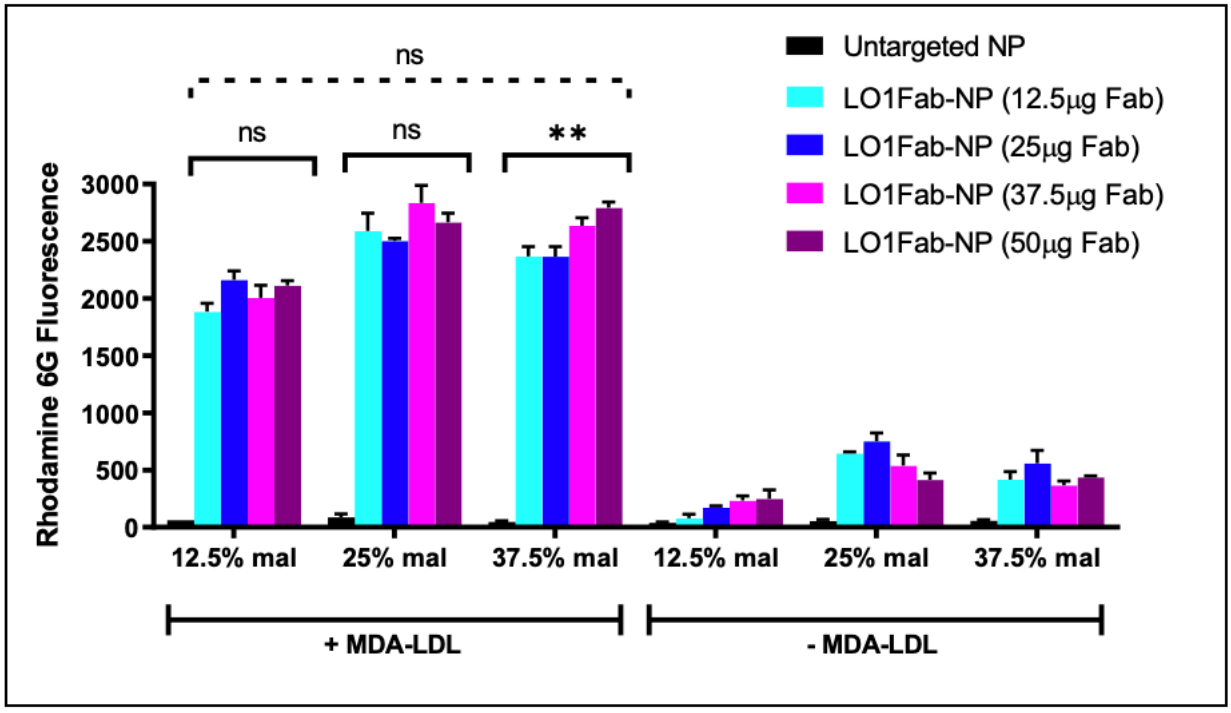

Figure 4-12. Optimisation of maleimide percentage and antibody fragment conjugation in nanoparticle formulation.

*This figure depicts a fluorescence ELISA with MDA-LDL or PBS on solid phase, with detection via Rhodamine 6G fluorescence. Nanoparticles were formulated with varying PLGA-PEG-MAL polymer compositions and differing quantities of LO1Fab added to the conjugation reaction. For all maleimide percentages there is much greater binding to MDA-LDL than the negative controls. With an increasing mass of LO1Fab added to the conjugation reaction there is no significant increase in MDA-LDL binding, except for the highest maleimide concentration (p=0.1452, p=0.2906, **p=0.0082 for 12.5%, 25% and 37.5% respectively, solid brackets). There is no significant difference when all maleimide percentages and quantities of LO1Fab are compared (p=0.7980, dashed bracket). One-way ANOVA used to assess significance. Performed in triplicate. Error bars represent SEM.*

Figure 4-12 above demonstrates no added benefit of larger amounts of LO1Fab added to the conjugation reaction, as had been suggested in Figure 4-11 above, but on this occasion, with smaller LO1Fab masses. In fact, even 12.5µg LO1Fab resulted in similar signal to larger quantities. In addition, there were no substantial differences in nanoparticle function with differing percentage maleimide compositions.

Next, I wanted to evaluate the biophysical properties of nanoparticles prepared with differing maleimide percentages and LO1Fab concentrations using DLS and a modified microBCA assay to quantify the amount of successfully bound Fab following the conjugation reaction. For this, the commercial microBCA assay was adapted to use a protein standard that comprised known amounts of Fab spiked into a fixed concentration of untargeted nanoparticles, to reduce any change in background colour due to nanoparticle presence Importantly, owing to the colorimetric readout of the microBCA assay, this could not be performed using the Cy5 nanoparticles or those with Rhodamine 6G within the core, and thus had to be performed using non-fluorescent constructs.

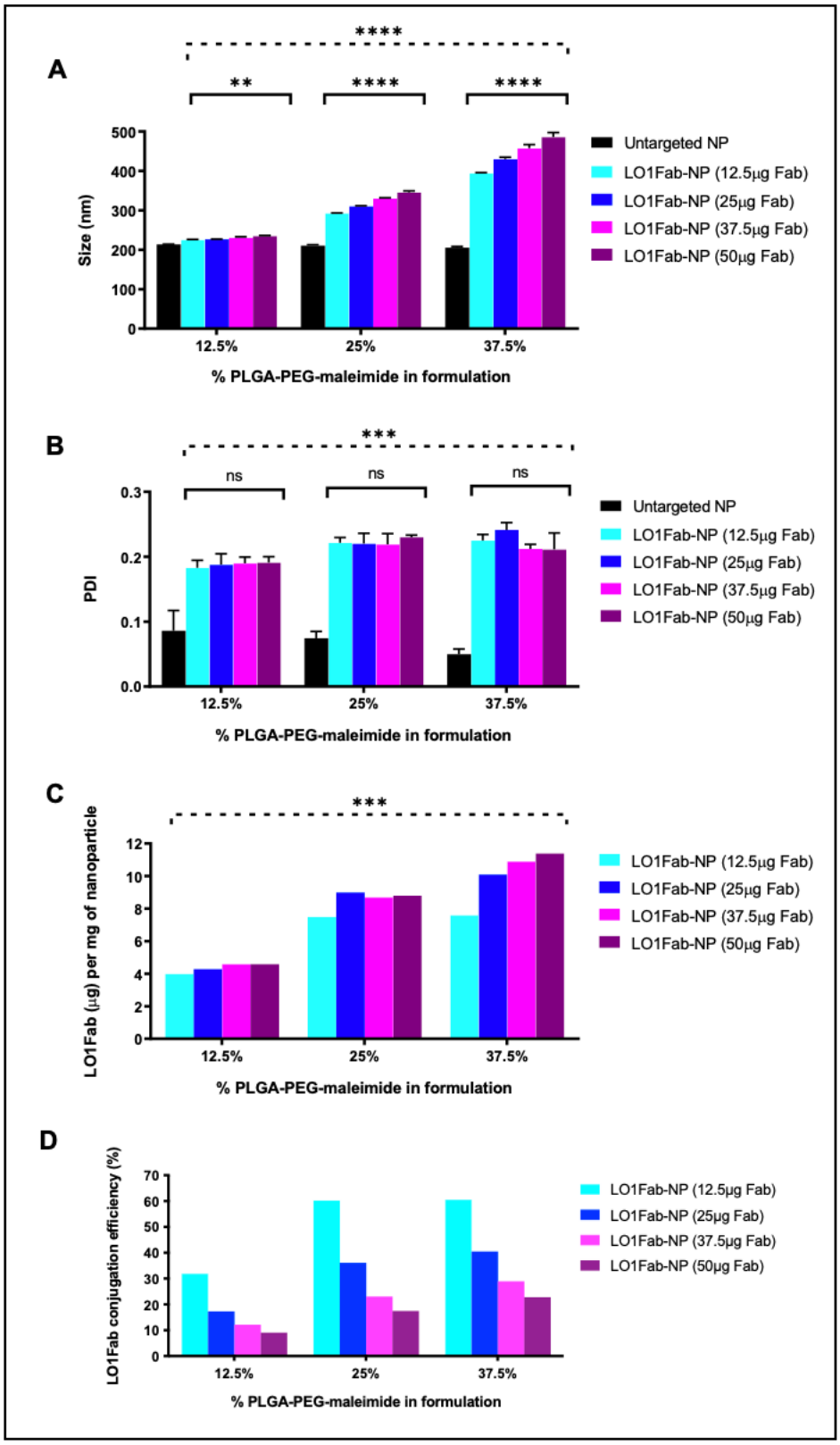

Figure 4-13. Evaluation of varying nanoparticle compositions.

The nanoparticle constructs from the figure above were then assessed for size and PDI by Dynamic Light Scattering (A & B). The nanoparticle constructs were also evaluated using a modified microBCA assay to quantify the amount of successfully bound Fab following the conjugation reaction, and is expressed in µg per mg of nanoparticle (C). Antibody conjugation efficiency is then calculated and is displayed in (D).

*(A) – As more LO1Fab was added to the conjugation reaction, the construct size increases (**p=0.0052 for 12.5%, ****p<0.0001 for both 25 and 37.5% PLGA-PEG-MAL, solid bracket). Constructs became larger as % PLGA-PEG-MAL increases (****p<0.0001, dashed bracket).*
*(B) – there was no significant difference in PDI with higher concentrations of LO1Fab (p=0.9680, p=0.9166 and p=0.4901 across % maleimide groups, solid bracket). There was however greater construct size variability with higher % maleimide formulations (***p=0.0004, dashed bracket).*
*(C) – There was more LO1Fab conjugated with higher % maleimide formulations (***p=0.0001, dashed bracket). However, as more LO1Fab was added to the conjugation reaction, there were no substantial increases in the amount of LO1Fab successfully bound at both 12.5 and 25% maleimide.*
(D) – The conjugation efficiency is then calculated from (C), with much greater efficiency demonstrated with lower initial Fab quantities.
(A) and (B) performed in triplicate. Error bars represent SEM. (C) and (D) are not carried out in replicates. One-way ANOVA used to assess significance.

As demonstrated in Figure 4-13A above, there is a stepwise increase in nanoparticle size with each maleimide percentage increase ($p<0.0001$), from ~226nm with 12.5% PLGA-PEG-MAL to ~394nm with 37.5% PLGA-PEG-MAL, at the lowest LO1Fab concentration. Interestingly, there was also an increase in nanoparticle size as more LO1Fab is added at each maleimide percentage, but the increase was much more substantial at the higher maleimide percentages ($p=0.0052$ for 12.5%, $p<0.0001$ for both 25 and 37.5% PLGA-PEG-MAL). This confirms the findings in Figure 4-11 and Figure 4-12 above and corroborates the explanations above as to why no more Fab can bind in those experiments: there is either saturation of all maleimide reaction ('binding') sites, or steric hindrance prevents further Fab binding. With greater maleimide percentages, there are of course more maleimide groups available for binding, but also the nanoparticle increases in size, reducing the effect of any potential steric hindrance. There was no significant difference in PDI (Figure 4-13B) within the maleimide percentage constructs with varying Fab added ($p=0.9680$, $p=0.9166$ and $p=0.4901$ for each maleimide percentage group); however, there was significantly more construct size heterogeneity with the higher maleimide percentage constructs (PDI 0.12, 0.24 and 0.25 at 12.5, 25 and 37.5% maleimide; $p=0.0004$ between groups), suggesting greater variability in antibody conjugation or construct clumping.

Figure 4-13C shows the results of the modified microBCA assay that was performed to quantify the amount of LO1Fab bound to each batch of nanoparticle construct. There was more LO1Fab conjugated with higher percentage maleimide formulations ($p=0.0001$). However, as more LO1Fab was added to the conjugation reaction, there were no substantial increases in the amount of LO1Fab successfully bound at both 12.5 and 25% maleimide. Figure 4-13D was then derived from C, through dividing the amount of successfully bound Fab by the amount initially added to the conjugation mix. Optimisation of conjugation efficiency is imperative, prior to upscaled construct production for *in vivo* (and later translational) studies. As can be clearly seen, conjugation efficiency was much greater with lower Fab masses. For example, ranging from 31.9% with 12.5µg to 9.1% with 50µg LO1Fab at 12.5% maleimide. Interestingly, conjugation efficiencies were significantly better at the higher maleimide percentages (60.2% and 60.6% for 25% and 37.5% maleimide respectively), again underlining that Fab conjugation is dependent on the maleimide reaction. Similar stepwise patterns of lesser conjugation efficiency with increasing Fab amounts are observed across each maleimide percentage.

These experiments suggested that lower maleimide percentages and less LO1Fab added to the conjugation reaction would produce nanoparticles with more optimal biophysical characteristics and improved conjugation efficiency. However, these experiments were conducted with non-fluorescent nanoparticles, and I wanted to be sure that I could replicate these results with Cy5 constructs, and that *in vitro* function was retained. Thus, I produced nanoparticles comprising 12.5% PLGA-PEG-MAL and conjugated varying amounts of

LO1Fab and tested them all three ELISA platforms (Figure 4-14, anti-PEG (A), Cy5 fluorescence (B) and anti-IgG-CH1 (C)).

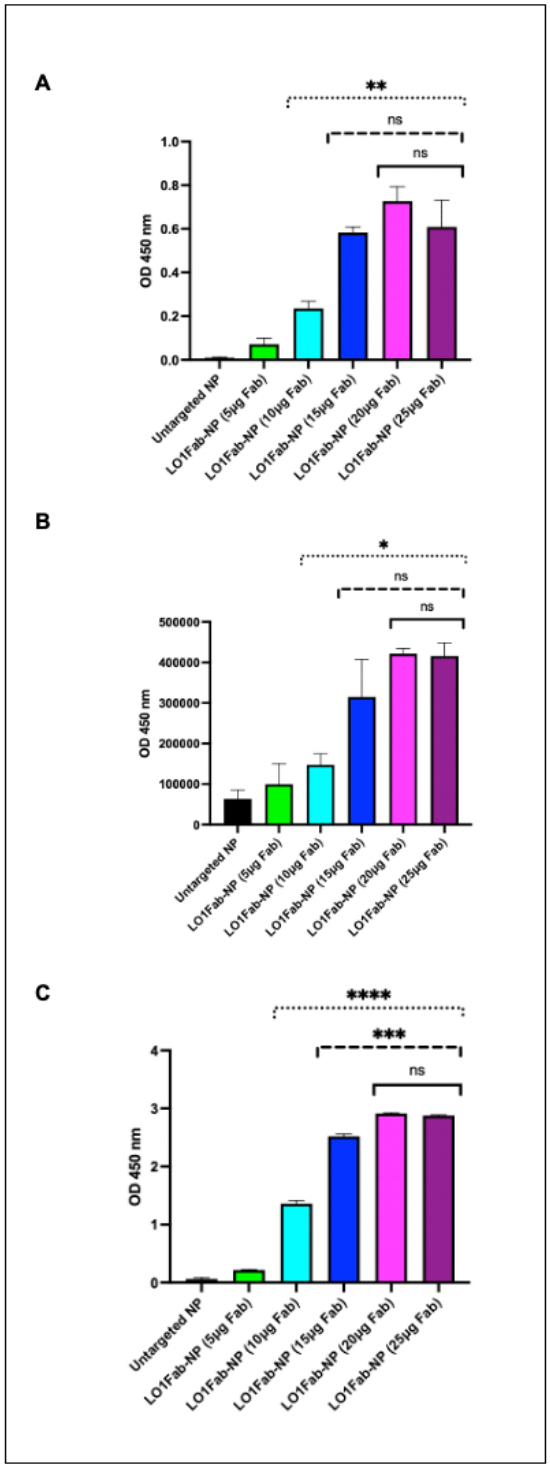

Figure 4-14. Optimisation of LO1Fab conjugation efficiency to Cy5 nanoparticles.

Cy5 nanoparticles were conjugated with varying concentrations of LO1Fab, and then tested for MDA-LDL recognition with 3 different ELISA designs. MDA-LDL was coated overnight, followed by blocking with 3% BSA and nanoparticles (250µg/mL). Detection was with anti-PEG (A), Cy5 fluorescence (B) and anti-IgG-CH1 (C).
*(A) – There was no significant difference between the top 2 (p=0.3528, solid bracket) or 3 (p=0.3114, dashed bracket) Fab concentrations. However, there was significant difference when 10µg/mL was included (**p=0.0097, dotted bracket).*
*(B) – There was no significant difference between the top 2 (0.8736, solid bracket) or 3 (p=0.2543, dashed bracket) Fab concentrations. However, there was significant difference when 10µg/mL was included (*p=0.0166, dotted bracket).*
*(C) – There was no significant difference between the top 2 (p=0.0873, solid bracket) Fab concentrations. However, there were significant differences when 15µg/mL or 10µg/mL were included (***p=0.0009, dashed bracket; ****p<0.0001 dotted bracket respectively).*
Unpaired t-test used to assess significance for 2 constructs, one-way ANOVA used for ≥ 3 constructs. All performed in duplicate. Error bars represent SEM.

Similar binding patterns are observed across all three ELISAs, with greater signal as more Fab is added to conjugation, up to 20µg, when there is no additional benefit. Again, this is analogous to the earlier experiments, demonstrating little extra gain of higher Fab concentrations. Of note however, from 15 to 20µg there would appear to be extra binding, which is statistically significant (p=0.0009) using the anti-IgG-CH1 assay in (C).

To ensure that maximal nanoparticle function was ensured, at least for the initial proof-of-concept experiments, I therefore chose to conjugate the nanoparticles with 20µg LO1Fab, at the cost of an expected poorer conjugation efficiency. That was with the knowledge that when large scale production is required after *in vivo* function has been demonstrated, the Fab concentration could be reduced in future studies.

4.5.3 Final nanoparticle physical properties

Using DLS as above, LO1Fab-nanoparticles manufactured using 12.5% maleimide and 20µg Fab measured 217.83 ± 1.13nm in size (mean ± SD), whilst untargeted nanoparticles measured 214.73 ± 0.26nm; both of which are within acceptable ranges. The slightly larger

targeted nanoparticle size is in keeping with Fab fragment conjugation. The PDI was 0.05 ± 0.03 and 0.08 ± 0.06 respectively, representing very good construct uniformity.

4.5.4 Final nanoparticle composition

Bringing this set of experiments together, I have demonstrated that Cy5 nanoparticles conjugated with LO1Fab are functional in three ELISA designs, assessing binding through different aspects of the nanoparticle construct. LO1Fab had more favourable binding results and physical properties than LO1, and thus has been taken forwards to construct development. I have optimised the nanoparticle design to improve physical properties, which now comprises 2.5 mg PLGA-PEG-MAL (12.5%), 10 mg PLGA-cyanine 5 (50%) and 7.5 mg PLGA (37.5%), to make 20mg of nanoparticles, conjugated to 20µg of LO1Fab. These quantities will now be used to produce standardised nanoparticle constructs throughout the rest of this chapter.

4.6 Control Fab production

To this point in the chapter, targeted nanoparticles have been compared to nanoparticles with no antibody fragment attached (‘untargeted nanoparticles’). However, this is an imperfect negative control, particularly for *in vivo* studies, where it is imperative to appreciate that any differences in binding/ signal are due to true on-target effects of the targeting antibody, rather than non-specific binding related to the presence of the antibody fragment. Thus, I searched commercial catalogues for a ‘control Fab'', ideally of human origin, that could be used to conjugate to the untargeted nanoparticles as a more representative control group. Unfortunately, I could not identify any commercially available Fab' fragments, so I set out to

develop a non-specific Fab fragment with capabilities for binding to nanoparticle constructs using maleimide chemistry.

4.6.1 F(ab')$_2$ reduction with 2-MEA

As there were no commercially available Fab' fragments, I purchased commercially available human IgG F(ab')$_2$ fragments (009000006 – Jackson ImmunoResearch, Philadelphia, USA) and performed reduction using the mild reducing agent 2-MEA, with the aim of selectively cleaving the two disulphide bonds in the hinge region, rendering two Fab' fragments, as has been performed previously (275). Following reduction with varying concentrations of 2-MEA for 1-hour (as detailed in *Section 2.3.3 Generation of control Fab fragments*), the resulting proteins were run on an SDS-PAGE gel and dyed with Coomassie stain (Figure 4-15 below).

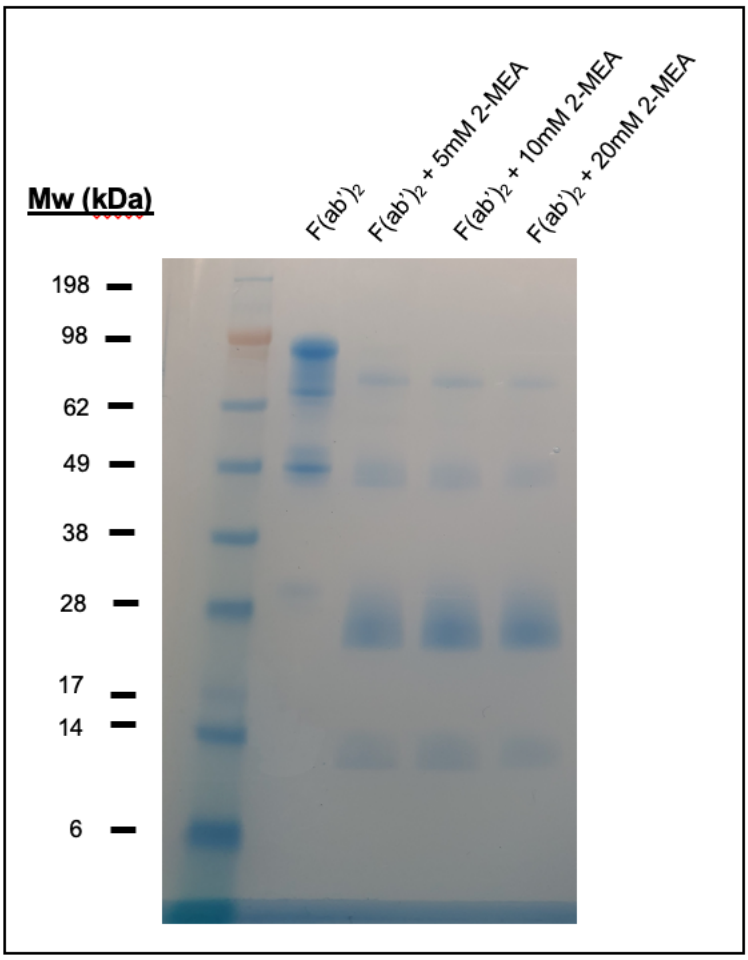

Figure 4-15. F(ab')2 reduction with 2-MEA.

4-12% Bis-Tris SDS-PAGE gel with Coomassie staining demonstrating F(ab')2 breakdown with different 2-MEA concentrations. Incubated at 37°C for 1 hour. 5µg of protein loaded per lane. There is effective reduction of the approximately 100kDa F(ab')2 into smaller fragments. However, the primary protein achieved through all reduction conditions is at approximately 25kDa, likely representing separate heavy and light chains, rather than the desired 50kDa proteins with paired heavy and light chains.

Figure 4-15 demonstrates that, as expected, non-reduced $F(ab')_2$ has ~100kDa weight. However, following reduction with 2-MEA, most of the $F(ab')_2$ protein has broken down, forming dense bands at ~25kDa. This suggests that the protein has been over-reduced, and other disulphide bonds have also broken in the $F(ab')_2$ structure, perhaps generating free heavy and light chains. Accordingly, I sought to vary the 2-MEA concentration and incubation period, to try to optimise Fab' generation, shown in Figure 4-16.

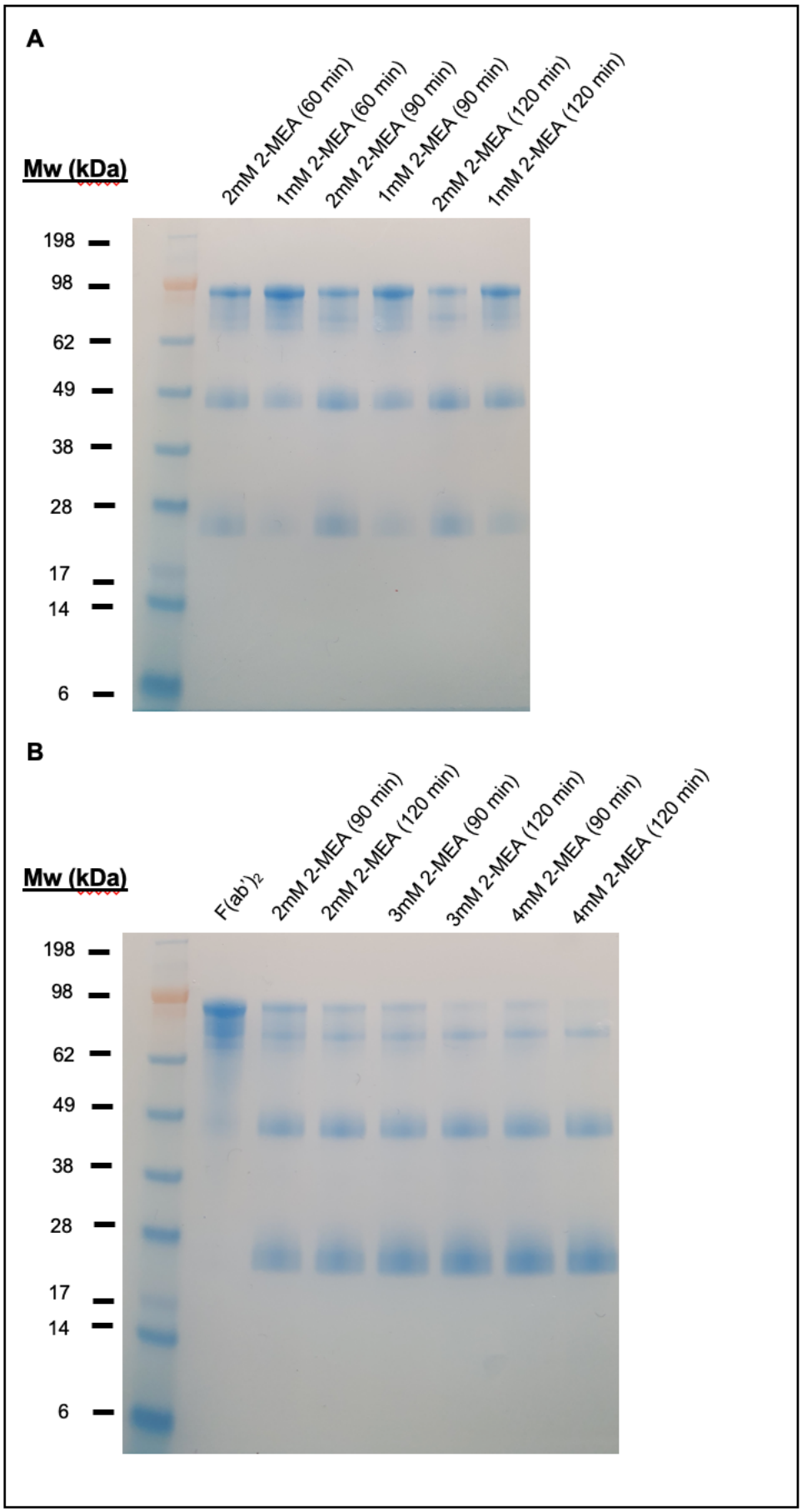
A
Mw (kDa)
198
98
62
49
38
28
17
14
6
2mM 2-MEA (60 min)
1mM 2-MEA (60 min)
2mM 2-MEA (90 min)
1mM 2-MEA (90 min)
2mM 2-MEA (120 min)
1mM 2-MEA (120 min)
B
Mw (kDa)
198
98
62
49
38
28
17
14
6
F(ab')2
2mM 2-MEA (90 min)
2mM 2-MEA (120 min)
3mM 2-MEA (90 min)
3mM 2-MEA (120 min)
4mM 2-MEA (90 min)
4mM 2-MEA (120 min)

Figure 4-16. Optimisation of F(ab')2 reduction with 2-MEA.

4-12% Bis-Tris SDS-PAGE gels with Coomassie staining demonstrating the degree of F(ab')2 breakdown with different concentrations and incubation duration of 2-MEA. Incubated at 37°C. 5µg of protein loaded per lane.
A) There is greater reduction (with stronger bands at approximately 50 and 25kDa) with the 2mM 2-MEA conditions, irrespective of incubation duration. However, the majority of the protein remains unreduced at ~100kDa.
B) There is greater reduction (with stronger bands at both ~25 and ~50kDa) with higher concentrations of 2-MEA, which was also mildly time-dependent. Therefore, the 4mM 2-MEA condition was taken forwards.

In Figure 4-16A, there is still significant amount of unreduced $F(ab')_2$ across all 2-MEA concentrations and incubation periods, despite incubating for twice as long as in Figure 4-15. There is increased degradation with 2mM than 1mM, at both incubation durations, with stronger bands at ~50 and ~25kDa. Thus, it became clear that finding a 'sweet spot' of Fab generation without also having an abundance of free heavy/ light chains was going to be problematic. In Figure 4-16B I then increased the 2-MEA concentrations further and utilised longer incubation periods. With higher 2-MEA concentrations there was less $F(ab')_2$ remaining, particularly at 120-minutes incubation, however with more significant bands at ~25kDa. I settled on 4mM 2-MEA for further control Fab production, considering how 5mM MEA had over-reduced the $F(ab')_2$ fragments in Figure 4-15.

4.6.2 Ultracentrifugation of reduced $F(ab')_2$ fragments

Given that obtaining a clean band at ~50kDa was proving difficult, I then used ultracentrifugation with an appropriate size filter to separate the proteins. A 50kDa filter was chosen to remove the free light and heavy chains, as the filter cut-off point should be two-fold higher than the molecular weight of the desired protein for exclusion. Moreover, having unreduced $F(ab')_2$ fragments in the control Fab mixture, although not ideal, should not cause

a major issue, unlike the free heavy and light chains, as it will not be able to react with and occupy the nanoparticle maleimide groups.

After ultracentrifugation according to the manufacturer's instructions (see *Section 2.3.3 Generation of control Fab fragments*), the filtrate and retentate were run on SDS-PAGE gels and Coomassie stained as above (Figure 4-17). Figure 4-17A demonstrated that some of the ~50kDa bands had crossed the filter membrane into the filtrate. However, importantly, the strength of ~25kDa bands had significantly reduced in the retentate, suggesting that the free heavy and light chains had successfully entered the filtrate. There were no significant differences between the protein bands that had been incubated with 2-MEA for either 90- or 120-minutes, and thus a 90-minute timepoint was chosen for all future control Fab generation. Figure 4-17B displays the final result of ultracentrifugation versus unreduced $F(ab')_2$ fragments, with some unreduced ~100kDa fragments remaining in the mixture, with a strong band at ~50kDa (representing Fab') and a very light band at ~25kDa.

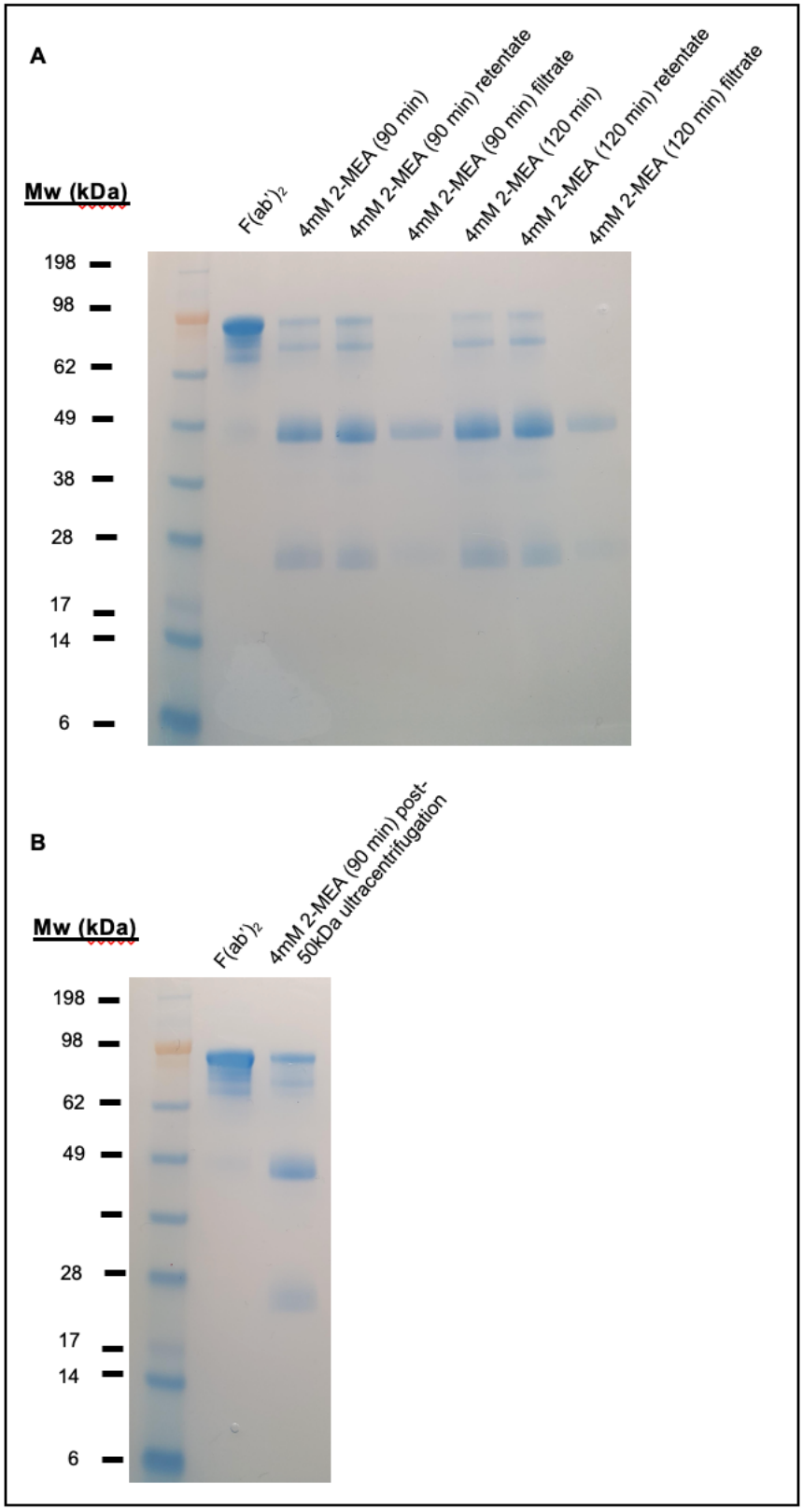

Figure 4-17. Ultracentrifugation of the reduced F(ab')2 fragments.

A) – 4-12% Bis-Tris SDS-PAGE gel with Coomassie staining demonstrating the degree of $F(ab')_2$ reduction with 4mM 2-MEA at either 90-minute or 120-minute incubation durations, before and after purification with a 50kDa ultracentrifugation column (filtrate and retentate both shown). There is a reduction in the strength of the ~25kDa band in the retentate following ultracentrifugation. There was little appreciable difference between the two time

conditions, and thus the 90-minute condition was chosen as optimum timepoint. Incubated at 37°C. 5µg of protein loaded per lane.
B) – The final optimised conditions for F(ab')2 reduction. 4-12% Bis-Tris SDS-PAGE gel with Coomassie staining, demonstrating F(ab')2 reduction with 4mM 2-MEA for 90-minutes after purification with a 50kDa ultracentrifugation column. There is a strong band at ~50kDa, representing a Fab fragment (with a free sulfhydryl group). There is a minimal ~25kDa band; however there does remain some unreduced $F(ab')_2$. Incubated at 37°C. 5µg of protein loaded per lane.

Thus, the final conditions were incubation with 4mM 2-MEA for 90-minutes. However, there is still scope to modify this reduction step further and increase the Fab' yield in future experiments, perhaps through trying different reducing agents, such as TCEP, dithiothreitol (DTT) or dithiobutylamine (275).

4.6.3 Quantification of free sulfhydryl groups on reduced $F(ab')_2$ fragments

Next, to confirm that the protein species produced via this reduction step possessed free sulfhydryl groups for the maleimide reaction, a commercial Ellman's assay was carried out, which is a colorimetric assay based upon the reaction between Ellman's Reagent and thiol groups.

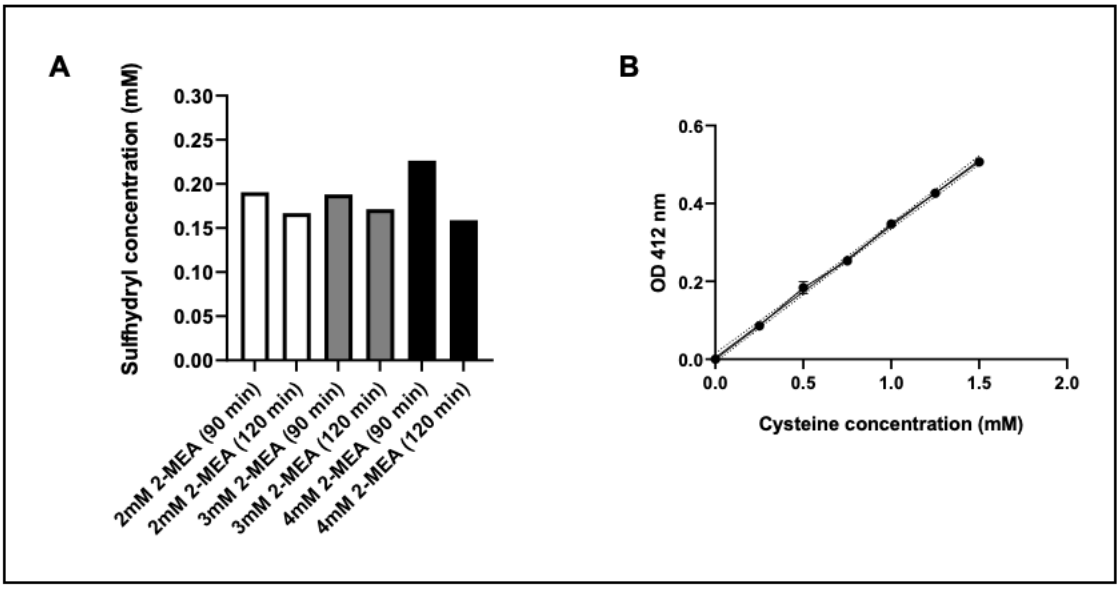

Figure 4-18. Quantification of free sulfhydryl groups on reduced F(ab')2 fragments.

A) – Displays the results of the Ellman's assay, a commercial assay to quantify the sulfhydryl concentration of unknown solutions, that was carried out as per manufacturer's instructions. Using the 2-MEA conditions shown above, this demonstrates preservation of free sulfhydryl groups across the reduction conditions.
B) – Shows the cysteine standard curve that was used to interpolate the unknown values using non-linear least squares regression (R^2 = 0.997). Performed in duplicate. Error bars represent SEM.

Figure 4-18A shows the results of the Ellman's assay, using control Fab that had been generated with different reducing conditions. There was evidence of free sulfhydryl groups across the range of conditions, with the strongest signal seen with 4mM 2-MEA incubated for 90-minutes (the optimum reduction conditions from above). Figure 4-18B displays the cysteine standard curve that was used to interpolate the unknown sulfhydryl group concentrations, with very good agreement with the line of best fit (R^2 = 0.997). This experiment confirmed that the reduction had produced Fab' rather than Fab fragments, which will be crucial for future conjugation reactions.

4.6.4 Fluorescent labelling of the control Fab fragment

I next wanted to ensure that I could label the Fab' construct with a fluorescent tag using maleimide chemistry, which itself will be needed for *in vivo* imaging, as well as providing evidence of successful conjugation. As such, both LO1Fab and control Fab were labelled with VivoTag-S-750 MAL, as performed previously (174) (see *Section 2.3.4 Fluorescent labelling of antibody fragments for in vivo studies*). There was a very good degree of labelling with the control Fab (ratio of dye: protein; 0.63 versus 0.21 with LO1Fab), suggesting good availability of free sulfhydryl groups for the maleimide reaction. Following conjugation, the fluorescently labelled Fab fragments were run on an SDS-PAGE gel and imaged at 800nm on a fluorescent scanner (Odyssey CLx Imaging System).

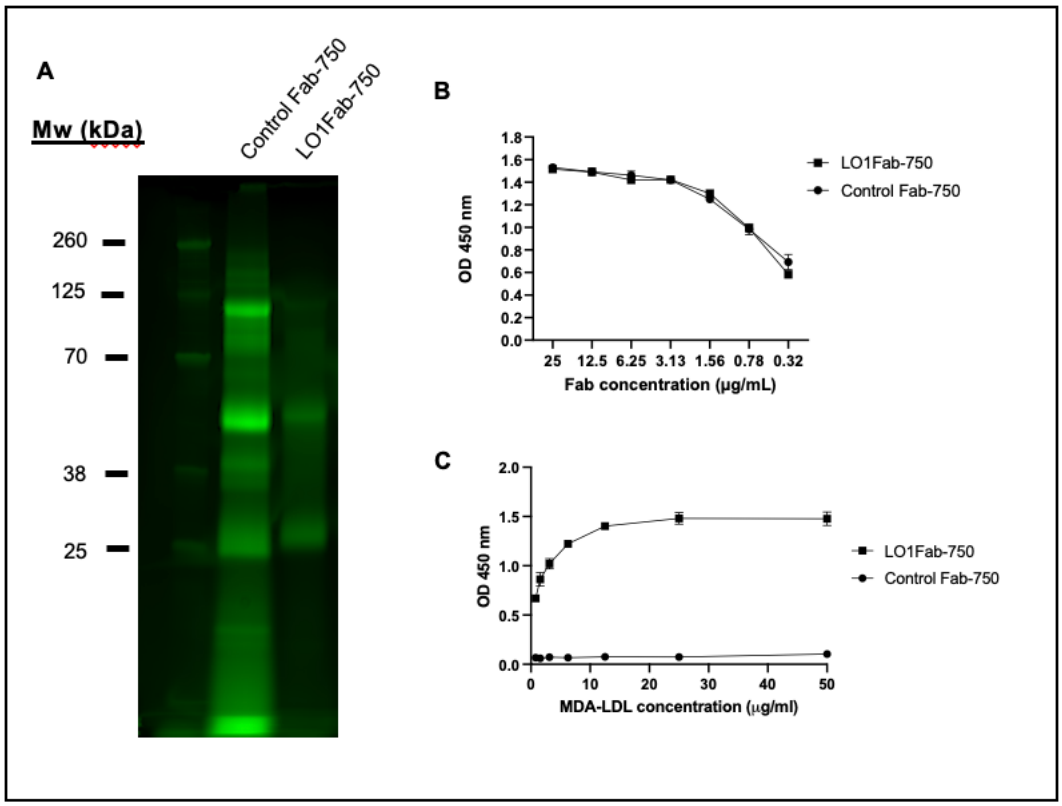

Figure 4-19. Fluorescent labelling of Fab constructs.

Control Fab and LO1Fab were then effectively labelled with a NIRF reporter (Vivotag-S-750 MAL), with a degree of labelling of 0.63 and 0.21 respectively.

A) – displays a 4-12% Bis-Tris SDS-PAGE gel that has been imaged at 800nm on the LICOR fluorescent scanner. There are clear fluorescent bands at around 50kDa, with less bright bands at approximately 25kDa.
B) – direct ELISA with the fluorescently labelled antibody fragments on solid phase was performed, with detection via a human anti-IgG-CH1 primary antibody. This demonstrates equivalent detection of both fluorescent constructs
C) – Demonstrates the reactivity of both fluorescently labelled constructs for MDA-LDL versus unlabelled LO1Fab in ELISA format, with detection via a biotinylated anti-ApoB primary antibody.
All ELISAs performed in duplicate. Error bars represent SEM.

Figure 4-19A demonstrates strong fluorescent bands at ~50kDa, representing successfully labelled Fab fragments for both LO1 and control Fab. The control Fab-750 band appears stronger, as would be expected given the three-fold better degree of fluorescent labelling. Next, I performed a direct ELISA (B), coating with the fluorescently labelled Fab constructs, and detecting with a human anti-IgG-CH1 primary antibody. There was equivalent detection between both proteins, demonstrating firstly that the Fab fragments were still intact post-conjugation, and secondly that the fragments were still detectable using the anti-IgG-CH1 ELISA. Finally in Figure 4-19C, I confirmed that control Fab-750 was not reactive in a functional ELISA versus MDA-LDL.

4.7 Effect of Fab fragment reduction for nanoparticle conjugation

4.7.1 Fab fragment reduction

For antibody-nanoparticle conjugation the protocol had involved reducing antibody fragments with 10M TCEP for 1-hour at RT prior to conjugation during nanoparticle development, based on prior experience in the Scott laboratory. However, I had not investigated the effect that this reduction step had on antibody structure and function. To explore this, I initially reduced both LO1Fab and control Fab with different TCEP concentrations 5-20M, and ran them on SDS-PAGE gels, shown in Figure 4-20 below.

Surprisingly, both Figure 4-20A and B demonstrate that unreduced LO1Fab had formed an oligomeric structure with a molecular weight of ~80kDa, likely representing a combination of three fragment chains (for example two heavy chains with one light chain). Control Fab had also oligomerised to a degree, despite resolubilising into reaction buffer containing EDTA after Fab generation. This entity was not robustly affected by reduction by TCEP at all tested concentrations. Reduction did further degrade the remaining ~50kDa fragments into ~25kDa fragments, however. All TCEP concentrations in A) degraded LO1Fab to form ~25kDa subunits. In B), with lower TCEP concentrations, there was some ~50kDa species formed, however there were much more significant ~25kDa species. Over-degradation to ~25kDa subunits is not ideal, as it means that it is not actually Fab fragments that are being conjugated to nanoparticles, but free heavy-light chains. Moreover, oligomerisation of both Fab fragments in solution suggests that fresh protein batches may be required (LO1Fab is stored at -80°C before storing at +4°C in aliquots for short term use), or that a degree of reduction may also be necessary prior to use.

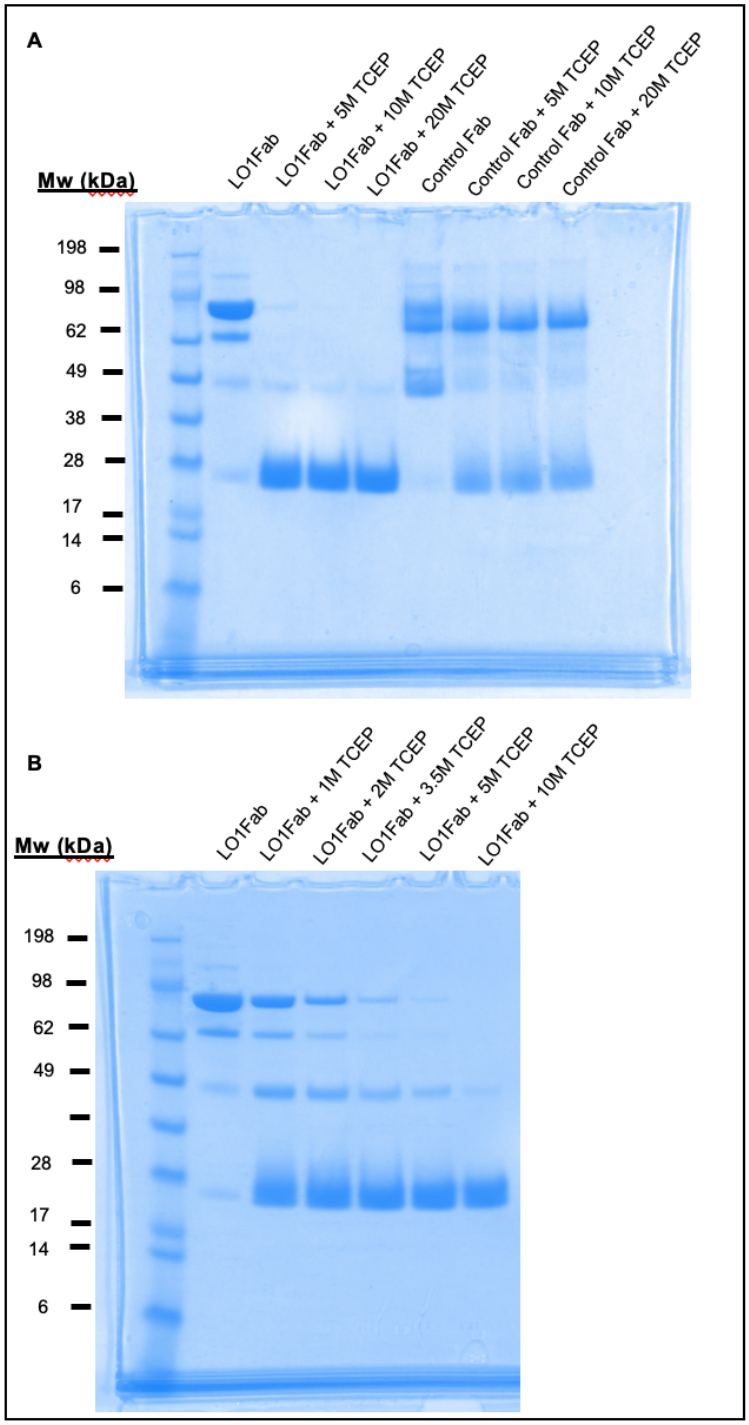

Figure 4-20. Fab fragment reduction using TCEP.

4-12% SDS-PAGE gels with Coomassie staining demonstrating the effect of different concentrations of selective disulphide bond reduction using TCEP on LO1Fab and control Fab. Unreduced LO1Fab is shown to have formed an oligomeric structure in both A & B, with a molecular weight of ~80kDa, which likely represents two heavy/ light chains with one light/ heavy chain accordingly (three chains in total). All TCEP reduction steps performed for 1 hour at room temperature. 5µg of protein loaded per lane.
A) – With the lowest (5M) TCEP molar excess there is complete loss of this LO1Fab band, with degradation to a ~25kDa subunit, and very little 50kDa Fab produced. In comparison, TCEP reduction of the control Fab seems to remove the ~50kDa band, with no significant effect on the higher molecular weight band.
B) – Milder LO1Fab reduction demonstrates some ~50kDa fragment formation with lower TCEP molar excess; however, together with this is persisting higher molecular weight bands.

To explore this further, I assessed whether the observed over-reduction with TCEP was a true effect, or an experimental artefact related to the reducing SDS-PAGE gel electrophoresis. As such, I ran reduced LO1Fab on identical SDS-PAGE and native-PAGE gels under reducing and non-reducing conditions respectively, and Coomassie stained for protein detection. Figure 4-21 below displays these gels. Of note, LO1Fab did not run on the non-reducing gel (B), perhaps related to the absence of denaturation/ reducing conditions prior to loading on the gels. Higher TCEP concentrations increased the strength of the ~25kDa band and reduced the oligomerised band in the reducing gel (A). Interestingly, the ~25kDa band in A) corresponded to a ~50kDa band in B), suggesting that the over-degradation with TCEP seen in Figure 4-20 may indeed be an experimental artefact.

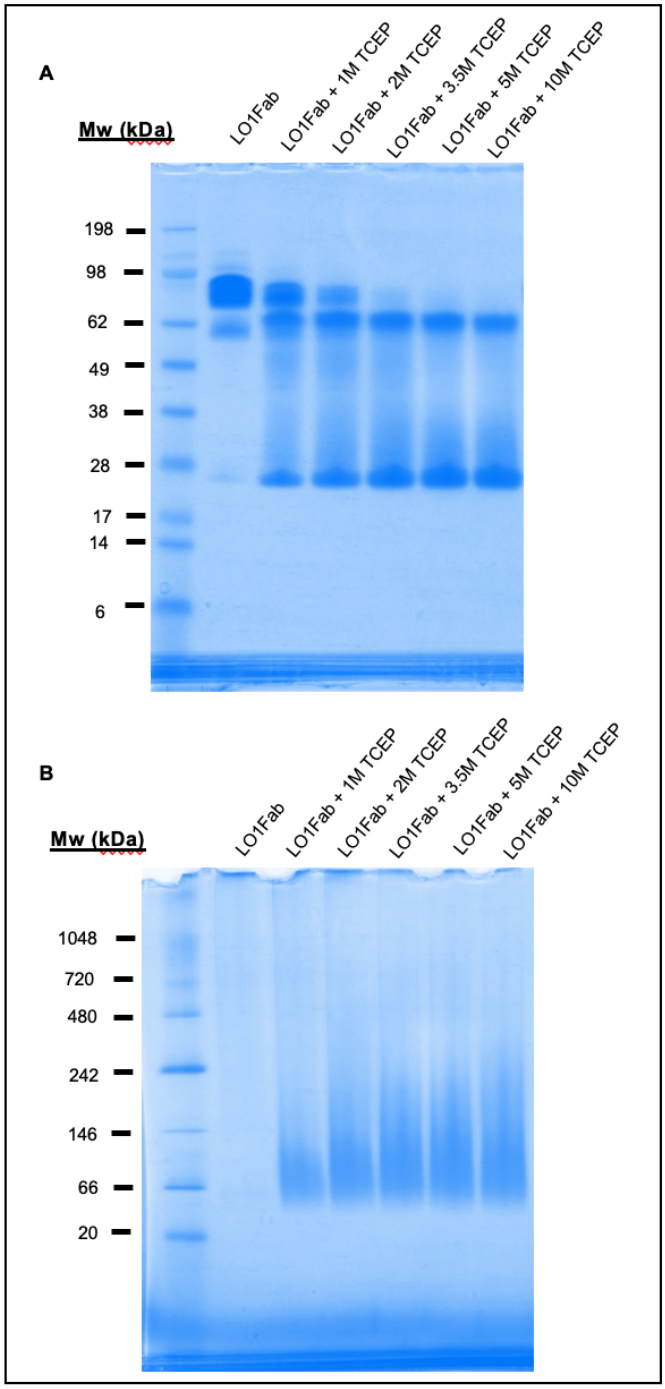

Figure 4-21. Gel electrophoresis of reduced LO1 Fab fragments.

4-12% SDS-PAGE Bis-Tris gel (A) and 4-16% Bis-Tris native-PAGE gel (B) with Coomassie staining demonstrating loss of higher molecular weight bands with increasing TCEP molar excess, coupled with the formation of lower weight fragments. The lowest band on the reduced gel (A) corresponds to ~25kDa, whilst on the non-reduced gel (B) this corresponds to ~50kDa. Unprepared and unreduced LO1Fab did not run on the non-reduced gel (B). 10µg of protein loaded per lane.

The next logical step was to assess the function of reduced Fab fragments, and confirm the absence of binding of reduced control Fab, on ELISA. An indirect ELISA was performed with MDA-LDL on solid phase, shown in Figure 4-22 below. This demonstrates substantially abrogated LO1Fab recognition for MDA-LDL, with TCEP reduction at 10M. There was no recognition of MDA-LDL by unreduced or reduced control Fab.

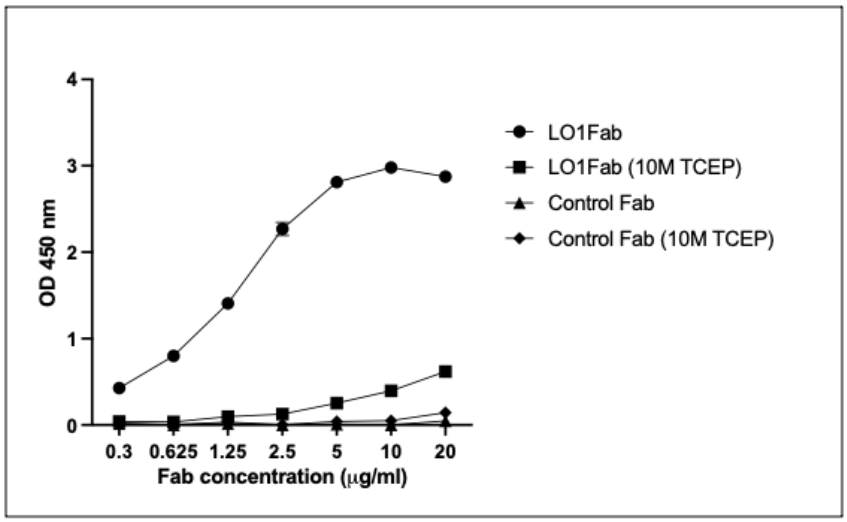

Figure 4-22. 10M TCEP-reduced Fab fragment recognition of MDA-LDL on ELISA.

This ELISA with MDA-LDL (10μg/mL) on solid phase and detection via an anti-IgG-CH1 primary antibody demonstrates a very significant loss of LO1Fab reactivity for MDA-LDL reduced with 10M TCEP molar excess for 1-hour at room temperature. Performed in duplicate. Error bars represent SEM.

Given the loss of LO1Fab function with TCEP reduction at TCEP concentrations that had been used for nanoparticle conjugation to date, I explored reducing LO1Fab with lower TCEP concentrations, in an attempt to identify more optimal reducing conditions.

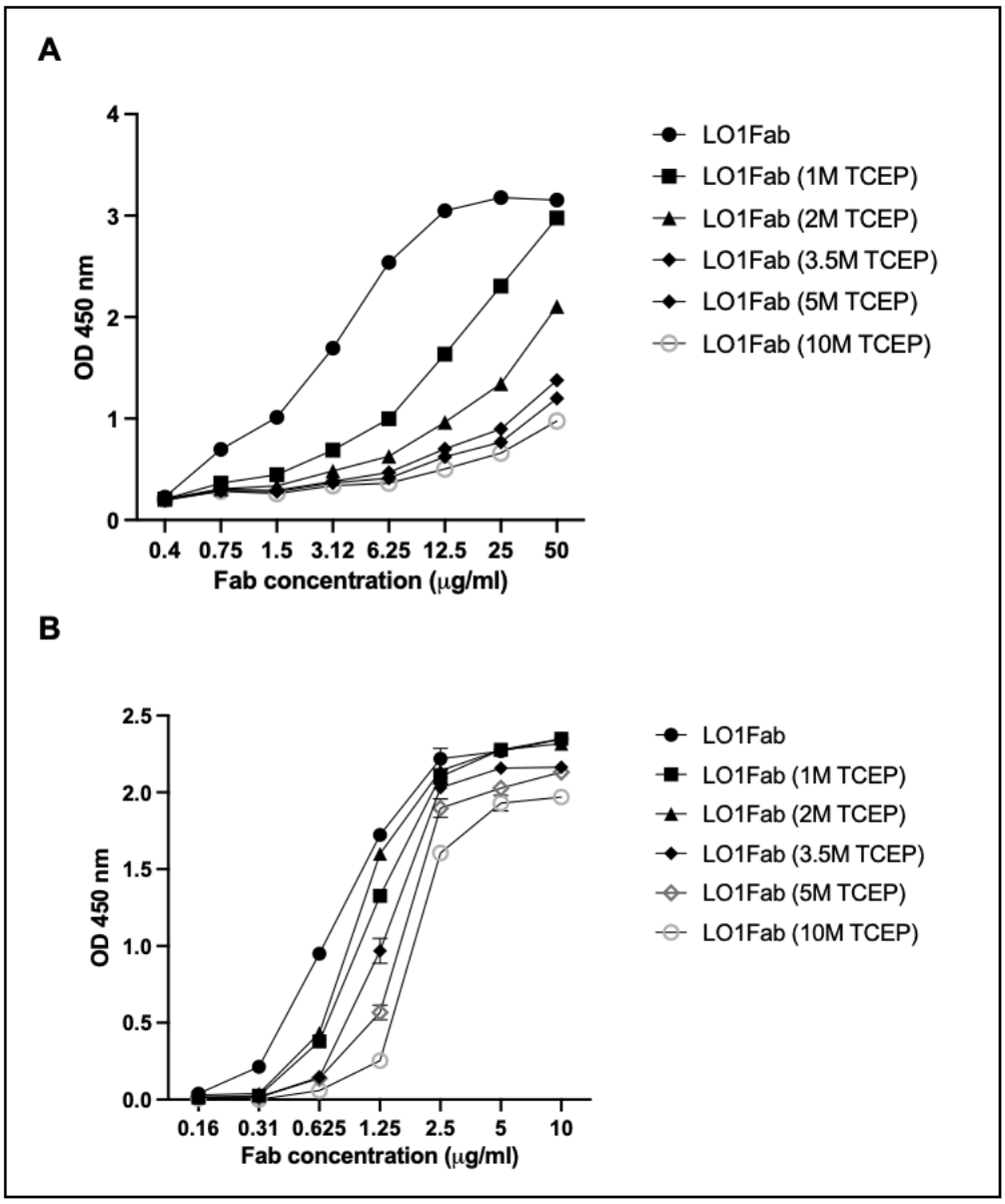

Figure 4-23. The reactivity of differentially reduced LO1Fab on ELISA.

LO1Fab was reduced with different molar excesses of TCEP for 1-hour at room temperature, and was assessed for reactivity with MDA-LDL (10μg/mL) in an indirect ELISA with detection via an anti-IgG-CH1 in (A), and in sandwich format with detection via an anti-ApoB in (B). Notably, although both ELISAs demonstrate a loss of function with increasing TCEP concentrations, this effect was much less marked on the ELISA in sandwich format. This suggests that the binding capability of LO1Fab for MDA-LDL in fluid-phase may be less susceptible to reduction than with MDA-LDL on solid phase, and that the significant loss of reactivity in (A) may be a function of the ELISA format. Performed in duplicate. Error bars represent SEM.

As Figure 4-23A clearly demonstrates, there is an apparent TCEP concentration-dependent loss of signal, evaluated in an indirect ELISA with MDA-LDL on solid phase and detection with anti-IgG-CH1. There is a significant loss of binding, with the 10M concentration resulting in ~2/3 reduction in function compared to unreduced or 1M TCEP reduced LO1Fab. I then repeated a functional ELISA with reduction using the same TCEP concentrations to ensure this a was true result and not due to experimental error or artefact. On this occasion I performed a sandwich ELISA, coating with reduced LO1Fab and detecting with an anti-ApoB antibody. Figure 4-23B displays the results of this ELISA. A graduated and concentration-dependent decrease in binding with TCEP reduction is again observed, however the degree of functional loss is much less sizable. This suggests that the binding capability of LO1Fab for MDA-LDL in fluid-phase may be less susceptible to reduction than with MDA-LDL on solid phase, and that the very significant loss of reactivity in A) may be a function of the ELISA format. I next demonstrated that the loss of reactivity was present even with very mild LO1Fab reduction (in case even less antibody reduction was desirable for nanoparticle conjugation in future studies), as shown in Figure 4-24 below.

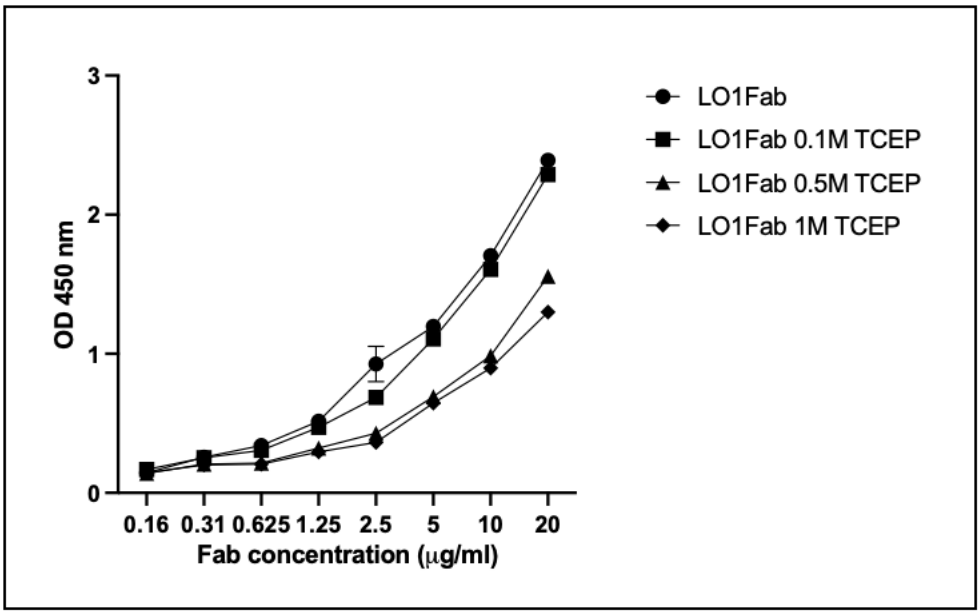

Figure 4-24. Effect of minimally reduced LO1Fab on MDA-LDL recognition in ELISA format.

This indirect ELISA with MDA-LDL (10μg/mL) on solid phase and detection with anti-IgG-CH1 demonstrates a concentration-dependent loss of reactivity, even at low TCEP molar excess. Performed in duplicate. Error bars represent SEM.

4.7.2 Reduced Fab fragment nanoparticle conjugation

Having now demonstrated that TCEP reduction affected Fab binding to MDA-LDL, to varying extents depending on the ELISA conditions, I then sought to explore how differentially reduced Fab prior to nanoparticle labelling altered nanoparticle conjugation and function. Additionally, 20μg control Fab was also reduced with TCEP prior to nanoparticle conjugation, under the same conditions as LO1Fab, to serve as a negative control.

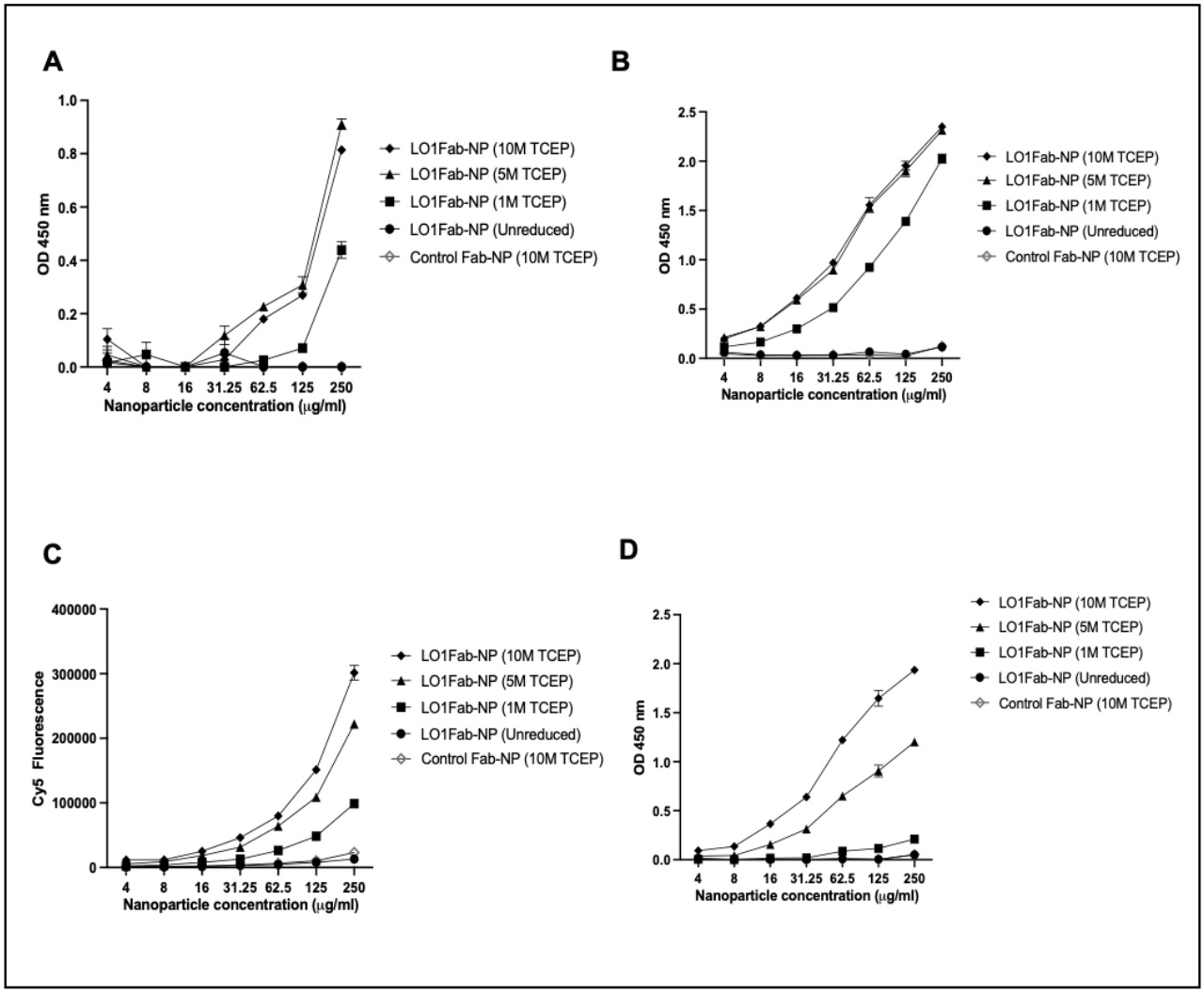

Figure 4-25. The effect of LO1Fab TCEP reduction prior to nanoparticle conjugation on ELISA.

Fab fragments were incubated with different molar excesses of TCEP for 1-hour at room temperature prior to nanoparticle conjugation. Nanoparticle function was assessed on various ELISAs. (A-C) with MDA-LDL (10μg/mL) on solid phase; (D) has nanoparticles on solid phase. All ELISAs performed in duplicate. Error bars represent SEM.
A) – Indirect ELISA with detection via anti-PEG primary antibody.
B) – Indirect ELISA with detection via anti-IgG-CH1 antibody.
C) – Fluorescence ELISA with MDA-LDL on solid phase and detection by Cy5 fluorescence.
D) – Sandwich ELISA with the addition of MDA-LDL (10μg/mL) and detection via an anti-ApoB antibody.
All ELISAs demonstrate greater nanoparticle reactivity with MDA-LDL using higher TCEP molar excesses for Fab fragment reduction.

Figure 4-25 above displays a panel of 4 nanoparticle functional ELISAs. A-C) are indirect ELISAs with detection via anti-PEG (A), anti-IgG-CH1 (B), Cy5 fluorescence (C); whilst D) is the anti-ApoB sandwich ELISA. All show similar reactivity patterns, with appreciably better

binding when LO1Fab was reduced with higher TCEP concentrations, in a concentration-dependent fashion. Importantly, there was no notable nanoparticle function when LO1Fab was unreduced prior to conjugation, validating the need for TCEP reduction prior to labelling. Indeed, these experiments also justify the use of 10M TCEP, rather than weaker concentrations.

In a follow-on experiment, I then conjugated nanoparticles with reduced or unreduced LO1Fab/ control Fab fragments and ran them on reducing and non-reducing gels, as performed in *Section 4.6 Control Fab production* above, to confirm antibody fragment presence on the nanoparticle constructs. Figure 4-26 below presents these gels.

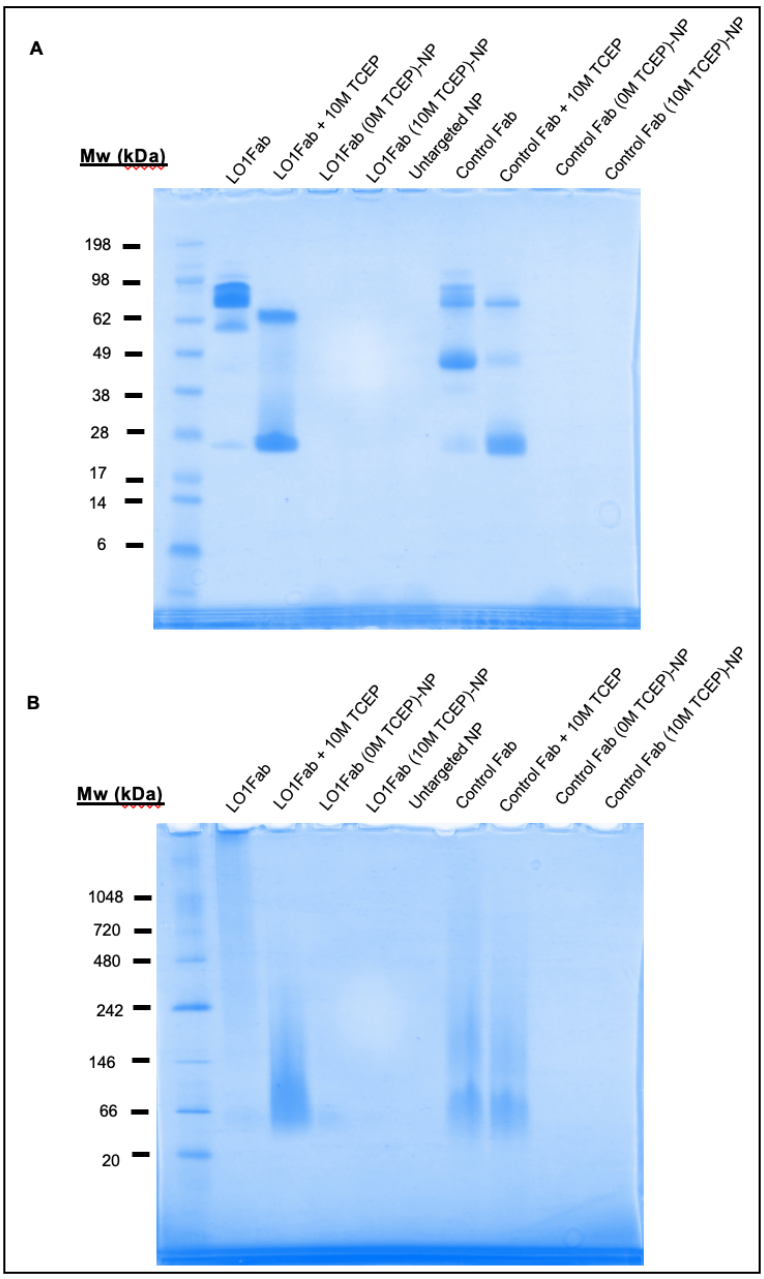

Figure 4-26. Gel electrophoresis of nanoparticle constructs.

4-12% SDS-PAGE Bis-Tris gel (A) and 4-16% Bis-Tris native-PAGE gel (B) with Coomassie staining, again demonstrating effective reduction of LO1Fab with 10M TCEP excess. Control Fab reduction appears highly significant in (A), whilst the TCEP-reduced and unreduced proteins behave similarly under non-reducing conditions. None of the nanoparticle constructs run on either gel, with no free antibody detectable. Again, the lowest molecular weight bands differ by method of gel electrophoresis: ~25kDa under reducing conditions and~50kDa under non-reducing conditions. 10µg of protein/ 1mg of nanoparticle loaded per lane.

The SDS-PAGE gel under reducing conditions again demonstrates oligomerisation of LO1Fab in the stock solution, which degrades with TCEP reduction. Control Fab stock is

predominantly a ~50kDa entity, however with TCEP reduction decreases to ~25kDa. Again, the lowest molecular weight bands differ by method of gel electrophoresis. Notably, and as expected, the nanoparticle constructs do not run on either SDS-PAGE or native-PAGE gels. This is most likely (and simply) due to the large nanoparticle molecular weight; however, nanoparticle gel migration is known to be influenced by a number of complex factors. These include corona architectures, corona and gel charge regulation as well as electrostatic and relaxation effects (321). To confirm that the lack of nanoparticle detection on the Coomassie-stained gels was indeed due to lack of nanoparticle migration, I performed another SDS-PAGE gel under reducing conditions and imaged under a fluorescent scanner (Odyssey CLx Imaging System), displayed in Figure 4-27 below.

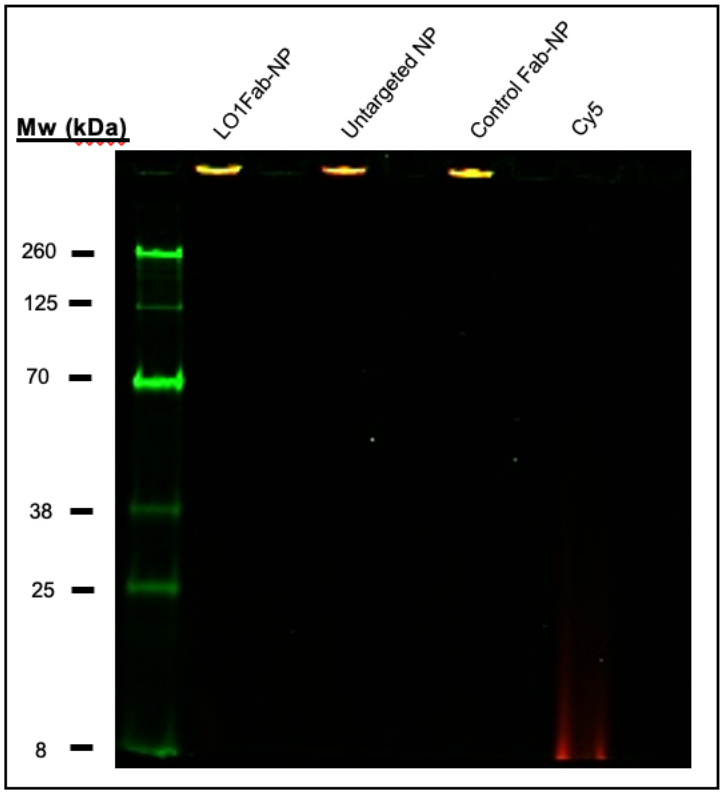

Figure 4-27. Gel electrophoresis with fluorescent imaging of nanoparticle constructs.

A 4-12% SDS-PAGE Bis-Tris gel was run with nanoparticle constructs and free Cy5 dye, and imaged at 700/ 800nm on the LICOR fluorescent scanner. Whilst the free Cy5 has migrated down the gel, none of the

nanoparticle constructs have run, and can be seen at the top of the lane. 5µg of protein/ 1mg of nanoparticle loaded per lane.

This demonstrates that all three Cy5 nanoparticle constructs have not migrated down the gel and have remained in the well. To compare, free Cy5-NHS Ester dye (13020 – Lumiprobe, Hannover, Germany) has successfully run off the gel.

In a final step to verify that there was indeed antibody present on the nanoparticles, I heavily reduced and boiled the antibody-nanoparticle complexes with Laemmli sample buffer and 5µL 2-mercaptoethanol for 10-minutes, in order to fragment the nanoparticle complexes into their constituent components. I then performed gel electrophoresis with these particles as above.

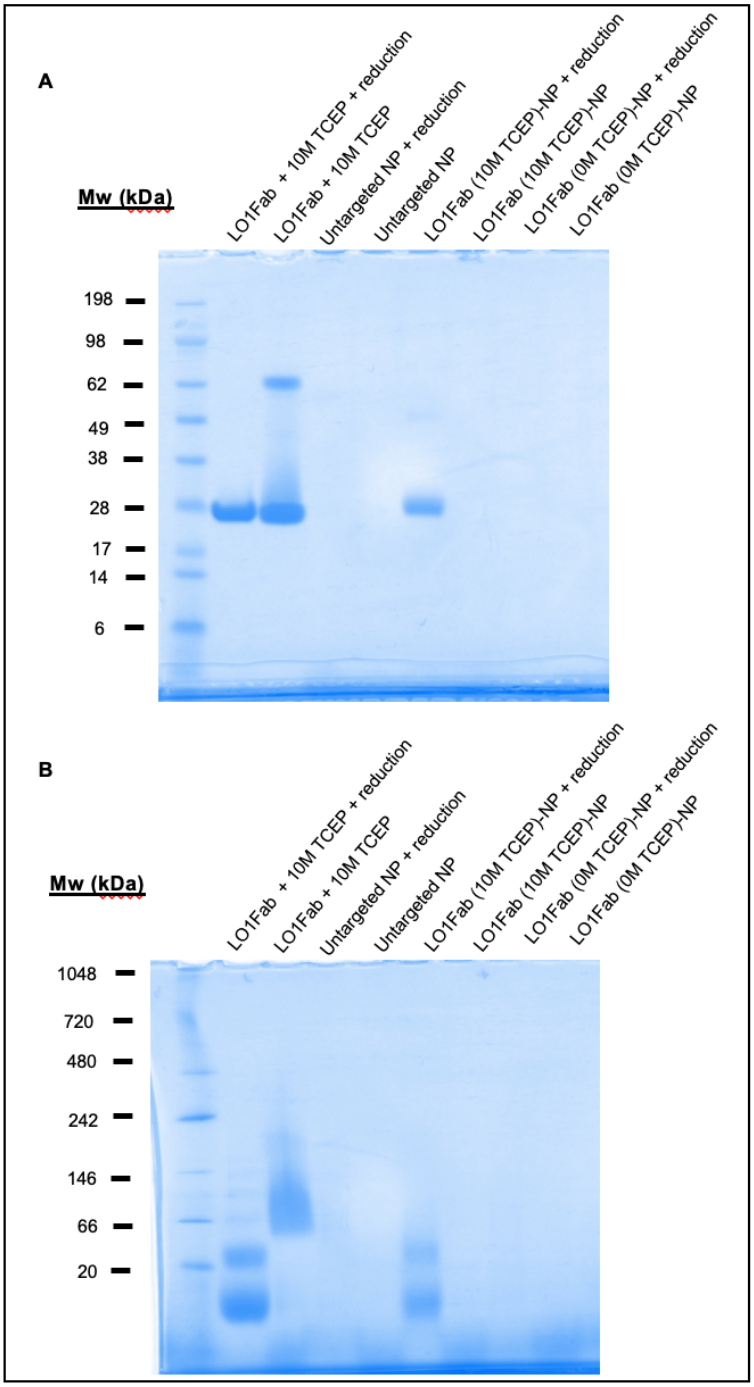

Figure 4-28. Gel electrophoresis of reduced nanoparticle constructs.

Nanoparticle/ Fab constructs were reduced via boiling at 95°C for 10 minutes with Laemelli buffer and BME, prior to gel electrophoresis. The resultant 4-12% SDS-PAGE Bis-Tris (A) and 4-16% Bis-Tris native-PAGE (B) gels with Coomassie staining are displayed. Again, the untargeted nanoparticles or non-reduced LO1Fab-NP do not run in either gel. However, a protein band is now evident in both (A) and (B) with reduced LO1Fab (10M TCEP)-NP. Dissimilarly, no band is seen with the reduced nanoparticles made with unreduced (0M TCEP) LO1Fab. This suggests that the LO1Fab (10M TCEP)-NP have LO1Fab conjugated, whilst LO1Fab (0M TCEP)-NP do not. Interestingly, under non-reducing conditions (B), much greater degradation of LO1Fab is evident following boiling/ reduction than in (A). 10µg of protein/ 1mg of nanoparticle loaded per lane.

Figure 4-28 displays the resultant gels. Boiling and heavily reducing unconjugated LO1Fab led to significant degradation, with the lowest band on the native-PAGE gel now decreasing to <20kDa. Untargeted nanoparticles without conjugated antibody were not detected on either gel. Crucially, a protein band was now detected on both gels after nanoparticle reduction and boiling, proving that Fab has successfully bound to nanoparticle. This band was not present when reduction and boiling was not performed, or when LO1Fab was not reduced with TCEP prior to conjugation. Ideally, I would also have performed these experiments with control Fab, to confirm that it could also effectively bind to the particles; however, this will be proven in subsequent work in following sections.

4.8 LO1 and LO1Fab binding properties

Despite the significant effort developing LO1, and more recently LO1Fab, for binding to oxLDL both in plasma and in tissues, to date, their binding kinetics for their epitope have not been evaluated. It is important to appreciate the strength of the antibody-antigen interaction for the future use of these antibodies as molecular probes themselves, as well as in the selection of which antibodies to serve as the targeting agents for nanoparticle constructs. The most traditional method of evaluating antibody binding affinity and kinetics is Biacore surface plasmon resonance, which has also been successfully utilised for analysing nanoparticle binding (322). However, this technique relies on being able to immobilise the antigen to the surface of a biosensor chip, which has proven very problematic with oxLDL in prior work in the Khamis laboratory, given its very high molecular weight (the ApoB molecule alone is over 550kDa) and that is has a heterogenous structure. As such, microfluidic antibody affinity profiling (MAAP) was explored as an alternative method for evaluating antibody binding. This technique can determine the dissociation constant (K_d), that is the

ligand concentration at which half the ligand binding sites on the protein are occupied at equilibrium, as well as maximum specific binding (B_{max}); both of which are widely utilised parameters of antibody binding.

4.8.1 Microfluidic antibody affinity profiling

MAAP is a novel technique that relies upon microfluidic diffusional sizing technology to measure changes in molecular size (hydrodynamic radius [R_h]) of the antibody as the ligand flows across it within a diffusion chamber. This method can be particularly useful with large complex antigens, such as oxLDL (323). This assay was performed in collaboration with Dr Sean Devenish and 'Fluid Analytics' (Cambridge, UK). For the MAAP assay, the antibodies need to be labelled with a fluorescent tag, so that the antibody, and therefore changes in R_h, can be detected. As such, LO1 and LO1Fab were tagged with AlexaFluor-647 using maleimide labelling chemistry. Table 4-1 below displays the change in the R_h of labelled LO1 and LO1Fab as unlabelled MDA-LDL is incubated, increasing in 1.60nm and 3.06nm respectively, confirming that both LO1 and LO1Fab bind MDA-LDL.

Antibody complex	***R*h (nm)**
LO1-AF647 (10nM)	2.54
LO1-AF647 (10nM) + MDA-LDL (5.46μM)	4.14
LO1Fab-AF647 (10nM)	2.93
LO1Fab-AF647 (10nM) + MDA-LDL (5.46μM)	5.99

Table 4-1. Fluorescently labelled LO1 and LO1Fab bind MDA-LDL using microfluidic diffusional sizing technology.

LO1 and LO1Fab were labelled with AlexaFluor-647 (AF647), prior to mixing with MDA-LDL and assayed using microfluidic diffusional sizing. The hydrodynamic radius (R_h) measurement confirmed that both labelled LO1

and LO1Fab underwent a respective size shift of 1.60nm and 3.06nm when incubated with MDA-LDL particles, confirming that both protein species were able to bind to the MDA-LDL particles. Performed in duplicate.

Next, the MAAP assay was performed for LO1 and LO1Fab versus MDA-LDL, and the binding curves are displayed in Figure 4-29 below.

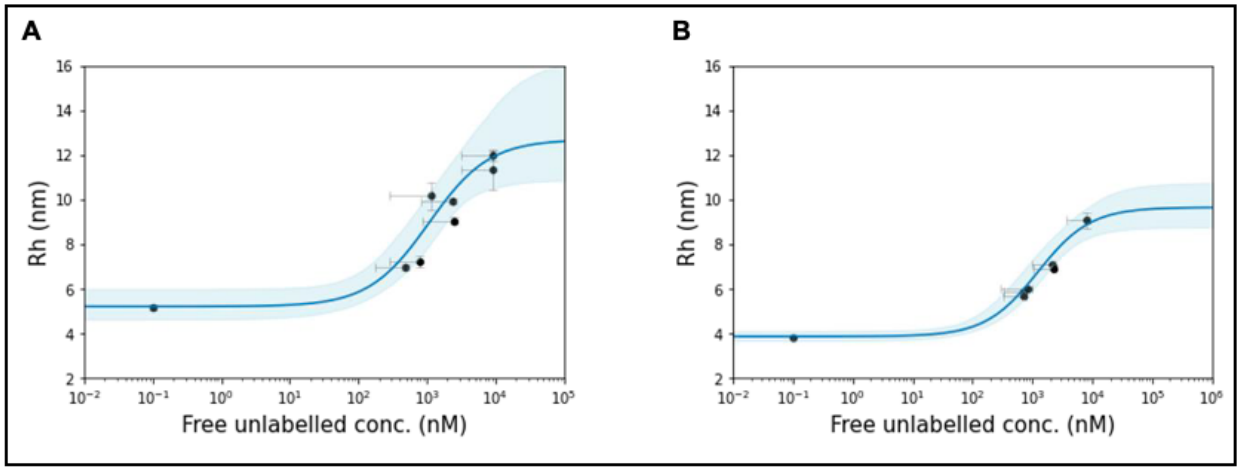

Figure 4-29. Binding curves for the interaction of MDA-LDL with LO1 and LO1Fab using microfluidic antibody affinity profiling.

LO1 (A) or LO1Fab (B) were assayed using microfluidic antibody affinity profiling at 4°C for 30-minutes at a size-range setting of 1.5 – 8nm to evaluate binding kinetics with MDA-LDL.
Performed in duplicate. 95% CI regions are indicated by the shaded areas. Performed in collaboration with 'Fluidic Analytics' using the 'Fluidity One-M'.

The MAAP assay results from Figure 4-29 can then be computed using Bayesian analysis (performed in collaboration with 'Fluid Analytics') to provide a K_d for LO1/ LO1Fab as well as the concentration of binding sites on MDA-LDL. There was a maximal MDA-LDL binding site concentration of ~9-10μM for both LO1 and LO1Fab, representing good assay consistency, whilst also suggesting that the antibodies are indeed binding to the same epitope. The K_d of LO1 with MDA-LDL was 546 (95% CI, 147-1214) nM, whilst LO1Fab was slightly less reactive at 678 (95%CI, 337-1104) nM; both of which are within the nanomolar range and would be

generally considered to represent high affinity protein-protein interactions. The Bayesian analysis can also generate molecular weight estimates of the antibody-ligand complex, based on the R_h. The LO1-MDA-LDL complex was 3.45 (95% CI, 2.20-7.60) MDa, whilst LO1Fab was 1.51 (95%CI, 1.10-2.10) MDa, which correspond to published values (324).

Parameter	Bayesian	95% Confidence Interval
	LO1	
K_d (nM)	546	147 – 1214
Binding sites (μM)	9.99	4.25 – 9.99
	LO1Fab	
K_d (nM)	678	337 – 1104
Binding sites (μM)	8.97	4.66 – 9.99

Table 4-2. Summary of microfluidic antibody affinity profiling assay results for LO1 and LO1Fab.

The predicted K_d for the interaction of both the LO1 IgG and Fab fragments with MDA-LDL were similar at approximately 500nM (546nM for LO1, 678nM for LO1Fab). Similarly, the calculated concentrations of binding sites present in MDA-LDL were consistent between the two experiments, at 9-10 μM. All values obtained by Bayesian analysis. Performed in duplicate. Performed in collaboration with 'Fluidic Analytics' using the 'Fluidity One-M'.

4.8.2 Immunohistochemistry

The MAAP assays provided an assessment of antibody binding kinetics in fluid phase, however it also remains important to evaluate the ability of LO1 and LO1Fab to access their MDA-LDL epitope in tissue, particularly human tissue, for clinical translation. To this end, I collaborated with Prof Jason Johnson (Bristol University, UK) who has access to human coronary artery atherosclerotic plaque sections from the Bristol Coronary BioBank. Accordingly, I performed immunohistochemistry with the antibodies on these tissue samples,

incubating with polyclonal goat anti-mouse and anti-IgG-CH1 antibodies for LO1 and LO1Fab respectively (see *Section 2.3.6.4.1 LO1 and LO1Fab immunohistochemistry in human atherosclerosis*). Adjacent slides had already been stained with mouse anti-human CD68 in prior work in the Johnson Laboratory, to allow co-localisation to tissue macrophages.

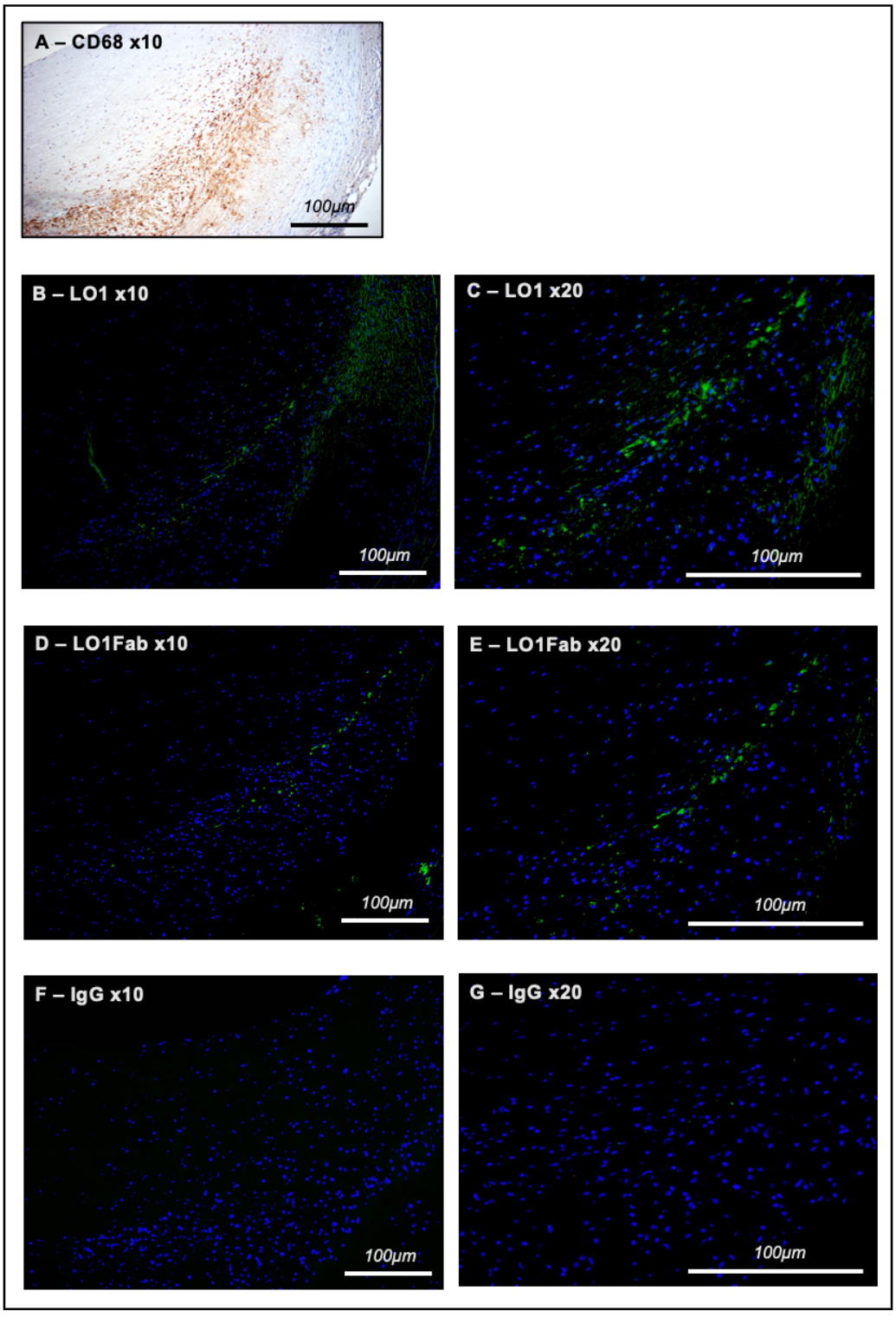

Figure 4-30. Immunohistochemistry with LO1 and LO1Fab on stable human coronary artery atherosclerotic plaques.

Adjacent 5µm sections were stained with CD68 (A), LO1 (B,C), LO1Fab (D,E) or IgG control (F,G) and imaged under white light (A) or DAPI/ 488 channels (B-G). (A, B, D, F) all 10x, (C, E, G) all 20x magnification. Scale bar is 100µm for all panels. Human coronary stable atherosclerotic plaque slides from the Bristol Coronary BioBank were used. Performed in collaboration with Prof Jason Johnson, Bristol University.

Figure 4-30 above displays adjacent stained slides of a fatty atherosclerotic plaque, with the vessel lumen in the top-left corner and adventitia in the bottom-right corner. There is dense brown CD68 macrophage staining in the middle of the plaque, which corresponds to green signal in both the LO1 and LO1Fab stained slides, that is not present in the control IgG slide. Thus, both antibodies are binding to their antigen within human atherosclerotic plaque, which appears to almost identically located, and as expected, in the vicinity of macrophages (325).

4.9 Nanoparticle in vitro characterisation

The previous sections have detailed the design, generation, and early *in vitro* functional assessment of LO1Fab- and control Fab-conjugated nanoparticles, as well as providing further exploration of LO1 and LO1Fab binding properties. However, further *in vitro* characterisation, proof of nanoparticle function and construct stability is needed prior to progression to *in vivo* study.

4.9.1 Physical nanoparticle properties

Although I have produced control Fab-nanoparticles in earlier sections in this chapter, I had made an assumption that control Fab had indeed effectively conjugated to the nanoparticle surface, using the same conditions and concentrations as with LO1Fab. As discussed, it is important for future *in vivo* study that the control nanoparticle construct is as genuine a control as possible (and therefore has a conjugated antibody fragment attached), to remove the possibility of non-specific binding related to the presence of an antibody fragment.

Thus, the first experiments in this section were to demonstrate successful control Fab nanoparticle binding.

4.9.1.1 ELISA

I performed a sandwich ELISA with Fab fragments or Fab-conjugated nanoparticles on solid phase, which, following blocking and washing, underwent detection using an anti-IgG-CH1 antibody, without the addition of an antigen. As both are treated under the same conditions and reagents, it should be possible to provide an approximation of protein concentration. The potential drawbacks of this method are that it cannot be assumed that Fab fragments and nanoparticles will adhere equally to the ELISA plate, as well as the possibility that there may be artificial signal amplification or reduction depending on the orientation of ligand-receptor binding and number of Fab fragments on each nanoparticle.

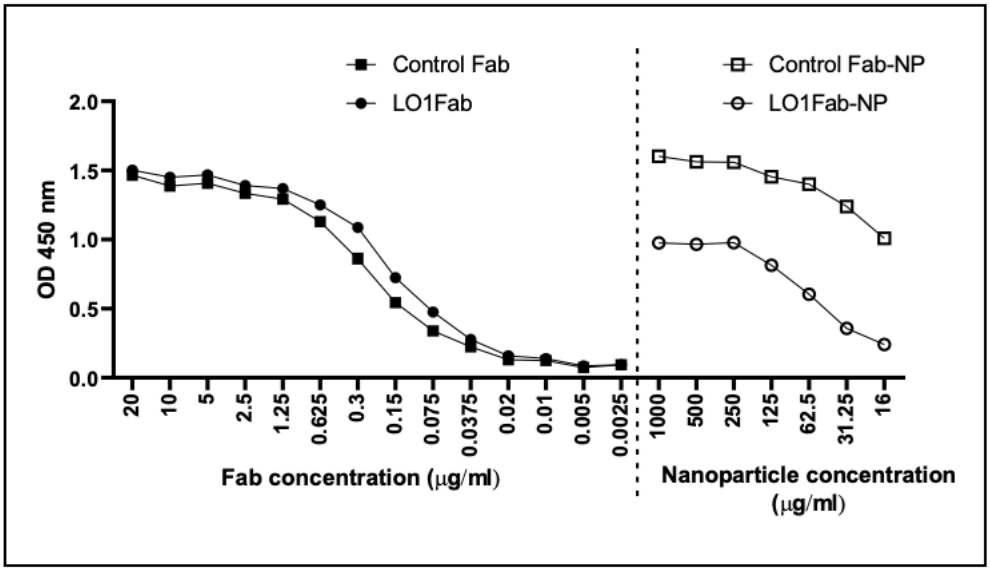

Figure 4-31. Confirmation of Fab presence on both LO1Fab and control Fab conjugated nanoparticles.

Nanoparticles or Fab fragments were coated on the same ELISA plate in dilution series. After blocking with 3% BSA, anti-IgG-CH1 was used to detect the presence of the bound Fab fragments directly (left panel), or nanoparticles via the conjugated Fab fragments (right panel). From this figure, an approximate estimation of the conjugated Fab concentration can be made. Performed in duplicate. Error bars represent SEM.

Figure 4-31 demonstrates that all four constructs plateaued and achieved receptor saturation. The control Fab-nanoparticle appeared to plateau at a higher OD than control Fab itself, whilst LO1Fab plateaued at lower OD than LO1Fab itself, perhaps due to experimental artefact as considered above. However, most importantly, the anti-IgG-CH1 bound to the control Fab nanoparticle construct, confirming Fab presence.

4.9.1.2 Dynamic Light Scattering analysis

DLS provides an important initial assessment of nanoparticle physical properties. Moreover, any change in construct size or dispersity detected by DLS after antibody incubation can be assumed to be due to successful conjugation. Accordingly, Table 4-3 below demonstrates an increase in size, within acceptable size limits, from the untargeted construct to both LO1Fab- and control Fab-nanoparticles.

Nanoparticle	Size (mean ± SD; nm)	PDI (mean ± SD)
Untargeted Nanoparticle	214.73 ± 0.26	0.08 ± 0.06
LO1Fab-Nanoparticle	217.83 ± 1.13	0.05 ± 0.03
Control Fab-Nanoparticle	218.34 ± 1.96	0.02 ± 0.02

Table 4-3. Average size and polydispersity index of nanoparticle constructs by Dynamic Light Scattering analysis.

Size and poydispersity index (PDI) expressed as mean ± standard deviation.

4.9.1.3 Nanoparticle tracking analysis

Another method of evaluating nanoparticle physical properties is nanoparticle tracking analysis, which visualises particles in suspension as they move under Brownian motion, generating size distribution and concentration readouts. The outputs for the three constructs are shown below in Figure 4-32 and Table 4-4.

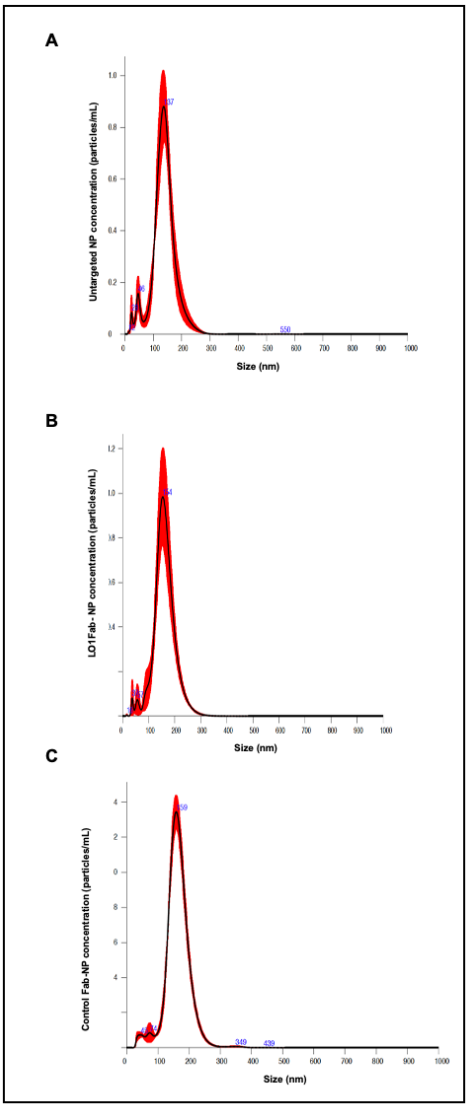

Figure 4-32. Nanoparticle construct size assessed by nanoparticle tracking analysis.

A) – Untargeted NP
B) – LO1Fab-NP
C) – Control Fab-NP
Shaded area represents SEM.

As can be seen, all constructs have relatively tight distributions around the average particle size. There is a difference in particle size versus those obtained using the DLS analysis, albeit with much larger standard deviations, which could be due to a difference in freshness of nanoparticle construct, degree of particle aggregation or methodological variations, which have been reported previously (326). Nonetheless, there is a clear increase in particle size following antibody conjugation, but again still within acceptable nanoparticle size parameters. Nanoparticle concentration is also provided, which although is somewhat contrived, will allow an approximation of number of Fab (in mass or moles) per each individual nanoparticle, detailed below in Table 4-4.

Nanoparticle	**Size (mean ± SD; nm)**	**Particle concentration in 10µg of particles per mL (mean ± SEM; particles/mL)**
Untargeted Nanoparticle	137.0 ± 41.1	$6.44\times10^{8} \pm 4.23\times10^{7}$
LO1Fab-Nanoparticle	159.7 ± 40.7	$7.76\times10^{8} \pm 1.64\times10^{8}$
Control Fab-Nanoparticle	162.7 ± 39.6	$9.72\times10^{8} \pm 3.52\times10^{7}$

Table 4-4. Average size and concentration of nanoparticle constructs by nanoparticle tracking analysis. *Expressed mean ± SD or mean ± SEM.*

4.9.1.4 Antibody conjugation estimations

After establishing that Fab fragments are conjugated on both nanoparticle constructs, I next wanted to quantify the amount of Fab that was present, to enable simple calculations for binding affinity and comparisons with the unconjugated antibodies. One method of achieving

this is through a modified microBCA assay (as performed in *Section 4.5.2 Antibody fragment conjugation efficiency*), displayed in Table 4-5.

Nanoparticle	Conjugation (µg/mg)	Conjugation efficiency (%)
Untargeted Nanoparticle	N/A	N/A
LO1Fab-Nanoparticle	4.01	31.9
Control Fab-Nanoparticle	1.20	9.6

Table 4-5. Antibody fragment conjugation and conjugation efficiency of nanoparticle constructs.

Similar to the earlier results, there is ~4µg of LO1Fab per 1mg of nanoparticle, with a conjugation efficiency of 31.9%; whilst there is ~1.2µg of control Fab per 1mg of nanoparticle, with a conjugation efficiency of 9.6%. It would be ideal to have a similar mass of Fab on both constructs, to ensure equivalence. Identification of the optimal conjugation conditions for control Fab could be carried out in future work, as performed earlier in this chapter with LO1Fab.

Nonetheless, utilising these masses and nanoparticle ratios enables the estimation of Fab per individual nanoparticle. An example of these calculations for LO1Fab-nanoparticle is shown below in Figure 4-33.

$LO1FabNP\ is\ at\ a\ concentration\ of\ 7.8\times10^{8}\ NPmL^{-1}$
$(10\mu g\ of\ NPmL^{-1})\ from\ Nanoparticle\ Tracking\ Analysis$

$There\ are\ 4\mu g\ LO1Fab\ per\ 1mg\ of\ NP\ from\ microBCA\ assay$
$\Longrightarrow 4\mu g\ LO1Fab\ \rightarrow\ 1mg\ NP$
$\Longrightarrow 0.04\mu g \rightarrow 10\mu g\ NP$
$\Longrightarrow\ 0.04\mu gFab\ in\ 7.8x10^{8}\ NP$

$\Longrightarrow {}^{0.04}/_{7.8\times10^{8}}\ gives\ amount\ of\ Fab\ (\mu g)\ per\ each\ NP$

$= 5.195\times10^{-11}\mu g\ per\ each\ NP$

$= 0.05195fg\ per\ each\ NP\ or\ 1.082\times10^{-21}\ moles\ per\ each\ NP$

Figure 4-33. Example calculations for the estimation of amount of Fab per each nanoparticle in the LO1Fab-nanoparticle construct.

NP, nanoparticle.

4.9.2 Nanoparticle MDA-LDL recognition on ELISA

4.9.2.1 Indirect ELISAs

Having ascertained that Fab fragments are present on both nanoparticles, I then wanted to finally compare all three constructs (LO1Fab, control Fab and untargeted nanoparticles) on ELISA, shown below in Figure 4-34.

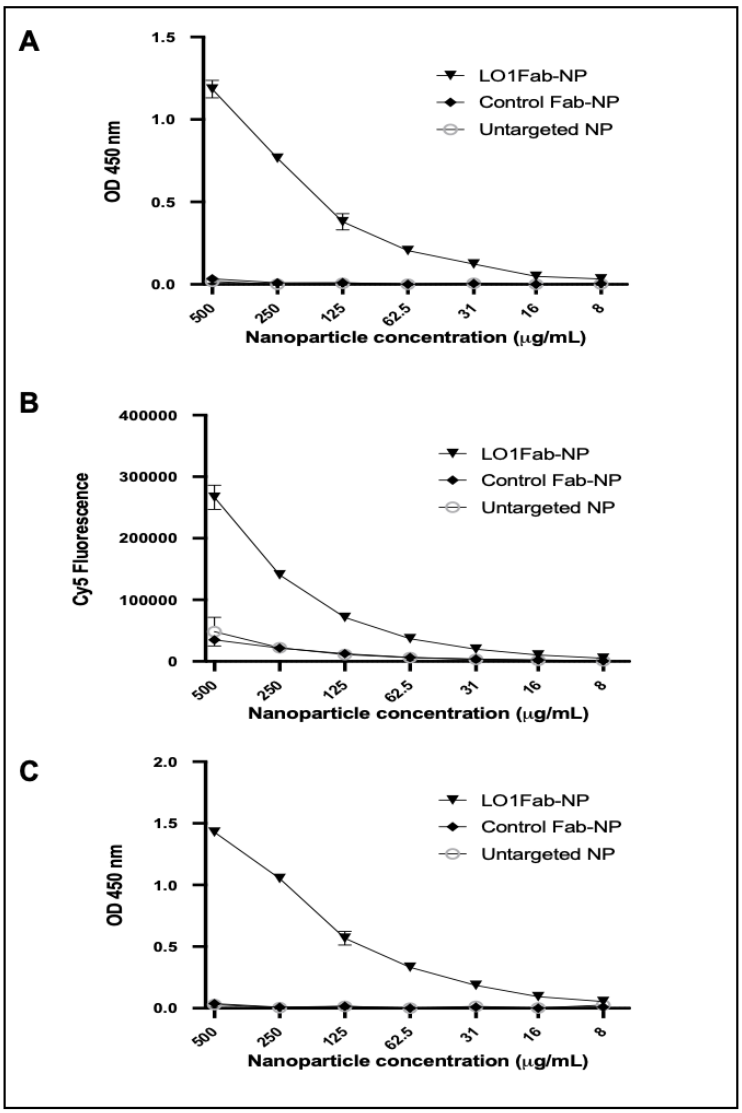

Figure 4-34. Nanoparticle function on ELISA.

MDA-LDL (10μg/mL) was coated on ELISA plates overnight and was blocked with 3% BSA prior to nanoparticles in dilution series. Detection was then performed using an anti-PEG secondary (A), Cy5 fluorescence (B) and anti-IgG-CH1 (C). All performed in duplicate. Error bars represent SEM.

Reassuringly, there was consistent LO1Fab-nanoparticle function on all three indirect ELISAs, with very little binding of both control constructs.

4.9.2.2 Competitive ELISAs

I next wanted to verify if the nanoparticles could compete with the unconjugated antibodies for their shared epitope in ELISA format.

4.9.2.2.1 Versus LO1

Figure 4-35 below displays three competitive ELISAs with different designs, each showing successful and statistically significant abrogation of LO1 binding (Rhodamine 6G fluorescence on fluorescence ELISA) by LO1Fab-nanoparticles, and vice versa, with MDA-LDL on solid phase. In A) LO1Fab-nanoparticles and LO1 were co-incubated for 2-hours; in B) LO1 was incubated for 1-hour prior to LO1Fab-nanoparticle incubation for 2-hours; and finally in C) LO1Fab-nanoparticles were pre-incubated with MDA-LDL for 1-hour, prior to adding to the ELISA plate for 2-hours. A) represents a traditional competitive ELISA, showing significant loss of nanoparticle binding in an LO1 concentration-dependent manner ($p<0.0001$). In B), pre-incubation of the MDA-LDL coated ELISA wells with LO1 prior to the addition of nanoparticles led to loss of signal ($p=0.0210$), suggesting that LO1 has occupied MDA-LDL epitopes and therefore there are fewer available binding sites for the targeted nanoparticle. In C), pre-incubating LO1Fab-nanoparticles with MDA-LDL significantly inhibited LO1Fab-nanoparticle binding to the solid phase MDA-LDL ($p=0.0013$), due to occupation of the Fab antigen binding sites by the MDA-LDL in fluid phase.

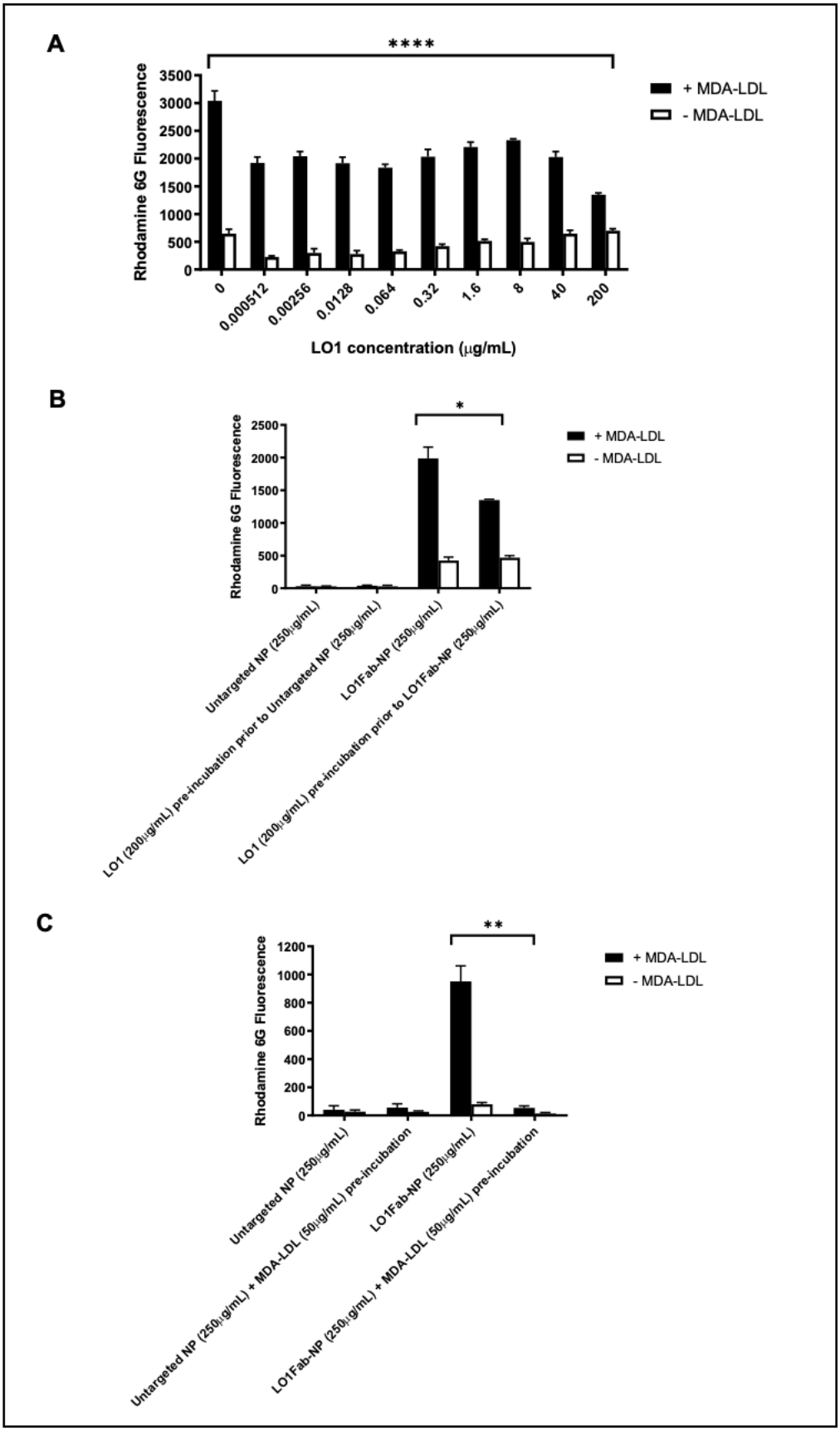

Figure 4-35. LO1Fab-NP competes with LO1 for MDA-LDL binding.

*A) – MDAL-LDL (10µg/mL) or PBS were added on solid phase overnight. After blocking with 3% BSA, a mixture of LO1Fab-NP at a fixed concentration of 250µg/mL and LO1 in dilution series was incubated for 2-hours. Read-out was Rhodamine 6G fluorescence intensity. There is a clear reduction in nanoparticle binding to MDA-LDL with increasing LO1 concentrations (****p<0.0001). One-way ANOVA used to assess statistical significance.*
*B) – MDAL-LDL (10µg/mL) or PBS were added on solid phase overnight. After blocking with 3% BSA, the wells were incubated with LO1 (200µg/mL) or PBS for 1-hour, followed by nanoparticles (250µg/mL) for 2-hours. There was a significant difference in nanoparticle fluorescent signal versus MDA-LDL with and without LO1 preincubation (*p=0.0210). Unpaired t-test used to assess statistical significance.*
*C) – MDAL-LDL (10µg/mL) or PBS were added on solid phase overnight followed by blocking with 3% BSA. Nanoparticles (250µg/mL) were preincubated with or without MDA-LDL (50µg/mL) for 1-hour, prior to plating for 2-hours. There was a significant difference in nanoparticle fluorescent signal versus MDA-LDL with and without MDA-LDL preincubation (**p=0.0013). Unpaired t-test used to assess statistical significance.*
All performed in triplicate. Error bars represent SEM.

4.9.2.2.2 Versus LO1Fab

Figure 4-36 below presents an ELISA with MDA-LDL on solid phase, in which, after washing and blocking, wells were incubated with LO1Fab for 1-hour, prior to LO1Fab-nanoparticles for a further hour. Following washing, nanoparticle presence was evaluated with the anti-PEG antibody. There is an LO1Fab concentration-dependent inhibition of nanoparticle binding, which, unsurprisingly, is more evident at the lower nanoparticle concentration.

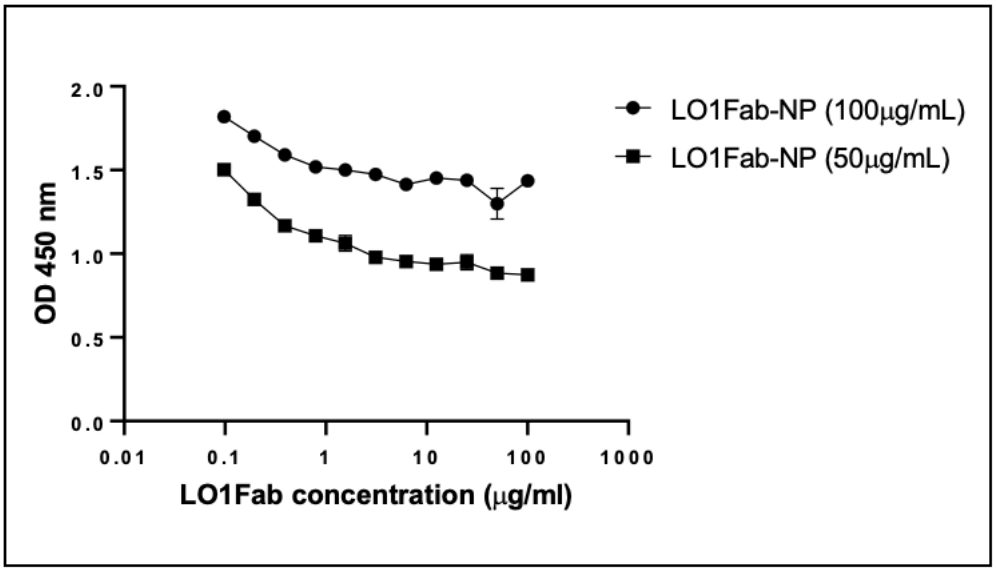

Figure 4-36. LO1Fab-NP competes with LO1Fab for MDA-LDL binding.

Wells were coated overnight with MDA-LDL (5µg/mL) prior to blocking with 2% BSA and then the addition of LO1Fab in dilution series for 1-hour. Following this, LO1Fab-NP were added at a concentration of either 50 or 100µg/mL for 1 further hour. Nanoparticle binding was then evaluated using the anti-PEG antibody. There is competition between LO1Fab and LO1Fab-NP for MDA-LDL on solid phase, suggesting a shared antigen. Performed in duplicate. Error bars represent SEM.

Consequently, both LO1 and LO1Fab are indeed able to compete with LO1Fab-nanoparticles, confirming that they bind the same epitope.

4.9.3 Varying antigenic loads

In further efforts to determine that the targeted nanoparticles are binding to the LO1 epitope on MDA-LDL, rather than another component of the LDL particle, I compared binding versus native, unmodified LDL, as well as MDA-LDL that had been oxidised for different periods of time.

4.9.3.1 Binding to MDA-LDL rather than native LDL

I performed the three indirect ELISAs, with plates coated with nLDL or MDA-LDL, as well as the ApoB sandwich ELISA, comparing LO1Fab- and control Fab-nanoparticles, shown in Figure 4-37 below.

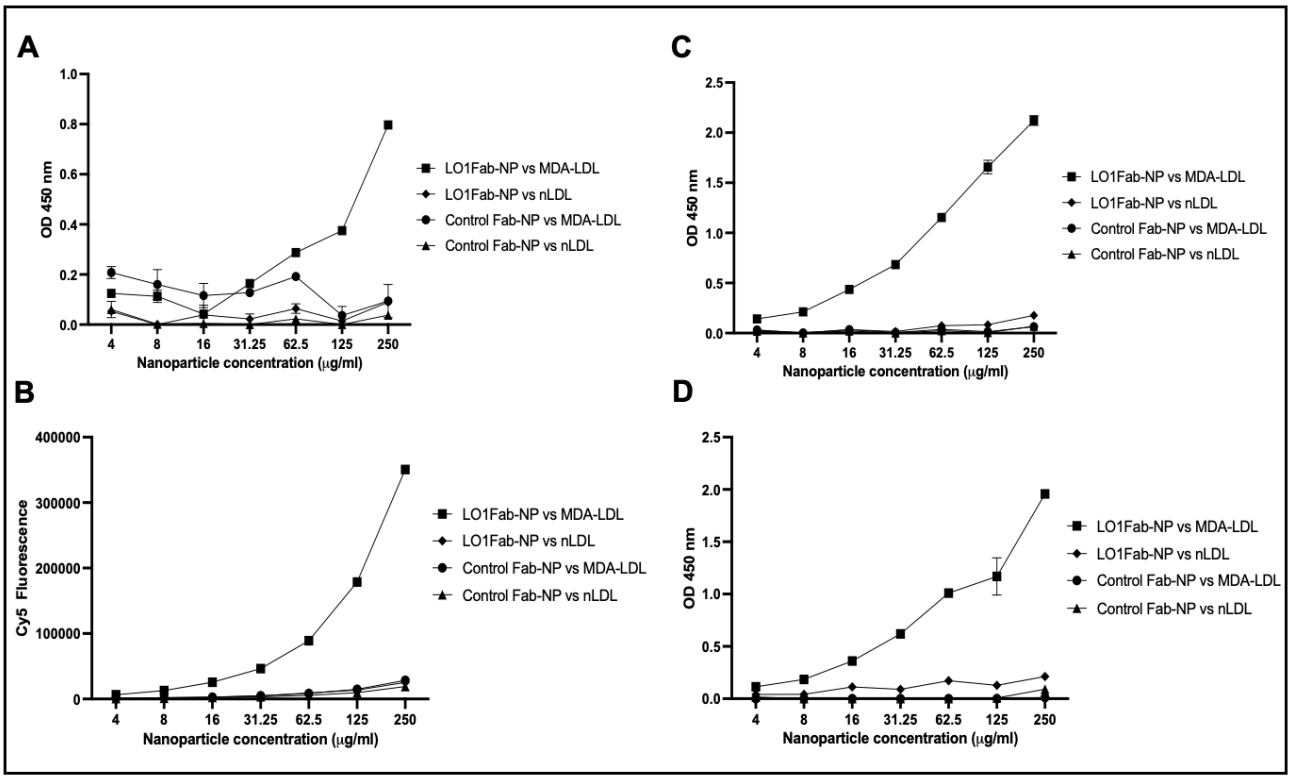

Figure 4-37. Nanoparticle binding to MDA-modified LDL but not native LDL on ELISA.

(A/B/C) – MDA-LDL (10μg/mL) or native LDL (10μg/mL) were coated overnight, prior to blocking with 3% BSA and then LO1Fab or control Fab conjugated nanoparticles were added in dilution series. Detection was using an anti-PEG secondary (A), Cy5 fluorescence (B) and anti-IgG-CH1 (C).
(D) – Sandwich ELISA with nanoparticle constructs coated in dilution series overnight, prior to blocking with 3% BSA and then the addition of MDA-LDL or native LDL (both at 10μg/mL). Detection was using a biotinylated anti-ApoB antibody.
All performed in duplicate. Error bars represent SEM.

Encouragingly, LO1Fab-nanoparticles only bound to MDA-LDL and not unmodified LDL; whilst control Fab-nanoparticles did not bind either.

4.9.3.2 Binding to differentially modified MDA-LDL

In a final step, I prepared MDA-LDL with varying MDA incubation durations, to demonstrate that with shorter MDA incubation durations (with presumably less LDL modification and therefore less LO1Fab epitope), there was reduced nanoparticle binding on ELISA.

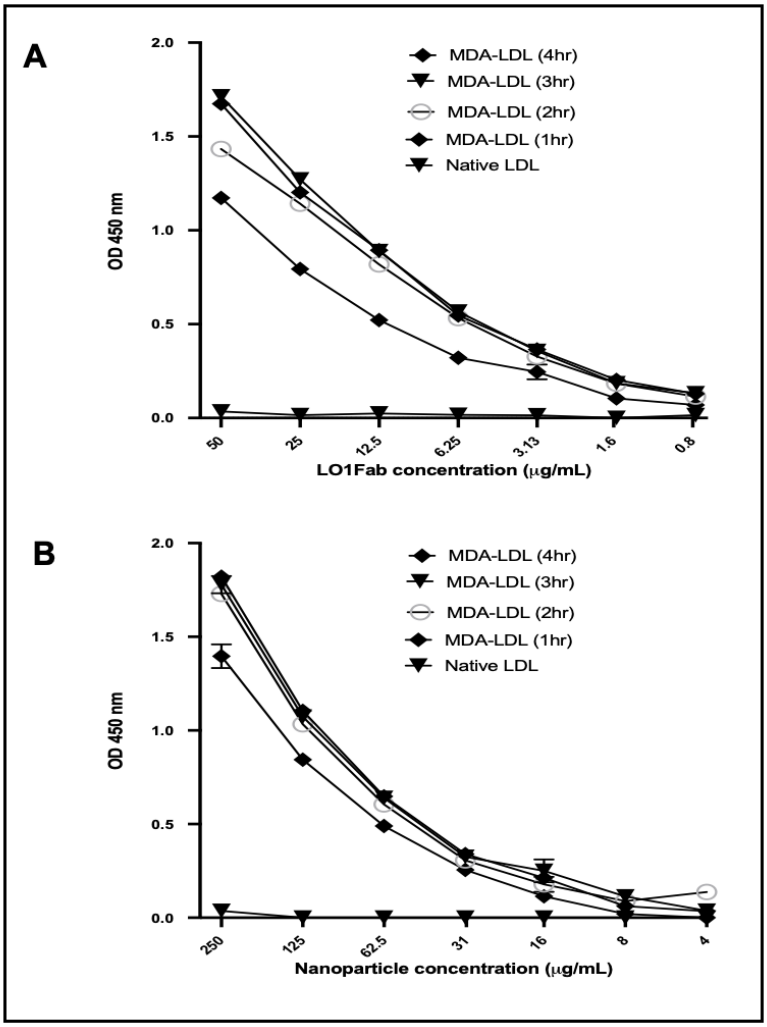

Figure 4-38. Preservation of nanoparticle binding to MDA-modified epitopes on MDA-LDL.

LDL was incubated for different durations with MDA to form differentially modified MDA-LDL. MDA-LDL or native LDL (10μg/mL) was then coated overnight, prior to blocking with 3% BSA and then LO1Fab (A) or LO1Fab-NP (B) in dilution series. Detection was with anti-IgG-CH1 for LO1Fab and anti-PEG for LO1Fab-NP. Similar binding patterns are observed for both constructs, with more signal with greater MDA-modification of LDL. Performed in duplicate. Error bars represent SEM.

In Figure 4-38 above, LO1Fab (A) and LO1Fab-nanoparticle (B) binding was compared, with differently modified MDA-LDL on solid phase. Detection was performed using anti-IgG-CH1 for LO1Fab and anti-PEG for the LO1Fab-nanoparticles. Similar binding patterns are observed between both constructs, with a modification duration-dependent increase in signal, most notably at the lower MDA modification periods. It may be that during the MDA-LDL

production, any additional modification beyond 2-hours renders little extra epitope (3-hour incubation is the standard protocol duration), as both constructs have almost overlapped curves for the 2-, 3- and 4-hour timepoints.

4.9.4 Nanoparticle stability

It is important to gain an appreciation of construct stability, particularly with episodes of freezing and thawing when transferring reagents between research and *in vivo* labs, as well being a key consideration further down the translational pipeline, where manufacture, storage and shipping become relevant. Accordingly, I subjected LO1Fab and LO1Fab-nanoparticles to up to 4 freeze-thaw cycles from -20°C to room temperature, and then assessed their function on indirect ELISA with MDA-LDL on solid phase, using anti-IgG-CH1 or anti-PEG for detection, as appropriate. Nanoparticles were freshly sonicated prior to ELISA plating.

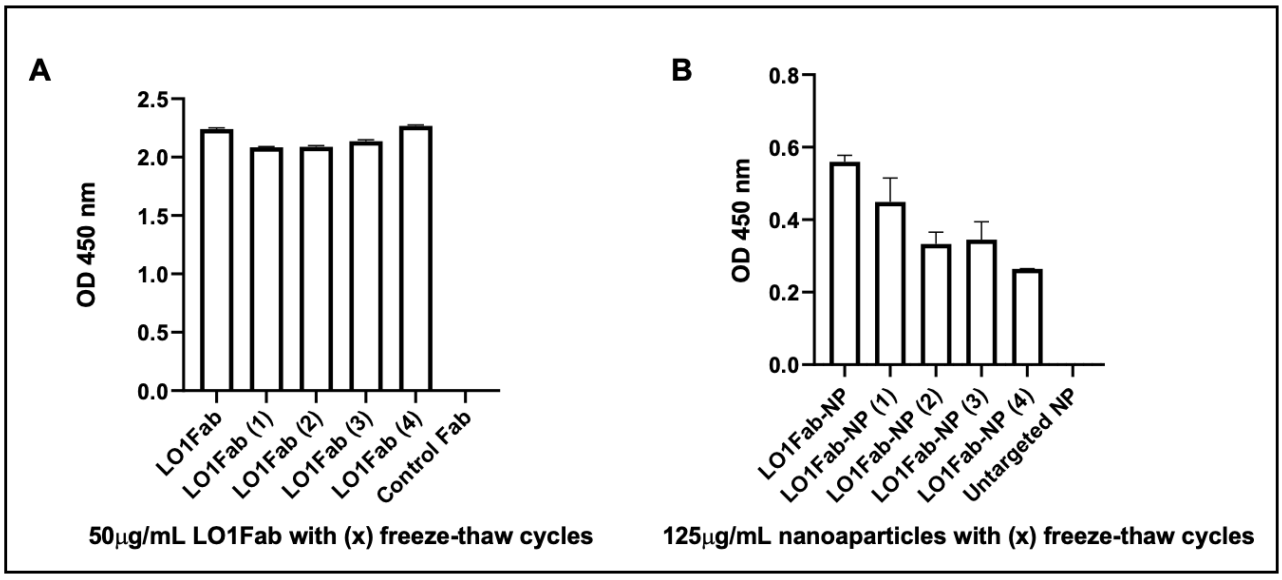

Figure 4-39. LO1Fab but not pre-conjugated LO1Fab-NP is resistant to freeze-thaw cycles.

LO1Fab (A) and LO1Fab-NP (B) were subjected to up to 4 freeze-thaw cycles from -20°C to room temperature. ELISA plates were coated with MDA-LDL (10μg/mL) prior to blocking with 3% BSA and the constructs, with fresh construct (positive control) and control constructs (negative control). Detection was with either anti-IgG-CH1 (A) or anti-PEG (B). Nanoparticles were freshly sonicated prior to plating. There was no loss of signal

across freeze-thaw cycles with LO1Fab, whereas there was significant loss of binding with repeated freeze-thaw cycles with LO1Fab-NP. (A) performed in triplicate, B performed in duplicate. Error bars represent SEM.

In Figure 4-39 it is evident that LO1Fab does not lose reactivity with repeated freeze-thaw episodes, unlike LO1Fab-nanoparticle, which loses function with each cycle. It is likely that each freeze-thaw cycle breaks more antibody-nanoparticle covalent bonds, denuding the nanoparticle and rendering it effectively untargeted. Going forwards, it will be important to note that the nanoparticles cannot be frozen post-conjugation, whereas LO1Fab fragment itself is relatively stable.

4.9.5 Fluorescence Microscopy

Next, I wanted to assess whether LO1Fab-nanoparticles could access their antigen within atherosclerotic tissue using immunohistochemistry/ fluorescence microscopy, having successfully demonstrated nanoparticle binding to an MDA-modified epitope on LDL in various ELISA formats. In particular, it was important to use murine tissue, given that this was the planned *in vivo* model, and I needed to ensure that the nanoparticle could bind in this species. As such, I generated tissue sections from LDL-$R^{-/-}$ mice fed a high-fat diet for 30-weeks (*Section 2.3.8.2 Murine model of atherosclerosis*), which were sacrificed via CO_2 inhalation and whole-body perfusion performed via infusion of formalin-saline via the left ventricle after incision of the right atrium (*Section 2.3.8.5 Mouse whole-body perfusion and aortic root sectioning*). After harvesting the heart and aortic root, the tissue was embedded in optimal cutting temperature embedding medium and frozen on dry ice. 5µm cryosections were then made, ensuring to transect the aortic root in short axis. Every 20^{th} slide was stained

with Oil Red O to confirm the presence of lipid deposits and counter-stained using haematoxylin.

4.9.5.1 LO1Fab

First, I wanted to ensure that LO1Fab could detect MDA-LDL within murine tissue, having shown that it could bind in human tissue (*Section 4.8 LO1 and LO1Fab binding properties*). Slides were blocked with avidin/ biotin prior to antibody incubation in a humidity chamber at 4ºC overnight. The next day, after washing, the secondary antibody anti-IgG-CH1 was incubated for 1-hour, followed by signal generation with Streptavidin-AlexaFluor-647. 5µm adjacent slides were stained with LO1Fab and control Fab to allow comparison. An adjacent slide was also stained with Oil Red O to allow signal localisation to fatty deposits. Figure 4-40 was produced after performing confocal microscopy at appropriate fluorescence channels for the antibody fragments, and widefield microscopy for Oil Red O.

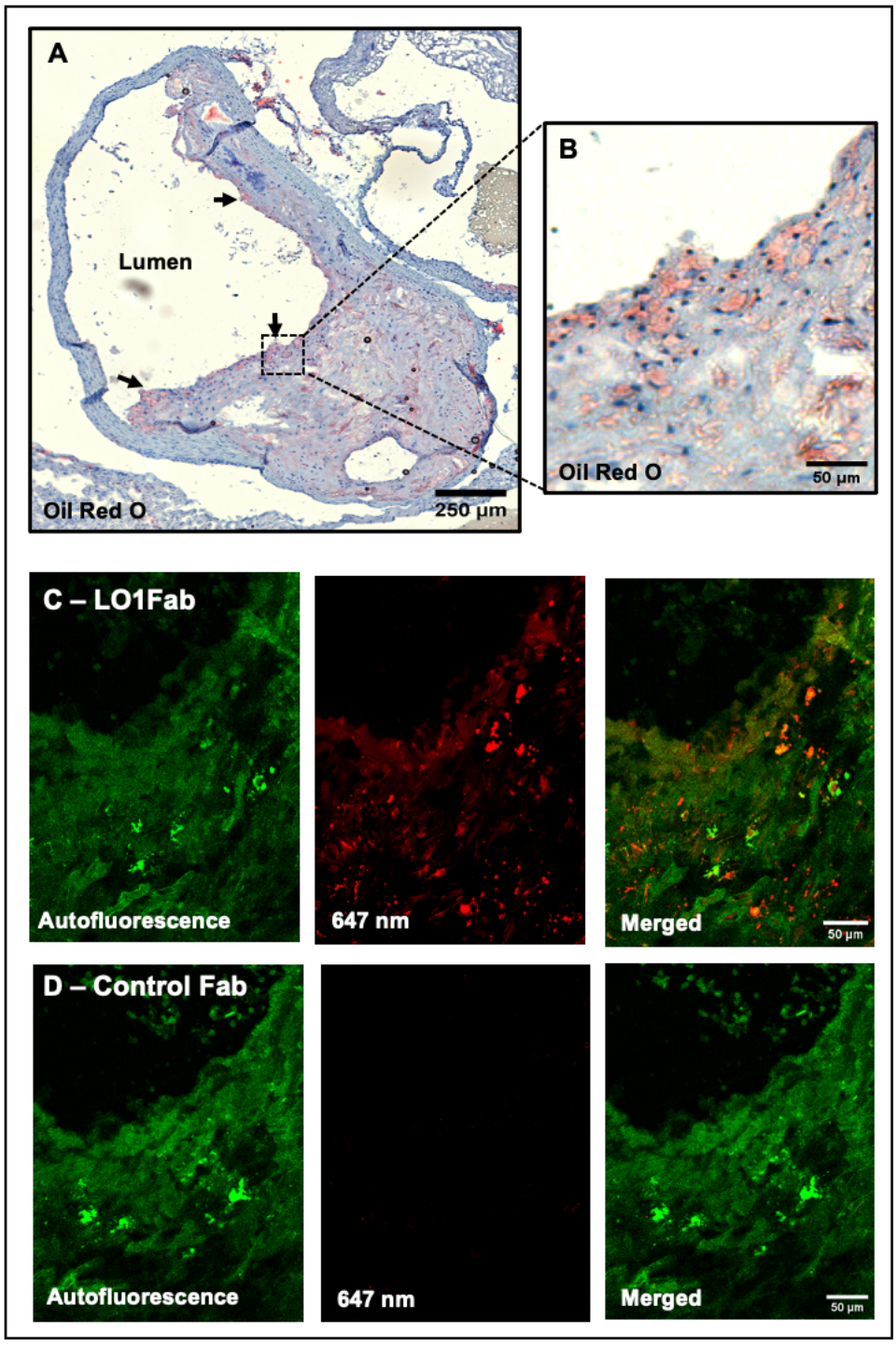

Figure 4-40. Immunohistochemistry with LO1Fab and control Fab in murine aortic root atherosclerosis (20x magnification).

An LDL-receptor deficient mouse fed a high-fat diet for 30 weeks was sacrificed via CO_2 inhalation and whole-body organ perfusion fixation carried out. The heart and aortic root were cryosectioned and 5µm adjacent sections were mounted on slides and stained with Oil Red O or antibodies.
(A) – the Oil Red O-stained slide was imaged using widefield microscopy (10x), demonstrating significant lipidic deposits in the aortic root. Scale bar = 250µm.

(B) – is an inset from A) at 20x magnification, showing an area of significant Oil Red O staining. Scale bar = 50µm.
(C,D) – 20x magnification of the section shown in (B), imaged using fluorescence confocal microscopy at autofluorescence (488nm, first panel)/ AlexaFluor-647 (647nm, second panel) channels and merged (third panel). (C – LO1Fab; D – Control Fab). Scale bar = 50µm.

There is a very large atherosclerotic plaque in this aortic root section, which heavily stains with Oil Red O, confirming its lipidic content. The 647nm signal is much greater with LO1Fab than control Fab, demonstrating successful binding of the targeted antibody fragment. Moreover, fluorescent signal is co-localised to regions of high Oil Red O signal.

4.9.5.2 LO1Fab-nanoparticle

Next, I wanted to assess whether the targeted nanoparticles could bind to its antigen in murine atherosclerotic tissue. As the nanoparticles contain Cy5 fluorophore in their core, direct fluorescence immunolabelling could be performed, without the need for secondary antibodies or signal generation. However, without the signal amplification step there was a poor SNR as may be expected (327), particularly given the 'stickiness' of the organic nanoparticle polymers to the microscope slide. As such, the staining protocols had to be carefully optimised (*Section 2.3.6.4.3 Nanoparticle staining in murine atherosclerosis*). Briefly, adjacent slides to those used in *Section 4.9.5.1 LO1Fab* above were blocked with 5% BSA overnight, prior to avidin/ biotin blocking and nanoparticle incubation for 2-hours. Adjacent slides were stained with LO1Fab-nanoparticles, control Fab-nanoparticles, untargeted nanoparticles, and Oil Red O. Figure 4-41 displays the fluorescence confocal microscopy, with widefield microscopy of the Oil Red O-stained slide.

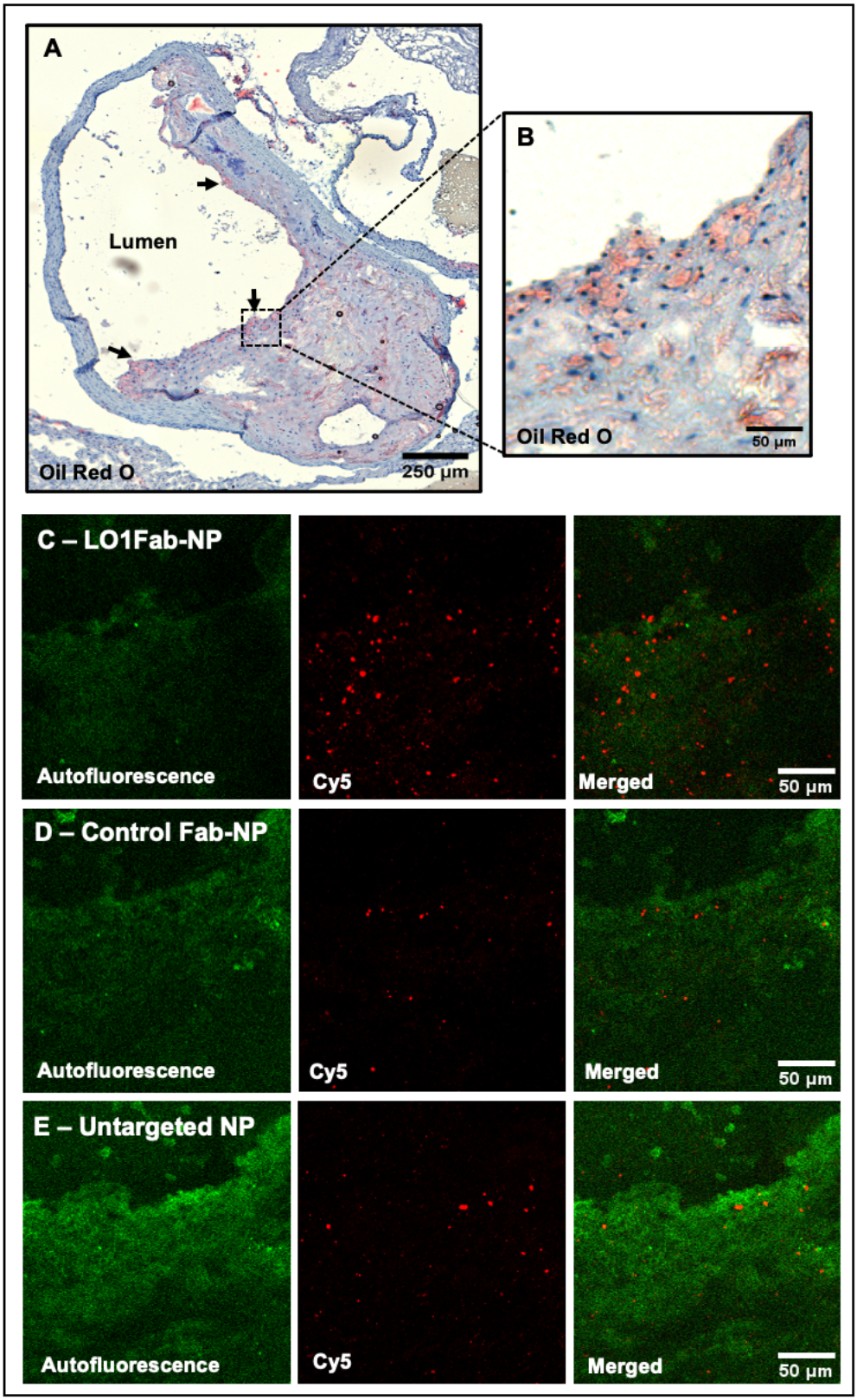

Figure 4-41. Fluorescence confocal microscopy with nanoparticle constructs in murine aortic root atherosclerosis (20x magnification).

An LDL-receptor deficient mouse fed a high-fat diet for 30 weeks was sacrificed via CO_2 inhalation and whole-body organ perfusion fixation carried out. The heart and aortic root were cryosectioned and 5µm adjacent sections were mounted on slides and stained with Oil Red O or nanoparticle constructs.
(A) – the Oil Red O-stained slide was imaged using widefield microscopy (10x), demonstrating significant lipidic deposits in the aortic root. Scale bar = 250µm.
(B) – is an inset from A) at 20x magnification, showing an area of significant Oil Red O staining. Scale bar = 50µm.
C-E) – 20x magnification of the section shown in (B), imaged using fluorescence confocal microscopy at autofluorescence (488nm, first panel)/ Cy5 (650nm, second panel) channels and merged (third panel). (C – LO1Fab-NP; D – Control Fab-NP; E – Untargeted NP). Scale bar = 50µm.

The fluorescence microscopy in Figure 4-41 demonstrates that LO1Fab-nanoparticles bind to the large atherosclerotic plaque, similar to LO1Fab in Figure 4-40 above. Therefore, both LO1Fab and LO1Fab targeted nanoparticles are able to bind their antigen in murine atherosclerotic lesions, specifically in lipid-rich regions of the plaque.

4.10 Foam cell assay

I have now designed and optimised LO1Fab nanoparticle production, developed a control construct, and demonstrated selective binding an MDA-modified epitope on LDL in a range of ELISA formats and within murine tissue. I thought it would be interesting to evaluate if macrophages could take up the nanoparticles in a cell-based assay, given that resident tissue macrophages in atherosclerotic plaques (foam cells) may represent the target cells for any cell-based therapeutic agents that could be delivered as the targeted nanoparticle payload. For imaging purposes this is less relevant, as the oxidatively modified LDL that the nanoparticles will react with will likely primarily be extracellular in the form of free lipid or cholesterol crystals within the atherosclerotic plaque necrotic core. However, if I could establish a reliable *in vitro* model of macrophage nanoparticle uptake, this may prove an invaluable assay for future experiments evaluating the effects of different nanoparticle

therapeutic cargo, for example on inflammatory cytokines or other relevant signalling peptides.

4.10.1 Isolation of monocytes and macrophage differentiation

PBMCs were isolated from healthy donors using density gradient centrifugation (*Section 2.3.7.1 Isolation of monocytes and macrophage differentiation*). Adherent cells were incubated at 37°C for 6-7 days with RPMI 1640 medium containing 10% autologous serum, L-glutamine, penicillin-streptomycin and M-CSF, to encourage macrophage differentiation.

4.10.2 Defining the macrophage population

It is important to establish the nature of the cellular population obtained using the steps above prior to addition of nanoparticle constructs, to confirm that monocyte-macrophages had indeed been isolated.

To this end, PCR was carried out as detailed in *Section 2.3.7.2 Quantitative real-time polymerase chain reaction*. Plated cells underwent lysis and lysates were collected, followed by RNA extraction, reverse transcription to generate cDNA, and finally quantitative real-time PCR. Probes were chosen to select cells of macrophage lineage. These included HLA-DRA and HLA-DRB1, which encode components of major histocompatibility complex class II, expressed in antigen presenting cells; CD11b, which encodes Integrin αM, a subunit of the αMβ2 molecule that is present on macrophages and other granulocytes; CD14, which encodes CD14 membrane glycoprotein and binds lipopolysaccharide, expressed on cells of the myelomonocyte lineage; CD16, which encodes FcγRIII, a transmembrane receptor expressed on granulocytes and macrophages; protein tyrosine phosphatase receptor type C

(CD45), expressed in all leucocytes; CD68, a transmembrane glycoprotein that is highly expressed in cells of monocyte lineage; and finally colony stimulating factor 1 receptor (CD115), a cell surface protein highly expressed in myeloid cells. The PCR results are displayed in Figure 4-42 below.

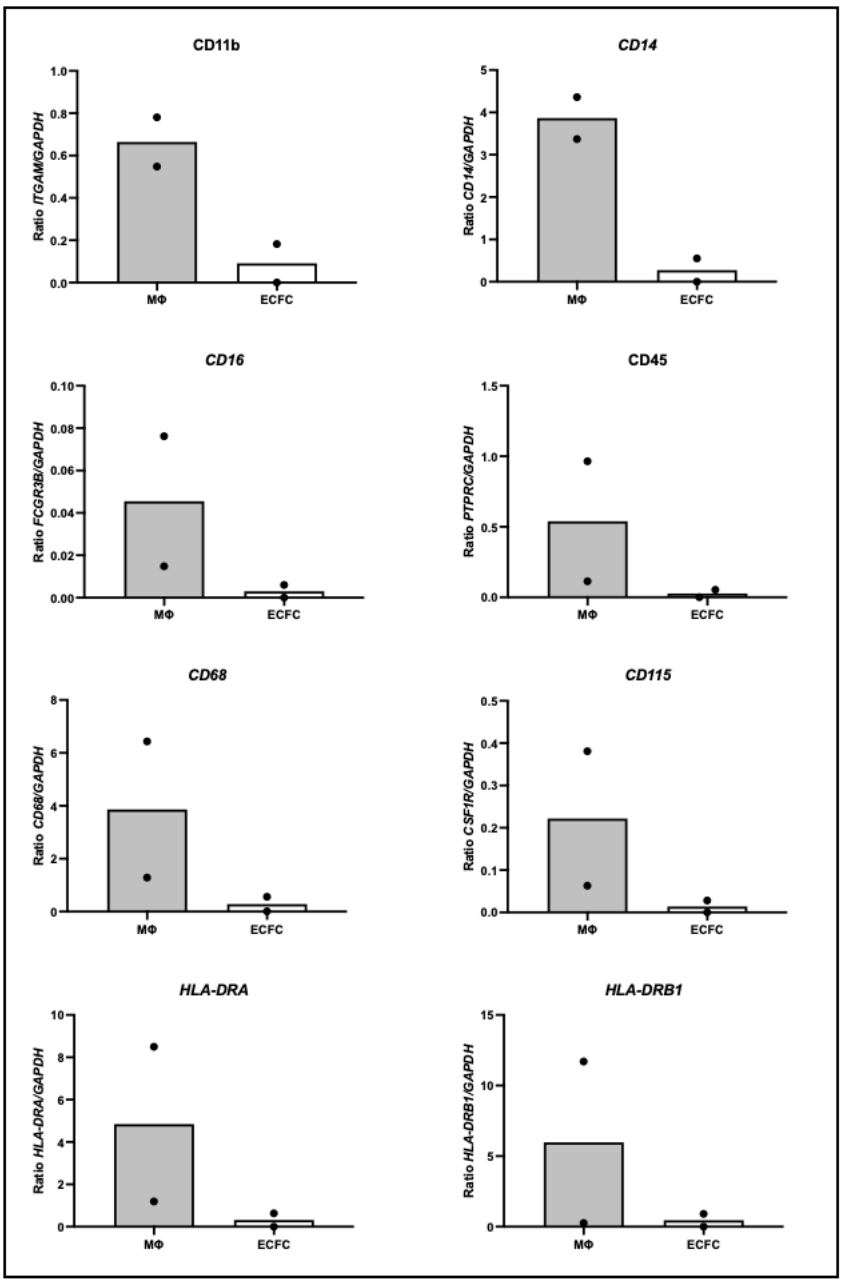

Figure 4-42. PCR of targeted macrophage genes.

Quantitative real-time polymerase chain reaction was performed on cultured macrophages (QuantStudio 6 Flex Real-time PCR system). Target gene expression was normalised to glyceraldehyde 3-phosphate

dehydrogenase (GAPDH) gene expression and fold change calculated. Performed using two macrophage (MΦ) colonies (different donors) and two endothelial colony forming cells (ECFCs) at passage two (different donors). There is greater expression of all targeted genes in the macrophage colonies, as compared to the ECFC colonies. Each bar represents the mean of individual values (dots).

Figure 4-42 confirms much greater targeted myeloid/ macrophage gene expression in the macrophage colonies than in the control endothelial colony forming cells at passage two. This is despite the endothelial colony forming cells being at a relatively early passage, where some non-endothelial cells may be present in the culture.

4.10.3 Foam cell formation

4.10.3.1 Fluorescent labelling of MDA-LDL

The techniques above confirmed that mononuclear cells were indeed obtained and cultured from peripheral blood. The next experimental stage was to turn the plated macrophages into foam cells (the nanoparticle target cell population), via ingestion of oxidatively modified LDL. To be able to demonstrate successful cellular oxLDL uptake, oxLDL needed to be fluorescently labelled, ideally with a fluorophore possessing different fluorescence characteristics to Cy5, so that nanoparticle binding could be evaluated. Labelling of oxLDL has traditionally been performed with DiI, a lipophilic dye with excitation 532nm/ emission 574nm (328). Although DiI-labelled oxLDL is commercially available (with unreported oxidative modifications), MDA-LDL was labelled with DiI in-house, to ensure that LO1Fab recognition of the antigen was retained. DiI-labelled MDA-LDL and nLDL were generated (*Section 2.3.7.3 Fluorescent labelling of native and MDA-modified LDL*) to demonstrate that labelling of MDA-LDL was onto the LDL particle itself, rather than the MDA component. These

reagents were then evaluated on ELISA to show that the labelling process was equivalent between both LDL particles and did not affect LO1 or LO1Fab reactivity.

Figure 4-43 below characterises DiI conjugation to MDA-LDL. These experiments determine that DiI labelling did not affect LO1 or LO1Fab binding in an indirect ELISA (Ai and ii) and sandwich ELISA (B). Moreover, reactivity in the indirect ELISA could be identified via antibody-mediated or fluorescence-mediated detection (C). There was no difference in fluorescence intensity between the two LDL constructs when added to an ELISA plate based on protein concentration gained from spectrophotometry post labelling (Figure 4-44).

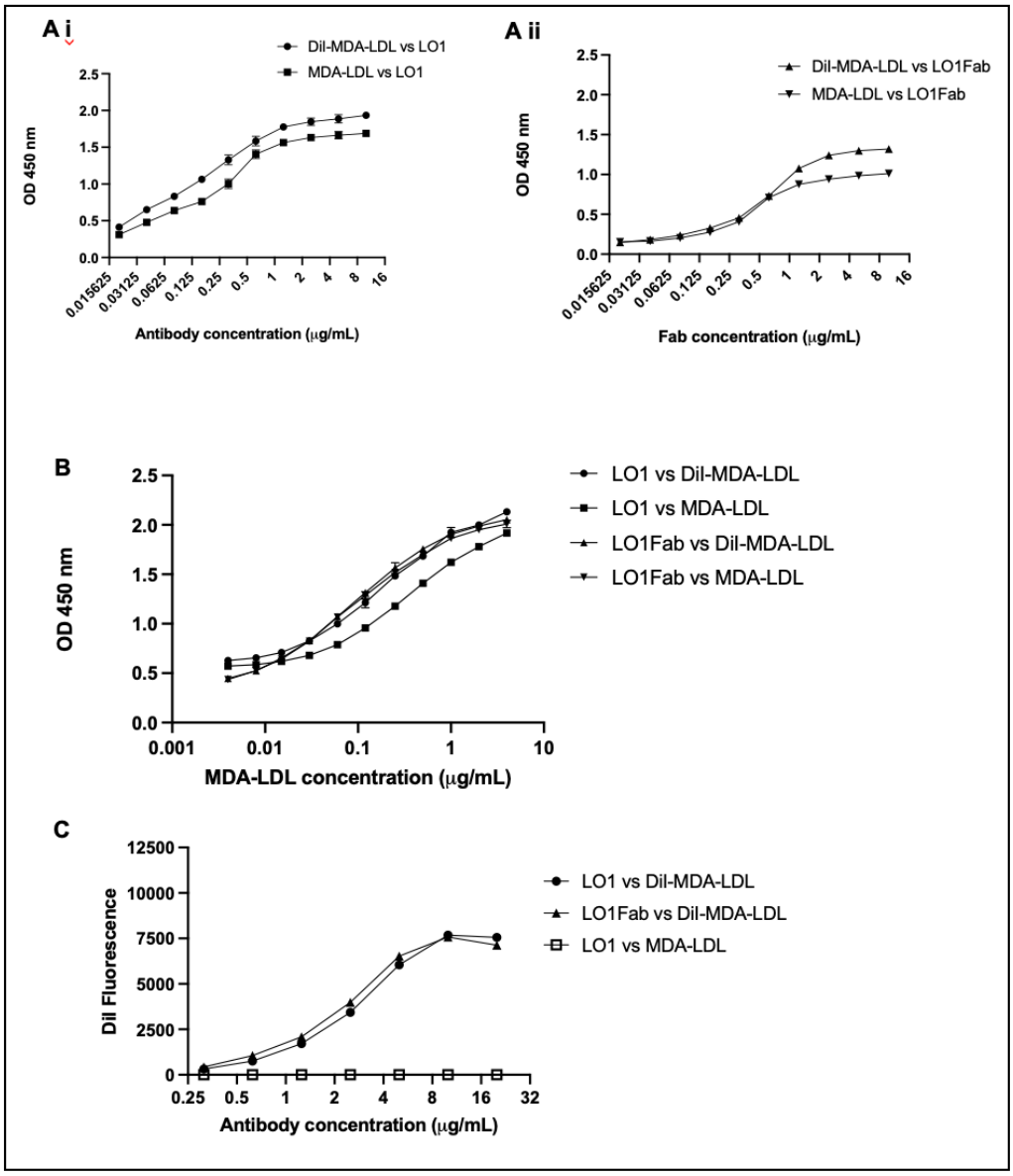

Figure 4-43. Fluorescent labelling of MDA-LDL.

MDA-LDL was labelled with DiI to enable assessment of cellular uptake.
(A i & ii) – DiI-MDA-LDL or unlabelled MDA-LDL were coated on ELISA plates overnight, followed by blocking with 3% BSA, LO1 (A i)/ LO1Fab (A ii) and then detection with either anti-IgG/ anti-IgG-CH1 as appropriate.
(B) – LO1 or LO1Fab were coated in dilution series on ELISA plates overnight, prior to blocking with 3% BSA and the addition of DiI-MDA-LDL or unlabelled MDA-LDL, followed by anti-ApoB for detection.
(C) – ELISA as performed in (A) except for detection was via DiI fluorescence.
There was no significant loss of recognition for MDA-LDL by either LO1 or LO1Fab following DiI labelling in any ELISA. Moreover, there was similar function between LO1 and LO1Fab, suggesting a conserved epitope. All performed in duplicate. Error bars represent SEM.

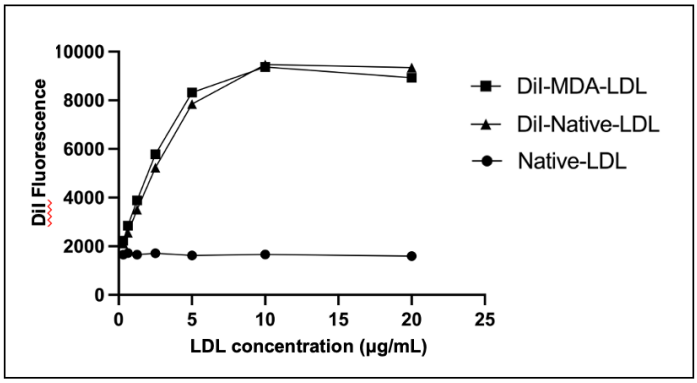

Figure 4-44. Equivalent fluorescent labelling of native and MDA-modified LDL.

To demonstrate that DiI labelling of MDA-LDL was onto LDL itself, rather than the malondialdehyde component of MDA-LDL, DiI-native LDL was produced in a similar fashion. This figure demonstrates no difference in fluorescence intensity between the labelled LDL constructs when read on an ELISA plate, suggesting equivalent DiI labelling. Performed in duplicate. Error bars represent SEM.

4.10.3.2 Foam cell formation

Foam cells were then generated from the macrophage population via incubation with DiI-labelled MDA-LDL for 24-hours, allowing the macrophages to engulf MDA-LDL. The cells were then washed, media changed to a non-fluorescent media and analysed on a fluorescent plate reader (CLARIOstar Plus). As an initial experiment, macrophages were incubated with DiI-labelled MDA-LDL or nLDL, aiming to demonstrate increased macrophage uptake of modified LDL. Figure 4-45 below displays the results of fluorescence intensity analysis on a fluorescence plate reader.

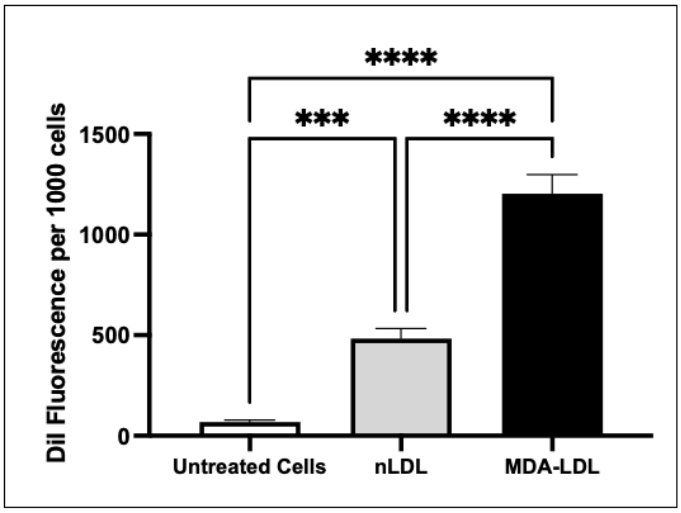

Figure 4-45. Increased macrophage uptake MDA-modified LDL versus native LDL.

Human peripheral blood monocytes were obtained and cultured. After culture for 6-days, macrophages were incubated with either native unmodified LDL or MDA-modified LDL (both 10µg/mL) for 1 further day. Macrophages were then changed into fresh media and imaged on a fluorescence plate reader and confocal microscope, after formaldehyde fixation. DiI fluorescence intensity was assessed, normalised to cell count per well, performed using widefield microscopy and expressed as DiI fluorescence per 1,000 cells (n=6 for all conditions).
*****p<0.0001 across all groups; ***p=0.0008 for untreated versus native LDL;**** p<0.0001 for native LDL versus MDA-LDL.*
Error bars represent SEM. One-way ANOVA used to assess statistical significance. Performed using cells obtained from 1 donor.

As would be expected, there is greater macrophage uptake of MDA-LDL in comparison to nLDL, likely due to the oxidative modification rendering the LDL particle more antigenic. There is some nLDL uptake (p=0.0008 versus untreated cells), however there is significantly greater MDA-LDL uptake (p<0.0001). Next, to prove internalisation and digestion of MDA-LDL by the cultured macrophages, a similar experiment was performed, using different concentrations of DiI-labelled MDA-LDL, and was also imaged using confocal microscopy. Figure 4-46 below displays the results, demonstrating a stepwise concentration-dependent increase in DiI fluorescence intensity (p=0.0149 for 10µg/mL versus untreated cells, p<0.0001 for 10 versus 20µg/mL), adding further supporting evidence that macrophages are indeed internalising the MDA-LDL. This is again corroborated in the representative confocal

images, which show more DiI fluorescence in the cells treated with the higher MDA-LDL concentration, with signal being localised around the DAPI-stained macrophage nuclei.

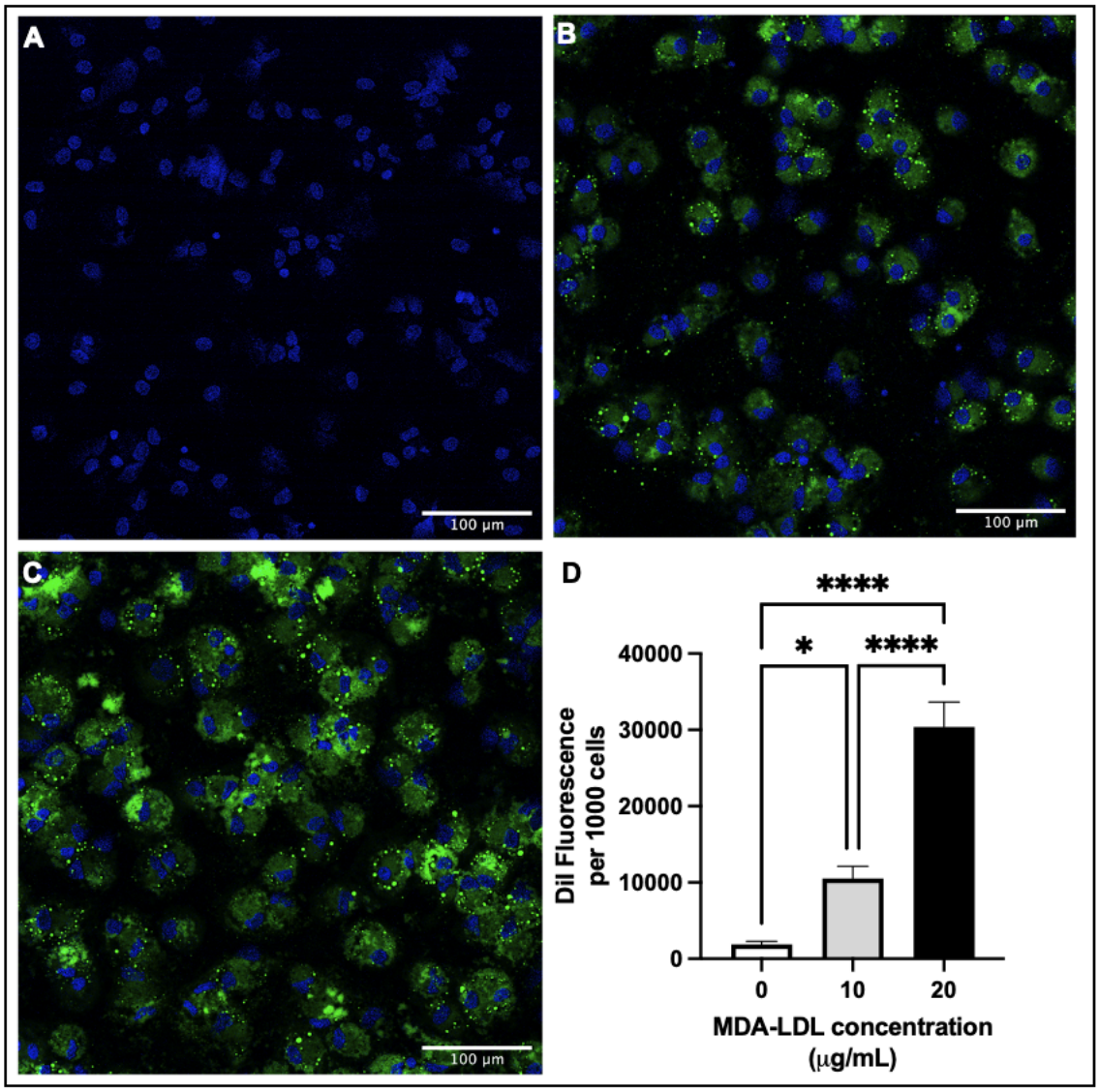

Figure 4-46. Macrophage MDA-LDL uptake is concentration dependent.

Human peripheral blood monocytes were obtained and cultured at 1x10^6/well. After culture for 6-days, macrophages were incubated with MDA-LDL (untreated, 10 or 20µg/mL) for 1 further day. Macrophages were then changed into fresh media and imaged on a fluorescence plate reader and confocal microscope, after formaldehyde fixation.
A-C) are representative images obtained using confocal microscopy of the three conditions (A – untreated; B – 10µg/mL MDA-LDL; C – 20µg/mL). Displaying merged images of the DAPI (blue) and DiI (green) channels. Scale bar = 100µm. Imaged at 20x magnification.
*D) – DiI fluorescence intensity of wells treated with each condition, normalised to cell count per well, performed using widefield microscopy. Expressed as DiI fluorescence per 1,000 cells. (Untreated, n=6; 10µg/mL MDA-LDL, n=7; 20µg/mL MDA-LDL, n=7). ****p<0.0001 across all groups; *p=0.0149 for untreated versus 10µg/mL; ****p<0.0001 for 10µg/mL versus 20µg/mL.*

Error bars represent SEM. One-way ANOVA used to assess statistical significance. Performed using cells obtained from 1 donor.

4.10.4 Macrophage uptake of nanoparticles

Finally, I added the nanoparticles (250µg/mL), which had been pre-incubated with DiI-MDA-LDL (10µg/mL) for 1-hour, to plated macrophages (1×10^6/well), and evaluated cellular uptake using confocal microscopy (*Section 2.3.7.5 Macrophage treatment with nanoparticle constructs*). Figure 4-47 below displays representative confocal imaging.

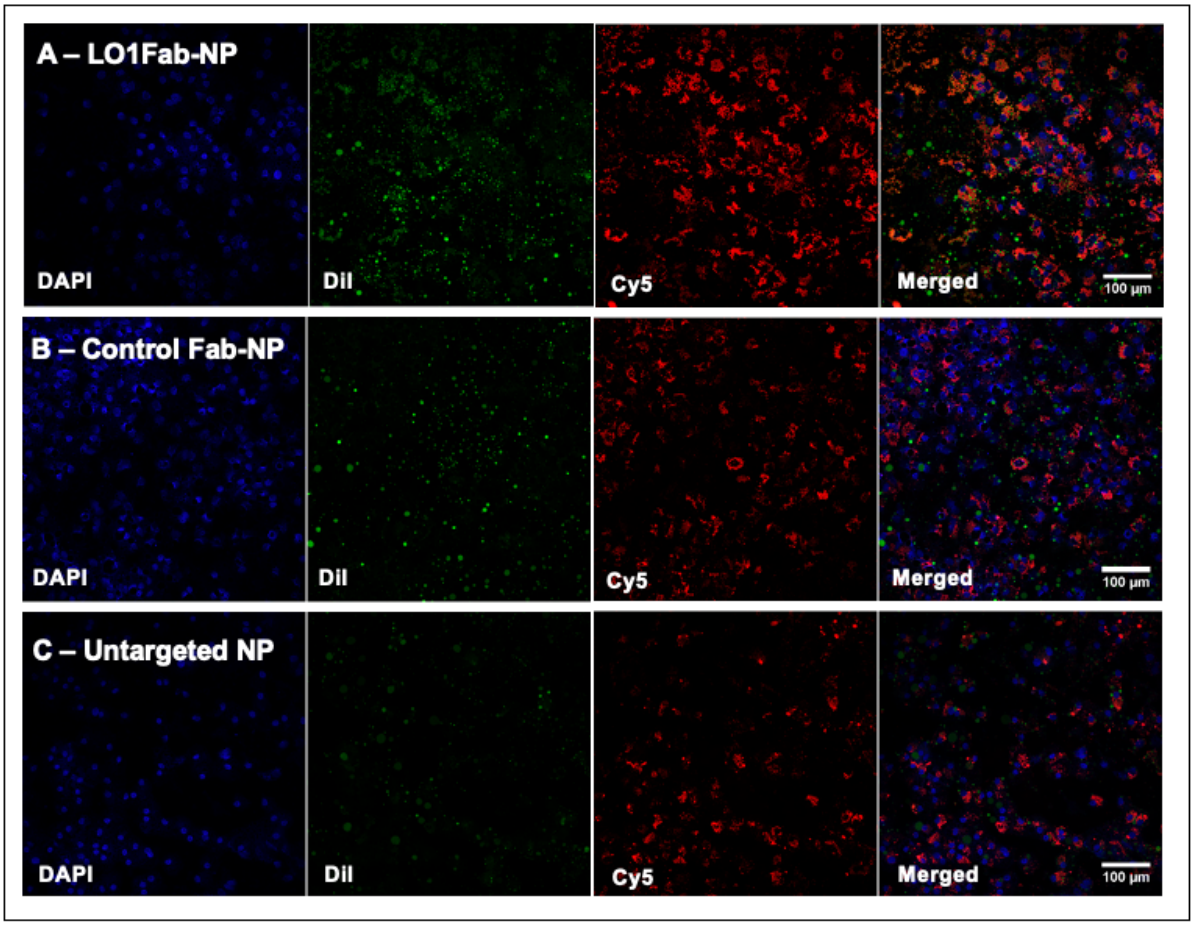

Figure 4-47. Confocal microscopy of macrophages treated with MDA-LDL and nanoparticle constructs.

Human peripheral blood monocytes were obtained and cultured at $1x10^6$/well for 6 days. DiI-MDA-LDL (10µg/mL) and nanoparticle constructs (250µg/mL) were mixed for 1-hour, prior to culturing with the

macrophages for 1 further day. Macrophages were then changed into fresh media and imaged on a confocal microscope after formaldehyde fixation. Imaged at 20x magnification.
1st column – DAPI channel, 2nd column – DiI channel, 3rd column – Cy5 channel; 4th column – Merged. Scale bar = 100µm.

In the LO1Fab-nanoparticle treated wells there is increased internalisation of MDA-LDL, as well as much greater nanoparticle presence, compared to wells treated with control Fab-nanoparticle and untargeted nanoparticles. Macrophage nanoparticle uptake is evident, rather than non-specific binding of the nanoparticles to the well surface, particularly in the fused images. One plausible explanation for the increased uptake of both LO1Fab-nanoparticles and MDA-LDL versus the control constructs is that the nanoparticles and MDA-LDL are forming complexes on mixing. These antibody-nanoparticle-antigen complexes may be more readily engulfed by macrophages. This is likely a function of the experimental design, rather than a true effect that would be expected *in vivo*, which requires optimisation and exploration in future work. Alternatively, LO1 may be masking the negative charge of MDA-LDL, and thus enhancing its interaction with macrophages. Initial further studies could simply vary the timing and method of nanoparticle addition to the macrophages, for example, forming foam cells prior to nanoparticle incubation. Nonetheless, an assay has been created that will be useful to model the cellular effects of different nanoparticle therapeutic payloads, when these are developed, prior to *in vivo* study.

4.11 LO1Fab-750 in vivo characterisation in murine atherosclerosis

The next important translational step was to evaluate the antibody fragments themselves *in vivo*, using FMT to ensure effective targeting of atherosclerotic plaques within the ROI in ascending aorta and aortic arch vessels. Prior work in the Khamis laboratory had compared LO1Fab to commercially available atherosclerotic plaque near-infrared reporters

(MMPSense-645 FAST and IntegriSense-680) and demonstrated favourable imaging atherosclerotic plaque localisation in high-fat fed LDL-$R^{-/-}$ mice (S Pandey's PhD thesis). However, no control construct had been developed as a comparator for these *in vivo* experiments. Testing against a control construct is important for the development of LO1Fab as a molecular imaging probe itself, as well as for the development of targeted nanoparticles.

4.11.1 The LDL-receptor deficient mouse model

There is much experience within the Haskard and Khamis laboratories with mouse models of atherosclerosis. The most commonly used model has been the high-fat fed LDL-$R^{-/-}$ mouse model, which is described earlier (*Section 1.6.1.1 Mouse models of experimental atherosclerosis*), and I have utilised in this thesis. Mice genetically engineered to possess a non-functioning LDL-receptor are unable to clear LDL from the circulation and thus develop significant hypercholesterolaemia (>2,000 mg/dL, [normal range 80-100 mg/dL]), particularly when coupled with a high-fat diet (280). Over the course of the mouse lifespan this leads to aggressive atherosclerotic plaque development, most prominently in the aorta, aortic root and major aortic branch vessels (329). To further promote an advanced model of atherosclerosis, female mice were utilised for imaging studies, given their propensity to develop larger atherosclerotic plaques than their male counterparts (133).

Thus, the model of atherosclerosis used in this thesis consisted of female homozygous LDL-$R^{-/-}$ mice transitioning to a high-fat diet from 10-weeks of age, and continuing this for 30-40 weeks, depending on the terminal timepoint of the individual experimental design. An advanced model of atherosclerosis was desirable for the imaging studies, given that atherosclerotic plaque necrotic cores rich in oxLDL (the imaging target of LO1Fab/ LO1Fab-

nanoparticles) should continue to develop with increasing mouse age and ongoing high-fat diet exposure, to maximise the chance of detecting a true difference between the tested constructs and therefore minimise experimental sample sizes. For the studies in this thesis no wild type mice were used. This limits the numbers of animals needed for the experiments, in line with the NC3Rs aims, and was felt to be unnecessary given the use of robust control constructs. Figure 4-48 displays a schematic representation of the murine model used in this thesis, as well as average mouse weights immediately prior to terminal imaging experiments and high-fat diet duration.

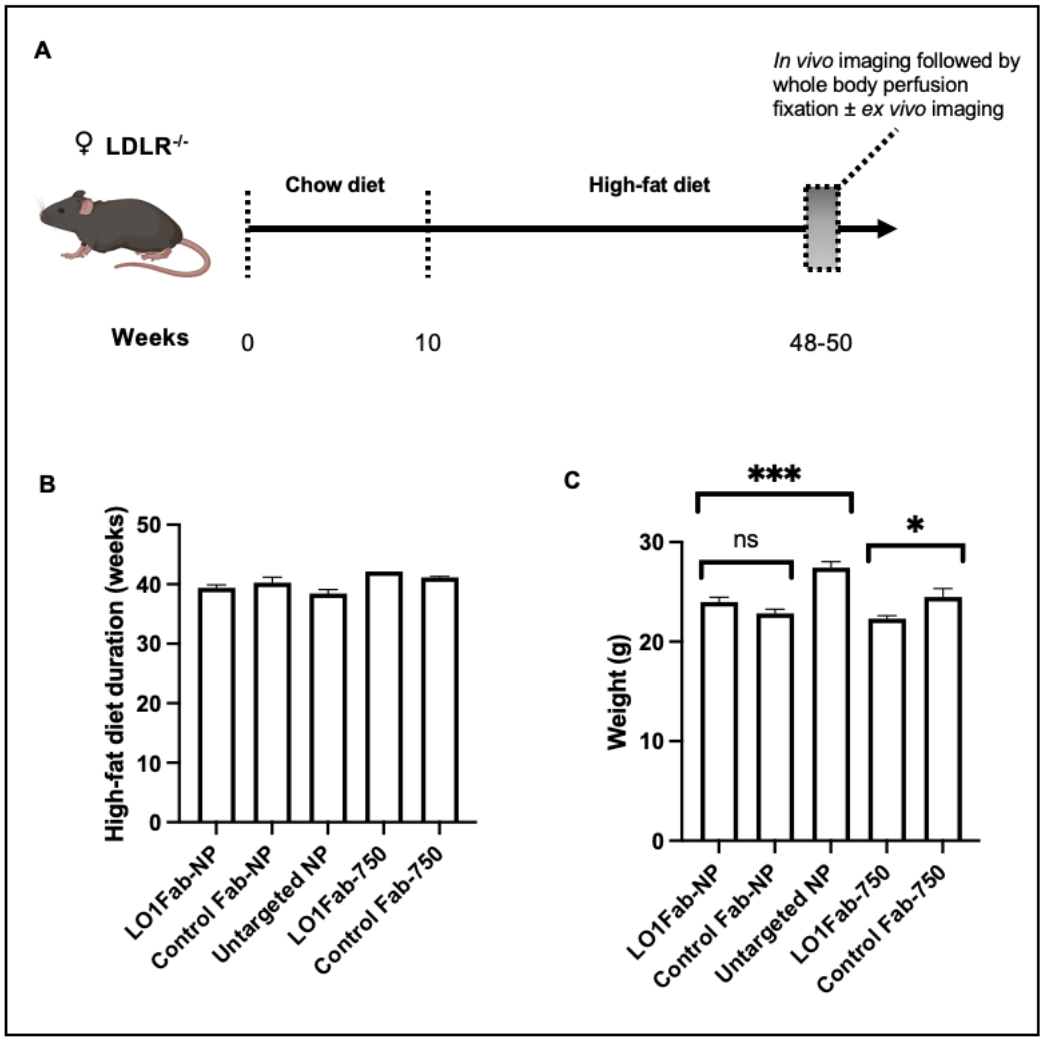

Figure 4-48. The atherosclerotic mouse model used for molecular imaging in this chapter.

A) – a schematic representation of the mouse model used in this thesis. LDL-receptor deficient mice were fed a chow diet up until 10 weeks of age, when they were switched to a high-fat diet. This continued until 45-50 weeks of age, where upon they underwent in vivo studies.
B) – average high-fat diet duration for mice undergoing experimental in vivo imaging.
*C) – average weights of mice used for each construct in the study. p=0.0894 for LO1Fab-NP vs control Fab-NP; ***p=0.0007 for LO1Fab-NP vs untargeted NP; *p=0.0484 for LO1Fab-750 vs control Fab-750.*
Unpaired t-test with Welch's correction used to assess statistical significance. Error bars represent SEM.

There were no substantial differences between the weights of mice used in each experimental arm. All mice undergoing *in vivo* studies received between 38-40 weeks of high-fat diet prior to imaging. The mice injected with untargeted nanoparticles or control Fab-750 were slightly heavier than those injected with the targeted constructs. The actual differences are small and would be expected to exert little experimental effect.

4.11.2 Whole body FMT

LO1Fab and control Fab were both conjugated with VivoTag-S-750 using maleimide labelling, as detailed in *Section 2.3.4 Fluorescent labelling of antibody fragments for in vivo studies*. The degree of labelling (ratio of 750 fluorescence signal: protein) was calculated individually per batch of conjugated antibodies used for *in vivo* imaging. This corrects the quantitative fluorescent signal obtained from FMT to a molar antibody concentration and permits direct comparison between injected constructs.

Prior to undertaking imaging studies, it is imperative to calculate construct circulating half-life, to ensure a significant number of half-lives have elapsed prior to imaging, to minimise the background signal from circulating construct, optimising the SNR. The half-lives or fluorescently labelled full LO1 IgG and LO1Fab fragment have previously been evaluated at 21-hours (174) and 12-minutes (S Pandey's thesis), respectively. The considerably shorter

half-life of the Fab is likely due to its much smaller molecular weight (48kDa versus 150kDa), rendering it under the renal clearance threshold for glomerular filtration. An imaging timepoint of 4-hours was previously selected for both LO1 and LO1Fab to allow comparison between constructs. No formal half-life evaluation of control Fab-750 was performed in this thesis, however, for consistency with prior work, equivalency to LO1Fab-750 was assumed, and a 4-hour imaging timepoint was a for both LO1Fab-750 and control Fab-750. All prior antibody imaging in the Khamis laboratory had been performed with intravenous injection of 1nmol of protein, scaled to a 25mg mouse, which was continued for this study.

FMT is a fluorescence-based three-dimensional imaging modality that permits the imaging and quantitative comparison of injected fluorescently tagged probes. Multiplexing different probes is possible, as long as there is a lack of significant overlap of the conjugated fluorescence spectra (there are 635, 680, 750 and 800nm lasers available). Hence, it is an invaluable imaging modality for the evaluation of molecular targeting agents, such as those being developed in this chapter, allowing signal quantification within customisable regions of interest and the location of that signal within three-dimensional space.

LDL-$R^{-/-}$ mice fed a high-fat diet for 35-40 weeks were injected with 1nmol of either LO1Fab-750 or control Fab-750 and FMT imaging undertaken using the 750nm channel 4-hours later. Figure 4-49 compares the two constructs, displaying representative mice with identical ROIs covering the ascending aorta and arch vessels, that were placed using a three-dimensional reconstruction.

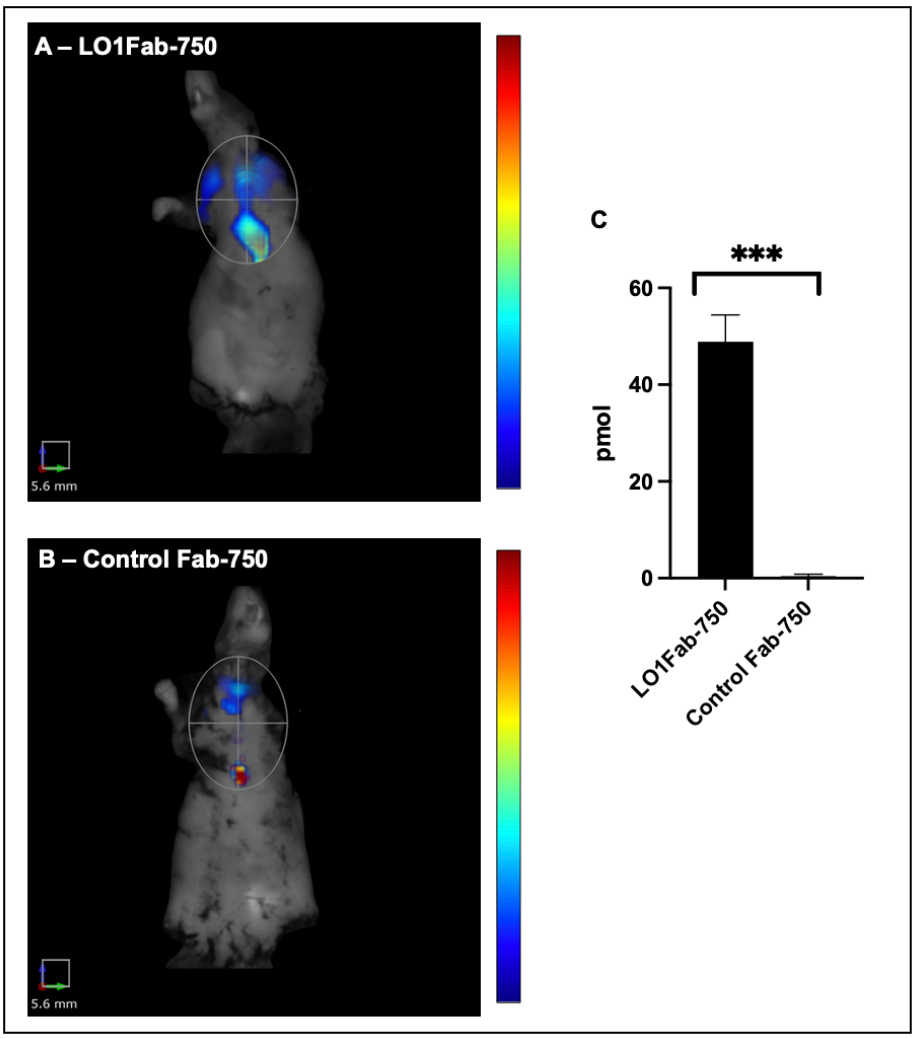

Figure 4-49. FMT quantitative imaging of LO1Fab-750 versus control Fab-750.

*LDL-receptor deficient mice fed a high fat diet for 38-40 weeks were injected with fluorescent LO1Fab (A) or control Fab (B) (1nmol scaled to a 25g mouse (~2mg/kg)) and imaged with fluorescence molecular tomography after 4-hours. Scale bar ranges from blue (0 signal) to red (high signal – 100nM). Following image reconstruction using TrueQuant 3.0, a region of interest was selected that included the heart and aortic arch vessels, which was standardised for all mice. Background correction was performed per scan in a blinded fashion. (C) Unpaired t-test with Welch's correction used to assess statistical significance, ***p=0.0003, n=6 for each group. Error bars represent SEM.*

There is greater fluorescent signal in the ROI in the mouse injected with LO1Fab-750. For quantitative construct comparison, 750nm signal within each ROI was corrected for background signal per mouse in a blinded fashion, and corrected for degree of fluorescent labelling. Figure 4-49C displays the amount of Fab fragment detected in each ROI, following

the above corrections, with n=6 per construct. There was a significant difference (p=0.0003) between each injected construct, with (mean ±SD) 48.9±13.6pmol LO1Fab versus 0.4±1.0pmol control Fab.

4.11.3 Confocal microscopy of in vivo injected mice

The above experiment confirms LO1Fab binding to tissue within the ROI in the *in vivo* mouse model of atherosclerosis. However, given the relatively poor spatial resolution of FMT, and the lack of CT co-registration performed in this study, it is not possible to conclusively demonstrate that the detected signal is indeed due to atherosclerotic plaque binding. To investigate this further, injected mice were culled via CO_2 inhalation and underwent formaldehyde perfusion fixation. Following organ extraction, cryosections of aortic root tissue were made and resultant slides imaged with fluorescence confocal microscopy, using identical microscope settings (Figures 4-50 and 4-51 below show representative sections). Slides that were 5µm adjacent to the selected slides for imaging were stained with Oil Red O, and counter-stained with haematoxylin, to confirm the presence of fatty lesions.

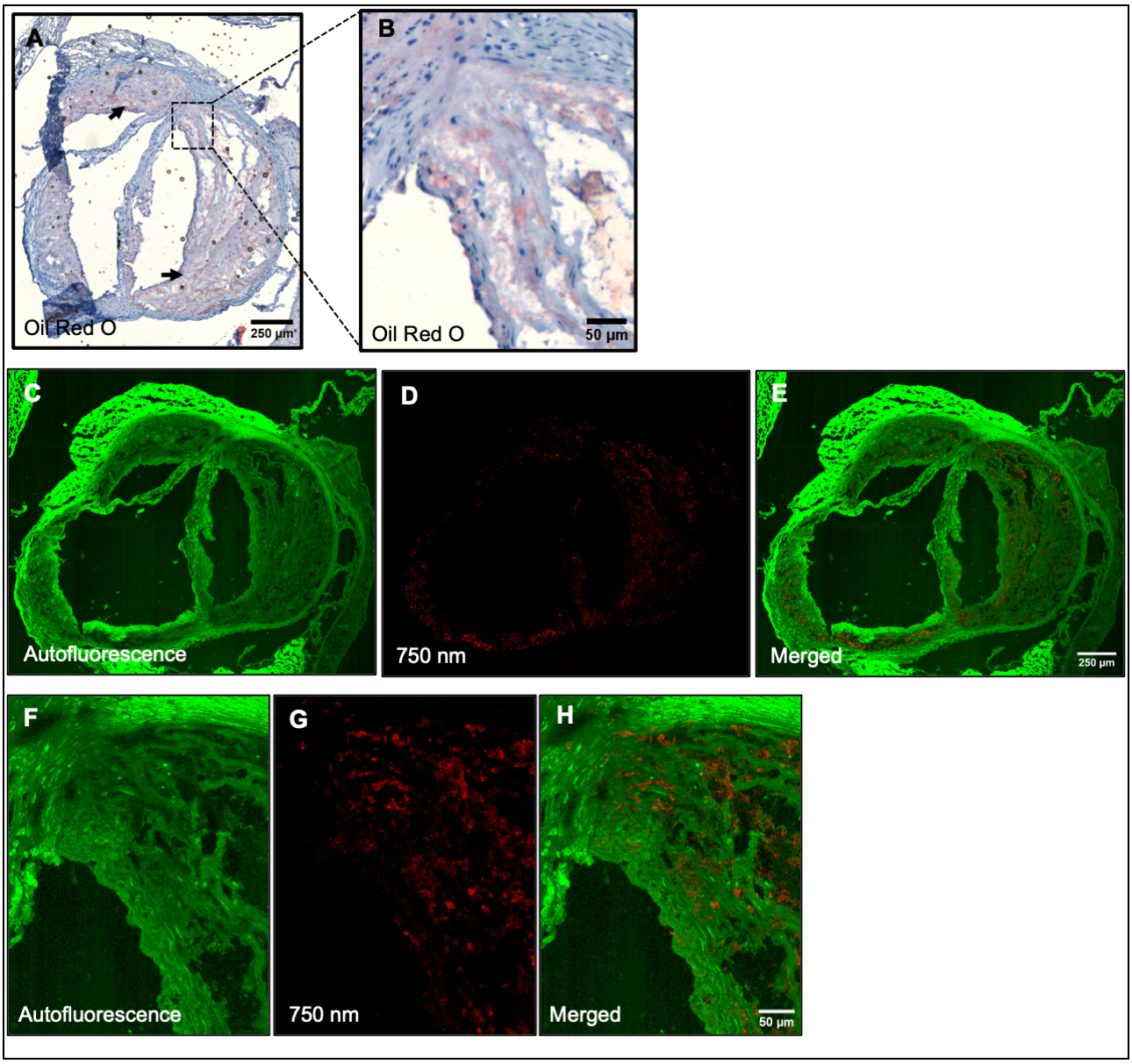

Figure 4-50. Fluorescent confocal microscopy of an aortic root section from a mouse injected in vivo with LO1Fab-750.

An LDL-receptor deficient mouse fed a high-fat diet for 40-weeks was injected with LO1Fab-750 and sacrificed via CO2 inhalation with whole-body perfusion fixation. The heart and aortic root were cryosectioned and 5µm adjacent sections were mounted on slides.
(A) – an Oil Red O-stained slide imaged using widefield microscopy (10x), demonstrating significant lipidic deposits in the aortic valve cusps (highlighted by arrows) in the aortic root. Scale bar = 250µm.
(B) – a 20x magnified view of the highlighted area in (A). Scale bar = 50µm.
(C-E) – a 5µm adjacent aortic root section was imaged using confocal microscopy at 10x magnification. (C – autofluorescence, D – 750 nm, E – merged). Scale bar = 250µm for all panels.
(F-H) – a 20x magnified view of the highlighted area in (A), that corresponds to the zoomed area in (B) with significant Oil Red O staining. (F – autofluorescence, G – 750 nm, H – merged). Scale bar = 50µm for all panels.

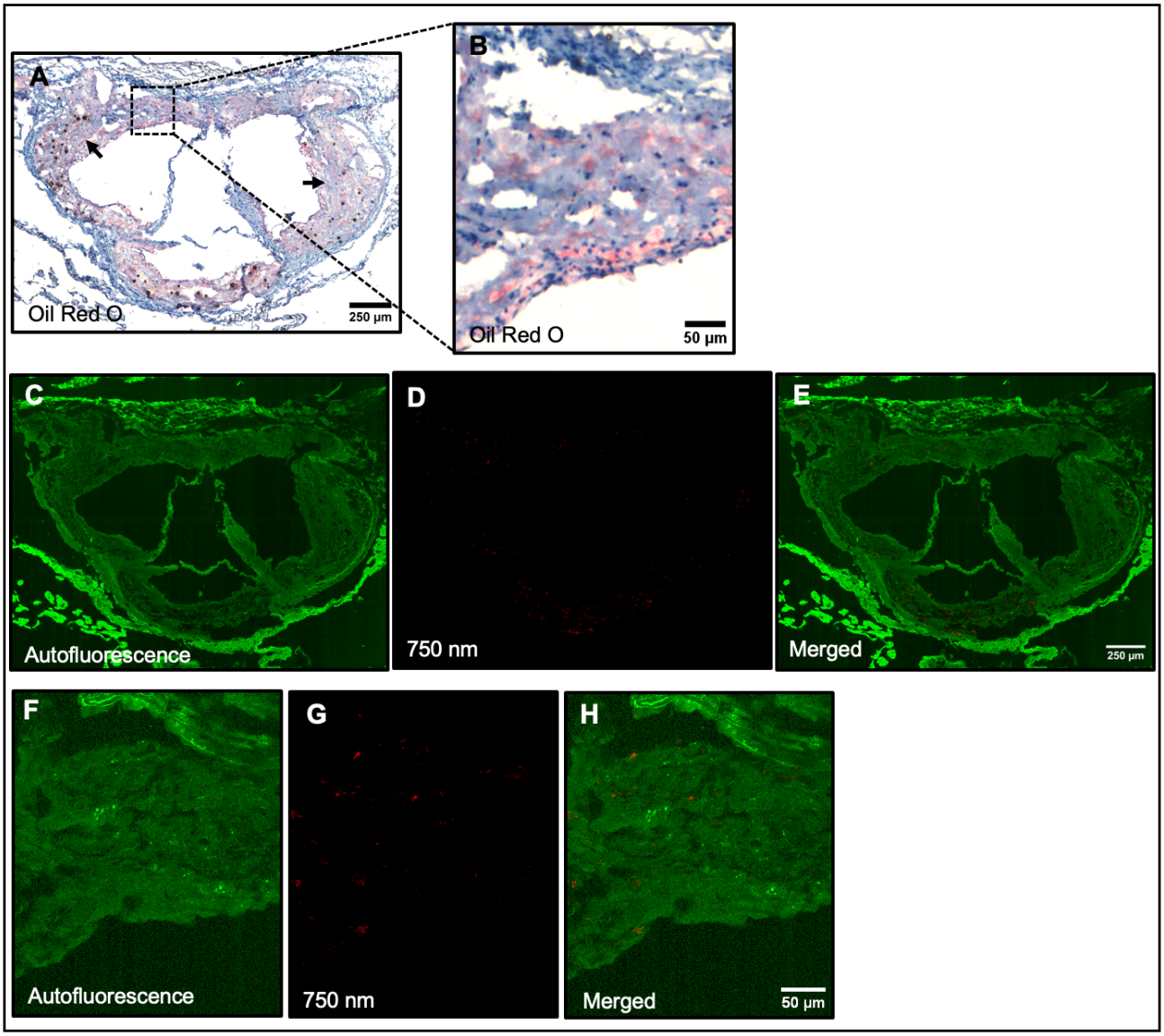

Figure 4-51. Fluorescent confocal microscopy of an aortic root section from a mouse injected in vivo with control Fab-750.

An LDL-receptor deficient mouse fed a high-fat diet for 40-weeks was injected with control Fab-750 and sacrificed via CO2 inhalation with whole-body perfusion fixation. The heart and aortic root were cryosectioned and 5µm adjacent sections were mounted on slides.
(A) – an Oil Red O-stained slide imaged using widefield microscopy (10x), demonstrating significant lipidic deposits in the aortic valve cusps (highlighted by arrows) in the aortic root. Scale bar = 250µm.
(B) – a 20x magnified view of the highlighted area in (A). Scale bar = 50µm.
(C-E) – a 5µm adjacent aortic root section was imaged using confocal microscopy at 10x magnification. (C – autofluorescence, D – 750 nm, E – merged). Scale bar = 250µm for all panels.
(F-H) – a 20x magnified view of the highlighted area in (A), that corresponds to the zoomed area in (B) with significant Oil Red O staining. (F – autofluorescence, G – 750 nm, H – merged). Scale bar = 50µm for all panels.

The sections display significant atherosclerotic lesions at the level of the aortic valve, involving the valve cusps as well as valve tips, which is confirmed to have a high lipid content with Oil Red O staining. When comparing the sections made from LO1Fab-750 and control Fab-750 injected mice, there is significantly greater red (750nm) signal for the targeted construct. On the merged and zoomed imaging panels, the increased signal is shown to localise to regions of atherosclerotic plaque on the valve cusps, suggesting binding to lipidic plaque contents. Moreover, LO1Fab-750 binding did not localise to areas of high DAPI (nuclear) staining in B) or high green autofluorescence (extracellular matrix) signal in E) or H). These findings indicate that LO1Fab is reacting with acellular or extracellular areas, such as the atherosclerotic necrotic core, as shown previously with the full LO1 IgG (174). These acellular areas are likely due to apoptotic cellular remnants within the plaque necrotic core. The failure of these apoptotic cells to be phagocytosed by resident macrophages, termed defective efferocytosis, is a key feature of advanced atherosclerosis and other chronic inflammatory diseases, and has the potential to render plaques unstable and vulnerable to rupture (330). Possible mechanisms for defective efferocytosis in advanced atherosclerosis include macrophage overload, oxidative stress and free radical excess, as well as competitive inhibition by oxLDL for the same macrophage scavenger receptors (331). These factors would all be expected to be present in our mouse model of atherosclerosis, and should result in an abundance of LO1Fab antigen.

4.12 Nanoparticle in vivo characterisation in murine atherosclerosis

Following the development of the LO1Fab targeted nanoparticle and appropriate control construct, *in vitro* function was demonstrated to be preserved on ELISA and immunohistochemistry. Given that *in vivo* testing of LO1Fab-750 versus control Fab-750 had

shown promising atherosclerotic plaque targeting in the mouse model of atherosclerosis, the next experimental phase in nanoparticle development was therefore to assess their *in vivo* function, taking forwards the most promising constructs and optimised formulations from the earlier sections. As such, nanoparticles, formulated with 2.5 mg PLGA-PEG-MAL (12.5%), 10 mg PLGA-cyanine 5 (50%) and 7.5 mg PLGA (37.5%), conjugated to 20μg of LO1Fab or control Fab were taken forwards for *in vivo* testing.

4.12.1 Blood clearance of constructs

The first experimental step in the development of a new imaging probe for *in vivo* imaging is to understand the construct plasma half-life, to ensure that imaging timepoints are appropriate, where there is sufficient blood pool clearance to limit background signal and improve the SNR. Accordingly, LDL-$R^{-/-}$ mice fed a high-fat diet for 38-40 weeks were injected intravenously via a tail vein with LO1Fab-nanoparticles or untargeted nanoparticles, and plasma fluorescence evaluated. Blood was then collected via serial tail vein sampling (*Section 2.3.8.3 Construct half-life determination*), using the opposite vein to that which was injected, at various timepoints up to 48-hours after injection. The first blood sample was obtained prior to injection for baseline fluorescence correction, with haemostasis ensured prior to intravenous injection. The second sample was obtained 15-minutes after injection, to provide a peak fluorescence signal, which was then taken as Time-0. Mice used for these experiments were the same model as will be used for the imaging studies, to ensure any changes in plasma half-life induced by advanced atherosclerosis are accurately accounted for. Mice were injected with 2mg of nanoparticles, based on empiric data and prior experience in the Scott laboratory. Of note, 2mg LO1Fab-nanoparticles equates to ~8μg LO1Fab; a much

lower quantity of LO1Fab than the 1nmol (48μg) than was injected in the LO1Fab-750 imaging studies.

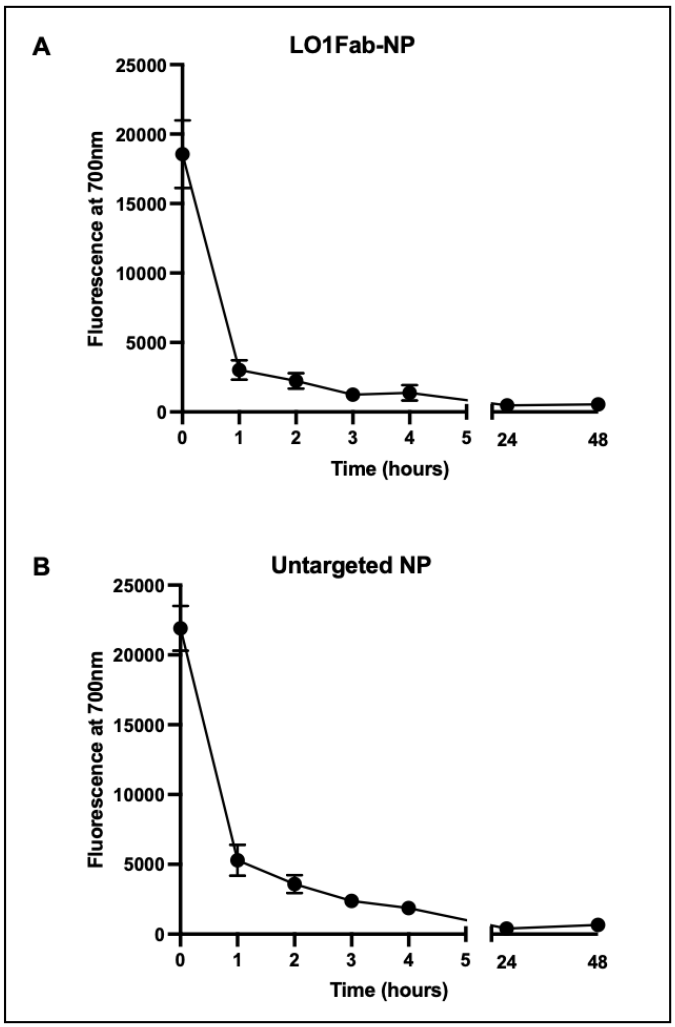

Figure 4-52. Nanoparticle construct in vivo half-lives.

Nanoparticle constructs (A – LO1Fab-NP; B – Untargeted NP) were injected intravenously in LDL-receptor deficient mice fed a high-fat diet for 35-40 weeks. Blood was drawn at multiple timepoints following injection and assessed for fluorescence intensity on the Odyssey CLx Imaging System. Time 0 on the x-axis represents 15-minutes post-injection. Error bars represent SEM. Non-linear regression using least squares fit estimated the blood clearance to vary in two phases (two-phase exponential model) with half-lives of:
A) – LO1Fab-NP – 1st $t_{1/2}$ – unstable (95% CI incalculable); 2nd $t_{1/2}$ – 1.5 hours (95% CI incalculable); n=5.
B) – Untargeted NP – 1st $t_{1/2}$ – 0.09 hours (95% CI incalculable) [5.4 minutes]; 2nd $t_{1/2}$ – 1.5 hours (95% CI 0.61-4.5 hours); n=4.

Figure 4-52 displays the plasma fluorescence curves, that has been background-corrected for each mouse. There are similar curves for both constructs, with a rapid initial clearance over the first hour, followed by a slower second clearance phase, reaching a steady state by 24-hours. A lower peak at Time-0 (15-minutes after injection), as well as lower fluorescence values over the first four hours, can be appreciated with the targeted constructs. Tentatively, it could be suggested that the lower quantity of circulating LO1Fab-nanoparticles at each timepoint may be due to on-target effects – i.e., LO1Fab construct binding to their oxLDL epitopes, within organs, such as the liver, where oxLDL will be abundant in the atherosclerotic mouse model, or possibly, within vascular endothelium of atherosclerotic plaques. Conversely, the presence of the Fab fragment on LO1Fab-nanoparticles would be expected to prolong the plasma half-life versus the untargeted nanoparticle, given the increased molecular weight.

A very rapid first pass metabolism of polymeric nanoparticles is a well-known phenomenon, mostly being taken to the reticuloendothelial system via the liver. However, PEGylation should reduce hepatic clearance through reduced immunogenicity, as well as the generation of a hydrated cloud surrounding each particle, sterically precluding particles from interaction with blood components as well as each other, reducing nanoparticle aggregation. The net result of these effects should be a substantially prolonged blood circulation half-life (319). One potential explanation for the rapid initial blood clearance seen with these nanoparticles is that, given their relatively large size for nanoparticle constructs (>100nm), that they accumulate rapidly in the liver, and undergo phagocytosis by resident macrophages. Larger particle sizes have also been shown to accumulate in lung vasculature, but generally with diameters towards 1μm (332).

Nanoparticle half-life was estimated using non-linear regression with least squares fit in a two-phase exponential model. The untargeted nanoparticle clearance more accurately fitted the statistical model, with a first half-life of 5.4 minutes and second half-life of 90 (95% CI, 37 – 270) minutes. The LO1Fab-nanoparticle first half-life was unstable, whilst the second half-life also was 90-minutes. Blood clearance was not performed for the control Fab-nanoparticle; however, given the very similar half-life values for the targeted and untargeted constructs, equivalence was assumed.

4.12.2 In vivo imaging at 24-hours

Subsequently, mice were injected intravenously with 2mg LO1Fab-nanoparticles or untargeted nanoparticles, and FMT performed using the 680nm channel, at 24-hours after injection. An imaging timepoint of 24-hours was selected given the almost complete blood pool clearance of both constructs at this timepoint. As detailed earlier, mice were depilated, warmed and placed under general anaesthesia prior to FMT imaging.

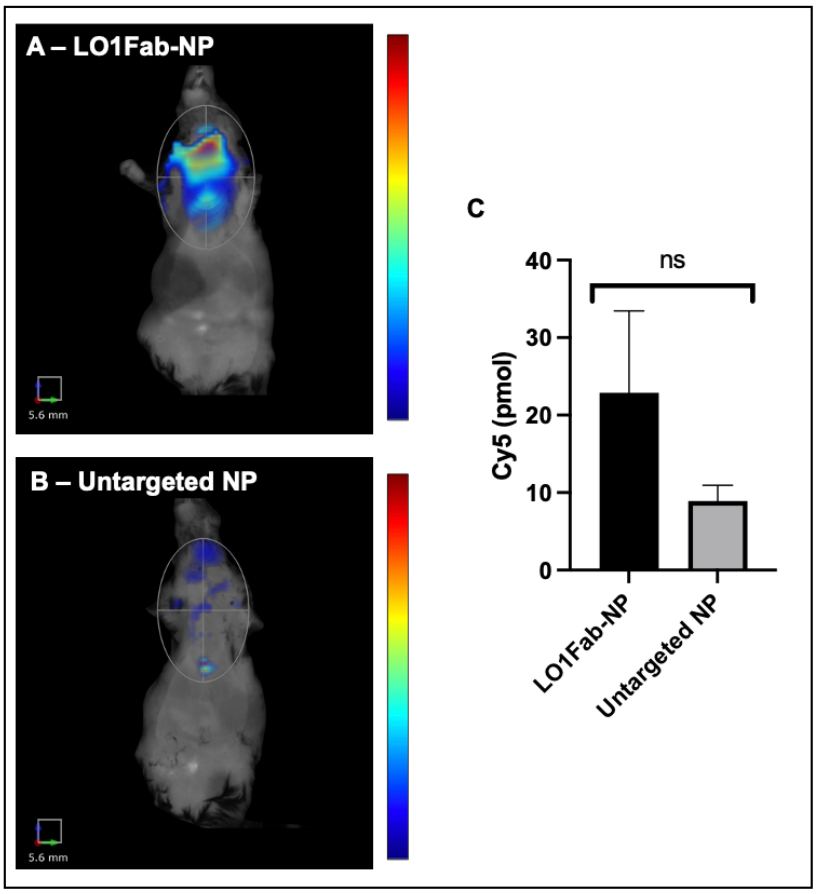

Figure 4-53. FMT imaging of LO1Fab targeted nanoparticles at 24-hours post-injection.

Representative FMT images at 24-hours post-injection of in vivo injected LO1Fab-NP (A) and untargeted NP (B) in LDL-receptor deficient mice fed a high-fat diet for 40-weeks. Scale bar ranges from blue (0 signal) to red (high signal – 250nM). Following image reconstruction using TrueQuant 3.0, a region of interest was selected that included the heart and aortic arch vessels, which was standardised for all mice.
(C) – quantitative analysis of Cy5 signal in the region of interest. Background correction was performed per scan in a blinded fashion. Unpaired t-test with Welch's correction used to assess significance, p=0.2395 (ns, non-significant), n=7 for each group. Error bars represent SEM.

Figure 4-53 displays the results of the imaging study, with n=7 per group. A) and B) show representative FMT images obtained using the 680nm (Cy5) channel, with signal shown within identical ROIs. C) presents the average moles of Cy5 within the background-corrected ROI for each group. There was no quantitative difference (p=0.2395) between the LO1Fab and untargeted nanoparticles, with (mean ±SD) 22.9±28.0pmol and 8.9±5.4pmol respectively, despite a more intense signal with the targeted construct visually. The FMT

signal does not appear to be particularly localised to the aortic root, which may relate to relatively poor spatial resolution of the imaging modality or represent true non-specific binding.

4.12.3 Construct organ distribution at 24-hours

Following *in vivo* imaging, the mice were sacrificed, and organs harvested using a dissecting microscope. Identical lengths of aorta, from the extra-cardiac ascending aorta to the iliac bifurcation were dissected and opened en face. All organs were thoroughly washed in PBS prior to quantitative fluorescence imaging with FMT at 680nm.

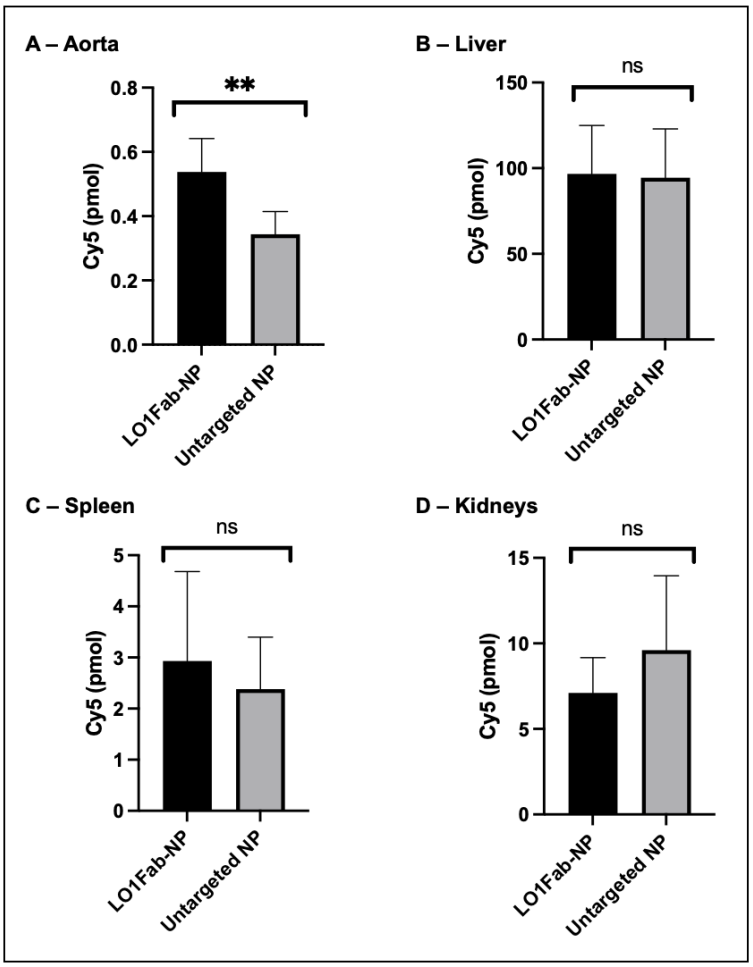

Figure 4-54. Organ distribution of nanoparticle constructs at 24-hours post-injection.

Following sacrifice, organs were extracted, washed in PBS and imaged with FMT at 680nm.
*A) – Aorta, **p=0.0020*
B) – Liver, p=0.9013
C) – Spleen, p=0.5470
D) – Kidneys, p=0.2928
Unpaired t-test with Welch's correction used to assess statistical significance, n=7. Error bars represent SEM.

Figure 4-54 displays the organ-specific fluorescence of aortae, as well as the liver, spleen and kidneys, with n=7 in each group. There was no statistically significant difference between the metabolic organs. Conversely, there was greater aortic fluorescence with the LO1Fab-nanoparticle ([mean ±SD] 0.54±0.10pmol) versus the untargeted nanoparticle (0.34±0.07pmol); p=0.0020. These results were promising, suggesting that there is on-target binding of the targeted nanoparticles in the *in vivo* mouse model, however the magnitude of signal versus the control construct was too small to detect with *in vivo* FMT. To combat this, the injected dose of nanoparticles (and therefore targeting Fab fragment) could be increased; the nanoparticles could be redeveloped to permit greater Fab fragment conjugation or greater Cy5 payload; a more sensitive method of *in vivo* detection could be used, such as PET; or a different imaging timepoint trialled to see if greater on-target signal could be achieved, with a potential trade-off of greater background signal.

4.12.4 In vivo imaging at 4-hours

Of the above options, rather than redevelop and re-optimise the nanoparticle, given that there was binding on *ex vivo* analysis, I elected to trial an earlier imaging timepoint. Of note, both the full LO1 IgG and LO1Fab had shown successful targeting with imaging 4-hours after injection. Therefore, I chose this timepoint, which would also permit construct comparison, if this was necessary in future studies.

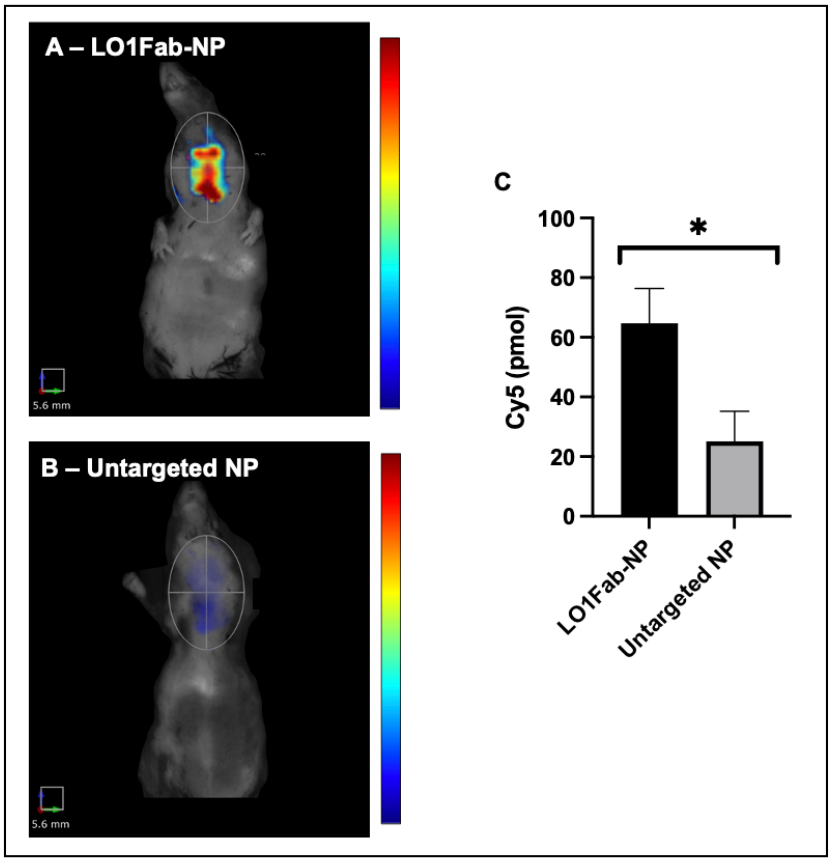

Figure 4-55. In vivo FMT imaging of LO1Fab targeted versus untargeted nanoparticles at 4-hours post-injection.

Representative FMT images at 4-hours post-injection of in vivo injected LO1Fab-NP (A) and untargeted NP (B) in LDL-receptor deficient mice fed a high-fat diet for 40-weeks. Scale bar ranges from blue (0 signal) to red (high signal – 250nM).
*(C) – quantitative analysis of Cy5 signal in the region of interest. Background correction was performed per scan in a blinded fashion. Unpaired t-test with Welch's correction used to assess significance, *p=0.0252, n=7 for each group. Error bars represent SEM.*

The same experimental protocols were carried out as above, with mice intravenously injected with LO1Fab- or untargeted nanoparticles via a tail vein and imaged with FMT using the 680nm channel at 4-hours post-injection. The results are shown in Figure 4-55 above, with example FMT images displaying identical ROIs. There was greater fluorescence signal with LO1Fab-nanoparticles versus the untargeted construct within the individually background-corrected ROIs, (mean ±SD) 64.7±28.7pmol versus 25.2±24.6pmol, respectively, p=0.0252.

4.12.5 Ex vivo imaging at 4-hours

The aortae were extracted as above, and underwent FRI prior to quantitative FMT, both at 680nm, to demonstrate localisation of signal to atherosclerotic lesions (Figure 4-56). Aortae were extracted from mice following injection with both constructs, and were imaged under white light (A), FRI (C) and FMT (D), followed by staining with Oil Red O to highlight atherosclerotic lipidic lesions (B). Fluorescence imaging was performed prior to the addition of Oil Red O, as the stain itself is fluorescent with a large emission spectrum (~576–750 nm) which may interfere with the fluorescence imaging (333).

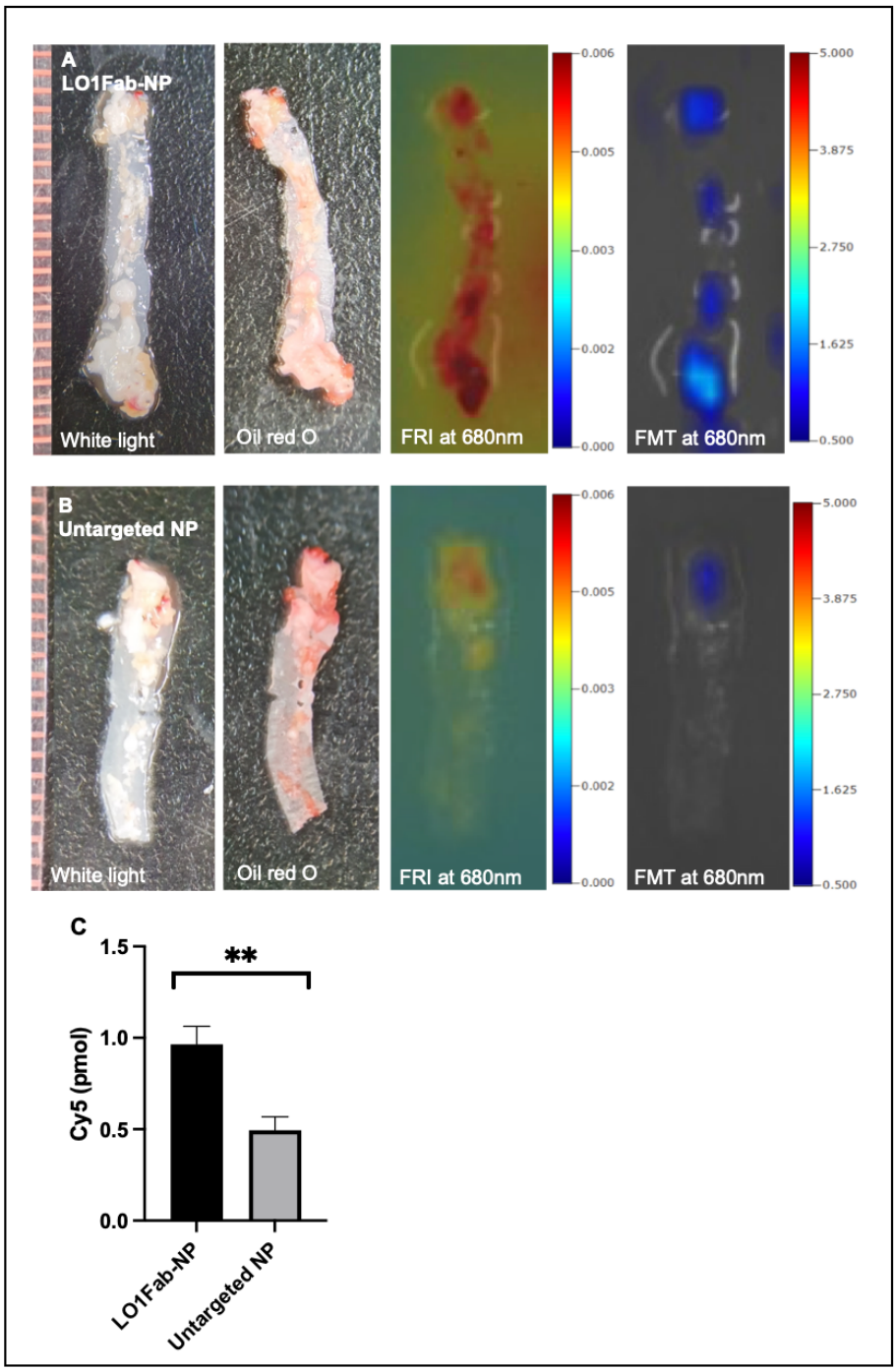

Figure 4-56. Ex vivo fluorescence analysis of aortae from mice injected with LO1Fab-targeted or untargeted nanoparticles.

*Representative extracted aortae from mice injected with LO1Fab-NP (top row, A) and untargeted NP (bottom row, B). Aortae were imaged ex vivo under white light (1st column), after staining with Oil Red O (2nd column), using FRI at 680nm (3rd column) and using FMT at 680nm (4th column). Quantitative analysis of FMT imaging is shown in (C). Unpaired t-test with Welch's correction used to assess significance, **p=0.0027, n=7). Each mark on the scale bar = 1mm. FRI imaging scale bar is in counts/ energy and ranges from blue (low, 0) to red (high, 0.006) signal. FMT imaging scale bar is in Cy5 nM and ranges from blue (low, 0.5) to red (high, 5.0) signal. Error bars represent SEM.*

There is a significant atherosclerotic burden from the aortic root throughout the length of both imaged aortae, as seen with white light and with Oil Red O staining. The FRI and FMT imaging confirm much more intense fluorescent signal with the LO1Fab-nanoparticle, which localises to the atherosclerotic plaques identified in A) and B). There was a significant difference between the LO1Fab and untargeted nanoparticles using the quantitative FMT signal, with 0.96±0.26pmol versus 0.49±0.20 respectively, p=0.0027. These results are very encouraging, determining that the targeted nanoparticles localise to lipid-rich aortic atherosclerotic plaques, which can be detected via both *in vivo* and *ex vivo* imaging techniques.

4.12.6 Construct organ distribution at 4-hours

I next wanted to evaluate the metabolic organ distribution of the nanoparticles, as performed for the 24-hour timepoint experiments. The liver, spleen and kidneys of three injected mice were harvested, washed, and imaged with FMT. There were no significant differences in the organ distribution between the two constructs, as illustrated by Figure 4-57 below.

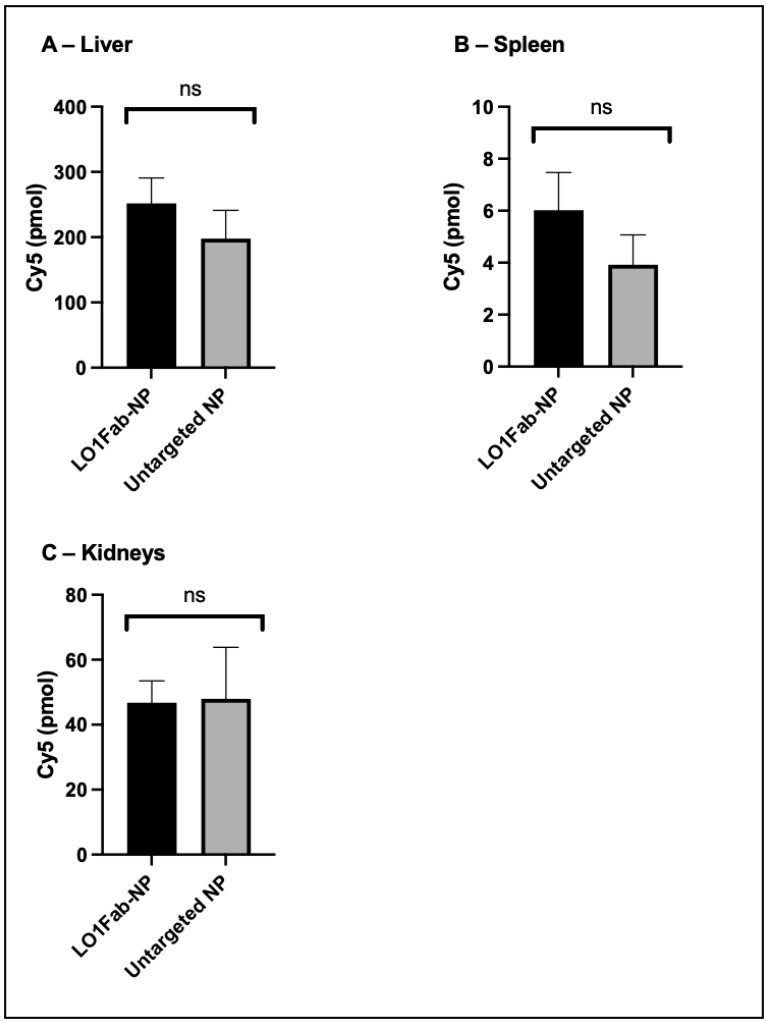

Figure 4-57. Organ distribution of nanoparticle constructs at 4-hours post-injection.

Following sacrifice, organs were extracted, washed in PBS and imaged with FMT at 680nm.
A) – Liver, p=0.4081
B) – Spleen, p=0.3212
C) – Kidneys, p=0.9495
Unpaired t-test with Welch's correction used to assess significance, n=3 for each group. Error bars represent SEM.

Interestingly, the greatest organ uptake for both constructs was seen in the liver, unlike the unconjugated Fab, which has been shown to be primarily detectable in the kidneys at 4-hours after injection (S Pandey's thesis). This is most likely due to construct size of the nanoparticles, being much greater in diameter than the renal clearance threshold (~8nm) (334).

4.12.7 In vivo imaging co-localised with a commercial plaque-targeted NIRF agent

Next, I wanted to co-localise *in vivo* injected LO1Fab-nanoparticles with an alternative NIRF probe that targets atherosclerotic plaque, to provide an *in vivo* imaging marker of atherosclerotic burden, whilst also permitting normalisation of quantitative nanoparticle fluorescence signal within identical ROIs. I also set out to perform hybrid imaging with micro-CT, to enable greater target signal localisation, which is possible given the superior spatial resolution of CT compared to FMT. As such, atherosclerotic mice were co-injected with MMPSense-750FAST. This is a commercially available (PerkinElmer, Massachusetts, USA) NIRF caged probe to detect inflammation that is optically silent on injection, that gets activated through cleavage by endogenous protease activity within MMP-rich environments that include MMPs such as 2, 3, 7, 9, 12, and 13; all of which may be found within the atherosclerotic plaque. Although the optimal imaging timepoints for this agent are 12-24 hours after injection according to the manufacturer, sufficient signal has been detected in prior studies at 4-hours in the Khamis laboratory (174). Moreover, the fluorescence properties of MMPSense-750FAST (excitation 749nm/ emission 775nm) lie outside of the Cy5 fluorescence spectrum, permitting multiplexing with the Cy5 nanoparticles, and is suitable for FMT imaging on the 750nm channel. For this final set of *in vivo* experiments, I compared LO1Fab-nanoparticles to control Fab-nanoparticles for the first time, following the successful development of the antibody-conjugated control nanoparticles, providing the most robust negative control construct.

Mice were injected with MMPSense-750FAST (2nmol, according to the manufacturer's instructions) alongside LO1Fab- or control Fab-nanoparticles (2mg). To maintain within the

acceptable volume of injection limits in mice, nanoparticles were re-sonicated and resuspended in the MMPSense agent, rather than PBS, immediately prior to injection. After 4-hours, mice were anaesthetised and underwent FMT at both the 680nm and 750nm channels, followed by micro-CT (*Section 2.3.8.4 Fluorescence molecular tomography - computerised tomography*).

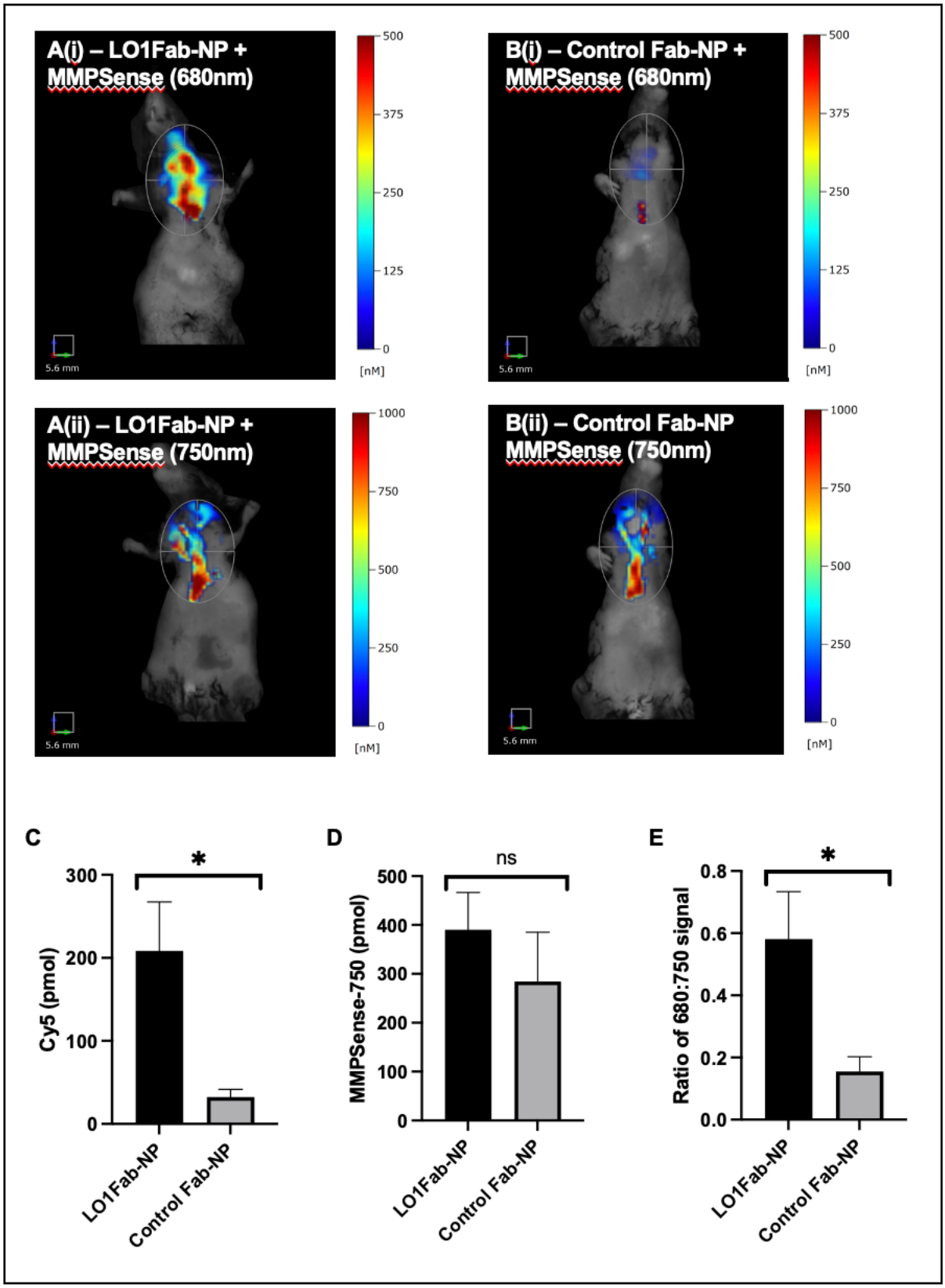

Figure 4-58. In vivo FMT imaging of LO1Fab-conjugated versus control Fab-conjugated nanoparticles, co-injected with MMPSense-750FAST at 4-hours post-injection.

Representative FMT images at 4-hours post-injection of in vivo injected with LO1Fab-NP (A) or control Fab-NP (B) in LDL-receptor deficient mice fed a high-fat diet for 40-weeks, co-injected with MMPSense-750FAST and

fluorescent signal within the region of interest shown. Scale bar for A(i) and B(i) ranges from blue (0 signal) to red (high signal – 500nM). Scale bar for A(ii) and B(ii) ranges from blue (0 signal) to red (high signal – 1,000nM).
A(i)) – LO1Fab-NP + MMPSense750-FAST, imaged at 680nm (Cy5 channel)
A(ii)) – A(i), imaged at 750nm (MMPSense channel)
B(i)) – Control Fab-NP + MMPSense-750FAST, imaged at 680nm (Cy5 channel)
B(ii)) – B(i), imaged at 750nm (MMPSense channel)
*C, D, E) – quantitative analysis of Cy5 nanoparticle signal (C – *p=0.0303), MMPSense-750FAST signal (D – p=0.4244) in the region of interest shown in (A-B), and 680nm (Cy5) signal normalised to 750nm (MMPSense) signal (E – *p=0.0371). Background correction was performed per scan in a blinded fashion. Unpaired t-test with Welch's correction used to assess significance, n=6 for each group. Error bars represent SEM.*

Figure 4-58 above displays representative FMT images obtained following co-injection of nanoparticle constructs and MMPSense-750FAST, using the 680nm and 750nm channels, with identical ROIs shown. A(i) and B(i) display the 680nm channel images with LO1Fab- and control Fab-nanoparticles respectively; whilst A(ii) and B(ii) display the corresponding 750nm channel images with MMPSense. There was much greater Cy5 nanoparticle 680nm signal in the ROI with the targeted construct versus control (208.3±144.5pmol versus 32.4±22.8pmol; n=6; p=0.0303) (C). There was no difference between the MMPSense 750nm signal between the groups of injected mice (p=0.4244) (D). Using identical ROIs, the 680nm nanoparticle signal could be divided by the MMPSense 750nm signal, therefore normalising the experimental nanoparticle signal to a commercially available and previously validated inflammation-specific molecular targeting agent. Accordingly, the difference between LO1Fab- and control Fab-nanoparticles remained (0.58±0.37 versus 0.15±0.12 respectively; p=0.0371) (E).

To better localise the *in vivo* fluorescent signal to internal structures, FMT imaging was fused with micro-CT imaging. The FMT images were reconstructed using TrueQuant 3.0 as above, whilst colocalisation of CT and FMT scans was performed via fiducial markers on the imaging cassette using 'Imalytics Preclinical' image analysis software, utilising a bespoke workflow

algorithm. Example mice injected with each construct is shown in Figure 4-59 below. A) and B) display the 680nm fused FMT-CT images, whilst C) and D) show the corresponding MMPSense 750nm fused FMT-CT images. There is visually much greater 680nm signal with the targeted construct than with control (A, B); whilst the MMPSense signal appears similar between the mice (C, D). It is easy to appreciate the origin of the fluorescence using the cross-sectional images, particularly with MMPSense, with signal predominantly arising from the ascending aorta and common carotid arteries. Conversely, the LO1Fab-nanoparticle is less discretely localised, but does originate in a similar distribution to MMPSense.

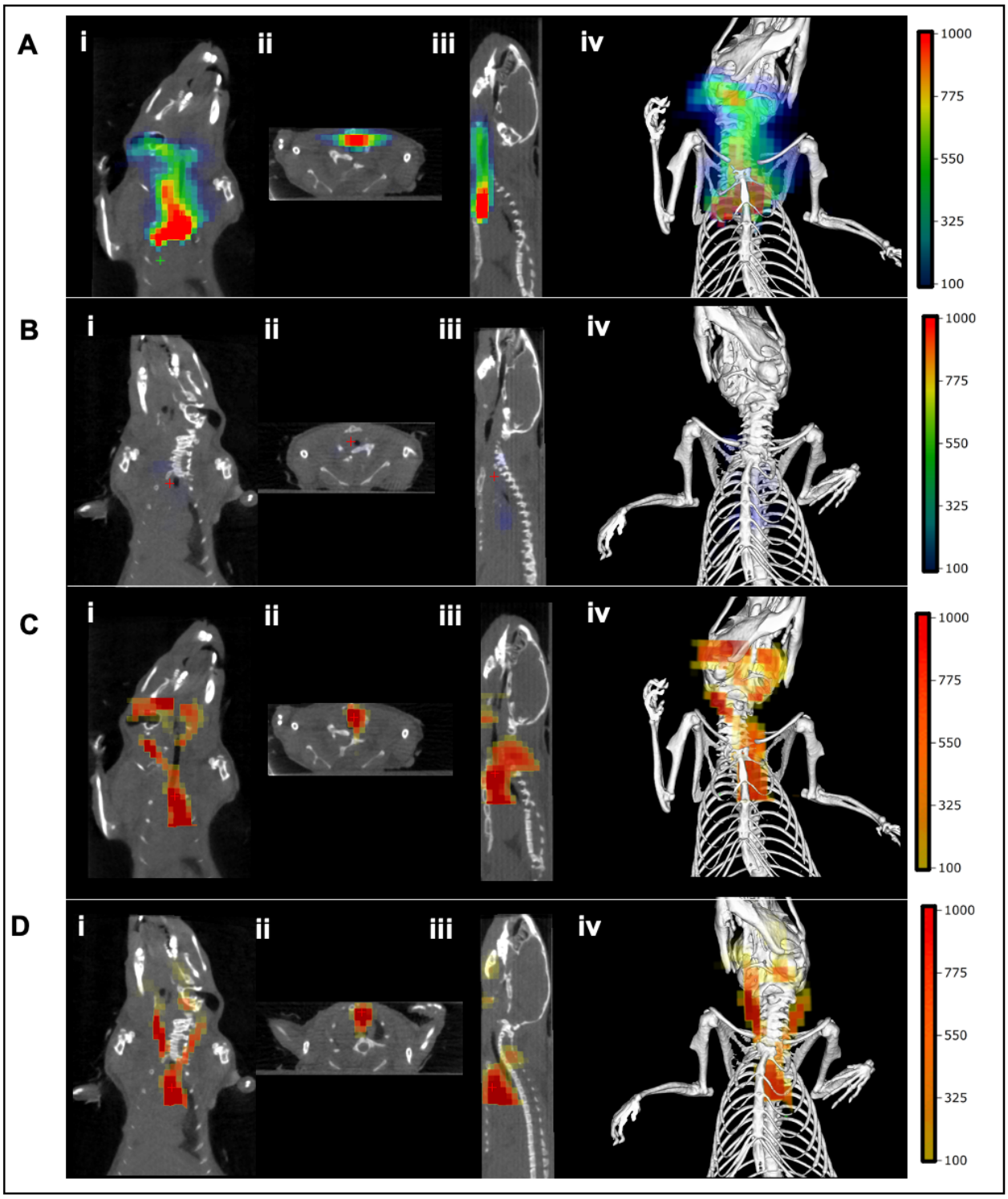

Figure 4-59. In vivo FMT-CT imaging of LO1Fab-conjugated versus control Fab-conjugated nanoparticles, co-injected with MMPSense-750FAST at 4-hours post-injection.

FMT fused with micro-CT imaging at 4-hours post-injection of in vivo injected LO1Fab-NP (A – 680nm, C – 750nm) or control Fab-NP (B – 680nm, D – 750nm) in LDL-receptor deficient mice fed a high-fat diet for 40-weeks, co-injected with MMPSense-750FAST, demonstrating fluorescent signal within the region of interest (ascending aorta and aortic arch vessels). Scale bar ranges from low (100nM) to high (1000nM). Imaging sections (i) – coronal; (ii) – axial; (iii) – sagittal; (iv) – 3D reconstruction.
A) – LO1Fab-NP + MMPSense-750FAST, imaged at 680nm (Cy5 channel)
B) – Control Fab-NP + MMPSense-750FAST, imaged at 680nm (Cy5 channel)

C) – A, imaged at 750nm (MMPSense-750FAST channel)
D) – B, imaged at 750nm (MMPSense-750FAST channel)

4.12.8 Ex vivo imaging co-localised with a commercial plaque-targeted NIRF agent

In a further attempt to demonstrate nanoparticle targeting to atherosclerotic plaque with MMPSense colocalisation, aortae were extracted and underwent FRI and quantitative FMT imaging at 680nm and 750nm channels, as above.

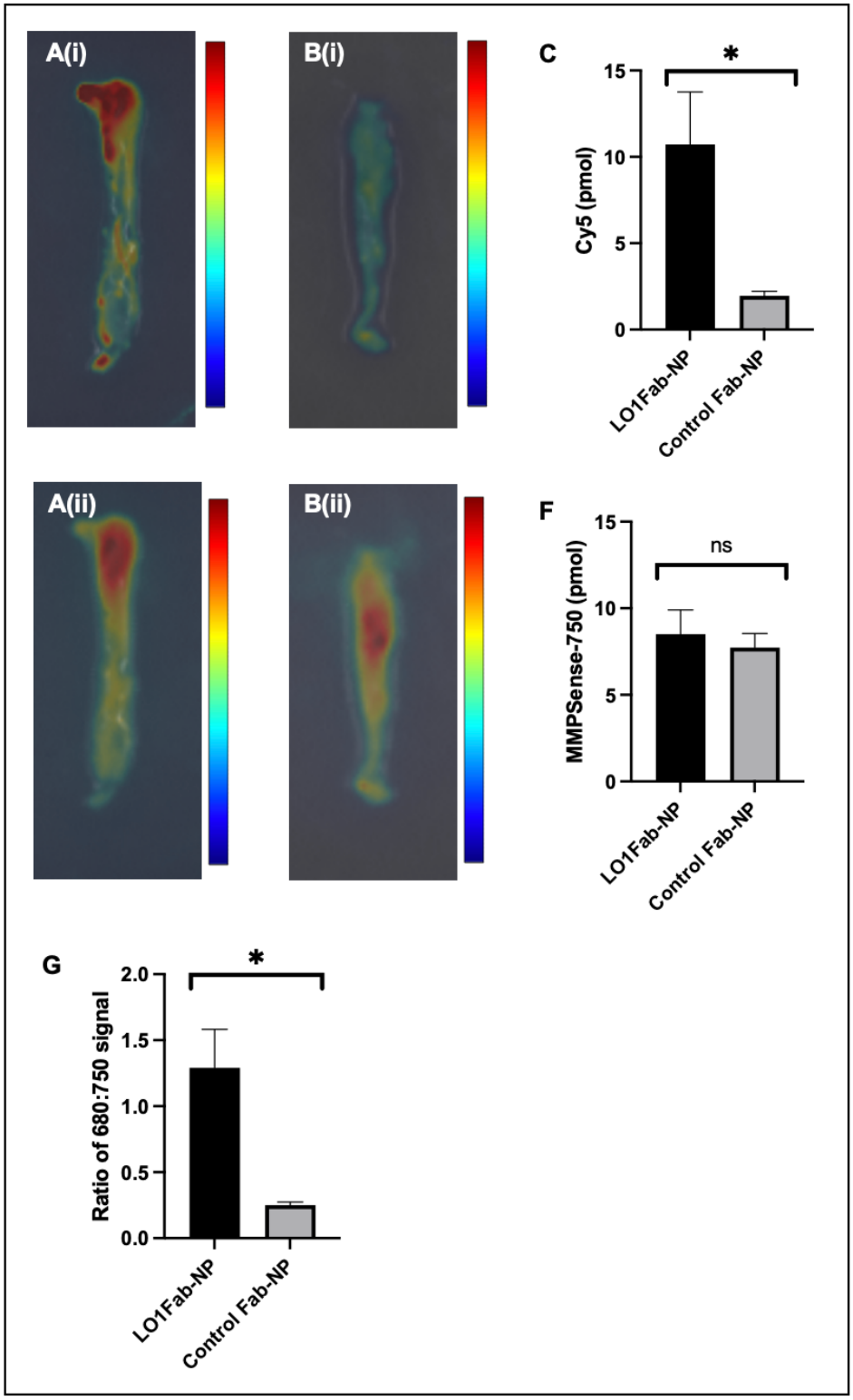

Figure 4-60. FRI and FMT of ex vivo aortae from mice injected with LO1Fab or control Fab conjugated nanoparticles and MMPSense-750FAST.

Following sacrifice, the aortae were extracted, washed in PBS and imaged with FRI and FMT at 680/ 750nm.
A(i)) – FRI of aorta from a mouse injected with LO1Fab-NP + MMPSense-750FAST, imaged at 680nm (Cy5 channel)
A(ii)) – As in A(i), imaged at 750nm (MMPSense channel)

B(i)) – FRI of aorta from a mouse injected with control Fab-NP + MMPSense-750FAST, imaged at 680nm (Cy5 channel)
B(ii)) – As in B(i), imaged at 750nm (MMPSense channel)
Scale bar for all images is in counts/ energy and ranges from blue (low, 0) to red (high, 0.03).
*(C, D, E) – quantitative FMT analysis of Cy5 nanoparticle signal (C – *p=0.0341) and MMPSense-750FAST signal (D – p=0.6487) from the aortae shown in A-B, and 680nm (Cy5) signal normalised to 750nm (MMPSense) signal (E – *p=0.0160).*
Unpaired t-test with Welch's correction used to assess significance, n=6 for each group. Error bars represent SEM.

Figure 4-60 above demonstrates example FRI images, as well as average FMT fluorescent signal per construct, at 680nm in (i) and 750nm in (ii). There was much greater aortic fluorescence with LO1Fab-nanoparticles (A(i)) than with control Fab-nanoparticles (B(i)); 10.7±7.4pmol versus 1.9±0.6pmol respectively; n=6; p=0.0341 (C). There was no difference between MMPSense groups (p=0.6487) (D). The difference between nanoparticle constructs remained when the 680nm was normalised to 750nm, as above (1.29±0.72 versus 0.25±0.06 for targeted and control constructs respectively; p=0.0160) (E).

4.12.9 Fluorescence microscopy of in vivo injected mice

In a final effort to establish atherosclerotic plaque nanoparticle targeting, hearts from injected mice from the experiments above were harvested and aortic root cryosections made. These slides were imaged using confocal microscopy at autofluorescence and Cy5 channels. Unfortunately, there was no 750nm signal identifiable on the sections to permit colocalisation with MMPSense. It is likely that the process of cryosectioning and freezing at -80°C had abolished MMPSense fluorescence, or that the fluorescence intensity had quenched over the time from injection to microscopy. Adjacent slides were stained with Oil Red O and counterstained with haematoxylin and imaged using widefield microscopy, as performed

above. Figures 4-61 (LO1Fab-nanoparticle) and 4-62 (control Fab-nanoparticle) present example images obtained, using the same microscope settings.

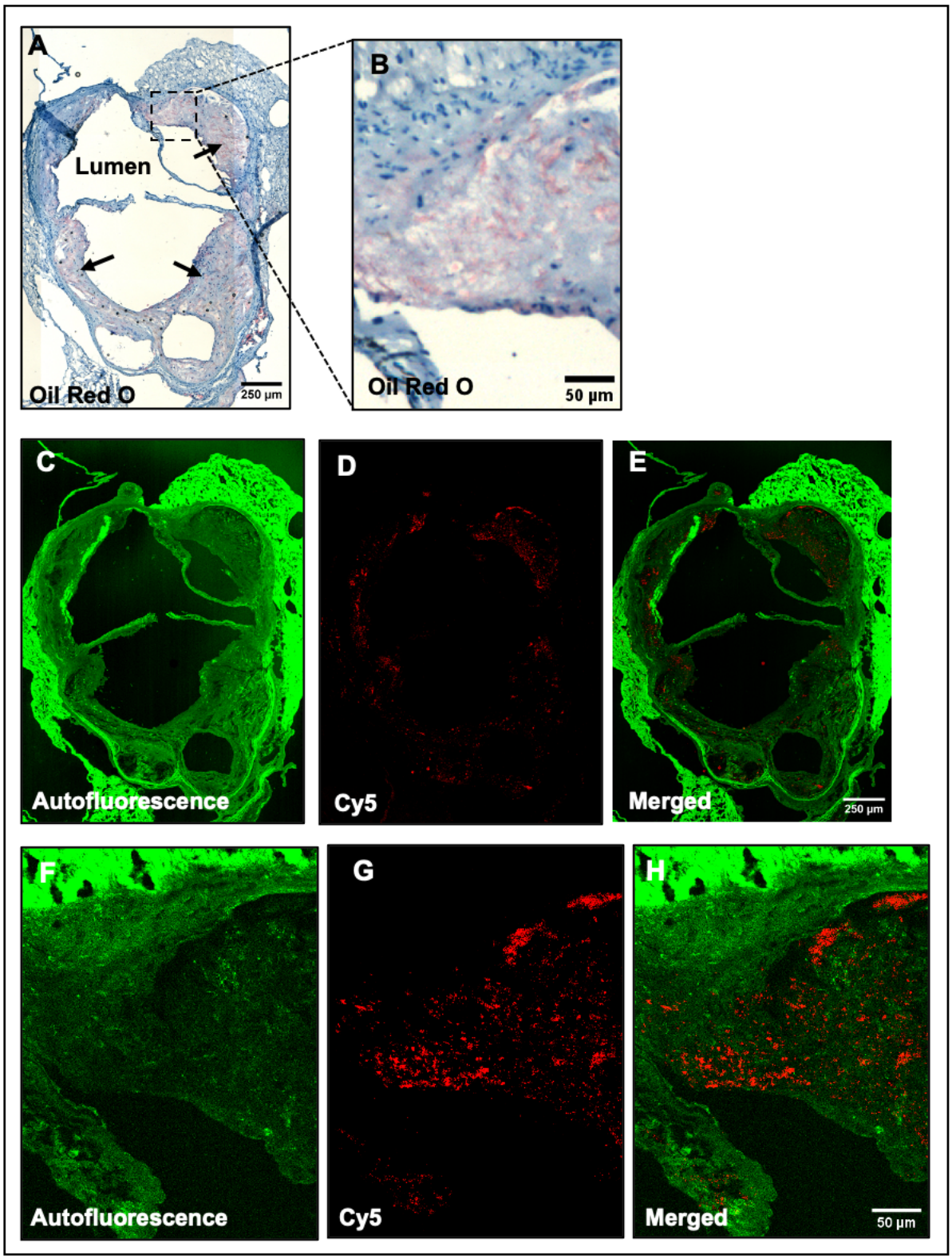

Figure 4-61. Fluorescent confocal microscopy of an aortic root section from a mouse injected in vivo with LO1Fab-targeted nanoparticles.

An LDL-receptor deficient mouse fed a high-fat diet for 40 weeks was injected with LO1Fab-NP and sacrificed via CO2 inhalation with whole-body perfusion fixation. The heart and aortic root were cryosectioned and 5µm adjacent sections were mounted on slides.

(A) – an Oil Red O stained slide imaged using widefield microscopy (10x), demonstrating significant lipidic deposits in the aortic valve cusps (highlighted by arrows) in the aortic root. Scale bar = 250µm.
(B) – a 20x magnified view of the highlighted area in (A), with significant lipidic deposits. Scale bar = 50µm.
(C-E) – a 5µm adjacent aortic root section was imaged using confocal microscopy at 10x magnification. (C – autofluorescence, D – Cy5, E – merged). Scale bar = 250µm for all panels.
(F-H) – a 20x magnified view of the highlighted area in (A), that corresponds to the zoomed area in (B) with significant Oil Red O staining. (F – autofluorescence, G – Cy5, H – merged). Scale bar = 50µm for all panels.

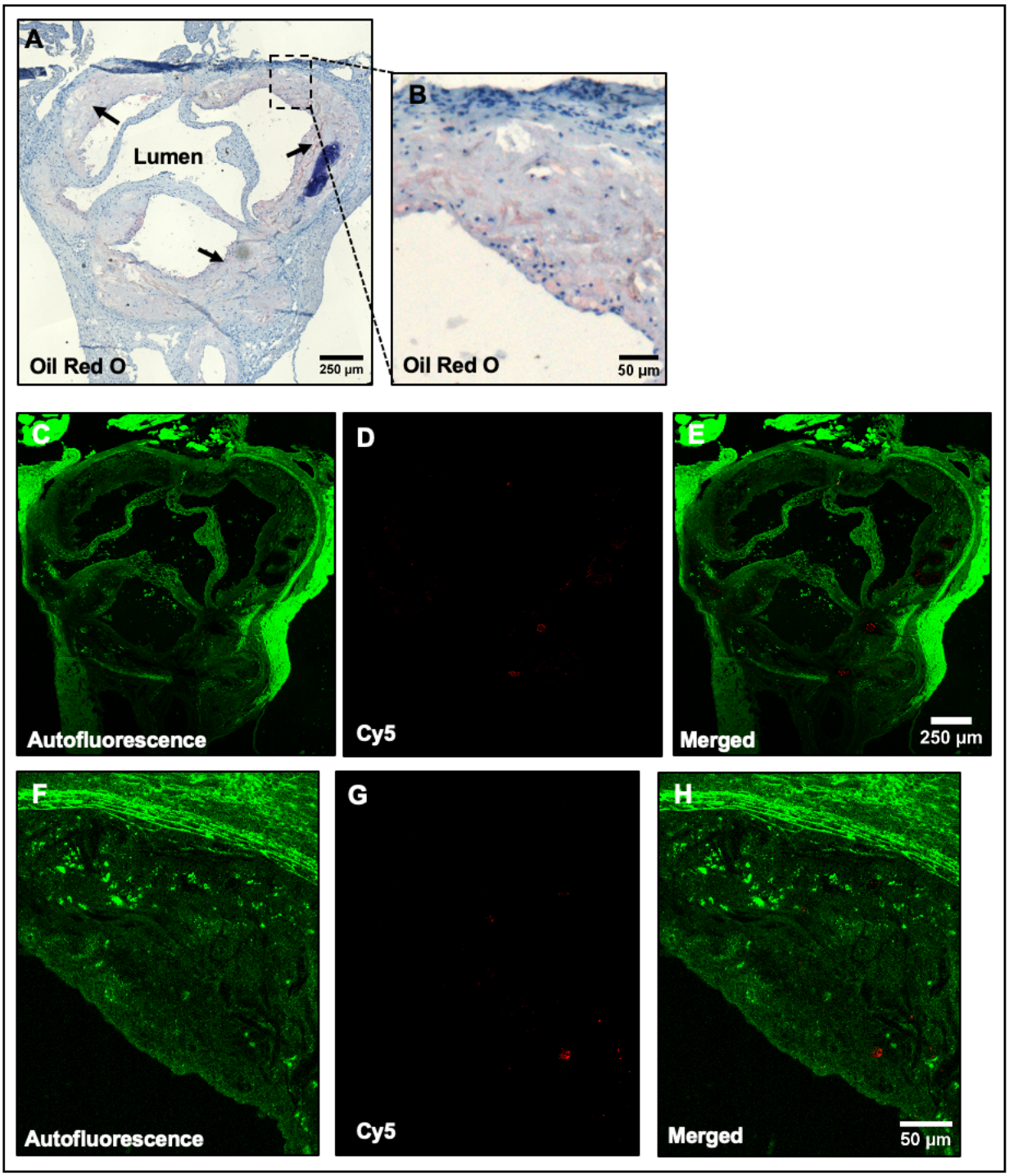

Figure 4-62. Fluorescent confocal microscopy of an aortic root section from a mouse injected in vivo with control Fab-targeted nanoparticles.

An LDL-receptor deficient mouse fed a high-fat diet for 40 weeks was injected with control Fab-NP and sacrificed via CO2 inhalation with whole-body perfusion fixation. The heart and aortic root were cryosectioned and 5µm adjacent sections were mounted on slides.
(A) – an Oil Red O stained slide imaged using widefield microscopy (10x), demonstrating significant lipidic deposits in the aortic valve cusps (highlighted by arrows) in the aortic root. Scale bar = 250µm.
(B) – a 20x magnified view of the highlighted area in (A), with significant lipidic deposits. Scale bar = 50µm.
(C-E) – a 5µm adjacent aortic root section was imaged using confocal microscopy at 10x magnification. (C – autofluorescence, D – Cy5, E – merged). Scale bar = 250µm for all panels.

(F-H) – a 20x magnified view of the highlighted area in (A), that corresponds to the zoomed area in (B) with significant Oil Red O staining. (F – autofluorescence, G – Cy5, H – merged). Scale bar = 50μm for all panels.

Both cryosections were made across the aortic valve and demonstrate marked thickening within the valve cusps, which stain brightly with Oil Red O, confirming the atherosclerotic plaque lipid content. The magnified sections reveal the acellular nature of the highlighted lesions, with little nuclear staining. LO1Fab-nanoparticles localise well to Oil Red O-stained areas on the Cy5 and merged confocal images. On the other hand, there is very little appreciable Cy5 signal within the aortic root of the mouse injected with control Fab-nanoparticle construct.

In summary, the *in vivo* nanoparticle studies have confirmed atherosclerotic plaque targeting of intravenously injected LO1Fab-nanoparticle constructs, which has been demonstrated using *in vivo* hybrid FMT-CT imaging, co-localised with a commercial plaque NIRF agent and validated using *ex vivo* FRI and confocal microscopy.

4.13 Discussion

This chapter has provided the *in vitro* to *in vivo* development of a targeted nanoparticle construct, that has been shown to both bind to oxLDL and localise to atherosclerotic plaque. This has to the potential to be utilised for the clinical imaging of oxLDL contained with atherosclerotic lesions, delivered intravascularly either by intravenous injection to target systemic atherosclerotic lesions, or catheter-directed therapy, delivering nanoparticles more locally to a coronary vascular bed at the time of coronary angiography. The translational importance of this lies in that larger plaque necrotic cores, of which oxidised lipid forms a

significant component, relate to an increased likelihood of plaque vulnerability to rupture, and thus precipitate a myocardial infarction (34). Multiple clinical intravascular imaging studies (*see Table 1.3*) have demonstrated that TCFA, defined as necrotic core with an overlying fibrous cap measuring <65μm (35), relate to MACE at both the lesional and patient level (335). The ability to detect these susceptible plaques, prior to their rupture, will provide the opportunity for aggressive cardiovascular risk factor profile modification with optimised medical therapy and lifestyle adaptations. There is evidence that tackling hypercholesterolaemia with a systemic agent, for example with PCSK9 inhibition, can remodel atherosclerotic lesions to a more stable phenotype. In the randomised PACMAN-AMI trial, 52-weeks of Alirocumab on top of high-potency statin therapy led to plaque regression, lower necrotic core volume and increased fibrous cap thickness (159). Additionally, in the YELLOW III study, 26-weeks of Evolocumab increased fibrous cap thickness from 70.9 to 97.3μm on OCT and the max$LCBI_{4mm}$ decreased from 306.8 to 213.1 on NIRS (both $p<0.001$) (336). However, these agents are injectable and require repeat administration, as well as being expensive and not free of side effects; thus should only be used in those who will benefit the most. Therefore, the ability to appropriately identify these at-risk patients early in their treatment course, prior to significant plaque progression and clinical presentation with MI, would be highly advantageous.

Moving on from the recognition of patients at-risk of plaque rupture and ensuing MI with LO1Fab-nanoparticles, a much more exciting avenue of development will lie in the potential targeted delivery of therapeutic agents directly to the necrotic core of atherosclerotic plaques. In this chapter, a Cy5 imaging cargo has been used within the nanoparticles to demonstrate localisation to areas of interest. However, plans are in place in subsequent research phases

to add a pharmaceutical or molecular agent into the nanoparticle core, and assess for payload delivery, followed by evaluation of therapeutic efficacy. Nanoparticle mediated payload delivery will permit the transport of a small quantity of a potent agent, directly to the necrotic core of vulnerable plaques, negating possible systemic toxicity. Potential agents include low molecular weight compounds, cytokines or nucleic acid constructs. The nature and desired effect of the therapeutic agent in question needs further detailed consideration, but clearly interfering with macrophage oxLDL uptake and foam cell formation, pro-inflammatory signalling or apoptotic pathways, would be expected to exert beneficial effects on the atherosclerotic plaque micro-environment. For example, oxLDL has been demonstrated to prime and activate the NLRP3 inflammasome in atherosclerotic mice, via direct oxLDL-mediated lysosomal damage following internalisation (337). Thus, given the importance of the NLRP3 inflammasome in atherosclerosis, interfering with this pathway via oxLDL targeting agents is a promising research avenue. It would also be interesting to evaluate the delivery of drugs known to beneficially affect ASCVD, such as colchicine or canakinumab, where mechanistic actions at the plaque level could be elucidated, without systemic toxicity. Aside from anti-inflammatories or immunotherapies, other candidate cargo therapeutics would include senolytic agents, affecting plaque cellular senescence and apoptotic processes (338) as well as MMP12 inhibition, via a drug or endogenous metallopeptidase inhibitor TIMP 1 (339), where MMP12 is thought to relate to plaque destabilisation and rupture (340). To help assess these potential nanoparticle cargo agents, this chapter has provided a foam cell assay in which therapeutic efficacy may be assessed at a cellular level, prior to subsequent *in vivo* study.

Further work is still required in the translational development of the targeted nanoparticles for imaging purposes, however. This includes planned experiments, such as switching the current NIR fluorophore, Cy5, to the IRDye 800CW (LI-COR, Nebraska, USA). This dye has been already safely evaluated in humans for tumour imaging following intravenous administration (341) and therefore should shorten translational timelines. The PLGA and PEG polymers used to formulate the nanoparticles have already been clinically translated, whilst the LO1Fab fragment itself has already undergone humanisation. In addition, the fluorescence properties of IRDye 800CW would be more favourable than Cy5 for clinical imaging (excitation 775nm/ emission 792nm), further reducing any tissue/ blood induced autofluorescence. To expedite future nanoparticle development, a bespoke polymer containing IRDye800CW (termed PLGA-IRDye800CW) has been developed with PolySciTech (Lafayette, USA), which is now available for use. As an initial first step in the nanoparticle customisation, constructs will be made containing both PLGA-IRDye800CW and PLGA-Cy5, as well as the PLGA conjugated fluorophores in isolation, followed by testing for function on ELISA and immunohistochemistry. This will allow assessment of whether any loss of signal seen on these *in vitro* experiments is related to the fluorophore itself, or an issue with nanoparticle conjugation.

Ideally, in future construct development, I would aim to assess whether a smaller *in vivo* dose of nanoparticles may be sufficient for plaque targeting. This would serve to reduce the dose required to be administered, saving on material to be injected and therefore associated costs. Experimentally, this could be reasonably easily assessed, with a dose-response quantitative FMT imaging study design. I would also like to explore further nanoparticle optimisation at

the formulation stage, aiming to increase the amount of conjugated LO1Fab and imaging cargo, hopefully without the trade-off of increased particle size.

If time had permitted in this PhD, I would also have performed an atherosclerosis progression-regression *in vivo* study, in an attempt to demonstrate that nanoparticle binding is related to atherosclerotic burden. For example, LDL-$R^{-/-}$ mice could be fed a high-fat diet for ~20 weeks then be switched to chow diet, or maintained on high-fat diet, until the imaging timepoint at ~40 weeks. As a further comparator, LDL-$R^{-/-}$ mice could be fed a chow diet for the entire 40-week period. This would create a murine model with varying levels of atherosclerosis, and could be used to determine the ability of LO1Fab-nanoparticles to differentiate the different atherosclerosis burdens using FMT. These experiments could also be conducted with multiplexing other commercially available plaque reporters, such as IVISense Integrin Receptor, which targets integrin αvβ3, expressed by plaque macrophages (342); IVISense Pan Cathepsin, which targets cathepsin-based protease activity, implicated in extracellular matrix proteolysis and degradation (343); or IVISense Neutrophil Elastase, which targets neutrophil elastase, involved in foam cell formation (344) (all PerkinElmer, Massachusetts, USA). These probes would add to the *in vivo* characterisation of nanoparticle binding, and permit detailed molecular localisation of targeting, especially if confocal microscopy could be successfully performed. Additionally, I would like to perform hybrid FMT-CT during this study, with injection of an iodinated contrast agent during CT acquisition, to better localise fluorescent signal to vascular structures.

Other planned *in vivo* studies include utilising the balloon-injured high-fat fed rabbit model of atherosclerosis, to evaluate nanoparticle function in an alternative animal model. A principal

reason to do this would be able to determine nanoparticle binding using high resolution hybrid catheter-based fluorescence technology, as may be conducted in humans following clinical translation. This will be performed in a research collaboration with Prof Michael Joner and Prof Vasilis Ntziachristos (both Technical University of Munich, Germany). The rabbit model consists of inducing atherosclerosis in male New Zealand White rabbits via balloon injury to the aorta and one iliac artery (with a second iliac artery serving as reference) followed by a 1% high-fat diet for one week and 0.025% high-fat diet for 16 further weeks. I will first determine blood half-life in the atherosclerotic rabbit model by serial ear bleeds 3-4 weeks prior to NIRF imaging. On the last day of the animal study, the nanoparticle construct will be injected intravenously at a time point appropriate to the half-life, prior to aortic cannulation via the femoral artery. Following guide wire placement under radiographic guidance, the novel NIRF-IVUS catheter will be advanced via a guiding catheter over the wire to sites of balloon injury. The multimodality catheter will simultaneously acquire both NIRF and IVUS images during pullback acquisition.

Following data acquisition, the NIRF signal will be calibrated based on IVUS measurement of the distance between the catheter and the artery wall. IVUS, cross-sectional images, two-dimensional NIRF maps and NIRF-IVUS fusion images will be created to visualize the data. IVUS metrics of plaque features will be computed using standardized methodology. We will conduct serial imaging under general anaesthetic and determine both TBR and SNR at optimal time points (at one and two half-lives). As a proof of concept, LO1-750 has been previously injected in a similar model, and imaged with two-dimensional NIRF, with plaque localisation confirmed on *ex vivo* analysis (174). Aside from successfully gaining ethical permissions for the rabbit studies, ongoing preparatory work includes performing

fluorescence microscopy with nanoparticle staining in rabbit atherosclerosis sections, to ensure functional binding in rabbit tissue.

Lastly, I would also like to modify the nanoparticles for PET, rather than fluorescence imaging, by incorporating a radiotracer inside the nanoparticle core, instead of a fluorophore. This will of course come with difficulties regarding radioactive labelling, but may provide a means whereby nanoparticle binding could be evaluated using an imaging modality in current clinical use. If successful, this could shorten pipelines for translation (there are no NIRF-based clinical imaging modalities), as well as permitting the non-invasive assessment of nanoparticle binding. Although whole body approaches will have inherently lower spatial resolution than catheter-based techniques, non-invasive approaches often result in lower costs, improved clinical safety and greater patient acceptance. Experimental plans to modify the nanoparticle for PET, colocalised with CT to improve resolution, using the LDL-$R^{-/-}$ high-fat fed mouse model of atherosclerosis, are in place with our collaborator Prof Jordi Llop (CIC biomaGUNE, San Sebastien, Spain).

4.14 Conclusions

In summary, this chapter has detailed the design, development and translational testing of fluorescent polymeric nanoparticles tagged with a LO1Fab targeting ligand for the specific diagnostic and therapeutic targeting of oxLDL-rich atherosclerotic lesions. Future experimental plans and ongoing nanoparticle optimisation have been discussed.

4.15 Related presentations and publications

4.15.1 Presentations

The work contained within this chapter has been presented at the following meetings:

In vivo targeting of vulnerable atherosclerotic plaque with novel humanised fab-targeted nanoparticles. **Royal Society of Medicine Cardiology President's Prize, London, 2023** (oral presentation)

Three constructs to target oxidised LDL *in vivo*. **Imperial Vulnerable Patient and Plaque Meeting, Valetta, Malta, 2023** (oral presentation)

Molecular imaging of experimental atherosclerosis using anti-oxidised low-density lipoprotein humanised antibody fragment targeted nanoparticles. **Royal Society of Medicine John Glyn Trainee Prize Event, London, UK, 2022** (poster presentation)

In vivo targeting of oxidised-LDL with novel humanised Fab-nanoparticles. **British Atherosclerosis Society, Oxford, UK, 2022** (poster presentation)

In vivo whole-body fluorescence molecular imaging of murine atherosclerosis using anti-oxidised low-density lipoprotein antibody fragment targeted nanoparticles. **National Heart and Lung Institute Away Day, Imperial College London, London, UK, 2022** (oral presentation)

Molecular imaging of experimental atherosclerosis using anti-malondialdehyde-modified low-density lipoprotein humanised antibody fragment targeted nanoparticles. ***European Society of Cardiology, Barcelona, Spain, 2022*** (moderated poster presentation)

Molecular imaging of experimental atherosclerosis using anti-malondialdehyde-modified low-density lipoprotein humanised antibody fragment targeted nanoparticles. ***European Society of Cardiology Basic Science Reception, Barcelona, Spain, 2022*** (poster presentation)

In vivo whole-body fluorescence molecular imaging of experimental atherosclerosis using anti-malondialdehyde-modified low-density lipoprotein humanised antibody fragment targeted nanoparticles. ***British Cardiovascular Society, Manchester, UK, 2022*** (poster presentation)

In vivo whole-body fluorescence molecular imaging of murine atherosclerosis using anti-oxidised low-density lipoprotein antibody fragment targeted nanoparticles. ***European Molecular Imaging Meeting, Thessaloniki,*** **Greece, 2022** (poster presentation)

Molecular targeting of oxidised LDL. ***Imperial Vulnerable Patient and Plaque Meeting, London, UK, 2021*** (oral presentation)

Chapter 5

A novel experimental model of atherosclerosis, the ex vivo pump-perfused amputated human limb model

CHAPTER 5 – A NOVEL EXPERIMENTAL MODEL OF ATHEROSCLEROSIS, THE *EX VIVO* PUMP-PERFUSED AMPUTATED HUMAN LIMB MODEL

5.1 Chapter summary

This chapter details the design, development, and initial proof-of-concept testing of a novel *ex vivo* pump-perfused amputated human limb model of atherosclerosis. The model aims to reduce the reliance on animal studies in preclinical atherosclerosis research, as well as streamlining and improving translational pipelines for molecular targeting agent development.

The experimental model involves the incorporation of a freshly amputated human limb into a novel bypass circuit. This circuit consists of a pulsatile pump that can achieve an output ('cardiac output') which the limb would receive prior to amputation, with a membrane oxygenator, modified from that used in paediatric cardiopulmonary bypass, in series. In parallel, a thermocirculator warms the circulating blood to 37°C. Packed red cells are pumped in a pulsatile fashion around the extracorporeal bypass circuit, perfusing the amputated limb with warmed, oxygenated blood, via a sheath sutured into a proximal artery. Following limb perfusion, blood exits via incised proximal veins, and drains under gravity into the oxygenator reservoir. A bespoke chamber houses the limb, collects the drained venous blood, and permits X-ray fluoroscopy. Limb perfusion is performed within a specially designed catheter laboratory, complete with C-arm for X-ray fluoroscopy, manifold for intra-arterial iodinated contrast injection for angiography and invasive haemodynamics, as well as intravascular imaging with IVUS and OCT. Regular monitoring can be performed via point-of-care blood

gas testing, with appropriate correction of pH, oxygenation, haemoglobin, lactate, and electrolytes.

The model has been successfully performed (n=3), maintaining oxygen saturations >99% for the length of perfusion (up to 6 hours). X-ray angiography, IVUS and OCT have been successfully performed. As a proof-of-principle of molecular targeting, in one limb, indocyanine green, a NIRF probe that localises to atherosclerotic plaque via leaky endothelium, was injected into the bypass circuit (2mg/kg) and left to circulate for 90-minutes. FRI of dissected tissue confirmed uptake in areas of calcific atherosclerotic plaque.

5.2 Introduction

5.2.1 Background

The traditional developmental pipeline of a novel molecular targeting agent, using atherosclerosis as an example, consists of the identification of an unmet clinical need, target discovery through interrogation and modulation of molecular cellular pathways in *in vitro* models, to *in vivo* translation with small animal models (e.g., mice and rats), prior to larger animal models, which are closer to human size and biology (e.g., rabbits and pigs), to demonstrate continued efficacy and absence of toxicity. Finally, following this, clinical studies must be conducted, ranging from small-scale first-in-man to large phase III clinical trials, testing against the current clinical standard. This translational pipeline is clearly fraught with difficulties, with significant dropout of potential agents even after extensive and very promising *in vivo* testing, when a large amount of time, money and research effort will already have been invested. One recent example of failed clinical translation of a novel therapeutic agent in atherosclerosis, after very successful *in vitro* and *in vivo* preclinical studies, is the

lipoprotein-associated-phospholipase A2 inhibitor, darapladib, developed by GSK. Darapladib did not demonstrate any effect on MACE in patients presenting with ACS at 2.5 years of follow-up in addition to current OMT and has now been taken out of development (345), despite previously significantly attenuating atherogenesis in a swine model of atherosclerosis (346). Accordingly, the validity of animal models of atherosclerosis to patients with ASCVD in clinical practice continues to be questioned, as reviewed in *Section 1.6 Experimental modelling of atherosclerosis*, with all models suffering from human translation applicability, cost, and ethical considerations.

5.2.2 Concept of the ex vivo pump-perfused amputated human limb model

The concept behind this novel experimental model is taking an amputated human limb, that would otherwise be incinerated as clinical waste, and incorporating it into a bespoke extra-corporeal perfusion circuit that maintains physiological parameters and facilitates modern clinical and preclinical intravascular imaging techniques, coupled with fluoroscopy. Given that the limbs are amputated on clinical grounds, the vast majority will be lower limbs and have a significant burden of atheroma, with chronic limb ischaemia representing the most common indication for amputation (347). In addition, limbs are amputated with a relatively healthy vascular bed proximal to the incision site to ensure adequate wound healing, which should provide suitable tissue for insertion of an arterial sheath for antegrade perfusion and also allow a comparison with the more heavily diseased distal vascular bed.

The limb will be perfused with warmed and oxygenated packed red cells mixed with balanced crystalloid via a modified oxygenator used in paediatric cardiopulmonary bypass, and a pulsatile pump. The pump will be set to mimic the cardiac output the limb would have received

in situ. Measurement of pH, electrolytes, haemoglobin, lactate and oxygenation will be performed via point-of-care blood gas analysis, with appropriate optimisation to ensure physiological parameters are maintained, as feasible. Maintenance of a physiological environment is desirable to allow the experimental set-up to continue running for a prolonged period without limb decomposition, to assess probe binding and localisation at a timepoint after initial administration, simulating intravenous construct injection. As an example, *ex situ* perfusion of an amputated human upper limb from brain-dead organ donors has been successfully performed for 24-hours (n=5), in an attempt to prolong allograft storage times for transportation and potential transplantation. Using a similar experimental circuit design, neuromuscular electrical stimulation resulted in appropriate contractile responses throughout perfusion and histological examination post-perfusion demonstrated no evidence of myocyte injury (348). The additional innovative aspects of the current proposed design however are the incorporation of a diseased limb into the perfusion system, integrated into an experimental cardiac catheter laboratory, with adaptations to allow the introduction of guiding catheters for angiography, invasive continuous haemodynamic monitoring and intravascular imaging.

Once perfusion is established, an angiogram will be performed with iodinated contrast injected via the side port of the perfusion sheath to identify sites of atherosclerosis. A guiding catheter can then be advanced over a 0.035” J-tipped wire to the area of interest, and a coronary 0.014” guidewire passed into the distal arterial bed. Over-the-wire devices, for example IVUS or OCT intravascular imaging catheters, can then be advanced distal to the sites of interest and imaging runs performed under manual or automated pullback. Using these techniques, co-registered with angiography, will permit the multi-modality evaluation of atherosclerotic lesions, which is becoming routine clinical interventional cardiology practice.

Following injection of a targeted probe of experimental interest into either the perfusate reservoir post-limb (imitating intravenous systemic injection) or intra-arterially via the sheath/ guiding catheter pre-limb (imitating catheter-based localised injection), the agent would be allowed to circulate within the closed loop circuit for a desired period. Next, repeat intravascular imaging could then be performed, depending on the imaging required for probe detection, for example fluoroscopy for iodinated agents or IVUS for microbubble-based agents. However, more innovatively, the possibility of using a hybrid NIRF-OCT (111), NIRF-IVUS (349) or even NIRF-IVUS-OCT (114) catheter is very exciting, permitting the *ex situ* colocalisation of novel developmental fluorescent molecular targeting agents with well anatomically characterised atherosclerotic lesions. To further aid in probe validation after finishing perfusion, vascular tissue can be dissected and repeat imaging runs performed. Following this, the lumen can then be opened en face and further imaging performed, with either a fluorescence scanner or cryosections made and fluorescence microscopy performed, colocalised with atherosclerotic plaque components using appropriate cellular stains.

5.2.3 Aims of the ex vivo pump-perfused amputated human limb model

This novel experimental model aims to reduce the reliance on animals for preclinical atherosclerosis research, in line with the NC3Rs requirements to develop and optimise animal research in the UK. This model would constitute a significant replacement step in the NC3Rs framework. Aside from purely reducing our reliance on animal studies, this novel experimental model also aims to reduce the time, money and research efforts required for the development of novel molecular targeting agents, thus streamlining and improving translational processes. For example, in Chapter 4 of this thesis, I have described the development of a novel targeted nanoparticle for imaging and therapeutics of atherosclerosis.

Great effort went into demonstrating retained molecular targeting using a range of tissues *ex vivo*, followed by *in vivo* murine studies, with further studies in rabbits planned. If this model had been available during nanoparticle development, much of the small animal studies and planned rabbit studies may have been able to be reduced. For example, the rabbit studies are planned to provide 1), verification of successful molecular targeting in another animal species, and 2), an experimental model that permits the use of intravascular imaging techniques similar to those used clinically in cardiac catheterisation laboratories, given the similar dimensions and disease processes of balloon-injured rabbit iliac and human coronary arteries. Moreover, as the tissue is of human origin, if successful molecular targeting could be demonstrated, this may be able to shorten clinical translation further. Advantages would be similar to that which may be achieved with perfusion of isolated cadaveric human coronary arteries, but perhaps with shorter ischaemic times (350).

5.3 Ethical permission

Ethical permission for the collection of, and research on, human clinical tissue for this study was granted by the Imperial College Healthcare Tissue Bank (REC Wales 17/WA/0161), as a formal subcollection (CAR_RK_17_070). No additional clinical samples were required or obtained for this study.

Patients were approached to donate tissue to the study following screening by the referring vascular surgical team and routine clinical pre-amputation counselling, arranged from pre-operative clinic. All participants received the appropriate patient information leaflet for use of leftover tissue for research purposes, as per the Imperial College Healthcare Tissue Bank,

prior to the consenting process. All patients provided written informed consent for tissue collection at the time of consenting for the operation.

5.4 The ex vivo pump-perfused amputated human limb model

5.4.1 Ex situ perfusion system

A custom-made radiolucent operating table was designed that incorporated a decline and funnel to facilitate venous blood return back into the bypass circuit. The funnel was connected via ¼'' tubing (Tygon Tubing – Harvard Apparatus, Cambridge, UK) to the venous inlet of a modified oxygenator with integrated arterial filter (CAPIOX Baby FX05RW – Terumo, Surrey, UK), allowing the venous reservoir to fill passively under gravity. The arterial filter served to remove any clots or debris generated within the perfusion system. The reservoir outlet was connected to the inlet of a pulsatile blood pump, with ball valves and smooth flow to minimise haemolysis (55-3321 pulsatile blood pump for dogs/ monkeys – Harvard Apparatus, Cambridge, UK), through a ¼''-½'' adapter (Harvard Apparatus, Cambridge, UK) and ½'' tubing. The pump outlet was connected through a ½''-¼'' adapter to ¼'' tubing back to the arterial inlet of the oxygenator. The oxygenator was supplied with a sweep gas of 40% oxygen: air mixture via ¼'' tubing. A parallel circuit supplying warmed water to the oxygenator at 37°C was set up using a thermocirculator (TC120 – Grant Instruments, Cambridge, UK), connected via ½'' tubing. The arterial outlet port of the oxygenator was connected via ¼'' tubing to one arm of a Y-connector (Harvard Apparatus, Cambridge, UK). Further ¼'' tubing incorporating a femoral sheath (9French Input Introducer Sheath – Medtronic, Dublin, Ireland) was connected to the other arm. The Y-connecter was then joined via further ¼'' tubing to a femoral arterial cannula (EOPA Elongated One-Piece Arterial cannula – Medtronic, Dublin, Ireland), supplying the amputated limb with warmed and oxygenated

perfusate. Figure 5-1 below provides a schematic representation of the limb circuit. Figure 5-2 is an annotated photograph of the limb model during use, with water used as perfusate in this example.

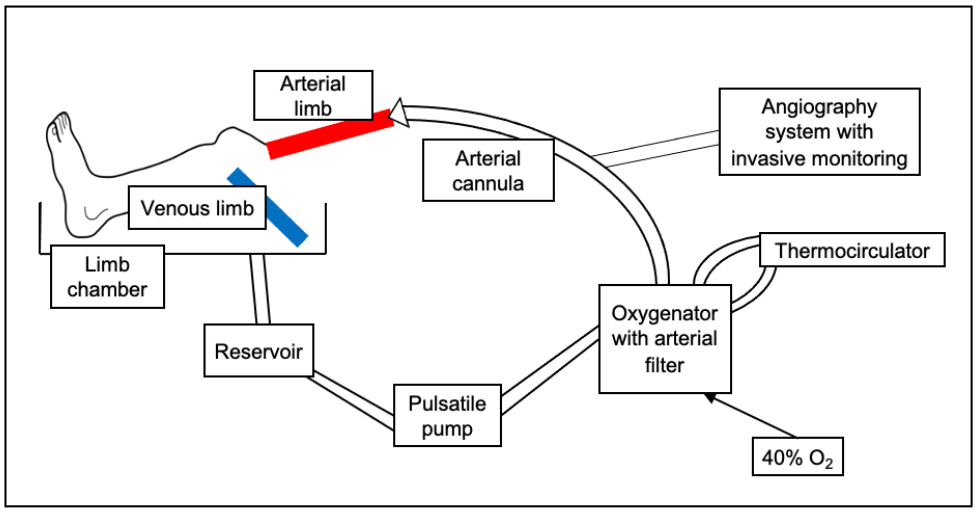

Figure 5-1. Schematic representation of the ex vivo pump-perfused amputated human limb model.

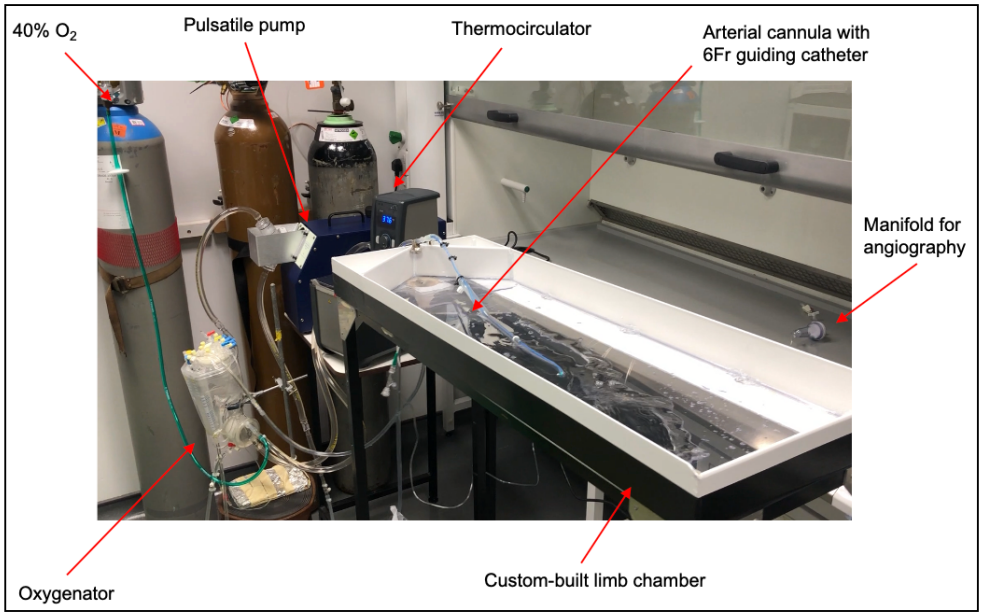

Figure 5-2. Annotated photograph of the ex vivo pump-perfused amputated human limb model.

5.4.2 Limb procurement

All patients undergoing elective planned limb amputations were eligible to donate tissue to the study. Prior to collecting tissue however, the patients were required to receive negative screening tests for potential infectious blood-borne viruses, including human immunodeficiency virus, as well as Covid-19, as was routine pre-operative practice, to reduce the risk of infectious transmission. In addition, selection of patients undergoing above-knee, rather than below-knee, amputations were prioritised given the inherent larger proximal vessel calibre (and thus easier subsequent experimental perfusion), although no limbs were declined on this basis. Suitability of limbs for subsequent perfusion was also assessed by the vascular surgical team, prior to referral to the research team. Of note, the concept of utilising their amputated limb for medical research was generally very acceptable to prospective donors, given that it would be otherwise incinerated.

Limbs were collected immediately from vascular operating theatre and flushed with heparinised saline to remove clots and prevent *in situ* thrombosis. Ligatures were tied around the main proximal artery that would be used for antegrade perfusion, as well as the large proximal veins for outflow, locking the heparinised saline within the vascular bed. The limbs were wrapped in insulating material and placed adjacent to cold ice packs within an insulation box. Limbs were then transported expediently to the perfusion circuit, limiting cold ischaemic time as much as feasible.

5.4.3 Limb perfusion

Firstly, the arterial cannula was sutured into the femoral/ popliteal artery (depending on length of resection), and corresponding veins incised to facilitate venous return. Following establishment of the perfusion circuit, the limb was flushed via the pulsatile pump with heparinised saline to remove any *in situ* clot. The system was then drained to remove the saline wash and exchanged for perfusate. The perfusate comprised either expired clinical-grade or research-grade packed red cells (which was not necessarily group-matched to the limb donor owing to limited availability; Non-Clinical Issue National Health Service Blood and Transplant Service, Colindale, UK) and balanced crystalloid (Plasma-Lyte 148 [pH 7.4] – Baxter, Berkshire, UK) in a 1:1 ratio. Packed red cells were used for their oxygen carrying capacity, rather than an acellular perfusate. Sodium heparin was added to the perfusate, at a concentration of 3,000 units/kg in 0.9% sodium chloride, to limit haemostasis. The pump was set at 60 systole % / 40 diastole % (to equate to an approximated clinical blood pressure) and at a pump output of 15mL per stroke (to represent approximately 10% of clinical stroke volume), with an average pump rate of 70 per minute (equating to a heart rate of 70 beats per minute). Thus, total pump output, or 'cardiac output' to the limb was estimated at 1,050mL/min. Circuit flow (mL/min) was approximated to 6% to 10% of donor estimated cardiac output (pulse pressure/ [(systolic blood pressure + diastolic blood pressure) * heart rate]), which is an approximation of the blood flow a leg would receive *in vivo*. Pump output and settings were adjusted according to the clinical parameters of the donor patient prior to anaesthetic induction for the amputation, using the formula above.

Monitoring for satisfactory limb perfusion was performed using continuous pulse oximetry (AVAX – Contec Medical Systems, China); hourly peripheral temperature of the skin on the

sole (TempIR, USA); and post-limb perfusate testing every hour for pH, oxygen saturation, lactate, glucose, bicarbonate, sodium, potassium, and haemoglobin concentrations (GEM 4000 – Werfen UK, Cheshire, UK). The perfusate was adjusted according to these parameters with sodium chloride containing 40mmol potassium, 1.26% sodium bicarbonate and 10% dextrose in solution as required, aiming for physiological electrolyte normal ranges. Haemoglobin concentration was targeted at 40-60g/L, with further packed red cells/ crystalloid added as needed. This haemoglobin target range was based on prior studies with upper limb perfusion, where this lower than physiologic level resulted in less vascular congestion (348). Oxygen saturations were targeted at >99%. In addition, continuous haemodynamic monitoring was performed using a S/5 Compact Anaesthesia Monitor with beat-to-beat invasive blood pressure, heart rate and oxygen saturation modules (M-ESTR module) (Datex-Ohmeda, Wisconsin, USA).

5.4.4 Imaging

Interventional cardiac guide catheters (for example, a 6French multipurpose MB1 Launcher guiding catheter [Medtronic, Dublin, Ireland]) were introduced over a J-tipped 0.035” wire to the artery of study and connected to a 3-port standard angiography manifold, that permits injection of iodinated contrast and invasive monitoring. Omnipaque 300 (GE Healthcare, Illinois, USA) was used as the contrast agent for angiographic studies. X-ray fluoroscopy was performed using a portable C-arm (Fluoroscan Insite FD Mini C-arm Extremities Imaging System – Hologic, Manchester, UK). Following this, 0.014” coronary guidewires, such as a Runthrough NS Extra Floppy (Terumo, Tokyo, Japan), could be manipulated to the distal arterial bed using conventional interventional techniques. Over this wire, intravascular imaging catheters could be passed distal to the area of interest and manual/automated

pullback performed. Readily available imaging systems included IVUS (Volcano Eagle Eye Platinum – Philips, Amsterdam, Netherlands) and OCT (Dragonfly Optis – Abbott Cardiovascular, Illinois, USA). IVUS was performed with manual pullback at a rate of 1mm/ second, whilst OCT was performed with an automated pullback of 20mm/second. Further imaging catheters or devices could be used to interrogate atherosclerotic plaques, as per experimental protocols.

5.5 Experimental progress

The limb perfusion circuit has been successfully set up and run with three limbs to date. This number is unfortunately considerably lower than is desirable and had been expected prior to commencement. The reasons for this are multifactorial, but in no small part is due to the restrictions on elective operations within the National Health Service, as well clinical research, imposed by the Covid-19 outbreak. The knock-on effect of reduced elective operating activity and intensive care recovery beds has extended past the national lockdown periods and has significantly reduced experimental limb availability. In addition, owing to the multiple comorbidities of patients with significant peripheral vascular disease, unfortunately it is possible that prospective patients could have become critically unwell with Covid-19 infections. Moreover, the direct effect of Covid-19-induced hypercoagulability may have resulted in more acute limb ischaemia, requiring emergency intervention (351), further reducing experimental limb availability. As detailed above, tissue from patients infected with Covid-19 was not possible to collect, and the requirement for fresh packed red cells meant that advanced planning was needed; which was not possible with emergency procedures.

Nonetheless, the limb model has been successfully established. The average cold ischaemic time, (the time taken from amputation to initiation of blood perfusion), was 40-minutes. This length of time is sub-optimal, but reducing this was difficult owing to the time necessary for limb transportation from vascular theatre to the experimental catheter laboratory. Figure 5-3 below displays the model during perfusion of an above-knee amputation.

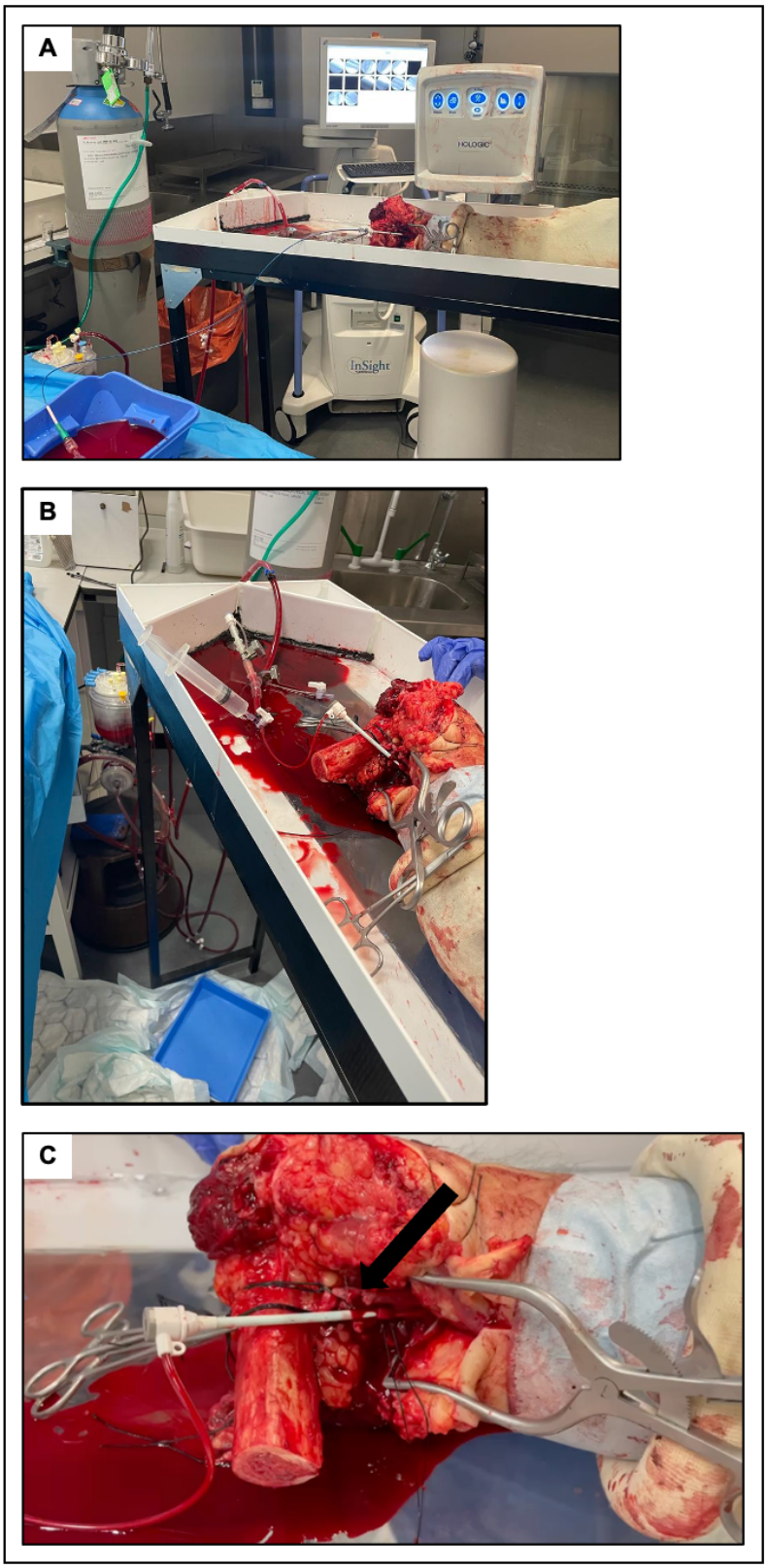

Figure 5-3. The amputated human limb model.

A) – an overview of the model set-up, with fluoroscopic C-arm, oxygen supply and limb chamber demonstrated.
B) – perfusion of the limb, with a 9French sheath sutured into the popliteal artery.
C) – a close-up image of the perfusing sheath inside the popliteal artery, demonstrating passive outflow from the incised popliteal vein directly above the inflow sheath (black arrow).

5.6 Maintenance within physiological parameters

As detailed above, I aimed to maintain the limb environment within physiological parameters, within the remits of what was achievable in an *ex situ* atherosclerotic amputated limb. Figure 5-4 displays physiological parameters that were assessed over the course of one experimental limb model set-up, with 5 hours of perfusion.

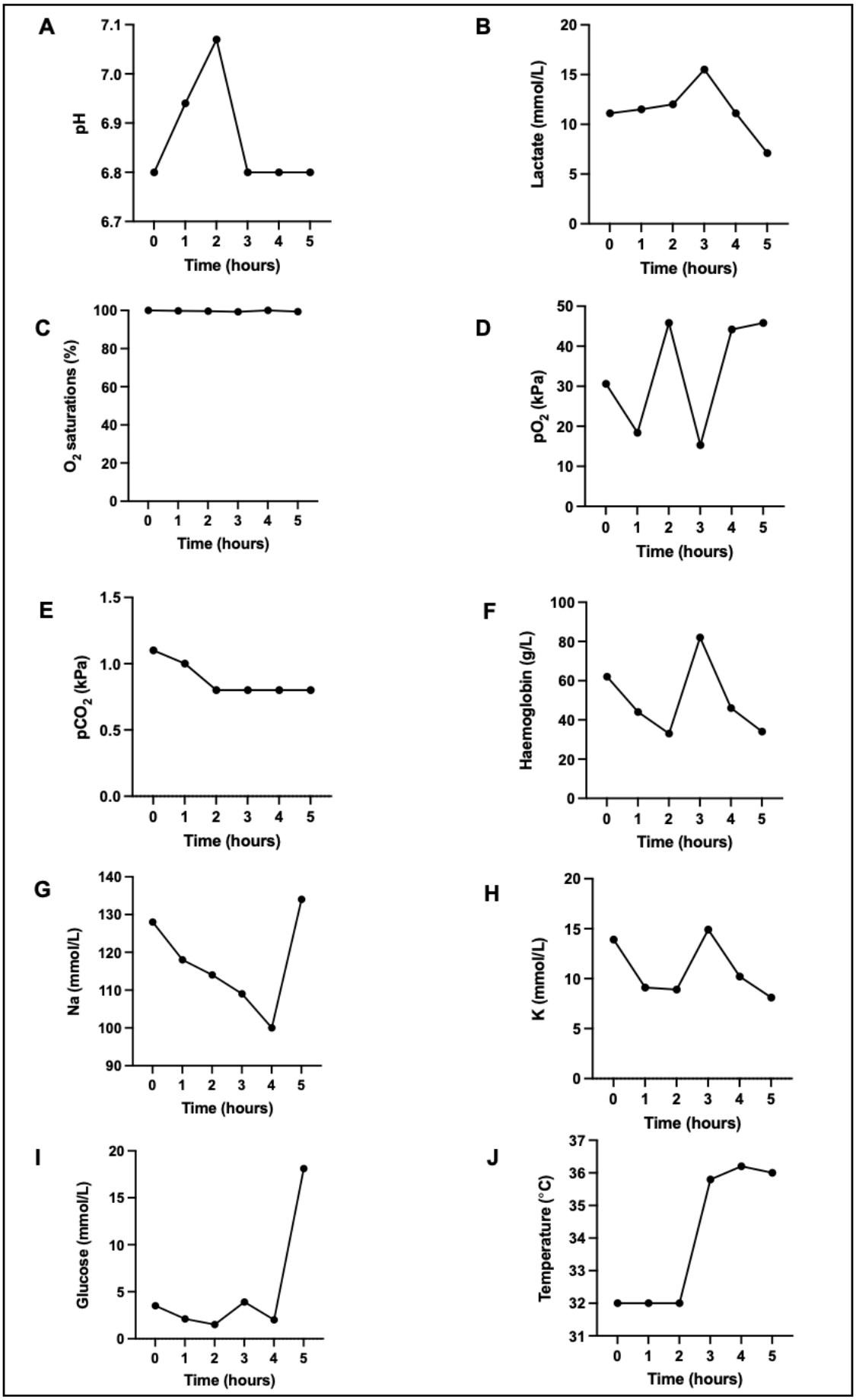
A
pH
7.1
7.0
6.9
6.8
6.7
0 1 2 3 4 5
Time (hours)
B
Lactate (mmol/L)
20
15
10
5
0
0 1 2 3 4 5
Time (hours)
C
O_2 saturations (%)
100
80
60
40
20
0
0 1 2 3 4 5
Time (hours)
D
pO_2 (kPa)
50
40
30
20
10
0
0 1 2 3 4 5
Time (hours)
E
pCO_2 (kPa)
1.5
1.0
0.5
0.0
0 1 2 3 4 5
Time (hours)
F
Haemoglobin (g/L)
100
80
60
40
20
0
0 1 2 3 4 5
Time (hours)
G
Na (mmol/L)
140
130
120
110
100
90
0 1 2 3 4 5
Time (hours)
H
K (mmol/L)
20
15
10
5
0
0 1 2 3 4 5
Time (hours)
I
Glucose (mmol/L)
20
15
10
5
0
0 1 2 3 4 5
Time (hours)
J
Temperature (°C)
37
36
35
34
33
32
31
0 1 2 3 4 5
Time (hours)

Figure 5-4. Physiological parameters measured during one limb perfusion experiment.

A) – pH
B) – lactate (mmol/L)
C) – oxygen saturations (%)
D) – partial pressure of oxygen (kPa)
E) – partial pressure of carbon dioxide (kPa)
F) – haemoglobin (g/L)
G) – sodium (mmol/L)
H) – potassium (mmol/L)
I) – glucose (mmol/L)
J) – temperature (°C)

As can be seen in Figure 5-4, gas exchange was very good through the oxygenator, especially bearing in mind that the blood gas samples were obtained post-limb from the reservoir (akin to venous blood). The partial pressure of oxygen was >15kPa throughout, varying as I altered the sweep gas oxygen rate, maintaining oxygen saturations >99% for the entirety of perfusion. In addition, carbon dioxide levels were very low at <1.5kPa. Haemoglobin stayed around the target range of 40-60g/L throughout. The skin temperature of the limb did take a significant length of time to rise towards normothermia, likely due to the prolonged cold ischaemic time on ice packs during transit pre-perfusion. Unfortunately, despite exchanging blood volume with fresh crystalloid and packed red cells, it was not possible during this experiment to generate a non-acidotic pH or suppress the lactataemia. This is likely a result of a degree of muscle breakdown and anaerobic respiration of the amputated limb tissue, as well as the lower pH and raised lactate concentration of stored packed red cells (352).

Achieving physiological levels of sodium, potassium and glucose was difficult, possibly due to the large swings in electrolyte/ glucose levels induced by the addition of large volumes of crystalloids within a smaller circulating volume (the circuit volume is approximately 2L,

compared to 5L in an adult male). The need for more fine-tuned adjustments of the electrolyte and glucose concentrations is required in future experiments. Using glucose as an example, a very large jump in glucose concentration is seen at 5-hours, due to blood sampling occurring soon after the administration of 10% dextrose solution. Transfusion-related hyperkalaemia is a well identified phenomenon, especially with blood that has been stored for longer periods, due to reduced cellular function and potassium leakage into the extracellular space (353). The red cells used in this experiment will have been stored for a prolonged period prior to use, and thus will carry a significant potassium load. Moreover, as above, given the smaller circulating volume of the limb circuit, any changes in electrolyte levels are magnified. Indeed, transfusion-related hyperkalaemia has been noted to be more problematic in neonatal and paediatric populations (354). In an attempt to combat hyperkalaemia in the future, insulin could be administered, to drive potassium into the cells down the large concentration gradient.

5.7 Angiography

Following the establishment of limb perfusion, the first imaging step was to perform angiography, using the fluoroscopic C-arm and iodinated contrast. This served to confirm successful cannulation of a proximal limb artery as well as identifying any target areas of atherosclerosis for further study (which all the limbs will have, owing to their need for amputation) and providing a roadmap for wiring of the vessel with a coronary guidewire.

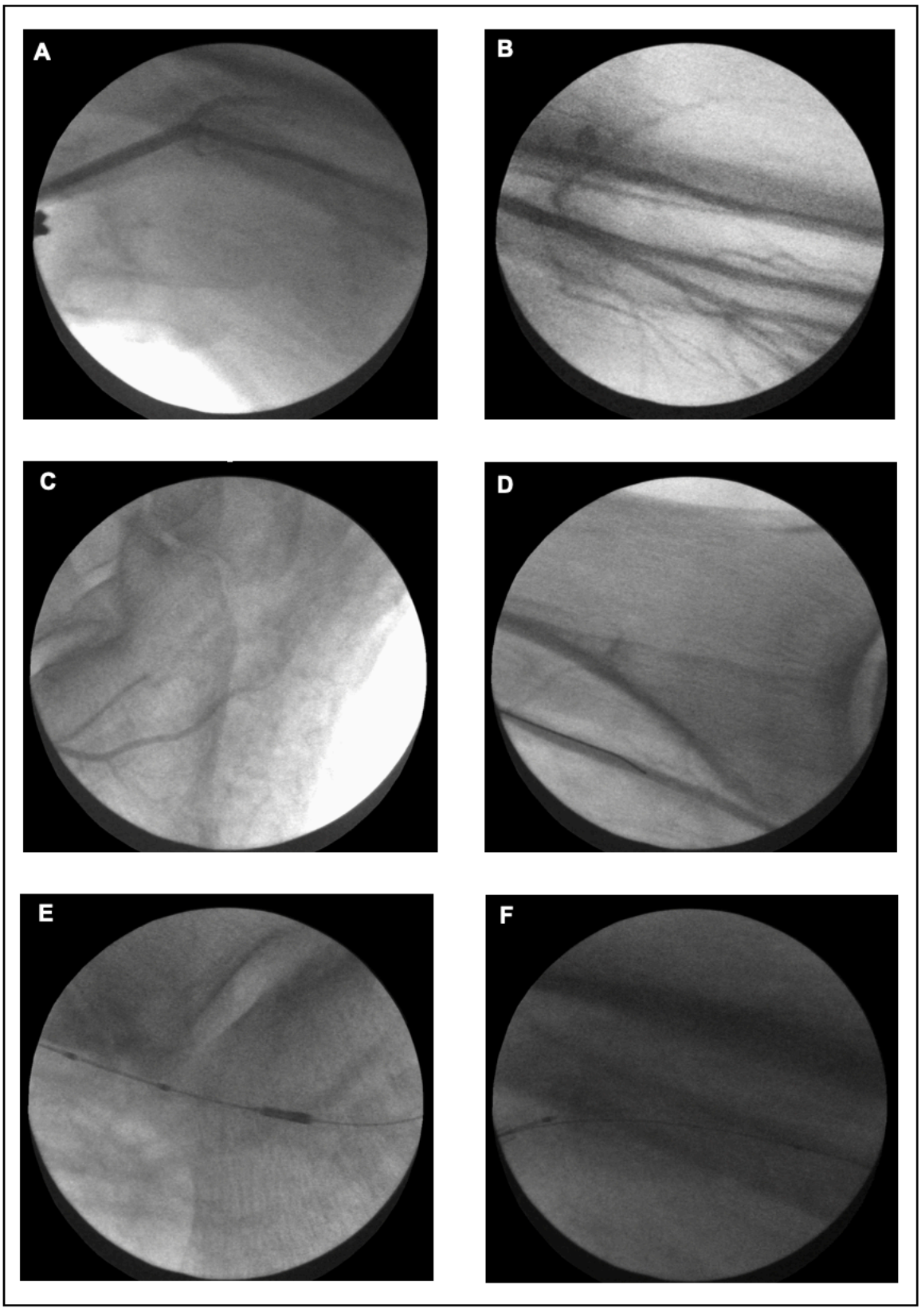

Figure 5-5. Angiography of the amputated human limb model.

A) – Perfusion of an above knee amputation via the popliteal artery, with an angiogram taken in posterior-anterior projection with the injection of iodinated contrast (Omnipaque 300, GE Healthcare, Illinois, USA) through a 6French multipurpose guiding catheter (MB1 Launcher, Medtronic, Ireland) at knee level.
B) – angiogram at the below knee level, demonstrating the anterior tibial artery (top), tibioperoneal trunk (bottom left) bifurcating into the posterior tibial and peroneal arteries.
C) – angiogram at the level of the foot, demonstrating the medial (top) and lateral (bottom) plantar arteries, arising from the posterior tibial artery.
D) – a coronary 0.014" guidewire (ChoICE PT Extra Support, Boston Scientific, Massachusetts, USA) was advanced within posterior tibial artery to level of ankle.
E) – an intravascular ultrasound catheter (Volcano Eagle Eye Platinum – Philips, Amsterdam, Netherlands) was advanced to level of ankle within the posterior tibial artery
F) – an optical coherence tomography catheter (Dragonfly Optis – Abbott Cardiovascular, Illinois, USA) was advanced to the proximal posterior tibial artery

Figure 5-5 above provides fluoroscopic still frames obtained during cine imaging in the posterior-anterior projection of one limb experiment. An angiogram performed via the guiding catheter demonstrates successful intubation of the popliteal artery at knee-level (A); just distal to the popliteal trifurcation below the knee, with anterior tibial, posterior tibial and peroneal branches shown (B); at foot-level with plantar arterial branches of the posterior tibial artery demonstrated (C). Interestingly, there were no significant obstructive angiographic stenoses identified during this study. On review of the pre-operative ultrasound doppler study, there was a significant popliteal stenosis with resultant reduced distal flow, and hence the need for amputation. The introducing sheath for limb perfusion has therefore crossed this stenosis, with relatively angiographically unobstructed distal arteries now evident. D) displays a coronary 0.014" guidewire being manipulated within the posterior tibial artery, with an injection of iodinated contrast used to confirm the intra-luminal position. Following wiring of the distal vessel, intravascular imaging runs were performed, with IVUS (E) and OCT (F) catheters passed distally over-the-wire.

5.8 Intravascular imaging

The use of intravascular imaging to guide PCI is becoming increasingly commonplace, to identify lesions for intervention, improve lesion preparation and optimise the post-intervention result. In this experimental limb model, intravascular imaging helps in the identification and characterisation of atherosclerotic plaques for study. As seen in Figure 5-5, there was no evidence of significant atheroma on angiography in this limb. However, as with clinical coronary angiography, the luminogram provided by angiography does not provide an assessment of the vessel wall, where positive remodelling, accommodating atherosclerotic plaques without lumen encroachment, will be missed. In addition, orthogonal views of the arterial bed were not taken during the angiogram in Figure 5-5, as is routine practice during coronary angiography, so there also remains the possibility that significant angiographic stenoses exist, but were not identified. Accordingly, IVUS and OCT analyses were performed of the entire vascular bed, from popliteal artery to distal posterior tibial artery of the same limb, shown in Figure 5-6 and 5-7 respectively, at similar angiographic locations as demonstrated in Figure 5-5 (A) and (B).

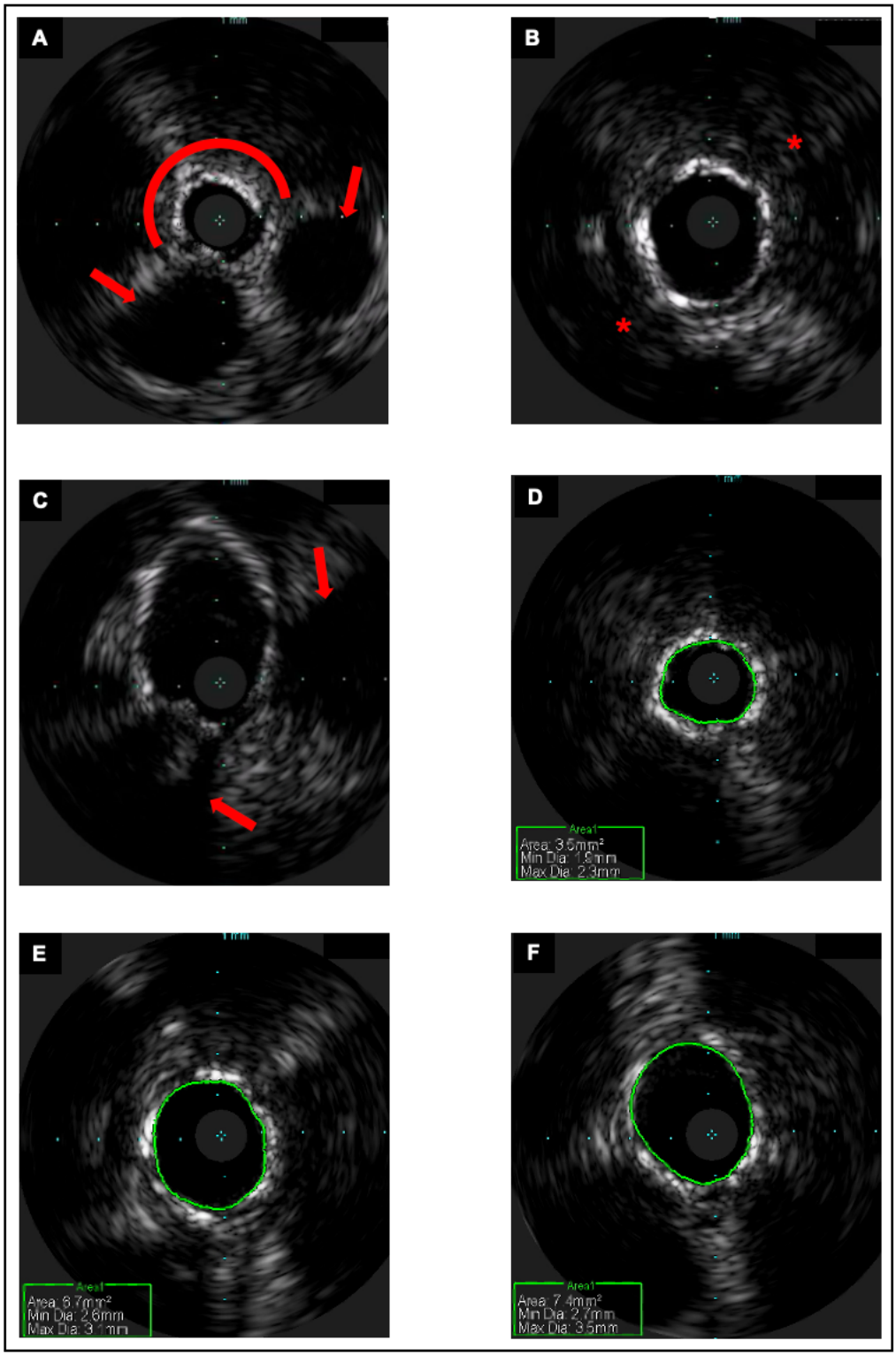

Figure 5-6. Intravascular imaging of the amputated human limb model using intravascular ultrasound.

Intravascular ultrasound study of the amputated human limb model performed using the Eagle Eye Platinum catheter (Volcano, Philips, Amsterdam, Netherlands).
A) – still frame of the distal posterior tibial artery, demonstrating superficial calcification (7 o'clock to 3 o'clock, highlighted by red arc) without significant luminal obstructive disease. There are surrounding extraluminal vessels (highlighted by red arrows), which likely represent posterior tibial venous branches veins running alongside the posterior tibial artery.

*B) – still frame of the mid posterior tibial artery, demonstrating concentric calcification, with loss of signal penetration beyond the calcium deposits (highlighted by red *).*
C) – still frame demonstrating the tibioperoneal bifurcation, as the posterior tibial artery joins the peroneal artery (highlighted by red arrows)
D-F) – minimal lumen area measurements in the distal (D), mid (E) and proximal (F) posterior tibial artery.
The interval between crosshair indicators represents 1mm.

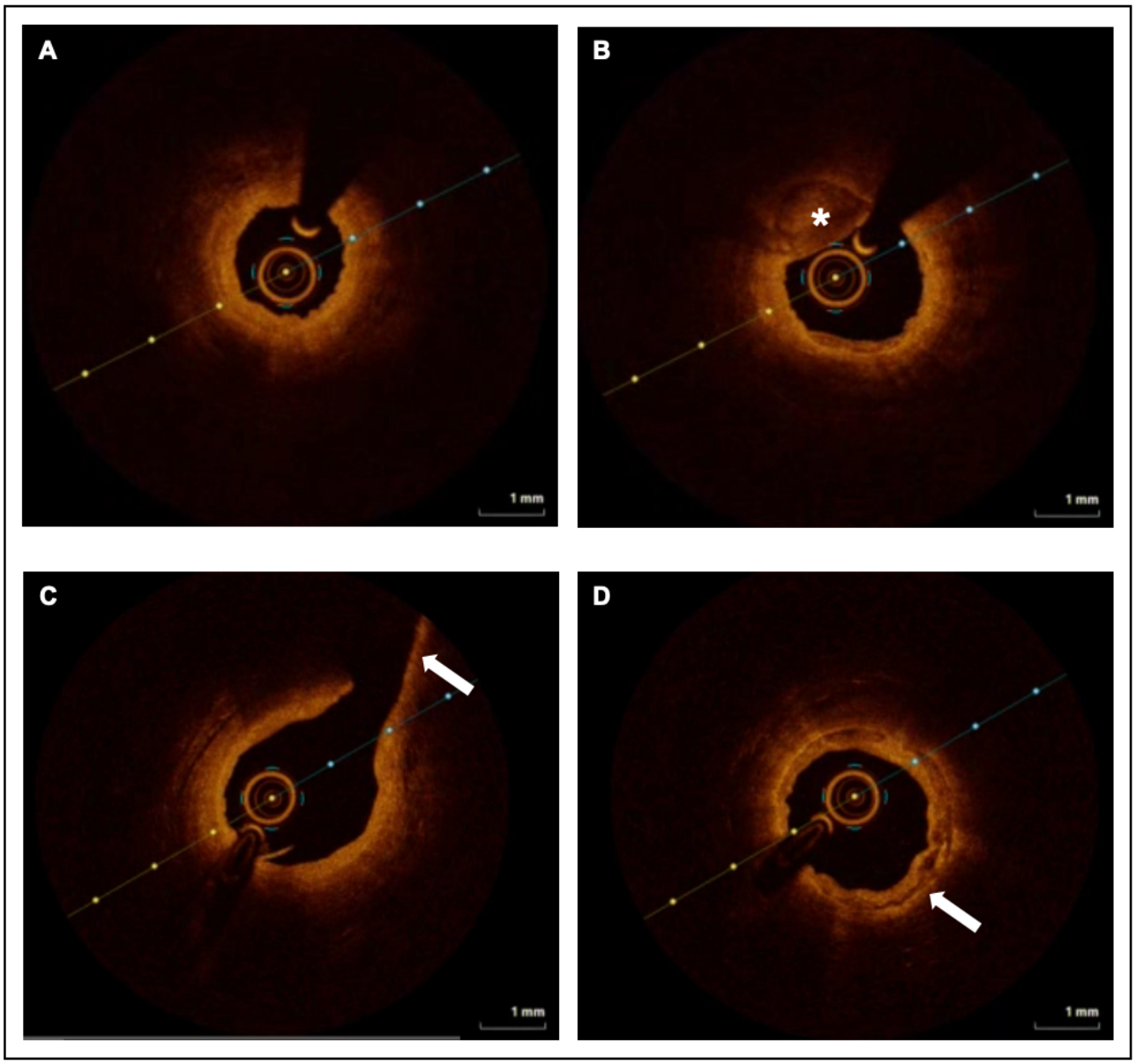

Figure 5-7. Intravascular imaging of the amputated human limb model using optical coherence tomography.

Optical coherence tomography study of the amputated human limb model performed using the Dragonfly Optis catheter (Abbott Cardiovascular, Illinois, USA). Injection of iodinated contrast was used to generate a blood-free field.
A) – still frame of the distal posterior tibial artery, demonstrating concentric fibrous plaque with a high backscatter and relatively homogenous signal

*B) – still frame of the mid posterior tibial artery, demonstrating a fibrous calcific plaque with a large area of calcification (indicated by *), appearing as a signal-poor well demarcated region with clear borders and no dramatic signal drop-out.*
C) – still frame demonstrating the tibioperoneal bifurcation, as the posterior tibial artery joins the peroneal artery (highlighted by white arrow).
D) – still frame of the popliteal artery showing concentric fibrous calcific plaque (highlighted by white arrow).
The interval between crosshair indicators represents 1mm.

Figures 5-6 and 5-7 demonstrate evidence of atherosclerotic plaques that could not be readily appreciated angiographically. The obtained intravascular imaging is of clinical calibre and is easily interpretable by a trained operator. In particular, the iodinated contrast injection for the OCT runs has generated a clear blood-free field, without significant swirling artefact. The superior spatial resolution provided by OCT is clearly evident, and permits greater lesion assessment and characterisation than with IVUS.

Both IVUS and OCT have been successfully utilised to provide data to assess the presence of atherosclerosis, which will be useful for colocalising signal from molecular targeted agents to diseased segments in future experiments. Importantly, these studies provide a proof-of-concept of the ability to perform detailed clinical-grade intravascular imaging within the arterial tree of the amputated limb model, confirming that more advanced research technologies, such as the hybrid NIRF catheter-based techniques for molecular imaging with fluorescent agents, is feasible.

5.9 Proof-of-principle atherosclerotic fluorescence molecular imaging

Following intravascular imaging, limb perfusion was continued, aiming for biological normal ranges of a plethora of factors, as outlined in *Section 5.6 Maintenance within physiological parameters*. As a proof-of-principle of utilising the limb model for the assessment of a

molecular targeting atherosclerosis agent, indocyanine green was tested. Indocyanine green is a NIR agent (excitation 780/ emission 830nm), which non-specifically targets lipid and macrophages in areas of increased endothelial permeability (atherosclerotic plaques). Moreover, indocyanine green is readily available as it is used clinically with laser ophthalmoscopy for the evaluation of the retinochoroidal circulation.

Indocyanine green at a dose of 2mg/kg (limb weight) was injected post-limb (akin to intravenous injection) and left to circulate within the perfusion system. Prior studies using indocyanine green for atherosclerotic imaging used a concentration of 0.25 mg/kg, however 2mg/kg was chosen, given the large dead space within the perfusion circuit. Indocyanine green usually has a human plasma half-life of 3-5 minutes, with hepatic excretion. Of course, in the limb model there is no liver metabolism; thus, the agent should remain in circulation until the perfusate is changed. In a successful *in vivo* human carotid study carried out by Verjans and colleagues (173), indocyanine green was injected prior to carotid endarterectomy, and atherosclerotic plaque uptake was confirmed *ex vivo*. In this study, the average time from intravenous injection to surgical resection was ~99 minutes. Accordingly, 90-minutes after injection, limb perfusion was ceased, and the system drained of all perfusate. The limb was then perfused with fresh crystalloid only, to flush out any residue or unbound indocyanine green and therefore reduce background fluorescent signal. Next, the perfused arterial tissue was dissected out and opened en face, prior to performing FRI, as shown in Figure 5-8 below.

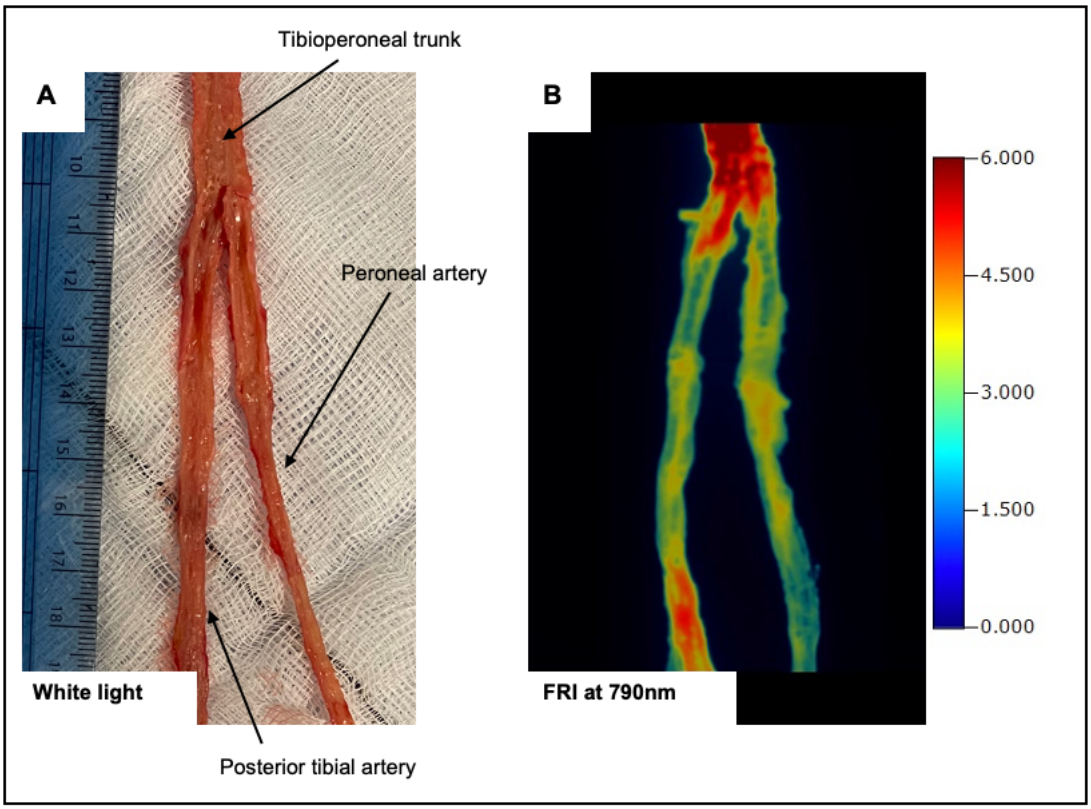

Figure 5-8. Targeting atherosclerosis near-infrared fluorescence imaging of atherosclerosis using the ex vivo pump-perfused amputated human limb model.

Indocyanine green (2mg/kg) was injected post-limb and left to circulate in the perfusion system for 90-minutes. Following this, the limb was flushed with fresh crystalloid and the perfused arterial tree dissected out, opened en face (lumen facing upwards) and imaged under white light. The tibioperoneal trunk bifurcation into posterior tibial artery on the left and peroneal artery on the right is shown (A). Fluorescence reflectance imaging was then performed using the FMT 4000 at 790nm (B). Scale bar in A) is in cm. Scale bar in B) is in counts/ energy, ranging from blue (low, 0) to red (high, 6.0).

Figure 5-8 above displays the dissected tibioperoneal trunk bifurcating into posterior tibial and peroneal arteries, imaged under white light in A) and using FRI in B). There is increased fluorescence signal in the tibioperoneal artery proximal to the bifurcation, which is a predilection site for atherosclerosis, as well as in the posterior tibial artery. The area of high intensity fluorescence towards the distal end of the posterior tibial artery section corresponds to regions of circumferential calcification seen on both IVUS and OCT in Figures 5-6 and 5-7 above. Interestingly in the above study by Verjans and colleagues (173), indocyanine green

signal was found to not diffusely and uniformly localise to all atherosclerotic plaque, but to favour areas of overt endothelial disruption possessing advanced atherosclerotic characteristics, such as intraplaque haemorrhage or plaque disruption. The FRI results here would corroborate those findings, without homogenous signal seen throughout the section, and greater signal in regions of greater calcification on intravascular imaging.

5.10 Discussion

This chapter details the design, development and initial validation of a novel experimental model of atherosclerosis. The benefits of this model lie in that it could reduce our dependency on animal models of atherosclerosis in preclinical research, whilst at the same time also improving applicability of the preclinical models to humans, thus optimising clinical relevance, and hopefully increasing the efficiency of clinical translation. Although establishing the limb perfusion circuit was expensive, once set up, there is a possibility that this model may be cost saving, versus breeding/ purchasing, feeding and housing animals (especially large species), as well as any necessary procedures, such as balloon iliac injury in the case of the rabbit model of atherosclerosis.

The next steps in model development principally involve repeating the experimental set up on multiple occasions, to increase experience and ensure model robustness and reliability. As discussed above, the Covid-19 pandemic has had a significant impact on elective operations, and therefore limb availability. Another means of increasing limb availability would be to explore establishing research collaborations with other vascular surgical departments outside of Imperial College NHS Healthcare Trust, however this will introduce the need for further ethical permissions whilst also prolonging ischaemic times in transit prior

to perfusion. I could also move to procuring limbs from emergency amputations, although this will not afford me the time for equipment set up or the ability to courier fresh packed red cells. I could keep blood permanently on standby to remedy this, but of course is likely to incur some wastage and added expense. Another option would be to switch to a readily available acellular perfusate, such as University of Wisconsin solution, a hydroxyethyl starch-based fluid used for transplant organ cold storage preservation (355). However, this may have a reduced oxygen carrying capacity, different NIR properties (relevant for future NIRF experiments) and is less clinically applicable.

Aside from low limb availability, the inability to perform experiments in batches (as would be performed in an animal study), procuring limbs on an ad hoc basis, is a limiting factor. There is also the possibility that an obtained limb would be too atherosclerotic to allow successful perfusion, with such a heavy disease burden that arterial blood simply cannot supply distal tissue, although this issue has not been encountered yet. Nevertheless, during circuit development I did move from a femoral perfusion cannula used for conventional clinical cardiopulmonary bypass, to a large bore femoral sheath used for vascular access during angiography, owing to its smaller calibre and easier arterial cannulation.

Similarly, refinements to the perfusion system will continue with greater experience. For example, I have had to develop perfusionist skills, and a greater appreciation of how the circuit responds to fluid and electrolyte changes will enable the optimisation of time spent within physiological ranges. I would also like to increase the frequency of blood gas sampling, perhaps to every 30-minutes, to minimise time spent outside of ideal parameters.

Nonetheless, the electrolyte abnormalities may not be purely correctable by modifying the perfusate, and haemofiltration may be required, if necessary.

Further adaptations to the model may avoid limb cooling between amputation and perfusion, to limit cold ischaemia time, which has been demonstrated to correlate with muscle damage (356). Moreover, providing an objective measure of muscle injury would be beneficial, to demonstrate satisfactory limb perfusion. Potential methods of doing this include measurement of free myoglobin in the perfusate over time, as well as cell viability testing (such as with the 'Cell Titer 96 non-radioactive cell proliferation assay' [Promega, Wisconsin, USA]), and histological examination for structural muscular injury on skin biopsies taken over the course of perfusion. To this end, I was not able to normalise pH and lactate concentration during limb perfusion. Werner and colleagues (348) were able to achieve an average pH of 7.4 during their upper limb perfusion experiments. However, as discussed earlier, their limbs were procured from brain-dead organ donors with no prior history of cardiovascular or peripheral vascular disease. Moreover, upper limbs are less prone to atherogenesis, further reducing the likelihood of significant atherosclerotic disease. Thus, with diseased lower limbs, accomplishing a neutral pH may not be achievable. In that study, lactataemia was also not correctable; but the authors note that rising lactate concentrations have been recognised with clinical *ex situ* lung perfusion, with successful functioning transplantation thereafter. The lactate elevations were attributed to failure of clearance of physiological levels of lactate, rather than pathological production (357).

Another potential modification to potentially reduce any immune-mediated cellular effects, and thus reduced limb longevity, would be to switch to packed red cells that are cross-

matched to the limb donor; however, this will add further delay to experimental set-up and would remove the option of procuring limbs from emergency operations. Additionally, I could measure activated clotting time, a measure of heparin activity, during perfusion and aim for a therapeutic range that is used as standard on cardiopulmonary bypass of >400 seconds (358). Free haemoglobin could also be measured on regular blood sampling to assess the degree of haemolysis within the circuit. These modifications would assess the adequacy of perfusate flow through the system and ensure the absence of haemostasis.

Moving forwards, the key innovative steps will be to perform more experiments with molecular atherosclerosis targeting agents, to demonstrate that a number of different probes are able to circulate within the system, bind to their molecular targets, and be detected by different methods. Regions of low atherosclerotic burden could be used as a negative control for each agent, to permit quantitative analysis. To date, indocyanine green has been used. Other investigational probes, such as those that we develop within the Khamis laboratory, including the LO1Fab-nanoparticles, those that we can access through collaboration, or even commercial agents should be considered. *Ex vivo* FRI was utilised in this chapter to demonstrate indocyanine green localisation to atherosclerotic plaques, but further validation is required. This could be performed with fluorescence microscopy on cryosectioned arterial tissue. Alternatively, and more uniquely, this could be performed using high resolution catheter-based hybrid NIRF intravascular imaging, as discussed earlier in the chapter. To this end, we have a collaboration with Prof Michael Joner and Prof Vasilis Ntziachristos (both Technical University of Munich, Germany) to perform nanoparticle studies in their rabbit model of atherosclerosis (Chapter 4). Together, their laboratories have developed a hybrid NIRF-IVUS catheter, which will be used for these experiments. If the catheter system could

be transported to the UK, it would be very exciting to trial it in the limb model. Aside from NIRF-based detection of atherosclerotic plaque directed agents, other imaging modalities may be possible to utilise with the limb model. These can include MRI or PET, opening the door to a plethora of possible molecular targeting candidates.

The limitations of the work in this chapter are firstly, and most importantly, the low number of occasions that the established limb model has been run. Further work is clearly required to address this, whilst also keeping the perfusion circuit running within physiological parameters for a prolonged period. In addition, although animal models are principally used to demonstrate targeting probe function, data on harm or toxicity is also generated. This will not be possible with the limb model. Moreover, animal models are routinely used to assess therapeutic efficacy of an investigational agent: this will be difficult to achieve with the limb model, without the ability to run the model for sufficient time to allow a therapeutic agent time to demonstrate efficacy. Additionally, although this is human-based and great efforts have gone to optimise the model within physiological parameters, it remains an artificial system, where clinical applicability and relevance will still be questioned.

5.11 Conclusions

This chapter details the design and development of a novel model of atherosclerosis that aims to provide a new method of assessing molecular targeting agent function. It utilises human tissue that would otherwise be incinerated and has the potential to reduce our reliance on animal models for preclinical atherosclerosis research, whilst also increasing translational efficiency. Future work with a greater number of experiments and more molecular targeting agents will be necessary to confirm model validity and reliability.

5.12 Related presentations and publications

5.12.1 Presentations

The work contained within this chapter has been presented at the following meetings:

Ex vivo pump-perfused human limb model for the molecular targeting in atherosclerosis. **Imperial Vulnerable Patient and Plaque Meeting, Galway, Ireland, 2022** (oral presentation)

A novel experimental model of atherosclerosis – the ex vivo pump-perfused amputated limb model. **British Atherosclerosis Society, Oxford, UK, 2022** (poster presentation)

The ex vivo on-ECMO amputated human limb model of atherosclerosis. ***European Society of Cardiology, Barcelona, Spain, 2022*** (moderated poster presentation)

First demonstration of a novel experimental model of atherosclerosis. The ex vivo on-ECMO amputated “living” human limb model. ***British Cardiovascular Society, Manchester, UK, 2022*** (poster presentation)

Chapter 6

Concluding remarks and future work

CHAPTER 6 – CONCLUDING REMARKS AND FUTURE WORK

6.1 Concluding remarks

There is a clear mandate for better risk stratification as well as targeted diagnostics and therapeutics in ASCVD. In this thesis I have described the development of anti-MDA-LDL antibodies as blood biomarkers reflecting atherosclerotic plaque characteristics that convey cardiovascular risk. In due course these can hopefully complement and add additional refinement to existing risk stratification techniques. However, the antibodies may be more than simple biomarkers of overall atherosclerotic burden; but may relate more specifically to vulnerable atherosclerotic plaque, and indeed may decline in response to oxidative stress induced by strenuous exercise. Whether or not this is the case should not affect their utility as prognostically important biomarkers of ASCVD.

We have previously demonstrated associations between anti-MDA-LDL antibodies, vulnerable atherosclerotic plaque and cardiovascular events; however, this is with a single invasive imaging modality. Providing additional validation is both important and necessary for translation. Moreover, demonstrating relationships with atherosclerotic plaque characteristics using a non-invasive anatomic imaging technique, such as CTCA, which is the now a first-line investigation for stable chest pain, is a significant step towards clinical translation.

The nanoparticle development as part of this PhD project has seen a major step forward in the molecular targeting of vulnerable atherosclerotic plaques. For imaging of vulnerable plaques, the NIR-emitting nanoparticles will deliver a greater amount of fluorophore per conjugated antibody fragment than antibody fragment-fluorophore complex alone, amplifying

the SNR. However, more intriguingly, local drug delivery to plaques is now a viable prospect. This would enable the target-specific delivery of therapeutics directly to atherosclerotic plaques with high lipid content, targeting all vascular beds with a single intravenous administration, or indeed coronary vessels with catheter-based administration, accompanied by few systemic adverse effects. The ideal nanoparticle cargo is yet to be established and will require significant further work; however potential candidates would include anti-inflammatory therapies or senolytic agents. There is an emerging understanding of the importance of inflammation in atherosclerosis, with limited focused treatment options at present, combined with significant off-target effects from systemic immunotherapies. If successful, and delivery of a suitable agent to highly lipidic plaque is achieved with therapeutic efficacy, there is the potential to revolutionise our approach to the management of vulnerable patients at risk of future cardiovascular events. Moreover, it is conceivable that a precision medicine approach could be adopted, akin to genomic or oncological medicine, with tailored nanoparticle therapies delivered depending on a patient's plaque features or biological activity.

Combining the serological and nanoparticle components of this thesis, perhaps low IgG/ IgM anti-MDA-LDL antibody levels on a simple blood test could identify high risk patients in primary prevention who would benefit from more intensive preventative medication optimisation. Nanoparticle-based molecular imaging could then further stratify patients at the highest risk in the secondary prevention setting following a cardiovascular event, where more expensive and invasive procedures are justified. Of course, if nanoparticle binding could be detected through non-invasive techniques, such as PET, this would be more acceptable.

These patients with the highest nanoparticle signal could then proceed to nanoparticle-based therapeutics.

The concept of the vulnerable plaque, one that is predisposed to rupture and precipitating a MI, is now a well-identified phenomenon and has led to the evolving notion of the vulnerable patient, one which is prone to future MACE, due to both the presence of identified vulnerable plaques and a high cardiovascular risk phenotype. Clearly, treating vulnerable patients is an important clinical priority, even more so than vulnerable plaques themselves, especially given the significant ongoing global burden of ASCVD. The work enclosed within this thesis should help go towards bridging the gap from vulnerable plaques to vulnerable patients and pave the way for a comprehensive personalised package of cardiovascular risk assessment. The development of antibodies against oxLDL that reflect low-attenuation plaque on CTCA (as well as other measures of coronary and valvular atherosclerosis), combined with prior research demonstrating relationships with MACE and lipid-rich plaque on NIRS-IVUS, supports the promise for these specific antibodies as serological biomarkers of cardiovascular risk, supplementary to current clinical risk stratification techniques. Next, the prospect of identification of vulnerable plaques using oxLDL-based targeted antibodies or nanoparticles, potentially with non-invasive imaging techniques, is exciting and raises the possibility of even more refined cardiovascular risk evaluation for vulnerable patients. Finally, there is the opportunity for anti-oxLDL antibody-based therapeutics, to treat these identified vulnerable plaques. The antibody constructs are due to be explored as localised therapeutic agents, in both their own right, with planned passive immunisation studies in the mouse model of atherosclerosis, as well as via targeting of nanoparticles containing a therapeutic agent cargo. Thus, this thesis provides meaningful steps in the translation of anti-oxLDL

antibody constructs in a bespoke package to hopefully identify, and treat, vulnerable plaques and patients.

Lastly, I have developed a novel model of atherosclerosis that has the potential to be invaluable as a new tool in preclinical atherosclerosis research. It requires further validation; however, the model poses the prospect of reducing our reliance on animal models, whilst also being cost effective and reducing time needed for clinical translation.

6.2 Suggestions for future work

For development of the anti-MDA-LDL antibodies as robust serological biomarkers of atherosclerotic CVD, further corroborative studies will be necessary prior to clinical translation. Links with clinical endpoints and atherosclerotic plaque characteristics have now been established in retrospective studies, independent of classical cardiovascular risk factors. Yet, the additional benefit of measuring these antibody levels has not been conclusively demonstrated in prospective studies. An important potential study would be to prospectively measure antibody levels at baseline in patients free from manifest CVD, perhaps with established cardiovascular risk factors to ensure a suitable event rate, and perform anatomic coronary imaging at various intervals (e.g., baseline, one and five years; ensuring the radiation dose is acceptable with CTCA) to quantitatively evaluate disease progression over time in relation to antibody levels. Long term cardiovascular event-driven follow-up could also be performed, via medical health record data linkage to minimise expenditure, to validate antibody relationships with immediately clinically relevant outcomes.

Furthermore, for clinical translation, the ELISAs will require testing in large disease-free populations to generate normal reference ranges, as well as reporting results in concentrations, to permit comparison between different patient populations. At present, in this thesis and all prior work in the laboratory, antibody levels are reported as OD AU at 450nm, and values are only evaluated across the cohort being studied (in tertiles or otherwise) – essentially comparing low-readers versus high-readers. Moreover, CTCA data here have been very useful to analyse the relationships between antibodies and coronary atherosclerosis, but of course serological biomarkers will reflect whole body disease processes. Coronary atherosclerosis in is the most well studied and characterised of the vascular territories, however gaining an appreciation of the associations between anti-MDA-LDL antibodies with peripheral or cerebral atherosclerosis would also be invaluable. Establishing any pathophysiological functions of the antibodies will also be important, to further validate their position as biomarkers as well as elucidating if there are any possible antibody-based therapeutic avenues. Planned passive immunisation with LO1/ LO1Fab anti-MDA-LDL antibodies *in vivo* using the LDL-$R^{-/-}$ mouse model of atherosclerosis will help shed light on any mechanistic roles and treatment applications.

Comprehensive future nanoparticle studies are planned, aiming to optimise nanoparticle function and clinical translation. These include modifying the nanoparticle construct for PET imaging, to provide an alternative, and importantly, non-invasive, clinically available, method of detection. Other intended optimisations include improving nanoparticle-antibody conjugation efficiency to increase on-target binding and reduce manufacture wastage; identifying an ideal quantity of nanoparticles for *in vivo* injection to reduce manufacturing costs; and perform *in vivo* FMT imaging colocalised with iodinated contrast-enhanced micro-

CT, to better delineate binding to vasculature. Progression-regression *in vivo* FMT imaging studies (switching a proportion of LDL-$R^{-/-}$ mice from high-fat to regular chow diet while the remainder remain on high-fat diet) will also evaluate whether the nanoparticle can discern different atherosclerotic burdens as well as lesion severity/ complexity, which will be important for clinical translation.

For future fluorescence studies, designs are in place to modify the current nanoparticle construct with an alternative NIR fluorophore (IRdye 800CW) that has already been conjugated to a PLGA polymer for this purpose. This fluorophore is further right-shifted into the infrared spectrum than Cy5, reducing background autofluorescence, optimising the TBR, and has already been safely evaluated in humans. These modified nanoparticles will also be evaluated for molecular targeting of lipidic atherosclerotic plaques in a rabbit model of atherosclerosis. Aside from simply providing confirmatory proof of nanoparticle binding in an additional species, the rabbit model will permit intravascular fluorescence and anatomic imaging using hybrid NIRF-IVUS/ OCT catheters. This has the additional benefit of greater *in vivo* plaque imaging resolution, and accompanied by *ex vivo* catheter runs as well as epifluorescence fluorescence microscopy, will conclusively establish nanoparticle atherosclerotic plaque binding. These experiments will precede necessary steps for clinical translation, including toxicity testing, ethical approval and obtaining funding for a first-in-human study.

As discussed above, loading the nanoparticles with a therapeutic cargo for payload delivery to atherosclerotic plaque will be a key ongoing research aim, and an *in vitro* foam cell assay has been established in this thesis to aid this process. After ascertaining that the nanoparticle

construct can deliver its payload in the vicinity of macrophages, the biological effect of the therapeutic needs to be established, perhaps using inflammatory PCR panels in the case of an anti-inflammatory cargo, such as the RT² Profiler PCR Array (Human Inflammatory Response & Autoimmunity – Qiagen, Hilden, Germany). Nanoparticle therapeutic payload delivery and efficacy, versus the therapeutic administered systemically, will then need to be determined *in vivo*, feasibly with repeat FMT imaging at different timepoints using inflammatory reporters, such as MMPSense (MMPs), IntegriSense (αvβ3 integrin) or ProSense (cathepsin) (all PerkinElmer, Massachusetts, USA), confirmed with *ex vivo* validation.

Planned future work for the novel experimental model of atherosclerosis principally involves repeating set-up on repeated occasions, to further perfect perfusion and maintenance of the limb environment within physiological conditions. This will include model refinements, such as assessing for cell viability, muscle breakdown with myoglobin assays and optimisation of heparinisation/ clotting times. More interestingly, a compelling experimental design would be to inject the fluorescent nanoparticles developed as part of this PhD project into the limb model and assess construct recognition of human atherosclerosis. LO1Fab versus control Fab-conjugated nanoparticle function could be evaluated in this way in separate limbs, as well as by comparing construct binding to atherosclerotic and disease-free arterial segments in the same limb. The experimental read-out could be *ex vivo* FRI or fluorescence microscopy, or more excitingly, with hybrid catheter-based NIRF signal co-registered with anatomic intravascular imaging, performed with ongoing limb perfusion.

Chapter 7

References

CHAPTER 7 – REFERENCES

1. WHO. The top 10 causes of death 2018 [Available from: http://www.who.int/news-room/fact-sheets/detail/the-top-10-causes-of-death.
2. Hartley A, Marshall DC, Salciccioli JD, Sikkel MB, Maruthappu M, Shalhoub J. Trends in Mortality From Ischemic Heart Disease and Cerebrovascular Disease in Europe: 1980 to 2009. Circulation. 2016;133(20):1916-26.
3. Roth GA, Mensah GA, Johnson CO, Addolorato G, Ammirati E, Baddour LM, et al. Global Burden of Cardiovascular Diseases and Risk Factors, 1990-2019: Update From the GBD 2019 Study. Journal of the American College of Cardiology. 2020;76(25):2982-3021.
4. Townsend N, Kazakiewicz D, Lucy Wright F, Timmis A, Huculeci R, Torbica A, et al. Epidemiology of cardiovascular disease in Europe. Nature reviews Cardiology. 2022;19(2):133-43.
5. Peters SAE, Muntner P, Woodward M. Sex Differences in the Prevalence of, and Trends in, Cardiovascular Risk Factors, Treatment, and Control in the United States, 2001 to 2016. Circulation. 2019;139(8):1025-35.
6. Hartley A, Haskard D, Khamis R. Oxidized LDL and anti-oxidized LDL antibodies in atherosclerosis - Novel insights and future directions in diagnosis and therapy(). Trends in cardiovascular medicine. 2018.
7. Maron DJ, Hochman JS, Reynolds HR, Bangalore S, O'Brien SM, Boden WE, et al. Initial Invasive or Conservative Strategy for Stable Coronary Disease. The New England journal of medicine. 2020;382(15):1395-407.
8. Bentzon JF, Otsuka F, Virmani R, Falk E. Mechanisms of plaque formation and rupture. Circulation research. 2014;114(12):1852-66.
9. Mann J, Davies MJ. Mechanisms of progression in native coronary artery disease: role of healed plaque disruption. Heart (British Cardiac Society). 1999;82(3):265-8.
10. Nigro P, Abe J, Berk BC. Flow shear stress and atherosclerosis: a matter of site specificity. Antioxid Redox Signal. 2011;15(5):1405-14.
11. Zhang X, Fernández-Hernando C. Transport of LDLs into the arterial wall: impact in atherosclerosis. Current opinion in lipidology. 2020;31(5):279-85.
12. Tsioufis P, Theofilis P, Tsioufis K, Tousoulis D. The Impact of Cytokines in Coronary Atherosclerotic Plaque: Current Therapeutic Approaches. International journal of molecular sciences. 2022;23(24).
13. Gui Y, Zheng H, Cao RY. Foam Cells in Atherosclerosis: Novel Insights Into Its Origins, Consequences, and Molecular Mechanisms. Front Cardiovasc Med. 2022;9:845942.
14. Libby P. Inflammation in atherosclerosis. Nature. 2002;420(6917):868-74.
15. Tozer EC, Carew TE. Residence time of low-density lipoprotein in the normal and atherosclerotic rabbit aorta. Circulation research. 1997;80(2):208-18.
16. Prassl R, Laggner P. Molecular structure of low density lipoprotein: current status and future challenges. Eur Biophys J. 2009;38(2):145-58.
17. Ridgway N, McLeod R. Biochemistry of lipids, lipoproteins and membranes: Elsevier; 2008.
18. Oppi S, Lüscher TF, Stein S. Mouse Models for Atherosclerosis Research-Which Is My Line? Front Cardiovasc Med. 2019;6:46.
19. Nordestgaard BG, Chapman MJ, Ray K, Borén J, Andreotti F, Watts GF, et al. Lipoprotein(a) as a cardiovascular risk factor: current status. European heart journal. 2010;31(23):2844-53.

20. Bergmark C, Dewan A, Orsoni A, Merki E, Miller ER, Shin MJ, et al. A novel function of lipoprotein [a] as a preferential carrier of oxidized phospholipids in human plasma. Journal of lipid research. 2008;49(10):2230-9.
21. Goldstein JL, Ho YK, Basu SK, Brown MS. Binding site on macrophages that mediates uptake and degradation of acetylated low density lipoprotein, producing massive cholesterol deposition. Proceedings of the National Academy of Sciences of the United States of America. 1979;76(1):333-7.
22. Miller YI, Choi SH, Wiesner P, Fang L, Harkewicz R, Hartvigsen K, et al. Oxidation-specific epitopes are danger-associated molecular patterns recognized by pattern recognition receptors of innate immunity. Circulation research. 2011;108(2):235-48.
23. Afonso CB, Spickett CM. Lipoproteins as targets and markers of lipoxidation. Redox Biol. 2019;23:101066.
24. Chou MY, Hartvigsen K, Hansen LF, Fogelstrand L, Shaw PX, Boullier A, et al. Oxidation-specific epitopes are important targets of innate immunity. Journal of internal medicine. 2008;263(5):479-88.
25. Haberland ME, Fong D, Cheng L. Malondialdehyde-altered protein occurs in atheroma of Watanabe heritable hyperlipidemic rabbits. Science (New York, NY). 1988;241(4862):215-8.
26. Shaw PX, Horkko S, Tsimikas S, Chang MK, Palinski W, Silverman GJ, et al. Human-derived anti-oxidized LDL autoantibody blocks uptake of oxidized LDL by macrophages and localizes to atherosclerotic lesions in vivo. Arteriosclerosis, thrombosis, and vascular biology. 2001;21(8):1333-9.
27. Tsimikas S, Miyanohara A, Hartvigsen K, Merki E, Shaw PX, Chou MY, et al. Human oxidation-specific antibodies reduce foam cell formation and atherosclerosis progression. Journal of the American College of Cardiology. 2011;58(16):1715-27.
28. van Dijk RA, Kolodgie F, Ravandi A, Leibundgut G, Hu PP, Prasad A, et al. Differential expression of oxidation-specific epitopes and apolipoprotein(a) in progressing and ruptured human coronary and carotid atherosclerotic lesions. Journal of lipid research. 2012;53(12):2773-90.
29. Amaki T, Suzuki T, Nakamura F, Hayashi D, Imai Y, Morita H, et al. Circulating malondialdehyde modified LDL is a biochemical risk marker for coronary artery disease. Heart (British Cardiac Society). 2004;90(10):1211-3.
30. Hartley A, Haskard D, Khamis R. Oxidized LDL and anti-oxidized LDL antibodies in atherosclerosis - Novel insights and future directions in diagnosis and therapy. Trends in cardiovascular medicine. 2019;29(1):22-6.
31. Gao S, Zhao D, Wang M, Zhao F, Han X, Qi Y, et al. Association between circulating oxidized LDL and atherosclerotic cardiovascular disease: a meta-analysis of observational studies. Canadian Journal of Cardiology. 2017.
32. Tsimikas S, Willeit P, Willeit J, Santer P, Mayr M, Xu Q, et al. Oxidation-specific biomarkers, prospective 15-year cardiovascular and stroke outcomes, and net reclassification of cardiovascular events. Journal of the American College of Cardiology. 2012;60(21):2218-29.
33. Ference BA, Yoo W, Alesh I, Mahajan N, Mirowska KK, Mewada A, et al. Effect of long-term exposure to lower low-density lipoprotein cholesterol beginning early in life on the risk of coronary heart disease: a Mendelian randomization analysis. Journal of the American College of Cardiology. 2012;60(25):2631-9.
34. Virmani R, Kolodgie FD, Burke AP, Farb A, Schwartz SM. Lessons from sudden coronary death: a comprehensive morphological classification scheme for atherosclerotic lesions. Arteriosclerosis, thrombosis, and vascular biology. 2000;20(5):1262-75.
35. Virmani R, Burke AP, Farb A, Kolodgie FD. Pathology of the vulnerable plaque. Journal of the American College of Cardiology. 2006;47(8 Suppl):C13-8.

36. Burke AP, Farb A, Malcom GT, Liang Y-h, Smialek J, Virmani R. Coronary risk factors and plaque morphology in men with coronary disease who died suddenly. New England Journal of Medicine. 1997;336(18):1276-82.
37. Narula J, Nakano M, Virmani R, Kolodgie FD, Petersen R, Newcomb R, et al. Histopathologic characteristics of atherosclerotic coronary disease and implications of the findings for the invasive and noninvasive detection of vulnerable plaques. Journal of the American College of Cardiology. 2013;61(10):1041-51.
38. Hafiane A. Vulnerable Plaque, Characteristics, Detection, and Potential Therapies. J Cardiovasc Dev Dis. 2019;6(3).
39. Burke AP, Kolodgie FD, Farb A, Weber DK, Malcom GT, Smialek J, et al. Healed plaque ruptures and sudden coronary death: evidence that subclinical rupture has a role in plaque progression. Circulation. 2001;103(7):934-40.
40. Farb A, Burke AP, Tang AL, Liang TY, Mannan P, Smialek J, et al. Coronary plaque erosion without rupture into a lipid core. A frequent cause of coronary thrombosis in sudden coronary death. Circulation. 1996;93(7):1354-63.
41. Jia H, Abtahian F, Aguirre AD, Lee S, Chia S, Lowe H, et al. In vivo diagnosis of plaque erosion and calcified nodule in patients with acute coronary syndrome by intravascular optical coherence tomography. Journal of the American College of Cardiology. 2013;62(19):1748-58.
42. Ehara S, Kobayashi Y, Yoshiyama M, Shimada K, Shimada Y, Fukuda D, et al. Spotty calcification typifies the culprit plaque in patients with acute myocardial infarction: an intravascular ultrasound study. Circulation. 2004;110(22):3424-9.
43. Michel JB, Virmani R, Arbustini E, Pasterkamp G. Intraplaque haemorrhages as the trigger of plaque vulnerability. European heart journal. 2011;32(16):1977-85, 85a, 85b, 85c.
44. Liu F, Wang Y, Yu J. Role of inflammation and immune response in atherosclerosis: Mechanisms, modulations, and therapeutic targets. Hum Immunol. 2023.
45. Ridker PM. From C-Reactive Protein to Interleukin-6 to Interleukin-1: Moving Upstream To Identify Novel Targets for Atheroprotection. Circulation research. 2016;118(1):145-56.
46. Bian F, Yang XY, Xu G, Zheng T, Jin S. CRP-Induced NLRP3 Inflammasome Activation Increases LDL Transcytosis Across Endothelial Cells. Front Pharmacol. 2019;10:40.
47. Ridker PM, Everett BM, Thuren T, MacFadyen JG, Chang WH, Ballantyne C, et al. Antiinflammatory Therapy with Canakinumab for Atherosclerotic Disease. The New England journal of medicine. 2017;377(12):1119-31.
48. Nidorf SM, Fiolet ATL, Mosterd A, Eikelboom JW, Schut A, Opstal TSJ, et al. Colchicine in Patients with Chronic Coronary Disease. The New England journal of medicine. 2020.
49. Tardif JC, Kouz S, Waters DD, Bertrand OF, Diaz R, Maggioni AP, et al. Efficacy and Safety of Low-Dose Colchicine after Myocardial Infarction. The New England journal of medicine. 2019;381(26):2497-505.
50. Fiolet ATL, Opstal TSJ, Mosterd A, Eikelboom JW, Jolly SS, Keech AC, et al. Efficacy and safety of low-dose colchicine in patients with coronary disease: a systematic review and meta-analysis of randomized trials. European heart journal. 2021.
51. Cockerill GW, Huehns TY, Weerasinghe A, Stocker C, Lerch PG, Miller NE, et al. Elevation of plasma high-density lipoprotein concentration reduces interleukin-1-induced expression of E-selectin in an in vivo model of acute inflammation. Circulation. 2001;103(1):108-12.
52. Jia C, Anderson JLC, Gruppen EG, Lei Y, Bakker SJL, Dullaart RPF, et al. High-Density Lipoprotein Anti-Inflammatory Capacity and Incident Cardiovascular Events. Circulation. 2021;143(20):1935-45.

53. Pan J, Cai Y, Wang L, Maehara A, Mintz GS, Tang D, et al. A prediction tool for plaque progression based on patient-specific multi-physical modeling. PLoS Comput Biol. 2021;17(3):e1008344.
54. Ridker PM, Devalaraja M, Baeres FMM, Engelmann MDM, Hovingh GK, Ivkovic M, et al. IL-6 inhibition with ziltivekimab in patients at high atherosclerotic risk (RESCUE): a double-blind, randomised, placebo-controlled, phase 2 trial. Lancet (London, England). 2021.
55. Ridker PM. From RESCUE to ZEUS: will interleukin-6 inhibition with ziltivekimab prove effective for cardiovascular event reduction? Cardiovascular research. 2021;117(11):e138-e40.
56. Ridker PM, Everett BM, Pradhan A, MacFadyen JG, Solomon DH, Zaharris E, et al. Low-Dose Methotrexate for the Prevention of Atherosclerotic Events. The New England journal of medicine. 2018.
57. Ridker PM, MacFadyen JG, Everett BM, Libby P, Thuren T, Glynn RJ. Relationship of C-reactive protein reduction to cardiovascular event reduction following treatment with canakinumab: a secondary analysis from the CANTOS randomised controlled trial. Lancet (London, England). 2018;391(10118):319-28.
58. Ridker PM, Bhatt DL, Pradhan AD, Glynn RJ, MacFadyen JG, Nissen SE. Inflammation and cholesterol as predictors of cardiovascular events among patients receiving statin therapy: a collaborative analysis of three randomised trials. Lancet (London, England). 2023;401(10384):1293-301.
59. Ridker PM, Hennekens CH, Buring JE, Rifai N. C-reactive protein and other markers of inflammation in the prediction of cardiovascular disease in women. The New England journal of medicine. 2000;342(12):836-43.
60. Koenig W, Sund M, Frohlich M, Fischer HG, Lowel H, Doring A, et al. C-Reactive protein, a sensitive marker of inflammation, predicts future risk of coronary heart disease in initially healthy middle-aged men: results from the MONICA (Monitoring Trends and Determinants in Cardiovascular Disease) Augsburg Cohort Study, 1984 to 1992. Circulation. 1999;99(2):237-42.
61. Morrow DA, Rifai N, Antman EM, Weiner DL, McCabe CH, Cannon CP, et al. C-reactive protein is a potent predictor of mortality independently of and in combination with troponin T in acute coronary syndromes: a TIMI 11A substudy. Thrombolysis in Myocardial Infarction. Journal of the American College of Cardiology. 1998;31(7):1460-5.
62. Cook NR, Paynter NP, Eaton CB, Manson JE, Martin LW, Robinson JG, et al. Comparison of the Framingham and Reynolds Risk scores for global cardiovascular risk prediction in the multiethnic Women's Health Initiative. Circulation. 2012;125(14):1748-56, s1-11.
63. Kaura A, Hartley A, Panoulas V, Glampson B, Shah ASV, Davies J, et al. Mortality risk prediction of high-sensitivity C-reactive protein in suspected acute coronary syndrome: A cohort study. PLoS Med. 2022;19(2):e1003911.
64. Wensley F, Gao P, Burgess S, Kaptoge S, Di Angelantonio E, Shah T, et al. Association between C reactive protein and coronary heart disease: mendelian randomisation analysis based on individual participant data. BMJ (Clinical research ed). 2011;342:d548.
65. Swerdlow DI, Holmes MV, Kuchenbaecker KB, Engmann JE, Shah T, Sofat R, et al. The interleukin-6 receptor as a target for prevention of coronary heart disease: a mendelian randomisation analysis. Lancet (London, England). 2012;379(9822):1214-24.
66. Ries W, Torzewski J, Heigl F, Pfluecke C, Kelle S, Darius H, et al. C-Reactive Protein Apheresis as Anti-inflammatory Therapy in Acute Myocardial Infarction: Results of the CAMI-1 Study. Front Cardiovasc Med. 2021;8:591714.
67. Moss A, Daghem M, Tzolos E, Meah MN, Wang KL, Bularga A, et al. Coronary Atherosclerotic Plaque Activity and Future Coronary Events. JAMA Cardiol. 2023.

68. Lim GB. Novel siRNA reduces plasma lipoprotein(a) levels. Nature reviews Cardiology. 2022;19(3):147.
69. Musunuru K, Chadwick AC, Mizoguchi T, Garcia SP, DeNizio JE, Reiss CW, et al. In vivo CRISPR base editing of PCSK9 durably lowers cholesterol in primates. Nature. 2021;593(7859):429-34.
70. Nilsson J, Hansson GK. Vaccination Strategies and Immune Modulation of Atherosclerosis. Circulation research. 2020;126(9):1281-96.
71. Libby P, Bornfeldt KE. How Far We Have Come, How Far We Have Yet to Go in Atherosclerosis Research. Circulation research. 2020;126(9):1107-11.
72. Vakhtangadze T, Singh Tak R, Singh U, Baig MS, Bezsonov E. Gender Differences in Atherosclerotic Vascular Disease: From Lipids to Clinical Outcomes. Front Cardiovasc Med. 2021;8:707889.
73. Aron-Wisnewsky J, Clément K. The gut microbiome, diet, and links to cardiometabolic and chronic disorders. Nature reviews Nephrology. 2016;12(3):169-81.
74. Vidarsson G, Dekkers G, Rispens T. IgG subclasses and allotypes: from structure to effector functions. Frontiers in immunology. 2014;5:520.
75. Kamisawa T, Zen Y, Pillai S, Stone JH. IgG4-related disease. The Lancet. 2015;385(9976):1460-71.
76. Janeway Jr CA. Immunobiology the immune system in health and disease. Artes Medicas. 1997.
77. Palma J, Tokarz-Deptuła B, Deptuła J, Deptuła W. Natural antibodies - facts known and unknown. Cent Eur J Immunol. 2018;43(4):466-75.
78. Hernandez AM, Holodick NE. Editorial: Natural Antibodies in Health and Disease. Frontiers in immunology. 2017;8:1795.
79. Gronwall C, Vas J, Silverman GJ. Protective Roles of Natural IgM Antibodies. Frontiers in immunology. 2012;3:66.
80. Chou MY, Fogelstrand L, Hartvigsen K, Hansen LF, Woelkers D, Shaw PX, et al. Oxidation-specific epitopes are dominant targets of innate natural antibodies in mice and humans. The Journal of clinical investigation. 2009;119(5):1335-49.
81. Iughetti L, Volta C, Maggi E, Palladini G, Perugini C, Bellomo G, et al. Circulating antibodies recognizing oxidatively modified low-density lipoprotein in children. Pediatr Res. 1999;45(1):94-9.
82. Shoji T, Nishizawa Y, Fukumoto M, Shimamura K, Kimura J, Kanda H, et al. Inverse relationship between circulating oxidized low density lipoprotein (oxLDL) and anti-oxLDL antibody levels in healthy subjects. Atherosclerosis. 2000;148(1):171-7.
83. Palinski W, Miller E, Witztum JL. Immunization of low density lipoprotein (LDL) receptor-deficient rabbits with homologous malondialdehyde-modified LDL reduces atherogenesis. Proceedings of the National Academy of Sciences of the United States of America. 1995;92(3):821-5.
84. Major AS, Fazio S, Linton MF. B-lymphocyte deficiency increases atherosclerosis in LDL receptor-null mice. Arteriosclerosis, thrombosis, and vascular biology. 2002;22(11):1892-8.
85. Chang MK, Bergmark C, Laurila A, Hörkkö S, Han KH, Friedman P, et al. Monoclonal antibodies against oxidized low-density lipoprotein bind to apoptotic cells and inhibit their phagocytosis by elicited macrophages: evidence that oxidation-specific epitopes mediate macrophage recognition. Proceedings of the National Academy of Sciences of the United States of America. 1999;96(11):6353-8.
86. Lewis MJ, Malik TH, Ehrenstein MR, Boyle JJ, Botto M, Haskard DO. Immunoglobulin M is required for protection against atherosclerosis in low-density lipoprotein receptor-deficient mice. Circulation. 2009;120(5):417-26.

87. Upadhye A, Srikakulapu P, Gonen A, Hendrikx S, Perry HM, Nguyen AT, et al. Diversification and CXCR4-Dependent Establishment of the Bone Marrow B-1a Cell Pool Governs Atheroprotective IgM Production Linked To Human Coronary Atherosclerosis. 2019.
88. Obermayer G, Afonyushkin T, Goederle L, Puhm F, Schrottmaier WC, Taqi S, et al. Natural IgM antibodies inhibit microvesicle-driven coagulation and thrombosis. Blood. 2020.
89. Iseme RA, McEvoy M, Kelly B, Agnew L, Walker FR, Handley T, et al. A role for autoantibodies in atherogenesis. Cardiovascular research. 2017;113(10):1102-12.
90. van den Berg VJ, Vroegindewey MM, Kardys I, Boersma E, Haskard D, Hartley A, et al. Anti-Oxidized LDL Antibodies and Coronary Artery Disease: A Systematic Review. Antioxidants (Basel). 2019;8(10).
91. Khamis RY, Hughes AD, Caga-Anan M, Chang CL, Boyle JJ, Kojima C, et al. High Serum Immunoglobulin G and M Levels Predict Freedom From Adverse Cardiovascular Events in Hypertension: A Nested Case-Control Substudy of the Anglo-Scandinavian Cardiac Outcomes Trial. EBioMedicine. 2016;9:372-80.
92. Sveen KA, Bech Holte K, Svanteson M, Hanssen KF, Nilsson J, Bengtsson E, et al. Autoantibodies Against Methylglyoxal-Modified Apolipoprotein B100 and ApoB100 Peptide Are Associated With Less Coronary Artery Atherosclerosis and Retinopathy in Long-Term Type 1 Diabetes. Diabetes care. 2021.
93. Nørgaard BL, Leipsic J, Gaur S, Seneviratne S, Ko BS, Ito H, et al. Diagnostic performance of noninvasive fractional flow reserve derived from coronary computed tomography angiography in suspected coronary artery disease: the NXT trial (Analysis of Coronary Blood Flow Using CT Angiography: Next Steps). Journal of the American College of Cardiology. 2014;63(12):1145-55.
94. Dey D, Diaz Zamudio M, Schuhbaeck A, Juarez Orozco LE, Otaki Y, Gransar H, et al. Relationship Between Quantitative Adverse Plaque Features From Coronary Computed Tomography Angiography and Downstream Impaired Myocardial Flow Reserve by 13N-Ammonia Positron Emission Tomography: A Pilot Study. Circulation Cardiovascular imaging. 2015;8(10):e003255.
95. Williams MC, Kwiecinski J, Doris M, McElhinney P, D'Souza MS, Cadet S, et al. Low-Attenuation Noncalcified Plaque on Coronary Computed Tomography Angiography Predicts Myocardial Infarction: Results From the Multicenter SCOT-HEART Trial (Scottish Computed Tomography of the HEART). Circulation. 2020;141(18):1452-62.
96. Investigators S-H. CT coronary angiography in patients with suspected angina due to coronary heart disease (SCOT-HEART): an open-label, parallel-group, multicentre trial. Lancet (London, England). 2015;385(9985):2383-91.
97. Williams MC, Hunter A, Shah ASV, Assi V, Lewis S, Smith J, et al. Use of Coronary Computed Tomographic Angiography to Guide Management of Patients With Coronary Disease. Journal of the American College of Cardiology. 2016;67(15):1759-68.
98. Hoffmann U, Ferencik M, Udelson JE, Picard MH, Truong QA, Patel MR, et al. Prognostic Value of Noninvasive Cardiovascular Testing in Patients With Stable Chest Pain: Insights From the PROMISE Trial (Prospective Multicenter Imaging Study for Evaluation of Chest Pain). Circulation. 2017;135(24):2320-32.
99. Hajhosseiny R, Munoz C, Cruz G, Khamis R, Kim WY, Prieto C, et al. Coronary magnetic resonance angiography in chronic coronary syndromes. Frontiers in Cardiovascular Medicine. 2021;8:682924.
100. Collet JP, Thiele H, Barbato E, Barthélémy O, Bauersachs J, Bhatt DL, et al. 2020 ESC Guidelines for the management of acute coronary syndromes in patients presenting without persistent ST-segment elevation. European heart journal. 2020.

101. Knuuti J, Wijns W, Saraste A, Capodanno D, Barbato E, Funck-Brentano C, et al. 2019 ESC Guidelines for the diagnosis and management of chronic coronary syndromes. European heart journal. 2020;41(3):407-77.
102. Sinclair H, Veerasamy M, Bourantas C, Egred M, Nair A, Calvert PA, et al. The Role of Virtual Histology Intravascular Ultrasound in the Identification of Coronary Artery Plaque Vulnerability in Acute Coronary Syndromes. Cardiology in review. 2016;24(6):303-9.
103. Thim T, Hagensen MK, Wallace-Bradley D, Granada JF, Kaluza GL, Drouet L, et al. Unreliable assessment of necrotic core by virtual histology intravascular ultrasound in porcine coronary artery disease. Circulation Cardiovascular imaging. 2010;3(4):384-91.
104. Jaguszewski M, Klingenberg R, Landmesser U. Intracoronary Near-Infrared Spectroscopy (NIRS) Imaging for Detection of Lipid Content of Coronary Plaques: Current Experience and Future Perspectives. Curr Cardiovasc Imaging Rep. 2013;6(5):426-30.
105. Madder RD, Goldstein JA, Madden SP, Puri R, Wolski K, Hendricks M, et al. Detection by near-infrared spectroscopy of large lipid core plaques at culprit sites in patients with acute ST-segment elevation myocardial infarction. JACC: Cardiovascular Interventions. 2013;6(8):838-46.
106. Khraishah H, Jaffer FA. Intravascular molecular imaging: near-infrared fluorescence as a new frontier. Frontiers in Cardiovascular Medicine. 2020;7:587100.
107. Muller J, Madder R. OCT-NIRS Imaging for Detection of Coronary Plaque Structure and Vulnerability. Front Cardiovasc Med. 2020;7:90.
108. Puri R, Madder RD, Madden SP, Sum ST, Wolski K, Muller JE, et al. Near-Infrared Spectroscopy Enhances Intravascular Ultrasound Assessment of Vulnerable Coronary Plaque: A Combined Pathological and In Vivo Study. Arteriosclerosis, thrombosis, and vascular biology. 2015;35(11):2423-31.
109. Terada K, Kubo T, Kameyama T, Matsuo Y, Ino Y, Emori H, et al. NIRS-IVUS for Differentiating Coronary Plaque Rupture, Erosion, and Calcified Nodule in Acute Myocardial Infarction. JACC Cardiovascular imaging. 2021;14(7):1440-50.
110. Abran M, Stähli BE, Merlet N, Mihalache-Avram T, Mecteau M, Rhéaume E, et al. Validating a bimodal intravascular ultrasound (IVUS) and near-infrared fluorescence (NIRF) catheter for atherosclerotic plaque detection in rabbits. Biomed Opt Express. 2015;6(10):3989-99.
111. Yoo H, Kim JW, Shishkov M, Namati E, Morse T, Shubochkin R, et al. Intra-arterial catheter for simultaneous microstructural and molecular imaging in vivo. Nature medicine. 2011;17(12):1680-4.
112. Ughi GJ, Wang H, Gerbaud E, Gardecki JA, Fard AM, Hamidi E, et al. Clinical Characterization of Coronary Atherosclerosis With Dual-Modality OCT and Near-Infrared Autofluorescence Imaging. JACC Cardiovascular imaging. 2016;9(11):1304-14.
113. Albaghdadi MS, Ikegami R, Kassab MB, Gardecki JA, Kunio M, Chowdhury MM, et al. Near-Infrared Autofluorescence in Atherosclerosis Associates With Ceroid and Is Generated by Oxidized Lipid-Induced Oxidative Stress. Arteriosclerosis, thrombosis, and vascular biology. 2021;41(7):e385-e98.
114. Li Y, Jing J, Qu Y, Miao Y, Zhang B, Ma T, et al. Fully integrated optical coherence tomography, ultrasound, and indocyanine green-based fluorescence tri-modality system for intravascular imaging. Biomedical optics express. 2017;8(2):1036-44.
115. Anderson L, Thompson DR, Oldridge N, Zwisler AD, Rees K, Martin N, et al. Exercise-based cardiac rehabilitation for coronary heart disease. The Cochrane database of systematic reviews. 2016;2016(1):Cd001800.
116. Visseren FLJ, Mach F, Smulders YM, Carballo D, Koskinas KC, Bäck M, et al. 2021 ESC Guidelines on cardiovascular disease prevention in clinical practice. European heart journal. 2021;42(34):3227-337.

117. Liao JK, Laufs U. Pleiotropic effects of statins. Annu Rev Pharmacol Toxicol. 2005;45:89-118.
118. Navarese EP, Lansky AJ, Kereiakes DJ, Kubica J, Gurbel PA, Gorog DA, et al. Cardiac mortality in patients randomised to elective coronary revascularisation plus medical therapy or medical therapy alone: a systematic review and meta-analysis. European heart journal. 2021;42(45):4638-51.
119. Chacko L, J PH, Rajkumar C, Nowbar AN, Kane C, Mahdi D, et al. Effects of Percutaneous Coronary Intervention on Death and Myocardial Infarction Stratified by Stable and Unstable Coronary Artery Disease: A Meta-Analysis of Randomized Controlled Trials. Circulation Cardiovascular quality and outcomes. 2020;13(2):e006363.
120. Wang J, Tan GJ, Han LN, Bai YY, He M, Liu HB. Novel biomarkers for cardiovascular risk prediction. J Geriatr Cardiol. 2017;14(2):135-50.
121. Stone GW, Maehara A, Lansky AJ, de Bruyne B, Cristea E, Mintz GS, et al. A prospective natural-history study of coronary atherosclerosis. The New England journal of medicine. 2011;364(3):226-35.
122. Preiss D, Thomas LE, Sun JL, Haffner SM, Holman RR, Standl E, et al. Predictors of cardiovascular events in a contemporary population with impaired glucose tolerance: an observational analysis of the Nateglinide and Valsartan in impaired glucose tolerance outcomes research (NAVIGATOR) trial. BMJ Open. 2012;2(6).
123. Emini Veseli B, Perrotta P, De Meyer GRA, Roth L, Van der Donckt C, Martinet W, et al. Animal models of atherosclerosis. Eur J Pharmacol. 2017;816:3-13.
124. Getz GS, Reardon CA. Animal models of atherosclerosis. Arteriosclerosis, thrombosis, and vascular biology. 2012;32(5):1104-15.
125. Van Herck JL, De Meyer GR, Martinet W, Van Hove CE, Foubert K, Theunis MH, et al. Impaired fibrillin-1 function promotes features of plaque instability in apolipoprotein E–deficient mice. Circulation. 2009;120(24):2478-87.
126. Watanabe Y. Serial inbreeding of rabbits with hereditary hyperlipidemia (WHHL-rabbit). Atherosclerosis. 1980;36(2):261-8.
127. Niimi M, Yang D, Kitajima S, Ning B, Wang C, Li S, et al. ApoE knockout rabbits: a novel model for the study of human hyperlipidemia. Atherosclerosis. 2016;245:187-93.
128. Jain M, Frobert A, Valentin J, Cook S, Giraud MN. The Rabbit Model of Accelerated Atherosclerosis: A Methodological Perspective of the Iliac Artery Balloon Injury. J Vis Exp. 2017(128).
129. Fan J, Kitajima S, Watanabe T, Xu J, Zhang J, Liu E, et al. Rabbit models for the study of human atherosclerosis: from pathophysiological mechanisms to translational medicine. Pharmacology & therapeutics. 2015;146:104-19.
130. Al-Mashhadi RH, Sørensen CB, Kragh PM, Christoffersen C, Mortensen MB, Tolbod LP, et al. Familial hypercholesterolemia and atherosclerosis in cloned minipigs created by DNA transposition of a human PCSK9 gain-of-function mutant. Science translational medicine. 2013;5(166):166ra1.
131. Pedrigi RM, Poulsen CB, Mehta VV, Ramsing Holm N, Pareek N, Post AL, et al. Inducing Persistent Flow Disturbances Accelerates Atherogenesis and Promotes Thin Cap Fibroatheroma Development in D374Y-PCSK9 Hypercholesterolemic Minipigs. Circulation. 2015;132(11):1003-12.
132. Shim J, Al-Mashhadi RH, Sørensen CB, Bentzon JF. Large animal models of atherosclerosis--new tools for persistent problems in cardiovascular medicine. J Pathol. 2016;238(2):257-66.
133. Man JJ, Beckman JA, Jaffe IZ. Sex as a Biological Variable in Atherosclerosis. Circulation research. 2020;126(9):1297-319.
134. Russell WMS, Burch RL. The principles of humane experimental technique: Methuen; 1959.
135. Prescott MJ, Lidster K. Improving quality of science through better animal welfare: the NC3Rs strategy. Lab animal. 2017;46(4):152-6.

136. Bom MJ, van der Heijden DJ, Kedhi E, van der Heyden J, Meuwissen M, Knaapen P, et al. Early Detection and Treatment of the Vulnerable Coronary Plaque: Can We Prevent Acute Coronary Syndromes? Circulation Cardiovascular imaging. 2017;10(5).
137. Waksman R, Di Mario C, Torguson R, Ali ZA, Singh V, Skinner WH, et al. Identification of patients and plaques vulnerable to future coronary events with near-infrared spectroscopy intravascular ultrasound imaging: a prospective, cohort study. Lancet (London, England). 2019;394(10209):1629-37.
138. Erlinge D, Maehara A, Ben-Yehuda O, Bøtker HE, Maeng M, Kjøller-Hansen L, et al. Identification of vulnerable plaques and patients by intracoronary near-infrared spectroscopy and ultrasound (PROSPECT II): a prospective natural history study. Lancet (London, England). 2021;397(10278):985-95.
139. Stone GW, Maehara A, Ali ZA, Held C, Matsumura M, Kjøller-Hansen L, et al. Percutaneous Coronary Intervention for Vulnerable Coronary Atherosclerotic Plaque. Journal of the American College of Cardiology. 2020;76(20):2289-301.
140. Kennedy MW, Fabris E, Ijsselmuiden AJ, Nef H, Reith S, Escaned J, et al. Combined optical coherence tomography morphologic and fractional flow reserve hemodynamic assessment of non-culprit lesions to better predict adverse event outcomes in diabetes mellitus patients: COMBINE (OCT-FFR) prospective study. Rationale and design. Cardiovascular diabetology. 2016;15(1):144.
141. Mol JQ, Volleberg R, Belkacemi A, Hermanides RS, Meuwissen M, Protopopov AV, et al. Fractional Flow Reserve-Negative High-Risk Plaques and Clinical Outcomes After Myocardial Infarction. JAMA Cardiol. 2023.
142. Jiang S, Fang C, Xu X, Xing L, Sun S, Peng C, et al. Identification of High-Risk Coronary Lesions by 3-Vessel Optical Coherence Tomography. Journal of the American College of Cardiology. 2023;81(13):1217-30.
143. Gallone G, Bellettini M, Gatti M, Tore D, Bruno F, Scudeler L, et al. Coronary Plaque Characteristics Associated With Major Adverse Cardiovascular Events in Atherosclerotic Patients and Lesions: A Systematic Review and Meta-Analysis. JACC Cardiovascular imaging. 2023.
144. Uchida Y, Nakamura F, Tomaru T, Morita T, Oshima T, Sasaki T, et al. Prediction of acute coronary syndromes by percutaneous coronary angioscopy in patients with stable angina. American heart journal. 1995;130(2):195-203.
145. Calvert PA, Obaid DR, O'Sullivan M, Shapiro LM, McNab D, Densem CG, et al. Association between IVUS findings and adverse outcomes in patients with coronary artery disease: the VIVA (VH-IVUS in Vulnerable Atherosclerosis) Study. JACC Cardiovascular imaging. 2011;4(8):894-901.
146. Oemrawsingh RM, Cheng JM, García-García HM, van Geuns RJ, de Boer SP, Simsek C, et al. Near-infrared spectroscopy predicts cardiovascular outcome in patients with coronary artery disease. Journal of the American College of Cardiology. 2014;64(23):2510-8.
147. Cheng JM, Garcia-Garcia HM, de Boer SP, Kardys I, Heo JH, Akkerhuis KM, et al. In vivo detection of high-risk coronary plaques by radiofrequency intravascular ultrasound and cardiovascular outcome: results of the ATHEROREMO-IVUS study. European heart journal. 2014;35(10):639-47.
148. Prati F, Romagnoli E, Gatto L, La Manna A, Burzotta F, Ozaki Y, et al. Relationship between coronary plaque morphology of the left anterior descending artery and 12 months clinical outcome: the CLIMA study. European heart journal. 2020;41(3):383-91.
149. Kubo T, Ino Y, Mintz GS, Shiono Y, Shimamura K, Takahata M, et al. Optical coherence tomography detection of vulnerable plaques at high risk of developing acute coronary syndrome. European heart journal cardiovascular Imaging. 2021.

150. Kedhi E, Berta B, Roleder T, Hermanides RS, Fabris E, AJJ IJ, et al. Thin-cap fibroatheroma predicts clinical events in diabetic patients with normal fractional flow reserve: the COMBINE OCT-FFR trial. European heart journal. 2021.
151. Jinnouchi H, Torii S, Sakamoto A, Kolodgie FD, Virmani R, Finn AV. Fully bioresorbable vascular scaffolds: lessons learned and future directions. Nature Reviews Cardiology. 2019;16(5):286-304.
152. Mol JQ, Bom MJ, Damman P, Knaapen P, van Royen N. Pre-Emptive OCT-Guided Angioplasty of Vulnerable Intermediate Coronary Lesions: Results from the Prematurely Halted PECTUS-Trial. J Interv Cardiol. 2020;2020:8821525.
153. Sehested TSG, Bjerre J, Ku S, Chang A, Jahansouz A, Owens DK, et al. Cost-effectiveness of Canakinumab for Prevention of Recurrent Cardiovascular Events. JAMA Cardiol. 2019;4(2):128-35.
154. Lee SE, Chang HJ, Sung JM, Park HB, Heo R, Rizvi A, et al. Effects of Statins on Coronary Atherosclerotic Plaques: The PARADIGM Study. JACC Cardiovascular imaging. 2018;11(10):1475-84.
155. Nicholls SJ, Puri R, Anderson T, Ballantyne CM, Cho L, Kastelein JJ, et al. Effect of Evolocumab on Progression of Coronary Disease in Statin-Treated Patients: The GLAGOV Randomized Clinical Trial. Jama. 2016;316(22):2373-84.
156. Kini AS, Baber U, Kovacic JC, Limaye A, Ali ZA, Sweeny J, et al. Changes in plaque lipid content after short-term intensive versus standard statin therapy: the YELLOW trial (reduction in yellow plaque by aggressive lipid-lowering therapy). Journal of the American College of Cardiology. 2013;62(1):21-9.
157. Komukai K, Kubo T, Kitabata H, Matsuo Y, Ozaki Y, Takarada S, et al. Effect of atorvastatin therapy on fibrous cap thickness in coronary atherosclerotic plaque as assessed by optical coherence tomography: the EASY-FIT study. Journal of the American College of Cardiology. 2014;64(21):2207-17.
158. Nicholls SJ, Kataoka Y, Nissen SE, Prati F, Windecker S, Puri R, et al. Effect of Evolocumab on Coronary Plaque Phenotype and Burden in Statin-Treated Patients Following Myocardial Infarction. JACC Cardiovascular imaging. 2022;15(7):1308-21.
159. Räber L, Ueki Y, Otsuka T, Losdat S, Häner JD, Lonborg J, et al. Effect of alirocumab added to high-intensity statin therapy on coronary atherosclerosis in patients with acute myocardial infarction: the PACMAN-AMI randomized clinical trial. Jama. 2022;327(18):1771-81.
160. Jaffer FA, Verjans JW. Molecular imaging of atherosclerosis: clinical state-of-the-art. Heart (British Cardiac Society). 2014;100(18):1469-77.
161. Duclos V, Iep A, Gomez L, Goldfarb L, Besson FL. PET Molecular Imaging: A Holistic Review of Current Practice and Emerging Perspectives for Diagnosis, Therapeutic Evaluation and Prognosis in Clinical Oncology. International journal of molecular sciences. 2021;22(8).
162. Knaapen P, de Haan S, Hoekstra OS, Halbmeijer R, Appelman YE, Groothuis JG, et al. Cardiac PET-CT: advanced hybrid imaging for the detection of coronary artery disease. Neth Heart J. 2010;18(2):90-8.
163. Osborn EA, Jaffer FA. The advancing clinical impact of molecular imaging in CVD. JACC Cardiovascular imaging. 2013;6(12):1327-41.
164. Tarkin JM, Joshi FR, Evans NR, Chowdhury MM, Figg NL, Shah AV, et al. Detection of Atherosclerotic Inflammation by (68)Ga-DOTATATE PET Compared to [(18)F]FDG PET Imaging. Journal of the American College of Cardiology. 2017;69(14):1774-91.
165. Singh SB, Ng SJ, Lau HC, Khanal K, Bhattarai S, Paudyal P, et al. Emerging PET Tracers in Cardiac Molecular Imaging. Cardiol Ther. 2023;12(1):85-99.
166. Tzolos E, Bing R, Andrews J, MacAskill MG, Tavares AAS, Macnaught G, et al. Noninvasive In Vivo Coronary Artery Thrombus Imaging. JACC Cardiovascular imaging. 2023;16(6):820-32.

167. Nazir MS, Bustin A, Hajhosseiny R, Yazdani M, Ryan M, Vergani V, et al. High-resolution non-contrast free-breathing coronary cardiovascular magnetic resonance angiography for detection of coronary artery disease: validation against invasive coronary angiography. J Cardiovasc Magn Reson. 2022;24(1):26.
168. Hajhosseiny R, Bahaei TS, Prieto C, Botnar RM. Molecular and nonmolecular magnetic resonance coronary and carotid imaging. Arteriosclerosis, thrombosis, and vascular biology. 2019;39(4):569-82.
169. Capuana F, Phinikaridou A, Stefania R, Padovan S, Lavin B, Lacerda S, et al. Imaging of dysfunctional elastogenesis in atherosclerosis using an improved gadolinium-based tetrameric MRI probe targeted to tropoelastin. Journal of Medicinal Chemistry. 2021;64(20):15250-61.
170. Briley-Saebo KC, Shaw PX, Mulder WJ, Choi SH, Vucic E, Aguinaldo JG, et al. Targeted molecular probes for imaging atherosclerotic lesions with magnetic resonance using antibodies that recognize oxidation-specific epitopes. Circulation. 2008;117(25):3206-15.
171. Briley-Saebo KC, Nguyen TH, Saeboe AM, Cho YS, Ryu SK, Volkova ER, et al. In vivo detection of oxidation-specific epitopes in atherosclerotic lesions using biocompatible manganese molecular magnetic imaging probes. Journal of the American College of Cardiology. 2012;59(6):616-26.
172. Briley-Saebo KC, Cho YS, Shaw PX, Ryu SK, Mani V, Dickson S, et al. Targeted iron oxide particles for in vivo magnetic resonance detection of atherosclerotic lesions with antibodies directed to oxidation-specific epitopes. Journal of the American College of Cardiology. 2011;57(3):337-47.
173. Verjans JW, Osborn EA, Ughi GJ, Calfon Press MA, Hamidi E, Antoniadis AP, et al. Targeted Near-Infrared Fluorescence Imaging of Atherosclerosis: Clinical and Intracoronary Evaluation of Indocyanine Green. JACC Cardiovascular imaging. 2016;9(9):1087-95.
174. Khamis RY, Woollard KJ, Hyde GD, Boyle JJ, Bicknell C, Chang SH, et al. Near Infrared Fluorescence (NIRF) Molecular Imaging of Oxidized LDL with an Autoantibody in Experimental Atherosclerosis. Scientific reports. 2016;6:21785.
175. Lipman NS, Jackson LR, Trudel LJ, Weis-Garcia F. Monoclonal versus polyclonal antibodies: distinguishing characteristics, applications, and information resources. Ilar j. 2005;46(3):258-68.
176. Holvoet P, Vanhaecke J, Janssens S, Van de Werf F, Collen D. Oxidized LDL and malondialdehyde-modified LDL in patients with acute coronary syndromes and stable coronary artery disease. Circulation. 1998;98(15):1487-94.
177. Holvoet P, Lee DH, Steffes M, Gross M, Jacobs DR, Jr. Association between circulating oxidized low-density lipoprotein and incidence of the metabolic syndrome. Jama. 2008;299(19):2287-93.
178. Couillard C, Ruel G, Archer WR, Pomerleau S, Bergeron J, Couture P, et al. Circulating levels of oxidative stress markers and endothelial adhesion molecules in men with abdominal obesity. J Clin Endocrinol Metab. 2005;90(12):6454-9.
179. Itabe H. Oxidative modification of LDL: its pathological role in atherosclerosis. Clin Rev Allergy Immunol. 2009;37(1):4-11.
180. Itabe H, Yamamoto H, Suzuki M, Kawai Y, Nakagawa Y, Suzuki A, et al. Oxidized phosphatidylcholines that modify proteins. Analysis by monoclonal antibody against oxidized low density lipoprotein. The Journal of biological chemistry. 1996;271(52):33208-17.
181. Palinski W, Horkko S, Miller E, Steinbrecher UP, Powell HC, Curtiss LK, et al. Cloning of monoclonal autoantibodies to epitopes of oxidized lipoproteins from apolipoprotein E-deficient mice. Demonstration of epitopes of oxidized low density lipoprotein in human plasma. The Journal of clinical investigation. 1996;98(3):800-14.
182. Tsimikas S, Shortal BP, Witztum JL, Palinski W. In vivo uptake of radiolabeled MDA2, an oxidation-specific monoclonal antibody, provides an accurate measure of atherosclerotic lesions rich

in oxidized LDL and is highly sensitive to their regression. Arteriosclerosis, thrombosis, and vascular biology. 2000;20(3):689-97.
183. Lehrer-Graiwer J, Singh P, Abdelbaky A, Vucic E, Korsgren M, Baruch A, et al. FDG-PET imaging for oxidized LDL in stable atherosclerotic disease: a phase II study of safety, tolerability, and anti-inflammatory activity. JACC Cardiovascular imaging. 2015;8(4):493-4.
184. Lorenzo C, Delgado P, Busse CE, Sanz-Bravo A, Martos-Folgado I, Bonzon-Kulichenko E, et al. ALDH4A1 is an atherosclerosis auto-antigen targeted by protective antibodies. Nature. 2021;589(7841):287-92.
185. Nelson AL. Antibody fragments: hope and hype. MAbs. 2010;2(1):77-83.
186. Bates A, Power CA. David vs. Goliath: the structure, function, and clinical prospects of antibody fragments. Antibodies. 2019;8(2):28.
187. Freise AC, Wu AM. In vivo imaging with antibodies and engineered fragments. Mol Immunol. 2015;67(2 Pt A):142-52.
188. Stephen ZR, Kievit FM, Zhang M. Magnetite Nanoparticles for Medical MR Imaging. Mater Today (Kidlington). 2011;14(7-8):330-8.
189. Anselmo AC, Mitragotri S. Nanoparticles in the clinic: An update. Bioeng Transl Med. 2019;4(3):e10143.
190. Khurana A, Allawadhi P, Khurana I, Allwadhi S, Weiskirchen R, Banothu AK, et al. Role of nanotechnology behind the success of mRNA vaccines for COVID-19. Nano Today. 2021;38:101142.
191. Silva S, Almeida AJ, Vale N. Combination of Cell-Penetrating Peptides with Nanoparticles for Therapeutic Application: A Review. Biomolecules. 2019;9(1).
192. Mitragotri S, Stayton P. Organic nanoparticles for drug delivery and imaging. Mrs Bulletin. 2014;39(3):219-23.
193. Alshammari BH, Lashin MM, Mahmood MA, Al-Mubaddel FS, Ilyas N, Rahman N, et al. Organic and inorganic nanomaterials: fabrication, properties and applications. RSC advances. 2023;13(20):13735-85.
194. Locatelli E, Franchini MC. Biodegradable PLGA-b-PEG polymeric nanoparticles: synthesis, properties, and nanomedical applications as drug delivery system. Journal of Nanoparticle Research. 2012;14(12):1-17.
195. Zhang M, He J, Jiang C, Zhang W, Yang Y, Wang Z, et al. Plaque-hyaluronidase-responsive high-density-lipoprotein-mimetic nanoparticles for multistage intimal-macrophage-targeted drug delivery and enhanced anti-atherosclerotic therapy. Int J Nanomedicine. 122017. p. 533-58.
196. Koga J, Matoba T, Egashira K. Anti-inflammatory Nanoparticle for Prevention of Atherosclerotic Vascular Diseases. J Atheroscler Thromb. 2016;23(7):757-65.
197. Zia A, Wu Y, Nguyen T, Wang X, Peter K, Ta HT. The choice of targets and ligands for site-specific delivery of nanomedicine to atherosclerosis. Cardiovascular research. 2020;116(13):2055-68.
198. van der Valk FM, van Wijk DF, Lobatto ME, Verberne HJ, Storm G, Willems MC, et al. Prednisolone-containing liposomes accumulate in human atherosclerotic macrophages upon intravenous administration. Nanomedicine : nanotechnology, biology, and medicine. 2015;11(5):1039-46.
199. Flores AM, Ye J, Jarr KU, Hosseini-Nassab N, Smith BR, Leeper NJ. Nanoparticle Therapy for Vascular Diseases. Arteriosclerosis, thrombosis, and vascular biology. 2019;39(4):635-46.
200. Di Mascolo D, C JL, Aryal S, Ramirez MR, Wang J, Candeloro P, et al. Rosiglitazone-loaded nanospheres for modulating macrophage-specific inflammation in obesity. J Control Release. 2013;170(3):460-8.

201. Zhang XQ, Even-Or O, Xu X, van Rosmalen M, Lim L, Gadde S, et al. Nanoparticles containing a liver X receptor agonist inhibit inflammation and atherosclerosis. Adv Healthc Mater. 2015;4(2):228-36.
202. Sanchez-Gaytan BL, Fay F, Lobatto ME, Tang J, Ouimet M, Kim Y, et al. HDL-Mimetic PLGA Nanoparticle To Target Atherosclerosis Plaque Macrophages. Bioconjug Chem. 2015;26(3):443-51.
203. Nakashiro S, Matoba T, Umezu R, Koga J, Tokutome M, Katsuki S, et al. Pioglitazone-Incorporated Nanoparticles Prevent Plaque Destabilization and Rupture by Regulating Monocyte/Macrophage Differentiation in ApoE-/- Mice. Arteriosclerosis, thrombosis, and vascular biology. 2016;36(3):491-500.
204. Zhao Y, Jiang C, He J, Guo Q, Lu J, Yang Y, et al. Multifunctional Dextran Sulfate-Coated Reconstituted High Density Lipoproteins Target Macrophages and Promote Beneficial Antiatherosclerotic Mechanisms. Bioconjug Chem. 2017;28(2):438-48.
205. Imanparast F, Paknejad M, Faramarzi MA, Kobarfard F, Amani A, Doosti M. Potential of mZD7349-conjugated PLGA nanoparticles for selective targeting of vascular cell-adhesion molecule-1 in inflamed endothelium. Microvasc Res. 2016;106:110-6.
206. Imanparast F, Faramarzi MA, Vatannejad A, Paknejad M, Deiham B, Kobarfard F, et al. mZD7349 peptide-conjugated PLGA nanoparticles directed against VCAM-1 for targeted delivery of simvastatin to restore dysfunctional HUVECs. Microvasc Res. 2017;112:14-9.
207. Koenig O, Zengerle D, Perle N, Hossfeld S, Neumann B, Behring A, et al. RNA-Eluting Surfaces for the Modulation of Gene Expression as A Novel Stent Concept. Pharmaceuticals (Basel). 2017;10(1).
208. Li Z, Huang H, Huang L, Du L, Sun Y, Duan Y. Prevention of Oxidized Low Density Lipoprotein-Induced Endothelial Cell Injury by DA-PLGA-PEG-cRGD Nanoparticles Combined with Ultrasound. International journal of molecular sciences. 2017;18(4).
209. Dou Y, Chen Y, Zhang X, Xu X, Chen Y, Guo J, et al. Non-proinflammatory and responsive nanoplatforms for targeted treatment of atherosclerosis. Biomaterials. 2017;143:93-108.
210. Le DQ, Kuriakose AE, Nguyen DX, Nguyen KT, Acharya S. Hybrid Nitric Oxide Donor and its Carrier for the Treatment of Peripheral Arterial Diseases. Scientific reports. 2017;7(1):8692.
211. Ameruoso A, Palomba R, Palange AL, Cervadoro A, Lee A, Di Mascolo D, et al. Ameliorating Amyloid-beta Fibrils Triggered Inflammation via Curcumin-Loaded Polymeric Nanoconstructs. Frontiers in immunology. 2017;8:1411.
212. Ochin CC, Garelnabi M. Berberine Encapsulated PLGA-PEG Nanoparticles Modulate PCSK-9 in HepG2 Cells. Cardiovasc Hematol Disord Drug Targets. 2018;18(1):61-70.
213. Zhang M, He J, Zhang W, Liu J. Fabrication of TPGS-Stabilized Liposome-PLGA Hybrid Nanoparticle Via a New Modified Nanoprecipitation Approach: In Vitro and In Vivo Evaluation. Pharm Res. 2018;35(11):199.
214. Ye M, Zhou J, Zhong Y, Xu J, Hou J, Wang X, et al. SR-A-Targeted Phase-Transition Nanoparticles for the Detection and Treatment of Atherosclerotic Vulnerable Plaques. ACS Appl Mater Interfaces. 2019;11(10):9702-15.
215. Chen C, Mei H, Shi W, Deng J, Zhang B, Guo T, et al. EGFP-EGF1-conjugated PLGA nanoparticles for targeted delivery of siRNA into injured brain microvascular endothelial cells for efficient RNA interference. PloS one. 2013;8(4):e60860.
216. Wu Z, Chen C, Zhang B, Tang L, Shi W, Liao D, et al. EGFP-EGF1-conjugated poly(lactic-co-glycolic acid) nanoparticles, a new diagnostic tool and drug carrier for atherosclerosis. Int J Nanomedicine. 2019;14:2609-18.

217. Wu Z, Chen C, Luo J, Davis JRJ, Zhang B, Tang L, et al. EGFP-EGF1-conjugated poly (lactic-co-glycolic acid) nanoparticles as a carrier for the delivery of CCR2- shRNA to atherosclerotic macrophage in vitro. Scientific reports. 2020;10(1):19636.
218. Wang L, Feng M, Li Y, Du Y, Wang H, Chen Y, et al. Fabrication of superparamagnetic nano-silica@ quercetin-encapsulated PLGA nanocomposite: Potential application for cardiovascular diseases. J Photochem Photobiol B. 2019;196:111508.
219. Wang Y, Zhang K, Qin X, Li T, Qiu J, Yin T, et al. Biomimetic Nanotherapies: Red Blood Cell Based Core-Shell Structured Nanocomplexes for Atherosclerosis Management. Adv Sci (Weinh). 2019;6(12):1900172.
220. Esfandyari-Manesh M, Abdi M, Talasaz AH, Ebrahimi SM, Atyabi F, Dinarvand R. S2P peptide-conjugated PLGA-Maleimide-PEG nanoparticles containing Imatinib for targeting drug delivery to atherosclerotic plaques. Daru. 2020.
221. Om H, El-Naggar ME, El-Banna M, Fouda MMG, Othman SI, Allam AA, et al. Combating atherosclerosis with targeted Diosmin nanoparticles-treated experimental diabetes. Invest New Drugs. 2020.
222. Yang H, Song Y, Chen J, Pang Z, Zhang N, Cao J, et al. Platelet Membrane-Coated Nanoparticles Target Sclerotic Aortic Valves in ApoE(-/-) Mice by Multiple Binding Mechanisms Under Pathological Shear Stress. Int J Nanomedicine. 2020;15:901-12.
223. Chen Q, Gao M, Li Z, Xiao Y, Bai X, Boakye-Yiadom KO, et al. Biodegradable nanoparticles decorated with different carbohydrates for efficient macrophage-targeted gene therapy. J Control Release. 2020;323:179-90.
224. Wang S, Guo X, Ren L, Wang B, Hou L, Zhou H, et al. Targeting and deep-penetrating delivery strategy for stented coronary artery by magnetic guidance and ultrasound stimulation. Ultrason Sonochem. 2020;67:105188.
225. Chen JA, Guo W, Wang Z, Sun N, Pan H, Tan J, et al. In Vivo Imaging of Senescent Vascular Cells in Atherosclerotic Mice Using a β-Galactosidase-Activatable Nanoprobe. Anal Chem. 2020;92(18):12613-21.
226. Yi X, Wang Y, Jia Z, Hiller S, Nakamura J, Luft JC, et al. Retinoic Acid-Loaded Poly(lactic-co-glycolic acid) Nanoparticle Formulation of ApoB-100-Derived Peptide 210 Attenuates Atherosclerosis. J Biomed Nanotechnol. 2020;16(4):467-80.
227. Khang MK, Kuriakose AE, Nguyen T, Co CM, Zhou J, Truong TTD, et al. Enhanced Endothelial Cell Delivery for Repairing Injured Endothelium via Pretargeting Approach and Bioorthogonal Chemistry. ACS Biomater Sci Eng. 2020;6(12):6831-41.
228. Wang Y, Zhang K, Li T, Maruf A, Qin X, Luo L, et al. Macrophage membrane functionalized biomimetic nanoparticles for targeted anti-atherosclerosis applications. Theranostics. 2021;11(1):164-80.
229. Yin T, Li Y, Ren Y, Fuad ARM, Hu F, Du R, et al. Phagocytosis of polymeric nanoparticles aided activation of macrophages to increase atherosclerotic plaques in ApoE(-/-) mice. J Nanobiotechnology. 2021;19(1):121.
230. Gao B, Xu J, Zhou J, Zhang H, Yang R, Wang H, et al. Multifunctional pathology-mapping theranostic nanoplatforms for US/MR imaging and ultrasound therapy of atherosclerosis. Nanoscale. 2021;13(18):8623-38.
231. Pillai SC, Borah A, Le MNT, Kawano H, Hasegawa K, Kumar DS. Co-Delivery of Curcumin and Bioperine via PLGA Nanoparticles to Prevent Atherosclerotic Foam Cell Formation. Pharmaceutics. 2021;13(9).

232. Katsuki S, Koga JI, Matoba T, Umezu R, Nakashiro S, Nakano K, et al. Nanoparticle-Mediated Delivery of Pitavastatin to Monocytes/Macrophages Inhibits Angiotensin II-Induced Abdominal Aortic Aneurysm Formation in Apoe(-/-) Mice. J Atheroscler Thromb. 2022;29(1):111-25.
233. Li Y, Che J, Chang L, Guo M, Bao X, Mu D, et al. CD47- and Integrin α4/β1-Comodified-Macrophage-Membrane-Coated Nanoparticles Enable Delivery of Colchicine to Atherosclerotic Plaque. Adv Healthc Mater. 2022;11(4):e2101788.
234. Shen JW, Li C, Yang MY, Lin JF, Yin MD, Zou JJ, et al. Biomimetic nanoparticles: U937 cell membranes based core-shell nanosystems for targeted atherosclerosis therapy. Int J Pharm. 2022;611:121297.
235. Leal BH, Velasco B, Cambón A, Pardo A, Fernandez-Vega J, Arellano L, et al. Combined Therapeutics for Atherosclerosis Treatment Using Polymeric Nanovectors. Pharmaceutics. 2022;14(2).
236. Chen Y, Chen Z, Duan J, Gui L, Li H, Liang X, et al. H(2)O(2)-responsive VEGF/NGF gene co-delivery nano-system achieves stable vascularization in ischemic hindlimbs. J Nanobiotechnology. 2022;20(1):145.
237. Zhou J, Niu C, Huang B, Chen S, Yu C, Cao S, et al. Platelet Membrane Biomimetic Nanoparticles Combined With UTMD to Improve the Stability of Atherosclerotic Plaques. Front Chem. 2022;10:868063.
238. Li G, Xu F, Yang B, Lu X, Li X, Qi Y, et al. A nanotherapy responsive to the inflammatory microenvironment for the dual-targeted treatment of atherosclerosis. Nanomedicine : nanotechnology, biology, and medicine. 2022;43:102557.
239. Fang F, Ni Y, Yu H, Yin H, Yang F, Li C, et al. Inflammatory endothelium-targeted and cathepsin responsive nanoparticles are effective against atherosclerosis. Theranostics. 2022;12(9):4200-20.
240. De Negri Atanasio G, Ferrari PF, Baião A, Perego P, Sarmento B, Palombo D, et al. Bevacizumab encapsulation into PLGA nanoparticles functionalized with immunouteroglobin-1 as an innovative delivery system for atherosclerosis. Int J Biol Macromol. 2022;221:1618-30.
241. Craciun I, Astete CE, Boldor D, Jennings MH, Gorman JD, Sabliov CM, et al. Nanoparticle coatings for controlled release of quercetin from an angioplasty balloon. PloS one. 2022;17(8):e0268307.
242. Zhang X, Misra SK, Moitra P, Zhang X, Jeong SJ, Stitham J, et al. Use of acidic nanoparticles to rescue macrophage lysosomal dysfunction in atherosclerosis. Autophagy. 2023;19(3):886-903.
243. Liu M, Gao T, Jiang L, Li S, Shi B, Li F. Enhancing the biopharmaceutical attributes of atorvastatin calcium using polymeric and lipid-polymer hybrid nanoparticles: An approach for atherosclerosis treatment. Biomed Pharmacother. 2023;159:114261.
244. Zhu Y, Xu Y, Han D, Zhang X, Qin C, Liu J, et al. Scavenger receptor-AI targeted theranostic nanoparticles for regression of atherosclerotic plaques via ABCA1 modulation. Nanomedicine : nanotechnology, biology, and medicine. 2023;50:102672.
245. Dash R, Yadav M, Biswal J, Chandra A, Goel VK, Sharma T, et al. Modeling of chitosan modified PLGA atorvastatin-curcumin conjugate (AT-CU) nanoparticles, overcoming the barriers associated with PLGA: An approach for better management of atherosclerosis. Int J Pharm. 2023;640:123009.
246. Groner J, Tognazzi M, Walter M, Fleischmann D, Mietzner R, Ziegler CE, et al. Encapsulation of Pioglitazone into Polymer-Nanoparticles for Potential Treatment of Atherosclerotic Diseases. ACS Appl Bio Mater. 2023;6(6):2111-21.
247. Huang JH, Huang CJ, Yu LN, Guan XL, Liang SW, Li JH, et al. Bioinspired PROTAC-induced macrophage fate determination alleviates atherosclerosis. Acta Pharmacol Sin. 2023;44(10):1962-76.
248. Karami Z, Mehrzad J, Akrami M, Hosseinkhani S. Anti-inflammation-based treatment of atherosclerosis using Gliclazide-loaded biomimetic nanoghosts. Scientific reports. 2023;13(1):13880.

249. Li Y, Zhang B, Liu X, Wan H, Qin Y, Yan H, et al. A bio-inspired nanoparticle coating for vascular healing and immunomodulatory by cGMP-PKG and NF-kappa B signaling pathways. Biomaterials. 2023;302:122288.
250. Duivenvoorden R, Tang J, Cormode DP, Mieszawska AJ, Izquierdo-Garcia D, Ozcan C, et al. A statin-loaded reconstituted high-density lipoprotein nanoparticle inhibits atherosclerotic plaque inflammation. Nature communications. 2014;5:3065.
251. McLeod O, Silveira A, Fredrikson GN, Gertow K, Baldassarre D, Veglia F, et al. Plasma autoantibodies against apolipoprotein B-100 peptide 210 in subclinical atherosclerosis. Atherosclerosis. 2014;232(1):242-8.
252. Chang SH, Johns M, Boyle JJ, McConnell E, Kirkham PA, Bicknell C, et al. Model IgG monoclonal autoantibody-anti-idiotype pair for dissecting the humoral immune response to oxidized low density lipoprotein. Hybridoma (2005). 2012;31(2):87-98.
253. Pandey SS, Hartley A, Caga-Anan M, Ammari T, Khan AHA, Nguyen BAV, et al. A Novel Immunoassay for Malondialdehyde-Conjugated Low-Density Lipoprotein Measures Dynamic Changes in the Blood of Patients Undergoing Coronary Artery Bypass Graft Surgery. Antioxidants (Basel). 2021;10(8).
254. Hartley A, Pradeep M, Van den Berg V, Khan AHA, Shah HA, Allaf M, et al. Depletion of Homeostatic Antibodies against Malondialdehyde-Modified Low-Density Lipoprotein Correlates with Adverse Events in Major Vascular Surgery. Antioxidants (Basel). 2022;11(2).
255. van den Berg VJ, Haskard DO, Fedorowski A, Hartley A, Kardys I, Caga-Anan M, et al. IgM anti-malondialdehyde low density lipoprotein antibody levels indicate coronary heart disease and necrotic core characteristics in the Nordic Diltiazem (NORDIL) study and the Integrated Imaging and Biomarker Study 3 (IBIS-3). EBioMedicine. 2018;36:63-72.
256. Skinner JS, Smeeth L, Kendall JM, Adams PC, Timmis A. NICE guidance. Chest pain of recent onset: assessment and diagnosis of recent onset chest pain or discomfort of suspected cardiac origin. Heart (British Cardiac Society). 2010;96(12):974-8.
257. Gulati M, Levy PD, Mukherjee D, Amsterdam E, Bhatt DL, Birtcher KK, et al. 2021 AHA/ACC/ASE/CHEST/SAEM/SCCT/SCMR Guideline for the Evaluation and Diagnosis of Chest Pain: A Report of the American College of Cardiology/American Heart Association Joint Committee on Clinical Practice Guidelines. Journal of the American College of Cardiology. 2021;78(22):e187-e285.
258. Newby DE, Adamson PD, Berry C, Boon NA, Dweck MR, Flather M, et al. Coronary CT Angiography and 5-Year Risk of Myocardial Infarction. The New England journal of medicine. 2018;379(10):924-33.
259. Williams MC, Golay SK, Hunter A, Weir-McCall JR, Mlynska L, Dweck MR, et al. Observer variability in the assessment of CT coronary angiography and coronary artery calcium score: substudy of the Scottish COmputed Tomography of the HEART (SCOT-HEART) trial. Open Heart. 2015;2(1):e000234.
260. Agatston AS, Janowitz WR, Hildner FJ, Zusmer NR, Viamonte M, Jr., Detrano R. Quantification of coronary artery calcium using ultrafast computed tomography. Journal of the American College of Cardiology. 1990;15(4):827-32.
261. de la Iglesia B, Potter JF, Poulter NR, Robins MM, Skinner J. Performance of the ASSIGN cardiovascular disease risk score on a UK cohort of patients from general practice. Heart (British Cardiac Society). 2011;97(6):491-9.
262. Woodward M, Brindle P, Tunstall-Pedoe H. Adding social deprivation and family history to cardiovascular risk assessment: the ASSIGN score from the Scottish Heart Health Extended Cohort (SHHEC). Heart (British Cardiac Society). 2007;93(2):172-6.

263. Øvrehus KA, Schuhbaeck A, Marwan M, Achenbach S, Nørgaard BL, Bøtker HE, et al. Reproducibility of semi-automatic coronary plaque quantification in coronary CT angiography with sub-mSv radiation dose. Journal of cardiovascular computed tomography. 2016;10(2):114-20.
264. Gudmundsson EF, Gudnason V, Sigurdsson S, Launer LJ, Harris TB, Aspelund T. Coronary artery calcium distributions in older persons in the AGES-Reykjavik study. European journal of epidemiology. 2012;27(9):673-87.
265. Boden WE, O'Rourke RA, Teo KK, Hartigan PM, Maron DJ, Kostuk WJ, et al. Optimal medical therapy with or without PCI for stable coronary disease. The New England journal of medicine. 2007;356(15):1503-16.
266. Sedlis SP, Hartigan PM, Teo KK, Maron DJ, Spertus JA, Mancini GB, et al. Effect of PCI on Long-Term Survival in Patients with Stable Ischemic Heart Disease. The New England journal of medicine. 2015;373(20):1937-46.
267. Stergiopoulos K, Boden WE, Hartigan P, Möbius-Winkler S, Hambrecht R, Hueb W, et al. Percutaneous coronary intervention outcomes in patients with stable obstructive coronary artery disease and myocardial ischemia: a collaborative meta-analysis of contemporary randomized clinical trials. JAMA Intern Med. 2014;174(2):232-40.
268. Al-Lamee R, Thompson D, Dehbi HM, Sen S, Tang K, Davies J, et al. Percutaneous coronary intervention in stable angina (ORBITA): a double-blind, randomised controlled trial. Lancet (London, England). 2018;391(10115):31-40.
269. Al-Lamee RK, Shun-Shin MJ, Howard JP, Nowbar AN, Rajkumar C, Thompson D, et al. Dobutamine Stress Echocardiography Ischemia as a Predictor of the Placebo-Controlled Efficacy of Percutaneous Coronary Intervention in Stable Coronary Artery Disease: The Stress Echocardiography-Stratified Analysis of ORBITA. Circulation. 2019;140(24):1971-80.
270. Team RC. R: A language and environment for statistical computing. R Foundation for Statistical Computing, Vienna, Austria.
. 2020.
271. Jr FEH. Regression Modeling Strategies. R package version 6.1-0.; 2020.
272. Khan TZ, Hartley A, Haskard D, Caga-Anan M, Pennell DJ, Collins P, et al. Oxidised LDL and Anti-Oxidised LDL Antibodies Are Reduced by Lipoprotein Apheresis in a Randomised Controlled Trial on Patients with Refractory Angina and Elevated Lipoprotein(a). Antioxidants (Basel). 2021;10(1).
273. Palinski W, Yla-Herttuala S, Rosenfeld ME, Butler SW, Socher SA, Parthasarathy S, et al. Antisera and monoclonal antibodies specific for epitopes generated during oxidative modification of low density lipoprotein. Arteriosclerosis (Dallas, Tex). 1990;10(3):325-35.
274. Linse S, Scheidt T, Bernfur K, Vendruscolo M, Dobson CM, Cohen SIA, et al. Kinetic fingerprints differentiate the mechanisms of action of anti-Aβ antibodies. Nat Struct Mol Biol. 2020;27(12):1125-33.
275. Crivianu-Gaita V, Romaschin A, Thompson M. High efficiency reduction capability for the formation of Fab' antibody fragments from F(ab)(2) units. Biochem Biophys Rep. 2015;2:23-8.
276. Nava-Arzaluz MG, Piñón-Segundo E, Ganem-Rondero A, Lechuga-Ballesteros D. Single emulsion-solvent evaporation technique and modifications for the preparation of pharmaceutical polymeric nanoparticles. Recent Pat Drug Deliv Formul. 2012;6(3):209-23.
277. Kirley TL, Greis KD, Norman AB. Selective disulfide reduction for labeling and enhancement of Fab antibody fragments. Biochem Biophys Res Commun. 2016;480(4):752-7.
278. Schneider CA, Rasband WS, Eliceiri KW. NIH Image to ImageJ: 25 years of image analysis. Nat Methods. 2012;9(7):671-5.
279. O'Brien J, Hayder H, Peng C. Automated Quantification and Analysis of Cell Counting Procedures Using ImageJ Plugins. J Vis Exp. 2016(117).

280. Ishibashi S, Brown MS, Goldstein JL, Gerard RD, Hammer RE, Herz J. Hypercholesterolemia in low density lipoprotein receptor knockout mice and its reversal by adenovirus-mediated gene delivery. The Journal of clinical investigation. 1993;92(2):883-93.
281. Wilson PW, D'Agostino RB, Levy D, Belanger AM, Silbershatz H, Kannel WB. Prediction of coronary heart disease using risk factor categories. Circulation. 1998;97(18):1837-47.
282. Hippisley-Cox J, Coupland C, Brindle P. Development and validation of QRISK3 risk prediction algorithms to estimate future risk of cardiovascular disease: prospective cohort study. BMJ (Clinical research ed). 2017;357:j2099.
283. Matsumoto H, Watanabe S, Kyo E, Tsuji T, Ando Y, Eisenberg E, et al. Improved Evaluation of Lipid-Rich Plaque at Coronary CT Angiography: Head-to-Head Comparison with Intravascular US. Radiol Cardiothorac Imaging. 2019;1(5):e190069.
284. Poznyak AV, Nikiforov NG, Markin AM, Kashirskikh DA, Myasoedova VA, Gerasimova EV, et al. Overview of OxLDL and its impact on cardiovascular health: focus on atherosclerosis. Frontiers in pharmacology. 2021:2248.
285. Linna M, Ahotupa M, Löppönen MK, Irjala K, Vasankari T. Circulating oxidised LDL lipids, when proportioned to HDL-c, emerged as a risk factor of all-cause mortality in a population-based survival study. Age and ageing. 2013;42(1):110-3.
286. Meisinger C, Baumert J, Khuseyinova N, Loewel H, Koenig W. Plasma oxidized low-density lipoprotein, a strong predictor for acute coronary heart disease events in apparently healthy, middle-aged men from the general population. Circulation. 2005;112(5):651-7.
287. Prasad A, Clopton P, Ayers C, Khera A, de Lemos JA, Witztum JL, et al. Relationship of Autoantibodies to MDA-LDL and ApoB-Immune Complexes to Sex, Ethnicity, Subclinical Atherosclerosis, and Cardiovascular Events. Arteriosclerosis, thrombosis, and vascular biology. 2017;37(6):1213-21.
288. Babakr AT, Elsheikh OM, Almarzouki AA, Assiri AM, Abdalla BEE, Zaki HY, et al. Relationship between oxidized low-density lipoprotein antibodies and obesity in different glycemic situations. Diabetes, Metabolic Syndrome and Obesity: Targets and Therapy. 2014:513-20.
289. Wu R, de Faire U, Lemne C, Witztum JL, Frostegård J. Autoantibodies to OxLDL are decreased in individuals with borderline hypertension. Hypertension (Dallas, Tex : 1979). 1999;33(1):53-9.
290. Greenland P, LaBree L, Azen SP, Doherty TM, Detrano RC. Coronary artery calcium score combined with Framingham score for risk prediction in asymptomatic individuals. Jama. 2004;291(2):210-5.
291. Larroche J, Panh L, Lhermusier T, Bataille V, Marachet MA, Chollet T, et al. Impact of aortic valve calcification severity on device success after transcatheter aortic valve replacement. The international journal of cardiovascular imaging. 2020;36(4):731-40.
292. Osaka S, Tanaka M. Strategy for Porcelain Ascending Aorta in Cardiac Surgery. Ann Thorac Cardiovasc Surg. 2018;24(2):57-64.
293. Greenland P, Blaha MJ, Budoff MJ, Erbel R, Watson KE. Coronary calcium score and cardiovascular risk. Journal of the American College of Cardiology. 2018;72(4):434-47.
294. Pawade T, Clavel MA, Tribouilloy C, Dreyfus J, Mathieu T, Tastet L, et al. Computed Tomography Aortic Valve Calcium Scoring in Patients With Aortic Stenosis. Circulation Cardiovascular imaging. 2018;11(3):e007146.
295. Fox CS, Vasan RS, Parise H, Levy D, O'Donnell CJ, D'Agostino RB, et al. Mitral annular calcification predicts cardiovascular morbidity and mortality: the Framingham Heart Study. Circulation. 2003;107(11):1492-6.

296. Williams MC, Massera D, Moss AJ, Bing R, Bularga A, Adamson PD, et al. Prevalence and clinical implications of valvular calcification on coronary computed tomography angiography. European heart journal cardiovascular Imaging. 2021;22(3):262-70.
297. Taleb A, Willeit P, Amir S, Perkmann T, Kozma MO, Watzenböck ML, et al. High Immunoglobulin-M Levels to Oxidation-Specific Epitopes Are Associated with Lower Risk of Acute Myocardial Infarction. Journal of lipid research. 2023:100391.
298. Chen Q, Reis SE, Kammerer C, Craig W, McNamara DM, Holubkov R, et al. Association of anti-oxidized LDL and candidate genes with severity of coronary stenosis in the Women's Ischemia Syndrome Evaluation study. Journal of lipid research. 2011;52(4):801-7.
299. Martos-Folgado I, del Monte-Monge A, Lorenzo C, Busse CE, Delgado P, Mur SM, et al. MDA-LDL vaccination induces athero-protective germinal-center-derived antibody responses. Cell Reports. 2022;41(2):111468.
300. Pattarabanjird T, Nguyen AT, McSkimming C, Dinh HQ, Marshall MA, Ghosheh Y, et al. Human circulating CD24hi marginal zone B cells produce IgM targeting atherogenic antigens and confer protection from vascular disease. Nature Cardiovascular Research. 2023:1-12.
301. Horkko S, Bird DA, Miller E, Itabe H, Leitinger N, Subbanagounder G, et al. Monoclonal autoantibodies specific for oxidized phospholipids or oxidized phospholipid-protein adducts inhibit macrophage uptake of oxidized low-density lipoproteins. The Journal of clinical investigation. 1999;103(1):117-28.
302. Que X, Hung M-Y, Yeang C, Gonen A, Prohaska TA, Sun X, et al. Oxidized phospholipids are proinflammatory and proatherogenic in hypercholesterolaemic mice. Nature. 2018;558(7709):301.
303. Sakai R, Sekimoto T, Arai T, Tanaka H, Ogura K, Oishi Y, et al. Contributions of small dense LDL and oxidized LDL on the formation of neoatherosclerosis in patients under statin treatment. European heart journal. 2021;42(Supplement_1):ehab724. 3370.
304. Caparevic Z, Kostic N, Celic V, Cosic Z, Marina D, Ilic S, et al. Effects of acute exercise on atherogenic lipids in untreated mild hypertensive patients. Vojnosanit Pregl. 2009;66(4):313-8.
305. Jorde UP, Colombo PC, Ahuja K, Hudaihed A, Onat D, Diaz T, et al. Exercise-induced increases in oxidized low-density lipoprotein are associated with adverse outcomes in chronic heart failure. Journal of cardiac failure. 2007;13(9):759-64.
306. Kostic N, Caparevic Z, Marina D, Ilic S, Radojkovic J, Cosic Z, et al. Clinical evaluation of oxidative stress in patients with diabetes mellitus type II -- impact of acute exercise. Vojnosanit Pregl. 2009;66(6):459-64.
307. Medlow P, McEneny J, Murphy MH, Trinick T, Duly E, Davison GW. Lipoprotein subfraction oxidation in acute exercise and ageing. Free Radic Res. 2016;50(3):345-53.
308. Medlow P, McEneny J, Murphy MH, Trinick T, Duly E, Davison GW. Exercise training protects the LDL I subfraction from oxidation susceptibility in an aged human population. Atherosclerosis. 2015;239(2):516-22.
309. Takashima A, Ise T, Yagi S, Iwase T, Kimura S, Ueda Y, et al. Cardiac rehabilitation reduces serum levels of oxidized low-density lipoprotein. Circulation journal : official journal of the Japanese Circulation Society. 2014;78(11):2682-7.
310. Benedetti S, Catalani S, Peda F, Luchetti F, Citarella R, Battistelli S. Impact of the 24-h ultramarathon race on homocysteine, oxidized low-density lipoprotein, and paraoxonase 1 levels in professional runners. PloS one. 2018;13(2):e0192392.
311. Fernandez AB, Chaudhry W, Thompson PD. Coronary Atherosclerosis in Masters Athletes: Mechanisms and Implications for Cardiovascular Disease Risk. Curr Treat Options Cardiovasc Med. 2019;21(12):87.

312. De Bosscher R, Dausin C, Claus P, Bogaert J, Dymarkowski S, Goetschalckx K, et al. Lifelong endurance exercise and its relation with coronary atherosclerosis. European heart journal. 2023.
313. Fujii H, Shimizu M, Ino H, Yamaguchi M, Yasuda T, Fujino N, et al. Acute increases in plasma oxidized low-density lipoprotein immediately after percutaneous transluminal coronary angioplasty. The American journal of cardiology. 2001;87(1):102-3, a8.
314. Tsimikas S, Lau HK, Han KR, Shortal B, Miller ER, Segev A, et al. Percutaneous coronary intervention results in acute increases in oxidized phospholipids and lipoprotein(a): short-term and long-term immunologic responses to oxidized low-density lipoprotein. Circulation. 2004;109(25):3164-70.
315. Leibundgut G, Lee JH, Strauss BH, Segev A, Tsimikas S. Acute and long-term effect of percutaneous coronary intervention on serially-measured oxidative, inflammatory, and coagulation biomarkers in patients with stable angina. Journal of thrombosis and thrombolysis. 2016;41(4):569-80.
316. Tomaniak M, Katagiri Y, Modolo R, Silva R, Khamis RY, Bourantas CV, et al. Vulnerable plaques and patients: state-of-the-art. European heart journal. 2020.
317. Mulligan C, Mindell JA. Pinning Down the Mechanism of Transport: Probing the Structure and Function of Transporters Using Cysteine Cross-Linking and Site-Specific Labeling. Methods Enzymol. 2017;594:165-202.
318. Poon C, Patel AA. Organic and inorganic nanoparticle vaccines for prevention of infectious diseases. Nano Express. 2020;1(1):012001.
319. Suk JS, Xu Q, Kim N, Hanes J, Ensign LM. PEGylation as a strategy for improving nanoparticle-based drug and gene delivery. Adv Drug Deliv Rev. 2016;99(Pt A):28-51.
320. Hong G, Antaris AL, Dai H. Near-infrared fluorophores for biomedical imaging. Nature biomedical engineering. 2017;1(1):0010.
321. Hill RJ. Electrokinetics of nanoparticle gel-electrophoresis. Soft Matter. 2016;12(38):8030-48.
322. Schneider CS, Bhargav AG, Perez JG, Wadajkar AS, Winkles JA, Woodworth GF, et al. Surface plasmon resonance as a high throughput method to evaluate specific and non-specific binding of nanotherapeutics. J Control Release. 2015;219:331-44.
323. Emmenegger M, Worth R, Fiedler S, Devenish SR, Knowles TP, Aguzzi A. Protocol to determine antibody affinity and concentration in complex solutions using microfluidic antibody affinity profiling. STAR protocols. 2023;4(1):102095.
324. Kahlon TS, Shore VG, Lindgren FT. Heterogeneity of molecular weight and apolipoproteins in low density lipoproteins of healthy human males. Lipids. 1992;27(12):1055-7.
325. Khamis RY, Hartley A, Caga-Anan M, Pandey SS, Marceddu C, Kojima C, et al. Monoclonal Autoantibody Against a Cryptic Epitope on Tissue-Adherent Low-Density Lipoprotein for Molecular Imaging in Atherosclerosis. JACC Cardiovascular imaging. 2022;15(8):1458-70.
326. Kim A, Ng WB, Bernt W, Cho NJ. Validation of Size Estimation of Nanoparticle Tracking Analysis on Polydisperse Macromolecule Assembly. Scientific reports. 2019;9(1):2639.
327. Alturkistani HA, Tashkandi FM, Mohammedsaleh ZM. Histological Stains: A Literature Review and Case Study. Glob J Health Sci. 2015;8(3):72-9.
328. Nagy L, Tontonoz P, Alvarez JG, Chen H, Evans RM. Oxidized LDL regulates macrophage gene expression through ligand activation of PPARgamma. Cell. 1998;93(2):229-40.
329. Teupser D, Persky AD, Breslow JL. Induction of atherosclerosis by low-fat, semisynthetic diets in LDL receptor-deficient C57BL/6J and FVB/NJ mice: comparison of lesions of the aortic root, brachiocephalic artery, and whole aorta (en face measurement). Arteriosclerosis, thrombosis, and vascular biology. 2003;23(10):1907-13.

330. Yurdagul A, Jr., Doran AC, Cai B, Fredman G, Tabas IA. Mechanisms and Consequences of Defective Efferocytosis in Atherosclerosis. Front Cardiovasc Med. 2017;4:86.
331. Schrijvers DM, De Meyer GR, Kockx MM, Herman AG, Martinet W. Phagocytosis of apoptotic cells by macrophages is impaired in atherosclerosis. Arteriosclerosis, thrombosis, and vascular biology. 2005;25(6):1256-61.
332. Pérez-Campaña C, Gómez-Vallejo V, Puigivila M, Martín A, Calvo-Fernández T, Moya SE, et al. Biodistribution of different sized nanoparticles assessed by positron emission tomography: a general strategy for direct activation of metal oxide particles. ACS Nano. 2013;7(4):3498-505.
333. Strauss JA, Shepherd DA, Macey M, Jevons EFP, Shepherd SO. Divergence exists in the subcellular distribution of intramuscular triglyceride in human skeletal muscle dependent on the choice of lipid dye. Histochem Cell Biol. 2020;154(4):369-82.
334. Adhipandito CF, Cheung SH, Lin YH, Wu SH. Atypical Renal Clearance of Nanoparticles Larger Than the Kidney Filtration Threshold. International journal of molecular sciences. 2021;22(20).
335. Jiang S, Fang C, Xu X, Xing L, Sun S, Peng C, et al. Identification of High-Risk Coronary Lesions by 3-Vessel Optical Coherence Tomography. Journal of the American College of Cardiology. 2023.
336. Gupta K, Balachandran I, Foy J, Hermel M, Latif A, Krittanawong C, et al. Highlights of Cardiovascular Disease Prevention Studies Presented at the 2023 American College of Cardiology Conference. Curr Atheroscler Rep. 2023;25(6):309-21.
337. Sheedy FJ, Grebe A, Rayner KJ, Kalantari P, Ramkhelawon B, Carpenter SB, et al. CD36 coordinates NLRP3 inflammasome activation by facilitating intracellular nucleation of soluble ligands into particulate ligands in sterile inflammation. Nat Immunol. 2013;14(8):812-20.
338. Garrido AM, Kaistha A, Uryga AK, Oc S, Foote K, Shah A, et al. Efficacy and limitations of senolysis in atherosclerosis. Cardiovascular research. 2022;118(7):1713-27.
339. Kremastiotis G, Handa I, Jackson C, George S, Johnson J. Disparate effects of MMP and TIMP modulation on coronary atherosclerosis and associated myocardial fibrosis. Scientific reports. 2021;11(1):23081.
340. Wang J, Wei G, Hu W, Li L, Ye Y, Wang H, et al. Expression of matrix metalloproteinases-12 in ST-segment elevation myocardial infarction: A case-control study. Medicine (Baltimore). 2017;96(40):e8035.
341. Krishnan G, van den Berg NS, Nishio N, Juniper G, Pei J, Zhou Q, et al. Metastatic and sentinel lymph node mapping using intravenously delivered Panitumumab-IRDye800CW. Theranostics. 2021;11(15):7188-98.
342. Antonov AS, Kolodgie FD, Munn DH, Gerrity RG. Regulation of macrophage foam cell formation by alphaVbeta3 integrin: potential role in human atherosclerosis. The American journal of pathology. 2004;165(1):247-58.
343. Wu H, Du Q, Dai Q, Ge J, Cheng X. Cysteine Protease Cathepsins in Atherosclerotic Cardiovascular Diseases. J Atheroscler Thromb. 2018;25(2):111-23.
344. Wen G, An W, Chen J, Maguire EM, Chen Q, Yang F, et al. Genetic and Pharmacologic Inhibition of the Neutrophil Elastase Inhibits Experimental Atherosclerosis. Journal of the American Heart Association. 2018;7(4).
345. O'Donoghue ML, Braunwald E, White HD, Lukas MA, Tarka E, Steg PG, et al. Effect of darapladib on major coronary events after an acute coronary syndrome: the SOLID-TIMI 52 randomized clinical trial. Jama. 2014;312(10):1006-15.
346. Mallat Z, Lambeau G, Tedgui A. Lipoprotein-associated and secreted phospholipases A_2 in cardiovascular disease: roles as biological effectors and biomarkers. Circulation. 2010;122(21):2183-200.

347. Kalbaugh CA, Strassle PD, Paul NJ, McGinigle KL, Kibbe MR, Marston WA. Trends in Surgical Indications for Major Lower Limb Amputation in the USA from 2000 to 2016. Eur J Vasc Endovasc Surg. 2020;60(1):88-96.
348. Werner NL, Alghanem F, Rakestraw SL, Sarver DC, Nicely B, Pietroski RE, et al. Ex Situ Perfusion of Human Limb Allografts for 24 Hours. Transplantation. 2017;101(3):e68-e74.
349. Abran M, Cloutier G, Cardinal MH, Chayer B, Tardif JC, Lesage F. Development of a photoacoustic, ultrasound and fluorescence imaging catheter for the study of atherosclerotic plaque. IEEE Trans Biomed Circuits Syst. 2014;8(5):696-703.
350. Petersen JL, Levin DB, Hou VW, Hagen CV, Anderson G, Block J, et al. Intact and Isolated Human Cadaveric Coronary Artery Perfusion Models to Facilitate Research and Education Regarding Coronary Anatomy and Pathology. J Invasive Cardiol. 2019;31(9):272-7.
351. Biswal JK, Mohanty SK, Behera SN, Swain SK, Sahoo AK. Acute Limb Ischemia: A Catastrophic COVID-19 Sequel Leading to Amputation. Cureus. 2021;13(7):e16456.
352. Oyet C, Okongo B, Onyuthi RA, Muwanguzi E. Biochemical changes in stored donor units: implications on the efficacy of blood transfusion. J Blood Med. 2018;9:111-5.
353. Raza S, Ali Baig M, Chang C, Dabas R, Akhtar M, Khan A, et al. A prospective study on red blood cell transfusion related hyperkalemia in critically ill patients. J Clin Med Res. 2015;7(6):417-21.
354. Altun D, Arnaz A, Doğan A, Yalçınbaş Y, Türköz R, Yüksek A, et al. Measuring potassium level in packed red blood cells before using: Word of caution for congenital cardiac surgery. J Card Surg. 2022;37(3):535-41.
355. Wang LC, Lawson SD, Fries CA, Davis MR. Hyperbaric sub-normothermic ex-vivo perfusion delays the onset of acute rejection in a porcine VCA model. Plastic and Reconstructive Surgery. 2015;136(4S):34.
356. Blaisdell FW. The pathophysiology of skeletal muscle ischemia and the reperfusion syndrome: a review. Cardiovascular surgery. 2002;10(6):620-30.
357. Koike T, Yeung JC, Cypel M, Rubacha M, Matsuda Y, Sato M, et al. Kinetics of lactate metabolism during acellular normothermic ex vivo lung perfusion. The Journal of heart and lung transplantation. 2011;30(12):1312-9.
358. O'Carroll-Kuehn BU, Meeran H. Management of coagulation during cardiopulmonary bypass. Continuing education in anaesthesia, critical care & pain. 2007;7(6):195-8.

APPENDIX

Appendix 1 – Related publications

Khamis RY., **Hartley A.**, Caga-Anan M., Pandey S., Marceddu C., Kojima C., Chang SH., Boyle JJ., Johnson JL., Björkbacka H., Guo L., Finn AV., Virmani, R., Nilsson, J., Haskard DO. Monoclonal Autoantibody Against a Cryptic Epitope on Tissue-Adherent Low-Density Lipoprotein for Molecular Imaging in Atherosclerosis. **Journal of American College of Cardiology: Cardiovascular Imaging**, 2022. DOI 10.1016/j.jcmg.2022.02.023. PMID: 35926905

Kaura A., **Hartley A.**, Panoulas V., Glampson B., Shah ASV., Davies J., Mulla A., Woods K., Omigie J., Shah AD., Thursz MR., Elliott P., Hemmingway H., Williams B., Asselbergs FW., O'Sullivan M., Lord GM., Trickey A., Sterne JAC., Haskard DO., Melikian N., Francis DP., Koenig W., Shah AM., Kharbanda R., Perera D., Patel RS., Channon KM., Mayet J., Khamis RY. Mortality risk prediction of high-sensitivity C-reactive protein in suspected acute coronary syndrome: A cohort study. **PLoS Medicine**, 2022. DOI: 10.1371/journal.pmed.1003911. PMID: 35192610

Hartley A., Pradeep M., Van den Berg V., Khan AHH., Shah HA., Allaf M., Chow A., Caga-Anan M., Shalhoub J., Koenig W., Fisher M., Haskard DO., Khamis RY. Depletion of homeostatic antibodies against malondialdehyde-modified low-density lipoprotein correlates with adverse events in major vascular surgery. **Antioxidants**, 2022. DOI: 10.3390/antiox11020271. PMID: 35204154

Pandey SS., **Hartley A. (joint first author),** Caga-Anan M., Ammari T., Khan AHA., Nguyen BAV., Kojima C., Anderson J., Lynham S., Johns M., Haskard DO., Khamis RY. A novel immunoassay for malondialdehyde-conjugated low-density lipoprotein measures dynamic changes in the blood of patients undergoing coronary artery bypass graft surgery. ***Antioxidants***, 2021; DOI: 10.3390/antiox10081298. PMID: 34439546

Hammond-Haley M., **Hartley A.**, Essa M., Delago AJ., Marshall DC., Salciccioli JD., Shalhoub J. Trends in Ischaemic Heart Disease and Cerebrovascular Disease Mortality in Europe: an Observational Study 1990-2017. ***Journal of American College of Cardiology***, 2021; DOI: 10.1016/j.jacc.2021.02.013. PMID: 33795044

Khan TZ., **Hartley A.**, Haskard D., Caga-Anan M., Pennell DJ., Collins P., Barbir M., Khamis, R. Oxidised LDL and Anti-Oxidised LDL Antibodies Are Reduced by Lipoprotein Apheresis in a Randomised Controlled Trial on Patients with Refractory Angina and Elevated Lipoprotein (a). ***Antioxidants***, 2021. DOI: 10.3390/antiox1001013210.3390/antiox8100484. PMID: 33477712

Appendix 2 – Related presentations

Baseline high sensitivity C-Reactive Protein predicts incident cardiovascular events and all-cause mortality in the ASCOT Study at 20-years. ***European Society of Cardiology, Amsterdam, Netherlands, 2023*** (moderated poster presentation)

High sensitivity CRP at baseline predicts cardiovascular outcomes at 20-year follow-up in the ASCOT Legacy Study. **British Society of Cardiovascular Research/ British Atherosclerosis Society/ British Cardiovascular Society, 2023** (poster presentation)

The Effect of Major Vascular Surgery on Oxidized LDL, its Antibodies, Complement and Complexes. ***European Atherosclerosis Society, 2020*** (oral presentation)